

Earl J. Kirkland

Advanced Computing in Electron Microscopy

Third Edition



Springer

Advanced Computing in Electron Microscopy

Third Edition

Earl J. Kirkland

Advanced Computing in Electron Microscopy

Third Edition



Springer

Earl J. Kirkland
School of Applied & Engineering Physics
Cornell University
Ithaca, NY, USA

ISBN 978-3-030-33259-4 ISBN 978-3-030-33260-0 (eBook)
<https://doi.org/10.1007/978-3-030-33260-0>

2nd edition: © Springer Science+Business Media, LLC, part of Springer Nature 2010

3rd edition: © Springer Nature Switzerland AG 2020

This work is subject to copyright. All rights are reserved by the Publisher, whether the whole or part of the material is concerned, specifically the rights of translation, reprinting, reuse of illustrations, recitation, broadcasting, reproduction on microfilms or in any other physical way, and transmission or information storage and retrieval, electronic adaptation, computer software, or by similar or dissimilar methodology now known or hereafter developed.

The use of general descriptive names, registered names, trademarks, service marks, etc. in this publication does not imply, even in the absence of a specific statement, that such names are exempt from the relevant protective laws and regulations and therefore free for general use.

The publisher, the authors, and the editors are safe to assume that the advice and information in this book are believed to be true and accurate at the date of publication. Neither the publisher nor the authors or the editors give a warranty, expressed or implied, with respect to the material contained herein or for any errors or omissions that may have been made. The publisher remains neutral with regard to jurisdictional claims in published maps and institutional affiliations.

This Springer imprint is published by the registered company Springer Nature Switzerland AG.
The registered company address is: Gewerbestrasse 11, 6330 Cham, Switzerland

Preface

Preface to Third Edition

A longer discussion of imaging with aberration correctors and the effects of the multitude of aberrations they produce has been added, along with a short discussion of ABF (annular bright field) and GPUs (graphical processing units) for faster numerical calculations.

The associated programs discussed in the text will be available on an associated web site (currently [sourceforge.com\computem](http://sourceforge.com/computem), but may move as time goes on).

Again, I apologize in advance for leaving out some undoubtedly outstanding references. I also apologize for the as yet undiscovered errors that remain in the text.

Earl J. Kirkland, July 2019

Preface to Second Edition

Several new topics have been added, some small errors have been corrected, and some new references have been added in this edition. New topics include aberration-corrected instruments, scanning confocal mode of operations, Bloch wave eigenvalue methods, and parallel computing techniques. The first edition included a CD with computer programs, which is not included in this edition. Instead the associated programs will be available on an associated web site ([currently people.ccmr.cornell.edu/~kirkland](http://people.ccmr.cornell.edu/~kirkland), but may move as time goes on).

I wish to thank Mick Thomas for preparing the specimen used to record the image in Fig. 5.25 and to thank Stephen P. Meisburger for suggesting an interesting biological specimen (α -Hemolysin) to use in a figure.

Again, I apologize in advance for leaving out some undoubtedly outstanding references. I also apologize for the as yet undiscovered errors that remain in the text.

Earl J. Kirkland, December 2009

Preface to First Edition

Image simulation has become a common tool in HREM (High-Resolution Electron Microscopy) in recent years. However, the literature on the subject is scattered among many different journals and conference proceedings that have occurred in the last two or three decades. It is difficult for beginners to get started in this field. The principal method of image simulation has come to be known as simply *the multislice method*. This book attempts to bring the diverse information on image simulation together into one place and to provide a background on how to use the multislice method to simulate high-resolution images in both conventional and scanning transmission electron microscopy. The main goals of image simulation include understanding the microscope and interpreting high-resolution information in the recorded micrographs. This book contains sections on the theory of image formation and simulation as well as a more practical introduction on how to use the multislice method on real specimens. Also included with this book is a CD-ROM with working programs to perform image simulation. The source code as well as the executable code for IBM-PC and Apple Macintosh computers is included. Although the programs may not have a very elegant user interface by today's standards (simple command line dialog), the source code should be very portable to a variety of different computers. It has been compiled and run on Macs, PCs, and several different types of UNIX computers.

This book is intended to be at the level of first-year graduate students or advanced undergraduates in physics or engineering with an interest in electron microscopy. It assumes a familiarity with quantum mechanics, Fourier transforms and diffraction, some simple optics, and basic computer skills (although not necessarily programming skills) at the advanced undergraduate level. Prior experience with electron microscopy is also helpful. The material covered should be useful to students learning the material for the first time as well as to experienced researchers in the field. The programs provided on the CD can be used as a black box without understanding the underlying programs (with a primary goal of understanding the transmission electron microscope image), or the source code can be used to understand how to write your own version of the simulation programs.

Although an effort was made to include references to most of the appropriate publications on this subject, there are undoubtedly some that were omitted. I apologize in advance for leaving out some undoubtedly outstanding references. I also apologize for the as yet undiscovered errors that remain in the text.

I wish to acknowledge the support of various funding agencies (principally DOE, NSF, and NIH) that have supported my research efforts over the past several

decades. My research experience has substantially contributed to my understanding of the material covered in this book.

I also wish to thank Dr. David A. Muller and Dr. Richard R. Vanfleet for providing many helpful suggestions and help in proofreading the manuscript and to thank Dr. M. A. O'Keefe for providing helpful comments on electron microscopy and image simulation.

Earl J. Kirkland, March 1998

MATLAB(R) is a registered trademark of The Mathworks, Inc.

Windows is a registered trademark of Microsoft, Inc.

The Octave and other programs listed in this book are supplied for instructional purposes, AS IS WITHOUT ANY WARRANTY, WITHOUT EVEN THE IMPLIED WARRANTY OF MERCHANTABILITY or FITNESS FOR A PARTICULAR PURPOSE to the extent permitted by law. Effort has been made to insure the programs are correct, but neither the author nor the publisher shall be held responsible or liable for any damage resulting from the use or failure to use these programs.

Contents

1	Introduction	1
1.1	Computing in Electron Microscopy	1
1.2	Organization of This Book	5
2	The Transmission Electron Microscope	9
2.1	Introduction	9
2.2	Modeling the Electron Microscope	13
2.3	Relativistic Electrons	15
2.4	Reciprocity	18
2.5	Confocal Mode	19
2.6	Aberrations	20
2.7	Aberration Correction	26
2.8	More Aberrations	30
2.9	Further Reading	35
3	Some Image Approximations	37
3.1	The Weak Phase Object in Bright Field	38
3.1.1	BF-CTEM with Aberration Correctors	44
3.2	Partial Coherence in BF-CTEM	44
3.2.1	Aberration Correctors and Partial Coherence	51
3.3	Detector Influence (CTEM)	53
3.4	Incoherent Imaging of Thin Specimens (CTEM)	53
3.5	Annular Dark Field STEM	58
3.5.1	Minimum Probe Conditions	65
3.5.2	Source Size	67
3.5.3	Defocus Spread	69
3.5.4	Aberration Tuning Errors	69
3.6	Compensation	72
3.6.1	Two Aberrations at a Time	74
3.6.2	Three Aberrations at a Time	75
3.7	Confocal Mode for Weak Phase Objects	76
3.8	Phase and Amplitude Contrast Revisited	78

4 Sampling and the Fast Fourier Transform	81
4.1 Sampling	81
4.2 Discrete Fourier Transform	86
4.3 The Fast Fourier Transform or FFT	87
4.4 Wrap Around Error and Rearrangement	90
4.5 Fourier Transforming Real Valued Data	91
4.6 Displaying Diffraction Patterns	93
4.7 An FFT Subroutine in C	95
4.8 Further Reading	97
5 Calculation of Images of Thin Specimens	99
5.1 The Weak Phase Object	99
5.2 Single Atom Properties	102
5.2.1 Radial Charge Distribution	103
5.2.2 Potential	103
5.2.3 Atomic Size	106
5.2.4 Scattering Factors	108
5.3 Total Specimen Potential	111
5.4 BF Phase Contrast Image Calculation	114
5.4.1 Single Atom Images	116
5.4.2 Thin Specimen Images	119
5.4.3 Partial Coherence and the Transmission Cross Coefficient	125
5.5 ADF STEM Images of Thin Specimens	128
5.5.1 Single Atom Images	130
5.5.2 Thin Specimen Images	132
5.6 Annular Bright Field (ABF)	135
5.7 Summary of Sampling Suggestions	138
6 Theory of Calculation of Images of Thick Specimens	143
6.1 Bloch Wave Eigenvalue Solution	146
6.1.1 Bloch Waves	146
6.1.2 Periodic Potential	148
6.1.3 Matrix Equation	149
6.1.4 Initial Conditions and the Exit Wave	153
6.1.5 Bloch Wave Eigenvalue Summary	154
6.1.6 Relative Performance	155
6.2 The Wave Equation for Fast Electrons	156
6.3 A Bloch Wave Differential Equation Solution	159
6.4 The Multislice Solution	162
6.4.1 A Formal Operator Solution	162
6.4.2 A Finite Difference Solution	166
6.4.3 Free Space Propagation	167
6.5 Multislice Interpretation	167
6.6 The Multislice Method and FFTs	170
6.7 Slicing the Specimen	171

6.8	Aliasing and Bandwidth	175
6.9	Interfaces and Defects	178
6.10	Multislice Implementation	180
6.10.1	The Propagator Function and Specimen Tilt	181
6.10.2	Convergence Tests	183
6.10.3	Partial Coherence in BF-CTEM	184
6.10.4	Parallel Computing	185
6.11	More Accurate Slice Methods	188
6.11.1	Operator Solutions	189
6.11.2	Finite Difference Solutions	190
7	Multislice Applications and Examples	197
7.1	Gallium Arsenide	197
7.1.1	BF-CTEM Simulation	199
7.1.2	ADF-STEM Simulation	202
7.1.3	Channeling	204
7.2	Silicon Nitride	208
7.3	Two-Dimensional Materials (MoS_2)	212
7.4	Reciprocity and Z-Contrast	216
7.5	CBED Simulations	218
7.6	Thermal Vibrations of the Atoms in the Specimen	220
7.6.1	Silicon 111 CBED with TDS	223
7.6.2	Silicon 110 ADF-STEM with TDS	225
7.7	Specimen Edges or Interfaces	226
7.8	Biological Specimens	227
7.9	Ronchigrams (in STEM)	231
7.10	Aberration Tuning	233
7.11	Quantitative Image Matching	235
7.12	Troubleshooting (What Can Go Wrong)	238
8	The Programs	241
8.1	TEMSIM Program Organization	242
8.1.1	Image Display	243
8.1.2	Disk File Format	244
8.2	BF-CTEM Sample Calculations for Periodic Specimens	246
8.2.1	Atomic Potentials	246
8.2.2	Multislice	250
8.2.3	Image Formation	252
8.2.4	Partial Coherence	253
8.3	ADF-STEM Sample Calculations for Periodic Specimens	256
8.4	Non-periodic Specimens	259
8.4.1	Fixed Beam Calculation	261
8.4.2	Scanned Beam Calculation	265
8.5	Program Incostem	270
8.6	Program Computem	272

A Plotting Transfer Functions	273
A.1 CTEM	274
A.2 STEM	276
B The Fourier Projection Theorem	281
C Atomic Potentials and Scattering Factors	283
C.1 Atomic Charge Distribution	284
C.2 X-ray Scattering Factors	286
C.3 Electron Scattering Factors	287
C.4 Parameterization	289
D The Inverse Problem	303
E Bilinear Interpolation	307
F 3D Perspective View	311
References	317
Author Index	341
Subject Index	351

Chapter 1

Introduction



1.1 Computing in Electron Microscopy

Electron microscopy continues to push the limits of resolution. At high resolution, image artifacts due to instrumental or specimen limitations can greatly complicate image interpretation. The computer is finding an ever increasing role in interpreting high-resolution transmission electron micrographs as well as extracting additional information from the recorded images. Computer technology has been progressing at a very rapid pace over the past several decades. The rate of improvement in computing is certainly much faster than the rate of improvement of the electron microscope. A very powerful computer is now much less than 1% of the cost of a respectable electron microscope even though this level of computer hardware used to cost much more than a high performance electron microscope. It is very worthwhile to try to exploit the computer in electron microscopy in any way possible to extract more information about the specimen or to reduce the cost or effort required to obtain this information. Various applications of computing to electron microscopy may be arranged in the following categories.

Image simulation: Numerically calculate electron microscope images from first principles and a detailed description of the specimen and the instrument. Usually involving various nonlinear imaging modes and dynamical scattering in thick specimens.

Image processing and data analysis: The inverse of image simulation. Try to extract additional information from the experimentally recorded electron micrographs by applying numerical computation to the digitized micrographs. Exit wave reconstructions, tomography, ptychography, and cryo-microscopy also require significant amounts of computation.

Instrument design: CAD (computer aided design) in electron optics. Numerical calculation of electron optical properties (i.e., aberration, etc.) of magnetic and electrostatic lens and deflectors in the electron microscope to optimize the performance of the instrument.

On-line control: Directly control the operation of the microscope and record images and spectra directly from the instrument. The computer is directly wired into the electron microscope electronics.

Data archiving: Save the recorded data. Manage the large volume of data generated when recording a series of images.

Image simulation of electron micrographs has a long history and is the principle topic of this book. There are two general types of image simulation. One group of methods involves Bloch wave eigenstates and a matrix formulation in reciprocal space (Bethe [31], Howie and Whelan [219]) and the other group involves mathematically slicing the specimen along the beam direction (the multislice method). The multislice method (Cowley and Moodie [78], Lynch and O'Keefe [325], Goodman and Moodie [162], Ishizuka and Uyeda [236], Van Dyck [506]) is usually more flexible for a computer simulation of crystalline specimens with defects or interfaces as well as completely amorphous materials. Bloch wave solutions are more amenable to analytical calculations with pencil and paper for small unit cells and can provide valuable insight into the scattering process.

Attempts to analytically derive the theory of image formation in the electron microscope for specimen with large unit cells (and defects and interfaces) quickly arrive at equations that do not have a closed form analytical solution or are too difficult to easily interpret. The only recourse is a numerical solution. Image simulation numerically computes the electron micrograph from first principles. Starting from a basic quantum mechanical description of the interaction between the imaging electrons in the microscope and the atoms in the specimen the wave function of the imaging electrons may be calculated at any position in the microscope. If the optical properties of the lenses in the microscope are known, then the two-dimensional intensity distribution in the final electron micrograph can be calculated with a relatively high precision. Image simulation can provide several sources of additional information about the specimen. First, it can reveal which features of the image are due to artifacts produced by aberrations in the electron microscope and which image features are due to the specimen itself (and possibly relate features in the image to unsuspected properties of the specimen). Image simulation is an aid in interpreting the image recorded in the electron microscope. Second, it is relatively simple to change instrumental parameters in the simulation that would be difficult if not impossible to change in practice. For example, it is easy to change the beam energy or spherical aberration to an arbitrary value to see what happens. It is much easier to use image simulation to determine what type of instrument is required to investigate a particular specimen than it would be to build each type of electron microscope and see what happens. Image simulation can be used as both an aid in image interpretation and a means of exploring new types of imaging in the microscope.

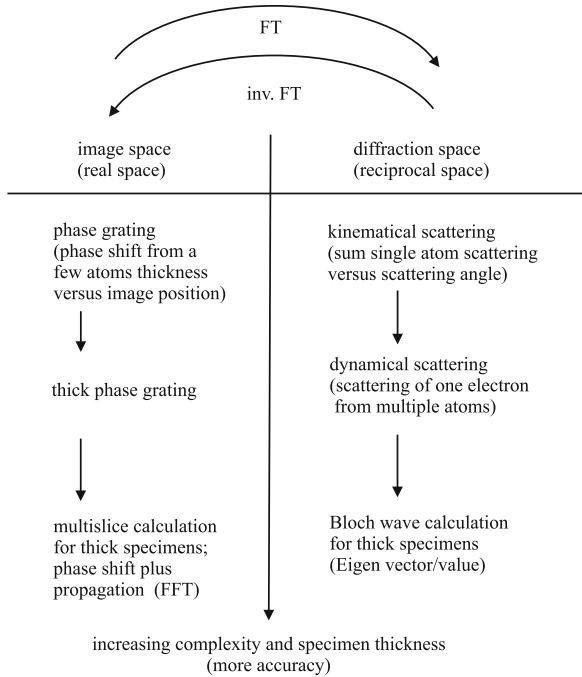


Fig. 1.1 Approximate relation between different theoretical concepts and methods in common use for the calculation of electron microscope images. The simplest start at the top and become more accurate and difficult going down. Concepts based mainly in image space (or real space) are on the left and diffraction space (reciprocal space) on the right. Real space concepts and diffraction space concepts are related by a Fourier transform, FT (and inverse Fourier transform). Some sophisticated methods still in development may not be shown here

The conceptual relationship between various theories and methods of calculation is shown in Fig. 1.1. The theory can be considered in a real space or diffraction space point of view, which are related by a Fourier transform. The simplest image interpretation is the so-called phase grating calculation in which the specimen is only a few atoms thick and the effect is a simple phase shift of the incident electron beam, which is roughly equivalent to a simple kinematical scattering model (electrons scattered at most once by a single atom). These are relatively simple to calculate and lead to some useful concepts but become inaccurate and misleading for specimens of a practical thickness. The most accurate and difficult calculations shown are the multislice and Bloch wave calculations. In particular, multislice is numerically more efficient because it makes use of the FFT (fast Fourier transform). The discussions that follows start with the simple approximations and works up (down in Fig. 1.1) to the more complicated calculations.

Image processing and data analysis are the inverse of image simulation. Starting from recorded experimental images the computer can process the micrographs to improve their interpretability or to try to recover additional information in the

micrographs. Image processing includes image enhancement such as simple contrast stretching or noise cleaning as well as image restoration or image reconstruction. Image restoration attempts to deconvolve the transfer function of the instrument from a single image to improve the apparent resolution of the recorded image. Image reconstruction attempts to combine several images (such as a defocus series) into one image with more information. In bright field phase contrast microscopy a series of images taken at different defocus values (a defocus series) together contain more information than any single image in the series. The computer can be used to reconstruct all of the information in the defocus series into a single image with more information (usually this means higher resolution) than any single isolated image in the series (see for example Kirkland [267, 270, 277], Kirkland et al. [284], Coene et al. [66] and Thust et al. [490]). Image reconstruction is inherently more difficult than image simulation because it must invert a complicated nonlinear process.

Electron tomography endeavors to reconstruct a 3D structure from a sequence of 2D images recorded at different tilt angles (for example, Midgley [346], Ercius et al. [121]) and can require significant computation. Cryogenic electron microscopy of biological specimens (for example, Frank [143], Kourkoutis et al. [294], Cheng et al. [63], Nogales [374]) involves substantial computation to average multiple low dose images of single particles at different orientations. Off-axis electron holography (Lichte [314]) may also involve a significant amount of computation. These important topics will be left to an author more knowledgeable in these areas.

Computer aided instrument design is a broad and rich field all of its own. It is more the realm of the manufacturers currently. This subject has been recently reviewed by Hawkes and Kasper [196, 197] and will not be considered here.

On-line control of the electron microscope received considerable attention in the literature in the last decade (see for example Erasmus and Smith [120], Smith [465], Skarnulis [458], Kirkland [271, 278]) but is now becoming mainly the province of the commercial instrument manufacturers. The original equipment manufacturers are perhaps in a better position to interface directly with the inner working of the instrument. Many new electron microscopes now come equipped with a computer to record the data (spectra and images) and possibly control the instrument. This can take the form of automatic alignment and focusing or simply a replacement for a traditional collection of knobs and switches. Aberration-corrected instruments have become so complicated that computer control is required and direct manual control is not practical. The related topic of telemicroscopy or remote access (see for example Fan et al. [125], Zaluzec [541] or O’Keeffe et al. [383]) involve accessing a microscope (or other instrument) over a network (the world wide web) from a computer in a location far away from the instrument. Many software packages now exist to remotely control a computer in a general sense and can easily be used to access computer controlled instruments without writing new specialized software.

Data archiving is now common place in many fields. Storing electron micrographs is in fact similar to storing any other type of image data. Digital storage has the advantage that the data will not degrade with time (as a photograph might) and the data can be readily transmitted electronically to any location. Also, digital storage can take up less space than a traditional collection of film or plates. Electron microscopy can readily take advantage of every day advances in data storage.

1.2 Organization of This Book

The level of discussion in this book is approximately at a beginning graduate student or advanced undergraduate student interested in the theory of image formation in the transmission electron microscope. It is assumed that the reader has some familiarity with quantum mechanics, Fourier transforms, and elementary optics. This book is not an introduction to computer programming. The reader is also assumed to understand the basic principles of computer programming. Numerical computer programming is discussed in a high level abstract manner.

Chapter 2 begins with an overview of the electron microscope instrument (scanning and conventional, STEM, and CTEM), the fundamental physics of electron dynamics, and the optical aberrations of electron lenses. Chapter 3 contains a theory of image formation for very thin specimens ignoring the geometrical thickness of the specimen. The transfer function is presented and investigated for several imaging modes. Chapter 4 is somewhat of a detour. It discusses numerical sampling and the fast Fourier transform (FFT) that will be needed in later chapters. Chapter 4 can be skipped if the reader is familiar with these topics. Chapter 5 starts the discussion of calculation methods, beginning with the electron atom interaction and very thin specimens. Chapter 6 is a long theoretical discussion of methods of calculating the propagation of the electron through thick (usually less than a few thousand Angstroms however) specimens. The Bloch wave eigenvalue and multislice methods are presented and discussed. Chapter 7 gives several applications of the multislice method. Some simple examples are first worked through in an educational approach, so the reader can learn how to use the method; then several more complicated examples are given to illustrate some interesting features of the electron microscope image. Chapter 8 documents how to use the programs used in this book and available to be downloaded from an associated web site.

Tables 1.1 and 1.2 show some frequently used symbols and acronyms. Some symbols may be used for more than one thing, but the usage should be clear from the context.

Table 1.1 Some symbols and their descriptions

Symbol	Description
a, b, c	Unit cell size of the specimen in x,y,z directions
a_0	Bohr radius (0.529 \AA)
$A(k)$	Aperture function (Eq. 3.54)
B	Debye Waller factor in \AA^2 or magnetic field
c	Speed of light in vacuum
$C_S = C_{S3}$	Third order spherical aberration
C_{S5}	Fifth order spherical aberration
D	Normalized defocus (Eq. 2.11)
$D(k)$	STEM detector function (Eq. 3.68)
e	Magnitude of the charge on the electron
f_e	Electron scattering factor (Eq. 5.15)
f_X	X-ray scattering factor (Eq. C.3)
G	Reciprocal lattice vector
$g(\mathbf{x})$	Recorded image intensity (with Fourier transform $G(\mathbf{k})$)
h	Planck's constant ($\hbar = h/(2\pi)$)
$J_0(x)$	Bessel function of order zero
k	2D spatial frequency in the Fourier transform of the image plane
$K = k(C_s \lambda^3)^{1/4}$	Dimensionless spatial frequency
m_0	Rest mass of the electron
$m = \gamma m_0$	Total mass of the electron
$t(\mathbf{x})$	Specimen transmission function (Eq. 3.3)
T_{nm}	Tunning tolerance for aberration C_{nm} (Eq. 2.29)
T_{CC}	Transmission cross coefficient (Sect. 5.4.3)
V	Accelerating voltage
x, y	Position in the image plane
z	Position along the optic axis
α	Electron scattering half angle
β	Condenser illumination half angle
β	Brightness
γ	Relativistic factor (Eq. 2.2)
Δf	Defocus
λ	Electron wavelength (Eq. 2.5)
σ_e	Electron interaction parameter (Eq. 5.6)
χ	Phase error due to aberration of a focused electron wave
$\psi(\mathbf{x})$	Electron wave function
$\frac{\partial \sigma}{\partial \Omega}$	Partial cross section for scattering

Also see Table 2.1 for more aberration symbols

Table 1.2 Some acronyms and their descriptions

Acronyms	Description
ABF	Annular Bright Field
ADF	Annular Dark Field
BF	Bright Field
CBED	Convergent Beam Electron Diffraction
CFEG	Cold Field Emission Gun
CPU	Central Processing Unit
CTEM	Conventional Transmission Electron Microscope
CTF	Contrast Transfer Function (MTF)
DFT	Discrete Fourier Transform or Density Functional Theory
DPC	Differential Phase Contrast
DOF	Depth Of Focus
EELS	Electron Energy Loss Spectroscopy
EHT	Extra High Tension (high voltage)
EWR	Exit Wave Reconstruction
FEG	Field Emission Gun
FT	Fourier Transform
FFT	Fast Fourier Transform
GPU	Graphics Processing Unit
GUI	Graphical User Interface
HAADF	High Angle Annular Dark Field
HREM	High-Resolution Transmission Electron Microscope (CTEM or STEM)
IAM	Independent Atom Model or Isolated Atom Model
LAADF	Low Angle Annular Dark Field
MPI	Message Passing Interface
MTF	Modulation Transfer Function (CTF)
PSF	Point Spread Function
SEM	Scanning Electron Microscope
SMP	Shared Memory Processor
SNR	Signal to Noise Ratio
STEM	Scanning Transmission Electron Microscope
TDS	Thermal Diffuse Scattering
WPOA	Weak Phase Object Approximation

Chapter 2

The Transmission Electron Microscope



2.1 Introduction

The modern transmission electron microscope has evolved over most of the twentieth century into a rather complex instrument. The twenty-first century is bringing forth a sequence of commercial aberration correction devices further complicating the instrument (as well as adding to their expense) in a never-ending quest for higher resolution. The Conventional Transmission Electron Microscope (CTEM) was first invented in the early 1930s by Knoll and Ruska [289, 432] as an extension of earlier work to perfect the cathode ray oscilloscope. Early microscopes had a resolution that was no better than a light microscope but there was considerable speculation at the time that atomic resolution should be possible. These speculations have been realized in current commercial instruments. For his work on the CTEM, Ruska shared the 1986 Nobel prize in physics with Binnig and Rohrer [35] for their invention of the scanning tunneling microscope (STM). In 2017, the Nobel prize for chemistry was awarded to Dubochet, Frank, and Henderson [56] for their achievements in cryogenic electron microscopy of biological molecules in which the three-dimensional structure is reconstructed from a large number of low dose images of the molecules in different orientations. The Scanning Transmission Electron Microscope (STEM) was invented shortly after the CTEM in the late 1930s by von Ardenne [512]. The utility of the STEM was greatly increased in the late 1960s by Crewe et al. [85] with the addition of a cold field emission gun (FEG) source with a small source size and high brightness. Both CTEM and STEM form an image from the electrons that are transmitted through a thin specimen and usually require a relatively high electron energy (60–1000 keV). Haguenau et al. [179] and the beginning chapters of Heidenreich [202] or Hall [184], the two contributed volumes edited by Hawkes [192] and Mulvey [366] have a more complete discussion of the history of the transmission electron microscope.

The scanning electron microscope (SEM) is related to the STEM in that both scan a focused electron beam across the specimen. However, the SEM usually uses an

electron beam of lower energy (approximately 1–30 keV versus 60 keV–1 MeV for CTEM and STEM) and forms an image signal from the secondary or backscattered electrons from a bulk specimen (the specimen is not necessarily thin). This results in a lower achievable resolution but has the advantage of being able to view the surface of bulk specimen without thinning. The SEM mode was first investigated around the same time as the CTEM and STEM were invented, and was refined by Oatley's group at Cambridge University. The history of the SEM has been reviewed by Oatley et al. [375] and McMullan [336]. The SEM itself has been reviewed by many authors (for example, Goldstein et al. [158] and Reimer [413]) and computer calculation of SEM images has been summarized by Joy [250]. Although the SEM is equally important it will not be discussed further in this book.

An approximate schematic cross section of a typical modern high-resolution aberration-corrected CTEM instrument is shown in Fig. 2.1. The specimen is loaded in the gap of the objective lens just above the objective aperture (not shown in the drawing) mechanism. Combined CTEM/STEMs and dedicated CTEMs and STEMs are commercially available. A probe corrector on a STEM would be located before the specimen and an image corrector is located after the specimen as in Fig. 2.1. An instrument as shown in Fig. 2.1 should have a field emission gun or FEG (Schottky electron source) instead of a thermionic source for improved brightness (and coherence). The condenser lenses transfer the beam onto the specimen. In a STEM scan coils would also be placed before (above in Fig. 2.1) the specimen. The aberration corrector corrects for the aberrations in the objective lens, and the projectors provide further magnification and transfer the image onto the detector (usually a CCD) at the bottom of the figure (detector not shown). In a CTEM the whole image is formed (in parallel) at one time whereas in the STEM a focused probe is scanned across the specimen in a raster fashion and the image is sequentially built up, one pixel (or image point) at a time. The CTEM is similar to a conventional light optical microscope and the STEM is similar to a scanning confocal light optical microscope (for example, Wilson and Sheppard [537]).

The electron source can be a simple thermionic, LaB₆, or field emission (hot or cold) source. The field emission source has a high brightness and small source size that makes it useful for both conventional and scanning electron microscopes. The small source size of the field emission source is essential for high-resolution STEM because the probe is essentially an image of the source (the smaller the source, the smaller the probe and better the resolution). The increased coherence of the FEG can also significantly increase the information limit in the CTEM (Otten and Coene [391]).

A CTEM image detector typically uses a scintillator plus an electronic CCD light detector. Some new direct electron detectors are sensitive enough to be capable of electron counting of low current signals in CTEM (McMullan et al. [337, 338]). A STEM detector also typically uses a scintillator to convert electrons into light which is detected with a photomultiplier tube (PMT) which can be integrated in analog for high signals and directly count electrons in low signal rates (Kirkland and Thomas [285], Findlay and LeBeau [134], Ishikawa et al. [229], and Kaneko et al. [253]).

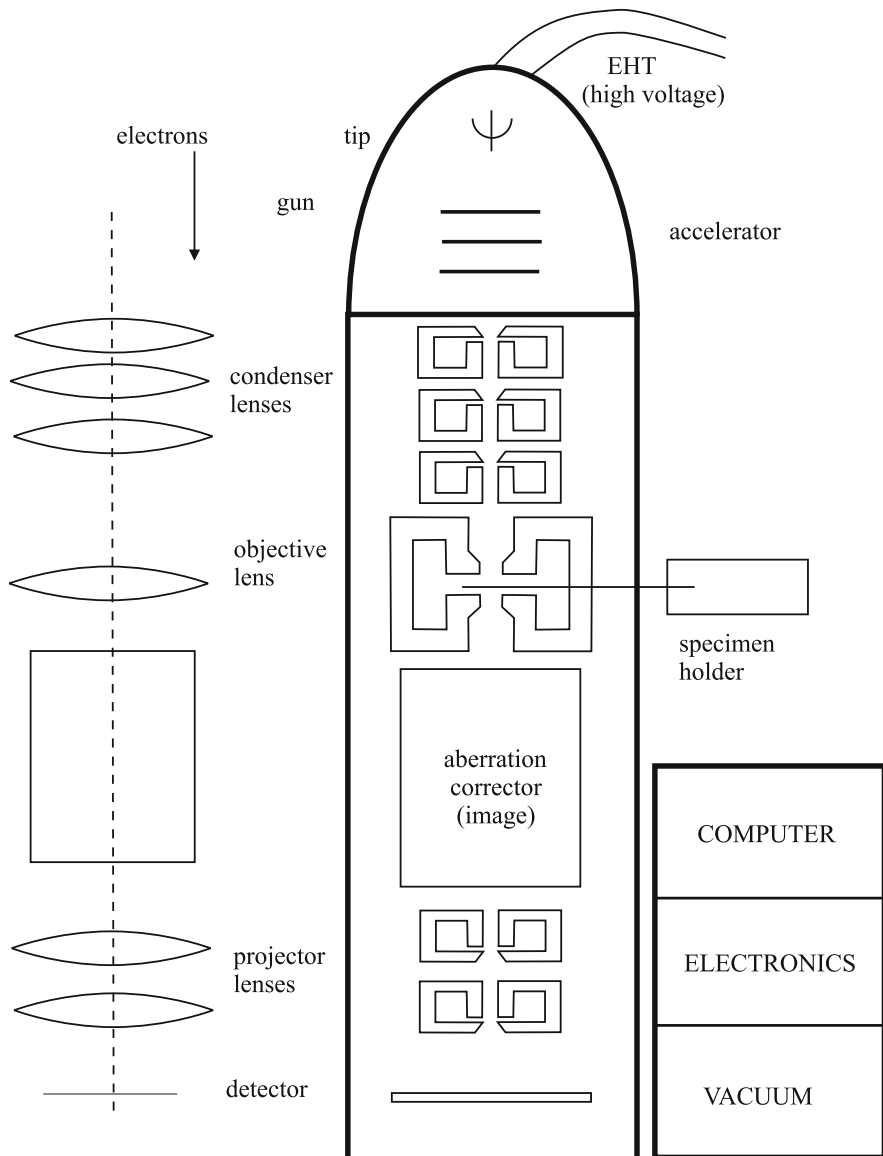


Fig. 2.1 Approximate cross section of a typical high-resolution CTEM column (not to scale) with an image corrector. There will be a CCD camera or other detector at the bottom of the instrument. There is an aberration corrector after the specimen to correct aberration of the objective lens. The electronics, vacuum, and computer systems are usually physically larger than the column unlike this simplified diagram

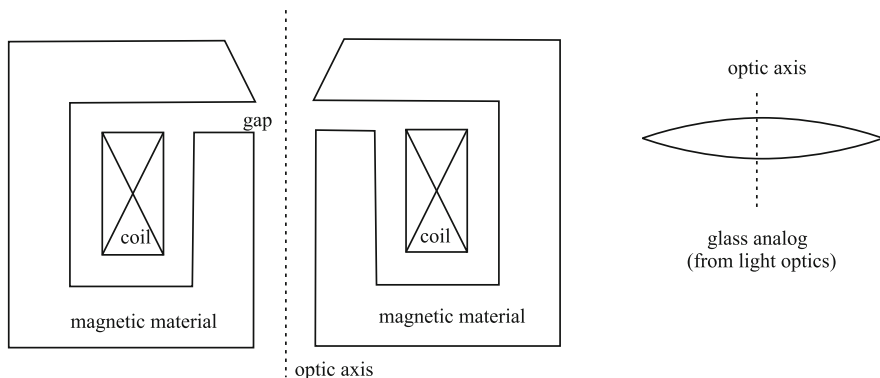


Fig. 2.2 Cross section of the general shape of a rotationally symmetric (about the optic axis), round lens (on left). The lens is symmetrical for rotation about the optic axis. The fringe fields in the gap focus the electron beam in a manner similar to that of a glass lens for visible light (on right). The electron beam travels up or down in this illustration (the optic axis, or z direction)

The general shape of a simple magnetic electron lens is shown (on the left) in Fig. 2.2. A large DC current flows through a coil of wire which produces a magnetic field. The field follows the magnetic material (typically an iron alloy) until it gets to the gap where it extends out towards the electron beam near the center of the lens. The specimen is usually placed in or near the gap of the objective lens. Lens designers expend a great amount of effort to shape the magnetic pole faces in the gap to shape the magnetic field and produce optimum focusing of the electron beam. The magnetic field forms a lens much like a glass lens for visible light. An analogous glass lens is shown on the right side of Fig. 2.2. Refer to the books on electron optics listed at the end of this chapter for more details on how magnetic lenses work.

There are typically two or three condenser lenses that gather the electrons emitted from the source and transfer them to the specimen. Three condenser lenses give three degrees of freedom allowing independent adjustment of angle, current, and focus. With the exception of the electrostatic lens in the electron gun (i.e., electron source), lenses in the electron microscope are usually rotationally symmetrical magnetic lenses (Fig. 2.2). The condenser lenses can illuminate the specimen with a wide collimated parallel beam (in CTEM) or present the objective lens with a parallel narrow beam (in STEM). The objective lens images the specimen in CTEM mode or forms a small probe of atomic dimensions on the specimen in STEM mode. In the CTEM mode the objective forms a virtual image which is further magnified by several projector lenses. STEM and CTEM modes require the objective lens to be on opposite sides of the specimen. A combined CTEM/STEM will usually sacrifice the performance in one mode because the specimen and objective lens are difficult to move. Most instruments currently available were initially CTEMs that have been converted to a combined STEM/CTEM instrument, so the STEM mode may not use the best portion of the objective lens field and hence has a reduced performance. STEM mode may be operated with or without post-specimen lenses.

Operation without post-specimen lenses can have advantages if there is significant inelastic scattering in the specimen (because of the inherent chromatic aberration of magnetic lens). However, the post-specimen portion of the objective lens magnetic field usually produces at least a small post-specimen lens. STEM mode also can be particularly useful for atomic resolution spectroscopy (X-ray, electron energy loss, etc.) from a localized volume of the specimen. The CTEM can also yield near atomic resolution spectroscopy using imaging energy loss filters (for example, see Reimer [415]). Herrmann [204, 205] and Smith [460, 461, 463] have reviewed the instrumental aspects of high-resolution electron microscope operation.

2.2 Modeling the Electron Microscope

If considered as a whole the TEM is a rather complicated instrument. However much of it can be ignored when considering the specific features of a high-resolution image. The vacuum system is essential and the TEM only works if there is a vacuum, but once it is established (with considerable effort in some cases!), it has no further effect. In a similar vein the illumination system (i.e., condenser lens) once aligned can be reduced to the properties of the illuminating rays (i.e., coherence and angular distribution). In CTEM mode the projector lenses magnify the virtual image formed by the objective lens. Because any defects in the objective lens are greatly magnified and the angles into the projector lenses are greatly reduced the projector lenses have little effect on the final image resolution so can also be ignored (in some instances the projectors may be responsible for small distortion in the image as opposed to a reduction in resolution). The simplest model to adequately describe the high-resolution imaging performance of a CTEM is shown in Fig. 2.3 and a similar model for a STEM is shown in Fig. 2.4. In each model the electrons will be assumed to be moving in the positive z direction (down in Figs. 2.3 and 2.4) and the image plane is assumed to be an x, y plane. The symbol α will denote the angle between the scattered electrons and the optic axis (and also the angle into the objective lens) in CTEM mode and the angle between the specimen perpendicular and the focused ray from the objective lens in STEM mode. The optic axis is typically perpendicular to the plane of the specimen.

The STEM may have several different types of detectors. The bright field (BF) detector (on the optic axis) detects the electrons that have passed through the specimen without significant deviation. The annular dark field (ADF) detector should detect the electrons that have been scattered to high angles (typically greater than three or four times the objective aperture angle). The annular bright field (ABF) detector is something in between, and collects electrons in the outer angles of the cone of rays in the objective angle (typically half). ABF is a relatively new imaging mode (for example, Findlay et al. [135, 136], Ishikawa et al. [228]). BF is typically coherent phase contrast, ADF is typically an incoherent image, and ABF is

Fig. 2.3 Simplified model (not to scale) of a high-resolution Conventional Transmission Electron Microscope (CTEM). The condenser lenses (above the top of the drawing) and projector lenses (below the bottom of the drawing) will be ignored

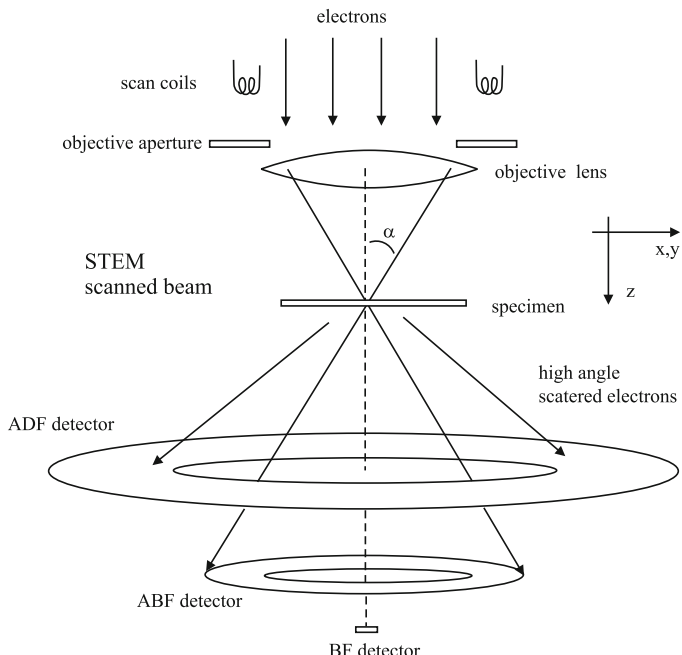
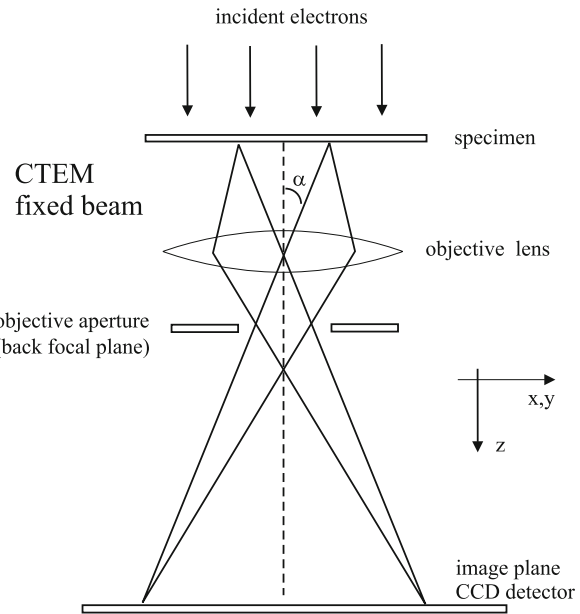


Fig. 2.4 Simplified model (not to scale) of a Scanning Transmission Electron Microscope (STEM). The condenser lenses (above the top of the drawing) are ignored. Different detectors are BF = bright field, ADF = annular dark field, ABF = annular bright field

a little of both. ABF should be equivalent to hollow cone illumination (Rose [424], Kunath et al. [302]) in CTEM by reciprocity (Sect. 2.4). Various other shapes of STEM detectors have been proposed including multiple rings and sectors (Haider et al. [180]). The ultimate detectors simply records the whole area from BF to ADF as another two-dimensional image at each point in the image (Tate et al. [485]) which can be called ptychography (Rodenburg [423], Nellist and Rodenburg [370], Plamann and Rodenburg [403], D’Alfonso et al. [90]) or 4D-STEM (for example, Ophus [388]). This approach produces a rather large amount of image data very quickly.

The STEM has a set of scan coils positioned before the objective lens. These are usually arranged so that the illumination electron trajectories rock about the principle plane of the objective lens (so that the beam does not move across the objective aperture during scanning). Alternately a virtual objective aperture (VOA) may be placed prior to the scan coils. At first glance it might seem as if the scan would cause the beam to move off the BF detector; however, the scan angles are so small that this is negligible. The objective lens usually gives a large demagnification, so that the specimen is essentially at the focal plane of the objective lens. The focal length is typically of order 2–3 mm. Therefore for a 1000 Å scan field the change in angle due to the scan is approximately $500 \text{ \AA}/2 \text{ mm} = 2.5 \times 10^{-5}$. At 100 keV typical angles on the BF detector are 2–3 mrad and about 40–200 mrad on the ADF detector. Therefore scanning the beam should not significantly affect the angles onto the detector.

2.3 Relativistic Electrons

The electron has a relatively small mass so that even a 100 keV electron is traveling at approximately one half the speed of light. This means that quantities such as velocity, wavelength, etc. should be calculated relativistically. The total energy E_T of a charged particle with charge e and rest mass m_0 accelerated through a potential V is given by:

$$E_T^2 = (m_0 c^2 + eV)^2 = p^2 c^2 + m_0^2 c^4 = m^2 c^4 \quad (2.1)$$

where c is the speed of light in vacuum, $p = mv$ is the particle’s momentum, v is its velocity, and m is the mass of the particle. From this expression it follows that the ratio of the electron’s mass to its rest mass is:

$$\frac{m}{m_0} = \gamma = \frac{1}{\sqrt{1 - v^2/c^2}} = 1 + \frac{eV}{m_0 c^2} \quad (2.2)$$

and that the velocity of the electron v relative to the velocity of light is:

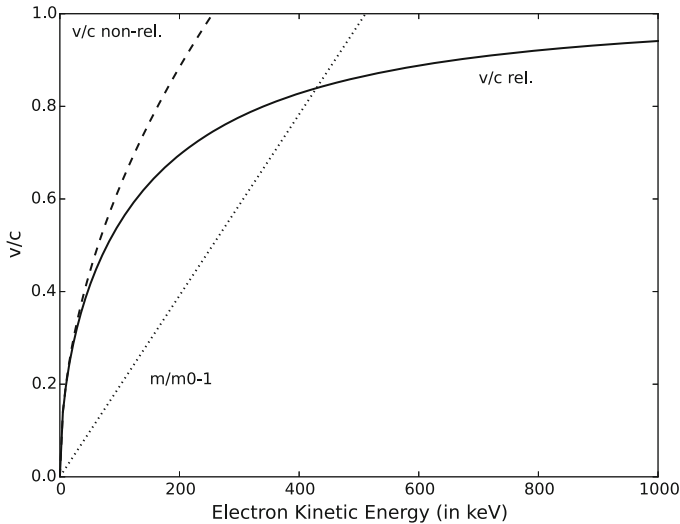


Fig. 2.5 Velocity v of the relativistic electron as a function of its kinetic energy eV . c is the speed of light in vacuum. For comparison the ratio of the electron mass to its rest mass (m/m_0) and the nonrelativistic velocity are also shown

$$\frac{v}{c} = \left[1 - \left(\frac{m_0 c^2}{m_0 c^2 + eV} \right)^2 \right]^{1/2} = \frac{[eV(eV + 2m_0 c^2)]^{1/2}}{m_0 c^2 + eV} \quad (2.3)$$

For comparison the nonrelativistic velocity is $v/c = \sqrt{2eV/(m_0 c^2)}$. The velocity is shown in Fig. 2.5 as a function of the kinetic energy eV of the electron.

The de-Broglie wavelength λ of the electron is:

$$\lambda = h/p \quad (2.4)$$

where h is Planck's constant. Substituting this in the above expression for the total energy (Eq. 2.1) yields:

$$(m_0 c^2 + eV)^2 = \left(\frac{hc}{\lambda} \right)^2 + m_0^2 c^4$$

$$\lambda = \frac{hc}{\sqrt{(m_0 c^2 + eV)^2 - m_0^2 c^4}}$$

$$\lambda = \frac{hc}{\sqrt{eV(2m_0 c^2 + eV)}} \quad (2.5)$$

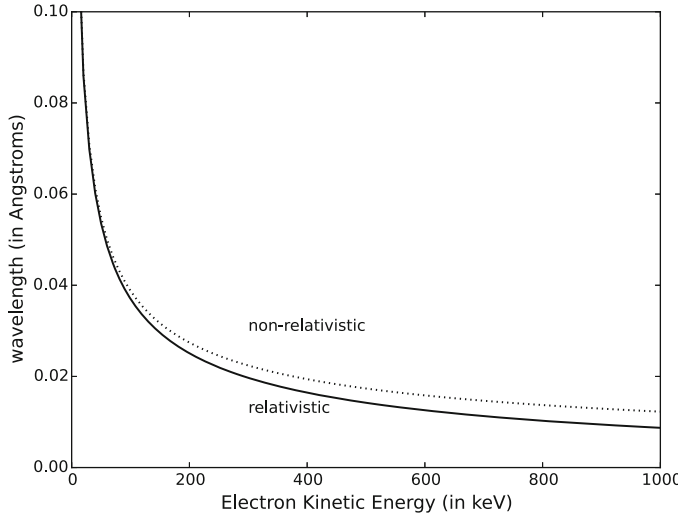


Fig. 2.6 Electron wavelength λ as a function of its kinetic energy. For comparison the nonrelativistic result is also shown

The relevant constants have values of $m_0c^2 = 511 \text{ keV}$, $hc = 12.398 \text{ keV}\cdot\text{\AA}$. For comparison the nonrelativistic result is $\lambda = hc/\sqrt{2m_0c^2eV}$. The electron wavelength is plotted as a function of kinetic energy in Fig. 2.6.

The Schrödinger wave equation of quantum mechanics is not relativistically correct. The electron is relativistic at the beam energies used in the electron microscope meaning that the Schrödinger equation should not be used directly. The relativistic Dirac equation would be the correct wave equation for relativistic electrons; however, it is significantly more difficult to work with mathematically (by hand or in the computer). It is now traditional to simply use the Schrödinger equation with a relativistically correct electron wavelength and mass. This approach has been compared to more accurate calculation using the Dirac equation by Fujiwara [153], Ferwerda [129, 130], and Jagannathan et al. [238, 239] and is usually accurate enough in the typical energy ranges used in the electron microscope. Op de Beck [92] recently found additional corrections to the use of the Schrödinger equation with relativistic mass and wavelength. The standard definition of the relativistic wavelength (Eq. 2.5) can lead to an additional error of order 10% at 100 keV and 20% at 400 keV in the electron wavelength. This error mostly cancels if the optical parameters (defocus, spherical aberration, etc.) are consistently determined using the same electron wavelength (which is usually the case) because only their product enters. The remaining error produces an apparent change in the crystal thickness (or equivalently the beam energy) of a few percent in image simulations. Rother et al. [430] have done a detailed comparison of relativistic and nonrelativistic electron scattering and also found good agreement with the

possible exception of very high angle scattering which might be a problem for ADF-STEM but probably not BF-CTEM. The form of the Schrödinger with a relativistic electron wavelength and mass as above will be used here because it is significantly easier to work with; however, some caution must be taken in a strict quantitative interpretation.

2.4 Reciprocity

The reciprocity theorem of scattering theory as adapted for electron microscopy (see Pogany and Turner [404]) states that the electron intensities and ray paths in the microscope (including a specimen) remain the same if their direction is reversed and the source and detector are interchanged (i.e., the electrons trajectories and elastic scattering processes have time reversal symmetry). Cowley [73], Zeitzer and Thomson [545], and Engel [117] have discussed the fact that this implies that the BF-CTEM and the BF-STEM should produce the same image. Reciprocity applies to all orders of the Born series for elastic interaction of the electrons and the specimen, so it is not necessary to restrict its implications to thin specimens. Figure 2.7 compares the ray paths in the CTEM with those in the STEM.

In the CTEM (on left in Fig. 2.7) the electrons start from a point source at the top and travel down. If the source is in the far field (either directly or by virtue of the condenser lens), then the specimen is illuminated by a nearly parallel beam. The objective lens then images each point on the specimen onto the image plane (film or other electron detectors such as a CCD). It is important to realize that the film or a CCD is an array of point detectors (one point detector for each image point in the specimen). In the STEM (on right in Fig. 2.7) the electrons start from a point source at the bottom and travel up (VG actually built their STEM's upside down but this orientation is only for this discussion and not necessary in practice). The objective lens forms a small probe on the specimen. The probe must be scanned to produce an image. A bright field detector is a small point detector on axis far away from the specimen (again in the far field). In each case the electron paths for only one image point are shown for simplicity. There is an obvious similarity between these two diagrams. If the direction of the electrons in the STEM is reversed and the source and detector interchanged, then the BF-STEM and the CTEM are identical. Both have a point source and a point detector on opposite sides of the specimen (the ADF-STEM is distinctly different however). This means that the image in the BF-STEM is equivalent to the BF image in the CTEM. It is even possible to measure the aberrations in an STEM using methods developed for the CTEM (Wong et al. [538]). It is not strictly necessary to have an exact point source (CTEM) or detector (STEM) for the equivalence of BF-STEM and BF-CTEM to hold. An increase in the illumination angles in the CTEM is equivalent to an increase in the size of the BF detector in the STEM.

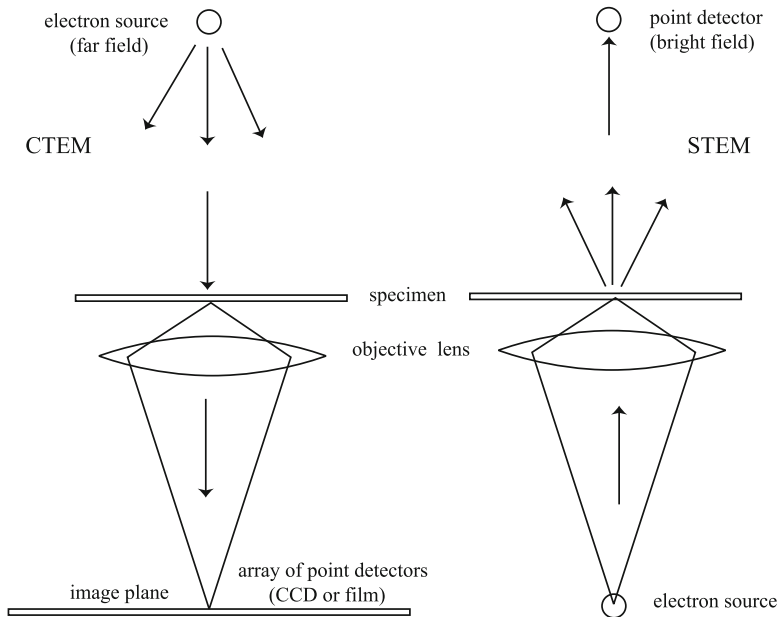
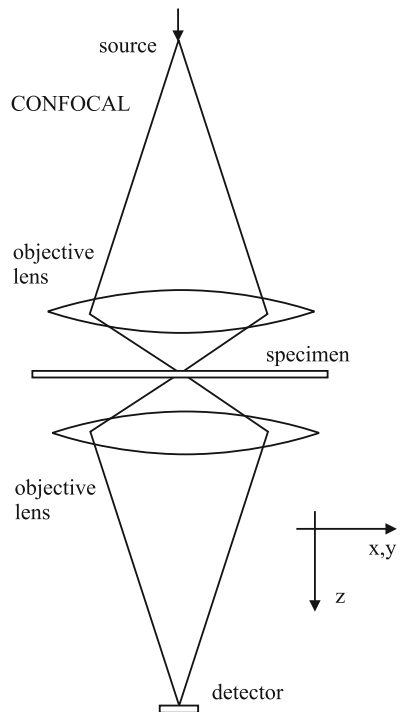


Fig. 2.7 Reciprocity applied to CTEM and STEM. The electrons are traveling downwards in the CTEM (left) and upwards in the STEM (right). The arrows indicate the direction of electron travel. Note that the geometry of the ray paths appear identical except for direction meaning that BF-CTEM is equivalent to BF-STEM

2.5 Confocal Mode

Confocal mode is a combination of both CTEM and STEM as in Fig. 2.8. The confocal optical microscope has demonstrated improved resolution and other advantages for many years. This mode has recently been adapted to electron microscopy (Frigo et al. [150], Zaluzec [542]). This mode is somewhat more difficult to implement in electron microscopy due to the added instrumentation. The top of the instrument (Fig. 2.8) is a STEM column (Fig. 2.4). The electron beam is focused to a small spot on the specimen. The bottom portion of the instrument after the specimen is basically a CTEM (Fig. 2.3) and images the probe transmitted through the specimen onto a small detector. There also has to be some way to scan the probe across the specimen in a raster and synchronously descans the image onto the detector. This can be done with two sets of scan coils carefully aligned or physically moving the specimen back and forth with a piezoelectric actuator (Takeguchi [482]) leaving the electron beam and lenses in a fixed position. Neither mechanism is shown in Fig. 2.8 for simplicity (may be difficult to implement in an actual instrument) but can be ignored in the calculations that will come later.

Fig. 2.8 Confocal mode is a combination of CTEM (bottom) and STEM (top). An STEM focuses a small probe onto the specimen (top) and a CTEM (bottom) images the probe transmitted through the specimen onto a small detector (bottom)



2.6 Aberrations

Most objective lenses in use today are rotationally (cylindrically) symmetric as in Fig. 2.2. Lens designers expend a great deal of effort in shaping the pole faces to get the best possible lens (minimum possible aberrations). Computer aided design of magnetic lenses is a sophisticated field by itself (see for example the recent books by Hawkes and Kasper [196–198]). It is also possible to form a lens by superimposing multipole elements such as quadrupole, hexapole, octopole, etc. Few if any microscopes currently use this approach for their primary focusing method because of its much greater complexity; however, several forms of aberration correction employ multipole elements.

The symmetry and shape of the magnetic fields in the objective lens are determined from Maxwell's equations which prevent the magnetic lens from performing exactly like the familiar ideal lens in classical light optics. There is however a close analogy between electron optics and light optics. An equivalent index of refraction and ray paths for electrons can be defined and magnetic lenses do approximately focus an image. The wavelength of the high energy electrons is much smaller than the dimensions of the lenses, so it is appropriate to think about the geometric rays in the lens just like those in a light optical glass lens. Furthermore the symmetries of Maxwell's equations are such that most of the primary light optical

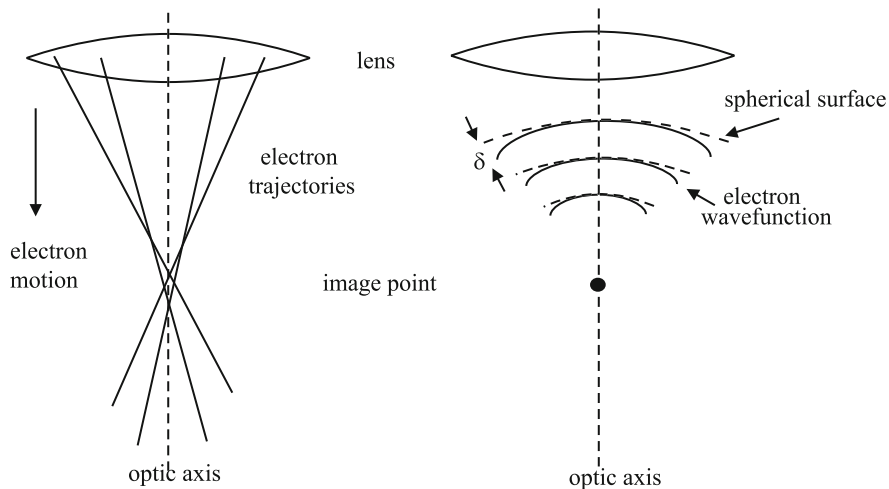


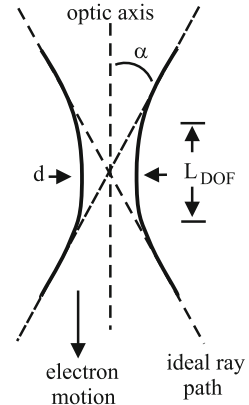
Fig. 2.9 The effect of spherical aberration C_s on the electron trajectories (left) and electron wave function (right). On the right the equivalent wave function without spherical aberration is shown as a dashed line

aberrations (see for example Born and Wolf [42]) also exist for magnetic lenses. These aberrations determine the deviation from an ideal lens and can be used to characterize the artifacts in the image.

In a high-resolution image only a small portion of the specimen near the optic axis is imaged. Therefore only the electron trajectories (or rays) near the optic axis need to be considered. This approach is called the paraxial ray approximation. If the electron microscope is well aligned, then off-axis aberrations are also negligible and the remaining lowest order effect is the third order spherical aberration C_s . Physically the magnetic field further away from the axis is stronger than is required so that electrons traveling at larger angles (α) are deflected more than is required to focus them (as in Fig. 2.9). C_s produces a position error in the electron trajectory or ray that is proportional to the third power of this angle and a phase error in the electron wave function that is proportional to the fourth power of the angle.

Ideally a lens forms a spherical wave converging on or emerging from a single point as on the right side of Fig. 2.9. The aberrations cause the wave to deviate from a spherical surface with an error δ , and the phase error is $\chi = (2\pi/\lambda)\delta$. The error δ can be represented in a variety of basis functions, the most obvious being a power series in positional deviations (x, y) and angular deviations (α_x, α_y) from the optic axis. In high-resolution microscopy the specimen should always be very near the optic axis, so positional deviations can be ignored leaving only the angular deviations (larger for higher resolution). If the lens is perfectly symmetric, then the deviation will not depend on the sign of α_x or α_y or which direction is chosen. Therefore the deviation δ can only depend on even powers of $\alpha = \sqrt{\alpha_x^2 + \alpha_y^2}$, leaving:

Fig. 2.10 Depth of focus of a focused probe (or image point). The solid line is the outline of the actual beam near its focus and the dashed line is the ideal ray path



$$\chi(\alpha) = \frac{2\pi}{\lambda} \delta = \frac{2\pi}{\lambda} \left(\frac{1}{2} C_1 \alpha^2 + \frac{1}{4} C_3 \alpha^4 + \frac{1}{6} C_5 \alpha^6 + \dots \right) \quad (2.6)$$

where the C_n coefficients have units of length. The deviations of the geometric rays are proportional to the derivative of χ and the leading numerical factors of each term are chosen to disappear after differentiation. $\Delta f = -C_1$ is defocus and $C_3 = C_{s3} = C_s$ is third order spherical aberration. There are an infinite number of higher order terms. $C_5 = C_{s5}$ is the fifth order spherical aberration. The subscript refers to the order of the geometric aberration (one less than the order of the wave aberration). If C_s is given without a numerical subscript it will be assumed to be the primary third order spherical aberration.

The ideal ray paths of a focused probe (or image point) would converge or cross over at a single point. The aberrations prevent the rays from meeting at a small point but instead expand the cross over point into a disk of diameter d as shown in Fig. 2.10. There is a short length L_{DOF} in which the cross over diameter is approximately constant. This distance can be called the depth of focus because an image of the specimen in this region is approximately the same focus. For small angles $\alpha \sim d/L_{DOF}$ giving $L_{DOF} \sim d/\alpha$. At modest resolution with an objective angle of $\alpha = 10$ mrad and a resolution of $d = 2$ Å $L_{DOF} \sim 200$ Å. With a high-resolution aberration corrector with angles $\alpha \sim 40$ mrad and resolution of 1 Å, $L_{DOF} \sim 25$ Å. There is the possibility of using this small depth of focus to perform optical depth sectioning in the specimen along the optic axis (for example, Einspahr and Voyles [111], Behan et al. [29], Lupini et al. [322], Hashimoto et al. [191], Xin et al. [540]).

Defocusing the lens also produces a deviation of the electron trajectory that departs from the ideal. Defocus can be changed by moving the specimen or changing the strength of the lens (proportional to the current through the lens coil). The amount of defocus, Δf is also defined as the deviation of the defocused image plane from the ideal Gaussian image plane. Defocus produces a phase error in the electron wave function but is proportional to the second power of the angle α .

Scherzer [442] found that a static, rotationally symmetric magnetic field with no sources on the axis will always produce a spherical aberration greater than zero because the expression for C_s can be written as the sum of quadratic terms. This is sometimes referred to as “Scherzer’s Theorem.” An electron microscope using this type of lens will have its instrumental resolution determined mainly by spherical aberration. Scherzer also noted that the defocus term can be used to partially offset the effect of C_s over some limited range of angles. For most microscopes, the net phase error is due to just spherical aberration and defocus as:

$$\chi(\alpha) = \frac{2\pi}{\lambda} \left(\frac{1}{4} C_s \alpha^4 - \frac{1}{2} \Delta f \alpha^2 \right) \quad (2.7)$$

Defocus Δf varies with the strength of the objective lens; however, C_s is essentially constant for a given specimen holder and beam energy. Equation 2.7 can be defined with the Δf term as positive or negative. Both sign conventions are used in the literature. With this definition, a positive Δf represents an underfocus (weaker lens current) of the objective lens. An accurate value of C_s is essential for image simulation or processing. Several methods for measuring C_s have been described by Budinger and Glasear [49], Krivanek [297], and others.

The semi-angle into the objective lens α (also the angle between the incident and scattered rays in CTEM) is related to the spatial frequency k in the image plane by multiplication by the electron wavelength λ as:

$$\alpha = \lambda k \quad (2.8)$$

The units of k are such that $1/k$ corresponds directly to a spacing d on the specimen (without multiplication or division by 2π). The literature on this subject can be very confusing because various authors add different factors of 2 and π . The simplest choice of $k = 1/d$ is used here (consistent with the optics literature but not with the traditional physics choice of $k = 2\pi/d$).

The aberration function $\chi(\alpha)$ rewritten as a function of k is:

$$\begin{aligned} \chi(k) &= \frac{2\pi}{\lambda} \left(\frac{1}{4} C_s \lambda^4 k^4 - \frac{1}{2} \Delta f \lambda^2 k^2 \right) \\ &= \pi \lambda k^2 (0.5 C_s \lambda^2 k^2 - \Delta f) \end{aligned} \quad (2.9)$$

Deviations from rotational symmetry are inevitable due to small machining errors in the magnetic lenses and small misalignments between lenses. The lowest order effect is the additional aberration of astigmatism and possibly coma which causes the defocus to vary with azimuthal angle ϕ .

$$\begin{aligned} \chi(k) &= \frac{\pi}{2} C_s \lambda^3 k^4 - \pi \Delta f \lambda k^2 + \pi f_{a2} \lambda k^2 \sin[2(\phi - \phi_{a2})] \\ &\quad + \frac{2\pi}{3} f_{a3} \lambda^2 k^3 \sin[3(\phi - \phi_{a3})] + \frac{2\pi}{3} f_{c3} \lambda^2 k^3 \sin[\phi - \phi_{c3}] \end{aligned} \quad (2.10)$$

where f_{a2} is twofold astigmatism, f_{a3} is threefold astigmatism, and f_{c3} is coma (Zemlin et al. [546]). ϕ_{a2} , ϕ_{a3} , and ϕ_{c3} are the azimuthal orientations of these aberrations. In principle astigmatism can be corrected but small amounts may remain in the image in practice. Astigmatism can result from small physical machining errors in the objective lens pole pieces or misalignments of the microscope column. Threefold astigmatism has recently been found to have a significant effect as resolution approaches or exceeds 2 Å (Ishizuka [232], Krivanek [298]). Zemlin et al. [546] described a coma-free alignment procedure using the so-called Zemlin tableau.

It is possible to write the aberration function in dimensionless form by scaling with appropriate powers of λ and C_s :

$$K = k(C_s \lambda^3)^{1/4} \quad (2.11)$$

$$D = \Delta f / \sqrt{C_s \lambda} \quad (2.12)$$

$$D_{a2} = \Delta f_{a2} / \sqrt{C_s \lambda} \quad (2.13)$$

$$D_{a3} = \Delta f_{a3} / (C_s^3 \lambda)^{1/4} \quad (2.14)$$

$$D_{c3} = \Delta f_{c3} / (C_s^3 \lambda)^{1/4} \quad (2.15)$$

$$\begin{aligned} \chi(K) = \pi & \left(0.5K^4 - DK^2 + D_{a2}K^2 \sin[2(\phi - \phi_{a2})] \right. \\ & \left. + \frac{2}{3}D_{a3}K^3 \sin[3(\phi - \phi_{a3})] + \frac{2}{3}D_{c3}K^3 \sin[\phi - \phi_{c3}] \right) \end{aligned} \quad (2.16)$$

The aberration function $\chi(K)$ is plotted in Fig. 2.11 for various amounts of defocus. $\chi(K)$ is the error (or deviation) of the wavefront from the ideal spherical wavefront.

The effect of the objective lens aberration function is to modulate different spatial frequencies (or different angles) by a complex function:

$$H_O(K) = \exp[-i\chi(K)] = \cos[\chi(K)] - i \sin[\chi(K)] \quad (2.17)$$

This function is plotted in Fig. 2.12.

The nonsymmetrical aberrations, such as astigmatism, etc., are not easily visualized in a simple graph. Some of these are illustrated in image form in Figs. 2.13 and 2.14 using computational methods that will be described later. These are images of a self-luminous point which is the probe function in STEM neglecting any remaining source size coming from the tip itself. It is not always obvious how different aberrations will combine in an image. The results of a few combinations are shown in Fig. 2.14.

A comparable results for a coherent BF image is shown in Fig. 2.15 for comparison. These aberrations look similar but have both black and white features (on a large background) and are a little larger than their incoherent counterparts.

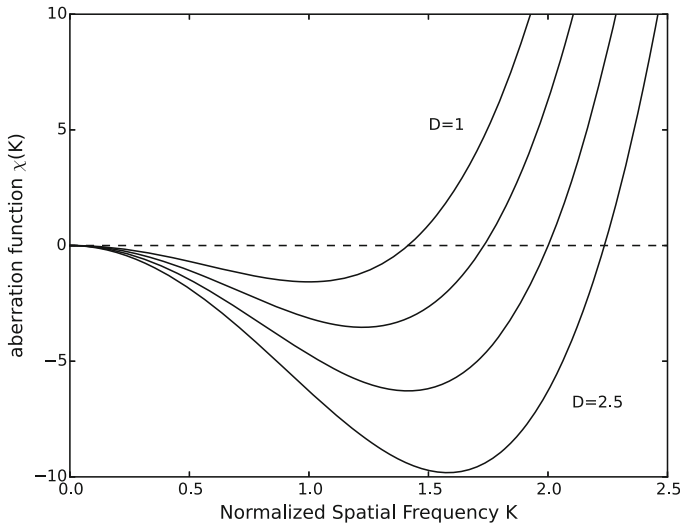


Fig. 2.11 The aberration function $\chi(K)$ as a function of the normalized spatial frequency K for different values of the normalized defocus $D = 1.0, 1.5, 2.0, 2.5$. Astigmatism and coma are assumed to be zero

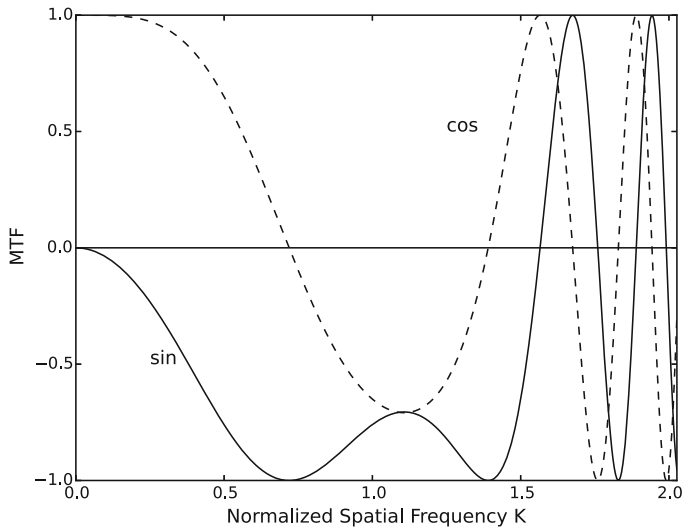


Fig. 2.12 The complex modulation function of the objective lens $H_O(K) = \cos[\chi(K)] - i \sin[\chi(K)]$ as a function of the normalized spatial frequency K for the special case of $\Delta f = \sqrt{1.5C_s\lambda}$. Astigmatism and coma are assumed to be zero

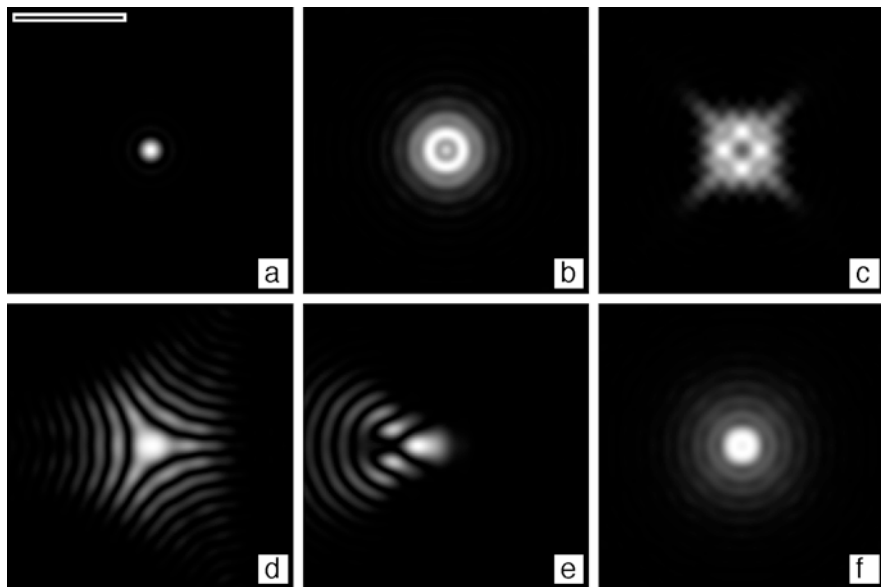


Fig. 2.13 Various single aberrations as an incoherent image. All images are of a 200 keV probe (or self-luminous point) with a 20 mrad aperture: (a) no aberrations (scale bar 5 Å), (b) defocus of 100 Å, (c) twofold astigmatism of 100 Å, (d) threefold astigmatism of 10,000 Å, (e) coma of 25,000 Å, and (f) spherical aberration of 0.057 mm

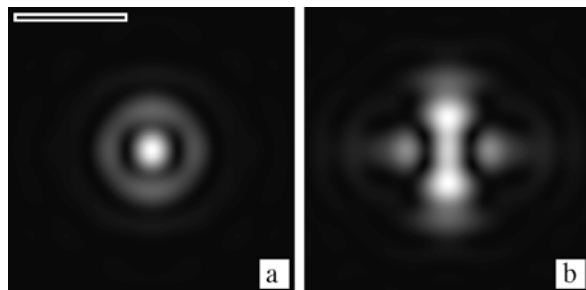


Fig. 2.14 Probe shape with combinations of aberrations. Both are for 200 keV, spherical aberration of 1.3 mm, an aperture of 10 mrad, and (a) defocus of 800 Å, and twofold astigmatism of 50 Å, (b) defocus of 800 Å, and twofold astigmatism of 200 Å. The scale bar in (a) is 5 Å

2.7 Aberration Correction

The most common electron lens is a rotationally symmetric lens similar to that shown in Fig. 2.2. The fringe field in the gap focuses the electron beam. Lens designers carefully shape the pole faces (of the magnetic material) near the gap to minimize the optical aberrations of the lens. Scherzer showed theoretically that a static round lens always has a positive spherical aberration. Theoretically,

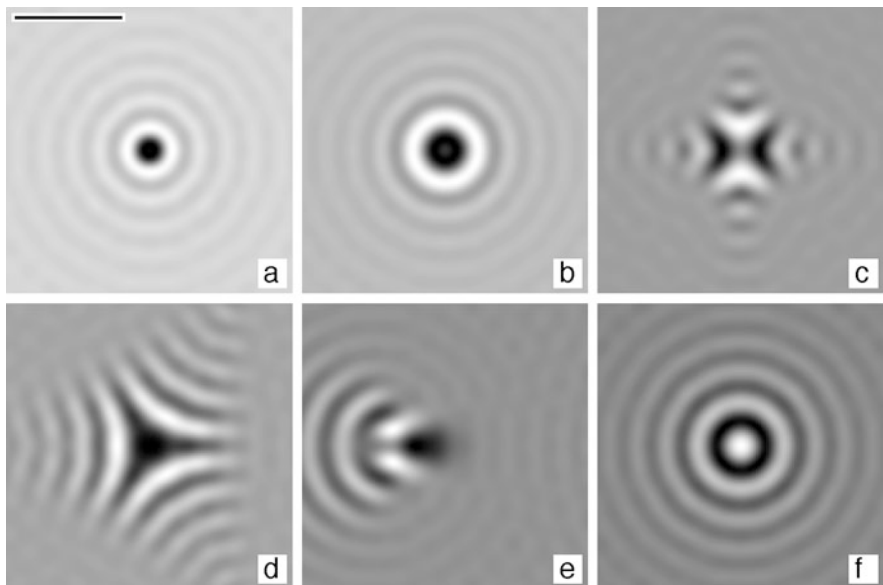


Fig. 2.15 Various single aberrations in phase contrast. All images are of a single gold atom at 200 keV with a 20 mrad aperture (to match Fig. 2.13): (a) no aberrations (scale bar 5 Å), (b) defocus of 100 Å, (c) twofold astigmatism of 100 Å, (d) threefold astigmatism of 10,000 Å, (e) coma of 25,000 Å, and (f) spherical aberration of 0.057 mm

spherical aberration can be arbitrarily small (but still positive), but in practice has reached a practical limit determined by the minimum size of the gap that can be practically utilized (the specimen usually must be inserted in the gap) and the maximum field strength that can be obtained by magnetic materials. The current practice is to utilize non-rotationally symmetric multipole lenses to produce negative spherical aberration to balance other positive spherical aberration in the system in a process similar to the design of light optical systems (except for multipole elements). Other approaches such as radio frequency microwave cavities (for example, Oldfield [384]) and foil lenses (with charges on the axis, for example, Hanai et al. [187]) have been tried but have not been aggressively pursued of late. Currently non-rotationally symmetric lenses have been developed commercially to correct for spherical aberrations.

Aberration correctors typically involve a rather sophisticated combination of multipole focusing elements. The general shape of a quadrupole element is shown in Fig. 2.16. The electron beam (optic axis) is into or out of the plane of the paper. A single quadrupole converges in one direction and diverges in the other direction (both are perpendicular to the optic axes), so more than one is needed to form an image. It is this ability to both converge and diverge that permits a negative spherical aberration unlike a round lens which is always converging. A set of three or four quadrupoles can be made to function as a conventional lens.

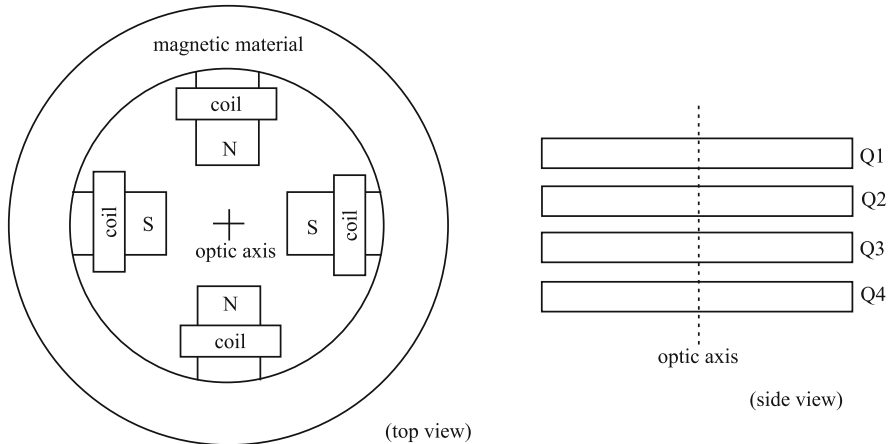


Fig. 2.16 General shape of a quadrupole lens. In the top view (on left) the electron travels into the plane of the page in the center of the lens. The beam converges in one direction and diverges in the other. A combination of quadrupole elements (side view on right) forms a lens. The magnetic field alternates direction in each element

Multipole elements can be formed with any even number of poles. A two pole element is just a deflector. Aberration correctors typically involve some combination of quadrupoles, hexapoles, and octopoles. Attempts were made many decades ago to build correctors but until recently did not significantly improve the images probably due to the difficulty of aligning such a complicated system manually. For example, Koops [291] demonstrated multipole correction of chromatic aberration with combined electric and magnetic dipoles. Rose [427, 428], Hawkes [193–195], and Septier [453] have given a review of the history of the development of aberration correctors starting with Scherzer. Smith [462] has also reviewed current progress in aberration-corrected microscopes. The recent success of correctors is largely due to advances in computer technology. Fast computer hardware and algorithms for automating the alignment of these complicated electron optical system is essential for utilizing this technology.

Scherzer [428, 441] originally proposed an image corrector using three octopoles with all electrostatic elements as in Fig. 2.17a. This corrector also includes two cylinder lenses, an eight pole stigmator, and one round lens. Unfortunately, this style of corrector has never been practical. A current probe corrector is shown in Fig. 2.17b. This uses all magnetic elements with three combined octopole-quadrupole units. There are four groups of four quadrupoles transferring the beam from one octopole to the next, focusing the appropriate rays into the octopole plane. In practice each quadrupole will have two set of quadrupoles rotated by 45° so that the superposition can be rotationally aligned to the other elements and each layer will have two pairs of dipole deflectors to steer the beam through the device (not shown in the figure for simplicity). The objective lens (OBJ) is a traditional round magnetic lens. Its position in each case is shown.

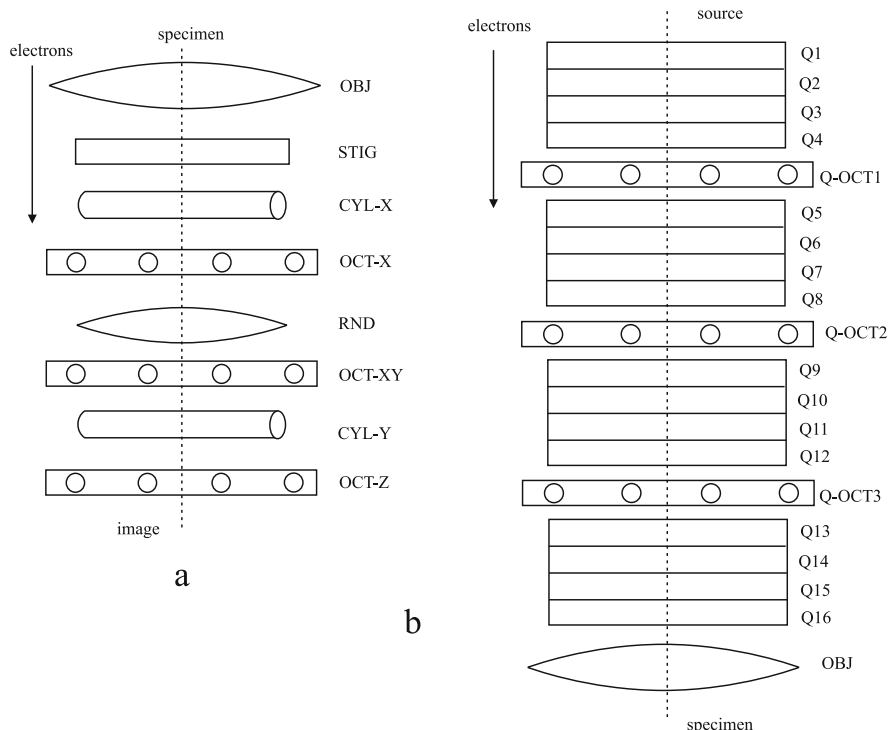


Fig. 2.17 Approximate configuration of some octopole aberration (C_{S3}) correctors. (OBJ = traditional round magnetic objective lens, OCT = octopole). (a) The original image corrector (CTEM) proposed by Scherzer [428, 441] using electrostatic elements. (STIG = stigmator, CYL = cylinder lens, RND = round lens). (b) A current probe corrector (STEM) using magnetic elements (similar to that described by Krivanek et al. [299], Q = quadrupole)

An approximate hexapole image corrector is shown in Fig. 2.18a. A single hexapole field produces a third order ($C_S = C_{30}$) aberration correction at the expense of adding significant second order aberrations ($C_{23} = A_2$). Rose [425, 426] realized that coupling two hexapole field with an inversion in between using two round telescopic transfer lenses can cancel the second order aberrations while retaining a negative third order aberration. Haider et al. [181] and Sawada et al. [181, 435] have added a third hexapole to further improve the corrector by correcting $C_{56} = A_5$. An approximate configuration of a three hexapole probe corrector is shown in Fig. 2.18b.

Multipole elements necessarily include many more non-rotationally symmetric aberrations. This complicates the imaging somewhat. Hexapole correctors generally involve significantly fewer elements (easier to use), but include several round lenses which are physically larger and use more power.

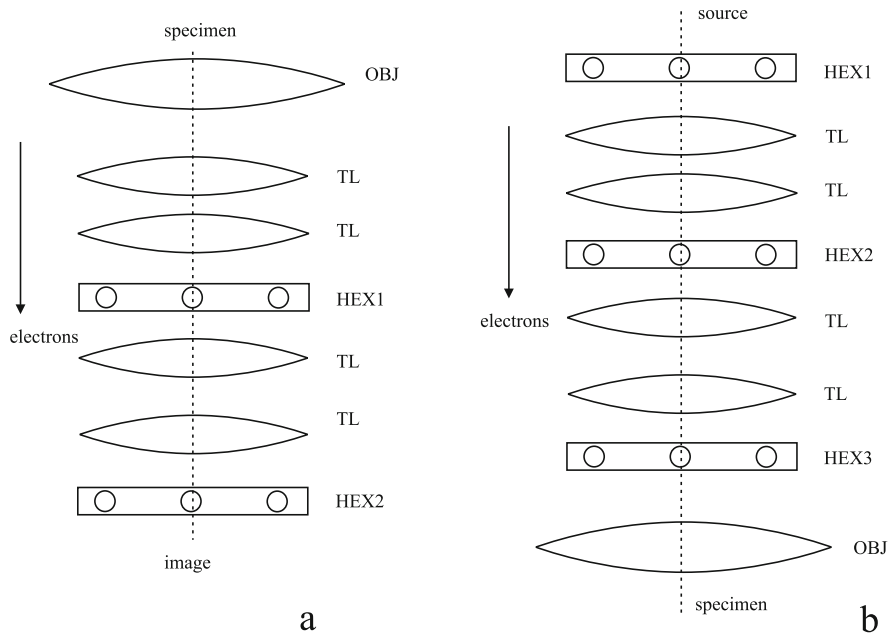


Fig. 2.18 Approximate configuration of some hexapole correctors. TL is a traditional round transfer lens. OBJ is the objective lens and HEX is a hexapole. (a) Image corrector with two hexapoles (Rose [425, 426]). (b) Probe corrector with three hexapoles (Haider et al. [181], Sawada et al. [435])

2.8 More Aberrations

A set of multipole elements (quadrupole, hexapole, octopole, etc.) may be used to correct for the unavoidable third order (and possibly higher) spherical aberration of a rotationally symmetric round lens. However, in the process, these multipoles by definition manifest a series of new rotational aberrations. Optical aberrations are like many other annoying things in life. Getting rid of one aberration causes another to pop up to take its place. These new aberrations must also be corrected. Some of these new aberrations will be described next.

There are a variety of ways to express the deviation δ of the wavefront from an ideal spherical wave (Fig. 2.9). For image points on the optic axis due to small (nonzero) angles with respect to the optic axis δ could be expanded in a double power series in angles $\alpha_x^n \alpha_y^m$, where α_x and α_y are components of α in the x and y directions, respectively. For high-resolution small lateral deviations (x and y) from the optic axis can be ignored, leaving just the axial aberrations. For example, there are four third order terms with $n + m = 3$ of α_x^3 , $\alpha_x^2 \alpha_y$, $\alpha_x \alpha_y^2$, and α_y^3 . Any set of four linear combinations of these terms (that are not linearly dependent) would also work. The usual practice is to group these terms into a basis set of functions, each with a particular rotational symmetry (not apparent in this set of functions). A compact

(slightly devious) mathematical notation using a complex angle $\omega = \alpha_x + i\alpha_y$ having a specific rotational dependence can generate a sequence of terms separated into separate rotational orders. The imaginary component is a temporary mathematical convenience and has no physical significance. Only the real part will be used in the end. A particular power is:

$$\omega^n = (\alpha_x + i\alpha_y)^n = \alpha^n \exp(in\phi) \quad (2.18)$$

where ϕ is the azimuthal angle and α is the polar angle. This expression has a rotational order of n . Now expand $\chi = (2\pi/\lambda)\delta$ in a double power series of ω and its complex conjugate ω^* with complex coefficients C_{nm} .

$$\chi(\omega) = \frac{2\pi}{\lambda} \text{Real} \left[\sum_{n=1}^{\infty} \sum_{s=0}^{n+1} \frac{1}{n+1} C_{nm} (\omega^*)^{n+1-s} \omega^s \right] \quad (2.19)$$

$$= \frac{2\pi}{\lambda} \text{Real} \left[\sum_{n=1}^{\infty} \sum_{s=0}^{n+1} \frac{1}{n+1} C_{nm} \alpha^{n+1} \exp[i(2s-n-1)\phi] \right] \quad (2.20)$$

where $m = 2s - n - 1$ is the rotational order of each term. Positive and negative m with the same magnitude yield the same thing. Several terms in this sequence may be repeated but only one of each form will be kept. The $n = 0$ term (C_{01}) is just a deflection (shift) and need not be considered here. Terms with $m \neq 0$ will have two terms with the same nm because C_{nm} is complex. Expanding to fifth order yields:

$$\begin{aligned} \chi(\omega) = & \frac{2\pi}{\lambda} \text{Real} \left[\frac{1}{2} C_{10} \omega^* \omega + \frac{1}{2} C_{12} \omega^{*2} + \frac{1}{3} C_{21} \omega^{*2} \omega + \frac{1}{3} C_{23} \omega^{*3} \right. \\ & + \frac{1}{4} C_{30} \omega^{*2} \omega^2 + \frac{1}{4} C_{32} \omega^{*3} \omega + \frac{1}{4} C_{34} \omega^{*4} \\ & + \frac{1}{5} C_{41} \omega^{*3} \omega^2 + \frac{1}{5} C_{43} \omega^{*4} \omega + \frac{1}{5} C_{45} \omega^{*5} \\ & \left. + \frac{1}{6} C_{50} \omega^{*3} \omega^3 + \frac{1}{6} C_{52} \omega^{*4} \omega^2 + \frac{1}{6} C_{54} \omega^{*5} \omega + \frac{1}{6} C_{56} \omega^{*6} + \dots \right] \end{aligned} \quad (2.21)$$

C_{10} is defocus, C_{12} is twofold astigmatism, C_{21} is coma, C_{23} is threefold astigmatism, C_{30} is third order spherical aberration, etc. In terms of polar angle α and azimuthal angle ϕ this series can be written as:

$$\chi(\alpha, \phi) = \frac{2\pi}{\lambda} \sum_{mn} \frac{1}{n+1} C_{nm} \alpha^{n+1} \cos[m(\phi - \phi_{nm})] \quad (2.22)$$

where this C_{nm} is real and ϕ_{nm} is the real rotational angle of each aberration. n and m take the indicated values in Eq. 2.21. Writing out these terms in a Cartesian like form to a little over third order yields:

$$\begin{aligned}
\chi(\alpha_x, \alpha_y) = & \frac{2\pi}{\lambda} \left[\frac{1}{2} C_{10} \alpha^2 + \frac{1}{2} C_{12a} (\alpha_x^2 - \alpha_y^2) + C_{12b} \alpha_x \alpha_y \right. \\
& + \frac{1}{3} C_{21a} \alpha_x \alpha^2 + \frac{1}{3} C_{21b} \alpha_y \alpha^2 + \frac{1}{3} C_{23a} \alpha_x (\alpha_x^2 - 3\alpha_y^2) \\
& + \frac{1}{3} C_{23b} \alpha_y (\alpha_y^2 - 3\alpha_x^2) + \frac{1}{4} C_{30} \alpha^4 + \frac{1}{4} C_{32a} (\alpha_x^4 - \alpha_y^4) \\
& + \frac{1}{2} C_{32b} \alpha_x \alpha_y \alpha^2 + \frac{1}{4} C_{34a} (\alpha_x^4 - 6\alpha_x^2 \alpha_y^2 + \alpha_y^4) \\
& + C_{34b} (\alpha_x \alpha_y^3 - \alpha_x^3 \alpha_y) + C_{41a} (\alpha_x^4 \alpha_y + 2\alpha_x^2 \alpha_y^3 + \alpha_y^5) \\
& \left. + C_{41b} (\alpha_x \alpha_y^4 + 2\alpha_x^3 \alpha_y^2 + \alpha_x^5) + \dots \right] \quad (2.23)
\end{aligned}$$

where the $C_{nma,b}$ coefficients are real valued. The sign of some of the $m \neq 0$ terms can be used either positive or negative (if used consistently) which can be a little confusing. This Cartesian like representation has some computational advantages because it does not require evaluating transcendental functions (like sin and cos) which may take a significant number of CPU cycles (sin and cos can also be efficiently generated using various recursion relations).

There are many ways to represent the aberrations. Every author seems to have a favorite form. Several forms of notation are listed in Table 2.1. The notation used in what follows is similar to that of Krivanek et al. [300, 301];

$$\chi(\alpha, \phi) = \frac{2\pi}{\lambda} \sum_{mn} \frac{\alpha^{n+1}}{n+1} [C_{nma} \cos(m\phi) + C_{nmb} \sin(m\phi)] \quad (2.24)$$

$$n = 0, 1, 2, 3, \dots \quad (2.25)$$

$$m = 0, 2, 4, \dots (n+1) \quad n \text{ odd} \quad (2.26)$$

$$= 1, 3, 5, \dots (n+1) \quad n \text{ even} \quad (2.27)$$

where n and m are positive integers and zero, and λ is the wavelength of the electron. Purists might wish to separate subscripts n and m with a comma, but until tenth order corrections becomes possible the comma may be dropped for convenience. Aberrations with $m \neq 0$ are sometimes referred to as parasitic because they are mostly introduced by the corrector itself.

Although currently the most common, this form of identifying the aberrations (with perhaps different symbols and names) is not the only possible method. These aberrations are not orthogonal which can be an occasional problem. For example, C_{23} and C_{43} have some small overlap which may make it difficult to separate which one is present (the opposite is also true, C_{23} can be used to compensate C_{43} which might be helpful). Another possible approach is the Zernike polynomials (for example, section 9.2 of Born and Wolf [42]) which are orthogonal over a unit circle (multipole parasitic aberrations may not be practical). Sheppard [457] has also given a general discussion of orthogonal aberration functions.

Table 2.1 Some aberration symbols through fifth order in some different systems of notation

Haider [182, 496]	Krivanek [299, 300]	Sawada [434]	Thust [489]	Description
A_0	C_{01}	A_1		Shift
C_1	C_{10}	O_2	C_{20}	Defocus
A_1	C_{12} (a,b)	A_2	C_{22}	Twofold astigmatism
$3B_2$	C_{21} (a,b)	P_3	C_{31}	Axial coma
A_2	C_{23} (a,b)	A_3	C_{33}	Threefold astig.
C_3	$C_{30} = C_S$	O_4	C_{40}	Third order spher.
$4S_3$	C_{32} (a,b)	Q_4	C_{42}	Axial star aber.
A_3	C_{34} (a,b)	A_4	C_{44}	Fourfold astig.
$4B_4$	C_{41} (a,b)	P_5	C_{51}	Fourth order axial coma
$4D_4$	C_{43} (a,b)	R_5	C_{53}	Three-lobe aberr.
A_4	C_{45} (a,b)	A_1	C_{55}	Fivefold astig.
C_5	$C_{50} = C_{55}$	O_6	C_{60}	Fifth order spher.
$6S_5$	C_{52} (a,b)	Q_6	C_{62}	Fifth order axial star
$6R_5$	C_{54} (a,b)	S_6	C_{64}	Fifth order rosette
A_5	C_{56} (a,b)	A_6	C_{66}	Sixfold astig.

Aberrations with (a,b) have two components at different azimuthal angles or equivalently a single rotation angle and combined magnitude. Chromatic aberration is usually represented as C_C

One method of displaying complicated aberrations is to show an image of the phase error inside the objective aperture. A few different aberrations are shown in Fig. 2.19 for 200 kV and a 70 mrad (half angle) objective aperture. Hexapole correctors have been demonstrated to work to about this angle by Haider et al. [181] (60 mrad at 200 kV) and Sawada et al. [435] (71 mrad at 60 kV). An octopole corrector has been shown to correct to 40 mrad at 100 kV by Krivanek et al. [299]. The phase error is modulo 2π . Each image is scaled so that $-\pi$ is black and $+\pi$ is white (the background is also arbitrarily set to white). The $-\pi$ to $+\pi$ transition produces a sharp boundary which helps visualize the structure in the aberration (visually similar to a contour plot). A properly tuned probe corrector would have a uniform flat gray tone (all images in this figure have significant aberrations and would not produce a sharply focused probe or image).

The traditional maximum allowed error is $\pi/4$ in each aberration at the maximum angle (outer circumference of the objective aperture). For simplicity ignore the azimuthal dependence (or equivalently look only in the maximum direction) and equate the residual aberration as:

$$\left| \frac{2\pi}{\lambda} \frac{\alpha_{\max}^{n+1}}{n+1} C_{nm} \right| \leq \frac{\pi}{4} \quad (2.28)$$

Fig. 2.19 Phase error $\chi(\alpha, \phi)$ at 200 kV in an objective aperture of 70 mrad (140 mrad diameter). The display is modulo 2π and scaled such that $-\pi$ is black and $+\pi$ is white. A zero phase error appropriate for a STEM probe corrector would be a uniform gray tone.

Various aberrations have been added. (a) $C_{21a} = 0.1 \mu\text{m}$, (b) $C_{23a} = 0.1 \mu\text{m}$, (c) $C_{30} = 0.1 \mu\text{m}$, (d) $C_{34a} = 0.8 \mu\text{m}$, (e) $C_{43a} = 80 \mu\text{m}$, (f) $C_{56a} = 800 \mu\text{m}$

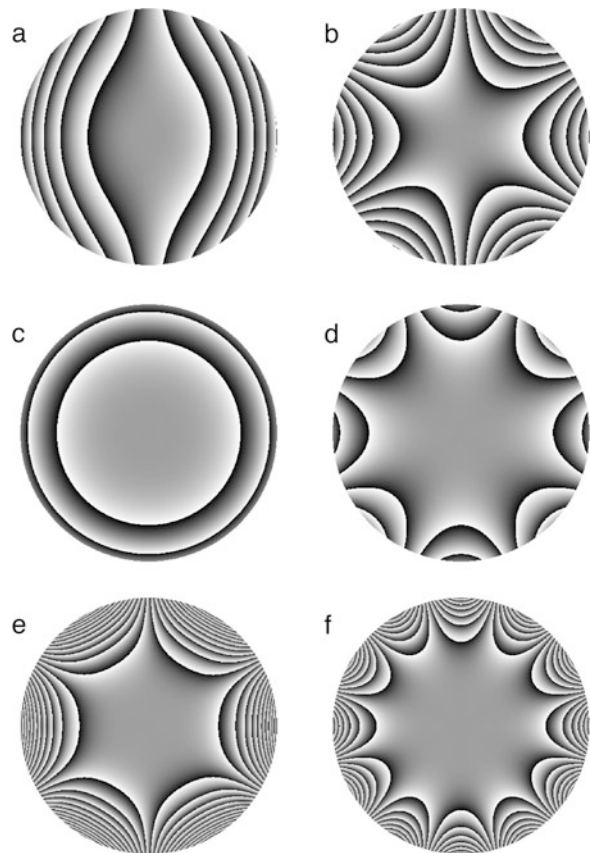


Table 2.2 Maximum allowed aberration tuning errors for 30 mrad objective aperture (Eq. 2.29) and 60 keV ($\lambda = 0.04866 \text{ \AA}$), 100 keV ($\lambda = 0.03701 \text{ \AA}$), 200 keV ($\lambda = 0.02508 \text{ \AA}$)

Aberration	Expression	60 keV	100 keV	200 keV
C_{1m}	$2\lambda/(8\alpha^2)$	1.35 nm	1.02 nm	0.70 nm
C_{2m}	$3\lambda/(8\alpha^3)$	67.6 nm	51.4 nm	34.8 nm
C_{3m}	$4\lambda/(8\alpha^4)$	3.00 μm	2.28 μm	1.55 μm
C_{4m}	$5\lambda/(8\alpha^5)$	125 μm	95.2 μm	64.5 μm
C_{5m}	$6\lambda/(8\alpha^6)$	5.01 mm	3.81 mm	2.58 mm

$$\left| C_{nm} \right| \leq T_{nm} = \frac{(n+1)}{8\alpha_{\max}^{n+1}} \lambda \quad (2.29)$$

where T_{nm} is the tolerance for aberration C_{nm} . Some values are shown in Table 2.2. In a probe corrector (STEM) all aberrations should be zero within this tolerance. In an image corrector (CTEM) all aberrations except defocus, C_{S3} and C_{S5} should be zero within this tolerance.

2.9 Further Reading

Some Books on Electron Microscopy

1. P. R. Buseck, J. M. Cowley and L. Eyring, edit., *High-Resolution Transmission Electron Microscopy*, Oxford Univ. Press, 1988 [52]
2. J. J. Bozzola and L. D. Russell, *Electron Microscopy, Princ. and Tech. for Biologists*, 2nd edit., Jones and Bartlett Pub., 1999 [45]
3. D. K. Bowen and C. R. Hall, *Microscopy of Materials*, MacMillan Press, 1975 [44]
4. M. De Graf, *Intro. to Conventional Transmission Electron Microscopy*, Cambridge Univ. Press, 2003 [164]
5. J. W. Edington, *Practical Electron Microscopy in Materials Science*, Van Nostrand Reinhold, 1976 [109]
6. R. Erni, *Aberration-Corrected Imaging in Transmission Electron Microscopy*, Imperial College Press, 2nd edit., 2015 [123]
7. J. Frank, *Three Dimensional Electron Microscopy of Macromolecular Assemblies*, Oxford Univ. Press, 2006 [143]
8. B. Fultz and J. Howe, *Transmission Electron Microscopy and Diffractometry of Materials*, fourth edit., Springer, 2013 [154]
9. C. E. Hall, *Introduction to Electron Microscopy*, 2nd edition, McGraw-Hill, 1966 [184]
10. R. D. Heidenreich, *Fundamentals of Transmission Electron Microscopy*, Wiley, 1964 [202]
11. P. Hirsch, A. Howie, R. B. Nicholson, D. W. Pashley, M. J. Whelan, *Electron Microscopy of Thin Crystals*, second edition , Krieger, 1977 [208]
12. S. Horiuchi, *Fundamentals of High Resolution Transmission Electron Microscopy*, North-Holland, 1994 [211]
13. R. Keyse et al, *Intro. to Scanning Transmission Electron Microscopy*, Springer, 1998 [255]
14. G. A. Meek, *Practical Electron Microscopy for Biologists*, second edition, Wiley, 1976 [341]
15. S. J. Pennycook and P. D. Nellist (edit.), *Scanning Transmission Electron Microscopy, Imaging and Analysis*, Springer-Verlag, 2010 [401]
16. L. Reimer, *Transmission Electron Microscopy*, third edition, Springer-Verlag, 1993 [414]
17. L. Reimer, *Scanning Electron Microscopy*, Springer-Verlag, 1985 [413]
18. J. C. H. Spence, *High-Resolution Electron Microscopy*, Oxford University Press, 2013 [470]
19. N. Tanaka (edit.), *Scanning Transmission Electron Microscopy of Nanomaterials*, Imperial College Press, 2015 [483]
20. D. B. Williams and C. B. Carter, *Transmission Electron Microscopy, A Textbook for Materials Science*, Springer, 2009 [534]
21. Jian Min Zuo and John C. H. Spencer, *Advanced Transmission Electron Microscopy, Imaging and Diffraction in Nanoscience*, Springer, 2017 [550]

Some Books on Electron Optics

1. P. Grivet, *Electron Optics, Parts 1 and 2*, 2nd English edition, Pergamon, 1972 [[174](#)]
2. P. W. Hawkes and E. Kasper, *Principles of Electron Optics*, Vol. 1,2,3, Academic Press, 1989, 1994 [[196–198](#)]
3. P. W. Hawkes (edit.), *Aberration-corrected Electron Microscopy, Adv. Imag. and Elect. Phys.*, vol. 153, Academic Press, 2008 [[193](#)]
4. O. Klemperer and M. E. Barnett, *Electron Optics, third edition*, Cambridge Univ. Press, 1971 [[287](#)]
5. A. B. El-Kareh and J. C. J. El-Kareh, *Electron Beams, Lenses, and Optics*, Vol. 1,2, Academic Press, 1970 [[115](#)]
6. J. Orloff, *Handbook of Charged Particle Optics*, 2nd edit., CRC Press, 2009 [[390](#)]
7. H. Rose, *Geometrical Charged Particle Optics*, 2nd edit., Springer, 2012 [[429](#)]
8. A. Septier, editor, *Applied Charged Particle Optics*, in: *Adv. in Electronics and Electron Physics*, Vol. 13A,B, Academic Press, 1980 [[454](#)]

Chapter 3

Some Image Approximations



At some level of approximation, human vision is a linear convolution of some function of light intensity with a spatial resolution response function. This simple linear image model is not quantitatively precise but allows for an easy interpretation of everyday observations. Electron microscope images do not in general follow a simple linear image model to any great precision. However it is useful to try to find the conditions under which an electron micrograph can be interpreted as a linear image of some physical property of the specimen.

In the linear image model the actual recorded image intensity $g(\mathbf{x})$ is related to the ideal image of the object $f(\mathbf{x})$ by a linear convolution of the object function with the point spread function $h(\mathbf{x})$ of the instrument:

$$\begin{aligned} g(x, y) &= f(x, y) \otimes h(x, y) = \int f(x', y') h(x - x', y - y') dx' dy' \\ g(\mathbf{x}) &= f(\mathbf{x}) \otimes h(\mathbf{x}) = \int f(\mathbf{x}') h(\mathbf{x} - \mathbf{x}') d\mathbf{x}' \end{aligned} \quad (3.1)$$

where $\mathbf{x} = (x, y)$ is a two-dimensional position vector in the image plane. The point spread function or PSF of the instrument is just the image of an isolated point in the object or specimen. The symbol \otimes represents the convolution. Using the Fourier convolution theorem the linear image model can also be written as a product in Fourier or reciprocal space.

$$G(\mathbf{k}) = F(\mathbf{k}) H(\mathbf{k}) \quad (3.2)$$

$H(\mathbf{k})$ is the transfer function (or modulation transfer function, MTF) and is the Fourier transform of $h(\mathbf{x})$. $G(\mathbf{k})$ and $F(\mathbf{k})$ are the Fourier transforms of $g(\mathbf{x})$ and $f(\mathbf{x})$, respectively. Capital letters will be used to denote a Fourier transformed quantity and lower case letters will denote a real space quantity. Goodman [161] has given an overview of the linear image model in light optics.

3.1 The Weak Phase Object in Bright Field

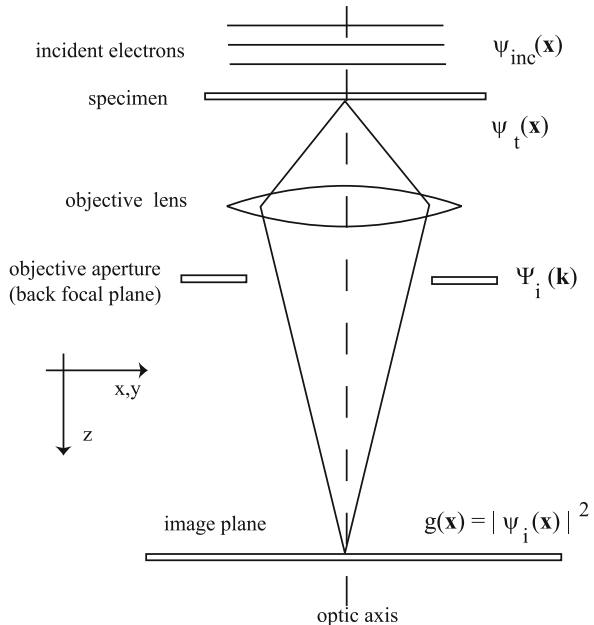
Under restricted conditions the BF image in a CTEM may be considered as a linear image model (for example, Erikson [122], Hansen [188], Lenz [309], Thon [487], Hoppe [210]). It should be noted that Scherzer [442] stated most of the features of this image model but did not take the final step of writing it as a convolution. This section will discuss the image formation in the context of the CTEM although BF-CTEM and BF-STEM are equivalent in this context due to the reciprocity theorem (see Sect. 2.4).

The electrons incident on the specimen have a relatively high energy (approximately 100–1000 keV) as compared to the electrons in the specimen. If the specimen is very thin, then the incident electrons pass through the specimen with only small deviations in their paths and the effect of the specimen can be modeled as a simple transmission function $t(\mathbf{x})$. The electron wave function after passing through the specimen is:

$$\psi_t(\mathbf{x}) = t(\mathbf{x})\psi_{\text{inc}}(\mathbf{x}) \quad (3.3)$$

where $\psi_{\text{inc}}(\mathbf{x})$ is the incident wave function. In the CTEM the incident electron wave function (see Figs. 2.3 and 3.1) is approximately a plane wave of constant intensity ($\psi_{\text{inc}} \sim 1$). Later chapters will discuss the effects of specimen thickness on the transmission function (i.e., $t(\mathbf{x})$ will no longer be a simple scalar function).

Fig. 3.1 The positions of the imaging wave functions in the CTEM column



The effect of the aberrations of the objective lens is to shift the phase of each frequency component by a different amount (angle and spatial frequency are proportional). If $\Psi_t(\mathbf{k})$ is the Fourier transform of $\psi_t(\mathbf{x})$ and $\Psi_i(\mathbf{k})$ is the electron wave function in the back focal plane of the objective lens, then:

$$\begin{aligned}\Psi_t(\mathbf{k}) &= FT[\psi_t(\mathbf{x})] \\ \Psi_i(\mathbf{k}) &= \Psi_t(\mathbf{k}) \exp[-i\chi(\mathbf{k})] = \Psi_t(\mathbf{k})H_0(\mathbf{k})\end{aligned}\quad (3.4)$$

where FT indicates a Fourier transform. The objective lens images this wave function into a virtual image which is equivalent to an inverse Fourier transform of the above equation (yielding $\psi_i(\mathbf{x})$ from $\Psi_i(\mathbf{k})$). The projector lenses further magnify this virtual image. Although magnification is the primary function of the microscope this magnification can be ignored (in the math) if the image coordinates are always referred to the dimensions on the specimen.

The actual recorded image is the intensity, or square magnitude of the image wave function. Denoting the intensity in the recorded image as $g(\mathbf{x})$ yields:

$$\begin{aligned}\psi_i(\mathbf{x}) &= FT^{-1}[\Psi_i(\mathbf{k})] \\ g(\mathbf{x}) &= |\psi_i(\mathbf{x})|^2 = |\psi_t(\mathbf{x}) \otimes h_0(\mathbf{x})|^2\end{aligned}\quad (3.5)$$

where $h_0(\mathbf{x})$ is the complex point spread function of the objective lens (the inverse Fourier transform of $H_0(\mathbf{k})$).

In the weak phase object (WPO) approximation the specimen is assumed to be very thin and composed mainly of light atoms. The primary effect of the specimen is to produce a spatially varying phase shift in the electron wave function as it passes through the specimen. This approximation can also be referred to as the Moliere [358], WKB, or eikonal [444] approximation. If the specimen is also weak, then the exponential phase factor can be expanded in a power series where only the low order terms are important. If the incident wave function is a plane wave ($\psi_{\text{inc}} = 1$) and the specimen is a weak phase object Eq. 3.3 becomes:

$$\psi_t(\mathbf{x}) \sim t(\mathbf{x}) \sim \exp[i\sigma_e v_z(\mathbf{x})] \sim 1 + i\sigma_e v_z(\mathbf{x}) + \dots \quad (3.6)$$

In later chapters $v_z(\mathbf{x})$ will be shown to be the projected atomic potential of the specimen and σ_e is an appropriate scaling factor (both are real). It is possible to use the opposite sign convention (reverse the sign of v_z in the exponent, with a corresponding change in $H_0(\mathbf{k})$) because only the square modulus of ψ will be important in the end. The result will be the same if all the signs are consistently changed, however this sign change can lead to some confusion when comparing different published versions of this theory in the literature (different authors use different sign conventions). The sign convention used here is consistent with the forward propagation of electrons (see Self et al. [452] for a discussion of the proper sign). Expanding the expression for $g(\mathbf{x})$ (Eq. 3.5) and keeping only the lowest order terms in $v_z(\mathbf{x})$ (i.e., the weak phase object approximation) yields:

$$\begin{aligned} g(\mathbf{x}) &= \left| \left[1 + i\sigma_e v_z(\mathbf{x}) + \mathcal{O}(v_z^2) \right] \otimes h_0(\mathbf{x}) \right|^2 \\ &= |1 \otimes h_0(\mathbf{x}) + i\sigma_e v_z(\mathbf{x}) \otimes h_0(\mathbf{x})|^2 + \mathcal{O}(v_z^2) \end{aligned} \quad (3.7)$$

using the Fourier convolution theorem:

$$1 \otimes h_0(\mathbf{x}) = FT^{-1} [\delta(\mathbf{k}) \exp[-i\chi(\mathbf{k})]] = 1 \quad (3.8)$$

where $\delta(\mathbf{k})$ is the Dirac delta function. This leaves:

$$\begin{aligned} g(\mathbf{x}) &= 1 + \sigma_e v_z(\mathbf{x}) \otimes [ih_0(\mathbf{x}) - ih_0^*(\mathbf{x})] + \mathcal{O}(v_z^2) \\ &\approx 1 + 2\sigma_e v_z(\mathbf{x}) \otimes h_{WP}(\mathbf{x}) \end{aligned} \quad (3.9)$$

where a superscript * denotes complex conjugation and $h_{WP}(\mathbf{x})$ is the point spread function for BF imaging in the weak phase object approximation. The cross term between the unscattered beam ($=1$) and the scattered beam ($\sigma_e v_z(\mathbf{x})$) can be identified as an in-line hologram or interference between these two beams. Gabor's [155] original paper on holography was actually about BF-CTEM although it was only tested on light optical holograms. The transfer function will be shown later to add an extra phase shift to produce a strong interference between the two beams.

It is easier to state the Fourier transform of the point spread function (i.e., the transfer function) than the PSF itself:

$$\begin{aligned} G(\mathbf{k}) &= FT[g(\mathbf{x})] = \delta(\mathbf{k}) + 2\sigma_e V_z(\mathbf{k}) H_{WP}(\mathbf{k}) \\ H_{WP}(\mathbf{k}) &= FT[h_{WP}(\mathbf{x})] \\ &= \frac{i}{2} \{\exp[-i\chi(\mathbf{k})] - \exp[i\chi(\mathbf{k})]\} \\ &= \sin \chi(\mathbf{k}) \end{aligned} \quad (3.10)$$

An oscillatory transfer function is about the worst thing that can happen. This means that some spacings (i.e., spatial frequencies \mathbf{k}) in the specimen will be transmitted as bright ($H_{WP}(\mathbf{k}) > 0$) at the same time that other spacings are transmitted as dark ($H_{WP}(\mathbf{k}) < 0$) because the transfer function is both positive and negative.

The minimum of the aberration function $\chi(\mathbf{k})$ remains approximately flat for a significant region near its minimum (see Fig. 2.11). If the defocus is adjusted so that $\sin \chi(\mathbf{k})$ is also near its minimum or maximum (± 1) when $\chi(\mathbf{k})$ is flat, then the transfer function will have a significant region of uniformly transferred information (i.e., the transfer function is large and constant in a band of spatial frequencies). Allowing $\sin \chi(\mathbf{k})$ to deviate slightly from unity magnitude in the passband increases the resolution slightly. Therefore look for conditions in which:

$$0.7 \leq |\sin \chi(k)| \leq 1.0$$

$$\chi(k) = -\left[\frac{2n_D - 1}{2}\right]\pi \pm \frac{\pi}{4}$$

$$n_D = 1, 2, 3, \dots \quad (3.11)$$

The minimum of the aberration function is found by setting its derivative equal to zero. Using the dimensionless form of $\chi(K)$ (Eq. 2.11) and ignoring the astigmatism (assumed small) yields:

$$\begin{aligned} \frac{\partial \chi(K)}{\partial K} &= \pi(2K^3 - 2DK) = 0 \\ K^2 - D &= 0 \\ K &= \sqrt{D} \end{aligned} \quad (3.12)$$

Next substitute this expression for K into the original expression for $\chi(K)$ (Eq. 2.16) and solve for defocus D to make $\sin[\chi(K)] \sim \pm 1$:

$$\begin{aligned} \chi(K) &= \pi(0.5(\sqrt{D})^4 - D(\sqrt{D})^2) \\ &= \pi(0.5D^2 - D^2) = -0.5\pi D^2 \\ &= -\left[\frac{2n_D - 1}{2}\right]\pi - \frac{\pi}{4} \end{aligned} \quad (3.13)$$

The optimum defocus is therefore:

$$\begin{aligned} D &= \sqrt{2n_D - 0.5} \\ \Delta f &= \sqrt{(2n_D - 0.5)C_s\lambda} \\ n_D &= 1, 2, 3, \dots \end{aligned} \quad (3.14)$$

The special case of $n_D = 1$ is referred to as Scherzer focus. Each positive integer value of n_D produces a band of uniformly transferred spatial frequencies (Eisenhandler and Siegel [114]). The transfer function for several values of n_D is shown in Fig. 3.2. The broad passband moves to higher spatial frequencies as n_D increases but unfortunately also gets smaller so that the resolution cannot be extended dramatically using large n_D . Eisenhandler and Siegel [114] and Hoppe [210] proposed using zone plates (in the objective aperture) to select appropriate bands in the transfer function to improve resolution. Image reconstruction from a defocus series may use these wide bands to advantage (for example, Kirkland et al. [282]).

Ideally a transfer function would be flat and have the same sign over the range of spatial frequencies that are transmitted to the image. The oscillatory nature of $H_{WP}(K)$ can cause serious problems because it is not flat and changes sign. Choosing an optimum defocus produces bands of uniform sign in the transfer

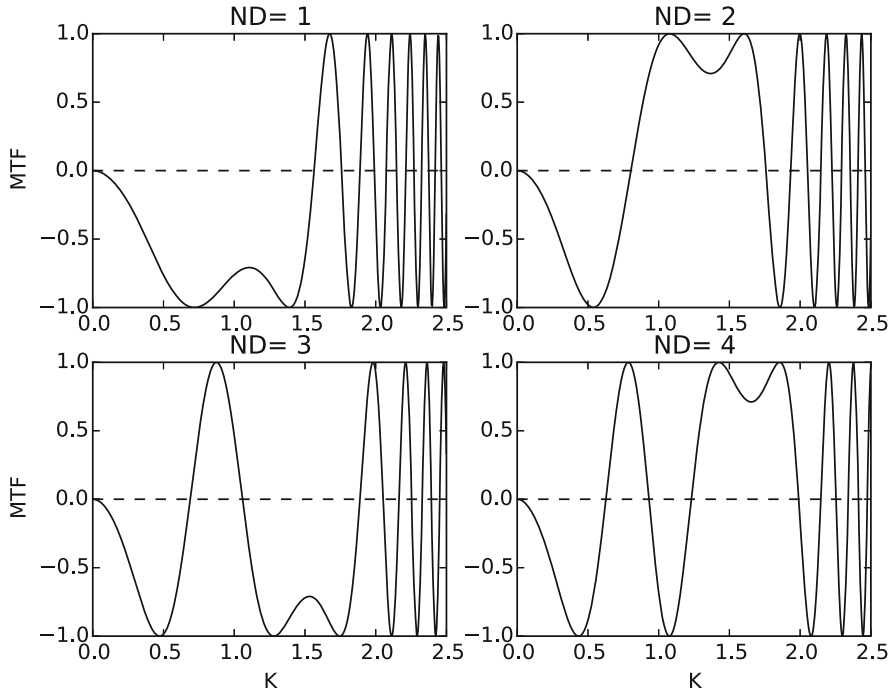


Fig. 3.2 The phase contrast transfer function H_{WP} for a weak phase object in bright field as a function of the normalized spatial frequency K for different values of the defocus index $n_d = 1, 2, 3, 4$. Astigmatism is assumed to be zero

function but the transfer function is still oscillating. Scherzer [442] realized that it is better to limit the range of spatial frequencies so that the transfer function at least has the same sign over its allowed range. An objective aperture is placed in the back focal plane of the objective lens (see Fig. 3.1) which is conveniently the Fourier transform plane. The radius in the aperture corresponds to spatial frequency in the image. The objective aperture allows all rays within a maximum distance from the optic axis to pass. This means that the objective aperture limits the maximum spatial frequency in the image. If this maximum cutoff is made to coincide with the first zero crossing of the transfer function (for Scherzer focus), then the transfer function will have the same sign over its range. The first zero crossing is found in dimensionless (normalized) form from:

$$\begin{aligned}\chi(K) &= \pi(0.5K_{\max}^4 - DK_{\max}^2) = 0 \\ 0.5K_{\max}^2 - D &= 0 \\ K_{\max} &= \sqrt{2D}\end{aligned}\tag{3.15}$$

At Scherzer focus $D = \sqrt{1.5}$. Substituting this value of D yields:

$$\begin{aligned} K_{\max} &= \sqrt{2\sqrt{1.5}} = k_{\max}(C_s \lambda^3)^{1/4} \\ k_{\max} &= \left(\frac{6}{C_s \lambda^3}\right)^{1/4} \\ \alpha_{\max} &= \lambda k_{\max} = \left(\frac{6\lambda}{C_s}\right)^{1/4} \end{aligned} \quad (3.16)$$

This value of α_{\max} is referred to as the Scherzer aperture. Together the Scherzer aperture and Scherzer focus are referred to as the Scherzer conditions. The corresponding resolution with Scherzer conditions is just:

$$d_s > \left(\frac{C_s \lambda^3}{6}\right)^{1/4} = 0.64(C_s \lambda^3)^{1/4} = 1/k_{\max} \quad (3.17)$$

This resolution is plotted versus spherical aberration in Fig. 3.3. This is a lower bound because the transfer function $H_{WP} = 0$ at this spacing and there is no information transferred. There is some ambiguity in the choice of Eq. 3.11. Other choices will change the value of various constants presented above by small amounts. The differences appearing in the literature mainly reflect the allowed variation of $\sin \chi(K)$ in the pass band (0.7–1.0 chosen here).

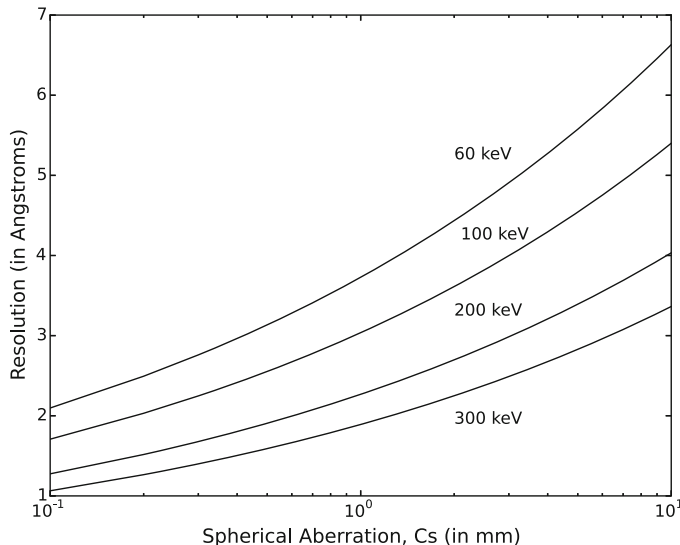


Fig. 3.3 The coherent bright field phase contrast resolution in the weak phase object approximation as a function of spherical aberration $C_s = C_{S3}$ for several different electron beam energies

3.1.1 BF-CTEM with Aberration Correctors

In BF, small aberrations are needed to produce a $\pi/2$ phase plate (Scherzer [443], Chang et al. [59], Lentzen [308], Erni [123]). For a CTEM with fixed fifth order spherical (C_{S5}) and controllable third order spherical aberration (C_{S3}) and defocus ($\Delta f = -C_{10}$), Scherzer [443] found the following condition to produce a $\pi/2 \pm \pi/4$ phase plate over the largest portion of the objective aperture:

$$\Delta f = -2(\lambda^2 C_{S5})^{1/3} \quad (3.18)$$

$$C_{S3} = -3.2(\lambda C_{S5}^2)^{1/3} \quad (3.19)$$

$$\alpha_{\max} = \frac{7}{4} \left(\frac{\lambda}{C_{S5}} \right)^{1/6} \quad (3.20)$$

with a resolution of:

$$d = \frac{4}{7} \left(C_{S5} \lambda^5 \right)^{1/6} \quad (3.21)$$

Figure 3.4 shows a graph of the BF-CTEM transfer function with a third order aberration corrector balancing the fifth order spherical aberration (C_{S5}) with third (C_{S3}) and first order aberrations (Δf). Successive terms in Eq. 2.6 have alternate signs. The C_5 term (fifth order spherical) is fixed and positive. The C_3 term (third order spherical) is set to be negative to balance C_5 and the C_1 term (defocus) is positive to balance the C_3 term.

3.2 Partial Coherence in BF-CTEM

In practice the electron microscope always has small deviations from the ideal. The incident illumination is never exactly collimated and parallel to the optic axis of the microscope. The electron energy is not completely monochromatic and the objective and condenser lens currents are never perfectly stable. The degree of collimation of the illumination incident on the specimen is related to the lateral coherence (i.e., spatial coherence) of the incident electron wave function and the stability of the beam energy and lens currents is related to the temporal coherence of the imaging process. The imaging described in the previous section assumes that these effects are negligible and that the imaging process is perfectly coherent. When the effects of a small spread in illumination angles and a small spread in beam energy and lens currents are included, the imaging process is said to be partially coherent. An analytical derivation of the effects of partial coherence on the transfer function in the weak phase object approximation has been given by Frank [142], Fejes [127], and Wade and Frank [515].

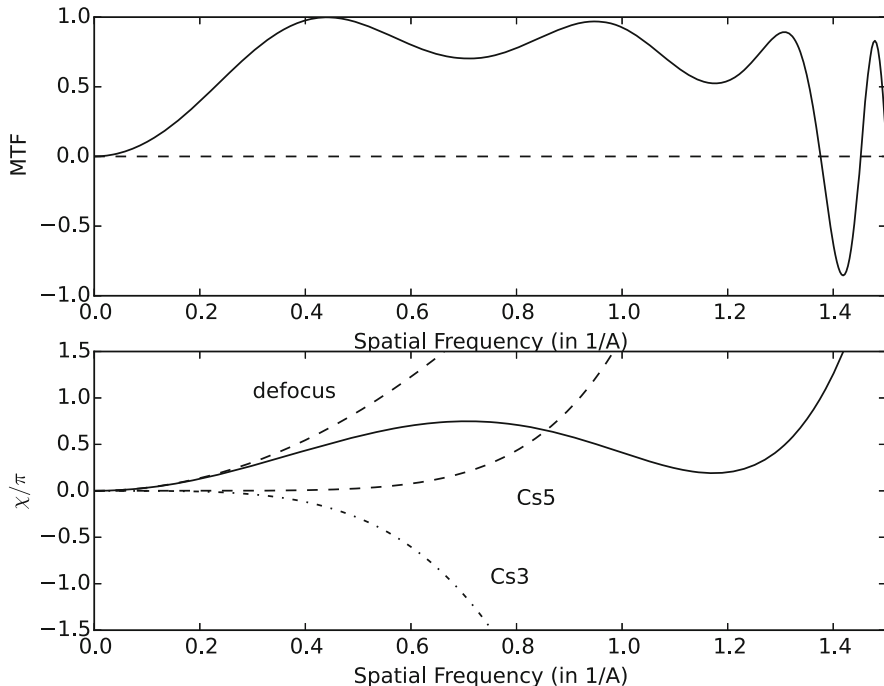


Fig. 3.4 BF-CTEM transfer function (top) with a third order aberration corrector with fixed fifth order spherical aberration for an electron energy of 200 keV. Third order spherical aberration and defocus are optimally adjusted to offset the fifth order spherical aberration using Scherzer's method. $C_{S5} = 50 \text{ mm}$, $C_{S3} = -59 \mu\text{m}$, $\Delta f = -C_1 = -136 \text{ \AA}$. The bottom curve shows the phase error χ and the various components due to each aberration

The transfer function oscillates both positive and negative. Partial coherence (for example, defocus shift due to beam energy or obj. lens current fluctuations) results in the superposition of adjacent portions of the transfer function (as in Fig. 3.5). When the transfer function is oscillating quickly (at high spatial frequencies) then partial coherence tends to reduce the transfer function to zero. Partial coherence limits the maximum information content of the image in the electron microscope by damping the high spatial frequency (large scattering angle) portion of the transfer function.

The electron beam illuminating the specimen (formed by the condenser system) will always have a small distribution of angles (see the right-hand side of Fig. 3.6). To calculate the effect on the image first consider an illumination at a single angle as shown in the left-hand side of Fig. 3.6. Previously in Eq. 3.3, the incident wave function was $\psi_{\text{inc}} \sim 1$, however, with the illumination at an angle β :

$$\psi_{\text{inc}}(\mathbf{x}) = \exp(2\pi i \mathbf{k}_\beta \cdot \mathbf{x}) \quad (3.22)$$

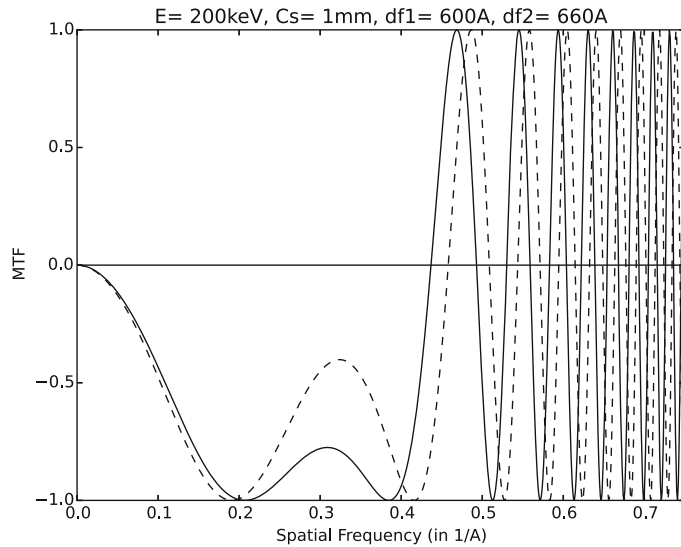


Fig. 3.5 BF-CTEM transfer function with two slightly different defocus values (solid line 600\AA , and dashed 660\AA) as might be caused by fluctuations in the objective lens current. When these are superposed in the image lower spatial frequencies are little affected but the high spatial frequencies tend to average to zero

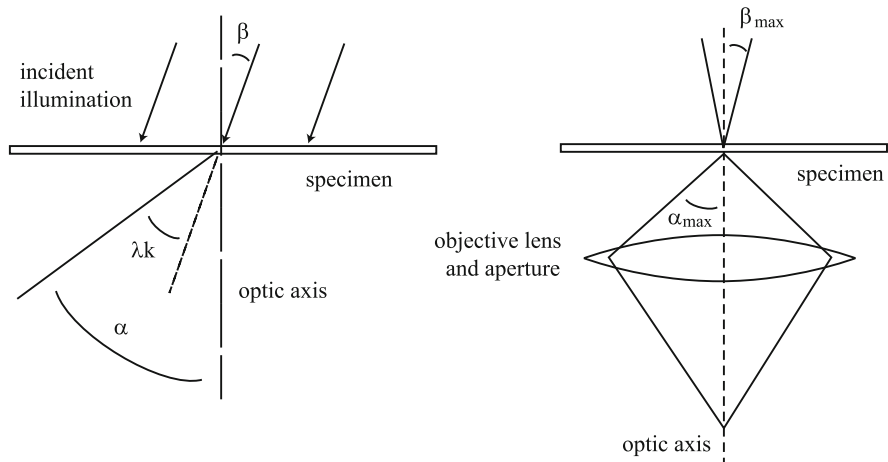


Fig. 3.6 Imaging with nonideal illumination. The incident electrons have an angle β . The specimen scatters at an angle λk and the final angle into the objective lens is α (angles measured with respect to the optic axis). A single electron trajectory is shown on the left and the total illumination of a single point on the image is shown on the right. β_{\max} is typically the condenser aperture and α_{\max} is the objective aperture

where $\mathbf{k}_\beta = \beta/\lambda$ and β is the angle of the incident illumination (with respect to the optic axis). Note that \mathbf{k}_β is a two-dimensional vector because β can vary in both the polar and azimuthal directions. The transmitted wave function (Eq. 3.3) now becomes:

$$\psi_t(\mathbf{x}) = t(\mathbf{x}) \exp(2\pi i \mathbf{k}_\beta \cdot \mathbf{x}) \quad (3.23)$$

Usually the condenser system will deliver a small cone of illumination angles onto the specimen. Typically each illumination angle will be incoherent with other illumination angles so the images due to each illumination angle should be summed incoherently by adding intensities $|\psi|^2$ and not amplitudes ψ . It is possible to operate a field emission gun to produce a coherent spread of illumination angles (in which case amplitudes and not intensities would be summed), however, this case will not be considered here. If $p(\mathbf{k}_\beta)$ represents the (probability) distribution of (incoherent) illumination angles, then Eq. 3.5 becomes:

$$\begin{aligned} g(\mathbf{x}) &= \int |\psi_i(\mathbf{x})|^2 p(\mathbf{k}_\beta) d^2 k_\beta \\ &= \int |[t(\mathbf{x}) \exp(2\pi i \mathbf{k}_\beta \cdot \mathbf{x})] \otimes h_0(\mathbf{x})|^2 p(\mathbf{k}_\beta) d^2 k_\beta \end{aligned} \quad (3.24)$$

A small spread in energy of the incident electron is equivalent to a small (incoherent) spread in defocus values due to the chromatic aberration of the objective lens. Fluctuations in the focusing currents in the objective lens also produce an incoherent spread in defocus values. When this spread in defocus values is combined and included in the image:

$$\begin{aligned} g(\mathbf{x}) &= \int |\psi_i(\mathbf{x})|^2 p(\mathbf{k}_\beta) p(\delta_f) d\delta_f d^2 k_\beta \\ &= \int |[t(\mathbf{x}) \exp(2\pi i \mathbf{k}_\beta \cdot \mathbf{x})] \otimes h_0(\mathbf{x}, \Delta f + \delta_f)|^2 p(\mathbf{k}_\beta) p(\delta_f) d\delta_f d^2 k_\beta \end{aligned} \quad (3.25)$$

where δ_f is the fluctuation in defocus and $p(\delta_f)$ is the distribution of this fluctuation. Both $p(\mathbf{k}_\beta)$ and $p(\delta_f)$ are normalized such that their integrated value is unity. This expression for $g(\mathbf{x})$ is formidable and should be treated numerically in general (see later chapters). However if the deviations from the ideal are assumed very small and the specimen is assumed to be a weak phase object, a modified transfer function can be obtained.

First examine the expression for the wave function in the image plane for one illumination angle and one defocus value:

$$\psi_i(\mathbf{x}) = [t(\mathbf{x}) \exp(2\pi i \mathbf{k}_\beta \cdot \mathbf{x})] \otimes h_0(\mathbf{x}) \quad (3.26)$$

Figure 3.6 shows that the tilt angle can appear in either the objective lens angle α or the incident wave function ψ_{inc} . To see this mathematically take the Fourier transform of ψ_i and use the Fourier convolution theorem:

$$\text{FT} \{ [t(\mathbf{x}) \exp(2\pi i \mathbf{k}_\beta \cdot \mathbf{x})] \otimes h_0(\mathbf{x}) \} = T(\mathbf{k} + \mathbf{k}_\beta) H_0(\mathbf{k}) \quad (3.27)$$

Now with a change of variable:

$$T(\mathbf{k} + \mathbf{k}_\beta) H_0(\mathbf{k}) = T(\mathbf{k}') H_0(\mathbf{k}' - \mathbf{k}_\beta) \quad (3.28)$$

The inverse Fourier transform is now an integration over \mathbf{k}' instead of \mathbf{k} (over all space) but gives the same result. This means that the image plane wave function can also be written as:

$$\psi_i(\mathbf{x}) = t(\mathbf{x}) \otimes h_0(\mathbf{x}, \mathbf{k}_\beta) \quad (3.29)$$

Using $h_0(\mathbf{x}, \mathbf{k}_\beta)$ will make the analytical calculation of the transfer function much simpler. This approximation would not be appropriate for thick specimens because the effect of the specimen is no longer a simple multiplicative function.

If the specimen is a weak phase object (Eq. 3.6), then the expression for the final image intensity will be similar to Eq. 3.9 except that the point spread function $h_0(\mathbf{x})$ of the objective lens will be integrated over illumination angles and defocus values as in Eq. 3.25. If \mathbf{k}_β is small, then the leading background constant can also be assumed to be close to unity (as in Eq. 3.8):

$$1 \otimes h_0(\mathbf{x}, \mathbf{k}_\beta) \sim 1 \quad (3.30)$$

The integral of the transfer function over a spread in illumination angles and defocus values using the dimensionless form of $\chi(\mathbf{K})$ is:

$$H_0(\mathbf{K}) = \int \exp\{-i\chi(\mathbf{K} + \mathbf{K}_\beta, D + D_p)p(D_p)p(\mathbf{K}_\beta)dD_p d^2 K_\beta \quad (3.31)$$

where the sign of \mathbf{K}_β has been changed to positive for simplicity (i.e., the integrand is symmetric) and:

$$\chi(\mathbf{K} + \mathbf{K}_\beta, D + D_p) = \pi[0.5(\mathbf{K} + \mathbf{K}_\beta)^4 - (D + D_p)(\mathbf{K} + \mathbf{K}_\beta)^2] \quad (3.32)$$

$p(\mathbf{K}_\beta)$ and $p(D_p)$ are the distribution of illuminations angles \mathbf{K}_β and defocus deviations D_p . The simplest assumption of a Gaussian distribution for each has the advantage of allowing an analytical solution.

$$p(\mathbf{K}_\beta) = \frac{1}{\pi K_s^2} \exp(-K_\beta^2/K_s^2) \quad (3.33)$$

$$p(D_p) = \frac{1}{\sqrt{\pi} D_s} \exp(-D_p^2/D_s^2) \quad (3.34)$$

where K_s is the $1/e$ width of the spread in illumination angles and D_s is the $1/e$ spread in defocus values. Taylor expanding $\chi(\mathbf{K}, D)$ to lowest order in \mathbf{K}_β and D_p :

$$\begin{aligned}\chi(\mathbf{K} + \mathbf{K}_\beta, D + D_p) &\sim \\ \chi(\mathbf{K}, D) + \mathbf{K}_\beta \cdot \mathbf{W}_1 + D_p W_2 + D_p \mathbf{K}_\beta \cdot \mathbf{W}_3 + \dots\end{aligned}\quad (3.35)$$

where

$$\mathbf{W}_1 = \frac{\partial \chi(\mathbf{K}, D)}{\partial \mathbf{K}} = 2\pi(|\mathbf{K}|^2 - D)\mathbf{K} \quad (3.36)$$

$$W_2 = \frac{\partial \chi(\mathbf{K}, D)}{\partial D} = -\pi K^2 \quad (3.37)$$

$$\mathbf{W}_3 = \frac{\partial^2 \chi(\mathbf{K}, D)}{\partial \mathbf{K} \partial D} = -2\pi \mathbf{K} \quad (3.38)$$

\mathbf{W}_1 and \mathbf{W}_3 are two-dimensional vector quantities. Equation 3.31 now becomes:

$$\begin{aligned}H_0(\mathbf{K}) = \frac{1}{\pi K_s^2 \sqrt{\pi} D_s} \exp[-i \chi(\mathbf{K}, D)] \int & \exp[-i \mathbf{K}_\beta \cdot \mathbf{W}_1 \\ & - i D_p W_2 - i D_p \mathbf{K}_\beta \cdot \mathbf{W}_3 - \mathbf{K}_\beta^2 / K_s^2 - D_p^2 / D_s^2] d^2 K_\beta d D_p\end{aligned}\quad (3.39)$$

First do the integration over \mathbf{K}_β :

$$\begin{aligned}H_0(\mathbf{K}) = \frac{1}{\sqrt{\pi} D_s} \exp[-i \chi(\mathbf{K}, D)] \int & \exp[-0.25 K_s^2 |\mathbf{W}_1 + D_p \mathbf{W}_3|^2 - \\ & i D_p W_2 - D_p^2 / D_s^2] d D_p\end{aligned}\quad (3.40)$$

Next do the integral over D_p :

$$\begin{aligned}H_0(\mathbf{K}) = \frac{1}{\sqrt{1 + E K^2}} \exp & \left[-i \chi(\mathbf{K}, D) + i \frac{D_s^2 K_s^2 \mathbf{W}_1 \cdot \mathbf{W}_3 W_2}{4(1 + E K^2)} \right] \\ & \times \exp \left[-0.25 K_s^2 |\mathbf{W}_1|^2 + \frac{D_s^2 [(0.5 K_s^2 \mathbf{W}_1 \cdot \mathbf{W}_3)^2 - W_2^2]}{4(1 + E K^2)} \right]\end{aligned}\quad (3.41)$$

Aside If the cross term $\mathbf{W}_3 = 0$ (implying $E = 0$) is neglected a somewhat more elegant expression results:

$$H_0(\mathbf{K}) = \exp[-i \chi(\mathbf{K}, D) - 0.25 K_s^2 |\mathbf{W}_1|^2 - 0.25 D_s^2 W_2^2] \quad (3.42)$$

Next substitute for the intermediate variables:

$$H_0(\mathbf{K}) = \exp \left[-i \frac{\pi K^2}{1 + EK^2} (0.5K^2(1 - EK^2) - D) \right] \\ \times \frac{1}{\sqrt{1 + EK^2}} \exp \left[\frac{-\pi^2 K_s^2 (K^2 - D)^2 K^2 - 0.25\pi^2 D_s^2 K^4}{1 + EK^2} \right] \quad (3.43)$$

$$\text{where } E = \pi^2 K_s^2 D_s^2$$

Now take the imaginary part to form the transfer function for the weak phase object image approximation (Eqs. 3.2 and 3.10) and substitute the dimensional form of the electron microscope parameters:

$$H_{WP}(k) = \sin \left[\frac{\pi \lambda k^2}{1 + \epsilon k^2} (0.5C_s(1 - \epsilon k^2)\lambda^2 k^2 - \Delta f) \right] \\ \times \frac{1}{\sqrt{1 + \epsilon k^2}} \exp \left[-\frac{[\pi \lambda k_s k (C_s \lambda^2 k^2 - \Delta f)]^2 + 0.25(\pi \lambda \Delta_0 k^2)^2}{1 + \epsilon k^2} \right] \quad (3.44)$$

where $\epsilon = (\pi \lambda k_s \Delta_0)^2$, $k_s = K_s(C_s \lambda^3)^{-1/4}$ and $\Delta_0 = D_s \sqrt{C_s \lambda}$. This transfer function (Eq. 3.44) should be substituted into the image model (Eqs. 3.9 and 3.10). Apart from the extra term with ϵ (typically small) the oscillatory portion of the transfer functions is the same as the coherent case. The main change is the addition of a damping envelope that attenuates the transfer function at high spatial frequencies. In a practical sense $\beta = \lambda k_s$ is the condenser (illumination) semiangle and Δ_0 is approximately the rms value of all of the appropriate fluctuations multiplied by the chromatic aberration C_c .

$$\Delta_0 \sim C_c \sqrt{\left(\frac{\Delta E}{E} \right)^2 + \left(2 \frac{\Delta I}{I} \right)^2 + \left(\frac{\Delta V}{V} \right)^2} \quad (3.45)$$

where E , I , and V are the electron energy, lens currents, and acceleration voltage, respectively, and ΔE , ΔI , and ΔV are the $1/e$ width of their fluctuations.

A graph of the WPO transfer function with (Eq. 3.44) and without (Eq. 3.10) partial coherence is shown in Fig. 3.7 for typical values of the electron optical parameters. It is interesting to note that the cross term W_3 produced the correction ϵ in the transfer function which can move the zero crossings in the transfer function but seems to have a negligible effect under Scherzer conditions.

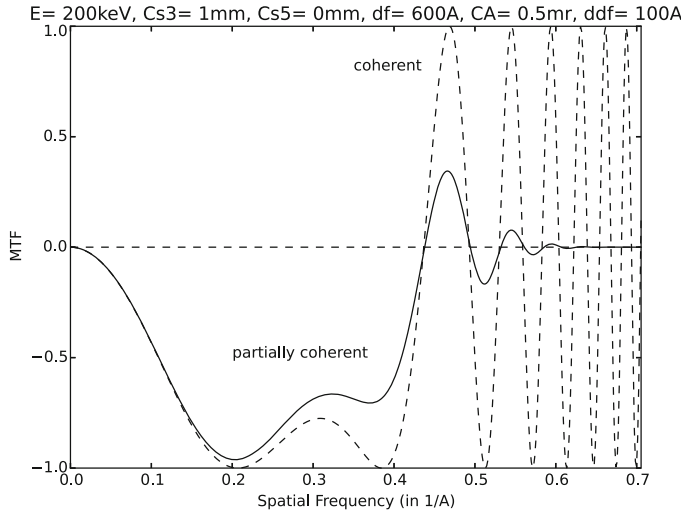


Fig. 3.7 The BF phase contrast transfer function with and without partial coherence (CA = condenser aperture)

3.2.1 Aberration Correctors and Partial Coherence

It is straightforward but somewhat tedious to add higher order aberrations to the above expressions for partial coherence. The transfer function with the fifth order spherical aberration is:

$$\begin{aligned}
 H_{WP}(k) &= \frac{1}{\sqrt{1 + \epsilon k^2}} \\
 &\times \sin \left[\frac{\pi \lambda k^2}{1 + \epsilon k^2} \left(\frac{1}{3} C_{S5} (1 - 2\epsilon k^2) \lambda^4 k^4 + 0.5 C_{S3} (1 - \epsilon k^2) \lambda^2 k^2 - \Delta f \right) \right] \\
 &\times \exp \left[-\frac{[\pi \lambda k_s k (C_{S5} \lambda^4 k^4 + C_{S3} \lambda^2 k^2 - \Delta f)]^2 + 0.25 (\pi \lambda \Delta_0 k^2)^2}{1 + \epsilon k^2} \right]
 \end{aligned} \quad (3.46)$$

Although an aberration corrector can produce very high resolution it is still very sensitive to partial coherence. Figure 3.8 shows the transfer function for high resolution with small amounts of partial coherence. The attenuation envelope for defocus spread (chromatic aberration) is not changed much by the corrector. Very small amounts of chromatic aberration destroy the transfer function and BF phase contrast with a geometric aberration corrector very likely requires a chromatic aberration corrector as well.

Terms such as the spherical aberration coefficient $C_s = C_{S3}$ are, however, no longer really constant. The spherical aberration of the round objective lens

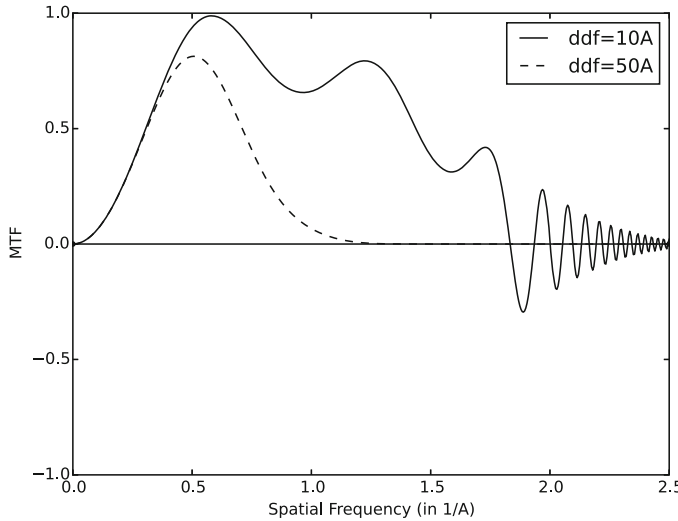


Fig. 3.8 The BF phase contrast transfer function (for thin specimens) with an aberration corrector and partial coherence for an electron energy of 300 keV. Third order spherical aberration and defocus are optimally adjusted to offset the fifth order spherical aberration using Scherzer's method. The condenser illumination angle was $\beta_{\max} = 0.05$ mrad, and $C_{S5} = 30$ mm, $C_{S3} = -38.7$ μm , $\Delta f = -97.6$ Å. Two different defocus spreads are shown to illustrate the effect of chromatic aberration

is essentially constant because it is due to the fixed geometry of the magnetic material used to shape the focusing fields and to lowest order insensitive to small fluctuations in the lens current (which instead produces fluctuations in defocus). An aberration corrector generates a large negative C_{S3} from a combination of strong focusing multipole fields. Fluctuations in currents in these elements can produce fluctuations in the net C_{S3} coefficients as well as all of the other dozen or so aberration coefficients. There can be of order 100 or more focusing currents (etc.) in the corrector that have their own fluctuations. These potentially cause all of the aberration coefficients to fluctuate (more study is needed here to determine how these all interact; may vary with the specific design of each corrector). Various groupings of the multipoles combine to form each aberrations (some elements may be a part of more than one aberration). If the cross terms between aberrations are ignored for simplicity, the aberration phase factor becomes:

$$H_0(\mathbf{K}) = \exp \left[-i\chi(\mathbf{K}, D) - \sum_k 0.25 W_k \left| \frac{\partial \chi}{\partial C_k} \right|^2 \right] \quad (3.47)$$

where W_k is the width of the fluctuations for parameter C_k and the summation is over all aberration components (C_k such as defocus, spherical aberrations C_{S3} , C_{S5} , etc.) and the illumination angle. Even though the aberration corrector can effectively

negate the existing aberrations in the main (round) objective lens, the fluctuations in the corrector causing partial coherence will be centered about the much larger aberrations (such as C_{S3}) of the original objective lens making this effect much larger than might be expected.

It may be easier to numerically integrate over small fluctuation in all parameters. Gauss–Hermite quadrature is very efficient for integration over a Gaussian weighting. With this many parameters it might even be worthwhile performing a Monte Carlo integration over a range of parameter values (which becomes more efficient when integrating over more than four dimensions). It is also not clear how fluctuations in the various aberration coefficient are coupled (mathematically in the aberration function and practically through common coils and currents).

3.3 Detector Influence (CTEM)

The detector that records the image may itself have a large influence on the image quality. Currently the detector is usually a CCD camera (plus scintillator). Film (or plates) were the most common detector in the not so distant past. It was common to record the image at not very high magnification and then magnify further in the darkroom enlarger, in which case the film may produce a large effect. Film (or plates) have a transfer function of their own (for example, Downing and Grano [98]). CCD detectors also have an associated transfer function which can be significant (Thust [488]). The effects of the detector can be included in the image by convolving the electron image (Eq. 3.5) with detector transfer function $h_{\text{det}}(\mathbf{x})$:

$$g(\mathbf{x}) = |\psi_t(\mathbf{x}) \otimes h_0(\mathbf{x})|^2 \otimes h_{\text{det}}(\mathbf{x}) \quad (3.48)$$

The detector may reduce the contrast in the high-resolution component of an image (for example, lattice fringes) by a large factor (like two or three).

3.4 Incoherent Imaging of Thin Specimens (CTEM)

The electron microscope image is generated from the electrons scattered by the specimen. For the electron wave scattered from two points of the specimen to interfere the incident electron wave from the condenser system must be coherent over the distance between these points (i.e., the specimen is not self-luminous). The illuminating electrons (using a thermionic source) are produced by a spatially incoherent, quasi-monochromatic source with nonzero size. The source size is typically translated into a maximum condenser angle β_{\max} (see Fig. 3.6). The electron rays incident on the specimen are not perfectly parallel but subtend a small cone of angles β_{\max} at the specimen plane. The lateral coherence length perpendicular to the optic axis (see section 10.4.2 of Born and Wolf [42]) of the illuminating electron wave function is approximately given by:

$$\Delta x_{coh} \sim \frac{0.16\lambda}{\beta_{max}} \quad (3.49)$$

If the coherence length is much smaller than the resolution element of the image, then the imaging will be essentially incoherent. If the coherence length is much bigger than the resolution element, then the imaging process will be essentially coherent. The resolution element of the image is approximately $d \sim \lambda/\alpha_{max}$, where α_{max} is the maximum objective angle (i.e., the size of the objective aperture). Combining these two expressions yields an approximate criteria for the image coherence:

$$\begin{aligned} \beta_{max} &<< 0.16\alpha_{max} && \text{coherent imaging} \\ \beta_{max} &>> 0.16\alpha_{max} && \text{incoherent imaging} \end{aligned} \quad (3.50)$$

In between these two extremes the image is partially coherent.

If the image is coherent, then the amplitudes ψ of the scattered electrons add, and if the image is incoherent, then the intensities of the scattered electrons $|\psi|^2$ add. The final image recording process is only sensitive to the intensity of the electrons and not their amplitudes. This means that phase contrast must have a coherent image process to be sensitive to the phase of the electron via some interference process. Reducing the coherence of the imaging process should also reduce the phase contrast transfer function. The ratio β_{max}/α_{max} can be used to control the coherence of the imaging process.

Because the phase contrast image will likely disappear in an incoherent image the transmission function should include the possibility of amplitude contrast. Assuming that the specimen is a weak phase, weak amplitude object yields a transmission function:

$$t(\mathbf{x}) \sim \exp[i\sigma_e v_z(\mathbf{x}) - u(\mathbf{x})] \sim 1 + i\sigma_e v_z(\mathbf{x}) - u(\mathbf{x}) + \dots \quad (3.51)$$

where $u(\mathbf{x})$ is the amplitude component of the specimen transmission function which can arise from scattering outside of the objective aperture (it is preceded by a minus sign because electrons cannot be created with elastic scattering). Alternately $u(\mathbf{x})$ can be considered as the next term in the Taylor expansion of $\exp[i\sigma_e v_z(\mathbf{x})]$, where $u(\mathbf{x}) \propto v_z^2(\mathbf{x})$. Both $\sigma_e v_z(\mathbf{x})$ and $u(\mathbf{x})$ are small compared to unity. The expression for the image intensity (Eq. 3.25) now becomes:

$$\begin{aligned} g(\mathbf{x}) &= \int |\psi_i(\mathbf{x})|^2 p(\mathbf{k}_\beta) p(\delta_f) d\delta_f d^2 k_\beta \\ &= \int |[(1 + i\sigma_e v_z(\mathbf{x}) - u(\mathbf{x})) \exp(2\pi i \mathbf{k}_\beta \cdot \mathbf{x})] \otimes h_0(\mathbf{x}, \Delta f + \delta_f)|^2 \\ &\quad \times p(\mathbf{k}_\beta) p(\delta_f) d\delta_f d^2 k_\beta \end{aligned} \quad (3.52)$$

The objective aperture will play a significant role in the following derivation so it should be included with the point spread function $h_0(\mathbf{x})$ or equivalently the transfer function:

$$H_0(\mathbf{k}) = \exp[-i\chi(\mathbf{k}, \Delta f + \delta_f)]A(\mathbf{k}) \quad (3.53)$$

where $A(\mathbf{k})$ is the aperture function:

$$\begin{aligned} A(\mathbf{k}) &= 1 ; \lambda|\mathbf{k}| = \alpha < \alpha_{\max} \\ &= 0 ; \text{ otherwise} \end{aligned} \quad (3.54)$$

and α_{\max} is the maximum semiangle allowed by the objective aperture.

Now expand the integrand keeping only the terms of the lowest order in $\sigma_e v_z(\mathbf{x})$ and $u(\mathbf{x})$ and drop the explicit reference to the independent arguments for simplicity:

$$\begin{aligned} g(\mathbf{x}) &= \int \{ |\exp(2\pi i\mathbf{k}_\beta \cdot \mathbf{x}) \otimes h_0|^2 \\ &\quad + [\exp(2\pi i\mathbf{k}_\beta \cdot \mathbf{x}) \otimes h_0]^* [i\sigma_e v_z \exp(2\pi i\mathbf{k}_\beta \cdot \mathbf{x}) \otimes h_0] \\ &\quad - [\exp(2\pi i\mathbf{k}_\beta \cdot \mathbf{x}) \otimes h_0]^* [u \exp(2\pi i\mathbf{k}_\beta \cdot \mathbf{x}) \otimes h_0] \\ &\quad + [\text{complex conjugate}] \} p(\mathbf{k}_\beta) p(\delta_f) d\delta_f d^2 k_\beta \end{aligned} \quad (3.55)$$

The first term is a constant of order unity that does not vary with position in the image. The rest of the right-hand side is rather unpleasant but can be simplified a little. Because $h_0(\mathbf{x})$ is simplest to write in reciprocal space, look at the Fourier transform of the term containing $v_z(\mathbf{x})$, and for simplicity drop explicit reference to the defocus Δf and its fluctuations δ_f :

$$\begin{aligned} FT\{[\exp(2\pi i\mathbf{k}_\beta \cdot \mathbf{x}) \otimes h_0]^* [i\sigma_e v_z \exp(2\pi i\mathbf{k}_\beta \cdot \mathbf{x}) \otimes h_0]\} \\ &= [\delta(\mathbf{k} - \mathbf{k}_\beta) H_0(-\mathbf{k})]^* \otimes [i\sigma_e V(\mathbf{k} + \mathbf{k}_\beta) H_0(\mathbf{k})] \\ &= i\sigma_e \int \delta(\mathbf{k}' - \mathbf{k}_\beta) H_0^*(-\mathbf{k}') V(\mathbf{k} + \mathbf{k}_\beta - \mathbf{k}') H_0(\mathbf{k} - \mathbf{k}') d\mathbf{k}' \\ &= i\sigma_e V(\mathbf{k}) H_0^*(-\mathbf{k}_\beta) H_0(\mathbf{k} - \mathbf{k}_\beta) \end{aligned} \quad (3.56)$$

where $\delta(\mathbf{k})$ is the Dirac delta function.

This expression is now a simple product so when inverse Fourier transformed back into real space $\sigma_e v_z(\mathbf{x})$ is convolved with a new form of the point spread function. Repeating this procedure with the amplitude component and combining the complex conjugate terms yield:

$$g(\mathbf{x}) \sim C_0 + 2\sigma_e v_z(\mathbf{x}) \otimes h_{WP}(\mathbf{x}) - 2u(\mathbf{x}) \otimes h_{WA}(\mathbf{x}) \quad (3.57)$$

where C_0 is a background constant of order unity:

$$C_0 = \int |\exp(2\pi i \mathbf{k}_\beta \cdot \mathbf{x}) \otimes h_0|^2 p(\mathbf{k}_\beta) p(\delta_f) d\delta_f d^2 k_\beta \quad (3.58)$$

and the transfer function for a weak phase object is:

$$\begin{aligned} FT[h_{WP}(\mathbf{x})] &= H_{WP}(\mathbf{k}) \\ &= \text{Imag} \int H_0(\mathbf{k}_\beta - \mathbf{k}) H_0^*(-\mathbf{k}_\beta) p(\mathbf{k}_\beta) p(\delta_f) d\delta_f d^2 k_\beta \end{aligned} \quad (3.59)$$

and the transfer function for a weak amplitude object is:

$$\begin{aligned} FT[h_{WA}(\mathbf{x})] &= H_{WA}(\mathbf{k}) \\ &= \text{Real} \int H_0(\mathbf{k}_\beta - \mathbf{k}) H_0^*(-\mathbf{k}_\beta) p(\mathbf{k}_\beta) p(\delta_f) d\delta_f d^2 k_\beta \end{aligned} \quad (3.60)$$

With the assumption of a small Gaussian spread of defocus (see Eq. 3.34) the integral over defocus can be done analytically yielding an expression for the transfer function for a weak phase object:

$$\begin{aligned} H_{WP}(\mathbf{k}) &= \int A(\mathbf{k}_\beta) A(\mathbf{k}_\beta - \mathbf{k}) \sin[\chi(\mathbf{k}_\beta - \mathbf{k}) - \chi(\mathbf{k}_\beta)] \\ &\quad \times \exp\{-0.25\pi^2\lambda^2\Delta_0^2[|\mathbf{k}_\beta - \mathbf{k}|^2 - |\mathbf{k}_\beta|^2]^2\} p(\mathbf{k}_\beta) d^2 k_\beta \end{aligned} \quad (3.61)$$

and an expression for the transfer function for a weak amplitude object:

$$\begin{aligned} H_{WA}(\mathbf{k}) &= \int A(\mathbf{k}_\beta) A(\mathbf{k}_\beta - \mathbf{k}) \cos[\chi(\mathbf{k}_\beta - \mathbf{k}) - \chi(\mathbf{k}_\beta)] \\ &\quad \times \exp\{-0.25\pi^2\lambda^2\Delta_0^2[|\mathbf{k}_\beta - \mathbf{k}|^2 - |\mathbf{k}_\beta|^2]^2\} p(\mathbf{k}_\beta) d^2 k_\beta \end{aligned} \quad (3.62)$$

The only difference between these two transfer functions is the switch between sin and cos. If \mathbf{k}_β is large then neither of these integrals can be done analytically and both must be done numerically (in two dimensions).

The phase and amplitude transfer functions are shown in Figs. 3.9 and 3.10, respectively, using Scherzer defocus and the Scherzer aperture. The phase contrast transfer function is initially similar to the coherent transfer (see Fig. 3.2) function but decays to zero as the condenser angle β_{\max} is increased as expected (i.e., when the image is incoherent there cannot be any interference to produce phase contrast). The amplitude contrast transfer function, however, transforms from an oscillatory function into a smoothly falling function similar to the transfer function in normal light optics (Black and Linfoot [37]). Note also that the first zero of the transfer function has moved by almost a factor of two in the incoherent ($\beta_{\max}/\alpha_{\max} = 1$) case. The improvement in resolution from incoherent imaging

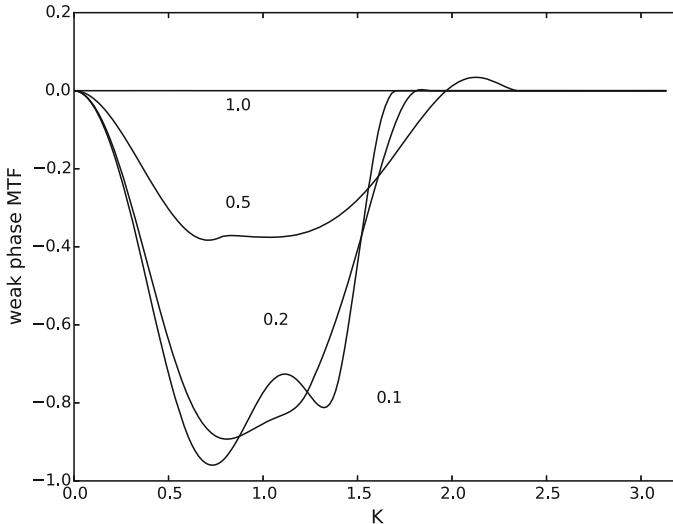


Fig. 3.9 BF-CTEM transfer function for weak phase objects with increasing condenser angle β_{\max} as a function of dimensionless spatial frequency K (Scherzer defocus and aperture α_{\max}). $\beta_{\max}/\alpha_{\max} = 0.1, 0.2, 0.5, 1.0$. The phase contrast transfer function is zero when the image process is incoherent $\beta_{\max}/\alpha_{\max} \geq 1$

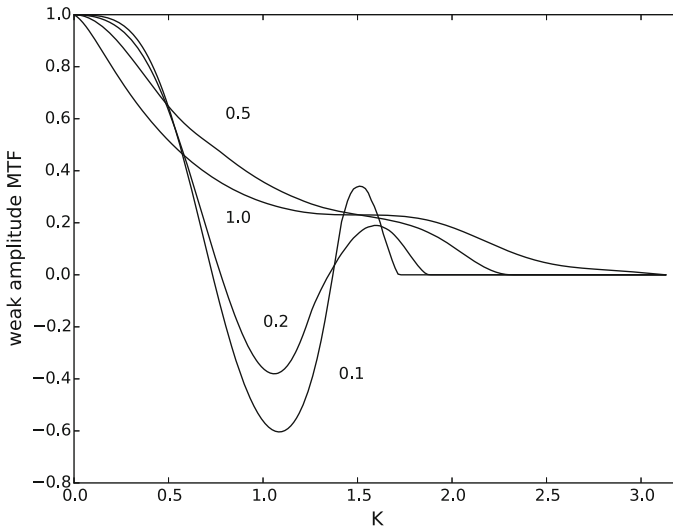


Fig. 3.10 BF-CTEM transfer function for weak amplitude objects with increasing condenser angle β_{\max} as a function of dimensionless spatial frequency K (Scherzer defocus and aperture α_{\max}). $\beta_{\max}/\alpha_{\max} = 0.1, 0.2, 0.5, 1.0$. The amplitude contrast transfer function is similar to normal light optics when the image process is incoherent $\beta_{\max}/\alpha_{\max} \geq 1$

over coherent imaging has been known for a long time (Rayleigh [411] and Goodman [161]). The essential features of this section were discussed by Hanszen [188], Hanszen and Trepte [189], and Thomson [486].

3.5 Annular Dark Field STEM

The order of the optical components of the STEM (Fig. 2.4) is reversed from that of the CTEM (Fig. 2.3). The objective lens is before the specimen and forms a focused probe on the specimen. The portion of the electrons transmitted through the specimen that fall on the detector form the image brightness at one point in the image. A whole image is built up by scanning the focused probe over the specimen and recording the transmitted intensity at each position of the probe. In bright field the detector integrates (incoherently) over a very small angle centered about zero scattering angle, and in annular dark field (ADF) the detector integrates everything except the center regions. The ADF-STEM image would be equivalent to the BF-CTEM image using incoherent hollow cone illumination by the reciprocity theorem (Engel [117]). In practice a CTEM condenser system may not be able to handle the large angles (typically 100–300 mrad at 100 keV) equivalent to the angles in the ADF-detector. Alternately an image similar to an ADF-STEM image but with reversed contrast may be obtained using BF-CTEM with a large solid cone that is mirror image of hollow cone illumination (Kirkland [272]). The simplified image model discussed in this section can be referred to as the incoherent image model.

A focused probe is calculated by integrating the aberration wave function $\exp[-i\chi(k)]$ over the objective aperture with translation to a particular point in the image. Figure 3.11 shows the relative placement of the wave functions in the STEM column. The aberrated electron probe wave function in the plane of the specimen when deflected to position \mathbf{x}_p is:

$$\psi_p(\mathbf{x}, \mathbf{x}_p) = A_p \int_0^{k_{\max}} \exp[-i\chi(\mathbf{k}) - 2\pi i \mathbf{k} \cdot (\mathbf{x} - \mathbf{x}_p)] d^2\mathbf{k} \quad (3.63)$$

where $\lambda k_{\max} = \alpha_{\max}$ is the maximum angle in the objective aperture and A_p is a normalization constant chosen to yield;

$$\int |\psi_p(\mathbf{x}, \mathbf{x}_p)|^2 d^2\mathbf{x} = 1 \quad (3.64)$$

With this normalization the total incident intensity in the electron probe is also unity (alternately the probe integral could be scaled to yield the actual value of the beam current in some appropriate choice of units). The probe is really just the demagnified image of the source and this expression assumes that the electron source (the electron gun demagnified by the condenser system) has a negligible size in the plane of the specimen (discussed later in Sect. 3.5.2). The probe size is

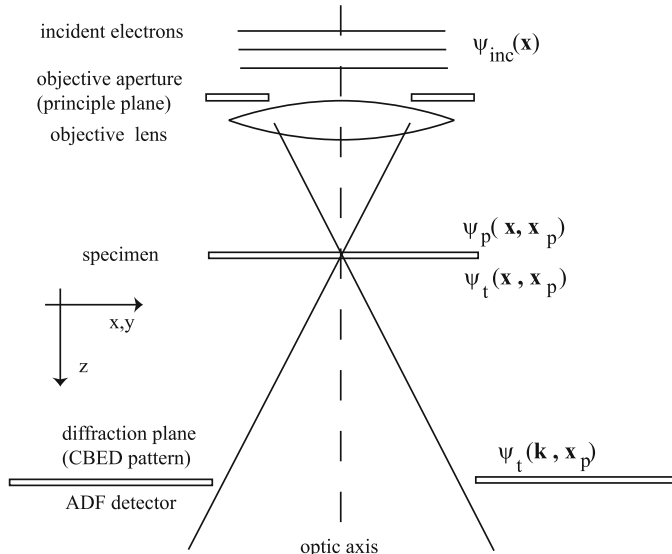


Fig. 3.11 Electron wave functions in the STEM column

limited instead by the aberrations of the objective lens. A dedicated STEM would usually use a high brightness field emission gun with a small virtual source size so that there is enough current left after demagnification to get a large enough signal to detect. Deflecting the beam to different positions on the specimen changes the angles through the objective lens. At high resolution this angle is of order 100 \AA divided by the focal length of the objective lens (of order 1 mm) producing a deflection angle of order 0.01 mrad which is negligible compared to a typical angle of 10 mrad in the objective aperture (large deflection angles would change the apparent aberrations but only occur at low magnification).

The electron probe passes through the specimen and is modulated by the specimen transmission function $t(\mathbf{x})$ (identical to the transmission function for the CTEM). $t(\mathbf{x})$ is in general a complex valued function for a weak phase, weak amplitude object (see Eq. 3.51). The transmitted wave function is:

$$\psi_t(\mathbf{x}, \mathbf{x}_p) = t(\mathbf{x})\psi_p(\mathbf{x}, \mathbf{x}_p) \quad (3.65)$$

Again a discussion of the effects of specimen thickness on the transmission function will be deferred to later chapters. This wave function is then diffracted onto the detector plane (represented by a Fourier transform).

$$\Psi_t(\mathbf{k}, \mathbf{x}_p) = FT[\psi_t(\mathbf{x}, \mathbf{x}_p)] = \int \exp(2\pi i \mathbf{k} \cdot \mathbf{x}) \psi_t(\mathbf{x}, \mathbf{x}_p) d^2\mathbf{x} \quad (3.66)$$

The intensity of this wave function $|\Psi_t(\mathbf{k}, \mathbf{x}_p)|^2$ as a function of scattering angle $\lambda\mathbf{k}$ is the convergent beam electron diffraction CBED pattern.

The CBED pattern is incoherently integrated over the detector geometry and the result is the final STEM image signal $g(\mathbf{x}_p)$ for one probe position \mathbf{x}_p .

$$g(\mathbf{x}_p) = \int |\Psi_t(\mathbf{k}, \mathbf{x}_p)|^2 D(\mathbf{k}) d^2\mathbf{k} \quad (3.67)$$

where $D(\mathbf{k})$ is the detector function.

$$D(\mathbf{k}) = 1 \text{ for } k_{D\min} \leq k \leq k_{D\max} \quad (3.68)$$

$$= 0 \text{ otherwise} \quad (3.69)$$

where $\lambda k_{D\min}$ and $\lambda k_{D\max}$ are the inner and outer angles of the ADF detector. This process is repeated for each probe position \mathbf{x}_p .

Equation 3.67 is difficult to intuitively relate to any specific structure in the specimen (later chapters will treat this equation more exactly using numerical calculations). However with some approximations a linear image model can be derived that is easier to understand. The ADF detector should go to very large angles (of order 200–300 mrad or more at 100 keV) so that all electrons that are incident on the specimen either fall on the ADF detector or go through the central hole in the ADF detector. This means that the signal formed by integrating all of the electrons in the central hole in the ADF detector is just one minus the ADF signal (where the total incident intensity is assumed to be unity). This effective signal from the central hole in the ADF detector is also equivalent to the BF-CTEM signal (via the reciprocity theorem) with a very large condenser illumination angle $\beta_{\max}/\alpha_{\max} \gg 1$. Therefore the ADF image process is incoherent if $k_{D\min} \gg k_{\max}$ (see Sect. 3.4). If the outer dimension of the ADF detector is essentially infinite then the large diameter of the central hole in the ADF detector produces an incoherent image. This means that phase contrast should be negligible and the image should be predominately amplitude contrast. Simple imaging approximations for ADF-STEM have been considered by Misell et al. [348], Cowley [75], Spence [472], Jesson and Pennycook [244], Treacy and Gibson [494], Loane et al. [317], and Jones and Nellist [249].

An approximate linear image model for thin specimens assuming an incoherent image process is:

$$g(\mathbf{x}) = f(\mathbf{x}) \otimes h_{\text{ADF}}(\mathbf{x}) \quad (3.70)$$

where the specimen function $f(\mathbf{x})$ is approximately the probability for scattering to the large angles of the ADF detector. If the specimen is modeled as a collection of isolated atoms with the signal from each atom j at position \mathbf{x}_j denoted by $S_j(\mathbf{x}_j)$ the total signal is approximately:

$$f(\mathbf{x}) = \sum_j S_j(\mathbf{x}_j) \quad (3.71)$$

$$S_j(\mathbf{x}_j) \sim \int D(\mathbf{k}) \frac{\partial \sigma_j(\mathbf{x})}{\partial k_s} d^2 k_s = \int_{k_{D\min}}^{k_{D\max}} \frac{\partial \sigma_j(\mathbf{x})}{\partial k_s} d^2 k_s \quad (3.72)$$

$\partial \sigma / \partial k_s$ is the partial cross section (the square of the scattering factor, calculated in the eikonal or Moliere approximate in Eq. 5.18) for atom j to scatter to angle k_s . The scattering from each atom is assumed to be independent of the scattering from all other atoms (which in general may not be true, see later chapters for thick specimens). With the incoherent image assumption an ADF-STEM image of a very thin specimen is essentially a mass thickness map of the specimen. The calculation with this approximation is simple enough to perform interactively on most computers and is useful to quickly build intuition on the imaging process although it may not be quantitatively accurate. This simple incoherent image model also is close to the assumed image models for a variety of sophisticated image restoration algorithms such as the Richardson-Lucy [320, 421] and maximum entropy methods (for example, [16]) so these methods can then be easily applied to ADF-STEM images (for example, Kirkland [269, 277]).

The point spread function (with the assumption of an incoherent image model) is just the intensity distribution in the focused probe. The aberration limited probe is:

$$\begin{aligned} h_{\text{ADF}}(\mathbf{x}) &= |\psi_p(\mathbf{x})|^2 \\ &= A_p \left| \int_0^{k_{\max}} \exp[-i\chi(\mathbf{k}) - 2\pi i \mathbf{k} \cdot \mathbf{x}] d^2 \mathbf{k} \right|^2 \end{aligned} \quad (3.73)$$

The constant A_p is chosen to normalize the point spread function to have a total integrated value of unity. Furthermore if the astigmatism is negligible, then the azimuthal integral can be done analytically leaving a one-dimensional integral for the probe intensity:

$$h_{\text{ADF}}(r) = A_p \left| \int_0^{k_{\max}} \exp[-i\chi(k)] J_0(2\pi kr) k dk \right|^2 \quad (3.74)$$

where $J_0(x)$ is the zeroth order Bessel function of the first kind and r is the radial coordinate. $\chi(k)$ is a function of only the magnitude of k when astigmatism is not present. This integral cannot be done analytically and must be done numerically. The point spread function is plotted in Fig. 3.12 versus position (on the specimen). Figure 3.13 shows a more condensed form of this graph for various values of defocus and objective aperture. The graph has been scaled to make $h_{\text{ADF}}(0) = 1$. Figure 3.13a shows the probe profile for Scherzer defocus and aperture with a full width at half max of approximately $0.43(C_s \lambda^3)^{1/4}$.

Fig. 3.12 The STEM probe intensity (approximate point spread function) when astigmatism and source size are negligible versus position. (200 keV, $C_s = 1.3$ mm, $\Delta f = 571 \text{ \AA}$, $\alpha_{\max} = 9.4 \text{ mrad}$)

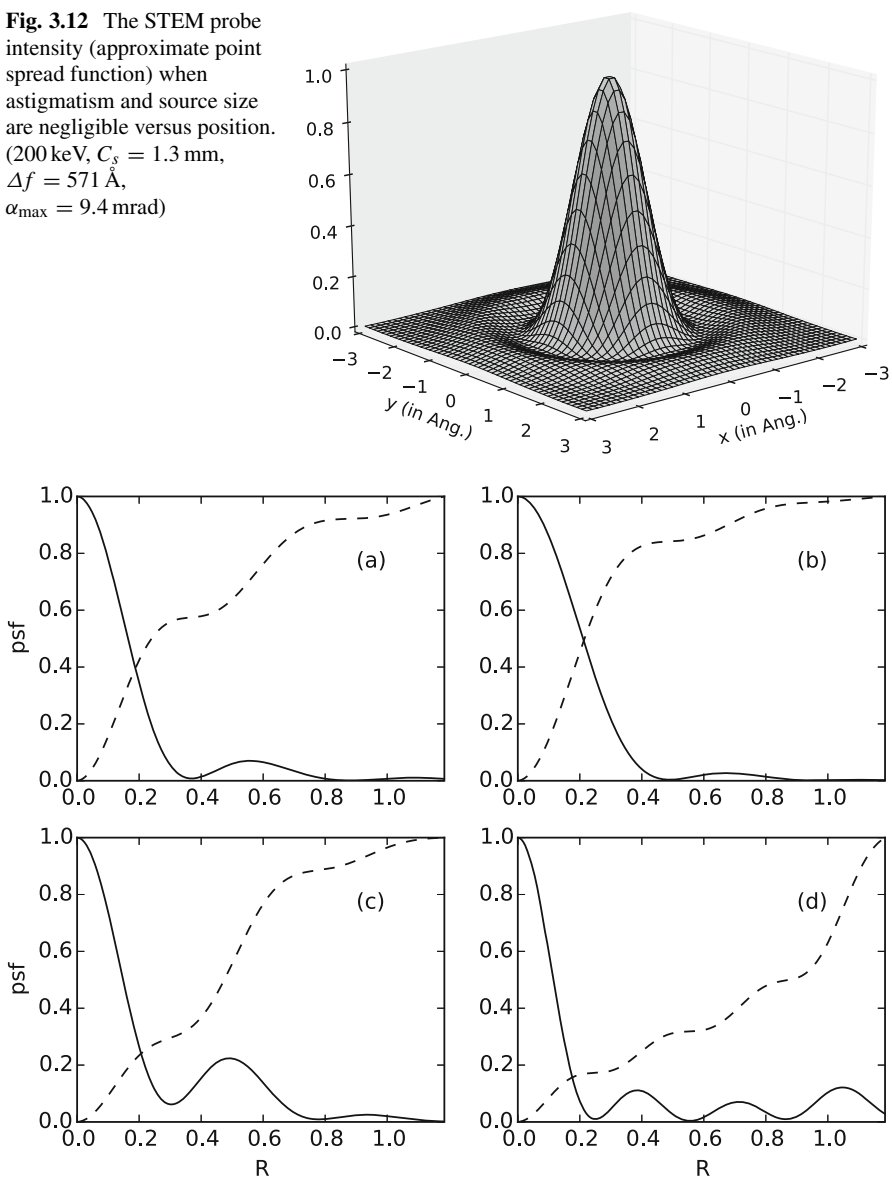


Fig. 3.13 The STEM probe intensity or approximate point spread function (solid line) when astigmatism and source size are negligible versus normalized radius $R = r(C_s \lambda^3)^{-1/4}$ for various values of the normalized defocus $D = \Delta f (C_s \lambda)^{-1/2}$ and objective aperture $K_{\max} = k_{\max} (C_s \lambda^3)^{1/4}$. (a) $D = 1.2$, $K_{\max} = 1.56$ (Scherzer conditions), (b) $D = 0.80$, $K_{\max} = 1.22$, (c) $D = 1.5$, $K_{\max} = 1.5$, (d) $D = 2.5$, $K_{\max} = 2.5$. The total integrated current is shown as a dashed line. All aberrations higher than third order have been ignored

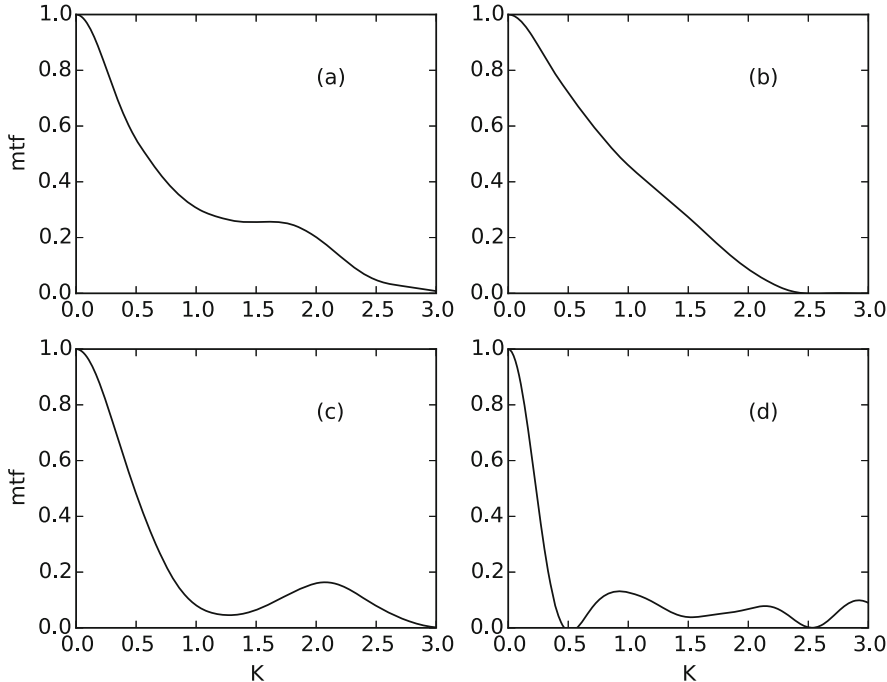


Fig. 3.14 The approximate STEM transfer function corresponding to the defocus values and objective apertures used in Fig. 3.13 versus the normalized spatial frequency $K = k(C_s\lambda^3)^{1/4}$. Source size is assumed negligible. All aberrations higher than third order have been ignored

The transfer function is just the inverse Fourier transform of the point spread function. With azimuthal symmetry (i.e., no astigmatism), and neglecting the source size the transfer function is:

$$H_{\text{ADF}}(k) = A'_p \int_0^\infty h_{\text{ADF}}(r) J_0(2\pi kr) r dr \quad (3.75)$$

where A'_p is the another normalization factor. The transfer function is plotted in Fig. 3.14 and BF-CTEM and ADF-STEM are compared in Fig. 3.15.

It is interesting to compare an aberration-corrected probe and an uncorrected probe (Maccagnano-Zacher et al. [326]). Figure 3.16 shows a probe at 100 keV with and without an aberration corrector. The curves are normalized to have the same integrated current. It is very surprising that the corrected probe is dramatically higher than the uncorrected probe. The tails of the probe at large radius have a very large contribution to the total current even though they appear small in this type of graph. An aberration corrector can increase the image contrast a lot more than might be expected.

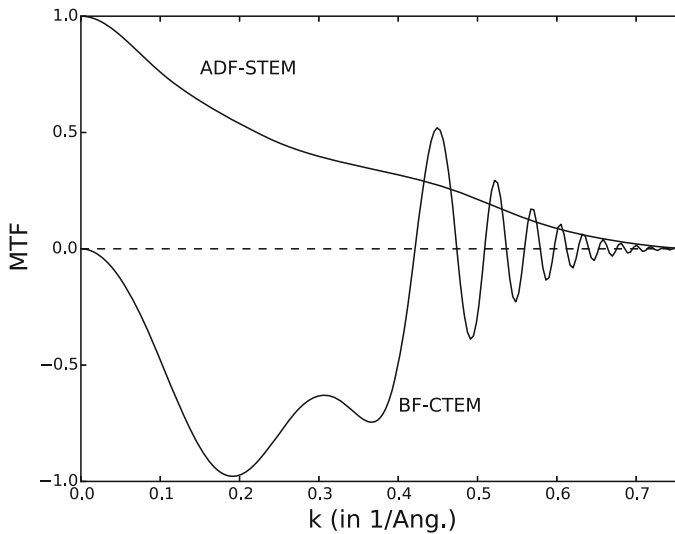


Fig. 3.15 Comparison of ADF-STEM and BF-CTEM transfer functions for the same spherical aberration, $C_s = 1.2$ mm at 200 keV. $\Delta f = 550 \text{ \AA}$ and $\alpha_{\max} = 9.5 \text{ mrad}$ for STEM and $\Delta f = 670 \text{ \AA}$ for BF-CTEM with a condenser half angle of 0.1 mrad and a defocus spread of 100 \AA

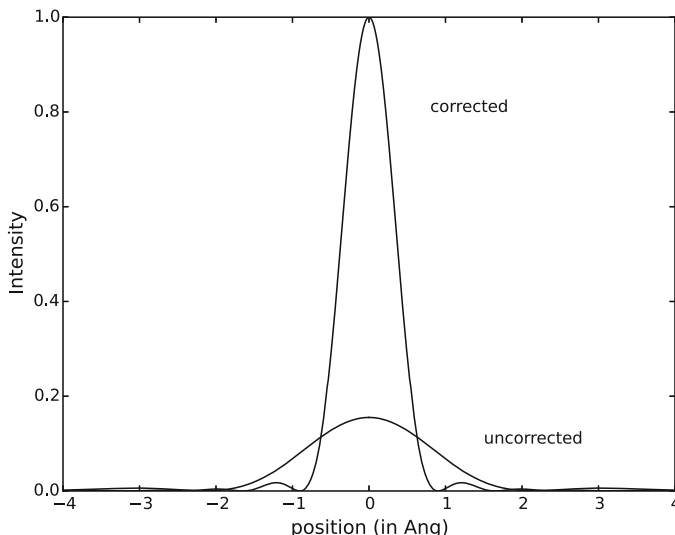


Fig. 3.16 Comparison of ADF-STEM probe with and without an aberration corrector at 100 keV. The uncorrected probe has $C_s = 1.3$ mm, $\Delta f = 694 \text{ \AA}$, and $\alpha_{\max} = 10.3 \text{ mrad}$. The corrected probe has $C_s = \Delta f = 0$ and $\alpha_{\max} = 25 \text{ mrad}$. Both curves are normalized to have the same total (integrated) current

3.5.1 Minimum Probe Conditions

It is difficult to define an optimum defocus and aperture to produce the best probe for the highest resolution. In Fig. 3.13d the full width at half maximum (FWHM) is clearly much smaller than the FWHM for Scherzer conditions (Fig. 3.13a); however, the tails (small wiggles at large radius) are dramatically increased in size. A small value at large radius can produce a large signal when integrated over a larger circumference. The total current inside a radius r in the probe is:

$$I(r) = 2\pi \int_0^r |\psi_p(\mathbf{x}')|^2 r' dr' \quad (3.76)$$

This current is shown in Fig. 3.13 as a dashed line. The extra factor of r inside the integral (Eq. 3.76) can shift the signal to a larger radius in a significant manner. The radius containing half of the current is a reasonable definition of the probe size (many other definitions are possible) and can be formally identified as the Sparrow [199, 468] condition of resolution. The Rayleigh criteria (see, for example, Hecht [199]) uses a width containing 59% of the total current. The Sparrow criteria is arbitrarily chosen here, although there are equally good reasons for either. This FWHM of the integrated intensity is a good measure of where the signal comes from.

A plot of this FWHM radius versus both defocus and objective aperture size is shown in Fig. 3.17. The minimum probe rms radius appears to be at defocus $D = 0.87$ and objective aperture $K_{\max} = 1.34$ (Fig. 3.13b). This produces the smallest tails but increases the FWHM (minimum rms radius approx. $0.43(C_s\lambda^3)^{1/4}$) to about twice that of the probe with Scherzer conditions. Scherzer conditions seem to be a compromise between a small full width half maximum and large tails. Mory et al. [362] have also considered the optimum probe defocus for STEM imaging and microanalysis. Crewe and Salzman [84], Krivanek et al. [299], and Intaraprasongk et al. [226] have discussed optimizing the probe with spherical aberration through fifth order. There is also a long history of balancing aberrations in incoherent light optics similar to the treatment here, starting with Maréchal [331] (see also section 4.4 of O’Neil [386] for balancing 3rd and 5th order spherical aberrations) and Black and Linfoot [37] and including annular objective apertures (for example, Barakt and Houston [21]).

A summary of the optimum condition found so far is given in Table 3.1 for BF-CTEM and ADF-STEM. The original paper of Intaraprasongk et al. [226] found an optimum value of $C_{S3} = C_{30}$ for a given $C_{S5} = C_{50}$, however, assumed a maximum phase error of $\lambda/4$ instead of the traditional $\pi/4$ which leads to an incorrect result. The results in the next to last column of Table 3.1 have been corrected for this problem (see the discussion in [277]). An example is shown in Fig. 3.18. With just the fifth order aberration C_{S5} , the probe is wider and has significant probe tails. Although small, the probe tails contain a large current (signal) due to a larger area (probe size 2.1 Å as defined above). Optimizing C_{S3} , α_{\max} (objective aperture) and

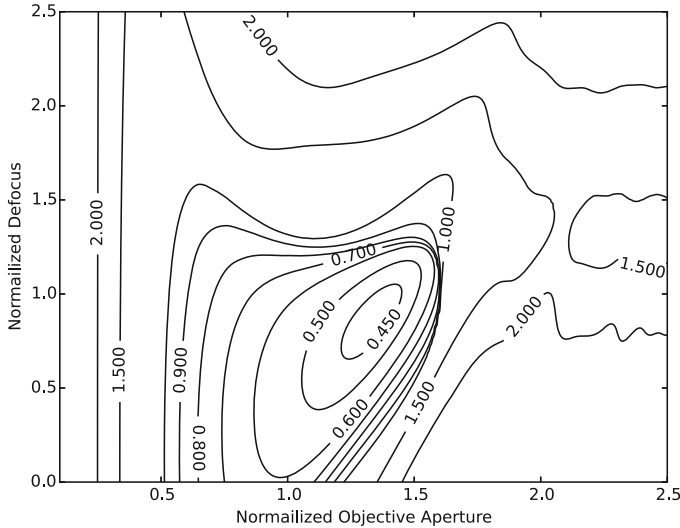


Fig. 3.17 The normalized rms radius containing half of the total probe current $r_{rms}(C_s \lambda^3)^{-1/4}$ of the STEM probe as a function of the normalized objective aperture $k_{max}(C_s \lambda^3)^{1/4}$ and the normalized defocus $\Delta f(C_s \lambda)^{-1/2}$ with a large $C_S = C_{S3}$ (no aberration corrector)

Table 3.1 Summary of optimum values for $m = 0$ aberrations when C_{S5} or C_{S3} is fixed, for phase contrast BF-CTEM [442, 443] and ADF STEM (this section and [226] with modification)

Parameter	BF-CTEM		ADF-STEM	
C_{S5}	Fixed	Ignored	Fixed	Ignored
C_{S3}	$-3.2(\lambda C_{S5}^2)^{1/3}$	Fixed	$-2.289(\lambda C_{S5}^2)^{1/3}$	Fixed
Δf	$-2(\lambda^2 C_{S5})^{1/3}$	$\sqrt{1.5} C_{S3} \lambda$	$-0.983(\lambda^2 C_{S5})^{1/3}$	$0.87\sqrt{C_{S3} \lambda}$
α_{max}	$\frac{7}{4}(\lambda/C_{S5})^{1/6}$	$(6\lambda/C_{S3})^{1/4}$	$1.513(\lambda/C_{S5})^{1/6}$	$1.34(\lambda/C_{S3})^{1/4}$
d_{min}	$\frac{4}{7}(C_{S5}\lambda^5)^{1/6}$	$0.67(C_{S3}\lambda^3)^{1/4}$	$0.403(C_{S5}\lambda^5)^{1/6}$	$0.43(C_{S3}\lambda^3)^{1/4}$

Chromatic aberration and all geometric aberrations higher than 5th order have been ignored

defocus can correct a significant fifth order aberration C_{S5} to a near optimum probe (probe size 0.65, corrected and 0.61 Å, ideal). Chromatic aberration has not been included here and will make the probe larger in all three cases.

This analysis is convenient and helps understand the interactions of these geometrical aberrations, but is somewhat oversimplified. All aberrations correctors currently in use have a large collection of multipoles, which will make many other parasitic $m \neq 0$ aberrations. Considering up to fifth order (Table 2.1) there are 25 aberrations, so selecting only three of these (Δf , C_{S3} , and C_{S5}) misses most of the problem. Some of this will be addressed more thoroughly in later sections.

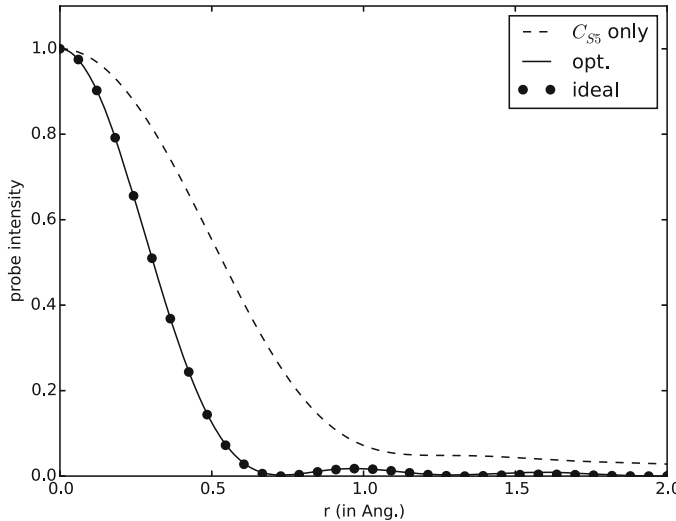


Fig. 3.18 The STEM probe profile for 100 keV with $C_{S5} = 50$ mm and $\alpha_{\max} = 31.0$ mrad. The dashed curve has just C_{S5} . The solid curve includes C_{S5} and the optimum $C_{S3} = -0.0481$ mm and $\Delta f = -C_{10} = -86.7$ Å (Table 3.1). The ideal curve (solid circles) with no aberrations overlaps the optimized curve (solid line). All other geometrical and chromatic aberrations were zero. Each curve normalized to be unity at the origin

3.5.2 Source Size

The probe is just the image of the electron source, which can also contribute to the probe size. The brightness of a source is defined as:

$$\beta = \frac{j}{\pi \alpha^2} \quad (3.77)$$

where j is the current density in the probe and α is the convergence half angle ($\pi \alpha^2$ is the solid angle). Brightness is conserved in a magnetic lens but may vary with beam energy. Various condenser lenses and the objective lens are used to demagnify the image of the source onto the specimen. More source demagnification produces less current (and a smaller source contribution to the probe size) in a predictable manner. If the probe is approximated as a disk of diameter d_S (the source size) and uniform intensity, then the current in the probe $I_P = j(\pi d_S^2/4)$ and the probe size are related as:

$$I_P = \frac{1}{4} \pi^2 \alpha^2 \beta d_S^2 \quad (3.78)$$

The probe current is shown in Fig. 3.19 for two different types of electron sources. A probe current of about 10–100 pAmp is needed for practical imaging. Only a field

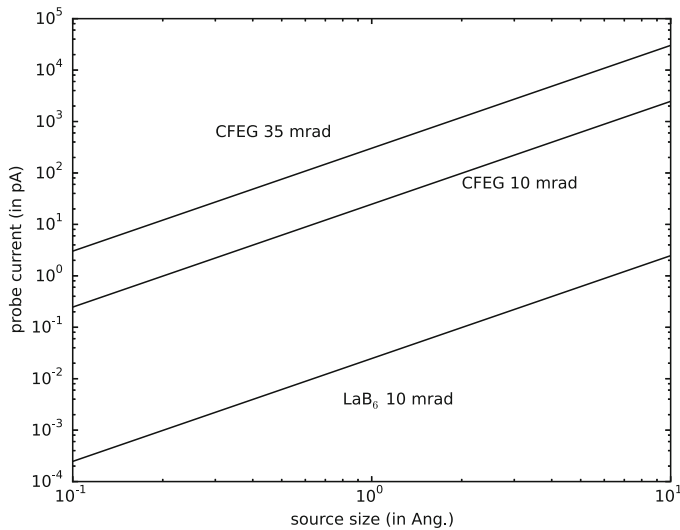


Fig. 3.19 Approximate probe current versus source size from brightness for a cold field emitter (CFEG) with brightness $\beta = 10^9$ amp/(cm²sr) for two different aperture sizes and a typical LaB₆ source with $\beta = 10^6$ amp/(cm²sr)

emission source can produce enough current to produce a source size of about 1 Angstrom (or smaller) and is preferred. This simple approximation is a convenient means of estimating the source contribution from just a measurement of the probe current and aperture size although it may not be that accurate.

Each part of the electron source can emit electrons that travel through the microscope and form an image of their own in some way. Each of these images is offset in position equivalent to the shift in position on the source demagnified by the lenses in the microscope. This can be summarized as a further convolution with an effective source size in the specimen plane (including appropriate demagnification).

$$g(\mathbf{x}) = f(\mathbf{x}) \otimes h_{\text{ADF}}(\mathbf{x}) \otimes h_{\text{source}}(\mathbf{x}) \quad (3.79)$$

The source contribution is typically taken as a Gaussian, and may become the dominate factor at high resolution. If there are other nondirectional instabilities in the microscope, then some of these may be treated in a similar manner. For example, if the stage has some small random vibrations convolving the final image with a small Gaussian may be an appropriate way to model this effect (stage vibrations likely have a preferred direction so the convolution kernel should match this asymmetry).

3.5.3 Defocus Spread

As in the CTEM, small fluctuations in the accelerating voltage, lens current and the thermal energy spread in the source itself produce a small spread in defocus values. The ADF-STEM transfer function does not vary as dramatically with defocus as the BF-CTEM transfer function so the effect of defocus spread is small on the ADF-STEM transfer function and can frequently be ignored. In a simple approximation the ADF-STEM transfer function (Eq. 3.75) can be integrated over a small range of defocus values to approx. the effects of these small fluctuations, leaving an effective transfer function:

$$h_{\text{ADF}}^{\text{eff}}(r) = \int_{-\infty}^{\infty} h_{\text{ADF}}(k, \Delta f) p(\Delta f) d(\Delta f) \quad (3.80)$$

$$H_{\text{ADF}}^{\text{eff}}(k) = \int_0^{\infty} h_{\text{ADF}}^{\text{eff}}(r) J_0(2\pi kr) r dr \quad (3.81)$$

where $p(\Delta f)$ is the probability distribution of defocus values. This integration may also be done in Fourier space in this linear imaging approximation. Typically $p(\Delta f)$ is a Gaussian distribution about its mean value, which is easily performed numerically using a Gauss–Hermite quadrature formula (5–9 points are probably sufficient in most cases), which conveniently includes a Gaussian weighting of the integrand (for example, section 4.6 of Press et al. [406], or chapter 25 of Abramowitz and Stegun [2]). Sheppard and Wilson [456] have considered partial coherence in scanning microscopy in a more general manner.

The STEM probe shape for several different values of defocus spread is shown in Fig. 3.20 using similar optical conditions as in Fig. 3.8 for the CTEM. The probe is much less sensitive to defocus spread as CTEM phase contrast, because it does not oscillate rapidly. The main effect is to add long probe tails (small wiggles at large r). The corresponding transfer function for each probe is shown in Fig. 3.21. Longer probe tails do not change the maximum resolution much; however, the intermediate spatial frequencies are significantly reduced.

3.5.4 Aberration Tuning Errors

Most (if not all) aberration correctors in current use utilize multipole optics, which produces a multitude of new parasitic aberrations (22 total to 5th order) that have to be corrected. Figure 3.22 compares two probes with and without a single parasitic aberration. Both probes have been normalized to have the same total integrated intensity. The surface plot of two probes has been merged into one for easy comparison. Half of the plot has no aberrations and half has a significant amount of C_{45b} . This multipole aberration produces small probe tails with a variety of small bumps. The tails are a small amplitude but have a very large area resulting in a significant reduction in the center intensity of the probe, which will result in a significant reduction of contrast (signal) in the image.

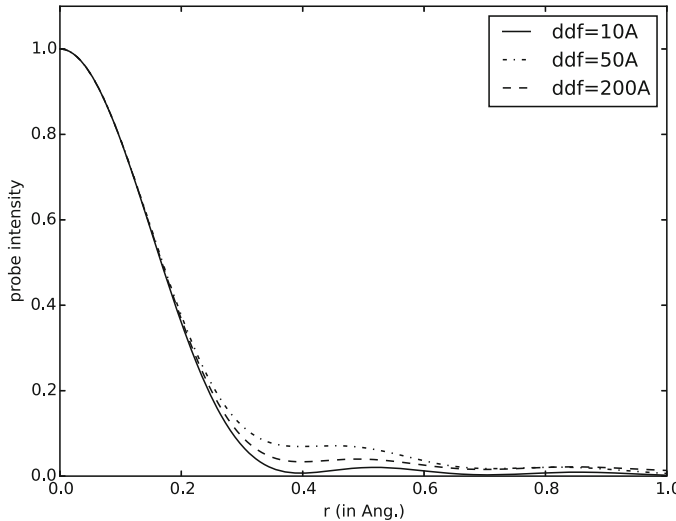


Fig. 3.20 Approximate ADF-STEM probe shape with different amounts of defocus spread for a beam energy of 300 keV. The objective angle was $\alpha_{\max} = 30.4$ mrad, and $C_{S5} = 30$ mm, $C_{S3} = -27.7$ μ m, $\Delta f = -48.0$ \AA . Three different defocus spreads are shown to illustrate the effect of chromatic aberration (ddf = defocus spread). Each curve is normalized to be unity at the origin

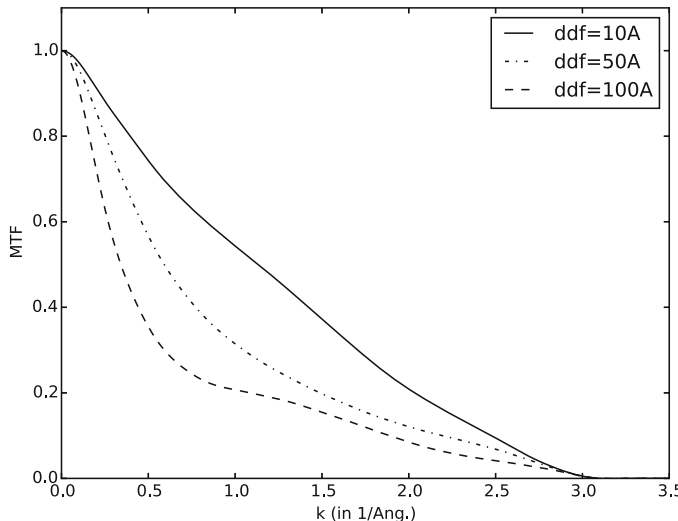
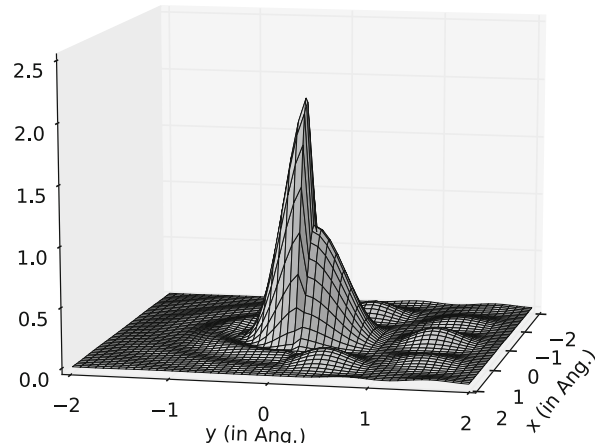


Fig. 3.21 Approximate ADF-STEM transfer function with different amounts of defocus spread, using the same parameters as in Fig. 3.20. Each curve is normalized to be unity at the origin

Fig. 3.22 Calculated ADF-STEM probe profile (100 keV, 30 mrad) with and without aberrations. The portion for $y < 0$ is an ideal probe with no aberrations, and the other portion has $C_{45b} = 0.4$ mm. Both probes are normalized to have the same total integrated intensity. Source size and defocus spread have been ignored



None of these parasitic aberrations will be corrected exactly to zero but will have a small random nonzero error (as in Table 2.2). There are enough that it is appropriate to think about the statistical properties of the probe. Figure 3.23 shows the azimuthal average of an average probe (calculated in two dimensions, in 5 by 5 Å with 1024 by 1024 pixels) with a random uniform distribution of errors in the aberrations within the allowed tolerance (for a $\pi/4$ error in the aberration function as in Table 2.2, including positive and negative values) averaged over 500 probes (100 keV, 30 mrad) with different random errors. This would generally be considered to be accurately tuned and usable. Some aberrations (such as C_{21} and C_{41}) can shift the probe position so each probe center was found numerically to produce the smallest probe size.

Most probes with random tuning errors show semi-random fluctuations that may vary azimuthally (for example, see Fig. 3.22). The average over many sets of random errors becomes smooth and symmetrical so only the azimuthal average (after summation) is shown. The mean probe is slightly larger but similar to the ideal probe. The probe tails (small values at large radius) can be particularly troublesome because the intensity grows as the square of the radius. The distribution of probe sizes in the set of probes in Fig. 3.23 is shown in Fig. 3.24. Probe size is defined as the diameter enclosing one half of the probe intensity (i.e., the Sparrow resolution criteria). The ideal size is shown as a single line. The resulting probe is larger than expected and has some random variation in size. This distribution is at least similar to a log-normal distribution (i.e., the log of the size has a normal or Gaussian distribution) typical of sizes that cannot become negative by definition. There is a slight asymmetry with more values on the large side. This random variation of sizes may change the apparent observed image contrast by almost a factor of two and greatly hinder efforts to quantitatively analyze aberration-corrected image. Each aberration will also have some instability (perhaps only a few parts per million) from noise in the driving electronics etc. (Kirkland [275]), but the measurement error is

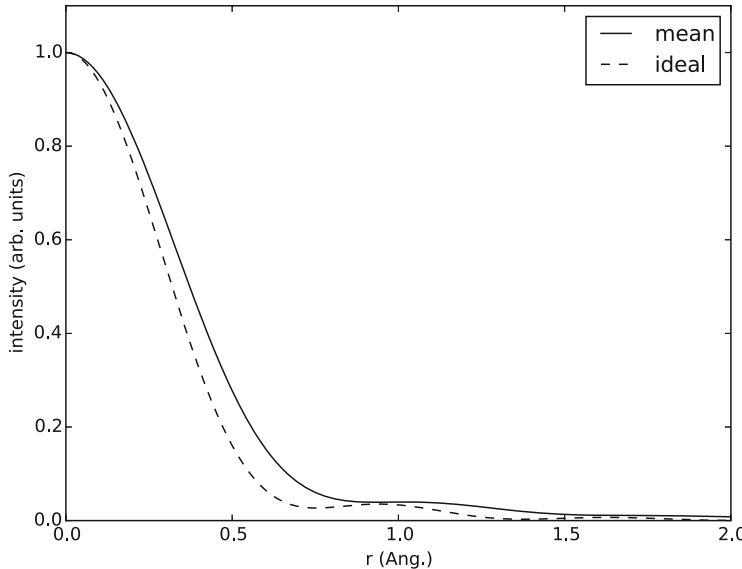


Fig. 3.23 Calculated azimuthally averaged ADF-STEM probe profile (100 keV, 30 mrad) with random aberration (up to and including 5th order) tuning errors uniformly distributed within the allowed tolerance in Table 2.2. Focus and astigmatism are assumed to be manually optimized and were not included. Each curve is normalized to be unity at the origin. A defocus spread of 50 Å has been included but source size has not. An ideal probe shape (including defocus spread) is shown as a dashed line for comparison

probably a much larger effect in typical cases. Any systematic errors in aberration measurement may also have a large detrimental effect.

A maximum phase error of $\pi/4$ for a single aberration may be about right but when more aberrations are included allowing a phase error of $\pi/4$ for each aberrations is overly optimistic. The error will accumulate, so allowing the same error for each of an arbitrary number of aberrations (as in Fig. 3.24) as seems to be the current practice, leads to a problem. If the random errors are assumed to add in quadrature, then the maximum error in each of N aberrations should be $\frac{\pi}{4\sqrt{N}}$. For $N = 22$ aberration the maximum allowed tuning error should be $\pi/19$ which may not be practical. Correcting to higher and higher order includes an unexpected penalty.

3.6 Compensation

An aberration corrector typically has some control over several low order aberrations but will not be able to directly control aberrations higher than some upper limit. The aberrations in the chosen form of the aberration function as in Eq. 2.27 are not

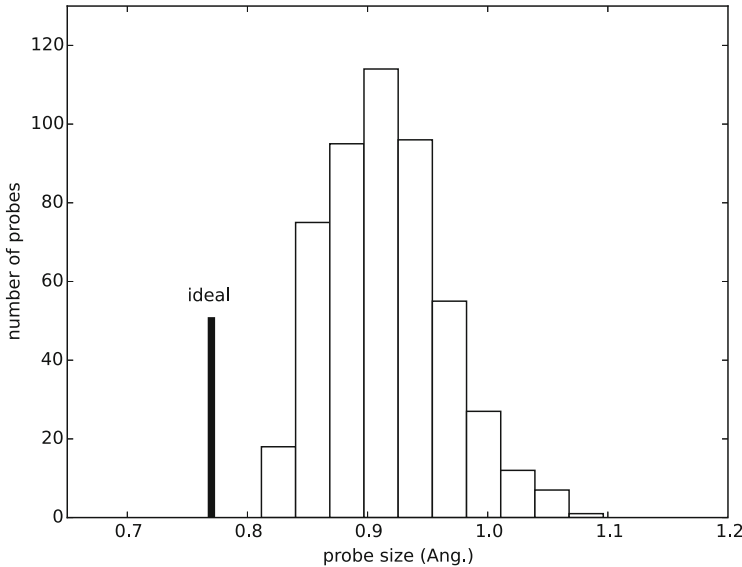


Fig. 3.24 Calculated distribution of STEM probe sizes (100 keV, 30 mrad) with random aberration tuning errors (up to and including 5th order) uniformly distributed within the allowed tolerance in Table 2.2 as in Fig. 3.23 for 500 probes with different random errors. Focus and astigmatism are assumed to be manually optimized and were not included. A defocus spread of 50 Å has been included but source size has not. The ideal probe size (including defocus spread) is shown as a single line

orthogonal. Lower order aberrations can be used to partially compensate small high order aberration of the same azimuthal symmetry over some small range of objective angle which can be referred to as compensation. The useful range of a corrector can be extended a little further than its original design might seem to imply. Scherzer focus can be said to compensate third order spherical aberration with defocus. In a multipole corrector system there will be a large number of aberrations. Each aberration will have a different optimal maximum objective aperture (as in Scherzer focus) but there has to be a single aperture size for all aberrations, so each aberration has to be compensated for an arbitrary aperture size chosen for some other reason. Kirkland et al. [264] have reviewed some approaches to compensation.

The process can be generalized to any combination of aberrations with the same azimuthal symmetry (same m and ab subscripts in Eq. 2.27). Aberrations with different azimuthal symmetry are orthogonal and independent (cannot compensate each other). Ideally, all aberrations should be zero in a STEM probe corrector, and all but the $m = 0$ aberrations (defocus, C_{S3} and C_{S5}) should be zero in a CTEM image corrector. For simplicity the following discussion will use just the a aberrations (and drop the a subscript) but can equally apply to a or b aberrations.

3.6.1 Two Aberrations at a Time

To compensate a high order fixed aberration C_{n+2} with a single variable lower order aberration C_n with the same m find the value to minimize the total squared aberration. Drop the a and m subscripts for simplicity. Minimize the total squared error in the objective aperture:

$$\min = \int_0^{\alpha_{\max}} \int_0^\pi \left[\frac{2\pi}{\lambda} \left(C_n \frac{\alpha^{n+1}}{n+1} + C_{n+2} \frac{\alpha^{n+3}}{n+3} \right) \right]^2 \cos^2[m\phi] \alpha d\phi d\alpha \quad (3.82)$$

The aberration may be both a type or b type or the combination at a specific angle (ratio) ϕ_0 . α_{\max} is the range of the objective aperture. Integrate over ϕ and drop leading constant factors:

$$\min = \int_0^{\alpha_{\max}} \left(C_n \frac{\alpha^{n+1}}{n+1} + C_{n+2} \frac{\alpha^{n+3}}{n+3} \right)^2 \alpha d\alpha \quad (3.83)$$

Differentiate with respect to C_n and equate to zero to find the minimum:

$$\int_0^{\alpha_{\max}} 2 \left(C_n \frac{\alpha^{n+1}}{n+1} + C_{n+2} \frac{\alpha^{n+3}}{n+3} \right) \frac{\alpha^{n+1}}{n+1} \alpha d\alpha = 0 \quad (3.84)$$

Integrate and drop constant leading factors:

$$\left[C_n \frac{\alpha^{2n+4}}{(2n+4)(n+1)^2} + C_{n+2} \frac{\alpha^{2n+6}}{(2n+6)(n+3)(n+1)} \right]_0^{\alpha_{\max}} = 0 \quad (3.85)$$

$$C_n \frac{1}{(2n+4)(n+1)} + C_{n+2} \frac{\alpha_{\max}^2}{(2n+6)(n+3)} = 0 \quad (3.86)$$

leaving:

$$C_n = -C_{n+2} \frac{(2n+4)(n+1)}{(2n+6)(n+3)} \alpha_{\max}^2 = -C_{n+2} \frac{(n+2)(n+1)}{(n+3)^2} \alpha_{\max}^2 \quad (3.87)$$

For example:

$$C_{23} = -C_{43} \frac{\alpha_{\max}^2 (8)(3)}{(10)(5)} = -0.480 C_{43} \alpha_{\max}^2 \quad (3.88)$$

$$C_{12} = -C_{32} \frac{\alpha_{\max}^2 (6)(2)}{(8)(4)} = -0.375 C_{32} \alpha_{\max}^2 \quad (3.89)$$

An example of a STEM probe with C_{23a} compensating C_{41a} is shown in Fig. 3.25. The probe tails are typically increased by a small amount with compensation

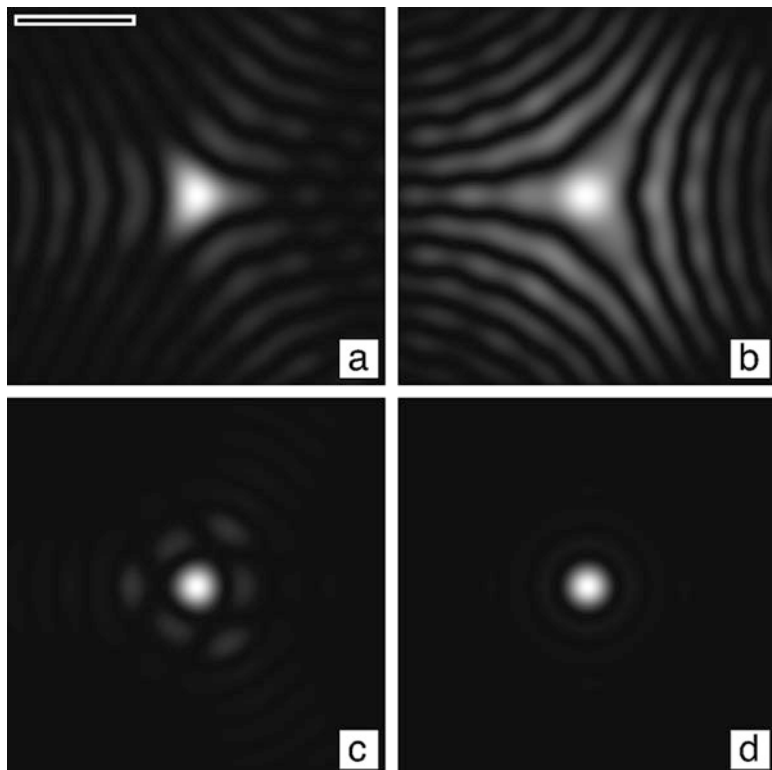


Fig. 3.25 Compensation at 100kV and obj. apert. of 40 mrad. Shown is a calculated image of the STEM probe with white being a larger electron intensity. (a) $C_{43a} = 0.30\text{ mm}$, (b) $C_{23a} = -230\text{ nm}$. (c) C_{43a} compensated with C_{23a} from (a) and (b). (d) Unaberrated probe (scale bar is 2 \AA)

although the intensity is too small to see in this figure. As the objective angle, α , or the higher order aberration get larger, this equation becomes less accurate although it is sometimes possible to find other values of the lower aberration to improve the compensation. The image of a single heavy atom in BF-CTEM should show a similar behavior (compare Figs. 2.13 and 2.15).

3.6.2 Three Aberrations at a Time

Repeating the derivation for two aberrations but including three aberrations with the highest order fixed and the two lower orders variable:

$$\min = \int_0^{\alpha_{\max}} \left(C_n \frac{\alpha^{n+1}}{n+1} + C_{n+2} \frac{\alpha^{n+3}}{n+3} + C_{n+4} \frac{\alpha^{n+5}}{n+5} \right)^2 \alpha d\alpha \quad (3.90)$$

Differentiate with respect to first C_n and then C_{n+2} and equate both to zero and integrate to find the minimum (after some tedious algebra) leaving:

$$\begin{aligned} C_n \frac{1}{(n+1)} + C_{n+2} \frac{\alpha_{\max}^2 (2n+4)}{(2n+6)(n+3)} &= -C_{n+4} \frac{\alpha_{\max}^4 (2n+4)}{(2n+8)(n+5)} \\ C_n \frac{1}{(n+1)} + C_{n+2} \frac{\alpha_{\max}^2 (2n+6)}{(2n+8)(n+3)} &= -C_{n+4} \frac{\alpha_{\max}^4 (2n+6)}{(2n+10)(n+5)} \end{aligned} \quad (3.91)$$

Now solve Eqs. 3.91 (two equations in two unknowns with messy coeff.). Subtract and factor:

$$\begin{aligned} C_{n+2} \left[\frac{(2n+6)}{(2n+8)} - \frac{(2n+4)}{(2n+6)} \right] \frac{1}{(n+3)} \\ = -C_{n+4} \alpha_{\max}^2 \left[\frac{(2n+6)}{(2n+10)} - \frac{(2n+4)}{(2n+8)} \right] \frac{1}{(n+5)} \end{aligned} \quad (3.92)$$

Insert back into original to obtain:

$$C_n = -C_{n+2} \frac{\alpha_{\max}^2 (2n+6)(n+1)}{(2n+8)(n+3)} - C_{n+4} \frac{\alpha_{\max}^4 (2n+6)(n+1)}{(2n+10)(n+5)} \quad (3.93)$$

More elaborate combination might be possible, but the algebra just gets more tedious.

3.7 Confocal Mode for Weak Phase Objects

The light optical scanning transmission microscope (in confocal mode) has exhibited improved performance relative to a conventional microscope, but what happens in the electron microscope? A simple imaging theory is similar to that of the light optical microscope (Wilson and Sheppard [537]). Nellist et al. [371] have also described the theory of imaging in a double corrected instrument.

Confocal mode is a combination of STEM and CTEM (Fig. 2.8). A focused electron probe is raster scanned across the specimen (much like a STEM). The electrons transmitted through the specimen are imaged by a collector lens (much like CTEM) onto a detector (usually a small point like detectors).

The incident probe focused onto the specimen has a complex wave function as given by Eq. 3.63. The wave transmitted through the specimen is given by Eq. 3.65. The probe is scanned across the specimen, and in confocal mode there is also a

collection lens that images the transmitted probe onto a detector. The collection lens adds a second complex points spread function. If the probe is scanned (moved) across the specimen, the transmitted beam must be inversely scanned so that there is no net motion on the detector. Alternately the electron beam may be fixed and the specimen moved in a raster fashion. The theory is slightly less complicated in this alternate mode (used here). The transmitted wave function is:

$$\psi_T(\mathbf{x}, \mathbf{x}_P) = h_P(\mathbf{x})t(\mathbf{x} + \mathbf{x}_P) \quad (3.94)$$

where \mathbf{x} is position in the specimen plane and \mathbf{x}_P is the position of the specimen (or probe). $t(\mathbf{x})$ is the complex transmission function of the specimen, and $h_P(\mathbf{x}) = \psi_P(\mathbf{x})$ is the point spread function of the probe forming lens (Eq. 3.63). The wave function incident on the detector is:

$$\begin{aligned} \psi_D(\mathbf{x}, \mathbf{x}_P) &= h_C(\mathbf{x}) \otimes [h_P(\mathbf{x})t(\mathbf{x} + \mathbf{x}_P)] \\ &= \int h_C(\mathbf{x}')h_P(\mathbf{x}' - \mathbf{x})t(\mathbf{x}' - \mathbf{x} - \mathbf{x}_P)d^2\mathbf{x}' \end{aligned} \quad (3.95)$$

where $h_C(\mathbf{x})$ is the point spread function of the collector lens. The subscript P or C refers to the probe or collector lens, respectively. If the detector is a point at position $\mathbf{x} = 0$, then:

$$\begin{aligned} \psi_D(\mathbf{x} = 0, \mathbf{x}_P) &= \int h_C(\mathbf{x}')h_P(\mathbf{x}')t(\mathbf{x}' - \mathbf{x}_P)d^2\mathbf{x}' \\ &= [h_C(\mathbf{x})h_P(\mathbf{x})] \otimes t(\mathbf{x}) \end{aligned} \quad (3.96)$$

In practice the detector must have a nonzero size so this is an unphysical approximation to simplify the mathematics. The transmitted intensity for a given probe position with this approximation is therefore:

$$g(\mathbf{x}) = |[h_p(\mathbf{x})h_c(\mathbf{x})] \otimes t(\mathbf{x})|^2 \quad (3.97)$$

where the distinction between \mathbf{x} and \mathbf{x}_P has been dropped for simplicity.

A transfer function is only defined for a linear system but this is still rather nonlinear. Approximate the transmission function of the specimen as a weak phase object as in Eqs. 3.6 to obtain a simplified linear theory:

$$t(\mathbf{x}) = \exp[i\sigma v_z(\mathbf{x})] \sim 1 + i\sigma v_z(\mathbf{x}) \quad (3.98)$$

or weak amplitude object (Eq. 3.51):

$$t(\mathbf{x}) = \exp[u(\mathbf{x})] \sim 1 + u(\mathbf{x}) \quad (3.99)$$

Using the weak phase object approximation, and keeping only the lowest terms in v_z , the image model becomes:

$$g(\mathbf{x}) \sim |[1 + i\sigma v_z(\mathbf{x})] \otimes (h_p(\mathbf{x})h_c(\mathbf{x}))|^2 \quad (3.100)$$

$$\sim 1 \otimes (h_p h_c) + 2Re[i\sigma v_z \otimes (h_p h_c)] \quad (3.101)$$

$$\sim 1 + 2\sigma v_z \otimes h_{WPA} \quad (3.102)$$

$$h_{WPA}(\mathbf{x}) = Re[ih_p(\mathbf{x})h_c(\mathbf{x})] \quad (3.103)$$

The transfer function is just the 2D Fourier transform of h_{WPA} . Using azimuthal symmetry the transfer function for weak phase objects in confocal mode is:

$$H_{WPA}(k) = \int_0^{r_{\max}} Re[ih_p(r)h_c(r)]J_0(2\pi kr)rdr \quad (3.104)$$

Remember that both $h_p(\mathbf{x})$ and $h_c(\mathbf{x})$ are complex valued functions. To repeat this derivation in the weak amplitude approximation just remove the factor of i , to obtain the transfer function for weak amplitude objects:

$$H_{WAA}(k) = \int_0^{r_{\max}} Re[h_p(r)h_c(r)]J_0(2\pi kr)rdr \quad (3.105)$$

Confocal mode has twice as many optical parameters and can produce a larger variety of features in the transfer function. Some examples are shown in Fig. 3.26 for the same set of parameters as ADF-STEM in Fig. 3.14. The confocal transfer function is compared to the BF-CTEM transfer function (both in the weak phase approximation) in Fig. 3.27. This particular choice of parameters produces a transfer function similar to ADF-STEM except that it is reversed in contrast (negative instead of positive). There is most likely a difference in the signal strength as well which is not apparent in this representation.

3.8 Phase and Amplitude Contrast Revisited

The theory presented above is a traditional view and seems plausible, but it is worth checking a little. Figure 3.28 shows how a pure amplitude and pure phase object (combined into a single image) are imaged in BF-CTEM and ADF-STEM, using methods that will be discussed later. The letters “AMP.” are a amplitude object and the letters “PHASE” are a phase object. The image transmission function is given by:

$$t(\mathbf{x}) = \exp(ip - a) \quad (3.106)$$

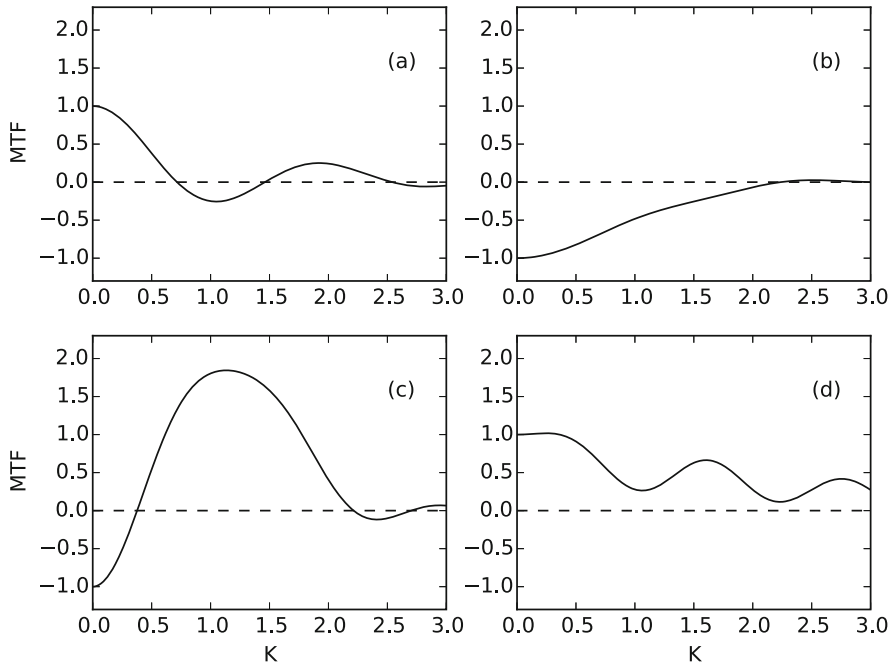


Fig. 3.26 Confocal transfer functions in the weak phase approximation (Eq. 3.104) for the same aberrations as ADF-STEM in Figs. 3.13 and 3.14. Both the probe and collectors lens aberration are the same in each graph

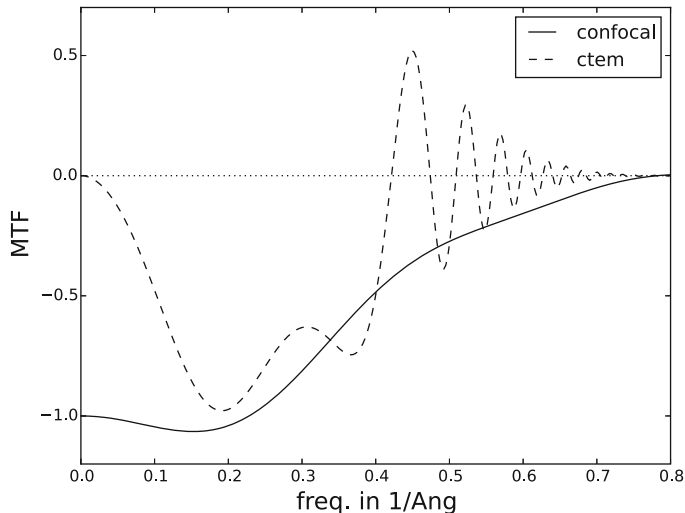
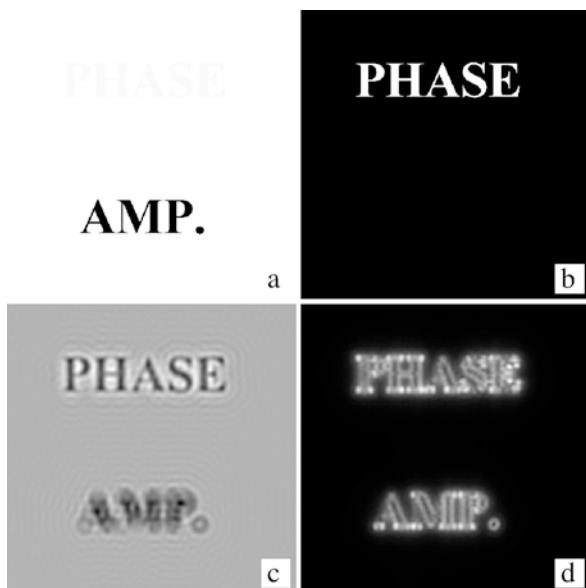


Fig. 3.27 Comparison of confocal and CTEM transfer functions in the weak phase approximation for the same spherical aberration, $C_s = 1.2$ mm, at 200 keV. $\Delta f = 550 \text{ \AA}$ and $\alpha_{\max} = 9.5 \text{ mrad}$ for confocal. Both the probe and collectors lens aberration in confocal were the same. $\Delta f = 670 \text{ \AA}$ for BF-CTEM with a condenser half angle of 0.1 mrad and a defocus spread of 100 \AA (Scherzer conditions)

Fig. 3.28 Phase and amplitude contrast in BF-CTEM and ADF-STEM. (a) Pure amplitude object, (b) pure phase object. The object was formed from the superposition of (a) and (b) and imaged as a (c) BF-CTEM image and (d) ADF-STEM image



where a and p are the amplitude and phase components (respect.) with a value of 0.05 on the appropriate letters and zero otherwise. The BF-CTEM and the ADF-STEM images contain both amplitude and phase contrast features. It is more the specimen that determines which form of contrast will be in the image. The ADF-STEM image only renders the high frequency components from the edges (scattered at high angle onto the ADF detectors). However, every specimen is composed of many small atoms, each of which scatters to high angle so this edge effect is not in a real specimen composed of many individual atoms (sharp edges, or points are everywhere). The simple theory is very helpful in developing an intuitive understanding of electron microscope image but there is still a need for more detailed simulations to more completely understand what the images mean. The property of coherence and incoherence also plays a large role in image formation

Chapter 4

Sampling and the Fast Fourier Transform



To go further with image calculations requires a detailed numerical calculation using a computer program. The mathematics gets too complicated (or long) to perform analytically with pencil and paper. This chapter gives some necessary computer background prior to calculating images in later chapters. The computer imposes its own set of rules that must be understood and dealt with to perform these calculations. Experienced computer users may prefer to skip this chapter.

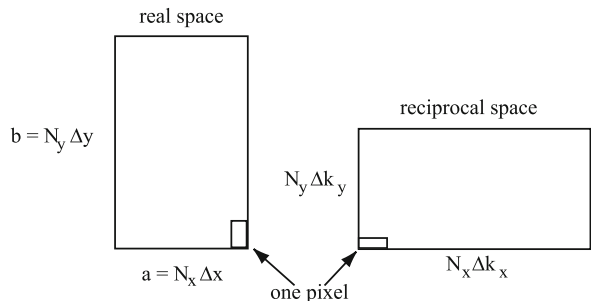
Image simulation or image processing with the computer presumes that the image is somehow represented inside the computer. A digital computer naturally operates on numerical data. Therefore an image must be represented as a two-dimensional array of numbers inside the computer. Each number is one pixel or spot in the image whose intensity is proportional to its numerical value. The trick is to have a sufficiently large number of pixels, so that when they are displayed as an image the individual numbers or pixels are not individually distinguishable. Sampling the image in this manner leads to some specific rules and limitations that are summarized in this chapter.

The fast Fourier transform or FFT is one of the most efficient computer algorithms available. The FFT computes the Fourier transform of discretely sampled data in a minimum amount of computer time. Image simulation, such as the multislice method, is usually organized around the FFT to reduce the computer time required for simulations. The mechanism of the FFT is closely coupled to discretely sampled data and is also included in this chapter.

4.1 Sampling

In practice each image is calculated in a rectangular grid of $N_x \times N_y$ pixels or picture elements as shown in Fig. 4.1. The images are sampled at N_x discrete points along x and N_y discrete points along y and form a supercell with dimensions of $a \times b$ in

Fig. 4.1 Sampling of an image of size $a \times b$ in a plane perpendicular to the optic axis of the microscope. There are $N_x \times N_y$ pixels with a size of $a/N_x \times b/N_y$ in real space and $1/a \times 1/b$ in reciprocal or Fourier transform space. Neither the pixels or the image have to be square



real space. Figure 4.2 shows the visual effects of changing the number of pixels in an image for the special case of $N_x = N_y$ and $a = b$. Each pixel has dimensions $a/N_x \times b/N_y$ in real space and has a single value associated with it that is the average over the area of the pixel (or in the case of a complex wave function two values representing the real and imaginary parts). The real space coordinates take on only discrete values of:

$$x = i \Delta x \quad i = 0, 1, 2, \dots, (N_x - 1) \quad (4.1)$$

$$y = j \Delta y \quad j = 0, 1, 2, \dots, (N_y - 1) \quad (4.2)$$

where $\Delta x = a/N_x$ and $\Delta y = b/N_y$.

The Fourier transform of this image will also have $N_x \times N_y$ pixels but the dimensions of each pixels change to $1/a \times 1/b$ and the reciprocal space coordinates take on values:

$$k_x = i \Delta k_x \quad i = 0, 1, 2, \dots, (N_x - 1) \quad (4.3)$$

$$k_y = j \Delta k_y \quad j = 0, 1, 2, \dots, (N_y - 1) \quad (4.4)$$

where $\Delta k_x = 1/a$ and $\Delta k_y = 1/b$. The supercell does not have to be square and there may be a different number of pixels in x and y although this is usually less efficient. Curiously, the longest dimension of the supercell will be reversed in real and reciprocal space (i.e., a tall narrow supercell in real space becomes short and wide in reciprocal space).

Discrete sampling also imposes a limit on the maximum spatial frequency in the image of:

$$\begin{aligned} |k_x| &< \frac{1}{2\Delta x} \\ |k_y| &< \frac{1}{2\Delta y} \end{aligned} \quad (4.5)$$

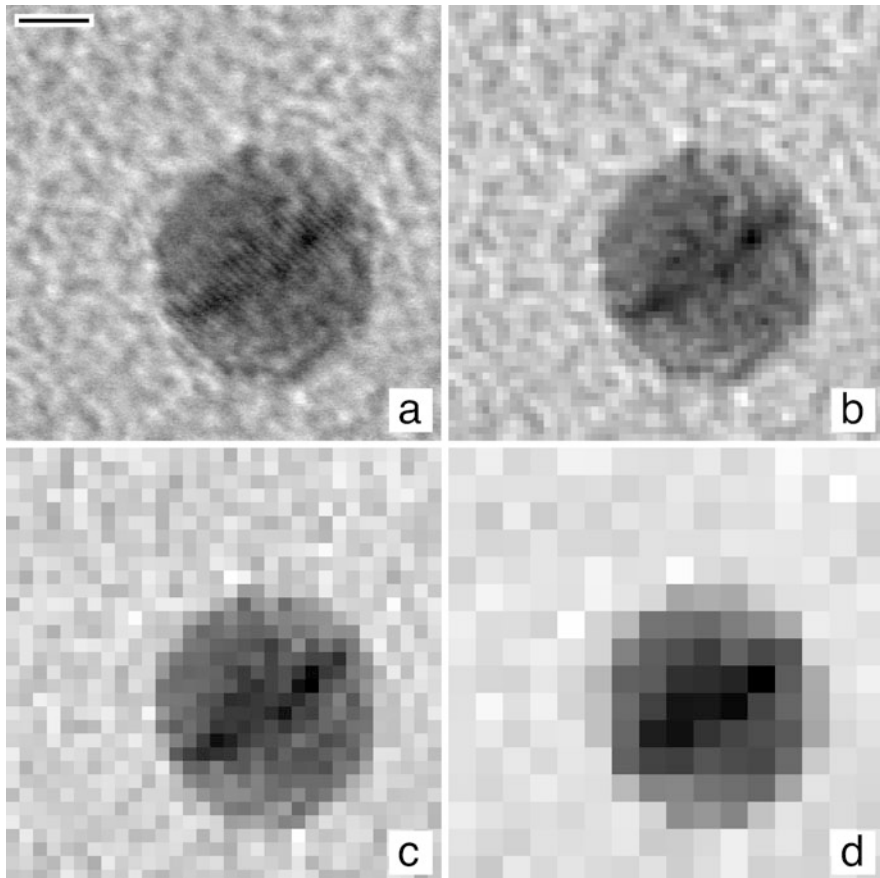


Fig. 4.2 The visual effects of changing the number of pixel in an image. (a) 256×256 pixels, (b) 64×64 pixels, (c) 32×32 pixels, and (d) 16×16 pixels. Each pixel has 8 bits. The image is a bright field STEM image of a gold particle on an amorphous carbon film recorded on a VG HB-501 STEM ($C_s = 1.3$ mm, 100 keV). The 2.35 \AA gold lattice fringes are barely visible in the center of the particle. The scale bar in (a) is approximately 20 \AA

This is referred to as the Nyquist limit. In principle this limit may be different in each direction; however, in practice the larger limit should be reduced to the smaller so that the effective resolution is isotropic in the image (i.e., to avoid sampling artifacts in the image). If the sampling size Δx or Δy is too large, then the signal is under-sampled and aliasing occurs. Figure 4.3 shows the effect of under-sampling a sine wave. The high frequency sine wave appears to be a low frequency sine wave if it is under-sampled. This should be avoided by making the sampling size smaller or explicitly limiting the bandwidth of the original signal.

It is often overlooked that the sampling in real space and reciprocal space is coupled. Increasing the sampling in real space decreases the sampling in reciprocal

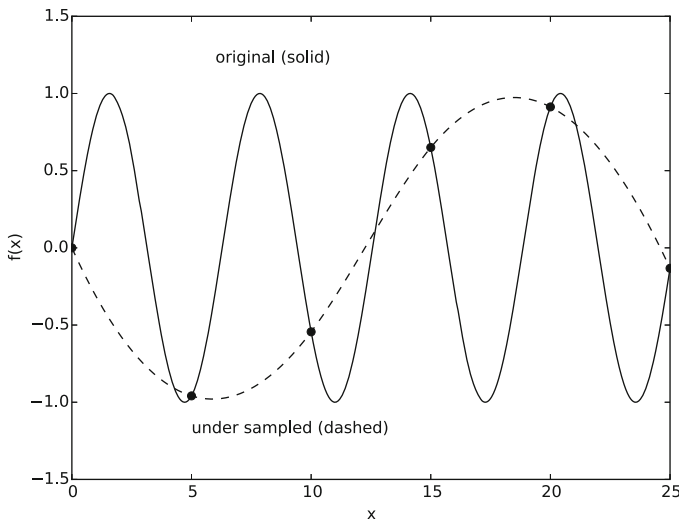


Fig. 4.3 The effect of under-sampling a function. The original function is shown as a solid line. It is under-sampled at regular intervals (circles). The apparent signal is shown as a dashed line. Under-sampling causes high frequencies to be improperly aliased as low frequencies

space and vice versa. Figure 4.4 illustrates some effects of how pixel size (sampling) changes the scale in real and reciprocal space. Methods of image calculation discussed in later chapters were used to calculate these images. The top row increases in size (full scale dimension) while keeping the total number of pixels fixed. The bottom row is the corresponding images of the objective aperture (of the same size in total angle) in reciprocal space for each image above it. Figure 4.4a, d have good sampling in real space (small pixel size) but poor sampling in reciprocal space (large pixels, only a few inside the aperture). Figure 4.4c, f have poor sampling in real space (large pixels) but good sampling in reciprocal space (small pixels, many inside the aperture, but high spatial frequencies may be missing). A compromise in the middle (Fig. 4.4b, e) is sometimes the best choice.

The numerical value associated with each pixel is itself discretely sampled. This value must be encoded as a finite number of bits (one bit has a value of 0 or 1) for each pixel in the computer. The human eye can distinguish at best about 30–50 different shades of gray. Figure 4.5 shows the effects on human perception of varying the number of bits in each pixel. The computer hardware is usually capable of conveniently handling data in units as small as 8 bits at a time. Therefore about 8 bits of information is needed for each pixel to display the image. Any substantial amount of calculation with only 8 bits per pixels will however quickly get into a lot of trouble. Rounding each value to 8 bits introduces an error of at least one in $2^8 = 256$. Even worse, dividing two eight bit integer numbers truncates the result to the lowest integer (for example, $1/2 = 0$, $128/50 = 2$, with integer arithmetic) which can introduce very large errors for each arithmetic operation between pixels.

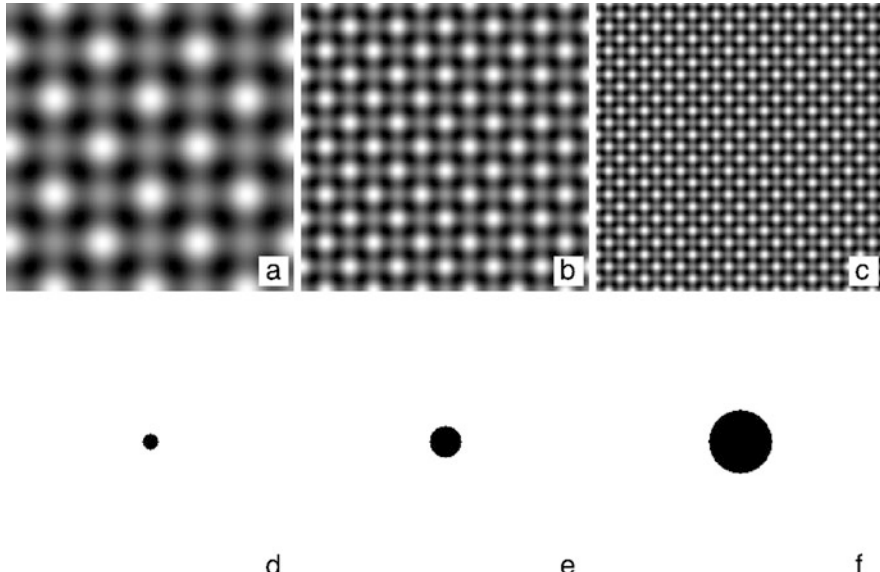


Fig. 4.4 The relationship between (a–c) real space (image) and (d–f) reciprocal space (Fourier) sampling for different supercell sizes (full scale size in real space). The real space image is of strontium titanate (Sr_3TiO_2 , unit cell, $a_0 = b_0 = c_0 = 3.9051 \text{ \AA}$) in BF-CTEM at 200 kV, $C_{S3} = 0.7 \text{ mm}$, obj. aperture of $\alpha = 15 \text{ mrad}$, defocus $\Delta f = 500 \text{ \AA}$, defocus spread 50 \AA , condenser illumination angle 0.5 mrad. Each image is 256×256 pixels. (d–f) are the corresponding objective aperture images in reciprocal space, for each of a–c. The supercell size is (a, d) $3a_0 \times 3b_0$, (b, e) $6a_0 \times 6b_0$, (d, f) $9a_0 \times 9b_0$

An image simulation may require thousands or millions of operations on each pixel. Therefore during image simulation each pixel should be represented as a floating point number with much more than 8 bits per pixel. Most computer hardware is equipped to handle 32-bit single precision (typically there is one sign bit, 8 exponent bits, and 23 mantissa bits) and 64-bit double precision floating point arithmetic. Single precision (32 bits) gives about six decimal digits of accuracy per pixel and is usually sufficient for most image calculations. Each arithmetic operation between two single precision floating point numbers can be thought of as adding an error of about ± 1 in 10^6 or 1 in 6 digits. This error is sometimes referred to as roundoff error, and calculations with a finite number of bits is sometimes referred to as finite precision arithmetic. Although this error may seem insignificant it may be necessary to perform a million operations on some numbers, so the errors can add up to be significant even with single precision (32-bit) floating point arithmetic. A good computer program should be organized in such a way as to minimize the effects of roundoff error. Storing several images of sizes of 512×512 pixels or more requires a lot of memory, so double precision is usually not used to keep the memory requirements to a reasonable level. During numerical simulation each pixels should

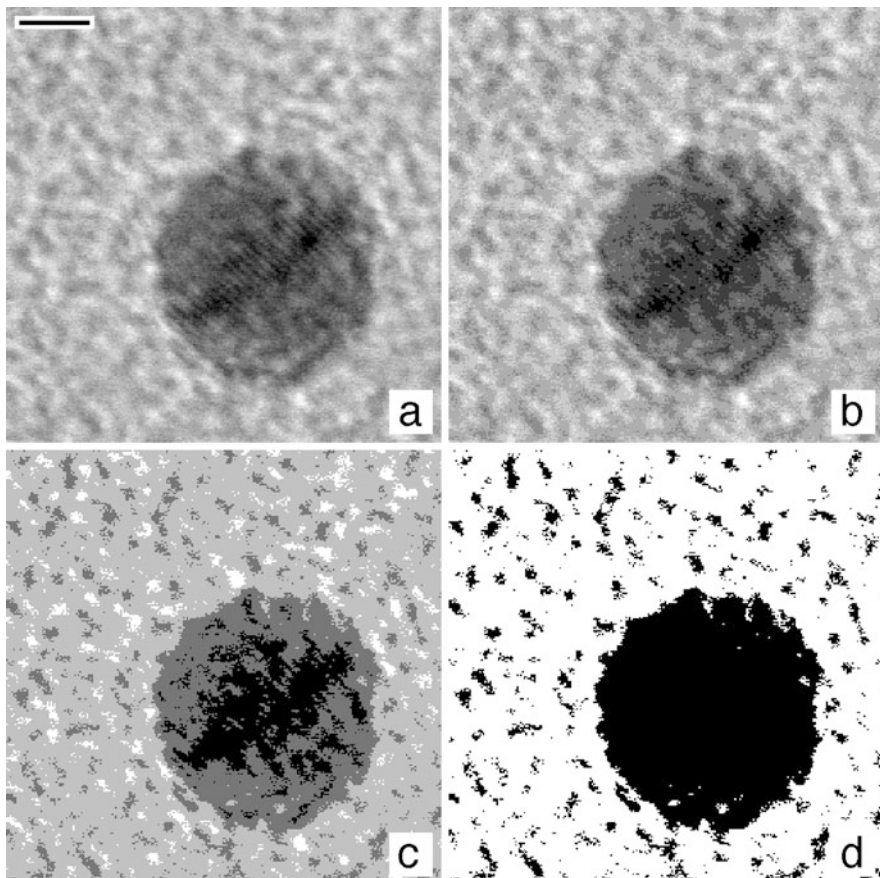


Fig. 4.5 The effect of limiting the number of bits in each pixel. (a) 4 bits/pixel, (b) 3 bits/pixel, (c) 2 bits/pixel, and (d) 1 bit/pixel. Each image was normalized to fill the available gray scale. The image is a bright field STEM image of a gold particle on an amorphous carbon film recorded on a VG HB-501 STEM ($C_s = 1.3$ mm, 100 keV). The 2.35 \AA gold lattice fringes are barely visible in the center of the particle. The scale bar in (a) is approximately 20 \AA (Fig. 4.2a is the same image with 8 bits per pixel)

be stored as a 32-bit (or more) floating point number and for the final displayed result 8 bits is probably sufficient.

4.2 Discrete Fourier Transform

Image simulation and image processing frequently use a discrete Fourier transform (DFT) to perform convolutions or to convert from reciprocal space to real space and

vice versa. There are several different ways to define a DFT that differ mainly in the placement of the minus signs and normalization constants. The specific definition of the Fourier transform FT and its inverse FT^{-1} that will be used here is:

$$FT[f(\mathbf{x})] = F(\mathbf{k}) = \sum_{x,y} \exp(2\pi i \mathbf{k} \cdot \mathbf{x}) f(\mathbf{x}) \quad (4.6)$$

$$FT^{-1}[F(\mathbf{k})] = f(\mathbf{x}) = \frac{1}{N_x N_y} \sum_{k_x, k_y} \exp(-2\pi i \mathbf{k} \cdot \mathbf{x}) F(\mathbf{k}) \quad (4.7)$$

where $\mathbf{x} = (x, y)$ and $\mathbf{k} = (k_x, k_y)$. The inverse Fourier transform can be written as the complex conjugate of the forward transform of the complex conjugate of $F(\mathbf{k})$.

$$FT^{-1}[F(\mathbf{k})] = \frac{1}{N_x N_y} \{FT[F^*(\mathbf{k})]\}^* \quad (4.8)$$

It is only necessary to program one or the other transform (forward or inverse) and the other can be obtained with suitable complex conjugation and scaling.

When expressed in (x, y) Cartesian coordinates the Fourier transform is separable in x and y .

$$F(k_x, k_y) = \sum_x \exp(2\pi i k_x x) \left[\sum_y \exp(2\pi i k_y y) f(x, y) \right] \quad (4.9)$$

A two-dimensional transform (forward or inverse) may be implemented by successive one-dimensional transforms. First perform a one-dimensional transform along all of the columns and then along all of the rows (or vice versa) of the sampled image (row-column decomposition). Therefore it is only necessary to program a single one-dimensional transform to perform both forward and inverse transforms on two-dimensional images. It is much easier in practice to arrange the images to be sampled in a rectangular (x, y) Cartesian grid to exploit the separability of the Fourier transform. Also note that the spacing in x and y may be different but it is usually advisable that the x and y spacings be within a factor of two or so of each other.

4.3 The Fast Fourier Transform or FFT

The one-dimensional discrete Fourier transform is:

$$F(n \Delta k) = F_n = \sum_j f(j \Delta x) \exp[2\pi i (n \Delta k)(j \Delta x)] \quad (4.10)$$

$$k = n\Delta k; \quad \Delta k = 1/a; \quad n = 0, 1, 2, \dots, (N - 1)$$

$$x = j\Delta x; \quad \Delta x = a/N; \quad j = 0, 1, 2, \dots, (N - 1)$$

with $f_j = f(j\Delta x)$ this simplifies to:

$$F_n = \sum_j f_j \exp[2\pi i(nj/N)] \quad (4.11)$$

The amount of computer time this requires typically scales as the number of floating point operations such as add, subtract, multiply, and divide. A one-dimensional DFT of length N requires N sums each with N terms and thus requires a computer time that is proportional to N^2 .

The computer time may be greatly reduced by use of the fast Fourier transform or FFT algorithm (Cooley and Tukey [68], Brigham [48], and Bracewell [46]). The FFT requires that the length N of the transform be a highly composite number (i.e., be factorable into many smaller integer prime factors). Usually factors of two are a little more efficient although this is not a strict requirement. If the length of the data array is some power of two, $N = 2^m$ (N and m integer), then the data array index j may be written as:

$$j = j_0 + j_1 2 + j_2 2^2 + j_3 2^3 + \dots + j_{m-1} 2^{m-1} \quad (4.12)$$

where each of the $j_0, j_1 \dots$ takes on values of 0 or 1. Equation 4.11 can then be written as:

$$\begin{aligned} F_n = & \sum_{j_0} \sum_{j_1} \sum_{j_2} \dots \sum_{j_{m-1}} f_{j_0 j_1 j_2 \dots j_{m-1}} \\ & \times \exp[2\pi i n(j_0 + j_1 2 + j_2 2^2 + \dots + j_{m-1} 2^{m-1})/N] \end{aligned} \quad (4.13)$$

The sums can be rearranged as:

$$\begin{aligned} F_n = & \sum_{j_0} \exp[2\pi i n j_0 / N] \sum_{j_1} \exp[2\pi i n j_1 2 / N] \dots \\ & \sum_{j_{m-1}} \exp[2\pi i n j_{m-1} 2^{m-1} / N] f_{j_0 j_1 j_2 \dots j_{m-1}} \end{aligned} \quad (4.14)$$

At first glance it seems as if this has just gotten a lot more complicated without any gain. However, a close inspection of the arithmetic reveals that there are $m = \log_2 N$ sums each with two terms. Each of the N Fourier components F_n requires m sums of length 2, so the total computer time becomes proportional to $Nm = N \log_2 N$. This is a huge savings in computer time for large N .

When N is decomposed into factors of 2 the FFT is said to be a radix-2 FFT. The radix-2 FFT requires frequent multiplication by sine and cosine of 0 and π (equals 0

and ± 1) which can be hand coded to avoid some floating point arithmetic operations. Curiously, if factors of 4 are also treated as prime factors, sine and cosine of 0, $\pi/2$, $3\pi/2$ and π appear (equals 0, ± 1 and $\pm i$). These can be hand coded without floating point arithmetic to produce an FFT that is a little faster than using only factors of 2. Factors of 8 also give a very small improvement in speed but significantly increase the code size, so only factors of 2 and 4 are commonly treated. When factors of four are used the FFT is said to be a radix-4 FFT. When N is decomposed into both factors of 2 and 4 the FFT is said to be a mixed radix FFT. It would first do all of the factors of 4 and then at most one factor of 2 to get any length that is a power of 2. If a two-dimensional (or higher) FFT is needed, an additional improvement in performance can also be obtained by using a look up table for the sines and cosines because they only need to be calculated once. Higher radix FFTs generally trade integer operations for floating point operation. Until recently floating point operations were almost always much slower than integer operation and higher radix FFTs run faster. Some new computer architectures close the gap (in speed) between integer and floating, and it is possible that radix-4 or radix-8 may not be significantly faster than radix-2 on some specific types of computers if floating point and integer operations are equally fast. Multidimensional transforms can also be limited by the memory bandwidth, and may benefit from careful attention to the order in which the data is accessed. The FFT is still a DFT in some sense (the FFT also satisfies Eq. 4.6 but just does it faster) but the two names will be used to distinguish the simple sum from the fast form of the sum.

The computer time for a radix-2 two-dimensional transform of length $N_x \times N_y$ for the DFT and the FFT (Eq. 4.6) is approximately proportional to:

$$\text{CPU time for simple DFT} \propto N_y N_x^2 + N_x N_y^2 \quad (4.15)$$

$$\text{CPU time for FFT} \propto N_x N_y \log_2(N_x N_y) \quad (4.16)$$

The constant of proportionality is of order unity in both cases. The advantage of the FFT over the DFT is very large as N gets bigger. Table 4.1 illustrates the relative CPU time of the DFT versus the FFT for some typical lengths of the data array. In two dimensions the ratio of the FFT to the DFT remains the same as in the table if $N_x = N_y = N$.

Table 4.1 Comparison of the relative CPU time required for a simple discrete Fourier transform (DFT) and a fast Fourier transform (FFT) for different lengths N

Number of data points N	$\log_2(N)$	DFT	FFT	Ratio
32	5	1024	160	6.4
64	6	4096	384	10.7
128	7	16,384	896	18.3
256	8	65,536	2048	32
512	9	262,144	4608	56.9
1024	10	1,048,576	10,240	102.4

The FFT is the workhorse of image simulation and image processing. It is worthwhile to optimize the code for efficient execution in the computer because it gets used over and over again. There are a variety of other tricks that can be incorporated into an actual program. Brigham [48] gives an excellent discussion of strategies for implementing an efficient FFT. Working code for the FFT has been given by Press et al. [406]. A version of a one-dimensional FFT using a mixed radix-2 and radix-4 approach in C is given at the end of this chapter.

Multidimensional FFTs can be implemented by successively applying a 1D FFT to each dimension. In a 2D FFT each row is transformed and then each column. This procedure is easy to adapt to multiple CPU (multithreaded) computer. Each row (or subset of rows) is independent so can be done simultaneously on a different CPU (many rows at the same time) and then each column (or subset of columns) on a different CPU. The openMP syntax for multithreading is relatively easy to use and has become commonly implemented in several different compilers and computer (and is mostly platform independent).

There are many freely available FFT subroutines. The currently popular FFTW package [149] seems to be one of the fastest (if not the fastest) available code. There are many ways to organize the FFT in small different ways. Different approaches work faster on different hardware, different compilers, and/or different data sizes. FFTW has an initialization phase that tests (at run time) several possible schemes for the FFT and discovers the fastest approach on the hardware, compiler, and data size being used. Subsequent FFTs are typically much faster. This initialization phase takes significant time and so is not effective if only a few FFTs are performed. However, if many more of the same size are executed (as is typical in many simulations, such as discussed here), then there can be an overall speed improvement of a factor of two or three, which is very helpful. In the current computer hardware large memory access is slower than many floating point calculation, so the organization of data in memory may be as important as the actual calculation. FFTW includes its own memory allocation routines which can be important in large multidimensional FFTs.

4.4 Wrap Around Error and Rearrangement

A consequence of a discrete Fourier transform (DFT or FFT) is that the sampled data is repeated indefinitely in a periodic array. An identical copy of the image appears on all four sides of the image. The image is usually not drawn this way but is implied by the use of discrete sampling and the discrete Fourier transform. In practice this periodic repetition means that the left and right edges of the image are effectively adjacent to one another and can interfere. ($x = 0$ is equivalent to $x = a$, $x = 2a$, etc.) The same is true of the top and bottom of the image. This effect is called the wrap-around error because the left and right or top and bottom edges effectively wrap around and touch each other. If the underlying specimen does not share this periodicity, then some rather dramatic artifacts that have nothing to do

with the specimen can be produced in simulated images. The underlying specimen periodicity should match the periodicity of the supercell (the supercell dimensions should be an integer multiple of the specimen unit cell size if the specimen is crystalline) or there should be a buffer zone around the edge of the image that can be discarded later. The width of this buffer zone varies with the application and may not always be obvious.

The wrap around effect applies in both real space and reciprocal space. This causes a strange distribution of spatial frequencies in the FFT. Large positive frequencies are the same as small negative frequencies. The sampled frequencies in reciprocal space (Eq. 4.4) may be written in order from left to right (in x) and bottom to top (in y) as:

$$k_x = 0, \Delta k_x, 2\Delta k_x, 3\Delta k_x, \dots, (N_x - 1)\Delta k_x \quad (4.17)$$

$$k_y = 0, \Delta k_y, 2\Delta k_y, 3\Delta k_y, \dots, (N_y - 1)\Delta k_y \quad (4.18)$$

With wrap around the $k_x = (N_x - 1)\Delta k_x$ position is touching the $k_x = 0$ position on the left. This means that the $N_x - 1$ position is the same as the -1 position (likewise in the y direction). The calculated order then becomes;

$$k_x/\Delta k_x = 0, 1, 2, \dots, \frac{N_x}{2}, -\frac{N_x}{2} + 1, \dots, -2, -1 \quad (4.19)$$

$$k_y/\Delta k_y = 0, 1, 2, \dots, \frac{N_y}{2}, -\frac{N_y}{2} + 1, \dots, -2, -1 \quad (4.20)$$

A circle with constant magnitude of spatial is drawn in FFT space on the left side of Fig. 4.6 (labeled default). The origin is in the lower left corner. What is normally the first quadrant is in the lower left corner, the second quadrant is in the lower right, the third quadrant in the upper right, and the fourth quadrant in the upper left. The distribution of spatial frequencies is normally used in this order during calculation because it would waste computer time to rearrange it. However, when displayed the FFT will be rearranged (as on the right-hand side of Fig. 4.6) to conform to a normal diffraction pattern with zero spatial frequency in the center.

4.5 Fourier Transforming Real Valued Data

The FFT discussed in Sect. 4.3 assumed a general case in which the data $f(x)$ is complex valued with a real and imaginary part (as in an electron wave function). Sometimes the data will be explicitly real valued (as in the potential $V(\mathbf{r})$ of the specimen). The special case of Fourier transforming real data allows a further reduction in computer time of about a factor of two. There are two possible methods to use. One is to transform a single real valued array more efficiently and the other is to transform more than one real array at a time with a single complex FFT. Both

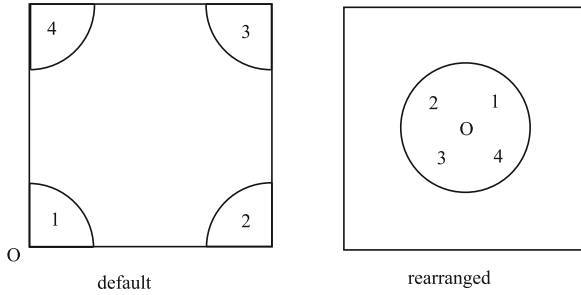


Fig. 4.6 Geometry of the FFT (or DFT). A circle of constant spatial frequency is drawn in the default configuration (left) and the rearranged configuration (right). The origin is at the lower left in the default configuration and in the center in the configuration at right rearranged for display purposes

of these methods are discussed in Press et al. [406]. Performing a two-dimensional FFT on real valued data is easiest using the second of these methods.

Consider two one-dimensional arrays of N real values, $f_a(x)$ and $f_b(x)$, linearly combined into a single complex valued array $f_c(x)$ as:

$$f_c(x) = f_a(x) + i f_b(x) \quad (4.21)$$

$f_c(x)$ is now in the form that can be used in a single FFT to produce N complex valued Fourier coefficients. The trick is to untangle the Fourier transform of $f_a(x)$ from that of $f_b(x)$. In real space $f_a(x)$ and $f_b(x)$ can be retrieved from $f_c(x)$ using Eq. 4.21 as:

$$f_a(x) = [f_c(x) + f_c^*(x)]/2 \quad (4.22)$$

$$f_b(x) = [f_c(x) - f_c^*(x)]/(2i) \quad (4.23)$$

In Fourier or reciprocal space:

$$F_c(k) = FT[f_c(x)] = \int f_c(x) \exp(2\pi i kx) dx \quad (4.24)$$

$$F_c^*(-k) = FT[f_c^*(x)] = \int f_c^*(x) \exp(2\pi i kx) dx \quad (4.25)$$

Therefore the transforms of $f_a(x)$ and $f_b(x)$ may be extracted from the transform of $f_c(x)$ (using Eq. 4.23) as:

$$FT[f_a(x)] = F_a(k) = [F_c(k) + F_c^*(-k)]/2 \quad (4.26)$$

$$FT[f_b(x)] = F_b(k) = [F_c(k) - F_c^*(-k)]/(2i) \quad (4.27)$$

If there are N real values in each of $f_a(x)$ and $f_b(x)$, then there are N complex values in $f_c(x)$ and $F_c(k)$. It follows that there are $N/2$ complex valued Fourier coefficients in each of $F_a(k)$ and $F_b(k)$ because:

$$F_a(k) = F_a^*(-k) \quad (4.28)$$

$$F_b(k) = F_b^*(-k) \quad (4.29)$$

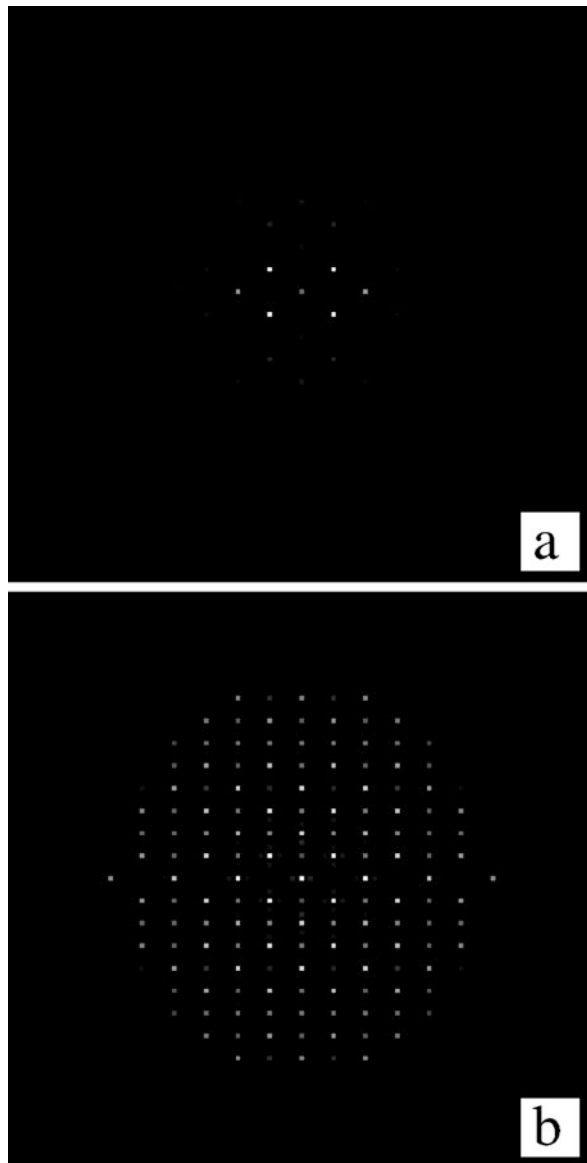
To calculate a two-dimensional Fourier transform of $N_x \times N_y$ real valued data points, first calculate the Fourier transform of all of the N_y columns two at a time, yielding N_y complex arrays of length $N_x/2$. Next Fourier transform N_x rows of $N_x/2$ complex values. This is referred to as a real to complex FFT and results in a net speed up of about a factor of two.

4.6 Displaying Diffraction Patterns

The square modulus of the Fourier transform of a function is called its power spectra. The power spectra of the wave function transmitted through the specimen is also equivalent to the electron diffraction pattern of the specimen. A diffraction pattern typically has a very large dynamic range in its intensity. The low spatial frequency information (low scattering angle) has a large amplitude but the high spatial frequency information (high scattering angle) has a much lower amplitude. A normal image display device (computer screen or printed paper) does not have a sufficient dynamic range to display both sets of information. The high spatial frequency information (which is frequently the interesting part) is not visible if the diffraction pattern is normalized to fill the available gray scale in a linear manner. In practice when a diffraction pattern is recorded the film or other detector may be saturated near the central beam to produce a nonlinear scale or multiple patterns may be recorded at different exposures to accommodate this large dynamic range. Gonzalez and Woods [160] and Pratt [405] suggest that a numerically calculated power spectra be displayed on a logarithmic scale to compress the dynamic range so that the entire diffraction pattern is visible. A simple logarithm will not work because some points of the power spectra (diffraction pattern) may be identically zero. The computer program must somehow limit the negative extent of the image scale. One method is to simply clip all the negative values (of the logarithm) to some minimum value. For example, the minimum gray scale can be set to the average value in some region of reciprocal space about half way between the minimum and maximum spatial frequencies. An alternative (similar to that proposed by Gonzalez and Woods [160] and Pratt [405]) is to transform the intensities as:

$$D(k_x, k_y) = \log(1 + c|F(k_x, k_y)|^2) \quad (4.30)$$

Fig. 4.7 The calculated diffraction pattern or power spectra of 110 silicon. (a) is shown on a linear scale and (b) is a logarithmic scale as in Eq. 4.30. White is a larger positive value



where $F(k_x, k_y)$ is the Fourier transform of the image, $D(k_x, k_y)$ is the actual value displayed, and c is a scaling constant that can be varied to adjust the contrast. Figure 4.7 shows the power spectra of the electron wave function transmitted through approximately 100 Å of silicon in the 110 orientation at an electron energy of 100 keV (simulated using the multislice method discussed in later chapters and a super cell size of 27×27 Å with 128×128 pixels). The linear gray scale in Fig. 4.7a

shows only the zero order beam in the center (rearranged as in Sect. 4.4) plus a few of the low order reflections. When displayed using Eq. 4.30 with $c = 0.1$ the higher order diffraction spots become visible in Fig. 4.7b. Most diffraction patterns shown in this book will use a compressed scale something like this.

4.7 An FFT Subroutine in C

The FFT is one of the most efficient (fast computation) algorithms available and is one of the primary drivers of the multislice algorithm to be considered in later chapters. There are many FFT subroutines available for downloading or purchase alone or as part of standard libraries. Below is the code for a simple one-dimensional FFT. Multidimensional transforms are typically performed as successive 1D FFTs in each direction, and can be easily implemented in parallel in a shared memory multiprocessor computer.

```

/*----- fft42 -----
fft42( fr[], fi[], n )           radix-4,2 FFT in C

fr[], fi[] = (float) real and imag. array with input data
n          = (long) size of array

calculate the complex fast Fourier transform of (fr,fi)
input array fr,fi (real,imaginary) indexed from 0 to (n-1)
on output fr,fi contains the transform

*/
void fft42 ( float *fr, float *fi, long n )
{
#define TWOPI    6.283185307

    long i, j, nv2, nm1, k, k0, k1, k2, k3, kinc, kinc2;
    float qr, qi, rr, ri, sr, si, tr, ti, ur, ui;
    double x1, w0r, w0i, wlr, wli, w2r, w2i, w3r, w3i;

    kinc = n;

    while( kinc >= 4 ) {      /* start radix-4 section */

        kinc2 = kinc;
        kinc = kinc / 4;

        for( k0=0; k0<n; k0+=kinc2 ) {
            k1 = k0 + kinc;
            k2 = k1 + kinc;
            k3 = k2 + kinc;

            rr = fr[k0] + fr[k2];
            ri = fi[k0] + fi[k2];

```

```

sr = fr[k0] - fr[k2];      si = fi[k0] - fi[k2];
tr = fr[k1] + fr[k3];      ti = fi[k1] + fi[k3];
ur = -fi[k1] + fi[k3];    ui = fr[k1] - fr[k3];

fr[k0] = rr + tr;      fi[k0] = ri + ti;
fr[k2] = sr + ur;      fi[k2] = si + ui;
fr[k1] = rr - tr;      fi[k1] = ri - ti;
fr[k3] = sr - ur;      fi[k3] = si - ui;
}

x1 = TWOPI/( (double) kinc2 );
w0r = cos( x1 );   w0i = sin( x1 );
w1r = 1.0;   w1i = 0.0;

for( i=1; i<kinc; i++ ) {
    x1 = w0r*w1r - w0i*w1i;   w1i = w0r*w1i + w0i*w1r;
    w1r = x1;
    w2r = w1r*w1r - w1i*w1i;   w2i = w1r*w1i + w1i*w1r;
    w3r = w2r*w1r - w2i*w1i;   w3i = w2r*w1i + w2i*w1r;

    for( k0=i; k0<n; k0+=kinc2 ) {
        k1 = k0 + kinc;
        k2 = k1 + kinc;
        k3 = k2 + kinc;

        rr = fr[k0] + fr[k2];      ri = fi[k0] + fi[k2];
        sr = fr[k0] - fr[k2];      si = fi[k0] - fi[k2];
        tr = fr[k1] + fr[k3];      ti = fi[k1] + fi[k3];
        ur = -fi[k1] + fi[k3];    ui = fr[k1] - fr[k3];

        fr[k0] = rr + tr;      fi[k0] = ri + ti;

        qr = sr + ur;      qi = si + ui;
        fr[k2] = (float) (qr*w1r - qi*w1i);
        fi[k2] = (float) (qr*w1i + qi*w1r);

        qr = rr - tr;      qi = ri - ti;
        fr[k1] = (float) (qr*w2r - qi*w2i);
        fi[k1] = (float) (qr*w2i + qi*w2r);

        qr = sr - ur;      qi = si - ui;
        fr[k3] = (float) (qr*w3r - qi*w3i);
        fi[k3] = (float) (qr*w3i + qi*w3r);
    }
}

} /* end radix-4 section */

while( kinc >= 2 ) { /* start radix-2 section */

    kinc2 = kinc;
    kinc = kinc / 2 ;

    x1 = TWOPI/( (double) kinc2 );

```

```

w0r = cos( x1 );    w0i = sin( x1 );
w1r = 1.0;    w1i = 0.0;

for( k0=0; k0<n; k0+=kinc2 ){
    k1 = k0 + kinc;
    tr = fr[k0] - fr[k1];    ti = fi[k0] - fi[k1];
    fr[k0] = fr[k0] + fr[k1];
    fi[k0] = fi[k0] + fi[k1];
    fr[k1] = tr;    fi[k1] = ti;
}

for( i=1; i<kinc; i++ ) {
    x1 = w0r*w1r - w0i*w1i;    wli = w0r*wli + w0i*w1r;
    w1r = x1;
    for( k0=i; k0<n; k0+=kinc2 ){
        k1 = k0 + kinc;
        tr = fr[k0] - fr[k1];    ti = fi[k0] - fi[k1];
        fr[k0] = fr[k0] + fr[k1];
        fi[k0] = fi[k0] + fi[k1];
        fr[k1] = (float) (tr*w1r - ti*wli);
        fi[k1] = (float) (tr*wli + ti*w1r);
    }
}
} /* end radix-2 section */

nv2 = n / 2;
nm1 = n - 1;
j = 0;

for (i=0; i< nm1; i++) { /* reorder in bit rev. order */
    if( i < j ){
        tr = fr[j];    ti = fi[j];
        fr[j] = fr[i];    fi[j] = fi[i];
        fr[i] = tr;    fi[i] = ti;    }
    k = nv2;
    while ( k <= j ) { j -= k;    k = k>>1;    }
    /* while ( k <= j ) {j=j-k;    k= k /2; }  is slower */
    j += k;
}

#endif TWOPI
} /* end fft42() */

```

4.8 Further Reading

Some Books on Computer Image Processing

1. K. R. Castleman, *Digital Image Processing*, Prentice Hall, 1979 [[58](#)]
2. R. C. Gonzalez and R. E. Woods, *Digital Image Processing, 3rd edition*, Prentice-Hall, 2008 [[160](#)]

3. B. K. Gunturk and X. Li, *Image Restoration, Fundamentals and Advances*, CRC Press, 2013 [175]
4. E. L. Hall, *Computer Image Processing and Recognition*, Academic Press, 1979 [186]
5. B. Jähne, *Digital Image Processing*, 3rd edition, Springer, 1995 [240]
6. A. Jain, *Fundamentals of Digital Image Processing*, Prentice Hall, 1989 [241]
7. D. L. Missel, *Image Analysis, Enhancement and Interpretation*, North Holland, 1978 [349]
8. W. K. Pratt, *Digital Image Processing*, Wiley, 1978 [405]
9. W. O. Saxton, *Computer Techniques for Image Processing in Electron Microscopy*, *Adv. in Electronics and Electron Physics, Supplement 10*, Academic Press, 1978 [436]

Some Books on Fourier Transforms and Fourier Optics

1. E. O. Brigham, *The Fast Fourier Transform*, Prentice-Hall, 1988 [48]
2. J. W. Goodman, *Intro. to Fourier Optics*, 3rd. edit., Roberts and Co., 2005 [161]
3. James S. Walker, *Fast Fourier Transforms*, 2nd edit., CRC Press, 1996 [516]

Chapter 5

Calculation of Images of Thin Specimens



This chapter discusses the calculation of an electron microscope image neglecting the geometrical thickness of the specimen (i.e., very thin specimens). Many practical specimens are too thick for this type of calculation to be quantitatively correct. However this approach can provide a qualitative insight into the structure in the image and it requires much less computer time. This type of image simulation is sometimes referred to as a phase grating, thick phase grating , or a kinematical image approximation because it does not properly include the effects of multiple or plural scattering within the specimen. Calculation of the transmission function of thin specimens is also a necessary part of more advanced calculations including a realistic specimen thickness that will be considered in later chapters. In particular the calculation presented in this chapter will form a single slice of the multislice algorithm

The kinetic energy of the imaging electrons in the electron microscope approaches their rest mass energy. A detailed quantum mechanical calculation of the motion of these electrons should properly be calculated using relativistic quantum mechanics (the Dirac equation with spin). As discussed in Sect. 2.3 the relativistic effects can be approximated by using the nonrelativistic Schrödinger equation (neglecting electron spin) with the relativistically correct wavelength and mass of the electron. This approximation is probably accurate enough at 100 keV but may be less accurate at 1 MeV. Nonrelativistic quantum mechanics is, however, dramatically easier to work with, and this approximation will be used here.

5.1 The Weak Phase Object

The primary interaction between the specimen and the imaging electrons is between the electrostatic potential of the specimen and the charge on the electron. The electrons traveling down the column of the microscope (before hitting the specimen)

are a superposition of one or more plane waves. In the CTEM the incident electrons are primarily in a single plane wave and the STEM probe is a superposition of many plane waves (i.e., a spherically convergent probe). It suffices to consider the effect of the specimen on one plane wave. The wave function ψ for one plane wave traveling along the optic axis in the z direction is:

$$\psi(\mathbf{x}) = \exp(2\pi i k_z z) = \exp(2\pi i z/\lambda) \quad (5.1)$$

where λ is the wavelength of the electron and $k_z = 1/\lambda$ is the propagation wave vector. The relativistic expression for the reciprocal of the electron wavelength in vacuum (see Eq. 2.5) is:

$$k_z = \frac{1}{\lambda} = \frac{\sqrt{eV(2m_0c^2 + eV)}}{hc} \quad (5.2)$$

where m_0 is the rest mass of the electron, c is the speed of light in vacuum, h is Planck's constant, and eV is the kinetic energy of the electron in vacuum.

The imaging electrons typically have a much higher energy than the electrons in the specimen. If the specimen is thin the imaging electrons pass through the specimen with only a small deviation in their path. This deviation can be approximated as a small change in wavelength of the electrons as they pass through the specimen (see Fig. 5.1). The specimen has a small electrostatic potential which influences the electron wavelength. If the potential inside the specimen is positive, then the imaging electrons are accelerated inside the specimen giving them a smaller wavelength. If eV_s is the additional electrostatic potential energy of the imaging electrons while in the specimen and λ_s is their wavelength, then while inside the specimen:

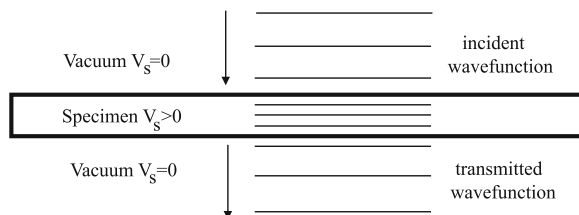


Fig. 5.1 An incident (high energy) electron plane wave passing through the electrostatic potential V_s of the specimen. The wave function is drawn as lines of constant phase, and the specimen is assumed to have a uniform constant potential (not usually true in practice). The electron wavelength is reduced by the positive potential inside the specimen. This drawing is not to scale

$$\begin{aligned}
\frac{1}{\lambda_s} &= \frac{[(eV + eV_s)(2m_0c^2 + eV + eV_s)]^{1/2}}{hc} \\
&= \frac{[eV(2m_0c^2 + eV) + eV_s(2m_0c^2 + 2eV + eV_s)]^{1/2}}{hc} \\
&= \frac{1}{\lambda} \left[1 + \frac{eV_s(2m_0c^2 + 2eV + eV_s)}{eV(2m_0c^2 + eV)} \right]^{1/2}
\end{aligned} \tag{5.3}$$

Expanding this equation and keeping only the lowest order terms in V_s/V yields:

$$\begin{aligned}
\frac{1}{\lambda_s} &\sim \frac{1}{\lambda} \left[1 + \frac{eV_s(2m_0c^2 + 2eV)}{2eV(2m_0c^2 + eV)} + \dots \right] \\
&\sim k_z + \frac{V_s(m_0c^2 + eV)}{\lambda V(2m_0c^2 + eV)} + \dots
\end{aligned} \tag{5.4}$$

Changing the wavelength inside the specimen is equivalent to shifting the phase of the electron as it passes through the specimen (i.e., changing the wave vector k_z). Therefore the electron wave function while passing through the specimen is:

$$\psi(\mathbf{x}) \sim \exp(2\pi i k_z z) \exp(i\sigma_e V_s z) \tag{5.5}$$

where the interaction parameter σ_e is:

$$\sigma_e = \frac{2\pi}{\lambda V} \left(\frac{m_0c^2 + eV}{2m_0c^2 + eV} \right) = \frac{2\pi m e \lambda}{h^2} \tag{5.6}$$

$m = \gamma m_0$ is the relativistic mass. This expression assumes that the specimen potential V_s is much smaller than the beam energy ($V_s/V \ll 1$). Also remember that the specimen potential varies with position although not explicitly written above. It is traditional to use the same symbol for both the interaction parameter and the scattering cross section, but the meaning should usually be clear from the context in which each is used. The interaction parameter is plotted versus the electron kinetic energy in Fig. 5.2. The interaction parameter decreases rapidly with increasing electron energy at low electron energy but is nearly constant for electron energies above about 300 keV.

If the specimen is very thin, then the electron wave function accumulates a total phase change while passing through the specimen that is just the integral of the potential of the specimen. The incident electrons pass through the specimen and the effect of the specimen is to multiply the incident wave function (Eq. 5.1) by the specimen transmission function $t(\mathbf{x})$. The wave function transmitted through the specimen is:

$$\begin{aligned}
\psi_t(\mathbf{x}) &= t(\mathbf{x}) \exp(2\pi i k_z z) \\
t(\mathbf{x}) &= \exp[i\sigma_e v_z(\mathbf{x})]
\end{aligned} \tag{5.7}$$

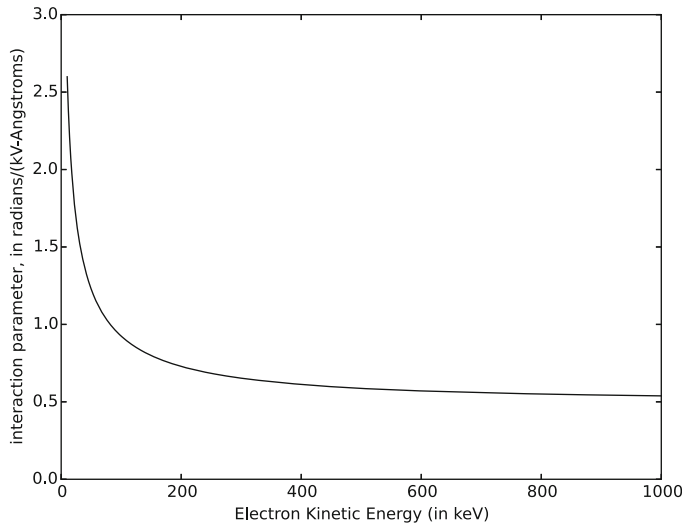


Fig. 5.2 The interaction parameter σ_e versus the electron kinetic energy

and the projected atomic potential $v_z(\mathbf{x})$ is the integral along the optic axis, z of the specimen:

$$v_z(\mathbf{x}) = v_z(x, y) = \int V_s(x, y, z) dz \quad (5.8)$$

This is the so-called weak phase object approximation (Cowley and Iijima [77]). There are really two assumptions in this approximation. One is that the potential inside the specimen is very small and the other is that the accumulated effect of the specimen can be replaced with a simple integral along z .

5.2 Single Atom Properties

Single atoms are a reasonable starting point to discuss the simulation of electron microscope images in the weak phase object approximation. Single isolated atoms with low to medium atomic number satisfy the thin specimen requirement and can actually be seen in some microscopes under the appropriate conditions. Furthermore the potential and charge distribution of single atoms can be calculated from first principles using relativistic Hartree–Fock theory in a reasonably well defined although tedious manner. To find the potential and charge distribution in a single atom requires finding the wave function of all electrons in the atom (to a good approximation the atomic nucleus may be regarded as a fixed point charge at the origin). Hydrogen is the only atom which can be solved analytically and a derivation

is usually given in most quantum mechanics text books (see for example Eisberg [112] or Schiff [444]). Unfortunately atoms with more than one electron (that is, the rest of the periodic chart) must be solved numerically with some approximations. The Hartree–Fock method forms an effective many-electron wave function obeying the Pauli exclusion principle that also satisfies the Schrödinger wave equation (or in the case of the relativistic Hartree–Fock method the Dirac wave equation). The method reduces to repeatedly solving a single particle wave equation for each electron orbital that is moving in an effective potential due to the charge on the nucleus and the average interactions with all other electrons in the atoms. Each electron orbital is calculated using the current distribution of the other electrons in the atoms and the process is repeated for all orbitals until the electron wave functions for all electrons converge to a final self-consistent result. Relativistic effects are probably negligible for low atomic numbers (like carbon) but are significant for high atomic numbers (like gold) because the core electrons near the nucleus experience a very large electric field and have a large kinetic energy (i.e., velocity). A detailed discussion of the Hartree–Fock method is beyond the scope of this book but may be found in the books by Froese-Fischer [151], Cowan [72], Szasz [481], and Froese-Fischer et al. [137]. Appendix C gives a detailed description of using a relativistic Hartree–Fock program to calculate a complete set of atomic potentials for the whole periodic chart (atomic number $Z = 1$ through $Z = 103$).

5.2.1 Radial Charge Distribution

The radial electron charge distribution $\rho(r)$ of each atom is generated as part of the Hartree–Fock atomic structure calculation. The calculated radial charge distribution for a few selected atoms is shown in Fig. 5.3. The peaks in the charge distribution correspond to the atomic orbitals (or electron shells) of each atom. It is interesting to note that although the total number of electrons increases with atomic number Z the actual size of the atoms does not change dramatically with atomic number. The increasing charge of the nucleus (with increasing Z) causes the electrons to be attracted more strongly to the nucleus roughly keeping the actual atomic size relatively constant at about one Angstrom in diameter.

5.2.2 Potential

The atomic potential is a more interesting quantity for electron microscopy because the imaging electrons in the microscope interact directly with the atomic potential (see Eq. 5.5). The charge distribution and potential are related via Poisson's equation from electromagnetic theory. The Mott–Bethe [32, 34, 363, 364] formula (Eq. C.7) is equivalent to Poisson's equation; however, it is stated in reciprocal space. Figure 5.3 only includes the electron charge distribution; however, the large point charge

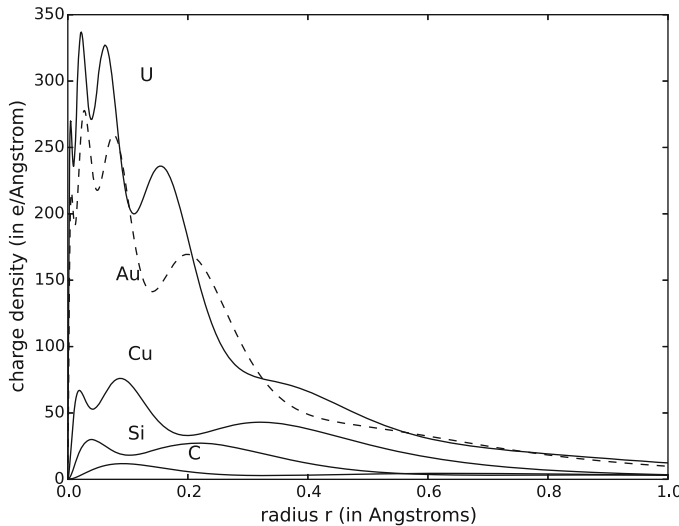


Fig. 5.3 The calculated electron charge distribution $4\pi r^2 \rho(r)$ (in electrons per \AA) for isolated single atoms at the origin versus the three-dimensional radius r . The atoms are carbon ($Z = 6$), silicon ($Z = 14$), copper ($Z = 29$), gold ($Z = 79$), and uranium ($Z = 92$)

on the atomic nucleus probably has the strongest interaction with the imaging electrons. The electron cloud in Fig. 5.3 mainly serves to shield the atomic nucleus (remember that the nucleus has a positive charge but the electron cloud has a negative charge). When the charge on the atomic nucleus is added to the atomic electron charge distribution and the resulting charge distribution is transformed into an atomic potential the total potential is much more strongly peaked near the nucleus (at the origin). The Hartree–Fock procedure of necessity ends up with a large table of numbers. Appendix C details how to parameterize the tabulated Hartree–Fock results. To a reasonably good approximation the atomic potential (including the nucleus) may be written as:

$$V_a(x, y, z) = 2\pi^2 a_0 e \sum_{i=1}^3 \frac{a_i}{r} \exp(-2\pi r \sqrt{b_i}) + 2\pi^{5/2} a_0 e \sum_{i=1}^3 c_i d_i^{-3/2} \exp(-\pi^2 r^2 / d_i) \quad (5.9)$$

with $r^2 = x^2 + y^2 + z^2$

where a_0 is the Bohr radius and the a_i , b_i , c_i , and d_i coefficients are tabulated in Appendix C. There is a different set of coefficients for each element. A graph of

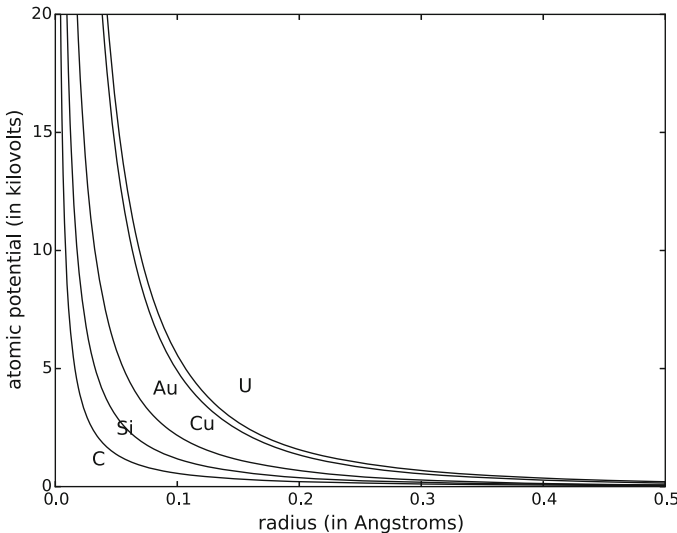


Fig. 5.4 Calculated atomic potential versus the three-dimensional radius r for isolated single atoms at $r = 0$. The atoms are carbon ($Z = 6$), silicon ($Z = 14$), copper ($Z = 29$), gold ($Z = 79$), and uranium ($Z = 92$)

the atomic potential versus radius in three dimensions is shown in Fig. 5.4 for a few selected elements.

When the atomic potential is integrated along the z direction (i.e., the optic axis of the microscope) the result is the projected atomic potential:

$$\begin{aligned}
 v_z(x, y) &= \int_{-\infty}^{+\infty} V_a(x, y, z) dz \\
 &= 4\pi^2 a_0 e \sum_{i=1}^3 a_i K_0(2\pi r \sqrt{b_i}) + 2\pi^2 a_0 e \sum_{i=1}^3 \frac{c_i}{d_i} \exp(-\pi^2 r^2 / d_i) \quad (5.10)
 \end{aligned}$$

with $r^2 = x^2 + y^2$

where $K_0(x)$ is the modified Bessel function of zeroth order. The projected atomic potential is shown in Fig. 5.5 for the same elements as in Fig. 5.4.

The atomic nucleus is essentially a point charge on this scale (typical nuclear sizes are of order a few times 10^{-5} Å). This causes a singularity in the projected atomic potential at $r = 0$ (there is also a singularity in the 3D atomic potential.) In reality the finite size of the nucleus removes the singularity so there is no real problem. No electron microscope that currently exists has enough resolution to see this strong singularity either, so the limited resolution of the microscope will further smear out this singularity in practice. In practical computer simulations the singularity will also be removed by finite sampling requirements because only the

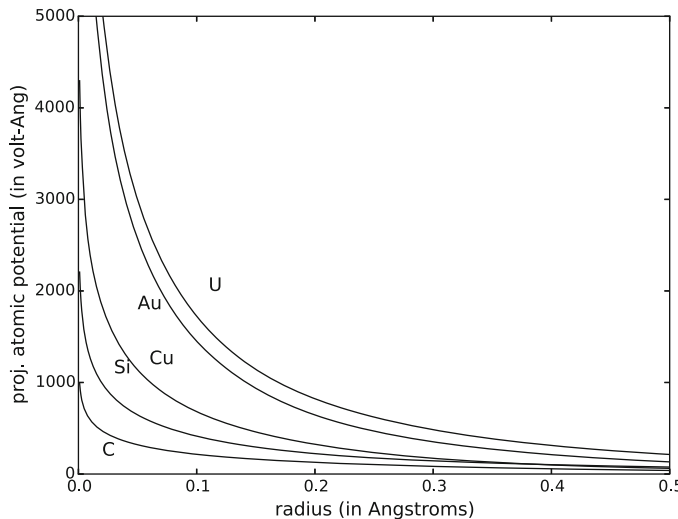


Fig. 5.5 Calculated projected atomic potential versus the two-dimensional radius r for isolated single atoms at $r = 0$. The atoms are carbon ($Z = 6$), silicon ($Z = 14$), copper ($Z = 29$), gold ($Z = 79$), and uranium ($Z = 92$)

projected atomic potential averaged over a nonzero sized sampling element or pixel is used. The projected atomic potential (Fig. 5.5) diverges less strongly than the atomic potential (Fig. 5.4).

At a radius of 0.1 Å the projected atomic potential of silicon (Si) is 0.41 kV-Å and the projected atomic potential of gold (Au) is 1.45 kV-Å (see Fig. 5.5). The interaction parameter σ_e (Eq. 5.6) is $0.92 \text{ radians/(kV-Å)}$ at a beam energy of 100 keV . This means that a single silicon atom will produce a total phase shift of 0.38 radians and a single gold atom will produce a phase shift of 1.34 radians (both at a beam energy of 100 keV and a radius of 0.1 Å). A single gold atom is not a weak phase object (in the sense of Eq. 3.6) but a single silicon atom is a reasonable weak phase object (at 100 keV). The situation improves slightly at beam energies of 300 keV or above because σ_e decreases by almost a factor of two. All atoms have a near singularity at a radius of zero so no single atom is truly a weak phase object in a strict sense.

5.2.3 Atomic Size

There is no single unambiguous method to calculate the effective size of single atoms. The rms (root-mean-square) radius is as good as any other method. The three-dimensional mean square (rms) radius of the charge distribution can be defined as:

$$r_q = \left[\frac{\int_0^\infty r^2 \rho(r) r^2 dr}{\int_0^\infty \rho(r) r^2 dr} \right]^{1/2} \quad \text{where } r = x^2 + y^2 + z^2 \quad (5.11)$$

where $\rho(r)$ is the radial charge density. In a similar manner the two dimensional mean square radius of the projected atomic potential is:

$$r_v = \left[\frac{\int_0^\infty r^2 v_z(r) r dr}{\int_0^\infty v_z(r) r dr} \right]^{1/2} \quad \text{where } r = x^2 + y^2 \quad (5.12)$$

Portions of the potential at large radius contribute more to this calculation due to their increased effective area. For example, if the projected atomic potential is multiplied by r the result is shown in Fig. 5.6. The rms atomic radii for all atoms as calculated from Eqs. 5.11 and 5.12 is shown in Fig. 5.7. The large tails of the potential increase the apparent size of the atoms. The effective rms size of the atoms as determined by the projected atomic potential is about two Angstroms in diameter (similar to the spacing between atoms). Note that the effective full-width-half-maximum of a single atom image may be smaller because of the strong potential near the nucleus of each atom.

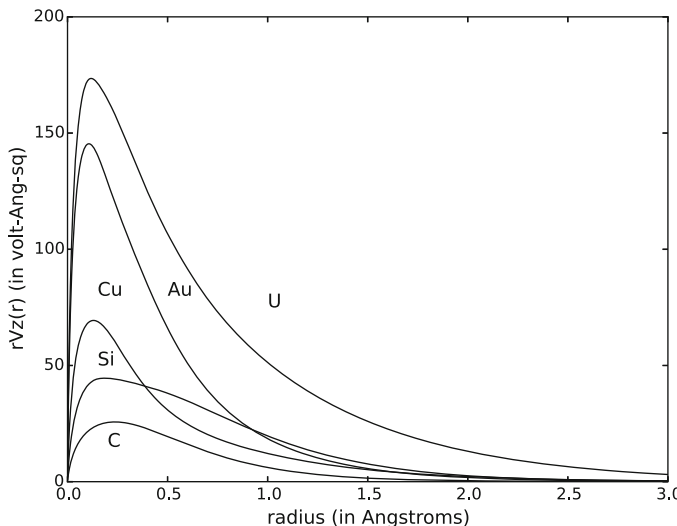


Fig. 5.6 Projected atomic potential multiplied by the radius r to illustrate the relative contribution to an image. Each curve is a different atom; carbon ($Z = 6$), silicon ($Z = 14$), copper ($Z = 29$), gold ($Z = 79$), and uranium ($Z = 92$)

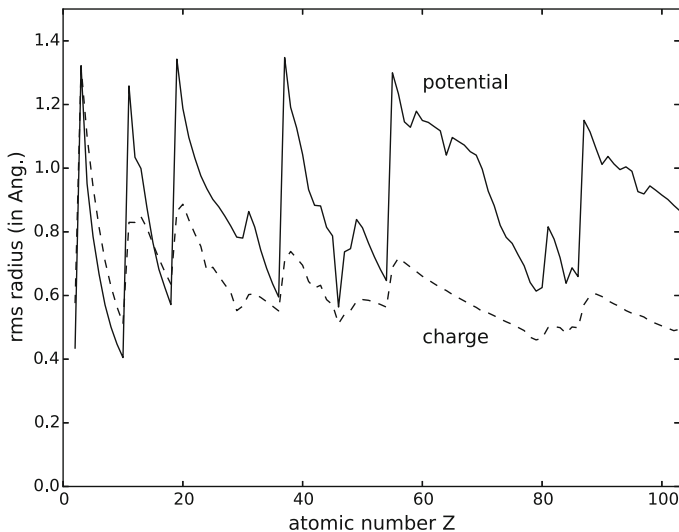


Fig. 5.7 The rms radius of isolated single atoms as determined from the (3D) electron charge and the (2D) projected atomic potential

5.2.4 Scattering Factors

The traditional physics view of electron scattering starts with a plane wave incident on the atom which gives rise to an outgoing plane wave plus an outgoing spherical wave (the atom has spherical symmetry) with amplitude $f_e(q)$.

$$\psi(\mathbf{x}) = \exp(2\pi i k_z z) \quad \text{incident} \quad (5.13)$$

$$= \exp(2\pi i k_z z) + f_e(q) \frac{\exp(2\pi i \mathbf{q} \cdot \mathbf{r})}{r} \quad \text{scattered} \quad (5.14)$$

where \mathbf{q} is the difference between the incident and scattered wave vectors (three-dimensional vector). The scattering amplitude $f_e(q)$ can also be referred to as the scattering factor. There are several methods of calculating the scattering amplitudes. The most popular approximation to the scattering amplitude is the first Born approximation that is simply the three-dimensional Fourier transform of the atomic potential (see for example section 38 of Schiff [444]):

$$\begin{aligned} f_e(\mathbf{q}) &= \frac{2\pi m_0 e}{h^2} \int V_a(\mathbf{r}) \exp(2\pi i \mathbf{q} \cdot \mathbf{r}) d^3 r \\ &= \frac{1}{2\pi e a_0} \int V_a(\mathbf{r}) \exp(2\pi i \mathbf{q} \cdot \mathbf{r}) d^3 r \end{aligned} \quad (5.15)$$

where $V_a(\mathbf{r})$ is the 3D atomic potential of the atom, m_0 is the rest mass of the electron, e is the magnitude of the charge of the electron, h is Planck's constant, and $a_0 = \hbar^2/m_0 e^2 = 0.5292 \text{ \AA}$ is the Bohr radius. $f_e(q)$ is in units of \AA and must be multiplied by the relativistic mass ratio m/m_0 for different incident electron energies. For the case where the atom is spherically symmetric this reduces to:

$$f_e(q) = \frac{1}{\pi e a_0 q} \int_0^\infty V_a(r) \sin(2\pi qr) r dr \quad (5.16)$$

The scattering factor is the amplitude for scattering of a single electron by a single atom. The first Born approximation is totally inadequate for directly calculating electron scattering in the electron microscope image (Zeitler and Olsen [543, 544], Glauber and Shoemaker [157]). In general $f_e(q)$ should be a complex valued quantity but the first Born approximation only yields a real valued quantity. However the first Born approximation is convenient because it is also the Fourier transform of the atomic potential. Image simulation will eventually use the specimen potential directly and not the scattering factors, so the Born approximation is still useful as a means of calculating the specimen potential. Combined with the Fourier projection theorem (Appendix B) the Born approximation provides a convenient method of calculating the projected atomic potential of thin specimens. It is also independent of the incident electron energy so that is easy to tabulate. As given in Appendix C the scattering amplitude in the first Born approximation can be written as:

$$f_e(q) = \sum_{i=1}^3 \frac{a_i}{q^2 + b_i} + \sum_{i=1}^3 c_i \exp(-d_i q^2) \quad (5.17)$$

where the a_i , b_i , c_i and d_i coefficients are tabulated in Appendix C for each element and are found by fitting the results of the relativistic Hartree–Fock program. The scattering factors for several atoms are plotted in Fig. 5.8. Note that the scattering factor for carbon ($Z = 6$) and silicon ($Z = 14$) cross at low angle. The low angle scattering factor is dependent on the state of the outer valence shell which fills periodically with increasing atomic number in the periodic chart. The scattering factor at large angles is primarily due to the scattering from the nucleus which is a monotonic function of atomic number Z . Doyle and Turner [100] have given the most popular tabulation currently in use. Many other authors have tabulated relevant parameters for single atoms and Table C.1 of Appendix C gives a more complete listing of the data available in the literature.

A more detailed derivation of the scattering factor in the Moliere [358] or eikonal [444] approximation yields an improved expression of:

$$f_e(q) = \frac{2\pi i}{\lambda} \int_0^\infty J_0(2\pi qr) \left\{ 1 - \exp \left[i\sigma_e \int V(x, y, z) dz \right] \right\} r dr \quad (5.18)$$

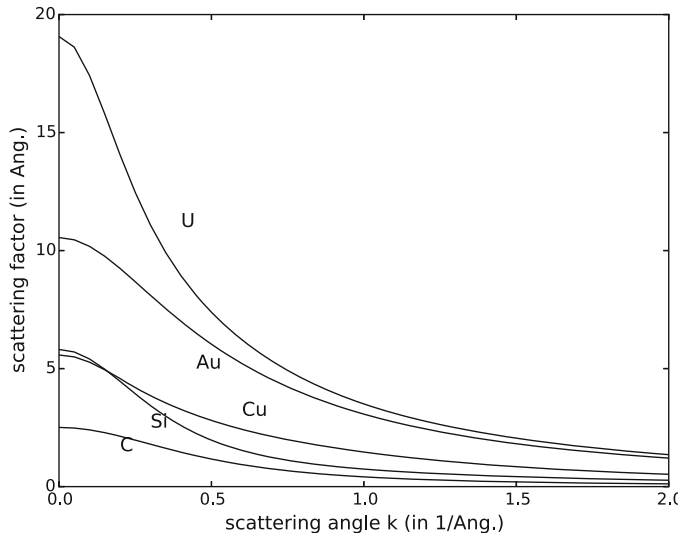


Fig. 5.8 The electron scattering factor in the first Born approximation versus scattering angle $k = \alpha/\lambda$ of isolated single atoms. Each curve is a different atom which are carbon ($Z = 6$), silicon ($Z = 14$), copper ($Z = 29$), gold ($Z = 79$) uranium ($Z = 92$)

where $r = \sqrt{x^2 + y^2}$ can also be interpreted as the impact parameter, $J_0(x)$ is the Bessel function of order zero which arises from the azimuthal integration of a spherically symmetric function and σ_e is the interaction parameter (Eq. 5.6). This expression for the electron scattering factor (Eq. 5.18) is a complex quantity (Zeitler and Olsen [543, 544], Frank [141], Reimer and Gilde [416], Ferwerda and Visser [131]) and can be recognized as the Fourier transform of the weak phase object approximation (Eq. 5.5). The scattering processes discussed here are purely elastic so electrons should not be created or destroyed. The optical theorem (for example, Schiff [444]) requires that the scattering factor $f_e(q)$ be complex to preserve the total number of electrons. A complex valued scattering factor does not imply that the atomic potential is complex. The atomic potential is a real valued function but a complete elastic scattering factor should be complex to preserve the total number of particles. The Moliere approximation for $f_e(q)$ (Eq. 5.18) is a different value for each incident electron energy and is therefore difficult to tabulate for a general incident electron energy. The first Born approximation can be tabulated independent of energy which probably accounts for its popularity. The scattering amplitude is plotted in Fig. 5.9 in both the Moliere and Born approximations for a low ($Z = 14$, silicon) and high ($Z = 79$, gold) atomic number atom. The Born approx. is fairly accurate for low atomic numbers like carbon and silicon but becomes less accurate at high atomic numbers like gold. At high atomic numbers the first Born approximation gets the magnitude about right but the phase of the scattering amplitude may have significant error. The phase of $f_e(q)$ increases at high angles whereas the phase of the first Born approximation is identically zero for all

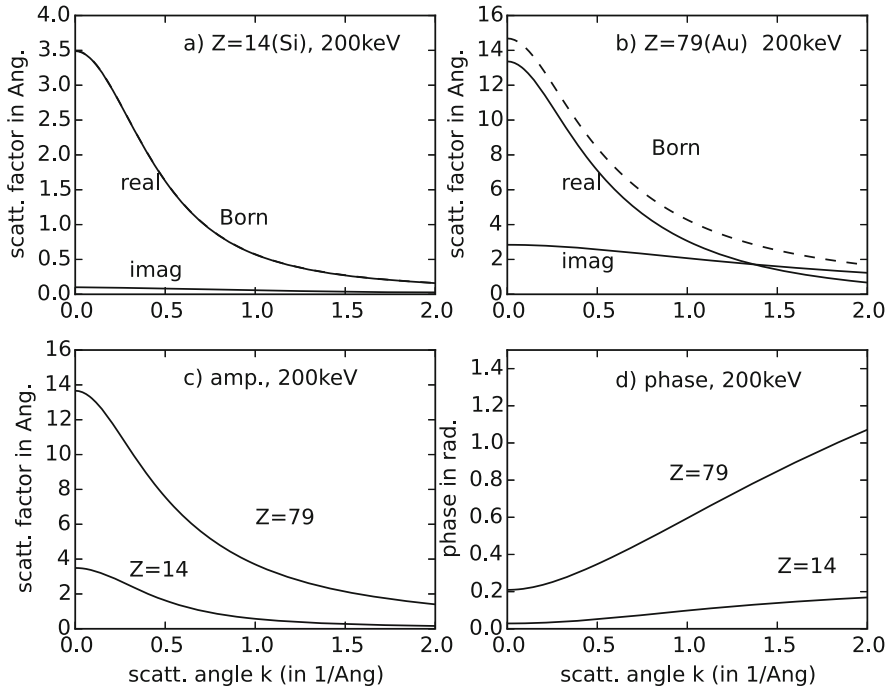


Fig. 5.9 The electron scattering factor for (a) silicon and (b) gold at 200 keV. The curves labeled real and imag. are the complex scattering factor in the Moliere approximation (Eq. 5.18) and the curves labeled Born are the scattering factor in the first Born approximation scaled by the relativistic mass ratio m/m_0 . (c) shows the amplitude and (d) the phase of the complex scattering factors

angles. The different behavior of heavy and light atoms in the imaginary part of the scattering factors has been proposed as a means of locating heavy atoms on a carbon support film using a defocus series reconstruction (for example, Frank [141]).

5.3 Total Specimen Potential

The imaging electrons in the microscope interact with the effective potential of the specimen as a whole. Simulation of a whole electron microscope image requires a knowledge of the position of all atoms in the specimen. The main question is how to combine the single atom potentials to get the potential of the whole specimen. The simplest approach is to form the potential of the specimen by a linear superposition of the potentials of each atom in the specimen as if all of the atoms were independent.

$$v_z(\mathbf{x}) = \sum_{j=1}^N v_{zj}(\mathbf{x} - \mathbf{x}_j) \quad (5.19)$$

where $\mathbf{x}_j = (x_j, y_j)$ is the position of atom j in a plane perpendicular to the optical axis of the microscope and $v_{zj}(\mathbf{x})$ is its projected atomic potential. In a thick specimen \mathbf{x}_j will become a three-dimensional quantity (see Chap. 6). This model may also be referred to (for example, Meyer et al. [343] and Susi et al. [480]) as an independent atom model (IAM). This linear superposition approximation would be exact for single atoms separated by a distance that is large compared to the size of the atom. However, in an actual solid specimen the atoms are bound together and their outer valence electrons will have been rearranged slightly. This electronic rearrangement will also alter the projected atomic potential (and low angle scattering) slightly. The principle interaction causing high angle scattering is the interaction between the imaging electrons (in the microscope) and the large point charge at the atomic nucleus. Because the nucleus is unaffected by bonding in the solid the high angle scattering (as in ADF-STEM) should be well represented by a simple linear superposition of atomic potentials. The bonding in the solid should primarily affect the low angle scattering such as in bright field phase contrast (STEM and CTEM).

Inherent in the discussion of Sect. 5.2 is the assumption that each atom is spherically symmetric. This is only true for atoms whose valence shells are in the $l = 0$ or s angular momentum state. Early work by McWeeny [339, 340] and Freeman [146, 147] showed that the X-ray scattering from aspherical atoms (p-state valence shells) may vary by approximately 5–10% with azimuthal angle in low Z atoms at small scattering angles. Electronic rearrangement in the solid should produce a similar magnitude of error in the projected atomic potential of the specimen. The error introduced with the linear superposition of atomic potentials approximation should be regarded as about 5–10% in the low angle scattering. This is an acceptable error for many calculations but caution should be taken when trying to extract precise quantitative information out of a simulation. Meyer et al. [343] and Susi et al. [480] have compared a detailed electronic structure calculation of monolayer specimens to the IAM approximation and found similar levels of error.

It is straight forward to write a general purpose computer program to calculate images of thin specimens with any element in the periodic chart that runs in a reasonable amount of computer time using the linear superposition (IAM) of tabulated single atom potentials from Appendix C (or other similar tabulations). As resolution improves to be comparable to the size of individual atoms the IAM becomes less accurate and should be replaced with a full electronic structure calculation including the core electrons. Unfortunately computing the electronic structure of solids including bonding is still a demanding task. It is not yet easy to write a general purpose computer program to calculate the electronic structure of an arbitrary solid, both because the theory is still under development to some extent and because of the large amount of computer time required. With the rapid advances

in computational science this situation will likely improve in the near future, but for now a simple linear superposition (Eq. 5.19) will have to suffice.

Previous tabulations of single atom properties usually were stated in terms of the electron scattering factors in the first Born approximation (Eq. 5.15). The first Born approximation is totally inadequate to describe the scattering process but has a simple relationship to the atomic potential (as well as the X-ray scattering factors, see Appendix C). The scattering factors in the first Born approximation naturally lend themselves to a calculation of the projected atomic potential in reciprocal (or Fourier) space. Once the potential has been calculated then a more correct scattering factor (Eq. 5.18) or specimen transmission function can be calculated (Eq. 5.7) from the specimen potential. The (2D) Fourier transform of Eq. 5.19 is:

$$V_z(\mathbf{k}) = \sum_{j=1}^N V_{zj}(\mathbf{k}) \exp(2\pi i \mathbf{k} \cdot \mathbf{x}_j) \quad (5.20)$$

substituting the electron scattering factor in the first Born approximation yields:

$$\sigma_e V_z(\mathbf{k}) = \lambda \frac{m}{m_0} \frac{1}{ab} \sum_j f_{ej}(k_x, k_y, 0) \exp(2\pi i \mathbf{k} \cdot \mathbf{x}_j) \quad (5.21)$$

where $f_{ej}(\mathbf{q})$ is the electron scattering factor in the first Born approximation for atom j . The total area of the specimen being simulated (with supercell dimensions $a \times b$) is ab and is required to normalize the Fourier transform properly. This constant may vary with different implementations of the Fourier transform. Note that $f_{ej}(\mathbf{q})$ is a function of a three-dimensional wave vector $\mathbf{q} = (k_x, k_y, k_z)$ but the inverse transform is with respect to only two dimensions ($\mathbf{k} = (k_x, k_y)$) with zero for the third coordinate k_z . This results in the projected atomic potential (i.e., integration along the z axis) because of the Fourier projection theorem (see Appendix B). The real space atomic potential can be found by inverse Fourier transforming $V_z(\mathbf{k})$ (in 2D) as:

$$v_z(\mathbf{x}) = FT^{-1}[V_z(\mathbf{k})] \quad (5.22)$$

This $v_z(\mathbf{x})$ can be used in Eq. 5.18 or 5.7. The summation on the right-hand side of Eq. 5.21 is formally called the structure factor of the specimen given by:

$$F(\mathbf{q}) = \sum_j f_{ej}(\mathbf{q}) \exp(2\pi i \mathbf{q} \cdot \mathbf{x}_j) \quad (5.23)$$

If the specimen is a crystal, then there will be a few discrete points \mathbf{k} at which the Fourier component of the potential $V_z(\mathbf{k})$ is significantly larger than its neighboring values. These correspond to the Bragg reflections for this particular projection of the crystal. The Fourier components of the potential are zero at points in between the Bragg reflections for crystalline specimens. Thermal vibration of the atoms in

the specimen may cause a small diffuse background in between the Bragg peaks (thermal diffuse scattering, TDS). If the specimen is amorphous, then there will be a nearly continuous distribution of values at all points \mathbf{k} in reciprocal space. Crystals containing defects or interfaces should be treated as if they are amorphous and all Fourier components of the potential should be calculated (i.e., not just the Bragg reflections).

5.4 BF Phase Contrast Image Calculation

This section will be discussed in the context of BF-CTEM image formation although it also applies to BF-STEM via the reciprocity theorem. In simple coherent BF-CTEM image formation the electron wave function incident on the specimen is a single plane wave of unit intensity. This wave function will pass through a thin specimen and experience a position dependent phase shift modeled as the specimen transmission function. Once the projected atomic potential of the specimen has been calculated (Eqs. 5.19 and 5.21) it is relatively straight forward to calculate the actual electron microscope image. From the projected atomic potential the wave function transmitted through the specimen is:

$$\psi_t(\mathbf{x}) = t(\mathbf{x}) \exp(2\pi i k_z z) \sim t(\mathbf{x}) \quad (5.24)$$

where a common factor of $\exp(2\pi i k_z z)$ has been ignored (it will drop out because only the intensity matters in the end and it is unaffected by the transfer function). The specimen transmission function is:

$$t(\mathbf{x}) = \exp[i\sigma_e v_z(\mathbf{x})] \quad (5.25)$$

where $v_z(\mathbf{x})$ is the total projected atomic potential of the specimen (Eqs. 5.8, 5.22) and σ_e is the interaction parameter (Eq. 5.6).

Electron microscope image formation is fundamentally cylindrically symmetric. It is essential that any simulation preserves this symmetry. Figure 5.10 shows a view of a sampled image in reciprocal space. The real space dimensions are $a \times b$ (in x and y). The general case in which a and b are very different is shown. There are two things that may alter the basic symmetry of the image and produce odd artifacts in the image. First, if the real space image size is not the same in x and y , then the maximum spatial frequency may be different in each direction. The second related problem is the few Fourier coefficient in the four corners. If the entire area of the Fourier transform is just filled completely, then various artifacts with rectangular symmetry can creep into the image. It is usually advisable to bandwidth limit the image with cylindrical symmetry. Only the spatially frequencies inside the largest inscribed circle as shown in Fig. 5.10 should be allowed to contribute to the final image. Although this may limit the resolution a little it at least does it with the proper symmetry and introduces fewer nonphysical artifacts in the image. This also

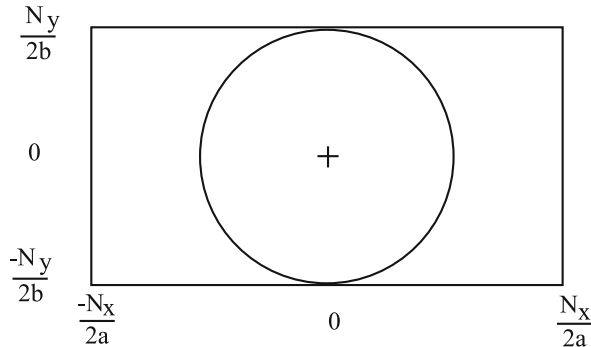


Fig. 5.10 Symmetrical bandwidth limiting the image in reciprocal space. The real space image has dimensions of $a \times b$ (in x and y) and is sampled with $N_x \times N_y$ pixels. Only those Fourier components inside the largest inscribed circle should be allowed to contribute to the image to avoid artifacts with an incorrect symmetry

means that it is best to make the image size square; otherwise, a large percentage of the pixels (in reciprocal space) will have to be set to zero and the calculation will not be very efficient. This bandwidth limit should be applied to both the projected atomic potential and the transmission function because the calculation in Eq. 5.25 is nonlinear and will generate many higher frequencies even though $v_z(\mathbf{x})$ may be properly bandwidth limited.

The transmitted wave function (Eq. 5.24) is imaged by the objective lens of the microscope. The effects of the aberrations of the objective lens are easiest to calculate by Fourier transforming the transmitted wave function and then multiplying by the transfer function of the objective lens.

$$\begin{aligned}\Psi_t(k) &= FT[\psi_t(\mathbf{x})] \\ \Psi_i(k) &= \Psi_t(\mathbf{k})H_0(\mathbf{k})\end{aligned}\quad (5.26)$$

where $\Psi_i(k)$ is the image wave function in the back focal plane of the objective lens and $H_0(k)$ is the transfer function of the objective lens. For simplicity, ignore aberrations other than defocus and third order spherical aberration.

$$\begin{aligned}H_0(\mathbf{k}) &= \exp[-i\chi(\mathbf{k})]A(\mathbf{k}) \\ \chi(k) &= \pi\lambda k^2(0.5C_s\lambda^2k^2 - \Delta f)\end{aligned}\quad (5.27)$$

where Δf is defocus, $C_s = C_{S3}$ is the coefficient of spherical aberration and $A(\mathbf{k})$ is the aperture function:

$$\begin{aligned}A(\mathbf{k}) &= 1 \quad ; \quad \lambda k = \alpha < \alpha_{\max} \\ &= 0 \quad ; \quad \text{otherwise}\end{aligned}\quad (5.28)$$

α_{\max} is the maximum semiangle allowed by the objective aperture. Other aberrations may be included but only the simplest few are given here for simplicity. The objec-

Table 5.1 Steps in the simulation of CTEM images of thin specimens (a phase grating calculation)

Step 1	Calculate the projected atomic potential $v_z(\mathbf{x})$ from Eq. 5.19 or 5.21
Step 2	Calculate the transmission function $t(\mathbf{x}) = \exp[i\sigma_e v_z(\mathbf{x})]$ (Eq. 5.25) and symmetrically bandwidth limit it. The incident wave function is a plane wave so the transmitted wave function is equal to the transmission function
Step 3	Fourier transform the transmission function $T(\mathbf{k}) = FT[t(\mathbf{x})]$
Step 4	Multiply the Fourier transform of the transmission function by the transfer function of the objective lens, $H_0(k)$ (Eq. 5.27) to get the image wave function in the back focal plane $\Psi_i(\mathbf{k}) = H_0(k)T(\mathbf{k})$
Step 5	Inverse Fourier transform the image wave function $\psi_i(\mathbf{k}) = FT^{-1}[\Psi_i(\mathbf{k})]$
Step 6	Calculate the square modulus of the image wave function (in real space) to get the final image intensity $g(\mathbf{x}) = \psi_i(\mathbf{x}) \otimes h_o(\mathbf{x}) ^2$

tive lens images this wave function to form the final electron microscope image. The actual magnification of the objective lens may be ignored in the calculation (but NOT in practice) if the image coordinates are always referred to the actual specimen dimensions.

The actual recorded image $g(\mathbf{x})$ is the magnitude squared of the image wave function after inverse Fourier transforming back into real space.

$$\begin{aligned}\psi_i(\mathbf{x}) &= FT^{-1}[\Psi_i(\mathbf{k})] \\ g(\mathbf{x}) &= |\psi_i(\mathbf{x})|^2 = |\psi_i(\mathbf{x}) \otimes h_o(\mathbf{x})|^2\end{aligned}\quad (5.29)$$

where $h_o(\mathbf{x})$ is the complex point spread function of the objective lens (the inverse Fourier transform of $H_0(\mathbf{k})$). The steps required to calculate the image of a thin specimen are summarized in algorithmic form in Table 5.1.

5.4.1 Single Atom Images

Figure 5.11 shows the specimen transmission function (Eq. 5.25) for the five single atoms plotted in Fig. 5.5. The atoms are arranged in a row 10 Å apart. The atomic potential was calculated in an image size of 50 Å on a side and 512 × 512 pixels using Eq. 5.21. The slight ringing near each atom is due to the finite bandwidth of the sampled image. There is also a slight asymmetry in some of the atoms. This occurs because there will always be some atom positions that are not exactly integer multiples of the pixel spacing. The atom potential is then spread across neighboring pixels in a nonsymmetrical manner. This asymmetry should be small and vanish in the final images. Also note that the real part of the transmission function has a stronger dependence on atomic number Z than the imaginary part.

The actual height of the peak for each atom is mainly a function of the sampling size. The actual potential has a singularity at the center of each atom (see Fig. 5.5). The value at the center of the atom is the average over one pixel. As this

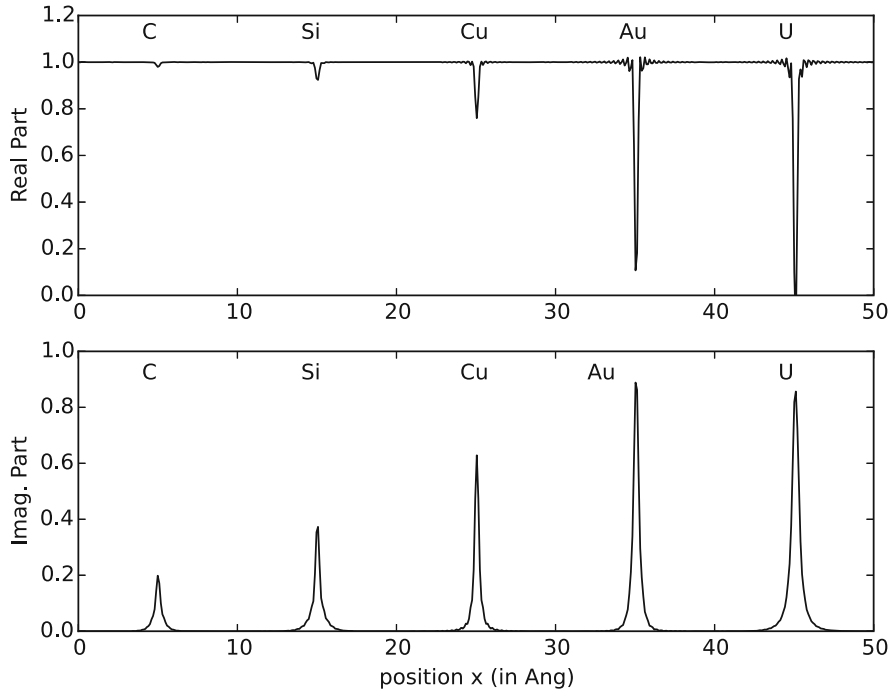


Fig. 5.11 Line scan of the complex transmission function for five isolated single atoms and an incident electron beam energy of 200 keV. This was calculated with a sampled image of 512×512 pixels. The scan goes through the center of each atom (atomic number $Z = 6, 14, 29, 79, 92$)

pixel gets smaller this value is closer to the singular value at the center of the atom. The integrated value should come through to the image properly with different pixel sizes although some care is required in choosing an appropriate pixel sampling size.

Figure 5.12 shows the image intensity (Eq. 5.29) of the five isolated single atoms calculated from Fig. 5.11 with Scherzer conditions. The incident electron intensity is assumed to be unity for this simulation so that the image intensity in between the atoms (i.e., vacuum) should be one. The rings surrounding each atom are part of the so-called Airy disk caused by a sharp cut off in reciprocal space due to the objective aperture. The rings on the right wrap around to interfere with the atom on the left (the wrap-around effect). Figure 5.13 shows a line scan through the center of each atom in Fig. 5.12. Eisenhandler and Siegel [113] and Reimer and Gilde [416] have also plotted single atom image profiles.

In the special case of isolated single atoms the image intensity $g(\mathbf{x})$ in bright field phase contrast may be written as:

$$g(\mathbf{x}) = \left| 1 + 2\pi i \int_0^{k_{\max}} f_e(k) \exp[-i\chi(k)] J_0(2\pi kr) k dk \right|^2 \quad (5.30)$$



Fig. 5.12 The coherent bright field phase contrast image of five isolated single atoms and an incident electron beam energy of 200 keV. The electron optical parameters are spherical aberration $C_s = 1.3$ mm, defocus $\Delta f = 700$ Å and an objective aperture of 10.37 mrad (Scherzer conditions). This was calculated with a sampled image of 512×512 pixels. Atomic number $Z = 6(\text{C})$, $14(\text{Si})$, $29(\text{Cu})$, $79(\text{Au})$, $92(\text{U})$ (left to right). The image ranges from 0.72 (black) to 1.03 (white)

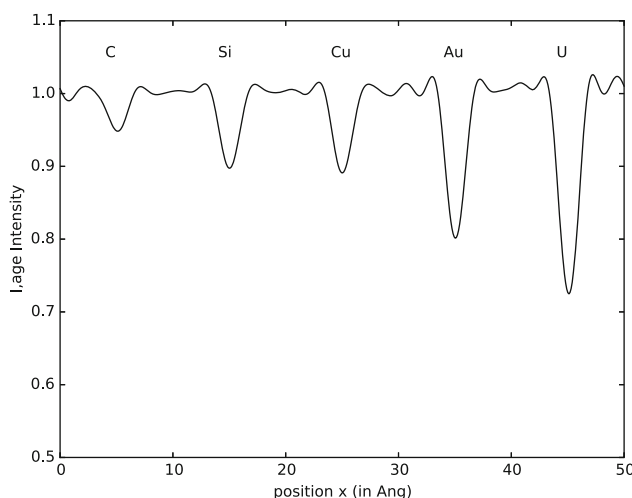


Fig. 5.13 Line scan through the center of the atoms in the coherent bright field phase contrast image in Fig. 5.12

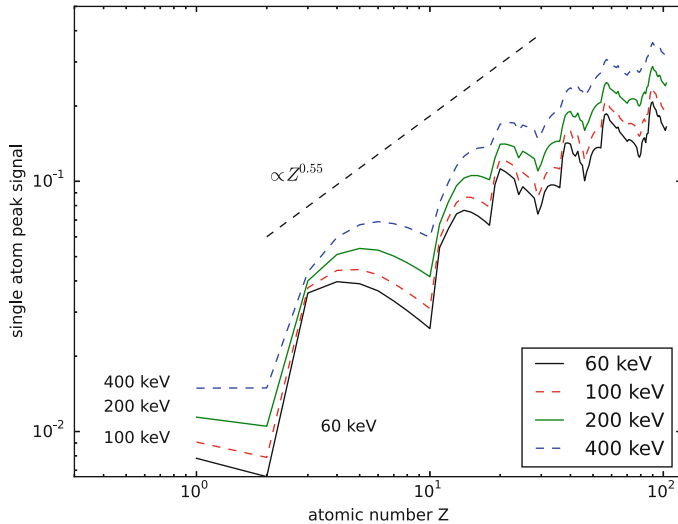


Fig. 5.14 Single atom peak signal in coherent bright field phase contrast versus atomic number Z for incident electron energies of 60, 100, 200, and 400 keV. Spherical aberration was fixed at $C_s = 1.3$ mm. Scherzer conditions were used for defocus and objective aperture

where $f_e(k)$ is the electron scattering factor in the Moliere approximation (found by numerical integration of Eq. 5.18 using the projected atomic potential from appendix C), $\chi(k)$ is the aberration function, $k_{\max} = \alpha_{\max}/\lambda$ is the maximum spatial frequency in the objective aperture, and $J_0(x)$ is the Bessel function of order zero. The first Born approximation for the scattering factor should not be used in this expression. A graph of the peak single atom signal $1 - g(0)$ in coherent bright field phase contrast found by numerical integration of Eq. 5.30 is shown in Fig. 5.14. The BF signal varies weakly with atomic number. The overall trend approximately follows $Z^{0.5}$ to $Z^{0.7}$; however, there is a significant variation reflecting the filling of different valence shells as in the periodic chart. Different atomic numbers can have the same signal and heavier atoms can have a smaller signal than lighter atoms (the signal is not monotonic in atomic number Z). It is possible to distinguish heavy atoms and light atoms but it would not be possible to precisely identify any specific atom by its bright field phase contrast signal alone.

5.4.2 Thin Specimen Images

Silicon is a reasonable starting point to begin discussing image simulation. It is a low enough atomic number that it is reasonable to approximate it as a weak phase object and it has a relatively simple structure. A precise simulation should still include thickness effects as covered in later chapters but for now the geometrical effects of

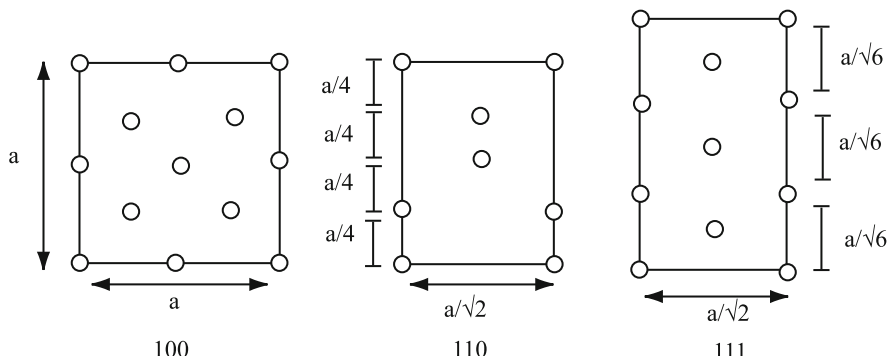


Fig. 5.15 Common projections of the silicon lattice (diamond structure with cubic cell size $a = 5.43 \text{ \AA}$). The circles represent the projected position of the silicon atoms. The indicated crystal direction (100, 110, or 111) is along the optic axis of the microscope and perpendicular to the plane of the paper

specimen thickness will be ignored. Thickness can be included in some sense by superimposing the atoms along the optic axis in the specimen but the position of each atom along the beam direction will be ignored until later.

Silicon is a technologically important material and is the basic building block of most electronic devices. Its common crystalline form is the diamond structure (two interpenetrating face centered cubic or fcc lattices). When viewed in the electron microscope the three-dimensional lattice is projected into a two dimensional image. The three common projections of the diamond lattice with a cubic cell dimension of a are shown in Fig. 5.15. The (100) projection has a repeat length of a along the beam direction with one atom per repeat length. The (110) projection repeats every $a\sqrt{2}$ with two atoms per repeat length and two different types of atomic layers. The (111) projection repeats every $a\sqrt{3}$ with two atoms per site and three different layers.

To calculate an image of silicon in the weak phase object approximation requires sampling the atomic potential of silicon in a rectangular grid with the atoms placed at their respective positions in the grid. The discrete Fourier transform (DFT or FFT) requires that the sampled image obey periodic boundary conditions so the boundaries of the sampled image should match the natural periodicity of the actual specimen. This means that the sampling grid size should be an integer number of unit cells shown in Fig. 5.15 or equivalent. The full scale dimensions of the sampling grid will be labeled a, b in the horizontal and vertical directions, respectively. This nomenclature is drawn from crystallography and should not be confused with the real physical dimensions of the crystal (which are also frequently labeled a, b, c). The meaning will usually be clear from the context in which they are used. As an example an image of the (110) projection of silicon will be calculated. The full scale dimensions of the (110) unit cell in Fig. 5.15 will be called $a_0 = a_{Si}/\sqrt{2}$ in the horizontal direction and $b_0 = a_{Si}$ in the vertical direction. a_{Si} is the real physical cubic cell size of silicon.

It is tempting to make the real space sampling grid the same size as the two dimensional unit cell in Fig. 5.15 but this is not a good idea. A typical electron microscope has a resolution of no better than about 1.5–2 Å. A good rule of thumb is to keep the real space sampling resolution (Δx , Δy) to be no bigger than about 1/3–1/4 of the final resolution. This way atoms still look round and not rectangular. With $a_0 = 3.84 \text{ \AA}$ and $b_0 = 5.43 \text{ \AA}$ this would mean that $N_x = a_0/\Delta x \sim 7.7$ pixels and $N_y = b_0/\Delta y \sim 10.9$ pixels. Rounding up to the nearest power of two would give an image of 8 by 16 pixels. Although the real space sampling size is adequate the reciprocal space sampling is very wrong in this simple argument. There are actually two sampling requirements that must be met. Both real space and reciprocal space are important. With a single unit cell of size $a_0 \times b_0$ the resolution in reciprocal space is $\Delta k_x = 1/a_0 = 0.26 \text{ \AA}^{-1}$ and $\Delta k_y = 1/b_0 = 0.18 \text{ \AA}^{-1}$. At 200 keV the electron wavelength is 0.02508 Å. Using $\alpha = \lambda k$ means that this choice has an angular resolution of about 6.5 and 4.6 mrad. In reciprocal space a typical objective aperture semiangle α is about 10 mrad. There would only be two or three pixels inside the objective aperture in the final image. This would be totally inadequate to sample the transfer function or the specimen. In practice it is a good idea to have at least 5–10 pixels in the radius of the objective aperture (much more is better).

The solution to this problem is slightly nonintuitive. The size of the sampled image should really be several times the size of the minimum unit cell of the crystal specimen. As long as a and b are integer multiples of a_0 and b_0 the periodic boundary conditions are satisfied, and the reciprocal space resolution can be improved (i.e., Δk_x and Δk_y made smaller). To get a reciprocal space sampling of about 1 mrad at 200 keV requires a supercell size of 7 × 5 unit cells (26.89 × 27.15 Å).

For this particular problem (a perfect crystal) expanding the number of unit cell in real space simply moves the Bragg peaks further apart in Fourier space with zero in between. The transfer function is not strictly needed at these in between zeros so there is no real improvement for this particular problem. However, in later examples with imperfect crystals and STEM probes this sampling will be important so this example will continue as if it were a more general problem, although there is some argument that this is not the most efficient approach (this is a quick calculation so CPU time is not much of a concern) for this particular problem.

The normalized coordinates for one projected unit cell of (110) silicon is shown in Table 5.2. The projected atomic potential for a four atom thick specimen of (110) silicon is shown in Fig. 5.16a with a super cell size of 7 × 5 silicon unit cells. Note the characteristic “dumbbell” shape of pairs of silicon atoms. Figure 5.16b, c is the

Table 5.2 The normalized coordinates for one projected unit cell of the silicon ($Z = 14$) lattice in the (110) projection

Atom	Occupancy	x/a	y/b
1	1	0	0
2	1	0.5	0.75
3	1	0	0.25
4	1	0.5	0.5

The two-dimensional unit cell dimensions are $a \times b$ where $a = a_{Si}/\sqrt{2} = 3.8396 \text{ \AA}$ and $b = a_{Si} = 5.43 \text{ \AA}$

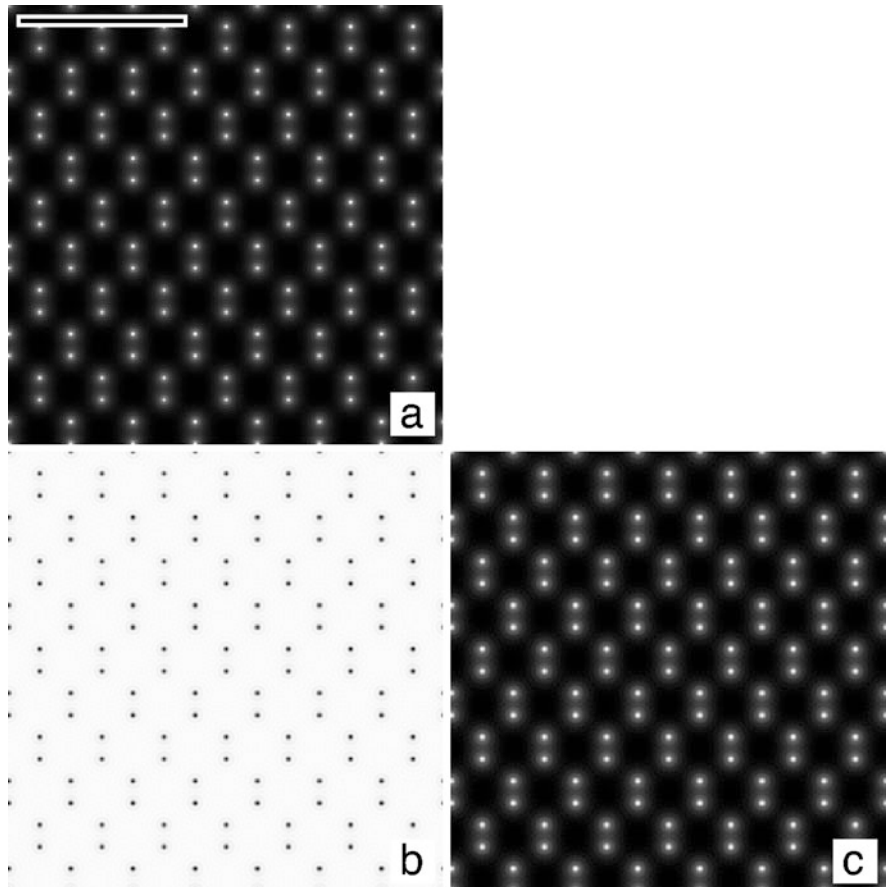


Fig. 5.16 Steps in simulating an image of 110 silicon in the weak phase object approximation. (a) Projected atomic potential (4 atoms thick, 256×256 pixels). (b, c) Real and imaginary part of the specimen transmission function at 200 keV. The scale bar in (a) is 10 Å. The image ranges are (b) 0.90–1.00, (c) 0.00–0.43. White is a larger positive number and atoms should appear white in (a)

complex transmission function at a beam energy of 200 keV for this specimen and Fig. 5.17a, b are the bright field images that would result at electron beam energies of 200 keV and 400 keV, respectively. The lattice is not easily visible at an energy of 100 keV under Scherzer conditions at this value of C_s . Deviations from Scherzer conditions can, however, produce some interesting effects (see for example Izui [237], Hutchison and Waddington [221]). When the image is calculated at 100 keV the result has a structure that resembles a crystal lattice but has a range that is of order (10^{-5} – 10^{-6}) of its average value. This is just the roundoff error of the numerical calculation and has no physical significance. This can happen often in simulation and you have to be careful to look at the actual numerical range of the

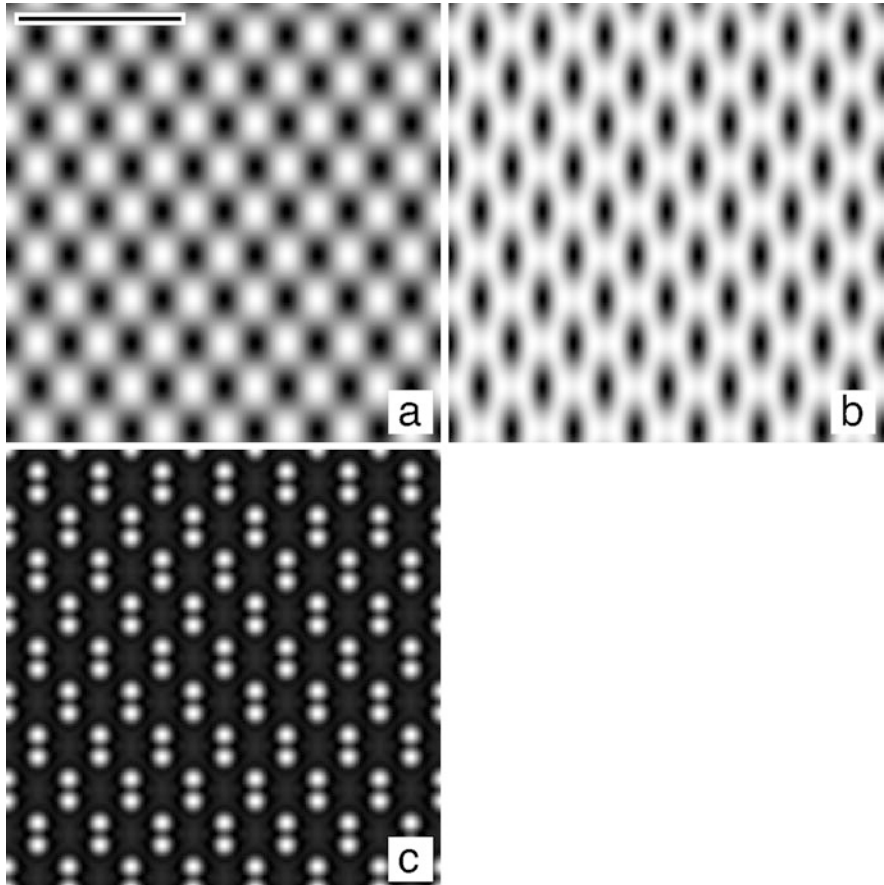


Fig. 5.17 Coherent bright field (BF) image of 110 silicon in the weak phase object approximation (256×256 pixels). (a) BF image at 200 keV, $\Delta f = 700 \text{ \AA}$, $\alpha_{\max} = 10.37 \text{ mrad}$. (b) BF image at 400 keV, $\Delta f = 566 \text{ \AA}$, $\alpha_{\max} = 9.33 \text{ mrad}$. Both (a) and (b) have a spherical aberration of $C_s = 1.3 \text{ mm}$ and Scherzer conditions. (c) BF image at 200 keV for an ideal aberration corrector with fixed $C_{S5} = 30 \text{ mm}$ similar to Fig. 3.8 ($C_{S3} = -38.7 \mu\text{m}$, $\Delta f = -97.6 \text{ \AA}$). The scale bar in (a) is 10 Å. The image ranges are (a) 0.91–1.09, (b) 0.87–1.07, and (c) 0.95–1.26. White is a larger positive number and atoms should appear black in (a, b) and white in (c)

image as well as its structure. The computer will just scale whatever numerical range is there to fill the available gray scale and produce an image. Although the dumbbell shape is not resolved at either energy the higher voltage does start to get an elongated shape for the atom pairs. Spence et al. [473] and Desseaux et al. [96] have given a similar discussion of 110 germanium.

Figure 5.17c shows the image for an ideal aberration corrector using the aberrations similar to Fig. 3.8 with a large fixed C_{S5} balanced by a small negative C_{S3} and positive C_{10} (or negative Δf) to produce a positive transfer functions over a large range of spatial frequencies (which changes the single atom signal from

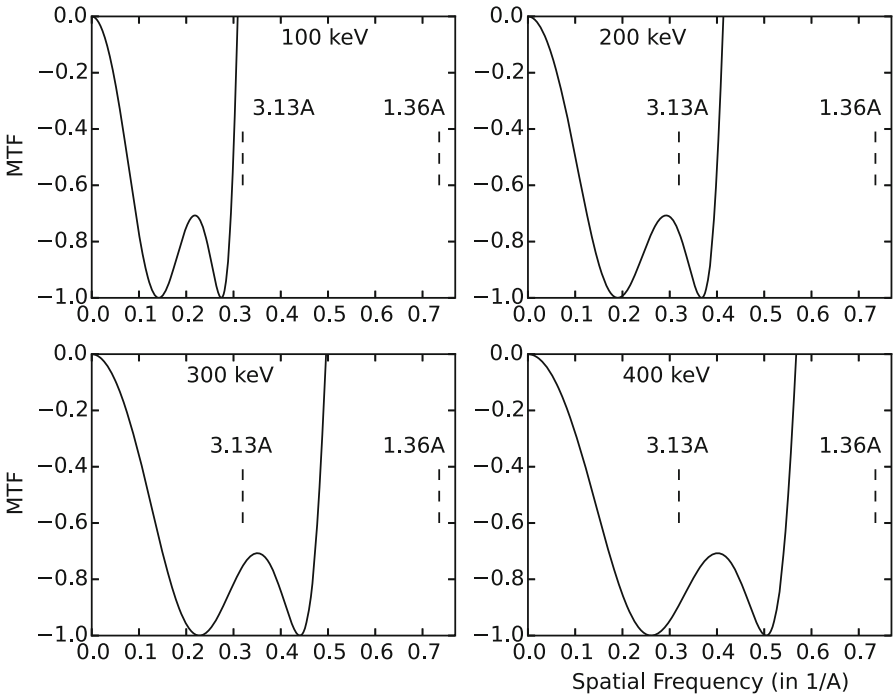


Fig. 5.18 The transfer function for a coherent bright field (BF) image in the weak phase approximation under Scherzer conditions. Spherical aberration is $C_s = 1.3 \text{ mm}$ and the electron energy varies from 100 to 400 keV. Two spacings relevant to the 110 projection of silicon are shown for comparison. 1.36 Å is the spacing between the dumbbells and 3.13 Å is the spacing for the lowest order allowed reflection

black to white). 200 kV was used here because 300 kV (in Fig. 3.8) will likely cause too much radiation damage in silicon. Other parasitic aberrations are assumed identically zero.

The apparent resolution of the simulated images in Fig. 5.17 is consistent with the linear image transfer function as shown in Fig. 5.18. The lowest order allowed reflection in the 110 projected unit cell (Fig. 5.15) are the 111 type beams with a spacing of $a_{Si}/\sqrt{3} = 3.13 \text{ \AA}$, and the distance between the two atoms in the pair in the center of the unit cell is $a_{Si}/4 = 1.36 \text{ \AA}$ (Edington [109]). The larger of these spacings should be clearly resolved in all but the 100 keV case, but the smaller of these two should not be resolved at all without an aberration corrector, consistent with the calculation in Fig. 5.17.

5.4.3 Partial Coherence and the Transmission Cross Coefficient

The BF image intensity distribution is the square modulus of the transmitted wave function $\psi_t(\mathbf{x})$ convolved with point spread function $h_0(\mathbf{x})$ of the objective lens:

$$g(\mathbf{x}) = |\psi_t(\mathbf{x}) \otimes h_0(\mathbf{x})|^2 = [\psi_t(\mathbf{x}) \otimes h_o(\mathbf{x})] [\psi_t^*(\mathbf{x}) \otimes h_o^*(\mathbf{x})] \quad (5.31)$$

The Fourier transform of this equation is:

$$\begin{aligned} G(\mathbf{k}) &= \int \Psi_t^*(\mathbf{k}') H_0^*(\mathbf{k}') \Psi_t(\mathbf{k}' + \mathbf{k}) H_0(\mathbf{k}' + \mathbf{k}) d^2\mathbf{k}' \\ &= \int T_{cc}(\mathbf{k}', \mathbf{k}' + \mathbf{k}) \Psi_t^*(\mathbf{k}') \Psi_t(\mathbf{k}' + \mathbf{k}) d^2\mathbf{k}' \end{aligned} \quad (5.32)$$

where $T_{cc}(\mathbf{k}', \mathbf{k}' + \mathbf{k})$ is the transmission cross coefficient that is similar to the function of the same name in light optics (for example, section 10.5.3 of Born and Wolf [42]). This relationship results in part because $g(\mathbf{x})$ is real, which also means that $G(\mathbf{k}) = G^*(-\mathbf{k})$ and yields an alternate form:

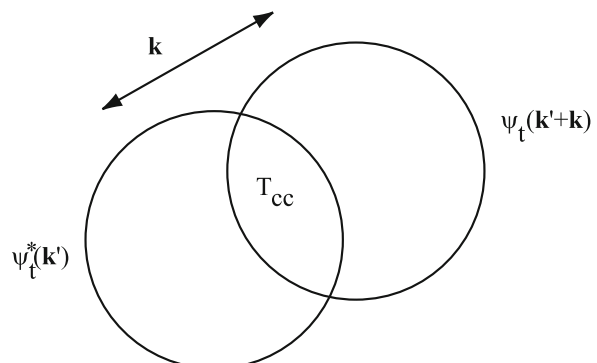
$$G(\mathbf{k}) = \int T_{cc2}(\mathbf{k}', \mathbf{k}' - \mathbf{k}) \Psi_t(\mathbf{k}') \Psi_t^*(\mathbf{k}' - \mathbf{k}) d^2\mathbf{k}' \quad (5.33)$$

(T_{cc} and T_{cc2} are slightly different functions). In the special case of perfectly coherent image formation the transmission cross coefficient (distinguished by an additional superscript *coh*) is:

$$T_{cc}^{coh}(\mathbf{k}', \mathbf{k}' + \mathbf{k}) = \exp[i\chi(\mathbf{k}') - i\chi(\mathbf{k}' + \mathbf{k})] A(\mathbf{k}') A(\mathbf{k}' + \mathbf{k}) \quad (5.34)$$

where $\chi(\mathbf{k})$ is the aberration function of the objective lens (Eq. 5.27) and $A(\mathbf{k})$ is the aperture function (Eq. 5.28). The portion of the transmitted wave function that passes through the objective aperture is combined with itself as illustrated in Fig. 5.19. $\Psi_t(\mathbf{k})$ is duplicated and offset by a vector \mathbf{k} . The overlap region is

Fig. 5.19 The transmission cross coefficient in reciprocal space. Each circle represents the objective aperture. Only the overlap region labeled T_{cc} contributes to Fourier coefficient \mathbf{k} in the image



multiplied by the transmission cross coefficient and the integrated value in the intersection of the two apertures forms a single Fourier component at position \mathbf{k} . The direct implementation (in a program) of the transmission cross coefficient for coherent imaging is rather inefficient. It would require the calculation of a two-dimensional convolution at each point of reciprocal space (i.e., for each Fourier coefficient of the image). The use of the FFT as described above is much more efficient for coherent image formation.

The transmission cross coefficient, however, provides a mechanism for including the effects of partial coherence of strong phase objects as was discussed by O'Keefe [377], Ishizuka [230] and Pulvermacher [408]. (Bonevich and Marks [39] have also considered some higher order terms that are not discussed here.) If the specimen is thin enough to satisfy the weak phase object approximation, then the form of the partial coherence derived in Sect. 3.2 is sufficient; however, if the specimen contains heavy atoms or is many atoms thick, then it may not be a weak phase object and a more detailed accounting of partial coherence is required. From the discussion on partial coherence in Sect. 3.2 the actual image will be formed with a small distribution of illumination angles and defocus values:

$$g(\mathbf{x}) = \int |\psi_t(\mathbf{x}) \otimes h_0(\mathbf{x}, \Delta f + \delta_f, \mathbf{k}_\beta)|^2 p(\mathbf{k}_\beta) p(\delta_f) d\delta_f d^2\mathbf{k}_\beta \quad (5.35)$$

where δ_f is the deviation in defocus, \mathbf{k}_β is the deviation in illumination angle, and $p(\delta_f)$ and $p(\mathbf{k}_\beta)$ are their distributions. If the specimen is thin enough so that its geometrical extent along the optic axis can be ignored (as has been assumed in this chapter), then the illumination angle can be included in either the specimen or the transfer function of the objective lens. When included as part of the objective lens the integration over δ_f and \mathbf{k}_β can be completely contained within the transmission cross coefficient without modifying the transmitted wave function $\psi_t(\mathbf{x})$. The transmission cross coefficient with partial coherence becomes:

$$\begin{aligned} T_{cc}(\mathbf{k}', \mathbf{k}' + \mathbf{k}) &= \int \exp [i\chi(\mathbf{k}' + \mathbf{k}_\beta, \Delta f + \delta_f) - i\chi(\mathbf{k}' + \mathbf{k} + \mathbf{k}_\beta, \Delta f + \delta_f)] \\ &\quad \times A(\mathbf{k}' + \mathbf{k}_\beta) A(\mathbf{k}' + \mathbf{k} + \mathbf{k}_\beta) p(\delta_f) p(\mathbf{k}_\beta) d\delta_f d^2\mathbf{k}_\beta \end{aligned} \quad (5.36)$$

If the deviations from the coherent mode are assumed to be small, then this expression can be Taylor expanded to first order in δ_f and \mathbf{k}_β as:

$$\begin{aligned} T_{cc}(\mathbf{k}', \mathbf{k}' + \mathbf{k}) &= T_{cc}^{coh} \int \exp \left\{ i \left[\mathbf{k}_\beta \cdot \frac{\partial}{\partial \mathbf{k}} + \delta_f \frac{\partial}{\partial \Delta f} + \delta_f \mathbf{k}_\beta \cdot \frac{\partial^2}{\partial \mathbf{k} \partial \Delta f} + \dots \right] \right. \\ &\quad \left. \times [\chi(\mathbf{k}') - \chi(\mathbf{k}' + \mathbf{k})] \right\} p(\delta_f) p(\mathbf{k}_\beta) d\delta_f d^2\mathbf{k}_\beta \end{aligned} \quad (5.37)$$

where the small variation of the aperture function with \mathbf{k}_β has been ignored (or equivalently the aperture diameter is much larger than the maximum spatial frequency of interest in the image). The indicated derivatives are:

$$\begin{aligned}\mathbf{W}_{C1} &= \frac{\partial}{\partial \mathbf{k}} [\chi(\mathbf{k}') - \chi(\mathbf{k}' + \mathbf{k})] \\ &= 2\pi\lambda^3 C_s [|\mathbf{k}'|^2 \mathbf{k}' - |\mathbf{k}' + \mathbf{k}|^2 (\mathbf{k}' + \mathbf{k})] + 2\pi\lambda\Delta f \mathbf{k} \\ &\quad + 2\pi\lambda^5 C_{s5} \left[|\mathbf{k}'|^4 \mathbf{k}' - |\mathbf{k}' + \mathbf{k}|^4 (\mathbf{k}' + \mathbf{k}) \right]\end{aligned}\quad (5.38)$$

$$\begin{aligned}W_{C2} &= \frac{\partial}{\partial \Delta f} [\chi(\mathbf{k}') + \chi(\mathbf{k}' + \mathbf{k})] \\ &= -\pi\lambda[|\mathbf{k}'|^2 + |\mathbf{k}' + \mathbf{k}|^2]\end{aligned}\quad (5.39)$$

$$\frac{\partial^2}{\partial \mathbf{k} \partial \Delta f} [\chi(\mathbf{k}') - \chi(\mathbf{k}' + \mathbf{k})] = 2\pi\lambda \mathbf{k}\quad (5.40)$$

where the auxiliary symbols \mathbf{W}_{C1} and W_{C2} will be used to simplify the derivation. Substituting for the derivatives yields:

$$\begin{aligned}T_{cc}(\mathbf{k}', \mathbf{k}' + \mathbf{k}) &= T_{cc}^{coh} \int \exp\{i\mathbf{k}_\beta \cdot \mathbf{W}_{C1} + i\delta_f W_{C2} + 2\pi i\lambda\delta_f \mathbf{k}_\beta \cdot \mathbf{k}\} \\ &\quad \times p(\delta_f) p(\mathbf{k}_\beta) d\delta_f d^2\mathbf{k}_\beta\end{aligned}\quad (5.41)$$

Note that \mathbf{W}_{C1} is a two-dimensional vector quantity, as are all odd powers of \mathbf{k} . Assume that both the defocus and illumination angles have a Gaussian distribution:

$$p(\delta_f) = \frac{1}{\Delta_0 \sqrt{\pi}} \exp(-\delta_f^2 / \Delta_0^2)\quad (5.42)$$

$$p(\mathbf{k}_\beta) = \frac{1}{k_s^2 \pi} \exp(-\mathbf{k}_\beta^2 / k_s^2)\quad (5.43)$$

where δ_f and k_s are the $1/e$ widths of the two distributions. First perform the integration with respect to \mathbf{k}_β giving:

$$\begin{aligned}T_{cc}(\mathbf{k}', \mathbf{k}' + \mathbf{k}) &= T_{cc}^{coh} \int \exp\left[+i\delta_f W_{C2} - k_s^2 |\mathbf{W}_{C1} + 2\pi\lambda\delta_f \mathbf{k}|^2 / 4\right] p(\delta_f) d\delta_f\end{aligned}\quad (5.44)$$

Note that this is equivalent to Fourier transforming the distribution function $p(\mathbf{k}_\beta)$. Next perform the integration with respect to δ_f , and use $\beta = \lambda k_s$ (i.e., the condenser angle in radians) to give:

$$\begin{aligned}T_{cc}(\mathbf{k}', \mathbf{k}' + \mathbf{k}) &= T_{cc}^{coh} \frac{1}{\sqrt{1 + \pi^2 \beta^2 \Delta_0^2 k^2}} \\ &\quad \times \exp\left[-\frac{\beta^2}{4\lambda^2} W_{C1}^2 + \frac{\Delta_0^2}{4} \frac{(\pi\beta^2 \mathbf{k} \cdot \mathbf{W}_{C1} / \lambda - i W_{C2})^2}{1 + \pi^2 \beta^2 \Delta_0^2 k^2}\right]\end{aligned}\quad (5.45)$$

The total transmission cross coefficient is a complicated damping factor whose net effect is similar to that for the weak phase approximation with linear imaging. However, the total transmission cross coefficient is much more complicated to calculate (note the vector nature of several components in the exponential factor). It is not separable into factors that depend only on \mathbf{k}' and factors that depends only on $\mathbf{k}' + \mathbf{k}$. The image calculation with this form of partial coherence cannot be done using FFTs but must be done by an explicit weighted convolution in two dimensions (at each point in reciprocal space). This adds considerably to the required computer time but it is valid for a strongly scattering specimen with a negligible geometrical thickness such as several atomic layers of heavy atoms. If one of the deviations (defocus or angle) is small it may be more efficient to perform one integration analytically and the other numerically (possibly using FFTs) than to calculate the two-dimensional convolution (Coene et al. [66]).

5.5 ADF STEM Images of Thin Specimens

In the STEM the objective lens acts on the electron beam before the beam interacts with the specimen in opposite order from the CTEM. The electrons that pass through the specimen and get scattered at high angles form the annular dark field or ADF signal. The wave function $\psi_p(\mathbf{x})$ of the focused probe incident upon the specimen at position \mathbf{x}_p is formed by integrating the aberration wave function $\exp[-i\chi(\mathbf{k})]$ over the objective aperture as:

$$\psi_p(\mathbf{x}, \mathbf{x}_p) = A_p \int_0^{k_{\max}} \exp[-i\chi(\mathbf{k}) - 2\pi i \mathbf{k} \cdot (\mathbf{x} - \mathbf{x}_p)] d^2\mathbf{k} \quad (5.46)$$

where $\lambda k_{\max} = \alpha_{\max}$ is the maximum angle in the objective aperture and A_p is a normalization constant chosen to yield:

$$\int |\psi_p(\mathbf{x}, \mathbf{x}_p)|^2 d^2\mathbf{x} = 1 \quad (5.47)$$

In a practical sense the probe wave functions are easiest to calculate in Fourier space and then apply an inverse FFT.

$$\psi_p(\mathbf{x}, \mathbf{x}_p) = A_p FT^{-1} \{ \exp[-i\chi(\mathbf{k}) + 2\pi i \mathbf{k} \cdot \mathbf{x}_p] A(\mathbf{k}) \} \quad (5.48)$$

where $A(\mathbf{k})$ is the aperture function (Eq. 5.28). A graph of the ADF-STEM probe wave functions with the optimum probe conditions is shown in Fig. 5.20. This is a complex valued function and the relative weighting of the real and imaginary parts can change dramatically with defocus, etc.

The probe wave function is incident on the specimen and is modulated by the specimen transmission function $t(\mathbf{x})$ as it passes through the specimen. The wave function transmitted through the specimen is:

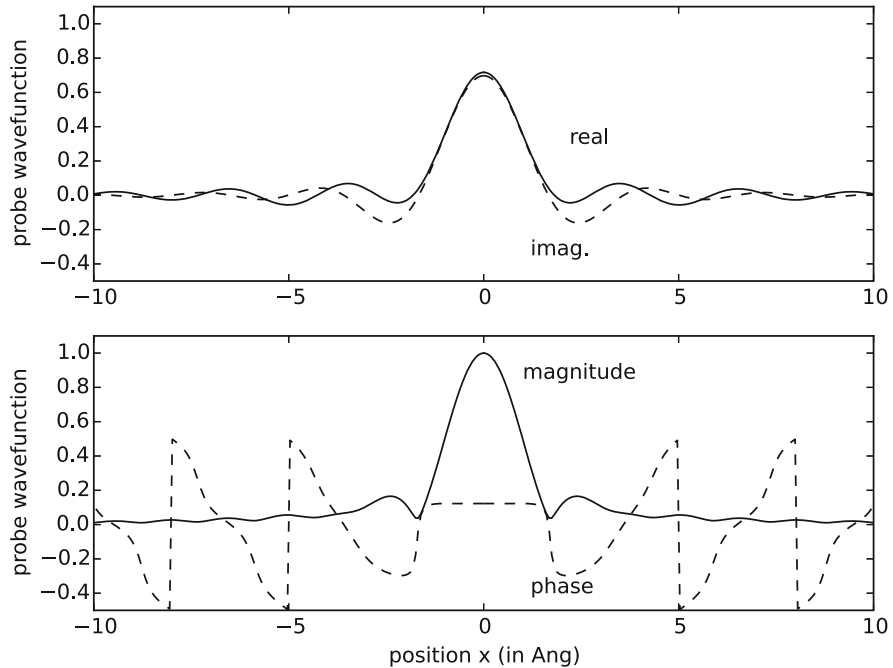


Fig. 5.20 Profile of the ADF-STEM probe wave functions (real and imaginary parts on top and amplitude and phase on bottom) for an electron energy of 200 keV, spherical aberration $C_s = 1.3$ mm, defocus $\Delta f = 497$ Å, and an objective aperture of $\alpha_{\max} = 8.88$ mrad (optimum probe conditions). The effects of a finite source size have been ignored. The phase is in units of 2π radians

$$\begin{aligned}\psi_t(\mathbf{x}, \mathbf{x}_p) &= \psi_p(\mathbf{x}, \mathbf{x}_p)t(\mathbf{x}) \\ &= \psi_p(\mathbf{x}, \mathbf{x}_p)\exp[i\sigma_e v_z(\mathbf{x})]\end{aligned}\quad (5.49)$$

In the STEM mode the transmitted wave function already has the effects of the objective lens aberration in it, unlike the CTEM mode where the objective lens effects enter after the wave function passes through the specimen. After passing through the specimen the transmitted wave function is then diffracted into the far field (i.e., the diffraction plane) and hits the ADF detector. Diffraction into the far field is equivalent to a Fourier transform of the transmitted wave function.

$$\Psi_t(\mathbf{k}) = FT[\psi_t(\mathbf{x})] \quad (5.50)$$

The detector integrates the square modulus of the wave function in the diffraction plane to form the ADF-STEM signal at this point in the image (corresponding to the probe position \mathbf{x}_p):

Table 5.3 Steps in the calculation of STEM images of thin specimens

Step 1	Calculate the projected atomic potential $v_z(\mathbf{x})$ from Eq. 5.19 or 5.21
Step 2	Calculate the transmission function $t(\mathbf{x}) = \exp[i\sigma_e v_z(\mathbf{x})]$ (Eq. 5.25) and symmetrically bandwidth limit it
Step 3	Calculate the probe wave function $\psi_p(\mathbf{x}, \mathbf{x}_p)$ at position \mathbf{x}_p (Eq. 5.46, and 5.48)
Step 4	Multiply the probe wave function by the specimen transmission function $t(\mathbf{x}) = \exp[i\sigma_e v_z(\mathbf{x})]$ to get the transmitted wave function $\psi_t(\mathbf{x})$
Step 5	Fourier transform the transmitted wave function to get the wave function in the far field (diffraction plane)
Step 6	Integrate the intensity (square modulus) of the wave function in the diffraction plane including only those portions that fall on the annular detector (Eq. 5.51). This is the signal for one point or pixel in the image
Step 7	Repeat step 3 through step 6 for each position of the incident probe \mathbf{x}_p

$$g(\mathbf{x}_p) = \int D(\mathbf{k}) |\Psi_t(\mathbf{k}, \mathbf{x}_p)|^2 d^2\mathbf{k} \quad (5.51)$$

where $D(\mathbf{k})$ is the detector function:

$$\begin{aligned} D(\mathbf{k}) &= 1 && \text{on the detector} \\ &= 0 && \text{otherwise} \end{aligned} \quad (5.52)$$

This process is repeated for each new position of the probe as it is scanned across the specimen (usually in a raster fashion). If $D(\mathbf{k})$ is a small point on the axis, then the image is a bright field image and the discussion of Sect. 5.4 also applies via the reciprocity theorem. If the detector is a large annulus covering only high angle scattering, then the image is an ADF (or annular dark field) image which is the focus of this section. This procedure is restated in algorithmic form in Table 5.3. The incoherent image model (Eq. 3.70) captures many of the features of this calculation but is much faster (approximately as fast as the phase grating calculation) and may be a better approach in many cases.

5.5.1 Single Atom Images

The ADF detector in the STEM typically covers very large angles which will require some changes to the sampling of the potential. First consider an image calculation of the five single atoms used in Fig. 5.13 for BF-CTEM phase contrast. The image is sampled in a 50 Å by 50 Å area. To get a scattering angle of 200 mrad at 200 keV it requires that $0.5\lambda N_x/a \geq 200$ mrad. Therefore the potential and wave functions should be sampled with 1024 pixels in each direction to get the large angles required for the ADF detector.

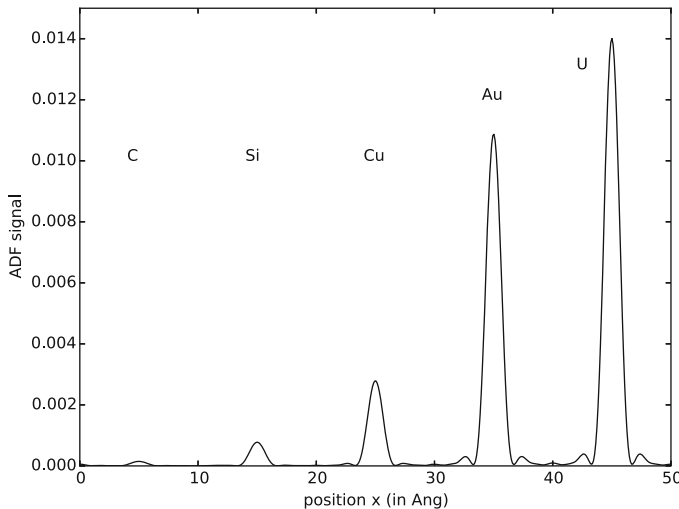


Fig. 5.21 Line scan of the ADF-STEM image intensity through the center of five isolated single atoms and an incident electron beam energy of 200 keV. The electron optical parameters are spherical aberration $C_s = 1.3$ mm, defocus $\Delta f = 500$ Å, and an objective aperture of 8.9 mrad (optimum probe conditions). The ADF detector covers 35–200 mrad. This was calculated with a sampled image of 1024×1024 pixels (atomic number $Z = 6, 14, 29, 79, 92$)

Figure 5.21 shows a line scan through the five single atoms used in Fig. 5.13. The transmission function (Fig. 5.11) is the same for both CTEM and STEM. The vertical axis is the portion of the incident probe intensity that falls on the ADF detector. The ADF signal (Fig. 5.21) is normalized slightly differently from the BF signal (Fig. 5.11) because of the different way in which they are generated. The ADF signal is relative to the total incident beam current but the BF signal is relative to the incident beam current density (the incident beam has a uniform intensity of one at all positions).

Even though the ADF signal and the BF signal are normalized differently it is apparent that the ADF signal is much weaker than the BF signal. However the ADF signal shows a much stronger contrast between heavy and light atoms. It is even possible to image single heavy atoms on thin carbon supports many atoms thick due to the large increase in signal with atomic number Z (see, for example, Crewe et al. [83], Isaacson et al. [227], and Langmore et al. [303]). The peak single atom signal in ADF-STEM for all atoms is shown in Fig. 5.22 as a function of atomic number Z for four different electron beam energies. This smooth variation of the ADF-STEM signal with atomic number Z leads to Z -contrast imaging as popularized by Pennycook [396, 397]. The ADF-STEM signal varies as approximately $Z^{1.5} - Z^{1.7}$ (mainly varies with the inner angle of the detector). Treacy [495] has compared the Z dependence for various atomic potential approximations. Spherical aberration was fixed at $C_s = 1.3$ mm and optimal conditions were used for the defocus and the objective aperture. The inner angle of the ADF detector was set to four times

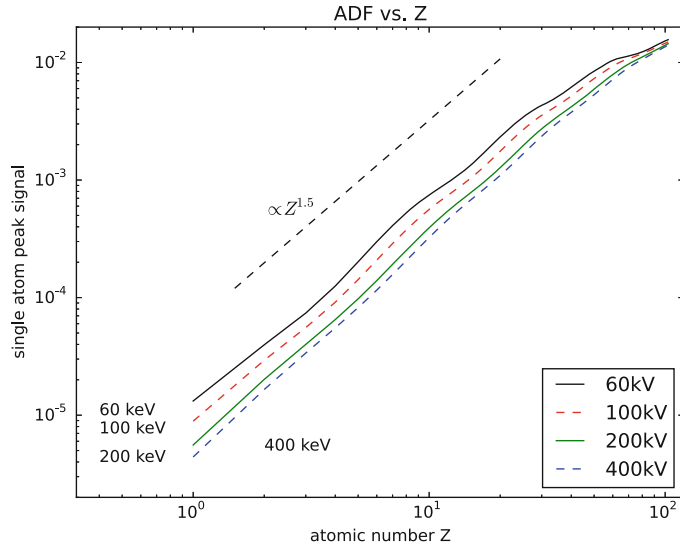


Fig. 5.22 Single atom peak signal in ADF-STEM versus atomic number Z for 60, 100, 200, and 400 keV. Spherical aberration was fixed at $C_s = 1.3$ mm with optimum values of defocus ($0.87\sqrt{C_{S3}\lambda} = 692, 603, 497, 402$ Å) and objective aperture of $(1.34(\lambda/C_{S3})^{1/4} = 10.5, 9.8, 8.9, 8.0$ mrad. The ADF detector extended from 4 to 20 times the objective aperture

the objective aperture and the outer angle was twenty times the objective aperture (this should integrate everything scattered beyond the inner angle). It is interesting that the single atom signal decreases with increasing electron beam energy contrary to BF phase contrast signal shown in Fig. 5.14. As energy increases the resolution should also increase making a larger peak signal. However, higher energy also scatters less to large angle (on the ADF detector) making the signal smaller which seems to be a larger effect here. The apparent signal decreases with increasing resolution in ADF-STEM. Also note that the weak phase object approximation may have small errors at 100 keV for very heavy atoms (Z near 100).

5.5.2 Thin Specimen Images

To simulate an image of (110) silicon also requires more sampling points than you might think at first. The image sequence given in Figs. 5.16 and 5.17 has a supercell size of $a \times b = 26.89 \times 27.15$ Å. The ADF-STEM detector collects large angles. To get $\theta_d \sim 200$ mrad on the detector requires that the number of pixels in each direction be increased to about $N_x > 2a\theta_d/\lambda \sim 429$ pixels. The nearest power of 2 (for the FFTs) is 512×512 pixels.

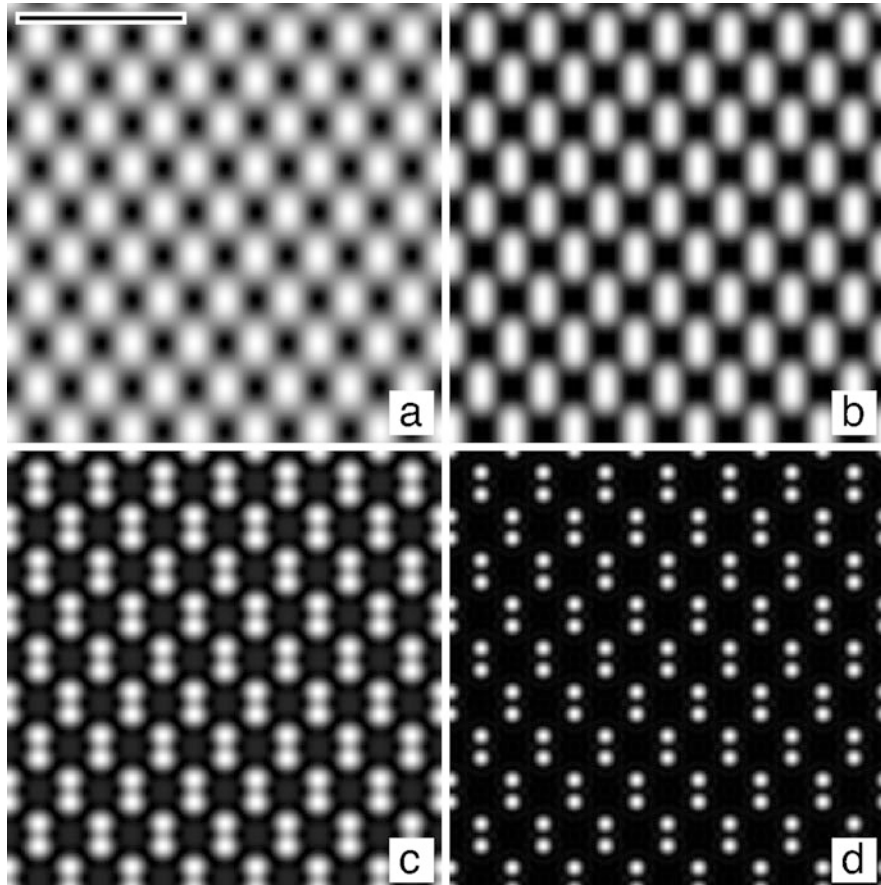


Fig. 5.23 Calculated ADF-STEM image of 110 silicon (4 atoms thick) in a thin phase object approximation with spherical aberration of $C_s = 1.3$ mm and three different beam energies. **(a)** 100 keV $\Delta f = 603 \text{ \AA}$, $\alpha_{\max} = 9.8 \text{ mrad}$. **(b)** 200 keV, $\Delta f = 497 \text{ \AA}$, $\alpha_{\max} = 8.9 \text{ mrad}$. **(c)** 400 keV, $\Delta f = 402 \text{ \AA}$, $\alpha_{\max} = 8.0 \text{ mrad}$. All are optimum STEM conditions. **(d)** 100 keV ideal aberration-corrected STEM image $\Delta f = 0$, $\alpha_{\max} = 30 \text{ mrad}$. The wave function was sampled with 512×512 pixels but the final image is calculated for 256×256 pixels. The scale bar in **(a)** is 10 \AA . The ADF detector extended to 200 mrad from **(a)** 45 mrad, **(b, c)** 40 mrad, and **(d)** 80 mrad. The image ranges are **(a)** 0.00033 – 0.00133 , **(b)** 0.00018 – 0.00072 , **(c)** 0.00003 – 0.00039 , and **(d)** 0 – 0.00331 . White is a larger positive number. Atoms should appear white in all images

Figure 5.23 shows the ADF-STEM image in the thin object approximation for three different energies (compare to Fig. 5.17). The specimen was four atoms thick and the signal is of the order of 10^{-3} – 10^{-4} of the incident beam intensity. The ADF detector spanned an angular range of 40–200 mrad for the 200 and 400 keV images, 45–200 mrad for the uncorrected 100 keV image, and 80–200 mrad for the aberration-corrected image. The ADF signal with a large detector is an incoherent image mechanism and gives a slightly better resolution, however, with a smaller

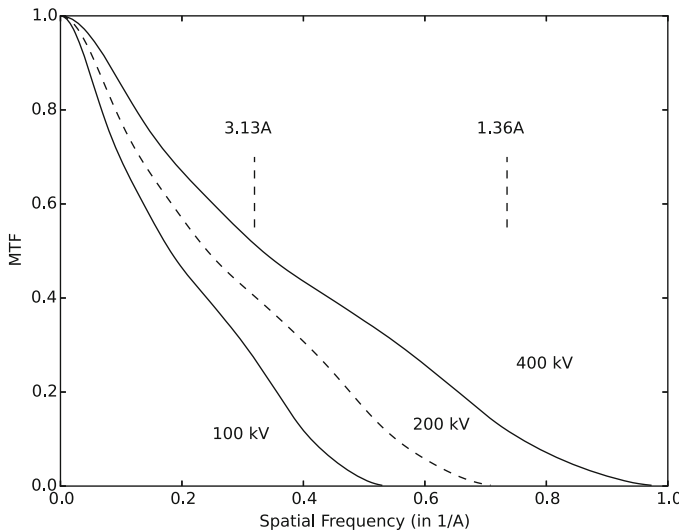


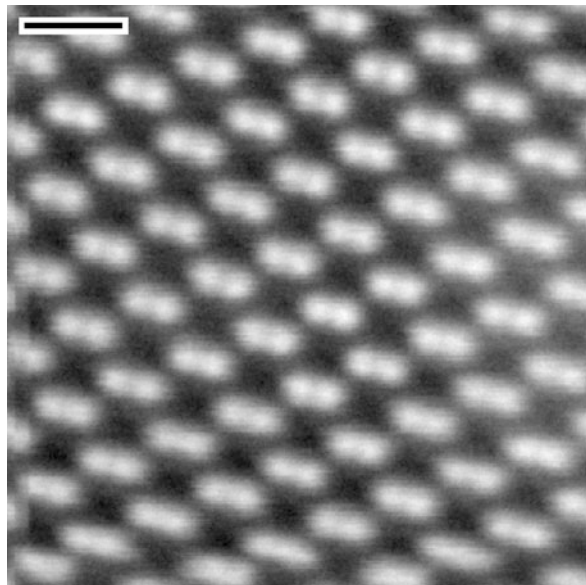
Fig. 5.24 The transfer function for an incoherent annular dark field STEM image in under optimum conditions. Spherical aberration is $C_s = 1.3 \text{ mm}$ and the electron energy varies from 100 to 400 keV. Two spacings relevant to the 110 projection of silicon are shown for comparison. 1.36 \AA is the spacing between the dumbbells and 3.13 \AA is the spacing of the lowest order allowed reflection in the projected unit cell

signal. The characteristic dumbbell structure of silicon atom pairs (in the 110 projection) should be resolved at these beam energies and spherical aberration values. This ADF image does not rely on complicated scattering mechanisms like thermal diffuse scattering or high order Laue zones, but does qualitatively reproduce the features of an ADF-STEM image.

The simulated images in Fig. 5.23 are consistent with the incoherent annular dark field transfer functions as shown in Fig. 5.24. Both of the indicated spacings for the 110 projection of silicon can be resolved at the higher beam energies (compare to Fig. 5.24).

An experimental image of the 110 projection of silicon taken at 100 keV with an aberration-corrected instrument is shown in Fig. 5.25. The dumbbell spacing of 1.36 \AA is just barely resolved in this image. If only the geometrical lens aberration were considered for this image the probe size should be 1.0 \AA or less (and 1.36 \AA should be better resolved); however, this image may be source limited. The tip was nearing the end of its life and probably produces a larger than normal source size (lower brightness). A sequence of images calculated in the simple incoherent image model (Eq. 3.70) with different source sizes (Eq. 3.79) is shown in Fig. 5.26. There is a reasonable match to image (d) with a 1 \AA source size. This produces more beam current (good) but reduces the obtainable resolution (usually bad). Part of this apparent source size blurring may also be due to a small stage vibration of about 0.5 \AA (which appears not to have a preferred direction). It is equally probable that

Fig. 5.25 Experimental ADF-STEM image of 110 silicon recorded on a NION Ultra-STEM at 100 keV (aberration corrected to third order with reduced fifth order) with 512×512 pixels and a 35 mrad objective aperture. The scale bar is 5 Å. Atoms should appear white. This image has been averaged over four frames and low pass filtered to a little above the instrumental resolution



this instrument has significant systematic aberration tuning errors (as in Figs. 3.23 and 3.24) which produces a larger probe with long Lorentzian like tails. Source size effects will vary with source magnification (condenser magnification) but tuning errors will not, which is one experimental approach of determining the cause but is rarely done (this instrument rarely showed much change of image quality with source magnification). The higher the resolution the more severe are the requirements on instrumental stability of all types.

5.6 Annular Bright Field (ABF)

Annular bright field (ABF) is a relatively new mode of operation, in which the STEM annular detector overlaps the outer half of the objective aperture (see Fig. 2.4, Findlay et al. [135, 136] and Ishikawa et al. [228]). This mode is something in between bright field (BF) and annular dark field (ADF) and should be similar to hollow cone illumination in CTEM (Rose [424], Kunath et al. [302]). Earlier theories tend to use only the weak phase approximation which leaves out some important features of the image. Bosch and Lavić [43] have also discussed the theory of ABF images for thin specimens. ABF images may be calculated with the same procedure as ADF-STEM images but integrating over smaller detector angles.

There is not yet an obvious easy approach to define the optimum optical conditions independent of the specimen as was done for BF and ADF. ABF will likely have some elements of phase contrast and involves low angle scattering so

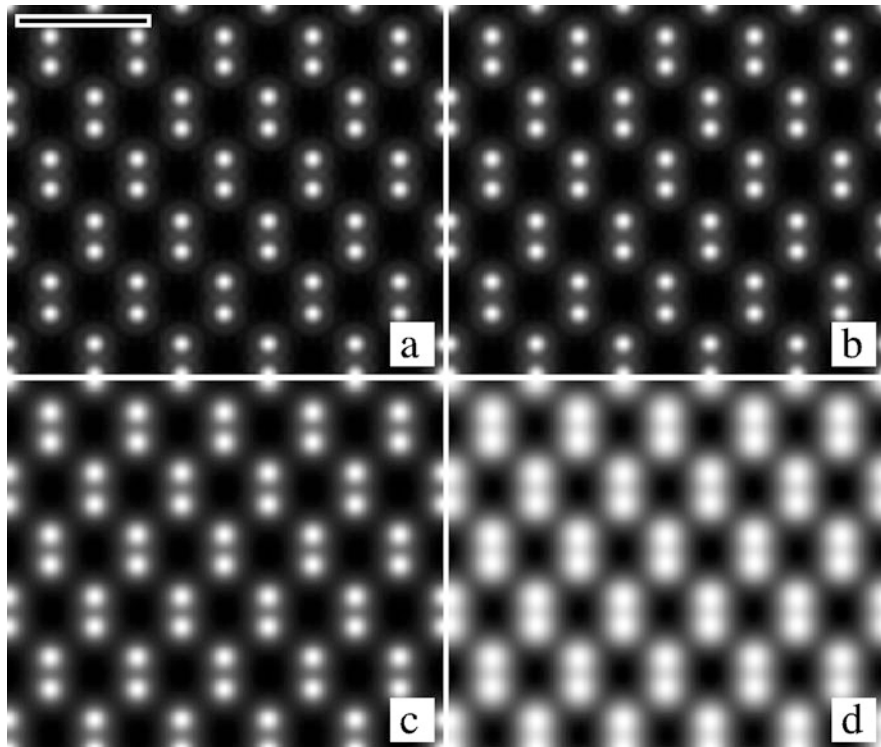


Fig. 5.26 Simple incoherent ADF-STEM images at 100 keV ($C_{s3} = 0$ and $C_{s5} = 5$ mm, 0 defocus and a 35 mrad obj. apert.). The scale bar is 5 Å. The source size is (a) 0.1 Å, (b) 0.2 Å, (c) 0.5 Å, (d) 1.0 Å

may vary significantly with specimen thickness. To find the appropriate optical conditions as independent of specimen thickness as possible, consider a single atom image in the middle of the periodic chart. The peak signal from a single iron ($Z = 56$) atom relative to the background is shown in Fig. 5.27 for similar conditions as for BF and ADF in the previous sections. Iron is approximately the middle of the periodic chart so is in some sense an average atom (the optimum optical conditions may vary with atomic number). The largest signal can be used as a proxy for the image with the best resolution (easy to calculate). Higher resolution likely produces a thin tall profile (a larger signal tends to be sharper). A similar calculation for low atomic number (carbon with $Z = 6$) produced a similar graph but small shifts in the optimum positions. This approach is only approximate but is a start until a more concrete theory presents itself. A similar calculation for ADF-STEM produced a result similar to Fig. 3.17 with a single well-defined position for the optimum conditions.

There are several different combinations (positions in Fig. 5.27) that seem to produce a large single atom signal. ABF can be optimized for both positive contrast

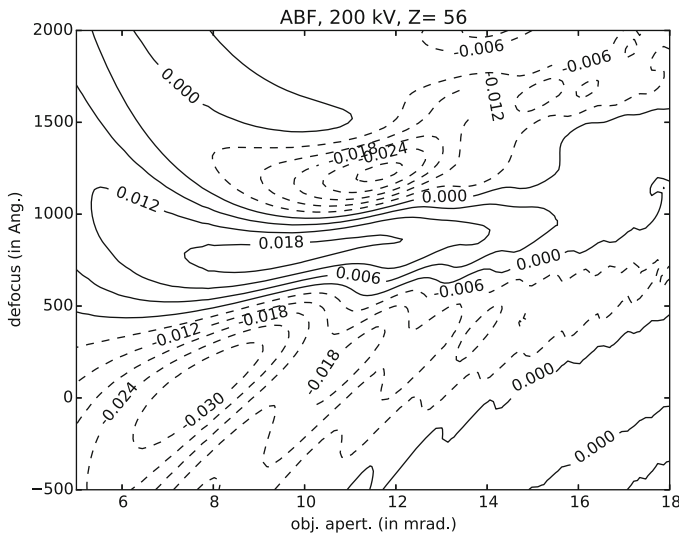


Fig. 5.27 ABF single atom signal ($Z = 56$, iron) versus defocus and objective aperture at 200 kV. $C_{S3} = 1.3$ mm. The ABF aperture covered the outer half of the objective aperture. Positive values are solid lines and negative values are dashed lines

and negative contrast. Two positions produce a maximum positive signal and one position produces a maximum negative signal. Negative contrast (negative peak signal) seems to produce a larger signal and might be more desirable. A line scan through several different atoms is shown in Fig. 5.28. The positive contrast conditions produce a smaller signal and may have a double peak for large atomic numbers (not good). The negative contrast conditions produce a larger signal with a more appropriate shape so the negative contrast conditions are probably better in general (for thin specimens).

The variation of the ABF signal versus atomic number is shown in Fig. 5.29. The dependence of the single atom signal on atomic number is in between that of BF and ADF as might be expected from the size and position of the detector. The ABF signal involves low angle scattering so still includes some variations of the periodic chart as conventional bright field.

With an aberration corrector spherical aberration and other low order aberrations can be controlled. Figure 5.30 show the variation of the single atom signal versus defocus and the inner angle of the ABF detector similar to that in Fig. 5.27. Again it is possible to obtain either positive or negative contrast. With a larger objective aperture the usable range of defocus becomes much smaller and the optimum defocus becomes closer to zero. Only a small change in defocus can switch the contrast from positive to negative which might make this imaging mode a little more ambiguous (are atoms white or black?). The optimum inner angle seems close to a relative value of 0.5 which is used typically.

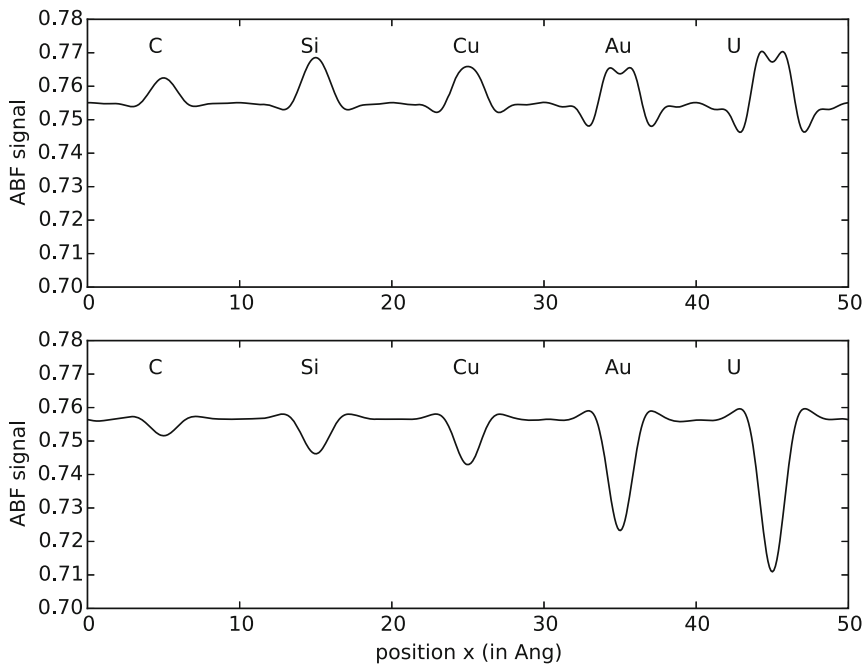


Fig. 5.28 ABF single atom profile at 200 kV and $C_{S3} = 1.3$ mm for a few atomic numbers. The ABF aperture covered the outer half of the objective aperture. Top: largest positive signal ($\Delta f = 763 \text{ \AA}$, $\alpha_{\max} = 9.07 \text{ mrad}$), and bottom: largest negative signal ($\Delta f = 100 \text{ \AA}$, $\alpha_{\max} = 7.95 \text{ mrad}$)

The calculated ABF images for 110 silicon are shown in Fig. 5.31. The images without an aberration corrector are shown in part (a) and (b). The images for an aberration-corrected ABF-STEM are shown in part (c) and (d) for negative contrast and positive contrast, respectively.

5.7 Summary of Sampling Suggestions

The previous sections discussed sampling requirements for some specific cases in an anecdotal manner. There is really no easy way to calculate the required pixel size (sampling requirements) for every case in general. Usually you have to make an estimate of the sampling requirements, calculate an image with this estimate and compare to another calculation with better sampling (more and smaller pixels, etc.). If there is no significant change between the calculated images at two different pixels sizes (and number of pixels per image), then this is an indication that the image is correct. The deviation between two different calculations with different pixels sizes and number of pixels can also be used to estimate the error of the simulation itself. Table 5.4 gives a list of suggestions for the initial sampling sizes.

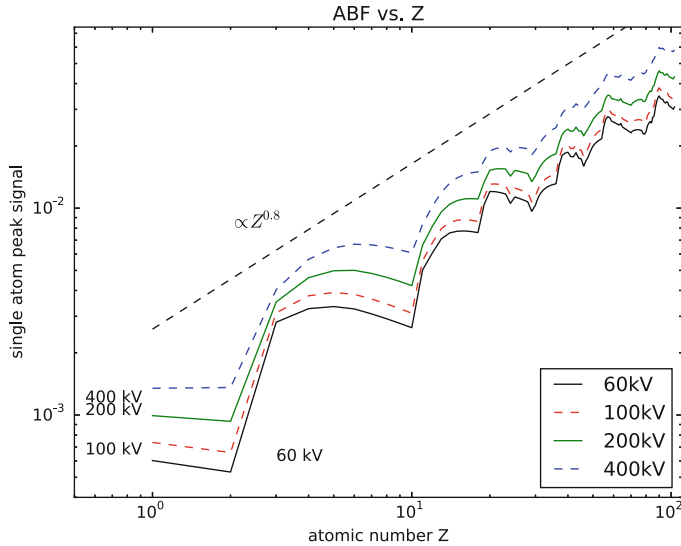


Fig. 5.29 The peak ABF single atom signal versus atomic number Z at 60, 100, 200, and 400 kV with the ABF aperture covering the outer half of the objective aperture. $C_{S3} = 1.3$ mm and optimum defocus values of 199, 135, 100, 49 Å, and objective aperture of 9.5, 8.8, 8.0, 7.0 mrad (to obtain the largest signal for $Z = 56$) were used.

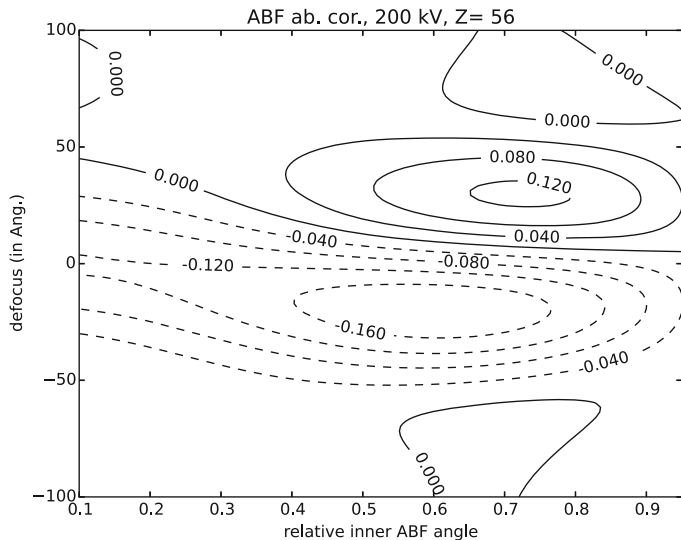


Fig. 5.30 The peak ABF single atom ($Z = 56$, iron) signal for 200 kV and an objective angle of $\alpha_{\max} = 30$ mrad versus defocus and the relative inner angle of the ABF detector for an ideal aberration-corrected image (all aberrations except defocus assumed negligible). Positive values are solid lines and negative values are dashed lines

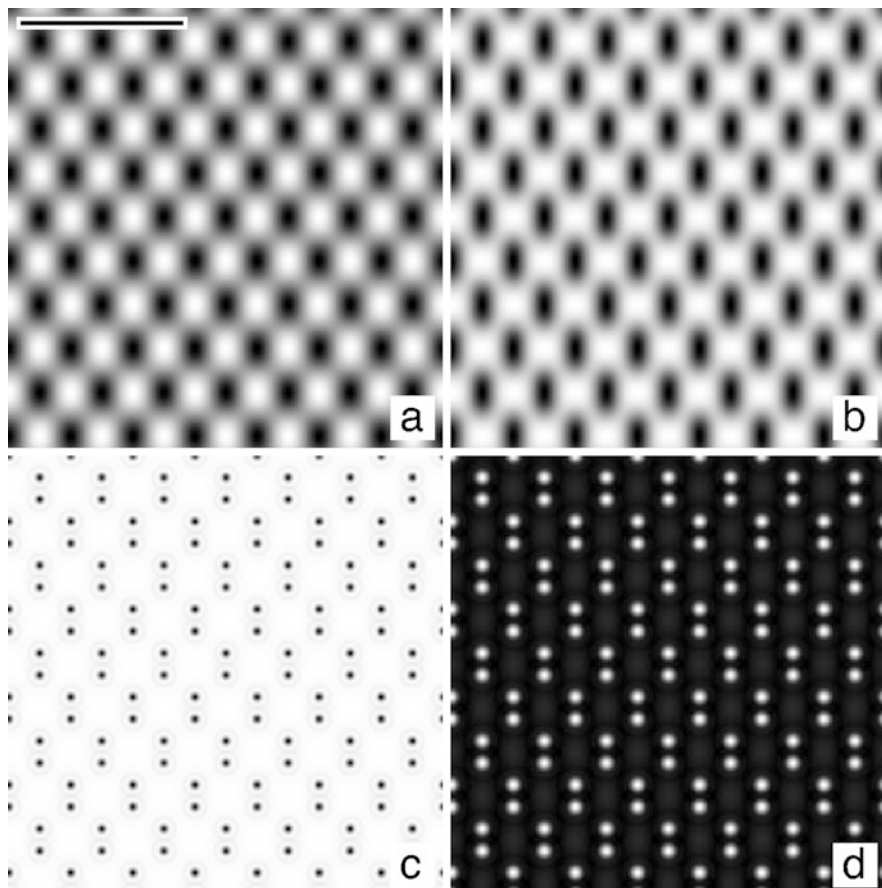


Fig. 5.31 Calculated ABF-STEM image of 110 silicon (4 atoms thick) in the thin specimen approximation with spherical aberration of $C_s = 1.3 \text{ mm}$ and three different beam energies. (a) 200 keV, $\Delta f = 100 \text{ \AA}$, $\alpha_{\max} = 8.0 \text{ mrad}$. (b) 400 keV, $\Delta f = 50 \text{ \AA}$, $\alpha_{\max} = 7.0 \text{ mrad}$. All are optimum ABF-STEM conditions. (c) 200 keV ideal aberration-corrected STEM image $\Delta f = 0$, $\alpha_{\max} = 30 \text{ mrad}$. (d) 200 keV ideal aberration-corrected STEM image $\Delta f = 20$, $\alpha_{\max} = 30 \text{ mrad}$. All have an inner detector angle of half the objective except (d) which is 0.7 of the objective. The wave function was sampled with 512×512 pixels but the final image is calculated for 256×256 pixels. The scale bar in (a) is 10 \AA . The image ranges are (a) 0.735–0.755, (b) 0.747–0.767, (c) 0.738–0.751, and (d) 0.548–0.598. White is a larger positive number. Atoms should appear black in (a) through (c) and white in (d)

Table 5.4 Initial sampling suggestions for calculating images of thin specimens

1	The transmission function $t(\mathbf{x})$ (Eq. 5.25) should be symmetrically bandwidth limited
2	The real space pixel size Δx and Δy should be less than about $d_0/3$ to $d_0/4$ where d_0 is the resolution of the instrument
3	The reciprocal space pixel size Δk_x and Δk_y should be less than about $k_{obj}/10$ where λk_{obj} is the maximum semiangle in the objective aperture
4	The maximum angle in reciprocal space $\lambda k_{x-\max}$ and $\lambda k_{y-\max}$ should be about twice the maximum angle in the objective aperture (for CTEM) or slightly bigger than the maximum angle on the ADF-STEM detector (for STEM)

Chapter 6

Theory of Calculation of Images of Thick Specimens



This chapter discusses how to calculate images of thick specimens including the effects of multiple or plural scattering in the specimen and the geometrical extent of the specimen along the optic axis of the electron microscope (the z direction). The electron interacts strongly with the specimen and can scatter more than once as it passes through specimens as thin as 10–50 Å. When the electron can scatter more than once as it passes through the specimen the scattering is said to be dynamical. If the electron can only scatter once when passing through the specimen the scattering is said to be kinematical. The electron interaction in Chap. 5 is kinematical and the scattering processes discussed in this chapter are dynamical. Dynamical scattering also exists in X-ray diffraction (Batterman and Cole [25]) of thick specimens.

The instrumental aspects of the electron microscope and the passage of the electrons through the microscope are identical to what has already been described in previous chapters. This chapter will focus almost entirely on the relatively short portion of the electron trajectory as it passes through the specimen. Although this is a very short part of the electron's trajectory it is the most difficult to fully calculate because the electron interacts strongly with the specimen and can be scattered many times while passing through the specimen. In many ways this is one of the most interesting portions of the electron's path through the microscope because of the information about the specimen that it reveals.

The theory of dynamical electron diffraction has been studied by many authors over a large portion of the last century. Bethe [31] first discussed dynamical scattering in 1928 in the context of electron diffraction (i.e., electron microscopes had not yet been invented). Bethe started with the Schrödinger equation and Fourier expanded the crystal potential and the electron wave function with components that match the underlying periodicity of the crystal lattice. The Fourier components of the wave function have since become known as Bloch waves in analogy with Bloch's Theorem in solid state physics (see for example Ashcroft and Mermin [20] or Kittel [286]). Bethe solved for the three dimensional eigenvalues of the electron wave

function in a crystalline specimen with the appropriate boundary conditions on the entrance and exit face of the crystal. Niehrs and Wagner [373], Fujimoto [152], and Sturkey [478] later organized the Bloch wave solution into a scattering matrix solution and Tournaire [493] developed a related reciprocal space matrix solution. Fertig and Rose [128], Pennycook and Jesson [398–400], and Nellist and Pennycook [369] have extended the Bloch wave analysis to scanning transmission (STEM) microscopy. Howie and Whelan [219] used a different starting point but ended up with a set of coupled first order differential equations similar to the Bloch wave solution. Van Dyck [501] and Jap and Glaeser [243] have independently developed a path integral formulation of dynamical scattering. The history of the development of the theory of dynamical diffraction of electrons has been given by Cowley [74], Self et al. [452], Van Dyck [506], and Watanabe [526].

Cowley and Moodie [78] considered the dynamical scattering problem by starting from a physical optics point of view and derived a method that has become known as the multislice method. In this method the specimen is divided into thin two-dimensional slices along the electron beam direction (like a loaf of sliced bread). The electron beam alternately gets transmitted through a slice and propagates to the next slice. Each slice is thin enough to be a simple phase object and the propagation between slices is determined using Fresnel diffraction. Goodman and Moodie [162] later expanded the multislice theory into an accessible form appropriate for numerical implementation on a computer and showed how various methods of dynamical scattering calculations were related. Allpress et al. [12] and Lynch and O’Keefe [325] first implemented the multislice method on a computer to confirm the interpretation of high-resolution CTEM images of niobium oxides. Comparison of simulated images to images of known structures confirmed that image simulation with the multislice method could reliably simulate the observed image structure (Allpress and Sanders [13]). The availability of simulation programs such as SHRLI O’Keefe et al. [380] and O’Keefe and Buseck [379] lead to wide spread use of simulation in high-resolution image interpretation in CTEM. Ishizuka and Uyeda [236] produced a more rigorous quantum mechanical derivation of the multislice method and coincident with Bursill and Wilson [51] introduced the use of the fast Fourier transform or FFT which greatly reduced the computer time required for an image simulation. Cowley and Spence [81] have extended the multislice method to the calculation of convergent beam electron diffraction patterns (CBED), Kirkland et al. [279] also extended it to include ADF-STEM image calculations, and Ishizuka [233] has presented some alternative suggestions to include the thermal diffuse scattering. Van Dyck [504, 505, 507], Coene and Van Dyck [64, 65], and Kilaas and Gronsky [258] recently proposed the so-called real space method which is related to the multislice method but performs the convolution and transmission in real space. The real space method may have advantages in some situations. O’Keefe [378] and Ishizuka [234] have recently reviewed the history of the multislice method.

If N is the number of Fourier components (also referred to as beams or Bloch waves), then any direct matrix solution will require the storage of N^2 elements in computer memory. The computer time required for a matrix multiplication scales as

N^2 and the time for the direct solution of a matrix equation or eigenvalue problem scales as N^3 (see for example Press et al. [406]). When there are a large number of beams (more than about 10 or 20) a direct matrix (Bloch wave) solution becomes very inefficient and the multislice solution using the FFT will prove to be much more efficient in computer time and memory requirements. Bloch wave matrix solutions can be obtained by hand with pencil and paper if there are only a small number of Bloch waves involved (two or three). This typically means that the specimen has to be a perfect crystal with a small unit cell projected along a high symmetry axis. Analytical Bloch wave solutions can provide valuable insight into the imaging process; however, small unit cell bulk crystal structures are already known (usually from X-ray diffraction) and there is no more than an academic interest in examining them again in the electron microscope. Most (nonbiological) specimens of interest contain interfaces or defects or are entirely amorphous. These specimens require relatively large numbers (many thousands) of beams or Bloch waves making a Bloch wave matrix solution impractical. The multislice method is generally much more efficient and easier to implement numerically on the computer and it is flexible enough to simulate defects and interfaces. The storage requirements for the multislice method scale as N and with the addition of the fast Fourier transform the computer time scales as approximately $N \log_2 N$. The multislice method is usually much more efficient for calculating dynamical electron diffraction patterns and images Goodman and Moodie [162] and Self et al. [452].

The multislice method solves the problem of propagation of a quantum mechanical wave packet through a potential. This is a rather general problem and it is not surprising that similar methods have evolved in fields other than electron microscopy. For example, the propagation of radio waves through an atmosphere can be treated in a method similar to the multislice method (Cordes et al. [69], French and Lovelace [148], and Pidwerbetsky and Lovelace [402]). Molecular dynamics problems in chemistry also can be studied using a method similar to the multislice method (Kosloff [293]). The split-step Fourier method (for example, Feit and Fleck [126, 138] or Agrawal [3] section 2.4) is a numerical method used to calculate the propagation of light through a nonlinear media that is essentially the same as the multislice method.

As discussed in Sect. 2.3 the electrons in the microscope have enough energy that they should be treated with the relativistic Dirac wave equation with spin for a precise calculation. However the simpler approach of ignoring the electron spin and using the nonrelativistic Schrödinger equation with the relativistic mass and wavelength will again be used because it is much easier to work with. This approximation is reasonably accurate at 100 keV but may introduce small errors at energies of order 1000 keV or higher.

The specimen is almost always placed near the peak magnetic field of the objective lens (of order 1 T or 10 kG). The electrons travel through the specimen while in a large magnetic field. Solving the problem with both the electrostatic interaction between the imaging electrons and the specimen and the imaging electrons and the magnetic field can be very difficult. The electron path deviation

due to the magnetic field of the objective lens is on the scale of the focal length of the objective lens (about 1 mm). The electron path deviation due to the electrostatic interaction with the atoms in the specimen is on the scale of the specimen thickness (a few hundred Angstroms). Therefore it is a reasonable approximation to neglect the action of the objective lens magnetic field on the scale of the specimen thickness. The electron trajectories while passing through the specimen will be calculated as if there were no external magnetic field present. This makes the problem somewhat easier to deal with.

Calculating the image given the atomic structure of the specimen is difficult enough (as will be seen). The inverse problem of calculating the atomic structure given the recorded image is even more difficult. The idea of an inverse multislice calculation has been around for a long time but few have had the courage to try it. Gribelyuk [168], Beeching and Spargo [27, 28] have proposed approaches for an inverse multislice calculation. Spargo et al. [467], Allen et al. [7, 9, 10], Spence et al. [469, 471], and O’Leary et al. [385] have considered the inverse problem using Bloch waves.

6.1 Bloch Wave Eigenvalue Solution

There is a long history of Bloch wave eigenvalue calculations starting with Bethe [31], with many worthwhile treatments in the literature, too numerous to mention all of them. Some recent reviews have been given by (for example) Humphreys [220], Spence [470], Spence and Zuo [474], deGraf [164], and Zuo and Spence [550]. Bloch wave solutions of ADF-STEM have been considered by Fertig and Rose [128], Pennycook and Jesson [398], Nellist and Pennycook [368], Watanabe et al. [529], and Allen et al. [8]. Bloch wave solutions for scanning confocal have been considered by Mitsuishi et al. [350].

6.1.1 *Bloch Waves*

The electron wave function can be expressed as a linear combination of any complete basis set. However, there is an advantage in using a basis set that also satisfies the Schrödinger equation in the specimen (with the same periodicity as the crystal) which are called Bloch waves. Expand the electron wave function in Bloch waves $b(\mathbf{k}_j, \mathbf{r})$ and their associated parameters \mathbf{k}_j (scattering wave vectors on the Ewald sphere):

$$\psi(x, y, z) = \psi(\mathbf{r}) = \sum_j \alpha_j b_j(\mathbf{k}_j, \mathbf{r}) \quad (6.1)$$

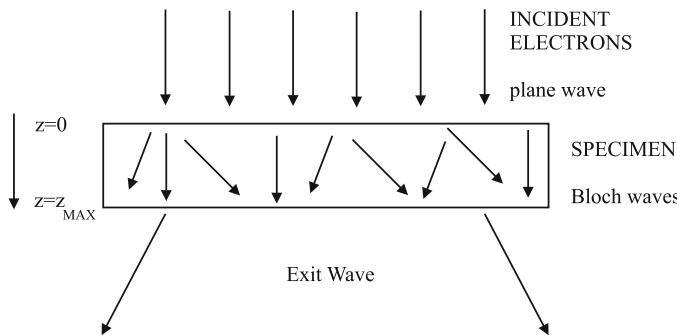


Fig. 6.1 The Bloch wave picture. The incident electron wave (plane wave for CTEM) becomes a superposition of Bloch waves inside the specimen. The properties of the Bloch wave determine the form of the wave that exits the specimen

With these Bloch waves any set of coefficients α_j are allowed inside the (crystal) specimen but only one set will also match the incident wave function. There is an implicit assumption that the specimen is crystalline (periodic) so this approach may not work well for amorphous specimens.

Conceptually, the specimen can be thought of as a converter or filter that converts the incident electron (plane wave for BF CTEM, and probe for STEM) into a superposition of Bloch waves inside the (crystalline) specimen as in Fig. 6.1. The wave function and its first derivative must be continuous at the (top) entrance surface, which determines which Bloch waves will be initiated in the specimen. After entering the specimen the electrons propagate as Bloch waves and finally leave through the exit surface (bottom) of the specimen and are imaged by the objective lens. The characteristics of these Bloch waves determine how the electrons travel through the specimen. Hopefully, the strongest Bloch waves are representative of the actual structure in the specimen.

Each Bloch wave must satisfy the Schrödinger equation in the (usually crystal) specimen:

$$\left[-\frac{\hbar^2}{2m} \nabla^2 - eV(x, y, z) \right] b_j(\mathbf{k}_j, \mathbf{r}) = Eb_j(\mathbf{k}_j, \mathbf{r}) \quad (6.2)$$

where $\hbar = h/2\pi$ is Planck's constant divided by 2π , $m = \gamma m_0$ is the relativistic mass of the electron, $e = |e|$ is the magnitude of the charge of the electron, E is the kinetic energy of the electron, and $-eV$ is the potential energy of the electron. V is the potential of the atoms in the specimen. The energy E will remain constant because elastic scattering is assumed, except for a slight increase due to the average inner potential of the specimen (with a related decrease in wavelength). The wave vector k_0 and energy of the incident wave (inside the specimen) are:

$$k_0 = \frac{1}{\lambda} \quad (6.3)$$

$$E = \frac{\hbar^2 k_0^2}{2m} = \frac{\hbar^2}{2m\lambda^2} \quad (6.4)$$

where λ is the relativistically corrected electron wavelength. The Schrödinger equation becomes:

$$\left[-\frac{\hbar^2}{2m} \nabla^2 - eV(x, y, z) \right] b_j(\mathbf{k}_j, \mathbf{r}) = \frac{\hbar^2 k_0^2}{2m} b_j(\mathbf{k}_j, \mathbf{r}) \quad (6.5)$$

$$\begin{aligned} \left[\nabla^2 + 4\pi^2 k_0^2 \right] b_j(\mathbf{k}_j, \mathbf{r}) &= -4\pi^2 \left(\frac{2me}{\hbar^2} \right) V(\mathbf{r}) b_j(\mathbf{k}_j, \mathbf{r}) \\ &= -4\pi^2 U(\mathbf{r}) b_j(\mathbf{k}_j, \mathbf{r}) \end{aligned} \quad (6.6)$$

$$U(\mathbf{r}) = \frac{2me}{\hbar^2} V(\mathbf{r}) = \frac{\sigma}{\pi\lambda} V(\mathbf{r}) \quad (6.7)$$

where σ is the interaction parameter.

Each Bloch wave is basically a plane wave that is forced to have the periodicity of the (crystalline) specimen by multiplying by a linear combination of plane waves in three dimensions (a Fourier series):

$$\begin{aligned} b_j(\mathbf{k}_j, \mathbf{r}) &= \exp[2\pi i \mathbf{k}_j \cdot \mathbf{r}] \sum_{\mathbf{G}} C_{\mathbf{G}j} \exp[2\pi i \mathbf{G} \cdot \mathbf{r}] \\ &= \sum_{\mathbf{G}} C_{\mathbf{G}j} \exp[2\pi i (\mathbf{k}_j + \mathbf{G}) \cdot \mathbf{r}] \end{aligned} \quad (6.8)$$

The set of vectors $\mathbf{G} = (G_x, G_y, G_z) = (h/a, k/b, l/c)$ are typically the reciprocal lattice vectors of the specimen. The unit cell size of the specimen is (a, b, c) and (h, k, l) are integer indexes. In principle there are an infinite number of \mathbf{G} vectors but in practice only a small number will typically be used. There is a different set of $C_{\mathbf{G}j}$ coefficients for each Bloch wave j .

6.1.2 Periodic Potential

Expand the specimen potential in a three-dimensional Fourier series in the independent atom model (Eq. 5.19) as:

$$V(x, y, z) = V(\mathbf{r}) = \sum_{\mathbf{G}} V_{\mathbf{G}} \exp[2\pi i \mathbf{G} \cdot \mathbf{r}] \quad (6.9)$$

$$\begin{aligned}
V_{\mathbf{G}} &= \frac{\hbar^2}{2\pi m_0 e} \frac{1}{\Omega} \sum_j f_{ej}(|\mathbf{G}|) \exp(-2\pi i \mathbf{G} \cdot \mathbf{r}_j) \\
&= \frac{2\pi e a_0}{\Omega} \sum_j f_{ej}(|\mathbf{G}|) \exp(-2\pi i \mathbf{G} \cdot \mathbf{r}_j) \\
&= \frac{47.86}{\Omega} \sum_j f_{ej}(|\mathbf{G}|) \exp(-2\pi i \mathbf{G} \cdot \mathbf{r}_j)
\end{aligned} \tag{6.10}$$

where $f_{ej}(q)$ is the electron scattering factor (in Angstroms) in the first Born approximation of the j^{th} atom, e and m are the charge and mass of the electron, a_0 is the Bohr radius, Ω is the unit cell volume (in cubic Angstroms), and $V_{\mathbf{G}}$ is in volts. The summation over j is over all atoms in the unit cell. The $\mathbf{G} = 0$ term in Eq. 6.9 is a uniform potential inside the specimen. There is a small computational advantage in absorbing this term into the electron wavelength (as already done in Eq. 6.3) so this term will be excluded in later equations.

If the specimen (crystal) has a center of symmetry (centro-symmetric), then for every atom at position \mathbf{r} there is an identical atom at position $-\mathbf{r}$ and the terms in Eq. 6.10 appear as pairs of complex conjugates making $V_{\mathbf{G}}$ real; otherwise, it may be complex. One possible strategy for finding the important \mathbf{G} values is to calculate all $V_{\mathbf{G}}$ up to some maximum magnitude $|\mathbf{G}|$ (scan through integers (h, k, l)) and keep all with $|V_{\mathbf{G}}| > \epsilon |V_{\mathbf{G}=0}|$ where ϵ is a small positive number chosen by the user (perhaps of order 10^{-5}).

6.1.3 Matrix Equation

Insert Eq. 6.9 for the potential (also using Eq. 6.7) and Eq. 6.8 for the Bloch waves into the Schrödinger equation (6.6). The summation indexes \mathbf{H} and \mathbf{G} will both be over the full range of allowed reciprocal lattice vectors \mathbf{G} but different letters are used to separate two different sums. The mean inner potential of the specimen $V_{\mathbf{G}=0}$ will be included in the wavelength so is dropped from the sum for the potential and the incident k_0 includes a small change of potential inside the specimen. Also dropping the common factor of $4\pi^2$ yields:

$$\begin{aligned}
&\sum_{\mathbf{G}} \left(k_0^2 - |\mathbf{k}_j + \mathbf{G}|^2 \right) C_{\mathbf{G}j} \exp[2\pi i (\mathbf{k}_j + \mathbf{G}) \cdot \mathbf{r}] \\
&= - \left[\sum_{\mathbf{H} \neq 0} U_{\mathbf{H}} \exp[2\pi i \mathbf{H} \cdot \mathbf{r}] \right] \left[\sum_{\mathbf{G}} C_{\mathbf{G}j} \exp[2\pi i (\mathbf{k}_j + \mathbf{G}) \cdot \mathbf{r}] \right]
\end{aligned}$$

$$\begin{aligned}
&= - \sum_{\mathbf{H} \neq 0} U_{\mathbf{H}} \left[\sum_{\mathbf{G}} C_{\mathbf{G}j} \exp[2\pi i(\mathbf{k}_j + \mathbf{G} + \mathbf{H}) \cdot \mathbf{r}] \right] \\
&= - \sum_{\mathbf{H} \neq 0} U_{\mathbf{H}} \left[\sum_{\mathbf{X}} C_{(\mathbf{X}-\mathbf{H})j} \exp[2\pi i(\mathbf{k}_j + \mathbf{X}) \cdot \mathbf{r}] \right] \\
&= - \sum_{\mathbf{H} \neq 0} U_{\mathbf{H}} \left[\sum_{\mathbf{G}} C_{(\mathbf{G}-\mathbf{H})j} \exp[2\pi i(\mathbf{k}_j + \mathbf{G}) \cdot \mathbf{r}] \right] \\
&= - \sum_{\mathbf{G}} \left[\sum_{\mathbf{H} \neq 0} U_{\mathbf{H}} C_{(\mathbf{G}-\mathbf{H})j} \right] \exp[2\pi i(\mathbf{k}_j + \mathbf{G}) \cdot \mathbf{r}] \\
&= - \sum_{\mathbf{G}} \left[\sum_{\mathbf{H} \neq \mathbf{G}} U_{\mathbf{G}-\mathbf{H}} C_{\mathbf{H}j} \right] \exp[2\pi i(\mathbf{k}_j + \mathbf{G}) \cdot \mathbf{r}]
\end{aligned} \tag{6.11}$$

where the substitution $\mathbf{X} = \mathbf{G} + \mathbf{H}$ was used in the second line and returned to \mathbf{G} at the end. Some of these steps are not strictly valid unless the range of summation is infinite, which may not be true in practice (a small approximation). The $\mathbf{H} = \mathbf{G}$ term is excluded from the summation because the $\mathbf{G} = 0$ term (inner potential) has been transferred into the electron wavelength (via k_0). Equating coefficients of $\exp[2\pi i(\mathbf{k}_j + \mathbf{G}) \cdot \mathbf{r}]$ yields:

$$(k_0^2 - |\mathbf{k}_j + \mathbf{G}|^2) C_{\mathbf{G}j} + \sum_{\mathbf{H} \neq \mathbf{G}} U_{\mathbf{G}-\mathbf{H}} C_{\mathbf{H}j} = 0 \tag{6.12}$$

This is a matrix equation where the first term (on the left-hand side) is the diagonal elements and the second term is the off-diagonal elements. So far no serious approximations have been made and this expression is reasonably exact. However, both the \mathbf{k}_j vectors and the $C_{\mathbf{G}}$ coefficients are unknown, so there is no obvious way to solve this equation. Next, several approximation will be made to get this equation into a linear form that can be solved. In the process half of the solutions will be lost, which turn out to be the backscattered electrons (deGraf [164]). These approximations are similar to those used in the multislice method.

A typical specimen is a thin slab of material perpendicular to the beam direction, and the incident electron beam is a very high energy traveling in a predominantly z direction. The incident beam is of order 100 keV or higher and the inner potential V_0 of the specimen is of order 10 eV so the kinetic energy does not change dramatically in the specimen.

$$k_0 \sim |\mathbf{k}_j| >> |\mathbf{G}| \tag{6.13}$$

This is sometimes referred to as the high energy approximation. Also within this approximation all backscattered electrons will be ignored. In general some small percentage of electron will reverse direction (backscattered) but these will be ignored to simplify the mathematics.

Both the electron wave and its first derivative must be continuous across the entrance surface of the specimen. The inner potential of the specimen (V_0) may change the kinetic energy in the beam direction ($k_{0,z}$) but the transverse wave vector must be continuous at the entrance of the specimen. Approximate this requirement as applying to each individual Bloch wave rather than the wave function as a whole (weighted sum of Bloch wave vectors). Therefore approximate the Bloch wave vector as the incident wave vector \mathbf{k}_0 plus a small term along the beam direction \hat{z} :

$$\mathbf{k}_j \sim \mathbf{k}_0 + \gamma_j \hat{z} \quad (6.14)$$

where γ_j is a small quantity. Inserting this expression yields:

$$\begin{aligned} k_0^2 - |\mathbf{k}_j + \mathbf{G}|^2 &= k_0^2 - |\mathbf{k}_0 + \gamma_j \hat{z} + \mathbf{G}|^2 \\ &= k_0^2 - |\mathbf{k}_0 + \mathbf{G}|^2 - 2\gamma_j (\mathbf{k}_0 + \mathbf{G}) \cdot \hat{z} - \gamma_j^2 \end{aligned} \quad (6.15)$$

The γ_j^2 term may be ignored because γ_j is a small quantity. Also expanding terms leaves:

$$\begin{aligned} k_0^2 - |\mathbf{k}_j + \mathbf{G}|^2 &= 2k_0 s_{\mathbf{G}} - 2\gamma_j (\mathbf{k}_0 + \mathbf{G}) \cdot \hat{z} \\ &= 2k_0 s_{\mathbf{G}} - 2\gamma_j (k_{0,z} + G_z) \end{aligned} \quad (6.16)$$

$$2k_0 s_{\mathbf{G}} = k_0^2 - |\mathbf{k}_0 + \mathbf{G}|^2 = -2k_{0,z} G_z - |\mathbf{G}|^2 \quad (6.17)$$

where $s_{\mathbf{G}}$ is a general excitation error. Insert this expression back into Eq. 6.12 to obtain:

$$[2k_0 s_{\mathbf{G}} - 2\gamma_j (k_{0,z} + G_z)] C_{\mathbf{G}j} + \sum_{\mathbf{H} \neq \mathbf{G}} U_{\mathbf{G}-\mathbf{H}} C_{\mathbf{H}j} = 0 \quad (6.18)$$

The high energy approximation says that:

$$|\mathbf{G}| \ll |k_{0,z}| \quad (6.19)$$

so the G_z term is usually dropped. However, at 100 kV $k_0 \sim 27 \text{ \AA}^{-1}$ and $|G_{\max}|$ may be 4 or 5 \AA^{-1} for high resolution, in which case G_z is important so this approximation may not be that good at high resolution (or for the higher order Laue zones). Rearranging terms and making the high energy approximation leaves:

$$2k_0 s_{\mathbf{G}} C_{\mathbf{G}j} + \sum_{\mathbf{H} \neq \mathbf{G}} U_{\mathbf{G}-\mathbf{H}} C_{\mathbf{H}j} = 2\gamma_j k_{0,z} C_{\mathbf{G}j} \quad (6.20)$$

This equation is repeated for each \mathbf{G} . This is an eigenvalue matrix equation for the eigenvalues $2\gamma_j k_{0,z}$ and the eigenvectors (set of $C_{\mathbf{G}j}$). If the specimen is a centro-symmetric crystal, then the matrix is real and symmetric; otherwise, it may be complex and Hermitian. The eigenvectors are orthogonal and can be normalized (most subroutines automatically normalize their results), which will be assumed later. The eigenvalues will be real.

With N Bloch waves then this is said to be an N-beam calculation. There will also be N vectors \mathbf{G} , N eigenvalues and N eigenvectors (N^2 coefficients $C_{\mathbf{G}j}$). The memory storage requirements scale as $\mathcal{O}(N^2)$. Solving the eigenvalue equation is a computationally difficult problem. The CPU time scales as $\mathcal{O}(N^3)$ so this approach is not competitive with the methods that will be discussed later for large N . However, small unit cells with a lot of symmetry may work well (small N). Finding eigenvalues and eigenvectors is also a difficult process. There are several existing free software libraries with well-developed subroutine for this purpose. Lapack [15] (www.netlib.org) is probably one of the better packages and in general it is probably best to use this or similar packages. Lapack is mainly in Fortran but there are translations in several different programming languages. The GNU Scientific Library or GSL (www.gnu.org/software/gsl/) is written in C and also has some useful eigenvalue subroutines. There are also several other eigenvalue software packages available.

The structure of Eq. 6.20 is easier to see when a specific example is written out. In practice there will be many hundreds or thousands of beams, but for simplicity use only a few for this example. The $\mathbf{G} = 0$ term is almost always included to match the incident beam (typically a plane wave) in CTEM. If there are only four beams $\mathbf{G} = 0, \mathbf{D}, \mathbf{E}$, and \mathbf{F} that are important then Eq. 6.20 becomes:

$$\begin{bmatrix} 0 & U_{-D} & U_{-E} & U_{-F} \\ U_D & 2k_0 s_D & U_{D-E} & U_{D-F} \\ U_E & U_{E-D} & 2k_0 s_E & U_{E-F} \\ U_F & U_{F-D} & U_{F-E} & 2k_0 s_F \end{bmatrix} \begin{bmatrix} C_0 \\ C_D \\ C_E \\ C_F \end{bmatrix} = 2\gamma k_{0,z} \begin{bmatrix} C_0 \\ C_D \\ C_E \\ C_F \end{bmatrix} \quad (6.21)$$

The off diagonal elements are essentially the convolution of U_G with itself which may require the calculation of many more values than in the original small set. There will be four different eigenvalues $2\gamma k_{0,z}$ (with associated eigenvectors) in this example. In condensed matrix notation:

$$\mathbf{AC} = 2\gamma k_{0,z} \mathbf{C} \quad (6.22)$$

\mathbf{A} is an $N \times N$ matrix and \mathbf{C} is a vector of length N . If the crystal (specimen) is centro-symmetric, then $U_G = U_{-G}^*$ and the matrix is real and symmetric; otherwise, it is Hermitian.

6.1.4 Initial Conditions and the Exit Wave

If the allowed Bloch wave have been determined (eigenvalues and eigenvectors as above), then the wave function anywhere in the (crystalline) specimen is known if the weighting coefficients α_j are known. The weighting coefficients can be determined by matching the wave function at the entrance surface of the specimen to the given incident wave function. First write the Fourier transform of the wave function with an explicit z dependence and a propagation in the beam direction \mathbf{k}_0 :

$$\psi(\mathbf{r}) = \sum_{\mathbf{G}} \psi_{\mathbf{G}}(z) \exp[2\pi i (\mathbf{k}_0 + \mathbf{G}) \cdot \mathbf{r}] \quad (6.23)$$

Now equate this equation to the Bloch wave expansion, Eqs. 6.1, 6.8, and 6.14:

$$\begin{aligned} \sum_{\mathbf{G}} \psi_{\mathbf{G}}(z) \exp[2\pi i (\mathbf{k}_0 + \mathbf{G}) \cdot \mathbf{r}] &= \sum_j \alpha_j b_j(\mathbf{k}_j, \mathbf{r}) \\ &= \sum_{\mathbf{G}} \sum_j \alpha_j C_{\mathbf{G}j} \exp[2\pi i (\mathbf{k}_j + \mathbf{G}) \cdot \mathbf{r}] \end{aligned} \quad (6.24)$$

$$= \sum_{\mathbf{G}} \left[\sum_j \alpha_j C_{\mathbf{G}j} \exp[2\pi i \gamma_j z] \right] \exp[2\pi i (\mathbf{k}_0 + \mathbf{G}) \cdot \mathbf{r}] \quad (6.25)$$

Now equate coefficients of $\exp[2\pi i (\mathbf{k}_0 + \mathbf{G}) \cdot \mathbf{r}]$ to obtain:

$$\psi_{\mathbf{G}}(z) = \sum_j \alpha_j C_{\mathbf{G}j} \exp[2\pi i \gamma_j z] \quad (6.26)$$

which illustrates how each Fourier coefficient of the wave functions propagates with depth z in the specimen. This equation is also in the form of a matrix equation. Using the previous example of four \mathbf{G} values 0,D,E,F and adding four eigenvalues 0,1,2,3 an example of this equation becomes:

$$\begin{bmatrix} \psi_0(z) \\ \psi_D(z) \\ \psi_E(z) \\ \psi_F(z) \end{bmatrix} = \begin{bmatrix} C_{00} & C_{01} & C_{02} & C_{03} \\ C_{D0} & C_{D1} & C_{D2} & C_{D3} \\ C_{E0} & C_{E1} & C_{E2} & C_{E3} \\ C_{F0} & C_{F1} & C_{F2} & C_{F3} \end{bmatrix} \times \begin{bmatrix} e^{2\pi i \gamma_0 z} & 0 & 0 & 0 \\ 0 & e^{2\pi i \gamma_1 z} & 0 & 0 \\ 0 & 0 & e^{2\pi i \gamma_2 z} & 0 \\ 0 & 0 & 0 & e^{2\pi i \gamma_3 z} \end{bmatrix} \begin{bmatrix} \alpha_0 \\ \alpha_1 \\ \alpha_2 \\ \alpha_3 \end{bmatrix} \quad (6.27)$$

In condensed matrix notation:

$$\psi(z) = \mathbf{C}[\exp(2\pi i \gamma_j z)]\alpha \quad (6.28)$$

where $\psi(z)$ is a column vector of ψ_G . Each column of the \mathbf{C} matrix containing the C_{Gj} coefficients is an eigenvector of Eq. 6.20. The vector $\psi(z)$ contains the $\psi_G(z)$ terms and $[\exp(2\pi i \gamma_j z)]$ denotes a diagonal matrix containing the eigenvalue dependence.

The form of the \mathbf{C} matrix has the very useful property that its inverse is equal to its Hermitian adjoint (transpose plus complex conjugation) $\mathbf{C}^{-1} = \mathbf{C}^\dagger$ because the eigenvectors are orthogonal and normalized. Multiplying each side by the inverse matrix for the special case of $z = 0$ (which is the known incident wave function) yields:

$$\mathbf{C}^{-1}\psi(z = 0) = \mathbf{C}^{-1}\mathbf{C}\alpha = \alpha \quad (6.29)$$

$$\alpha = \mathbf{C}^{-1}\psi(z = 0) = \mathbf{C}^\dagger\psi(z = 0) \quad (6.30)$$

which determines the weighting coefficients α_j . Then the Fourier coefficients of the wave function $\psi_G(z)$ may be calculated at any depth in the specimen from the eigenvalues, eigenvectors, and weighting coefficients. This result can be elegantly summarized as a scattering matrix \mathbf{S} (Sturkey [478]):

$$\psi(z) = \mathbf{C}[\exp(2\pi i \gamma_j)]\mathbf{C}^{-1}\psi(z = 0) = \mathbf{S}\psi(z = 0) \quad (6.31)$$

$$\mathbf{S} = \mathbf{C}[\exp(2\pi i \gamma_j)]\mathbf{C}^{-1} \quad (6.32)$$

The wave function at the exit surface of the specimen is then calculated by inserting these weighting coefficients α_j (Eq. 6.30) into Eq. 6.26 to obtain the set of ψ_G values at depth z . The slowly varying portion of the exit wave (similar to the multislice result), dropping the rapidly oscillating portion $\exp(2\pi i \mathbf{k}_0 \cdot \mathbf{r})$, is then given by an inverse Fourier transform (a single FFT) in two dimensions on Eq. 6.23;

$$\psi(x, y, z) = FT_{xy}^{-1} \left[\sum_G \psi_G \exp(2\pi i G_z z) \right] \quad (6.33)$$

where FT_{xy}^{-1} is a 2D inverse (fast) Fourier transform over (G_x, G_y) .

6.1.5 Bloch Wave Eigenvalue Summary

The steps in a Bloch wave eigenvalue calculation are summarized in algorithmic form in Table 6.1.

Table 6.1 Steps in the Bloch wave eigenvalue calculation of the wave function at the exit surface of the specimen

- | | |
|--------|---|
| Step 1 | Calculate the Fourier coefficients of the atomic potential V_G from Eq. 6.9 up to some maximum $ \mathbf{G} $ |
| Step 2 | Solve for the eigenvalues (proportional to γ_j) and eigenvectors (C_G), both in Eq. 6.20 |
| Step 3 | Find the weighting coefficients α_j to match the incident wave function at $z = 0$ (typically a plane wave for CTEM, or a focused probe for STEM) as in Eq. 6.30 |
| Step 4 | Calculate the electron wave function at the exit surface of the specimen (Eqs. 6.28 and 6.33) |

The remaining steps to add the effects of the objective lens in CTEM (imaging) or STEM (probe forming) are similar to other approaches (not given here)

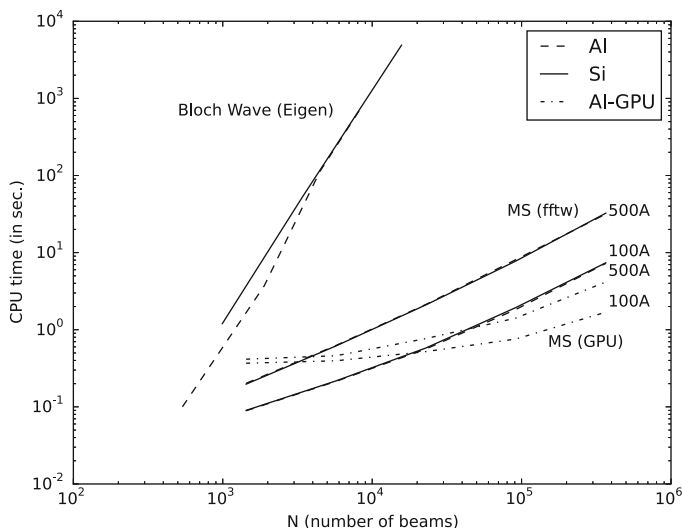


Fig. 6.2 Scaling of CPU time in the Bloch wave eigenvalue method with the number of beams N compared to the FFT multislice method (labeled MS) for the 100 projection of aluminum. Two forms of FFT multislice are shown, one using a GPU and one run entirely on a single host CPU (fftw). Two specimens were tested, silicon (nonsymmetric) and aluminum (symmetric). Two different thickness are shown for the FFT multislice times (100 and 500 Å). The measured CPU time has an error that is some small fraction of a second

6.1.6 Relative Performance

The scaling of computer (CPU) time of the Bloch wave method is compared to the multislice method (discussed in later sections) in Fig. 6.2 for two different specimens (100 aluminum and 100 silicon). The CPU time is for the transmission of a single plane wave through the indicated specimen (i.e., part of a simple BF-CTEM calculation). The 100 projection of aluminum is centro-symmetric and

the Bloch wave calculation took advantage of the real (not complex) matrix to be more efficient (about a factor of two) whereas the multislice calculation was a general complex valued calculation. The calculations were carried out on the same inexpensive desktop computer (using a single CPU or thread) using the same operating system and compiler with similar compiler options. The Bloch wave calculation used the Eigen C++ linear algebra library (eigen.tuxfamily.org) to perform the eigenvalue calculation and the multislice calculation used the FFTW [149] software package. Also shown is a multislice calculation using a GPU (graphical processor unit with nearly 3000 small processors) and its parallel FFT. All data was kept on the GPU (without transfer back to the host) as much as possible. The GPU calculation by definition uses many GPU processors and requires its own compiler; however, it was run on the same host computer as the other two calculations for comparison (CPU time refers to elapsed time on the host not total processor time on the GPU).

All of the programs could probably be improved a little in terms of efficiency so the absolute time is not so important but it is reasonable to compare the relative performance. The Bloch wave method is the same time for all thickness but the multislice method scales linearly with thickness so two different specimen thickness are shown. Having all thickness available from a single Bloch wave calculation can be an advantage or a disadvantage (all thickness are calculated whether needed or not). The number of beams for the multislice method is taken to be the number of Fourier components in a single two-dimensional slice after removing aliasing. There is an argument for counting each slice as a different beam (not done here) in which case the two curves for the multislice method would likely come together and move to a larger N . The GPU calculation has more initialization overhead so does not have a big advantage for very small calculations (flat portion of the curve for small N), but does produce a significant reduction in calculation time for large problems.

The Bloch wave CPU time grows very fast as the number of beams is increased which is a significant problem. Generally speaking, both methods require a similar number of beams and high resolution of nontrivial specimens requires many beams, so the multislice method has a clear advantage except for some simple cases requiring only a small number of beams. The memory storage requirements scale as N^2 for a Bloch wave calculation and N for a multislice calculation which is also a significant advantage of the multislice approach for large N . Third party software does exist for the eigenvalue calculations on a GPU, but this has not been tested here.

6.2 The Wave Equation for Fast Electrons

In principle the full time dependent Schrödinger equation could be used to solve for the time dependent electron wave function at all positions in the specimen or microscope column (in three dimensions) at each point in time. The initial wave function is a Gaussian wave packet that would propagate through the crystal.

The time evolution could in principle be traced using something like the Crank–Nicholson numerical method (for example, see Press et al. [406]). However this approach is prohibitively expensive in both computer memory and computer time. The wavelength of a 200 keV electron is $\lambda = 0.025 \text{ \AA}$. A straightforward numerical sampling of this wavelength would require of order 10 points per wavelength. To sample a small specimen in a cube of 100 Å per side would require about $(100/0.0025)^3$ or 6.4×10^{13} points. Even in single precision (four bytes per value) this would require 2.6×10^5 Gbytes of memory, which is clearly not possible in the near future. Clearly some other approach must be found. The Bloch wave method solves this problem by expanding in a small basis set of plane waves so real space sampling is not really used. However there is still a finite sample in reciprocal space.

An alternative approach described below will use the time independent Schrödinger equation mainly for mathematical simplicity. This section will further approximate the Schrödinger for fast electrons and later sections will discuss numerical solutions with the goal of reducing the computer memory and time requirements.

The Schrödinger equation for the full wave function $\psi_f(x, y, z)$ as a function of three spatial coordinates (x, y, z) in an electrostatic potential $V(x, y, z)$ of the specimen is:

$$\left[-\frac{\hbar^2}{2m} \nabla^2 - eV(x, y, z) \right] \psi_f(x, y, z) = E\psi_f(x, y, z) \quad (6.34)$$

where $\hbar = h/2\pi$ is Planck's constant divided by 2π , $m = \gamma m_0$ is the relativistic mass of the electron, $e = |e|$ is the magnitude of the charge of the electron, E is the kinetic energy of the electron, and $-eV$ is the potential energy of the electron. In an electron microscope the energy of the incident electrons (60–1000 keV) is much greater than the additional energy they gain (or lose) inside the specimen $eV(x, y, z)$. The electron motion will be predominately in the forward z direction (i.e., along the optic axis of the microscope) and the specimen will be a relatively minor perturbation on the electron's motion. It is useful to separate the large velocity in the z direction from other small effects due to the specimen. First write the full wave function $\psi_f(x, y, z)$ as a product of two factors, one of which is a rapidly varying plane wave traveling in the z direction, $\exp(2\pi iz/\lambda)$ and the other factor $\psi(x, y, z)$ is the remaining portion of the wave function that varies slowly with position z :

$$\psi_f(x, y, z) = \psi(x, y, z) \exp(2\pi iz/\lambda) \quad (6.35)$$

where λ is the electron wavelength. This step is just a simple mathematical operation of factoring out $\exp(2\pi iz/\lambda)$ (which is treated analytically) from the full wave function. The remaining portion is slowly varying and may have a larger (numerical) step size for ease of calculation. It is tempting to identify the phase in the exponent as proportional to the electron wave number in the z direction (k_z). However the

squared magnitude of the total wave vector is $k_x^2 + k_y^2 + k_z^2 = 1/\lambda^2$ so this is not strictly true once the electron scatters out of a pure plane wave and k_x and k_y are nonzero. Only elastic processes will be considered so the total kinetic energy of the electron is:

$$E = \frac{\hbar^2}{2m\lambda^2} \quad (6.36)$$

To use Eq. 6.35 in Eq. 6.34 requires the calculation of the following derivatives:

$$\begin{aligned} \nabla^2 \psi_f(x, y, z) &= \left[\frac{\partial^2}{\partial x^2} + \frac{\partial^2}{\partial y^2} + \frac{\partial^2}{\partial z^2} \right] \psi_f(x, y, z) \\ &= \left[\nabla_{xy}^2 + \frac{\partial^2}{\partial z^2} \right] \psi_f(x, y, z) \\ &= \exp(2\pi iz/\lambda) \nabla_{xy}^2 \psi(x, y, z) + \frac{\partial^2}{\partial z^2} [\psi(x, y, z) \exp(2\pi iz/\lambda)] \end{aligned} \quad (6.37)$$

where ∇_{xy}^2 is the sum of second derivatives with respect to x and y only. Now concentrate on the derivative with respect to z . The first derivative is:

$$\frac{\partial}{\partial z} [\psi \exp(2\pi iz/\lambda)] = \exp(2\pi iz/\lambda) \left[\frac{\partial \psi}{\partial z} + \frac{2\pi i}{\lambda} \psi \right] \quad (6.38)$$

and the second derivative is:

$$\begin{aligned} \frac{\partial^2}{\partial z^2} [\psi \exp(2\pi iz/\lambda)] &= \exp(2\pi iz/\lambda) \left[\frac{\partial^2 \psi}{\partial z^2} + \frac{4\pi i}{\lambda} \frac{\partial \psi}{\partial z} + \left(\frac{2\pi i}{\lambda} \right)^2 \psi \right] \\ &= \exp(2\pi iz/\lambda) \left[\frac{\partial^2 \psi}{\partial z^2} + \frac{4\pi i}{\lambda} \frac{\partial \psi}{\partial z} \right] - \frac{4\pi^2}{\lambda^2} \psi_f \end{aligned} \quad (6.39)$$

Now substitute Eq. 6.39 into Eq. 6.34. The last term on the right-hand side of Eq. 6.39 cancels the right-hand side of Eq. 6.34 given the value for E in Eq. 6.36. Dropping the common factor of $\exp(2\pi iz/\lambda)$ leaves:

$$-\frac{\hbar^2}{2m} \left[\nabla_{xy}^2 + \frac{\partial^2}{\partial z^2} + \frac{4\pi i}{\lambda} \frac{\partial}{\partial z} + \frac{2meV(x, y, z)}{\hbar^2} \right] \psi(x, y, z) = 0 \quad (6.40)$$

The motion of the high energy electrons is predominately in the forward z direction meaning that ψ changes slowly with z and λ is very small. Therefore:

$$\left| \frac{\partial^2 \psi}{\partial z^2} \right| << \left| \frac{4\pi}{\lambda} \frac{\partial \psi}{\partial z} \right| \quad (6.41)$$

so Eq. 6.40 may be approximated as:

$$\left[\nabla_{xy}^2 + \frac{4\pi i}{\lambda} \frac{\partial}{\partial z} + \frac{2meV(x, y, z)}{\hbar^2} \right] \psi(x, y, z) = 0 \quad (6.42)$$

Ignoring the term containing the second derivative with respect to z is referred to as the “high energy approximation” and sometimes interpreted as ignoring the backscattered electrons (appropriate for high energy electrons, Howie and Basinski [218], Lynch and Moodie [324]). However, it is probably more accurate to refer to Eq. 6.42 as the paraxial approximation to the Schrödinger equation. Including the second derivative term does not automatically include backscattered electrons because some initial conditions may further prohibit the backscattered electrons. Lewis et al. [311] have further considered the effect of neglecting the second order derivative term. Bird [36] has concluded that dropping the second order derivative (with respect to z) produces an error of about one percent in the position of the FOLZ (first order Laue zone) ring (the error decreases with increasing beam voltage). The importance of the second order term is approximately investigated in Sect. 6.11.2.

The Schrödinger equation (Eq. 6.34) for fast electrons traveling in the z direction may be written as a first order differential equation in z as:

$$\begin{aligned} \frac{\partial \psi(x, y, z)}{\partial z} &= \left[\frac{i\lambda}{4\pi} \nabla_{xy}^2 + \frac{2mei\lambda}{4\pi\hbar^2} V(x, y, z) \right] \psi(x, y, z) \\ &= \left[\frac{i\lambda}{4\pi} \nabla_{xy}^2 + i\sigma_e V(x, y, z) \right] \psi(x, y, z) \end{aligned} \quad (6.43)$$

where $\psi(x, y, z)$ is defined in Eq. 6.35, λ is the wavelength of the incident electrons, and $\sigma_e = 2\pi me\lambda/\hbar^2$ is the interaction parameter (Eq. 5.6). An identical equation would result if the exponent in Eq. 6.35 were replaced with $(2\pi z/\lambda - iEt/\hbar)$ (where t is time) and the time dependent Schrödinger equation were used.

6.3 A Bloch Wave Differential Equation Solution

If the specimen is periodic (i.e., crystalline), then the specimen potential can be expanded in a three-dimensional Fourier series as:

$$V(x, y, z) = V(\mathbf{r}) = \sum_{\mathbf{G}} V_{\mathbf{G}} \exp[2\pi i \mathbf{G} \cdot \mathbf{r}] \quad (6.44)$$

where the set of vectors $\mathbf{G} = (G_x, G_y, G_z)$ are typically the reciprocal lattice vectors of the specimen. Next expand the electron wave function in Bloch waves with the same crystal periodicity:

$$\psi(x, y, z) = \psi(\mathbf{r}) = \sum_{\mathbf{G}} \phi_{\mathbf{G}}(z) \exp[2\pi i \mathbf{G} \cdot \mathbf{r}] \quad (6.45)$$

where the coefficients ϕ_G vary weakly with depth in the crystal z . Substituting Eqs. 6.44 and 6.45 into the Schrödinger wave equation for fast electrons (Eq. 6.43) yields:

$$\begin{aligned} & \sum_{\mathbf{G}} \left(\frac{\partial \phi_{\mathbf{G}}}{\partial z} + 2\pi i G_z \phi_{\mathbf{G}} \right) \exp[2\pi i \mathbf{G} \cdot \mathbf{r}] \\ &= \frac{i\lambda}{4\pi} \sum_{\mathbf{G}} (-4\pi^2 G_x^2 - 4\pi^2 G_y^2) \phi_{\mathbf{G}} \exp[2\pi i \mathbf{G} \cdot \mathbf{r}] \\ &+ i\sigma_e \sum_{\mathbf{G}} \left[\sum_{\mathbf{G}'} V_{\mathbf{G}-\mathbf{G}'} \phi_{\mathbf{G}'} \right] \exp[2\pi i \mathbf{G} \cdot \mathbf{r}] \end{aligned} \quad (6.46)$$

Equating coefficients of $\exp[2\pi i \mathbf{G} \cdot \mathbf{r}]$ yields:

$$\begin{aligned} \frac{\partial \phi_{\mathbf{G}}(z)}{\partial z} &= -\pi i (2G_z + \lambda G_x^2 + \lambda G_y^2) \phi_{\mathbf{G}}(z) + i\sigma_e \sum_{\mathbf{G}'} V_{\mathbf{G}-\mathbf{G}'} \phi_{\mathbf{G}'}(z) \\ &= 2\pi i s_{\mathbf{G}} \phi_{\mathbf{G}}(z) + i\sigma_e \sum_{\mathbf{G}'} V_{\mathbf{G}-\mathbf{G}'} \phi_{\mathbf{G}'}(z) \end{aligned} \quad (6.47)$$

This set of first order differential equation is known as the Howie–Whelan [219] equations. If there are N Fourier coefficients in Eqs. 6.44 and 6.45, then there are N coupled first order equations. The excitation error, $s_{\mathbf{G}} = G_z + 0.5\lambda(G_x^2 + G_y^2)$ for the reflection G is illustrated in Fig. 6.3 for the case where $G_z = 0$. The incident wave vector \mathbf{k}_z is along the positive z direction. Only elastic scattering is considered here so the scattered wave vector \mathbf{k}_s must be the same length as the incident wave vector. This means that the end of the scattered wave vector must lie on the Ewald sphere centered at the beginning of the incident wave vector. The distance between the end of the scattered wave vector and the nearest reciprocal lattice point is labeled as s_G .

The Howie–Whelan equations (6.47) can also be written as a matrix equation for a column vector of N components $\phi_{\mathbf{G}}$ and a matrix of N^2 components $V_{\mathbf{G}-\mathbf{G}'}$. A general matrix multiplication on the right-hand side would scale as N^2 for computer time. Calculating $V_{\mathbf{G}}$ in three dimensions with a thousand or more beams is itself a formidable task. In the CTEM all of the initial $\phi_{\mathbf{G}}$ components (at $z = 0$) would be zero except for a single plane wave in the z direction. This set of equations can be solved using standard numerical differential equations methods such as Runge–Kutta methods (see for example Press et al. [406]) to advance the vector

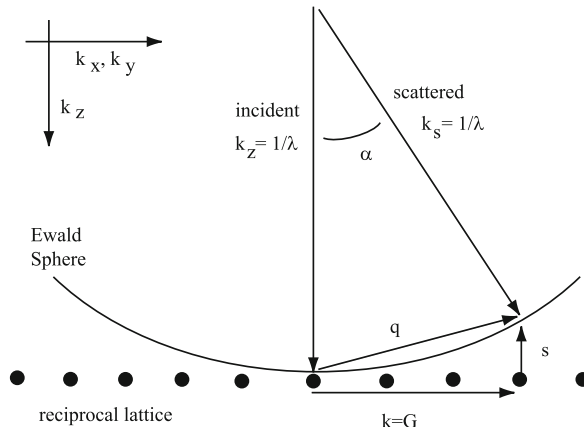


Fig. 6.3 Scattering geometry in reciprocal space. The incident electron is traveling in the positive z direction and is scattered through an angle α . The reciprocal lattice points of the specimen are shown as solid dots. Elastic scattering requires that the incident wave vector k_z and the scattered wave vector k_s both lie on the Ewald sphere. s is the extinction error for this scattering angle. In the small angle approximation $|\mathbf{q}| \sim \alpha/\lambda$ and $|s| = |\mathbf{q}| \sin(\alpha/2) \sim 0.5\alpha^2/\lambda$

of ϕ_G components for each small step Δz . There are several different Bloch wave formulations of the dynamical scattering problem. This is only one specific example but does illustrate some of the general features of a Bloch wave or reciprocal space solution. The Howie–Whelan equations are conceptually very similar to the multislice equation taken up in the next section. The first term on the right-hand side of Eq. 6.47 is similar to the propagator function and the second term is similar to the transmission function in the multislice method. The main difference is that the Howie–Whelan equations are stated completely in reciprocal space. Other, general analytical Bloch wave solutions are discussed at length in Hirsch et al. [208] and Reimer [414].

Watanabe et al. [527, 528] have recently proposed an alternate approach to the solution of the Howie–Whelan equations. They find that a direct integration of the equations (with the appropriate boundary conditions at the entrance and exit surface of the crystal) yields a method that has about the same accuracy as the multislice solution but is in between Bethe’s eigenvalue solution and the multislice solution in efficiency (i.e., computer time).

6.4 The Multislice Solution

6.4.1 A Formal Operator Solution

The wave equation for fast electrons (Eq. 6.43) can be written in operator form as:

$$\frac{\partial \psi(x, y, z)}{\partial z} = [A + B]\psi(x, y, z) \quad (6.48)$$

$$A = \frac{i\lambda}{4\pi} \nabla_{xy}^2$$

$$B = i\sigma_e V(x, y, z)$$

where A and B are non-commuting operators. This equation has a formal operator solution of:

$$\psi(x, y, z) = \exp \left[\int_0^z [A(z') + B(z')] dz' \right] \psi(x, y, 0) \quad (6.49)$$

This can be verified by formal differentiation. Offsetting the initial value to z and integrating from z to $z + \Delta z$ yields:

$$\begin{aligned} \psi(x, y, z + \Delta z) &= \\ &\exp \left[\int_z^{z+\Delta z} \left(\frac{i\lambda}{4\pi} \nabla_{xy}^2 + i\sigma_e V(x, y, z') \right) dz' \right] \psi(x, y, z) \end{aligned} \quad (6.50)$$

Δz will become a small slice of the specimen and this solution may be further simplified as:

$$\psi(x, y, z + \Delta z) = \exp \left[\frac{i\lambda}{4\pi} \Delta z \nabla_{xy}^2 + i\sigma_e v_{\Delta z}(x, y, z) \right] \psi(x, y, z) \quad (6.51)$$

where $v_{\Delta z}(x, y, z)$ is the projected potential of the specimen between z and $z + \Delta z$.

$$v_{\Delta z}(x, y, z) = \int_z^{z+\Delta z} V(x, y, z') dz' \quad (6.52)$$

The appearance of the operator ∇_{xy}^2 in the exponent complicates the solution somewhat because the $\exp(\dots)$ factor must also be regarded as an operator. If A and B are non-commuting operators or matrices and ϵ is a small real number, then:

$$\begin{aligned} \exp(A\epsilon + B\epsilon) &= 1 + (A + B)\epsilon + \frac{1}{2!}(A + B)^2\epsilon^2 + \dots \\ &= 1 + (A + B)\epsilon + \frac{1}{2!}(A^2 + AB + BA + B^2)\epsilon^2 + \dots \end{aligned} \quad (6.53)$$

If A and B were simple scalar variables, then this expression could be easily factored; however, the most common factorizations do not yield the expected results if A and B do not commute.

$$\begin{aligned}\exp(A\epsilon) \exp(B\epsilon) &= \left[1 + A\epsilon + \frac{1}{2!}A^2\epsilon^2 + \dots\right] \left[1 + B\epsilon + \frac{1}{2!}B^2\epsilon^2 + \dots\right] \\ &= 1 + (A + B)\epsilon + \frac{1}{2!}(A^2 + 2AB + B^2)\epsilon^2 + \dots\end{aligned}\quad (6.54)$$

and:

$$\begin{aligned}\exp(B\epsilon) \exp(A\epsilon) &= \left[1 + B\epsilon + \frac{1}{2!}B^2\epsilon^2 + \dots\right] \left[1 + A\epsilon + \frac{1}{2!}A^2\epsilon^2 + \dots\right] \\ &= 1 + (B + A)\epsilon + \frac{1}{2!}(B^2 + 2BA + A^2)\epsilon^2 + \dots\end{aligned}\quad (6.55)$$

By comparison Eq. 6.53 may be factored to lowest order in either of two ways:

$$\exp(A\epsilon + B\epsilon) = \exp(A\epsilon) \exp(B\epsilon) + \frac{1}{2}[B, A]\epsilon^2 + \mathcal{O}(\epsilon^3) \quad (6.56)$$

or

$$\exp(A\epsilon + B\epsilon) = \exp(B\epsilon) \exp(A\epsilon) + \frac{1}{2}[A, B]\epsilon^2 + \mathcal{O}(\epsilon^3) \quad (6.57)$$

where $[B, A] = BA - AB$ is the commutator of operators (or matrices) B and A . (A more accurate answer can be obtained simply by averaging Eqs. 6.56 and 6.57.) This result is referred to as the Zassenhaus theorem (Goodman and Moodie [162]). Feynman [132], Weiss and Maradudin [531], and Wilcox [533] have given a more detailed discussion of exponentiation of operators.

The traditional form of the multislice solution uses one of Eqs. 6.56 and 6.57 in Eq. 6.51.

$$\begin{aligned}\psi(x, y, z + \Delta z) &= \exp\left(\frac{i\lambda\Delta z}{4\pi}\nabla_{xy}^2\right) \exp[i\sigma_e v_{\Delta z}(x, y, z)] \psi(x, y, z) + \mathcal{O}(\Delta z^2) \\ &= \exp\left(\frac{i\lambda\Delta z}{4\pi}\nabla_{xy}^2\right) t(x, y, z) \psi(x, y, z) + \mathcal{O}(\Delta z^2)\end{aligned}\quad (6.58)$$

where $t(x, y, z)$ is the transmission function for the portion of the specimen between z and $z + \Delta z$ (compare to Eq. 5.7).

$$t(x, y, z) = \exp\left[i\sigma_e \int_z^{z+\Delta z} V(x, y, z') dz'\right] \quad (6.59)$$

The remaining factor of $\exp(\dots)$ is a little more difficult to interpret. First form the two-dimensional Fourier transform of the right-hand side of Eq. 6.58:

$$\begin{aligned} FT \left[\exp \left(\frac{i\lambda\Delta z}{4\pi} \nabla_{xy}^2 \right) (t\psi) \right] \\ = \int \left[\exp \left(\frac{i\lambda\Delta z}{4\pi} \nabla_{xy}^2 \right) (t\psi) \right] \exp[2\pi i(k_x x + k_y y)] dx dy \end{aligned} \quad (6.60)$$

The derivatives with respect to x and y commute so the exponential operator may be split into two factors (one with x and one with y) without further error.

$$\begin{aligned} FT \left[\exp \left(\frac{i\lambda\Delta z}{4\pi} \nabla_{xy}^2 \right) (t\psi) \right] \\ = \int \left[\exp \left(\frac{i\lambda\Delta z}{4\pi} \frac{\partial^2}{\partial x^2} \right) \exp \left(\frac{i\lambda\Delta z}{4\pi} \frac{\partial^2}{\partial y^2} \right) (t\psi) \right] \\ \times \exp[2\pi i(k_x x + k_y y)] dx dy \end{aligned} \quad (6.61)$$

Each exponential operator may be expanded in a power series as:

$$\begin{aligned} \exp \left(\frac{i\lambda\Delta z}{4\pi} \frac{\partial^2}{\partial x^2} \right) &= \sum_{n=0}^{\infty} \frac{1}{n!} \left(\frac{i\lambda\Delta z}{4\pi} \frac{\partial^2}{\partial x^2} \right)^n \\ \exp \left(\frac{i\lambda\Delta z}{4\pi} \frac{\partial^2}{\partial y^2} \right) &= \sum_{n=0}^{\infty} \frac{1}{n!} \left(\frac{i\lambda\Delta z}{4\pi} \frac{\partial^2}{\partial y^2} \right)^n \end{aligned} \quad (6.62)$$

Inserting the power series expansions for the exponentials in Eq. 6.61 and repeatedly integrating each term by parts (with the assumption that $t\psi$ vanishes at infinity or obeys periodic boundary conditions) yields:

$$\begin{aligned} FT \left[\exp \left(\frac{i\lambda\Delta z}{4\pi} \nabla_{xy}^2 \right) (t\psi) \right] &= \sum_{n=0}^{\infty} \frac{1}{n!} (-i\pi\lambda\Delta z k_x^2)^n \\ &\times \sum_{n=0}^{\infty} \frac{1}{n!} (-i\pi\lambda\Delta z k_y^2)^n FT[(t\psi)] \\ &= \exp[-i\pi\lambda\Delta z(k_x^2 + k_y^2)] FT[(t\psi)] \\ &= P(k, \Delta z) FT[t\psi] \end{aligned} \quad (6.63)$$

where $k^2 = (k_x^2 + k_y^2)$ and $P(k, \Delta z)$ is the propagator function. A multiplication in Fourier space converts to a convolution in real space so the operator may be interpreted as:

$$\exp\left(\frac{i\lambda\Delta z}{4\pi}\nabla_{xy}^2\right) = p(x, y, \Delta z) \otimes \quad (6.64)$$

where \otimes is a two-dimensional convolution (in x and y) and $p(x, y, \Delta z)$ is the propagator function in real space for a distance Δz :

$$P(k, \Delta z) = \exp(-i\pi\lambda k^2 \Delta z)$$

$$p(x, y, \Delta z) = FT^{-1}[P(k, \Delta z)] = \frac{1}{i\lambda\Delta z} \exp\left[\frac{i\pi}{\lambda\Delta z}(x^2 + y^2)\right] \quad (6.65)$$

Combining Eqs. 6.63 and 6.58 yields:

$$\psi(x, y, z + \Delta z) = p(x, y, \Delta z) \otimes [t(x, y, z)\psi(x, y, z)] + \mathcal{O}(\Delta z^2) \quad (6.66)$$

If the slices in the specimen are labeled $n = 0, 1, 2, \dots$, then the depth in the specimen is z_n ($z_n \sim n\Delta z$ if all slices were the same thickness). The wave function at the top of each slice is labeled $\psi_n(x, y)$ and the propagator and transmission functions for each slice are labeled as $p_n(x, y, \Delta z_n)$ and $t_n(x, y)$, respectively. The multislice equation (6.66) can be written in compact form as:

$$\psi_{n+1}(x, y) = p_n(x, y, \Delta z_n) \otimes [t_n(x, y)\psi_n(x, y)] + \mathcal{O}(\Delta z^2) \quad (6.67)$$

If the other identity (Eqs. 6.56 and 6.57) is used, then another equally accurate expression results.

$$\psi_{n+1}(x, y) = t_n(x, y) [p_n(x, y, \Delta z_n) \otimes \psi_n(x, y)] + \mathcal{O}(\Delta z^2) \quad (6.68)$$

The initial wave function $\psi_0(x, y)$ is a plane wave in the CTEM and the probe wave function in the STEM.

The last term in Eqs. 6.67 and 6.68 indicates the order of magnitude of the error caused by the approximation used to get the remaining terms in the equations and is called the error term. The error term should not be used in the actual calculation but is for informational purposes only. The error associated with one step of the multislice equations (6.66, 6.67, and 6.68) is of order Δz^2 . This error is referred to as the local error. If the specimen is divided into N_s slices, then typically $N_s \propto 1/\Delta z$. If the multislice equation is applied N_s times to advance the wave function all of the way through the specimen, then the error term of the final result is reduced by approximately one order. The error of the final result is therefore of order Δz . The final error is referred to as the global error.

6.4.2 A Finite Difference Solution

The traditional numerical analysis approach to solving a differential equation given an initial value is to Taylor expand the dependent variable (ψ in this case) in powers of Δz and approximate the derivatives by their finite difference approximations. Expanding $\psi(x, y, z)$ about the point z (and temporarily dropping explicit reference to x and y in ψ for simplicity) yields:

$$\psi(z + \Delta z) = \psi(z) + \Delta z \frac{\partial \psi(z)}{\partial z} + \frac{1}{2!} \Delta z^2 \frac{\partial^2 \psi(z)}{\partial z^2} + \dots \quad (6.69)$$

Substituting the first derivative from Eq. 6.43 yields:

$$\begin{aligned} \psi(z + \Delta z) &= \psi(z) + \Delta z \left[\frac{i\lambda}{4\pi} \nabla_{xy}^2 + i\sigma_e V(x, y, z) \right] \psi(z) + \mathcal{O}(\Delta z^2) \\ &= \left\{ 1 + \Delta z \left[\frac{i\lambda}{4\pi} \nabla_{xy}^2 + i\sigma_e V(x, y, z) \right] \right\} \psi(z) + \mathcal{O}(\Delta z^2) \end{aligned} \quad (6.70)$$

The Taylor series expansion for $\exp(x)$ with small x is:

$$\exp(x) = 1 + x + \frac{1}{2!} x^2 + \frac{1}{3!} x^3 + \dots \quad (6.71)$$

By comparison to Eqs. 6.70 and 6.71 may be written to lowest order (with the x, y dependence reinstated) as:

$$\begin{aligned} \psi(x, y, z + \Delta z) &= \exp \left[\Delta z \frac{i\lambda}{4\pi} \nabla_{xy}^2 + i\sigma_e \Delta z V(x, y, z) \right] \psi(x, y, z) \\ &\quad + \mathcal{O}(\Delta z^2) \end{aligned} \quad (6.72)$$

Keeping the leading factor as $\exp(\dots)$ where the exponent is predominately imaginary tends to keep the total integrated intensity constant.

$$\int |\psi(x, y, z + \Delta z)|^2 dx dy = \int |\psi(x, y, z)|^2 dx dy = \text{constant} \quad (6.73)$$

This is physically relevant because elastic scattering should be unitary. Without this constraint the result is essentially Euler's method (for example see Press et al. [406]) which is known to require an excessively small step size (Δz) to be stable. Furthermore to this level of accuracy the term containing the specimen potential may be written as:

$$\begin{aligned} V(x, y, z) \Delta z &= \int_z^{z+\Delta z} V(x, y, z') dz' + \mathcal{O}(\Delta z^2) \\ &= v_{\Delta z}(x, y, z) + \mathcal{O}(\Delta z^2) \end{aligned} \quad (6.74)$$

where $v_{\Delta z}(x, y, z)$ is the projected potential of the specimen between z and $z + \Delta z$. Therefore Eq. 6.72 may be written as:

$$\begin{aligned}\psi(x, y, z + \Delta z) &= \exp \left[\Delta z \frac{i\lambda}{4\pi} \nabla_{xy}^2 + i\sigma_e v_{\Delta z}(x, y, z) \right] \psi(x, y, z) \\ &\quad + \mathcal{O}(\Delta z^2)\end{aligned}\quad (6.75)$$

This is just the previous result (Eq. 6.51) and the rest of the derivation follows that of Sect. 6.4.1.

6.4.3 Free Space Propagation

In the special limiting case in which the specimen potential vanishes the formal multislice solution (Eq. 6.51) takes the simpler form of:

$$\psi(x, y, z + \Delta z) = \exp \left[\frac{i\lambda}{4\pi} \Delta z \nabla_{xy}^2 \right] \psi(x, y, z) \quad (6.76)$$

which can be written in terms of the propagator function without introducing any further approximations (or errors) as:

$$\psi(x, y, z + \Delta z) = p(x, y, \Delta z) \otimes \psi(x, y, z) \quad (6.77)$$

Closer inspection of the error term in the full multislice solution (Eq. 6.67, or 6.68) reveals that it should be written as $\mathcal{O}(\Delta z^2 v_{\Delta z})$ where $v_{\Delta z}$ is the projected atomic potential of the specimen and Δz is the slice thickness. This means that for a given slice thickness the accuracy of the multislice solution increases as the specimen potential gets smaller. The multislice solution should be more accurate for light atoms with low atomic numbers and less accurate for heavy atoms with high atomic numbers.

It is interesting to observe that the two components of the multislice solution (the transmission function and the propagation function) are nearly exact when used separately. The phase grating approximation (Sect. 5.1) of the transmission function and the propagation function are individually more accurate than when they are combined into the multislice solution (van Dyck [506]). The main error in the multislice solution is due to how these operations are combined.

6.5 Multislice Interpretation

If the initial value of the wave function $\psi(x, y, z = 0)$ is given in an x, y plane at the entrance face of the specimen (i.e., unity for the CTEM and the probe wave function for the STEM), then the electron wave function can be calculated at any depth z inside the specimen given a description of the potential inside the specimen by

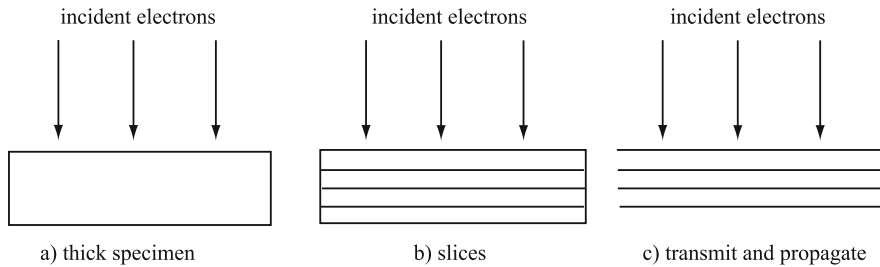


Fig. 6.4 Multislice decomposition of a thick specimen. (a) Original thick specimen, (b) the specimen divided into thin slices, (c) each slice is treated as a transmission step (solid line) followed by a propagator (vacuum between slices)

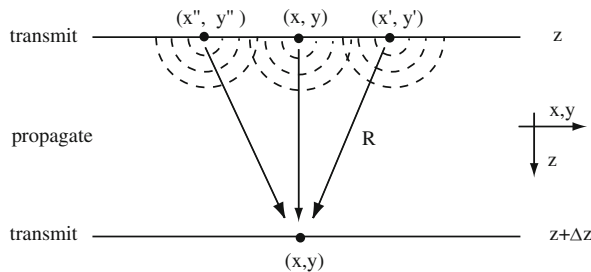


Fig. 6.5 Physical optics interpretation of the multislice propagator. The wave function in an x, y plane at z propagates to the x, y plane at $z + \Delta z$. Each point in the wavefront at z emits a spherically outgoing wave. All of these waves combine at each point in the x, y plane at $z + \Delta z$

repeated application of Eq. 6.66. The specimen is first divided into many thin slices as in Fig. 6.4. At each slice the electron wave function experiences a phase shift due to the projected atomic potential of all atoms in the slice and then is propagated along z for the thickness of the slice. In general each slice is independent of all other slices, so both the slice thickness Δz and transmission function $t(x, y, z)$ may vary from one slice to another.

The original derivation of Cowley and Moodie [78] was done from a physical optics viewpoint. The transmission function $t(x, y, z)$ can be associated with the phase grating approximation of a thin specimen for the layer of the specimen between z and $z + \Delta z$ as in Sect. 5.1. The propagator function $p(x, y, \Delta z)$ can be associated with the Fresnel (near zone) diffraction over a distance Δz .

Huygens' principle (of classical optics) states that every point of a wave front gives rise to an outgoing spherical wave. These outgoing spherical waves propagate to the next position of the wavefront and interfere with one another. The wave function in an x, y plane at $z + \Delta z$ is the interference of all of these spherically outgoing waves that originated in an x, y plane at z as illustrated in Fig. 6.5

The propagation of a wavefront as described by the Huygens' principle may be calculated using the Fresnel–Kirchhoff diffraction integral (for example, see Born and Wolf [42] section 8.3.2).

$$\psi(x, y, z + \Delta z) = \frac{1}{2i\lambda} \int \psi(x', y', z) \frac{\exp(2\pi i R/\lambda)}{R} (1 + \cos \theta) dx' dy' \quad (6.78)$$

where θ is the angle between the plane of the initial wavefront and the direction of the outgoing spherical wave at point (x', y') . R is the total distance the outgoing spherical wave must travel to point (x, y) on the next wavefront.

$$R = \sqrt{(x - x')^2 + (y - y')^2 + \Delta z^2} \quad (6.79)$$

The maximum scattering angle for high energy electrons is only about 100–200 mrad. The angle θ is very close to zero for high energy electrons so Eq. 6.78 may then be written as:

$$\psi(x, y, \Delta z) = \frac{1}{i\lambda} \int \psi(x', y', z) \frac{\exp(2\pi i R/\lambda)}{R} dx' dy' \quad (6.80)$$

Small angle scattering also means that the lateral distances ($|x - x'|$ and $|y - y'|$) are also small compared to Δz . For example, if the slice thickness is $\Delta z \sim 3 \text{ \AA}$, then $|x - x'| \sim 0.3 \text{ \AA}$ at a scattering angle of 100 mrad. The distance R may then be approximated as:

$$\begin{aligned} R &= \Delta z \sqrt{1 + (x - x')^2/\Delta z^2 + (y - y')^2/\Delta z^2} \\ &\sim \Delta z \left[1 + 0.5(x - x')^2/\Delta z^2 + 0.5(y - y')^2/\Delta z^2 + \dots \right] \end{aligned} \quad (6.81)$$

Substituting Eq. 6.81 into Eq. 6.80 and keeping only lowest powers of $(x - x')$ and $(y - y')$ yields:

$$\begin{aligned} \psi(x, y, \Delta z) &= \frac{1}{i\lambda} \frac{\exp(2\pi i \Delta z/\lambda)}{\Delta z} \int \psi(x', y', z) \\ &\quad \times \exp \left\{ \frac{i\pi}{\lambda \Delta z} [(x - x')^2 + (y - y')^2] \right\} dx' dy' \end{aligned} \quad (6.82)$$

The right-hand side of this expression is just the convolution of ψ with the propagator function (Eq. 6.65).

$$\psi(x, y, \Delta z) = \exp(2\pi i \Delta z/\lambda) [\psi(x, y, z) \otimes p(x, y, \Delta z)] \quad (6.83)$$

where the propagator function is:

$$p(x, y, \Delta z) = \frac{1}{i\lambda\Delta z} \exp\left[\frac{i\pi}{\lambda\Delta z}(x^2 + y^2)\right] \quad (6.84)$$

The leading exponential factor in Eq. 6.82 is just the forward propagation of the plane wave and is part of the full wave function (as in the Fresnel–Kirchhoff diffraction integral, Eq. 6.78) but not part of the slowly varying part of the wave function (see Eq. 6.35) as used in the multislice derivation. Expression 6.82 is then identical to the convolution with the propagator derived in the multislice method (Eq. 6.66). The multislice propagator function can be interpreted simply as the Fresnel diffraction over a distance Δz . Also note that this is equivalent to a defocus of $\Delta f = \Delta z$.

6.6 The Multislice Method and FFTs

When implemented numerically in the computer the wave function $\psi(x, y)$ will be sampled as discrete points in x and y . The solution of Eqs. 6.67 and 6.68 will require computer storage for only a small number of two-dimensional arrays of $\psi(x, y)$ at any one time because only the values at two positions of z are needed at the same time. Furthermore the convolution can be efficiently calculated using the fast Fourier Transform as first discussed by Ishizuka and Uyeda [236] and Bursill and Wilson [51]. The Fourier convolution theorem says that:

$$\begin{aligned} f(x, y) \otimes h(x, y) &= FT^{-1}[F(k_x, k_y)H(k_x, k_y)] \\ F(k_x, k_y) &= FT[f(x, y)] \\ H(k_x, k_y) &= FT[h(x, y)] \end{aligned} \quad (6.85)$$

where $FT[]$ is a two-dimensional Fourier transform. Equations 6.67 and 6.68 can be rewritten using Fourier transforms as:

$$\begin{aligned} \psi_{n+1}(x, y) &= FT^{-1}\{P_n(k_x, k_y, \Delta z_n)FT[t_n(x, y)\psi_n(x, y)]\} \\ &\quad + \mathcal{O}(\Delta z^2) \end{aligned} \quad (6.86)$$

and

$$\begin{aligned} \psi_{n+1}(x, y) &= t_n(x, y)FT^{-1}\{P_n(k_x, k_y, \Delta z_n)FT[\psi_n(x, y)]\} \\ &\quad + \mathcal{O}(\Delta z^2) \end{aligned} \quad (6.87)$$

Equation 6.86 will turn out to be the best form to eliminate aliasing (see Sect. 6.8). If the wave function is sampled with N_x points in the x direction and N_y points in the y directions, then there are $N = N_x N_y$ Fourier coefficients all together. Using the fast Fourier transform (Chap. 4) means that the total computation time then

scales roughly as $N \log_2 N$ instead of N^2 as in a direct matrix solution (or the direct convolution in Eqs. 6.67 and 6.68). In a matrix algebra description the transmission function is diagonal in real space and the propagator is diagonal in reciprocal space. The FFT is a convenient and fast way to convert back and forth between real and reciprocal space. The combined efficiency of small memory requirements and fast computation makes the multislice method preferable over a direct matrix or eigenvalue solution.

The multislice solution is formally equivalent to a solution of the Howie–Whelan equation (6.47) if the slice thickness Δz is small enough. Both are derived from the wave equation for fast electron (6.43) and both neglect the second derivative of ψ with respect to z (Eq. 6.41). The principle difference is the relative efficiency of the two solutions. When the multislice solution is implemented using the fast Fourier transform (FFT) it can be dramatically faster (i.e., less computer time) than a Bloch wave solution.

6.7 Slicing the Specimen

Generating a description of the specimen in a form that can be used in a multislice program can be the most difficult part of simulating an image (often involving many long hours staring at the crystallographic data for the specimen at hand). Overall the specimen needs to be described as a sequence of layers (x , y planes) and the spacing between each layer (thickness of the layer along z , the optic axis of the electron microscope). Deciding on a strategy (and input format) for listing the specimen parameters is part of designing the program and part of actually using the program once it is written. The FFT (fast Fourier transform) has an enormous advantage in computational efficiency (i.e., computer time) and is almost always used in a multislice program. The FFT is factorable into independent x and y components (see Chap. 4). The easiest way to use the FFT is to describe the specimen as a rectangular unit cell. Obviously not all specimens have a convenient rectangular unit cell so this may require some work by the person using the multislice simulation program. If the specimen naturally has a rectangular unit cell it is easy to simulate it if viewed along one of the major crystal axis. If the specimen is not viewed along a major crystal axis or is not naturally rectangular, it is necessary to redefine a larger unit cell to get something that is rectangular. It is technically possible to define a multidimensional Fourier transform with non-orthogonal coordinates (for example, Dudgeon and Mersereau [103]); however, this is beyond the scope of this book (and this author). It is generally easier to write one program and rearrange the specimen coordinates than to write a new program for every possible specimen with different symmetry. There is no general procedure for all specimens. Each specimen may require a different approach to generate its multislice description.

The multislice method requires that the specimen be divided into a sequence of thin rectangular slices. Each slice must be thin enough to be a weak phase object and is in a plane perpendicular to the optic axis of the electron microscope (along z)

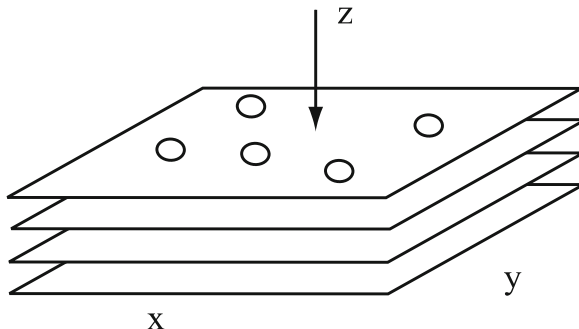


Fig. 6.6 The standard multislice description of the specimen as many thin slices perpendicular to the optic axis of the electron microscope (four slices shown). Each slice must be thin enough to be a weak phase object and is typically one atomic layer of the specimen. The optic axis of the electron microscope is in the positive z direction. Each slice should obey periodic boundary conditions in x and y

as in Fig. 6.6. All of the atoms within z to $z + \Delta z$ are compressed into a flat plane or slice at z . When viewed along the optic axis each slice must be aligned with the natural periodicity of the specimen. The edges of the slice (in the x , y plane) must obey periodic boundary conditions (in x and y) in the plane of the slice. This is a requirement for using the FFT and is identical to the requirements of the phase grating calculation (Chap. 5). If the slices do not obey periodic boundary conditions in the x and y direction, serious artifacts may be generated in the image due to the so-called wrap-around error (see Chap. 4). The transmission function for each slice should also be symmetrically bandwidth limited as in the phase grating calculation (Fig. 5.10) even though the sample spacing may be different in each direction (x and y).

The slices do not necessarily have to be periodic along the optic axis (the z direction), although this is frequently the case. Many crystalline specimens of interest are organized into layers of atoms. If the specimen is aligned such that these layers are perpendicular to the electron beam direction, then it is usually best to identify the slices with the atomic layers in the specimen. Many crystalline specimens can be described as a repetitive sequence of a small number of identical layers. For example, the (111) projection of silicon has a stacking sequence of $abcabc\dots$ with three repeating layers. Each layer can be used as one slice for the multislice method. In this case it is more efficient to calculate the transmission function for each of these three layers and store them in three arrays in computer memory. A multislice simulation program would then just reuse each layer over and over again without recalculation (to reduce the overall computer time required). The opposite extreme would be a completely disordered structure with no obvious repetitive structure along z . In this case there is no advantage to saving the transmission function of each slice. The transmission function for each slice can be calculated when needed and then discarded. This reduces the computer memory requirements significantly and has little or no effect on the computer time. The total

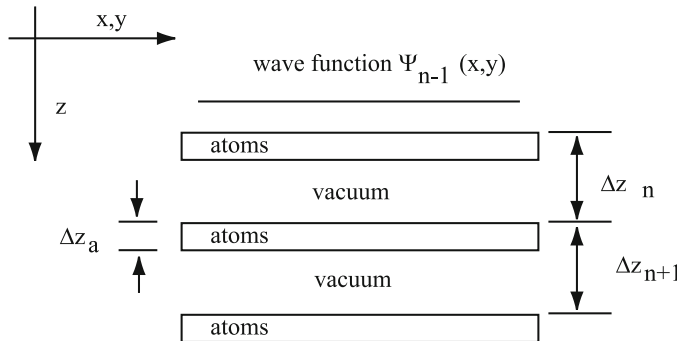


Fig. 6.7 The multislice error may be reduced by aligning atomic layers with the slice boundaries. The potential for each atomic layer is relatively thin (Δz_a) and the vacuum space between the slices is a free space propagation. The multislice slice thickness is Δz_n

computer time will increase with the number of slices that must be calculated but there is no advantage to saving the slices because they cannot be reused. These two strategies (precalculating the slices and reusing them versus calculating each slices as needed) may produce two different types of computer programs.

Aligning the natural atomic layers of the specimen with the slices can have beneficial side effects in the accuracy of the multislice solution. Figure 6.7 illustrates how this can occur. The atomic potential is strongly peaked near the atomic nucleus and falls off quickly away from the nucleus (the potential is approximately a screened $1/r$ dependence where r is the distance from the nucleus). The effective range of the potential in the atoms in one layer can be smaller than the distance between layers (see the rectangular box labeled “atoms” in Fig. 6.7). The potential is identically zero in between the layers. The transmission in vacuum is nearly exact but the multislice error occurs only over the thickness of the layer Δz_a . The propagator may be cascaded as:

$$p(x, y, \Delta z) = p(x, y, \Delta z - \Delta z_a) \otimes p(x, y, \Delta z_a) \quad (6.88)$$

In effect the multislice equations are a transmission plus propagator over a distance Δz_a followed by a propagation over a distance $\Delta z - \Delta z_a$. The effective multislice error is of order Δz_a which can be significantly smaller than total slice thickness Δz .

Furthermore if there are an integer number of slices in one repeat distance (along z) of the specimen then the multislice simulation can correctly reproduce the upper layer lines (higher order Laue zones) in the scattering process (Goodman and Moodie [162], Van Dyck [506]). If the specimen has a nonzero extent along the beam direction (the z axis) then its reciprocal lattice will have a definite three-dimensional structure. The simple case of a cubic unit cell is shown in Fig. 6.8. The wave vector of the incident electron beam is shown as k_z . The multislice calculation considers only elastic scattering so the scattered electron wave vector k_s must lie on the Ewald sphere to keep the length (or energy) of the incident

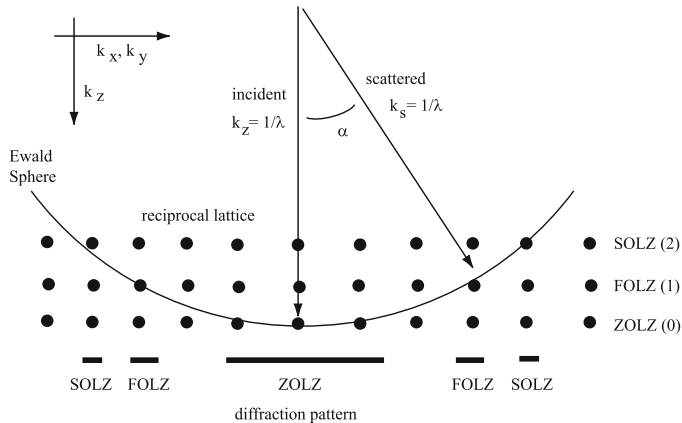


Fig. 6.8 The upper layer lines or higher order Laue zones (HOLZ). If the specimen is periodic in three dimensions (crystalline) then the reciprocal lattice will have additional diffraction conditions along the third dimension which can give rise to additional diffraction spots at high angle

and scattered electrons equal. The reciprocal lattice of the specimen (dark spots in Fig. 6.8) represents the only allowed changes in electron wave vector that can occur via elastic scattering in the specimen. Only the electron scattering angles on the Ewald sphere that cross spots in the reciprocal lattice of the specimen are allowed to contribute to the final transmitted electron wave function. The reciprocal lattice sites with a nonzero offset along the k_z direction are referred to as the higher order Laue zones (HOLZ). Only the bottom layer is allowed in the thin specimen calculations in Chap. 5 and is referred to as the zero order Laue zone (ZOLZ). The first nonzero (along z) layer is referred to as the first order Laue zone (FOLZ), the second layer is the second order Laue zone (SOLZ), etc. The ZOLZ gives rise to a large region in the diffraction pattern near the origin. The HOLZ regions give rise to rings at successively higher angles. If the slice thickness in the multislice calculation matches the natural periodicity in the specimen (i.e., an integer number of slices in the repeat length of the specimen), then the multislice simulation will reproduce the higher order Laue zones. If the slice thickness does not match the specimen periodicity, then beating can occur between the slice thickness and the specimen periodicity to produce artifacts in the image. The slice thickness can produce an artificial periodicity in the specimen if it does not match the natural periodicity of the specimen. If the multislice slice thickness is much larger than the natural periodicity of the specimen, then false HOLZ lines can be created at:

$$k = \sqrt{\frac{2}{\Delta z \lambda}} \quad (6.89)$$

where Δz is the multislice slice thickness, λ is the electron wavelength and $\alpha = \lambda k$ is the electron scattering angle. The slice thickness effectively takes the place of the

normal crystal lattice spacing along z . An overly large slice thickness can produce serious artifacts in a simulated image and should be avoided. Kilaas et al. [260] have discussed methods of including the upper layers lines in more detail.

The standard multislice method (Eqs. 6.86 and 6.87) is only accurate to order Δz . It is tempting to just let Δz get smaller and smaller to obtain more accuracy. However there is a competing effect that limits the minimum value of the slice thickness in most practical implementations. The standard multislice is frequently stated in terms of the total projected atomic potential $v_z(x, y)$ of the specimen, which is the integrated potential (along z) from minus infinity to plus infinity. Typically the total projected atomic potential is equated with the projected atomic potential for only the slice thickness:

$$v_{\Delta z}(x, y) = \int_z^{z+\Delta z} V(x, y, z) dz \sim \int_{-\infty}^{+\infty} V(x, y, z) dz = v_z(x, y) \quad (6.90)$$

As long as the slice thickness is large compared to the effective range of the atomic potential this approximation is valid. However if the slice thickness Δz is made less than the range of the atomic potential (about 1 Å), then this approximation is no longer valid. Therefore if the total projected atomic potential is used (as is typical) the minimum slice thickness is about 1 Å, which sets a limit on the maximum achievable accuracy of the multislice calculation. There is some question if 1 Å is thin enough for heavy atoms, such as gold, at 100 keV, however, higher voltage or lower atomic number should be all right (Watanabe [526]). The electron wavelength is typically of order 0.03 Å, which is much smaller than the minimum slice thickness. If the full wave function were used then the slice thickness would have to be much smaller than the electron wavelength, and the multislice method would not work at all. However, only the slowly varying part of the wave function is calculated so a slice thickness of several Angstroms is acceptable.

6.8 Aliasing and Bandwidth

Each slice in the multislice method produces two operations on the wave function (propagation and transmission). The first step is multiplication by the transmission function in real space and the second step is a convolution with the propagator function (a multiplication in reciprocal or Fourier space). Multiplication in real space is equivalent to a convolution in reciprocal space. Using a discretely sampled image for the wave function allows the use of the FFT with its computational efficiency but the discrete sampling also creates some subtle problems with aliasing (see Sect. 4.1) caused by multiplication by the transmission function in real space (or any other nonlinear operation).

In reciprocal space, multiplication of the wave function $\psi(x, y)$ by the specimen transmission function $t(x, y)$ is:

$$\begin{aligned} FT[t(x, y)\psi(x, y)] &= T(k_x, k_y) \otimes \Psi(k_x, k_y) \\ &= \int T(k'_x, k'_y) \Psi(k_x - k'_x, k_y - k'_y) dk'_x dk'_y \quad (6.91) \end{aligned}$$

where $T(k_x, k_y)$ is the Fourier transform of $t(x, y)$ and $\Psi(k_x, k_y)$ is the Fourier transform of $\psi(x, y)$. If each function is bandwidth limited to a maximum spatial frequency of k_{\max} (required when discretely sampled), then each function is only nonzero within a circle whose radius is k_{\max} . As shown earlier in Fig. 5.10 it is best to symmetrically bandwidth limit each function as:

$$k_{\max} = \min \left[\frac{N_x}{2a}, \frac{N_y}{2b} \right] \quad (6.92)$$

where the supercell size is $a \times b$ in real space with $N_x \times N_y$ pixels. A convolution is equivalent to sliding one circle across the other as in Fig. 6.9. The result of the convolution is a two-dimensional function whose value is the integration of the overlap between the two circles and the distance between the circles is the spatial frequency associated with this value. Multiplying two functions of bandwidth k_{\max} in real space produces a function with twice the original bandwidth ($2k_{\max}$).

When the functions are discretely sampled the spectra of each function is periodically repeated in both direction as shown in Fig. 6.10. Both the wave function $\Psi(k_x, k_y)$ and the transmission function $T(k_x, k_y)$ are repeated periodically although only $\Psi(k_x, k_y)$ is shown as being repeated to make the drawing easier to understand. When a discretely sampled wave function and transmission function

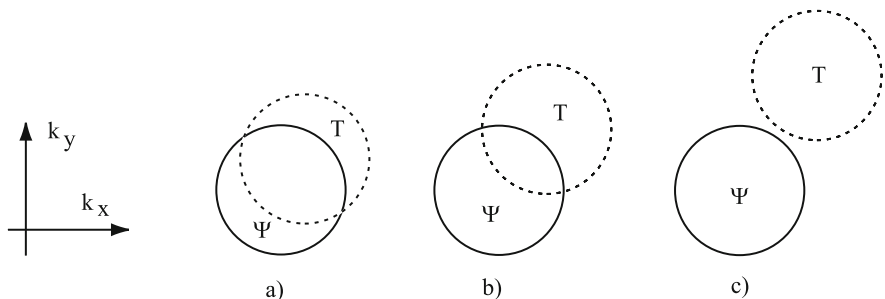


Fig. 6.9 The convolution of two continuous bandwidth limited Ψ and T in reciprocal space (equivalent to multiplication in real space). When limited to a symmetrically maximum frequency (or bandwidth) of k_{\max} each function is only nonzero within a circle of radius k_{\max} . Each point in the convolution is a different offset of the two circles and the value is the integrated intensity in the overlap region. The sequence (a), (b), (c) illustrate the process of sliding one disk across the other to form the convolution

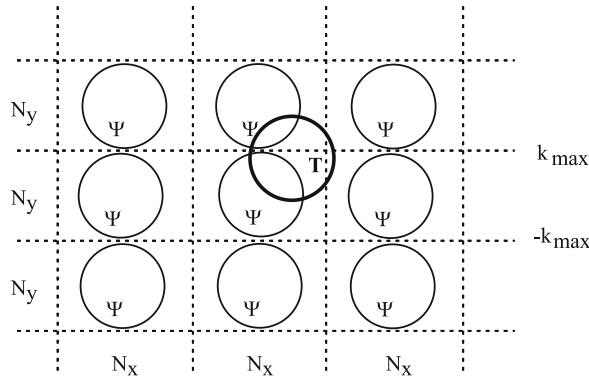


Fig. 6.10 The convolution of two discretely sampled bandwidth limited functions (the wave function Ψ and the transmission function T) in reciprocal space (equivalent to multiplication in real space). The bandwidth limit of each function appears as a circle

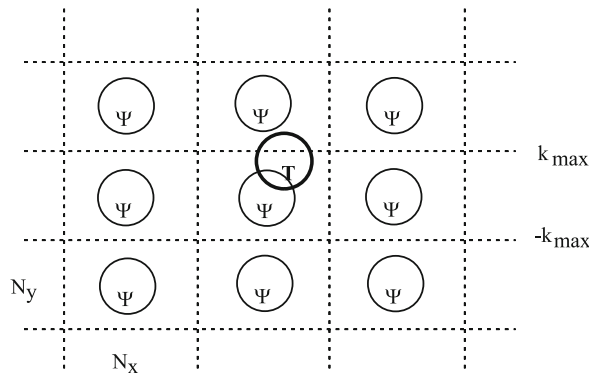


Fig. 6.11 The convolution of two discretely sampled bandwidth limited functions (the wave function Ψ and the transmission function T) in reciprocal space (equivalent to multiplication in real space). The bandwidth limit of each function appears as a circle and is limited to 2/3 of its maximum to eliminate aliasing

are convolved in reciprocal space, one function slides across the other and will overlap the adjacent periodically repeated functions. The other repeated functions improperly appear as very high spatial frequencies. It is equivalent to say that low spatial frequencies are aliased as high spatial frequencies. This can produce rather serious artifacts in the final simulation if not corrected.

The solution to this aliasing problem is to set the maximum spatial frequency (or bandwidth) of both functions to be 2/3 of the maximum sampling frequency (k_{\max}) in the wave function (Self et al. [452]). This way one function no longer overlaps the other when its offset reaches the maximum allowed spatial frequency (Fig. 6.11). Frequencies greater than 2/3 still overlap more than one Ψ function so the final result must be explicitly bandwidth limited again to $(2/3)k_{\max}$. If there are $N_x \times N_y$ pixels in the wave function and $N = N_x = N_y$, then there are a total

of N^2 possible Fourier coefficients. Limiting the bandwidth to 2/3 of its maximum symmetrical value limits the number of Fourier coefficients to $\pi[(2/3)(N/2)]^2 = \pi N^2/9 = 0.35N^2$. Even though nearly two thirds of the Fourier coefficients must be set to zero the overall benefit of the FFT is still worth the effort. A convenient way of limiting both functions is to set both the specimen transmission function and the propagator function to zero outside of $(2/3)k_{\max}$. When the electron wave function is multiplied by the transmission function (at each step or slice of the multislice method) its bandwidth doubles and is then reduced to the required maximum by convolution with the propagator function (multiplication in reciprocal space). This requires using the form of the multislice method in which convolution with the propagator function is performed after multiplication by the transmission function (Eq. 6.67 and not Eq. 6.68).

Without the appropriate bandwidth limit the simulated image can have serious artifacts and dramatically differ from the correct result. Reducing the effective bandwidth can also reduce the convergence of the multislice method. Usually the best recourse is to increase the number of pixels in one or both directions (N_x, N_y).

An alternate approach to eliminate aliasing was suggested by O'Keefe and Kilaas [381]. The wave function can be limited to $(1/2)k_{\max}$ (before and after each slice) and the transmission function limited to k_{\max} to get a similar elimination of aliasing.

6.9 Interfaces and Defects

Crystal defects and interfaces pose a problem for image simulation. The FFT is very efficient and produces a multislice calculation with an acceptable amount of computer time, but requires that the specimen potential and electron wave function be periodic in the xy plane (perpendicular to the optic axis of the microscope). The specimen does not need to be periodic along the z or beam direction although if it is not periodic along the beam it may require significantly more computer time.

An isolated point defect at a particular point in the specimen is obviously not periodic. If the defect is simply placed in the super cell of the specimen then the discrete nature of the sampled potential periodically reproduces an infinite number of point defects with the periodicity of the super cell as shown in Fig. 6.12. If the super cell dimensions $a \times b$ are too small, then the image from one defect can interfere with the image from the periodically produced adjacent defects. The solution to this problem is to use an artificially large unit cell. If the super cell dimensions $a \times b$ are large, then the point defects become essentially isolated and do not interfere. A good starting point is to keep the defects separated by about 25–30 Å. This method has been given the name periodic continuation and has been discussed by Grinton and Cowley [173], MacLagan et al. [327], Fields and Cowley [133], Anstis and Cockayne [19], Wilson and Spargo [535], and Matsuhata et al. [335].

A similar problem occurs for crystal interfaces as shown in Fig. 6.13. Consider an interface between material A on the left and material B on the right. The interface

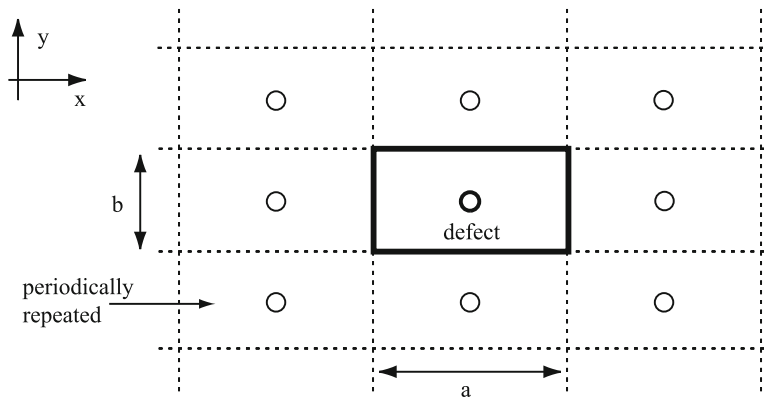
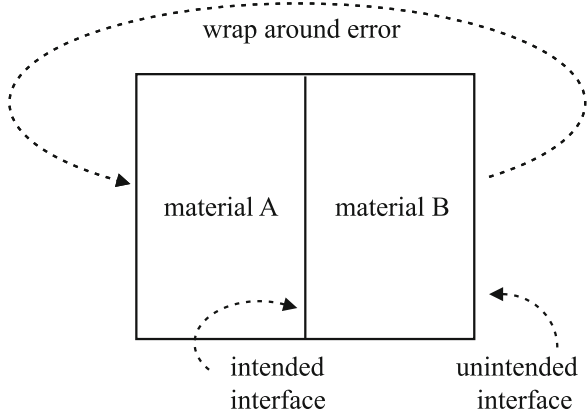


Fig. 6.12 Modeling a point defect (the small circle) in the center of the specimen of size $a \times b$. Periodic continuation of the image causes the defect to be repeated infinitely many times in both directions. The unit cell dimension $a \times b$ should be increased so that adjacent (periodically continued) defects do not interfere

Fig. 6.13 Modeling an interface in the center of the sampled area. The wrap-around error causes an extra interface to be created due to the interaction of the right-hand side and the left-hand side of the image



between the two materials in the center can be correctly modeled; however, the so-called wrap-around effect (or periodic continuation similar to Fig. 6.12) causes an additional interface to be produced when the right-hand side of material B wraps around to touch material A on the right for a second time. In this problem the super cell should again be made large enough so that these two interfaces do not interfere with one another. Usually the edges of the image (with the second unintended interface) can just be ignored, and the interface in the center will contain the correct simulation (assuming that the super cell size is large enough). Alternately, the presence of two interfaces can be explicitly acknowledged by sandwiching a narrow region of material B in the center of two regions of material A on the left and right. Then two interfaces are simulated. Note that the two regions of material A must match in orientation when wrapped around.

6.10 Multislice Implementation

The multislice method is particularly well suited for numerical implementation on a computer. There are several subtle problems and strategies associated with the multislice method, some of which will be discussed in this section. O’Keefe and Buseck [379] were the first to describe a specific computer implementation. Several other programs that have been described in the literature are listed in Table 6.2. Many other multislice program have likely been produced but have not been specifically described in the literature or otherwise missed in this abbreviated survey.

Table 6.2 Some image simulation software packages appearing in the literature or online

Program	Author	Year	Type	Comments
SHRLI	O’Keefe and Buseck [379]	1978, 1979	M	
TEMPAS	Kilaas [256]	1987	M	
EMS	Stadelmann [475]	1987	B	
NCEMSS	O’Keefe and Kilaas [381]	1988	M	
MacTEMPAS	Kilaas [257]	?	M	Online
CASINO	Hovington et al. [102, 215, 216]	1997	SEM	
TEMSIM	Kirkland [273]	1998	M	Online, openMP
?	Ishizuka [235]	2001	B, M	Online
?	deGraf [164]	2003	B	Online
JEMS	Stadelmann [476]	2004	B, M	Online
WebEMAPS	Zuo [474, 549]	2005	B	Online
EDM	Marks et al. [332]	2006	B,M	Online
CASINO-2	Drouin et al. [101]	2007	SEM	
SimulateM	Gómez-Rodríguez et al. [159]	2010	M	Online
TEM Simulator	Rullgård et al. [431]	2011	M	Online
STEM CELL	Grillo et al. [171, 172]	2013	M	Online, MPI
STEMSIM	Krause [295]	2013	M	Online
computem	Kirkland [276]	2013	M	Online, openMP
QSTEM	Koch [290]	2015	M	Online
MULTEM	Lobato [319]	2015	M	Online, GPU
μ STEM	Allen [6]	2015	B,M	Online
FDES	van den Broek [500]	2015	M	Online
STEMsalabim	Oelerich et al. [376]	2017	M	Online, MPI
PRISM	Ophus [387]	2017	M	Online, GPU
STEMcl	Radek et al. [410]	2018	M	Online, GPU
Dr. Probe	Barthel [24]	2018	M	Online
MS-STEM-FEM	Julian [251]	2018	M	MPI
Ronchigram.com	Schnitzer et al. [448]	2019		Ronchigram

Type M is multislice and type B is Bloch wave. Parallel programming models are openMP (shared memory) and MPI (networked, distributed memory) and graphics processing unit (GPU). Some of the listed programs may be commercial. Many other private programs likely exist

Table 6.3 Steps in the simulation of CTEM images of thick specimens

Step 1	Divide the specimen into thin slices
Step 2	Calculate the projected atomic potential $v_{zn}(\mathbf{x})$ (Eq. 5.19 or 5.21) for each slice and symmetrically bandwidth limit them
Step 3	Calculate the transmission function $t_n(\mathbf{x}) = \exp[i\sigma_e v_{zn}(\mathbf{x})]$ (Eq. 5.25) for each slice and symmetrically bandwidth limit each to 2/3 of its maximum to prevent aliasing
Step 4	Initialize the incident wave function $\psi_0(x, y) = 1$
Step 5	Recursively transmit and propagate the wave function through each slice $\psi_{n+1}(x, y) = p_n(x, y, \Delta z_n) \otimes [t_n(x, y)\psi_n(x, y)]$ using FFTs as in Eq. 6.86. Repeat until the wave function is all the way through the specimen
Step 6	Fourier transform the wave function at the exit surface of the specimen $\Psi_n(k_x, k_y) = FT[\psi_n(x, y)]$
Step 7	Multiply the transmitted wave function $\Psi_n(k_x, k_y)$ by the transfer function of the objective lens, $H_0(k)$ (Eq. 5.27) to get the image wave function in the back focal plane $\Psi_i(\mathbf{k}) = H_0(k)\Psi_n(\mathbf{k})$
Step 8	Inverse Fourier transform the image wave function $\psi_i(\mathbf{x}) = FT^{-1}[\Psi_i(\mathbf{k})]$
Step 9	Calculate the square modulus of the image wave function (in real space) to get the final image intensity $g(\mathbf{x}) = \psi_i(\mathbf{x}) ^2 = \psi_n(\mathbf{x}) \otimes h_o(\mathbf{x}) ^2$

If there are a small number of distinct layers repeated several times, then the transmission function for each can be calculated and stored; otherwise, they can be calculated as needed and discarded

The basic procedure for calculating CTEM and STEM images is similar to the procedure for simulating thin specimens given in Tables 5.1 and 5.3 except that the steps that propagate the electron wave function through the specimen are changed into the recursive relation Eq. 6.67 or 6.86. The portion of the electron path in the electron microscope that does not involve the specimen is identical for thin and thick specimens. Tables 6.3 and 6.4 summarize the multislice method for CTEM and STEM

6.10.1 The Propagator Function and Specimen Tilt

Small amounts of specimen tilt may be included with a small modification to the propagator function (Eq. 6.65):

$$P(k, \Delta z, \theta) = \exp \left[-i\pi\lambda k^2 \Delta z + 2\pi i \Delta z (k_x \tan \theta_x + k_y \tan \theta_y) \right] \quad (6.93)$$

where θ_x, θ_y is the crystal tilt in the x, y directions, $k^2 = k_x^2 + k_y^2$, and Δz is the slice thickness. This is equivalent to shifting the wave function between slices and is only valid for small tilts of no more than about 1° (Cowley [74]). A specimen tilt is not the same as a beam tilt because the beam direction has a strong interaction with the electron optical aberrations of the objective lens. Ishizuka [231] and Chen et al. [61] have given a more detailed discussion of tilt in multislice simulations.

Table 6.4 Steps in the simulation of STEM images of thick specimens

- | | |
|--------|---|
| Step 1 | Divide the specimen into thin slices |
| Step 2 | Calculate the projected atomic potential $v_{zn}(\mathbf{x})$ (Eq. 5.19 or 5.21) for each slice and symmetrically bandwidth limit them |
| Step 3 | Calculate the transmission function $t_n(\mathbf{x}) = \exp[i\sigma_e v_{zn}(\mathbf{x})]$ (Eq. 5.25) for each slice and symmetrically bandwidth limit each to 2/3 of its maximum to prevent aliasing |
| Step 4 | Calculate the probe wave function $\psi_p(\mathbf{x}, \mathbf{x}_p)$ at position \mathbf{x}_p (Eqs. 5.46 and 5.48) |
| Step 5 | Recursively transmit and propagate the probe wave function through each slice
$\psi_{n+1}(x, y) = p_n(x, y, \Delta z_n) \otimes [t_n(x, y)\psi_n(x, y)]$ using FFTs as in Eq. 6.86. Repeat until the wave function is all the way through the specimen |
| Step 6 | Fourier transform the transmitted wave function to get the wave function in the far field (diffraction plane) |
| Step 7 | Integrate the intensity (square modulus) of the wave function in the diffraction plane including only those portions that fall on the detector (Eq. 5.51). This is the signal for one point or pixel in the image |
| Step 8 | Repeat step 4 through step 7 for each position of the incident probe \mathbf{x}_p |

There is a multislice simulation for each point in the final image. If there are a small number of distinct layers repeated several times, then the transmission function for each can be calculated first and stored; otherwise, they can be calculated as needed and discarded. In a parallel computing environment, many probes can be propagated at the same time on different processors

The propagator function requires a small but significant amount of computation because of the transcendental functions. If the specimen contains many layers with the same slice thickness it is advantageous to calculate the propagator once, in advance, and then reuse it for each slice. The whole two-dimensional propagator can require a significant amount of computer memory. However the propagator function may be factored into an x component and a y component as:

$$\begin{aligned} P(k, \Delta z, \boldsymbol{\theta}) &= P_x(k_x, \Delta z, \theta_x)P_y(k_y, \Delta z, \theta_y) \\ P_x(k_x, \Delta z, \theta_x) &= \exp \left[-i\pi\lambda k_x^2 \Delta z + 2\pi i \Delta z k_x \tan \theta_x \right] \\ P_y(k_y, \Delta z, \theta_y) &= \exp \left[-i\pi\lambda k_y^2 \Delta z + 2\pi i \Delta z k_y \tan \theta_y \right] \end{aligned} \quad (6.94)$$

This factorization can be put to good use when programming the multislice simulation. $P_x(k_x, \Delta z, \theta_x)$ and $P_y(k_y, \Delta z, \theta_y)$ can be precalculated and stored in two one dimensional arrays that require much less computer memory than a whole two-dimensional array and then multiplied together when the whole two dimensional propagator function is needed. This produces about the same reduction in computer time as precalculating the whole two dimensional propagator (and reusing it for each slice) but requires only a relatively small amount of additional computer memory.

6.10.2 Convergence Tests

The computer will merrily calculate the wave function with total disregard for the accuracy of the calculation. It is the responsibility of the human user to interpret the results and decide if they are correct or not. There are a variety of approximation that go into the derivation of the multislice method and it is not guaranteed to give the right answer for every possibly set of input parameters. The user must specify the atomic coordinates of the specimen, the slice thickness, the size and number of pixels in the wave function, and specimen potentials. In a practical sense there are a lot more ways to make the simulation fail than there are to make it succeed. When using a multislice simulation program (or any other simulation program) it is always a good idea to be a little skeptical and do some testing to try and verify that the result is correct or at least internally consistent.

The multislice algorithm has a built in parameter that can be used to verify that it is running correctly. The electron wave function only interacts with the specimen with elastic scattering as far as the simulation is concerned. This means that the total number of electrons should be conserved. One easy test is to watch the total integrated intensity of the electron wave function as it progresses through the specimen. If the wave function incident on the specimen (plane wave for CTEM and a focused probe for STEM) is normalized such that:

$$I_n = \int |\psi_n(x, y)|^2 dx dy = 1 \quad \text{for } n = 0 \quad (6.95)$$

where n is the slice index and $n = 0$ for the incident wave function, then I_n should remain constant. The integrated intensity can become less than one if the sampling is inadequate. When the specimen scatters electrons to high angle some of them may be scattered outside of the maximum allowed angle (the 2/3 maximum bandwidth limit required to eliminate aliasing). Once they are scattered outside of this maximum limit then they are effectively lost to the calculation and I_n decreases. The actual value of I_n has no particular physical significance other than indicating whether or not the simulation is working. The electrons scattered outside the maximum limit are just as likely to continue to higher angles or to be scattered back to low angles. An I_n less than one only indicates the relative precision of the simulation. In practice this number is not very sensitive to the accuracy of the calculation. A value of $I_n \leq 0.90$ is probably wrong (although it may give a qualitatively valid image) and the sampling should be increased. This may mean a smaller pixel size in real space or reciprocal space, more pixels or some combination of these. Values of $0.95 \leq I_n \leq 1.00$ are typical for well-behaved calculations. On the other extreme values of $I_n > 1.0$ can also occur. An integrated intensity greater than one is also a clear indication that the calculation is not correct (typically this means that the slice thickness is too large).

Even if the total integrated intensity is within bounds the simulation is not guaranteed to be correct either. One of the best tests is to compare two different

simulations performed with slightly different sampling sizes (usually about a factor of two apart is good). The multislice simulation is only accurate in the limit of an infinitesimally small pixel size and slice thickness. If the sampling is adequate, then reducing the pixel size or slice thickness by a factor of two should have no effect. Therefore if two simulations with different sampling sizes produce the same result, then the simulation is likely to have the proper sampling. The phrase “pixel size” refers to both the real space pixel size and the reciprocal space pixel size. If one simulation is performed with an image size of $a \times b$ and $N_x \times N_y$ pixels, then increasing the number of pixels to $2N_x \times 2N_y$ only tests the pixel size in real space but not in reciprocal space. To test both pixel sizes the image size should be increased to about $\sqrt{2}a \times \sqrt{2}b$ and the number of pixels doubled in each direction to $2N_x \times 2N_y$. This approach tests the pixel size in both real space and reciprocal space at the same time.

All of the schemes for testing the accuracy of the simulation discussed above are only testing the internal consistency of the calculation. In the end no amount of internal consistency will guarantee that the simulation is correct. The only real test is to compare to experimentally observed images. Comparisons between real experimentally recorded image and theoretically simulated images have been performed and the multislice simulation is generally agreed to produce acceptable simulation of real images. Note, however, that most comparisons are done in a rather qualitative manner. The simulated images are subjectively judged to look like the experimentally observed image. This is due in part to the lack of quantitative experimental image data. Usually important parameters such as defocus or the incident beam intensity are simply not known, so a detailed quantitative comparison is difficult.

6.10.3 Partial Coherence in BF-CTEM

The electron microscope image is never perfectly coherent as assumed in Table 6.3. There is always a small spread in illumination angles from the condenser lens and a small spread in defocus values due to small instabilities in the high voltage and lens current supplies. When these effects are included the image is said to be partially coherent. Section 3.2 discussed partial coherence in the linear image model and Sect. 5.4.3 introduced the transmission cross coefficient for partial coherence in nonlinear imaging of thin specimen.

If the specimen is not too thick and the amount of incoherence is small (small condenser angle), then the transmission cross coefficient (Sect. 5.4.3) can be applied to the wave function transmitted through the specimen via the multislice algorithm. However if the spread in illumination angles is significant and the specimen is thick, then the transmission cross coefficient is not quite right. Each illumination angle incident on the specimen may interact differently with the specimen. Different illumination angles may satisfy different diffraction conditions in the specimen. The best way to simulate a large spread in illumination angles in a thick specimen is to

perform a multislice simulation for each angle in the condenser aperture and sum the results incoherently (OKeefe and Sanders [382]) assuming the source is incoherent. If \mathbf{k}_β is one angle in the condenser aperture, then the initial wave function is:

$$\psi_0(\mathbf{x}) = \exp(2\pi i \mathbf{k}_\beta \cdot \mathbf{x}) \quad (6.96)$$

This wave function is then recursively transmitted through the specimen using the multislice algorithm (Eq. 6.86) yielding a transmitted wave function of $\psi_n(\mathbf{x}, \mathbf{k}_\beta)$. Each of these wave functions should then be convolved with the objective lens point spread function $h_0(\mathbf{x})$ and incoherently summed to give a final image intensity of:

$$g(\mathbf{x}) = \frac{1}{N_\beta} \sum_{\mathbf{k}_\beta} |\psi_n(\mathbf{x}, \mathbf{k}_\beta) \otimes h_0(\mathbf{x})|^2 \quad (6.97)$$

where N_β is the number of condenser illumination angles used. The illumination angles vary in two dimension and must match the existing periodic boundary conditions of the specimen (i.e., only integer coordinates in the Fourier transform). This summation can require a significant amount of computer time but is not excessive on currently available computer hardware for reasonable sizes of condenser angles. If the condenser aperture is not uniformly illuminated, then a suitable weighting factor can be added to Eq. 6.97. A defocus spread can also be included by simply integrating over a range of defocus values Δf as:

$$g(\mathbf{x}) = \frac{1}{CN_\beta} \sum_{\mathbf{k}_\beta} \sum_{\Delta f} p(\Delta f) |\psi_n(\mathbf{x}, \mathbf{k}_\beta) \otimes h_0(\mathbf{x}, \Delta f)|^2 \quad (6.98)$$

$$C = \sum_{\Delta f} p(\Delta f)$$

where $p(\Delta f)$ is the probability distribution of defocus values. The integration over defocus is relatively quick compared to the integration over illumination angles because it does not require a multislice simulation for each defocus value.

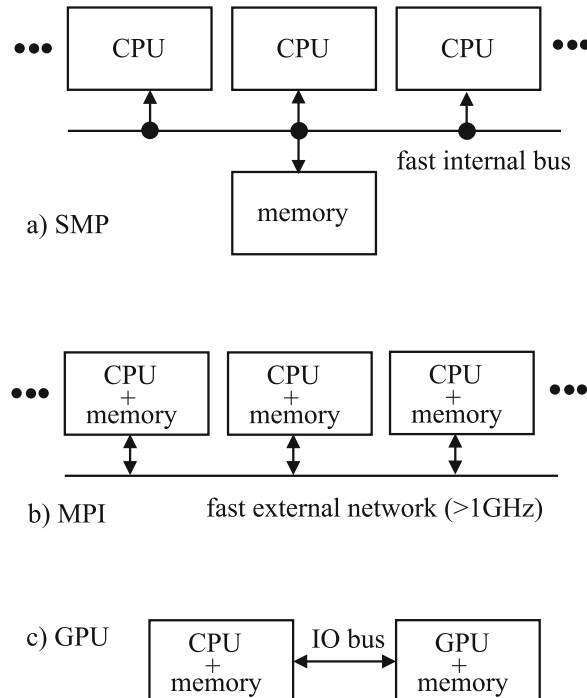
6.10.4 Parallel Computing

The current trend in computer hardware is to organize many processors (or CPUs) to cooperatively work on a common calculation. Improvements in the speed of individual processors appear to be nearing a physical speed limit. Historically, the transistors in the CPU were made faster by making them smaller to reduce parasitic capacitance, etc. This leads to Moore's Law [360] stating that the number of transistors on an IC doubles about every 2 years. The dimensions of a single transistor are now approaching the spacing between atoms in the semiconducting

material the transistors are made of, so cannot get much smaller. The speed of an individual CPU seems to be approximately constant over the last few years. The principle method of increasing computer capabilities is to use more than one CPU on a given problem. Moore's Law is still in effect after 50 years because more transistors on an IC are being used to make more CPUs on a single IC. This trend of multiprocessing may be here to stay. Even inexpensive computers intended for personal use can have much more than a single processor, so this trend is worth exploiting. Most of the algorithm development in the past was modeled on a single processor approach, so many algorithms require a complete reorganization to use more than one processor at a time and many new algorithms are being developed for this mode of computation. Fortunately, there are several relatively easy ways to use multiple CPUs in the multislice simulation method, which have been used by many authors in recent years (see Table 6.2).

There are currently three different popular methods of connecting multiple processors together that mainly differ in how the memory is accessed as outlined in Fig. 6.14. One is the shared memory processing (SMP, Fig. 6.14a) approach in which many processors share the same large block of memory with a fast data path to and from this memory. The CPUs are typically on the same IC or circuit board. The processors communicate by reading or writing data from or to this fast memory. This approach is usually limited to a small number (of order 2–16, but increasing every year) of processors due to the hardware difficulty of connecting

Fig. 6.14 Parallel computing architecture models. (a) Shared memory processors (SMP), (b) distributed memory architecture with message passing over a fast network (cluster), and (c) graphical processing unit (GPU)



multiple processors to the same memory at high speed. SMP has the advantage of being easier to program.

A second approach uses distributed memory and many physically separate computers, each with their own memory, connected together on a very fast external network switching hub (connection), collectively called a cluster (Fig. 6.14b). This has the advantage of using existing computers and allows a vast numbers (perhaps thousands) of processors to be coupled into one system. The only limit on the maximum size is the available money and space. The disadvantage is that the communications between processors is relatively slow (compared to SMP) which is a little harder to program in some cases. Each node in a computing cluster can also have the SMP mode of operation. Robertson [422] and Grillo et al. [57, 170] have implemented ADF-STEM on an MPI cluster.

A third new approach uses specialized graphics processors (GPUs) with thousands of very inexpensive processors (Fig. 6.14c). Video display processors have evolved to render images very fast in real time, principally for the computer gaming market. Conceptually a GPU board tries to produce a dedicated numerical processor (CPU) for each pixel in the display (a goal not yet achieved in practice). The manufacturers have also realized a more scientific use for this computing capability and allow a programmer to access this large array of dedicated CPUs for numerical processing independent of a video display. There are typically several thousand simple cores or CPUs on a single GPU board. However these cores are not general purpose CPUs capable of running stand-alone programs but must be controlled from the host computer. The host launches a large number of similar tasks to run in parallel on all of the GPU cores at once. Each core runs one thread or simple instruction sequence. This can be referred to as a SIMD (Single Instruction Multiple Threads) architecture (for example, Sanders and Kandrot [433]). These may be difficult to program but can be very inexpensive. TEM image simulations have been studied by Dwyer [105, 106] and Lobato et al. [319], and diffraction simulation by Eggman et al. [110]. Hosokawa et al. [212] have benchmarked GPU multislice code. A GPU approach currently seems to be an economical approach to parallel multislice computations.

Multiprocessing has been around for a long time. Recent software developments have made it a lot more attractive in recent years. SMP hardware has moved into the mainstream of inexpensive every day computers (not just expensive research computers) and the software tools have become easy to use. Two packages are worth mentioning; openMPI is a message passing environment for a distributed memory cluster and openMP for a shared memory (SMP) environment (see, for example, Quinn [409]). Many compilers now support one or both of these in some manner. This software is relatively easy to use (compared to previous vendor specific approaches) and is nonproprietary. It is being implemented on a variety of different computing platforms, so is likely to last for a long time. Parallel programming can be thought of as a collection of instruction sequences or threads that run at the same time and combine their results at the end. Each thread is controlled in software in openMP and openMPI so there is a large overhead for starting and stopping a thread. To be effective, each thread should perform a large amount of calculations;

otherwise, the CPU time just goes into managing the threads and not the calculation. This may be referred to as coarse grain parallelization, and requires reorganizing the program flow so that various parts of the calculation can proceed independently at the same time on different CPUs. GPUs, however, seem to manage a very large number of threads in parallel with little or no overhead per thread (probably in hardware not software). Each GPU core is less capable than the host CPUs but there are a very large number of them. To be effective there should be a large number of simple operations performed in parallel at the same time organized in a fine-grain parallelization mode. Some operations do not easily translate into a GPU mode. For example, a simple integral (or long summation) cannot be easily performed using a fine-grain parallelization because all threads need to access the same summation variable at the same time (a slightly complicated work around is to divide the summation into sub-sums). Fine and coarse grain programming are opposite programming strategies. A fine-grain approach is like attaching the problem with a large swarm of bees and the coarse grain approach is more like using a small pack of wolves. Each has its limitations. Typically there may be 10–20% of the code that cannot be converted to run in parallel and must remain sequential on a single host CPU. This limits the maximum increase in speed to about 5 \times to 10 \times without an heroic programming effort.

There are several ways to utilize multiple processors in parallel in a multislice calculation. It is not so obvious for a Bloch wave calculation, although the ScaLapack subroutine package targets a many processor distributed cluster and may help with the eigenvalue calculation which is the main portion of the calculation. At a low level the multidimensional FFT (in this case 2D, used in the multislice method) can easily be split into many parallel paths. Each row can be done by a different processor in one direction and then each col. in the other direction. Various sums in the transmission function can also be split into separate processors. Both of these methods are a relatively fine-grain parallelization and work best on an SMP machine. A distributed memory cluster may not yield an improvement this way due to the increased communications overhead. An ADF-STEM calculation can be extremely compute intensive. However, it is also very easy to expand into a multiprocessor mode. The transmission of each probe position in the image can be put on a separate processor and run in parallel. This has the advantage of a coarse grain parallelization and may work well in a distributed memory environment. The ADF-STEM code used here uses this approach in an SMP mode or GPU mode.

6.11 More Accurate Slice Methods

There are (at least) four main approximations that limit the accuracy of the calculation. First is the neglect of backscattered electron. Second is the neglect of the second order term, Eq. 6.41 (also known as the high energy approximation). Third is the independent atom approximation (Eq. 5.19) and fourth is a nonzero slice thickness and limited accuracy relating to the slice thickness. The first three

are also in the Bloch wave solution. Improving any of these may in principle improve the accuracy of the calculation. The multislice solution is automatically stable because each step is a unitary operation which is a big advantage, but it is not that accurate (stability and accuracy are two different things).

Watanabe et al. [527, 528] have proposed an alternate approach to the solution of the Howie–Whelan equations using a direct integration of the second order equations plus a convolution; however, their approach requires a very small step size so is not that practical. Hiller et al. [206] have discussed the effects of the second order term using a direct Runge–Kutta method. Dulong et al. [104] have done a similar study for Bloch wave calculations.

Chen et al. [60, 62], Cai et al. [55], Cai and Chen [54], and Wacker and Schöder [514] have proposed more accurate (higher order) multislice formulations. Ming and Chen [347] have compared three possible multislice methods (standard as in this chapter and two more accurate methods) and found that the standard multislice method agrees with more accurate methods at beam energies of 50 kV and higher but deviates significantly at 20 kV. Kirkland [277] compared the standard multislice method (with a special slice integration method for thin slices) to a multislice method with a slice thickness less than about 0.1 Å (i.e., more accuracy) and found a similar result in crystalline gold. Generally speaking, the standard multislice formulation is fast and accurate for beam energies above about 50 V or 60 kV, and higher order methods are much slower but probably required for lower energies such as 40 kV and lower

The standard multislice expression is only accurate to first order in Δz . There is some incentive to find more accurate solutions in which the error term is a higher power (or order) of the small quantity Δz . An obvious idea is to simply average Eqs. 6.67 and 6.68 to increase the accuracy by one order in Δz . This approach is more accurate but unfortunately also doubles the computer time. Averaging would also have the benefit of insuring that reciprocity is obeyed.

6.11.1 Operator Solutions

One obvious weak spot in the multislice derivation is factoring the combined operator Eqs. 6.56 and 6.57. An alternate approach to factorizing the combined operator is:

$$\begin{aligned}
 & \exp(A\epsilon/2) \exp(B\epsilon) \exp(A\epsilon/2) \\
 &= \left[1 + A\frac{\epsilon}{2} + \frac{1}{2!}A^2\left(\frac{\epsilon}{2}\right)^2 + \dots \right] \left[1 + B\epsilon + \frac{1}{2!}B^2\epsilon^2 + \dots \right] \\
 &\quad \times \left[1 + A\frac{\epsilon}{2} + \frac{1}{2!}A^2\left(\frac{\epsilon}{2}\right)^2 + \dots \right] \\
 &= 1 + (A + B)\epsilon + \frac{1}{2!}(A^2 + AB + BA + B^2)\epsilon^2 + \mathcal{O}(\Delta z^3) \quad (6.99)
 \end{aligned}$$

where A and B are non-commuting matrices or operators and ϵ is a small scalar quantity. By comparison to Eq. 6.53 the operator relevant to the multislice method can be written in symmetrical form as:

$$\exp(A\epsilon + B\epsilon) = \exp(A\epsilon/2) \exp(B\epsilon) \exp(A\epsilon/2) + \mathcal{O}(\epsilon^3) \quad (6.100)$$

The error term is proportional to $\mathcal{O}(\Delta z^3)$ which is one order better than the previous identities (Eqs. 6.56 and 6.57) used in the standard multislice derivation. This symmetrical operator approximation has been used to simulate the paraxial propagation of laser beams by Fleck et al. [138] with a method very similar to the multislice method.

van Dyck [502, 506] has pointed out that this new operator identity allows the standard multislice equation to be re-interpreted in a more accurate manner. Applying Eq. 6.100 to the multislice Eq. 6.51 yields:

$$\begin{aligned} \psi_{n+1}(x, y) &= p_n(x, y, \Delta z/2) \otimes \{t_n(x, y) [p_n(x, y, \Delta z/2) \otimes \psi_n(x, y)]\} \\ &\quad + \mathcal{O}(\Delta z^3) \end{aligned} \quad (6.101)$$

where $\psi_n(x, y)$, $p_n(x, y, \Delta z/2)$, $t_n(x, y)$ are the wave function, propagator function, and transmission functions of the n^{th} layer. The propagator function of the n^{th} layer is split into two component each with thickness $\Delta z/2$. When Eq. 6.101 is applied recursively the convolution with the propagator on the right combines with the convolution with the propagator of the left to yield:

$$p_{n+1}(x, y, \Delta z_{n+1}/2) \otimes p_n(x, y, \Delta z_n/2) \otimes = p(x, y, \Delta z) \otimes \quad (6.102)$$

if $\Delta z_n = \Delta z_{n+1} = \Delta z$. The final result is a succession of convolutions with the propagator and multiplication by the transmission function that is identical to the standard multislice formulation with only one additional propagation by $\Delta z/2$ at the end. This means that the standard multislice method (Eqs. 6.67 and 6.68) can be interpreted as being accurate to $\mathcal{O}(\Delta z^3)$ locally and $\mathcal{O}(\Delta z^2)$ globally if the result is offset by one half of a slice thickness. The defocus is rarely known with much accuracy so this offset is negligible. Van Dyck [503, 505, 506] and Chen [60, 62] have proposed other possible higher order methods.

6.11.2 Finite Difference Solutions

Another approach to increasing the accuracy is to include more terms in the Taylor series expansion for ψ in Δz . Consider the following expansions for both positive and negative steps in z and temporarily drop explicit reference to the independent variables x and y in ψ .

$$\begin{aligned}\psi(z + \Delta z) \\ = \psi(z) + \Delta z \frac{\partial \psi(z)}{\partial z} + \frac{1}{2!} \Delta z^2 \frac{\partial^2 \psi(z)}{\partial z^2} + \frac{1}{3!} \Delta z^3 \frac{\partial^3 \psi(z)}{\partial z^3} + \dots\end{aligned}\quad (6.103)$$

$$\begin{aligned}\psi(z - \Delta z) \\ = \psi(z) - \Delta z \frac{\partial \psi(z)}{\partial z} + \frac{1}{2!} \Delta z^2 \frac{\partial^2 \psi(z)}{\partial z^2} - \frac{1}{3!} \Delta z^3 \frac{\partial^3 \psi(z)}{\partial z^3} + \dots\end{aligned}\quad (6.104)$$

Subtracting Eqs. 6.103 and 6.104 yields:

$$\frac{\partial \psi(z)}{\partial z} = \frac{\psi(z + \Delta z) - \psi(z - \Delta z)}{2\Delta z} + \mathcal{O}(\Delta z^2) \quad (6.105)$$

All terms containing even derivatives vanish identically leaving only the higher order error term proportional to Δz^2 . If instead Eqs. 6.103 and 6.104 are added, then:

$$\frac{\partial^2 \psi(z)}{\partial z^2} = \frac{\psi(z + \Delta z) - 2\psi(z) + \psi(z - \Delta z)}{\Delta z^2} + \mathcal{O}(\Delta z^2) \quad (6.106)$$

where all terms containing odd derivatives vanish identically leaving only the error term proportional to Δz^2 . These are the finite difference approximations to both the first and second derivatives of $\psi(z)$ with respect to z . The Schrödinger wave equation (6.40) for the slowly varying portion of the wave function contains both first and second derivatives with respect to z . Rewriting it using the interaction parameter $\sigma_e = 2\pi me\lambda/h^2$:

$$\left[\frac{\partial^2}{\partial z^2} + \frac{4\pi i}{\lambda} \frac{\partial}{\partial z} + \nabla_{xy}^2 + \frac{4\pi\sigma_e}{\lambda} V(x, y, z) \right] \psi(x, y, z) = 0 \quad (6.107)$$

Next substitute the finite difference approximations for the first and second derivatives (Eqs. 6.105 and 6.106) without ignoring the second derivative with respect to z as was done for the Howie–Whelan equations and the traditional multislice solution.

$$\begin{aligned}\frac{\psi(z + \Delta z) - 2\psi(z) + \psi(z - \Delta z)}{\Delta z^2} + \frac{4\pi i}{\lambda} \frac{\psi(z + \Delta z) - \psi(z - \Delta z)}{2\Delta z} \\ + \nabla_{xy}^2 \psi(z) + \frac{4\pi\sigma_e}{\lambda} V(x, y, z) \psi(z) + \mathcal{O}(\Delta z^2) = 0\end{aligned}\quad (6.108)$$

Multiply by Δz^2 , rearrange terms and restore the reference to the x, y dependence in ψ :

$$\begin{aligned}\psi(x, y, z + \Delta z) &= \frac{1}{c_+} \left[2 - \Delta z^2 \left(\nabla_{xy}^2 + \frac{4\pi\sigma_e}{\lambda} V(x, y, z) \right) \right] \psi(x, y, z) \\ &\quad - \left(\frac{c_-}{c_+} \right) \psi(x, y, z - \Delta z) + \mathcal{O}(\Delta z^4/c_+)\end{aligned}\quad (6.109)$$

$$c_+ = 1 + 2\pi i \Delta z / \lambda$$

$$c_- = 1 - 2\pi i \Delta z / \lambda$$

$\Delta z / \lambda \gg 1$ so that dividing by c_+ does not necessarily reduce the order of the error term. The values of $\psi(x, y)$ are calculated in an xy plane at $z + \Delta z$ from ψ in an xy plane at z and $z - \Delta z$. This is also a slice method but of higher accuracy because the error term is a higher power of the small quantity Δz and because the second derivative of ψ with respect to z has not been ignored. This method can be referred to as a three plane slice method (or finite difference method) because the values of $\psi(x, y)$ in three planes are related to one another in each iteration. The standard multislice method can be referred to as a two plane slice method. When using a discretely sampled wave function and potential this method should also be bandwidth limited to 2/3 of its maximum (both $\psi_n(x, y)$ and $V(x, y)$) just as in the standard multislice method to avoid aliasing. The potential $V(x, y, z)$ is not a very well-behaved function. It is strongly peaked near the center of each atom (with a logarithmic singularity) which may defeat the higher accuracy of this equation. For comparison repeating the above derivation without the second derivative term yields the result:

$$\begin{aligned}\psi(x, y, z + \Delta z) &= 2 \left[\Delta z \frac{i\lambda}{4\pi} \nabla_{xy}^2 + i\sigma_e \Delta z V(x, y, z) \right] \psi(x, y, z) \\ &\quad + \psi(x, y, z - \Delta z) + \mathcal{O}(\Delta z^3)\end{aligned}\quad (6.110)$$

The other second derivative term $\nabla_{xy}^2 \psi$ can be approximated with its finite difference equivalent:

$$\begin{aligned}\nabla_{xy}^2 \psi(x, y) &= \frac{\psi(x + \Delta x, y) - 2\psi(x, y) + \psi(x - \Delta x, y)}{\Delta x^2} \\ &\quad + \frac{\psi(x, y + \Delta y) - 2\psi(x, y) + \psi(x, y - \Delta y)}{\Delta y^2} \\ &\quad + \mathcal{O}(\Delta x^2) + \mathcal{O}(\Delta y^2)\end{aligned}\quad (6.111)$$

or by using a pair of FFTs as:

$$\nabla_{xy}^2 \psi(x, y) = FT^{-1} \left[-4\pi^2 k^2 FT[\psi(x, y, z)] \right] \quad (6.112)$$

where FT is the two-dimensional Fourier transform with respect to x and y and $k^2 = k_x^2 + k_y^2$ is the spatial frequency. Using the Fourier transform does not add a significant error if the sampling is adequate.

Equation 6.109 uses the atomic potential directly (without projection) and does not suffer from a minimum slice thickness limitation as in the standard multislice method although it has an opposite problem. If the slice thickness is too thick (greater than about 1 Å), then Eq. 6.109 can possibly lose some atoms in between slices.

This method (Eq. 6.109) is accurate to about one order better than the standard multislice method and is more complete because it includes the second derivative (with respect to z) term. The local (or per step) error is $\mathcal{O}(\Delta z^4)$ and the total or global error is $\mathcal{O}(\Delta z^3)$ if each slice is symmetrical about its center. This solution requires two FFTs to calculate $\nabla_{xy}^2 \psi(x, y)$ plus several pairs of FFTs to bandwidth limit the appropriate functions (to avoid aliasing) for each iteration. This amount of computation is similar to the amount of computation in the standard multislice method. However it requires the storage of an additional set of wave function values $\psi(x, y, z - \Delta z)$ (which is only a mild inconvenience with the current low cost of memory) and it requires that each slice thickness be identical (which can be a significant problem with some specimens). Also, the initial values ψ are required at two values of z . If there are $N = N_x N_y$ Fourier coefficients, then the computer memory requirements scale as N and the computer time scales as $N \log_2 N$, similar to the standard multislice method. This method (Eq. 6.109) is similar to that tested by Kosloff and Kosloff [292] for solution of the time dependent Schrödinger wave equation in molecular dynamics calculations and may eventually have some value in electron microscope image simulation.

Although more accurate this method is not stable for an arbitrary slice thickness. At each step the current solution $\psi_n(x, y, z)$ will include some small error either from the finite precision arithmetic of the computer or from the errors arising from truncating the Taylor series at only the first few terms. It is important to consider how the recursive calculation in Eq. 6.109 treats this error. If a small error increases with each step, then the method is unstable and if it decreases with each step, then the method is stable. First consider a small error with a particular two-dimensional spatial frequency $\mathbf{k}_e = (k_{xe}, k_{ye})$ and amplitude ϵ_n in the wave function $\psi_n(x, y)$. This error will give rise to an associated error in the wave function in the next plane $\psi_{n+1}(x, y)$.

$$\begin{aligned} \psi_n(x, y) &\rightarrow \psi_n(x, y) + \epsilon_n \exp(2\pi i \mathbf{k}_e \cdot \mathbf{x}) \\ \psi_{n+1}(x, y) &\rightarrow \psi_{n+1}(x, y) + \epsilon_{n+1} \exp(2\pi i \mathbf{k}_e \cdot \mathbf{x}) \end{aligned} \quad (6.113)$$

Substituting these into Eq. 6.109 yields an expression relating the amplitude of the error at each step (neglecting a possible error in $\psi_{n-1}(x, y)$).

$$\begin{aligned}\epsilon_{n+1} \exp(2\pi i \mathbf{k}_e \cdot \mathbf{x}) &= \frac{1}{c_+} \left[2 - \Delta z^2 \left(\nabla_{xy}^2 + 4\pi\sigma_e V/\lambda \right) \right] \\ &\times \epsilon_n \exp(2\pi i \mathbf{k}_e \cdot \mathbf{x})\end{aligned}\quad (6.114)$$

The rate of growth g of the error must be less than or equal to one to produce a stable recursive solution.

$$g = \left| \frac{\epsilon_{n+1}}{\epsilon_n} \right| = \left| \frac{1}{c_+} \left[2 - \Delta z^2 \left(-4\pi^2 k_e^2 + 4\pi\sigma_e V/\lambda \right) \right] \right| \leq 1 \quad (6.115)$$

This is the von Neuman stability analysis (for example Press et al. [406]). Further rearranging Eq. 6.115 yields:

$$k_e^2 < \frac{1}{4\pi^2 \Delta z^2} \left[\sqrt{1 + 4\pi^2 \Delta z^2 / \lambda^2} - 2 \right] + \frac{\sigma_e V}{\lambda \pi} \quad (6.116)$$

Note that the last term is always positive. This expression means the bandwidth of the calculation (the maximum of $|k_e|$) is coupled to the slice thickness. Either the bandwidth or the slice thickness should be reduced to produce a stable solution. Unfortunately the slice thickness must typically be reduced to about the same size as the pixel (of order 0.1 Å) so this method is not competitive with the standard multislice method (with a slice thickness of order 2–3 Å). This argument does, however, explain why the standard multislice method is stable and well behaved. Each multislice step is unitary meaning that ψ_n is multiplied by a factor whose magnitude is identically one (i.e., the exponential of a pure imaginary number). This means that each step of the standard multislice is unconditionally stable (there is a distinction between stability and accuracy, however).

In the long run any higher order solution may be defeated by the ill behaved nature of the specimen potential $V(x, y, z)$ (i.e., it has a sharp cusp or singularity near the atomic nucleus). The error term is proportional to Δz^3 , and the other factors of the error term involve various derivatives of the wave function which indirectly involve various derivatives of the potential. If there are singularities in the potential, then the higher order derivatives in the Taylor series can grow abnormally large making convergence slow at best.

This finite difference method with three slices (Eq. 6.109) will be very slow in comparison to the standard two slice multislice method so is not very competitive in most ways. However, it is worth comparing results as a test of accuracy. Figure 6.15 shows the results of the standard multislice and the three slice finite difference (labeled MS and FD, respectively) for 60 kV along the c axis of gold (face centered cubic lattice). The principle 000 beam and one diffracted beam are shown versus depth into the specimen.

A single gold atom is not a weak phase object at 60 kV so this energy is a good test of the accuracy of the standard multislice method (MS). The three slice FD solution was calculated with a step size of $c/400$ (about 0.01 Å) and $c/800$ (about

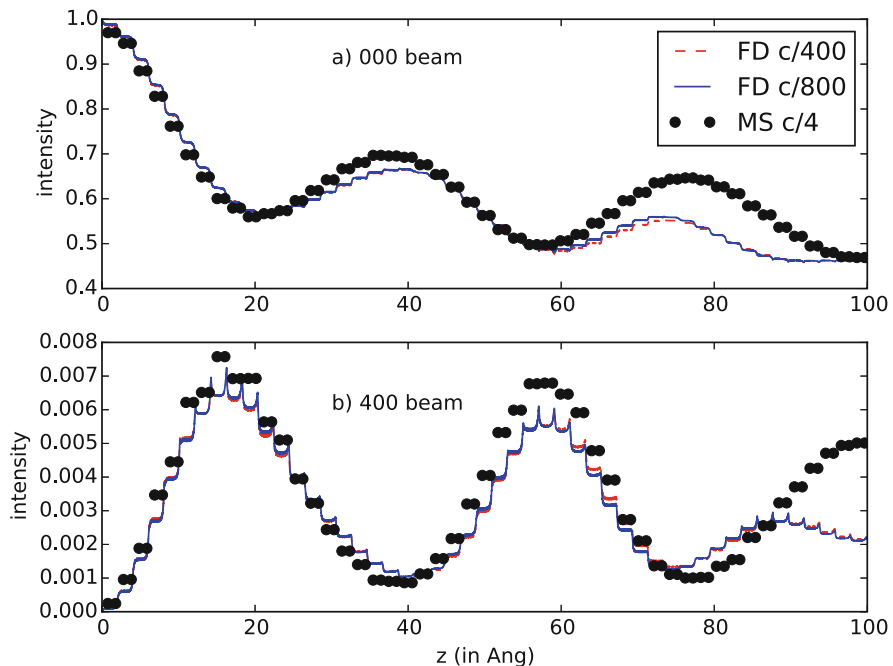


Fig. 6.15 Comparison of the conventional multislice calculation (MS) to a more accurate three-slice finite difference solution (FD) for a beam energy of 60 kV in gold ($c = 4.078 \text{ \AA}$). The intensity of the 000 and 400 (about 1 Å) beams are plotted versus distance into the specimen (z). The specimen supercell size was 7 by 7 unit cells and the wave function was sampled with 1024 by 1024 pixels

0.005 Å), which should be sufficient to subdivide the atom (the full 3D potential not the projected atomic potential was used). The two step sizes agree which indicates that this step size is small enough. The MS and FD method agree fairly well to a depth of about 60 Å, which is very good. This result seems to say that neglecting the second derivative (in z , the high energy approximation) and using a slice thickness of an atom or so does not cause significant problems in the standard multislice (MS) method. This thickness of gold is much greater than would be usable in the microscope. The agreement should get better as the beam energy is increased or the atomic number of the specimen is decreased. This test has not tested the significance of ignoring the backscattered electron (of which there may be a large amount) or the independent atom approximation (IAM), but is encouraging for continued use of the standard multislice method. The IAM is not really part of the numerical method but rather the specimen model. Further attempts to use a more accurate specimen potential will likely require a method similar to this FD calculation with a finer sampling of the potential which will be a computational challenge.

Chapter 7

Multislice Applications and Examples



The multislice method simulates electron transmission in a thick specimen including dynamical scattering. Chapter 6 presented the theory of the multislice method and discussed how to use it in general terms. This chapter will give some specific examples of performing a multislice simulation. The examples serve to illustrate some typical multislice results and also provide a more detailed description of using the multislice method.

A prerequisite for image simulation is a detailed description of the coordinates of the atoms in the specimen. The two-volume set of Wyckoff [539] is a good starting point for many common materials with a crystalline structure. The books by Megaw [342] and Vainshtein et al. [498, 499] give a thorough discussion of crystal structure. There are also numerous journal articles (see, for example, the journal *Acta Cryst.*) and web sites with crystal structure information. For example, the Crystallography Open Database (www.crystallography.net) and the Protein Data Bank or PDB (www.rcsb.org) [30], and the Electron Microscopy Data Bank (www.ebi.ac.uk/pdbe/emdb) for biological structure information using cryo-EM.

7.1 Gallium Arsenide

Gallium arsenide (GaAs) is a relatively simple structure similar to that of silicon (the diamond structure) except that adjacent atoms alternate between gallium and arsenic in the zinc sulfide (or zincblende) structure. The cubic lattice constant is slightly bigger (5.65 Å) than that of silicon (5.43 Å) so that it may be slightly easier to image in the electron microscope. However the atoms in GaAs are significantly heavier (atomic number $Z = 31$ and 33 for Ga and As, respectively) and scatter more strongly than silicon ($Z = 14$). GaAs may be expected to have more dynamical scattering than silicon, so a simple phase grating calculation (as in Chap. 5) may not be sufficient. This is a good place to start testing the multislice

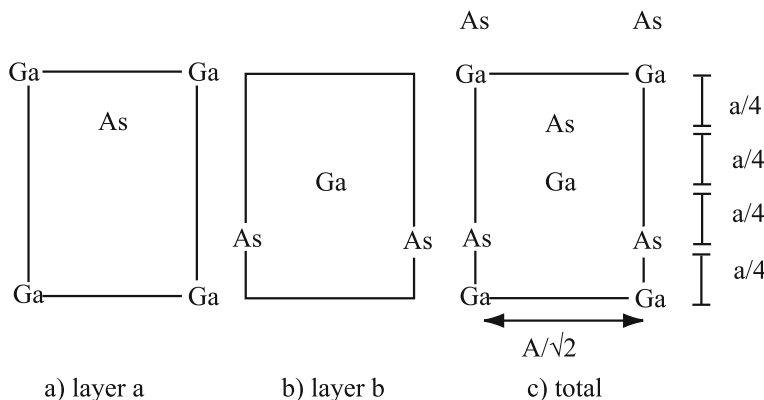


Fig. 7.1 The structure of gallium arsenide (GaAs) projected along the $\bar{1}\bar{1}0$ direction. GaAs has a zincblende structure with a cubic lattice constant of $a_{GA} = 5.65 \text{ \AA}$. (a) and (b) are two different atomic layers suitable for use in a multislice calculation and (c) is the projection of whole specimen. The layers are stacked in the sequence $ababa \dots$. Each layer is 1.998 \AA thick (along z or the optic axis) and $3.995 \times 5.65 \text{ \AA}$ in x and y (in the plane of the paper)

method because this specimen may produce significant dynamical scattering but is relatively simple to describe.

In the $\bar{1}\bar{1}0$ projection GaAs has a projected structure as shown in Fig. 7.1. The main difference between silicon (Fig. 5.15) and GaAs is that there are two different types of atoms (Ga and As). In the $\bar{1}\bar{1}0$ projection, GaAs naturally divides into two different layers (labeled a and b in Fig. 7.1). The layers are stacked in the sequence $ababa \dots$ with a spacing along the z axis (optic axis) of $\sqrt{2}a_{GA}/4 = 1.9976 \text{ \AA}$. Silicon can be divided in the same manner if the Ga and As atoms are replaced with Si and the lattice constant is changed. It is best to use these two layers as the slices in the multislice method. The thickness is small enough to get an accurate answer (which is usually the case for the natural layers in a small unit cell crystal) and using the natural layers of the specimen will ensure that the multislice simulation correctly reproduces the HOLZ (or upper layer lines) portion of the diffraction patterns. Although the HOLZ lines may not contribute directly to a BF CTEM phase image of a thin specimen, getting the HOLZ lines correct is frequently required for an accurate simulation of thick specimens in BF (to get the phase of the low order reflections correct) and is usually required for ADF-STEM images because the ADF detector collects large scattering angles (where the HOLZ lines are). The actual atomic coordinates for each layer are shown in Table 7.1.

Table 7.1 The normalized coordinates for two layers in one projected unit cell of the (110) projection of GaAs. The two-dimensional unit cell dimensions are $a_0 \times b_0$ where $a_0 = a_{GA}/\sqrt{2} = 3.995 \text{ \AA}$ and $b_0 = a_{GA} = 5.65 \text{ \AA}$. a_{GA} is the cubic lattice constant of GaAs

Atom	Layer	x/a_0	y/b_0
Ga	a	0	0
As	a	0.5	0.75
As	b	0	0.25
Ga	b	0.5	0.5

7.1.1 BF-CTEM Simulation

Once the structure of the specimen has been determined and a convenient way of layering or slicing the specimen has been identified, the next step is to find the correct sampling for the simulation. The general guidelines for simulating thin specimens (Table 5.4) are a good starting point. Dynamical scattering in a thick specimen will also introduce further constraints on the sampling. The easiest way to discover these sampling requirements is to simply try a range of super cell sizes with different numbers of pixels. A sequence of trial multislice runs (using an incident plane wave) is shown in Table 7.2 for two different thicknesses of 110 GaAs. The super cell sizes were chosen to yield a reciprocal space sampling size of about 1 mrad at 200 keV to get adequate sampling inside the objective aperture. The columns labeled “Intensity” refer to the total integrated intensity in the final electron wave function at the exit surface of the specimen. As discussed in Sect. 6.10.2 the integrated intensity should remain constant at unity if there is adequate sampling. Typically this value will decrease with thickness but should not go below about 0.90 for a reasonable simulation, and a value of 0.95 or higher is typical for a good simulation. Table 7.2 shows that this simulation probably needs about 512×512 pixels (or more) to simulate a thickness of 200 Å.

The magnitude $|\psi(x, y)|$ of the electron wave function $\psi(x, y)$ after passing through a thickness of 10(ab) and 50(ab) layers (40 and 200 Å) is shown in Fig. 7.2. An ideal perfect microscope with amplitude contrast would produce an image similar to that in Fig. 7.2. A phase grating calculation (as in Chap. 5) would yield identically $|\psi(x, y)| = 1$ across the whole area because it approximates the transmission process as a pure phase shift. Figure 7.2 illustrates that the specimen is not a pure phase object. The electron intensity accumulates near the atom sites (a white spot in Fig. 7.2). The imaging electrons see a large positive charge at the atom nucleus that is screened by the bound electrons of the atom. Far away from the atom the imaging electrons (at 200 keV in this example) do not see any net charge (for neutral atoms the positive charge on the nucleus equals the number of negatively charged bound electrons), but near the nucleus the imaging electrons see the large positive charge on the nucleus and are attracted to the center of the atoms in the specimen. The imaging electrons effectively get channeled into the atomic

Table 7.2 The effects of sampling on a multislice calculation of 110 GaAs

Unit cells	Size (in Å)	Number of pixels	Max angle (mrad)	Intensity at 10(ab)	Intensity at 50(ab)
$5a_0 \times 3b_0$	19.98×16.95	128×128	53.6	0.969	0.821
		256×256	107.1	0.987	0.906
		512×512	214.3	0.997	0.978
$6a_0 \times 4b_0$	23.97×22.2	128×128	44.6	0.964	0.802
		256×256	89.3	0.980	0.871
		512×512	178.6	0.995	0.967
$7a_0 \times 5b_0$	27.97×28.25	128×128	37.9	0.967	0.812
		256×256	75.8	0.975	0.849
		512×512	151.5	0.993	0.951
$8a_0 \times 6b_0$	31.96×33.9	128×128	31.6	0.969	0.807
		256×256	63.1	0.972	0.834
		512×512	126.3	0.991	0.938
		1024×1024	252.5	0.998	0.982

The two-dimensional unit cell dimensions are $a_0 = a_{GA}/\sqrt{2} = 3.995 \text{ \AA}$ and $b_0 = a_{GA} = 5.65 \text{ \AA}$. a_{GA} is the cubic lattice constant for GaAs. 10(ab) means that there are 10 repeats of both the a and b layers (about 40 Å thick). 50(ab) results in a thickness of about 200 Å.

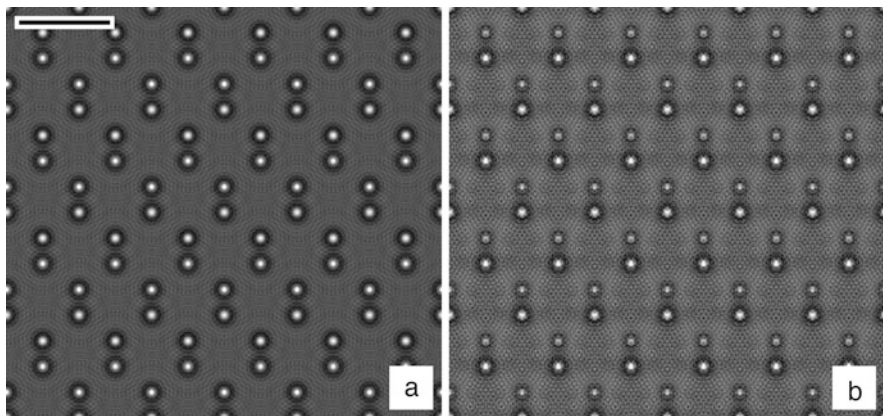
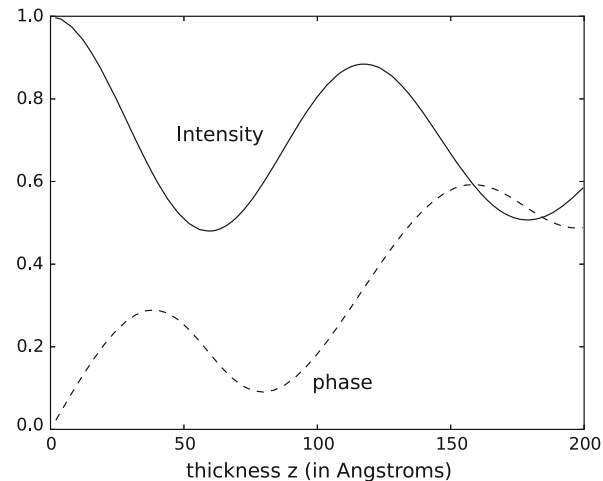


Fig. 7.2 The magnitude of the electron wave function $|\psi(x, y)|$ (in real space) after passing through (a) 40 Å and (b) 200 Å of 110 GaAs at an electron energy of 200 keV. The super cell size is $6a_0 \times 4b_0$ with 512×512 pixels. The scale bar in (a) is 5 Å. The numerical range of each image is (a) 0.18–3.70 and (b) 0.01–3.30 (white is a larger positive number)

columns in the specimen. The black ring surrounding each atom site is a depletion of electron intensity.

Channeling is not a static process either. As the imaging electrons progress further through the specimen, they may be scattered out of the atomic column as well. Figure 7.2b shows this effect. The As atoms have a slightly larger positive charge on the nucleus. The white spot at the As sites is less bright than the white

Fig. 7.3 The intensity and phase of the $k_x = k_y = 0$ Fourier coefficient of the 200 keV electron wave function as it passes through the 110 projection of GaAs. The super cell size is $6a_0 \times 4b_0$ with 512×512 pixels



spot at the Ga sites indicating that the imaging electrons are diminishing in intensity at the As sites. This is a dynamical scattering effect. The relative intensities of the channeling peaks on the Ga and As sites will likely oscillate with thickness. There is a faint structure in the magnitude of the electron wave function that looks like standing waves between the atom sites. This occurs when the HOLZ lines appear and it is not always clear whether this is the real space manifestation of the HOLZ lines or simply a sampling error.

Figure 7.3 shows the intensity and phase of the $k_x = k_y = 0$ Fourier coefficient (or zero order beam) of the wave function of the electron as it is passing through the specimen. Both the intensity and the phase oscillate with depth, clearly indicating the dynamical nature of the scattering process. All of the nonzero Fourier coefficients or beams will oscillate with depth, although with a different period. The period of oscillation is referred to as the extinction depth for the particular beam (or Fourier coefficient). The dynamical nature of the scattering process is completely lacking in a phase grating calculation (as in Chap. 5) and the multislice calculation (or equivalently a Bloch wave calculation) is required to correctly simulate strongly scattering specimen (more than about 10–20 Å in the case of 110 GaAs).

The simulated bright field (BF) phase contrast image is shown in Fig. 7.4 for various thickness of the specimen. Scherzer conditions were used for the defocus and partial coherence was approximately included using the transmission cross coefficient (Sect. 5.4.3). Figure 7.4a is for two layers of the specimen and is approximately the same as a phase grating calculation. Each pair of atoms (Ga and As) in the dumbbell appears as a black ellipse. Figure 7.4b is for a slightly thicker crystal. The relative phases of the Fourier coefficients have already changed significantly. Some features that should be white are black and vice versa. The image has a lot of artifacts. These artifacts can vary dramatically with small changes in defocus and the size of the objective aperture. Figure 7.4c is a thick crystal. Although the overall periodicity is again correct there has been a contrast reversal.

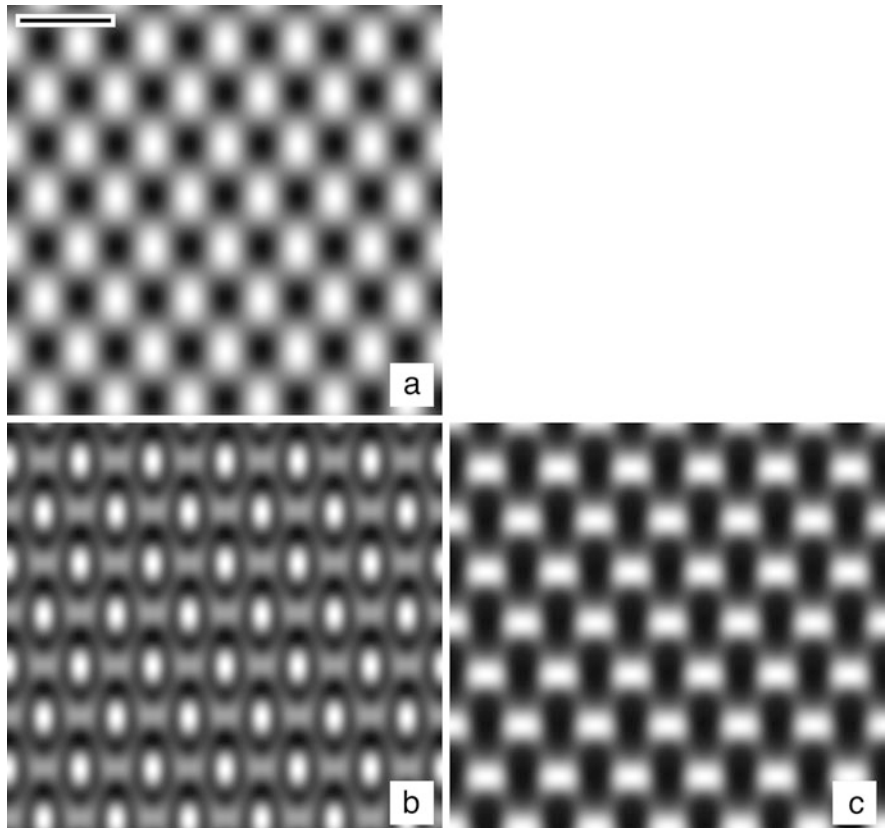


Fig. 7.4 Calculated bright field phase contrast images for different thickness of 110 GaAs at 200 keV. $C_s = 0.7$ mm, $\Delta f = 513$ Å, obj. apert. 14 mrad, with partial coherence (1 mrad spread in illumination and 100 Å defocus spread). (a) 4 Å(2 layers), (b) 40 Å(20 layers), and (c) 200 Å(100 layers). The super cell size is $6a_0 \times 4b_0$ with 512×512 pixels. The range of each image is (a) 0.90–1.05, (b) 0.57–1.20, (c) 0.35–1.43 (white is a larger positive number). The scale bar in (a) is 5 Å

This illustrates why image simulation is necessary to interpret a high-resolution phase contrast image.

7.1.2 ADF-STEM Simulation

The annular dark field (ADF) STEM image is a small signal (compared to phase contrast BF) and directly involves high angle scattering. Both of these effects are more difficult to calculate and an ADF-STEM image simulation requires more attention to the accuracy and tolerance of the calculation (i.e., sampling

requirements). Finding the super cell size and number of pixels to achieve a total integrated intensity of nearly unity (as in Table 7.2) is the first requirement. It is also a good idea to test the accuracy more directly. This is conveniently done by comparing two different simulations with slightly different sampling. If the sampling is adequate, then there should be no difference between using $N_x \times N_y$ pixels and $2N_x \times 2N_y$ pixels with a similar real space super cell size. There are two different sampling requirements that should be tested. The pixel size (and number of pixels) in both real space and reciprocal space is important. The number of pixels is restricted to powers of two (for the most efficient FFT) so the two simulations must differ by a factor of two in the number of pixels. If the real space super cell size were left the same, then the sampling in real space (Δx and Δy) would double; however, the pixel size in Fourier or reciprocal space ($\Delta k_x = 1/a$ and $\Delta k_y = 1/b$) would remain the same. To vary both at the same time the super cell size should be increased by about a factor of $\sqrt{2}$ (within the constraints of the specimen periodicity) to get approximately the same reduction in the pixel size in both real space and reciprocal space.

Figure 7.5 shows a comparison between two different simulations with different sampling sizes on the 110 projection of GaAs. This is only a test of the sampling, so a full image simulation is not necessary. An ADF-STEM multislice simulation requires a full multislice calculation for each position of the scanned probe which can require a lot of computer time. A simple one-dimensional line scan through an appropriate feature of the specimen is usually sufficient to test the sampling, but requires substantially less computer time. Figure 7.5 shows a scan through adjacent Ga and As atoms along the direction of their closest position (vertical in Fig. 7.1). The low resolution simulation had a super cell size of $6a_0 \times 4b_0$ with 512×512 pixels and the high-resolution simulation had a super cell size of $8a_0 \times 6b_0$ with 1024×1024 pixels. There is a good agreement between the two curves so this sampling is probably adequate for performing the simulation. The difference between the two curves can also serve as an estimate of the sampling error in the simulation. The As atom is slightly heavier ($Z = 33$) than the Ga atom ($Z = 31$) so the peak on the As position is slightly higher (stronger scattering at the As position). Also, there is a slight peak in between the main dumbbells (at about $y = 3.5 \text{ \AA}$ in Fig. 7.5). This is caused by the tails of the probe (compare to Fig. 3.13).

Figure 7.6 shows the magnitude of the electron wave function $|\psi(x, y)|$ of the focused probe as it is passing through the specimen. The probe was positioned at an offset of $(8 \text{ \AA}, 10 \text{ \AA})$ with $(0, 0)$ being in the lower left corner of the image. Although the initial probe is smooth and round the atomic columns of the specimen again attract the imaging electron which get channelled into the atomic columns. After a thickness of 200 \AA (Fig. 7.6b) the electron distribution in the probe can get fairly distorted by the specimen.

The actual (simulated) ADF-STEM images calculated using the multislice method are shown in Fig. 7.7. These images require a multislice calculation for each point (or pixel) in the image. To save computer time only 32×32 pixels

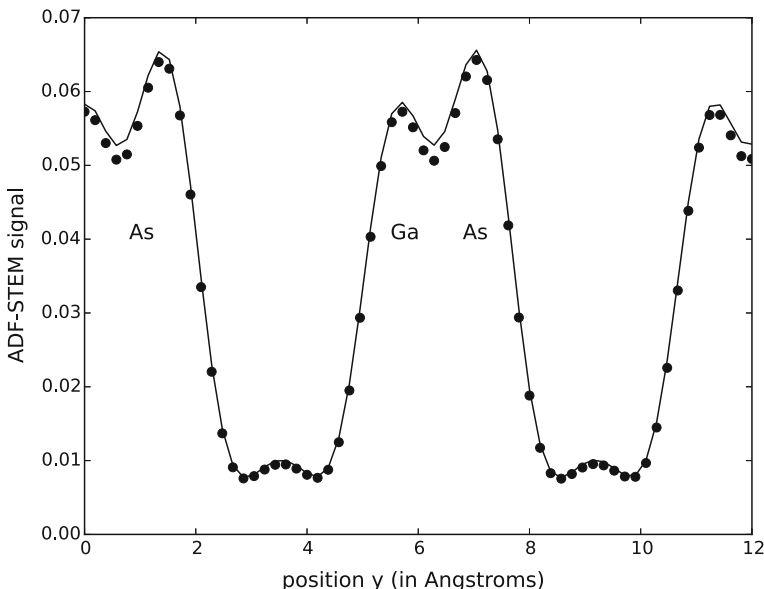


Fig. 7.5 Sampling test for ADF-STEM of 110 GaAs (40 Å thick) at an electron energy of 200 keV. The curve shows the ADF signal in a vertical line through pairs of Ga and As atoms. The optical parameters were $C_s = 0.7$ mm, $\Delta f = 365$ Å, with an objective aperture of 10.37 mrad (optimum conditions). The ADF detector covered 40–175 mrad. The solid curve is for a super cell size of $8a_0 \times 6b_0$ with 1024×1024 pixels and the circles are for a super cell size of $6a_0 \times 4b_0$ with 512×512 pixels. The agreement between the two curves indicates that the sampling is sufficient

in one unit cell were calculated, and the unit cell was duplicated to fill the same area as the BF-CTEM simulation (Fig. 7.4). The specimen potential and electron wave function were each sampled with 512×512 pixels. The effective extinction distance for scattering to high angles (as on the ADF detector) is much larger than that for low angle scattering, which makes the ADF-STEM image much less sensitive to specimen thickness in the way that BF phase contrast is (compare to Fig. 7.4). The atomic columns are imaged as white in both the 40 Å (Fig. 7.7a) and 200 Å (Fig. 7.7b) images. The dumbbells are nearly resolved in these images. The magnitude of the ADF signal increases with thickness but there is not a contrast reversal as there was in BF phase contrast. The price paid for this improvement in image interpretation is a much smaller overall signal.

7.1.3 *Channeling*

When the specimen is aligned along a major zone axis columns of atoms line up in a row along the optic axis. This is usually desirable because the atom columns may be imaged in their corresponding atomic location (in the 2D projection). As the

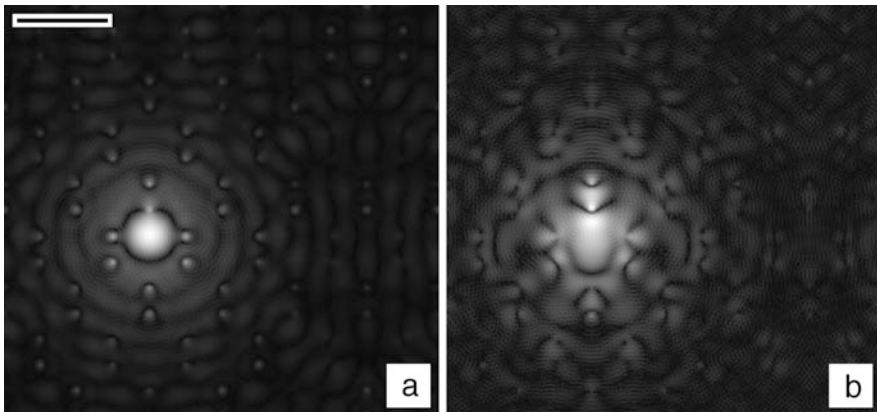


Fig. 7.6 The calculated intensity distribution in the electron probe as it passes through 110 GaAs at an electron energy of 200 keV. (a) 40 Å thick and (b) 200 Å thick. The optical parameters were $C_s = 0.7$ mm, $\Delta f = 365$ Å, with an objective aperture of 10.37 mrad (optimum conditions). The super cell size had dimensions of $6a_0 \times 4b_0$ with 512×512 pixels. The range of each image is (a) 0.0–15.7, (b) 0.0–11.2 (white is a larger positive number). The scale bar in (a) is 5 Å

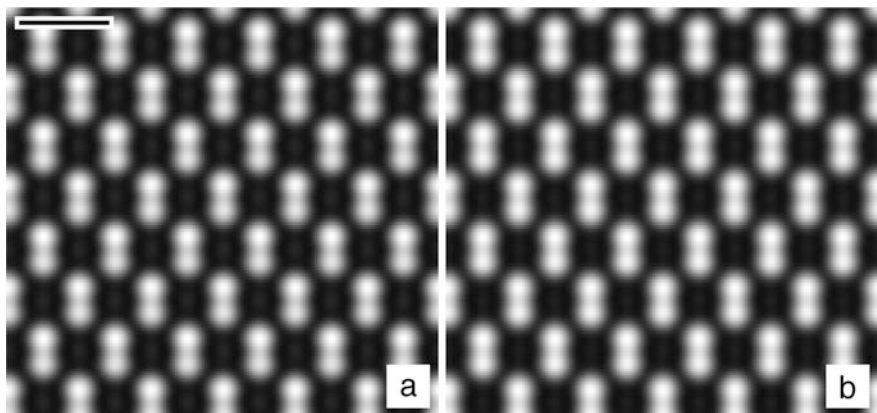


Fig. 7.7 Calculated ADF-STEM images of 110 GaAs at an electron energy of 200 keV for a thickness of (a) 40 Å and (b) 200 Å. The optical parameters were $C_s = 0.7$ mm, $\Delta f = 365$ Å, with an objective aperture of 10.37 mrad (optimum conditions). The specimen super cell size had dimensions of $6a_0 \times 4b_0$ with 512×512 pixels. The image was calculated as 32×32 pixels (in one unit cell) and periodically replicated to 192×128 pixels for display. Black is (a) 0.0053, (b) 0.021 and white is (a) 0.065, (b) 0.179, where the total incident beam current is one. The scale bar in (a) is 5 Å

electrons travel through the specimen they tend to channel along these atomic columns in a process called channeling as is already evident in Figs. 7.2 and 7.6. This name can also apply to ion scattering in which the ions travel through the hollow space between atomic columns. Electrons are negatively charged and are attracted to the positive charge on the nucleus, so they tend to get pulled into

the atomic columns and channel down a narrow channel that can be very small. The channeling width can be smaller than the outer electron shell in the atom and have a significant effect on low loss EELS (electron energy loss spectroscopy) signals (Kirkland [274]).

One advantage of a simulation is the ability to display signals that are not normally accessible in a real experiment. Figure 7.8a shows the electron intensity along a row of atom pairs in 110 GaAs versus depth in the specimen (vertical direction) in an y, z plane (along a vertical line in Fig. 7.7) for an incident plane wave. An incident uniform plane wave is incident at the bottom of the image and exists the specimen at the top of the image (the electron wave is traveling up in this particular image). The channeling peak intensity increases significantly about half way through this specimen and then spreads out again as it travels further through the specimen. Channeling will oscillate with specimen thickness. The channeling peak will form (or oscillate) quicker with heavier atoms (and atom density along the beam) and lower electron energy. This particular example was chosen to reasonably fit on the page (low energy so it oscillates in a short distance). Channeling occurs in both fixed beam (CTEM) and scanned probe (STEM).

Figure 7.8b shows the channeling for an incident aberration correct probe placed in between atom pairs. The probe slowly gets pulled onto the atom columns as it passes through the specimen. Figure 7.8c is the same as (b) but with a saturated gray scale to bring out the low intensity portion of the image. If the atomic columns are close enough, the channeling peak may oscillate between adjacent columns with thickness (Hovden et al. [213]).

Channeling is sometimes an annoyance, but can be used to advantage. If the specimen (substrate) thickness is chosen so that the channeling peak is sharp and intense at the exist surface any atoms deposited on the exit surface will be strongly imaged only if they are on atomic columns but not in between, which may help distinguish where these atoms are.

In the Bloch wave picture, the electron eigenfunctions (or eigenvectors) have a high density near the atomic columns. In a two-dimensional plane perpendicular to the beam direction the electrons appear as states loosely bound to the atomic columns much like the lower energy atomic electrons are bound to the nucleus (but in this case the high energy beam electrons are bound to the screened nucleus). These states can be identified using atomic quantum numbers 1s, 2p, etc. (Kambe et al. [252] and Buxton et al. [53]) with similar symmetry. These eigenfunctions indicate a preference for propagation along the atomic columns (channeling). Pennycook and Jesson [399] were able to develop an intuitive understanding of ADF-STEM imaging based on the s-state eigenstates for well separated atomic columns. Anstiss et al. [17, 18] have shown that more states are needed for high resolution if the atomic columns are close. An atomic sized probe (with aberration corrector) placed on one atomic columns with another atomic column close by may oscillate between columns as it propagated through the specimen.

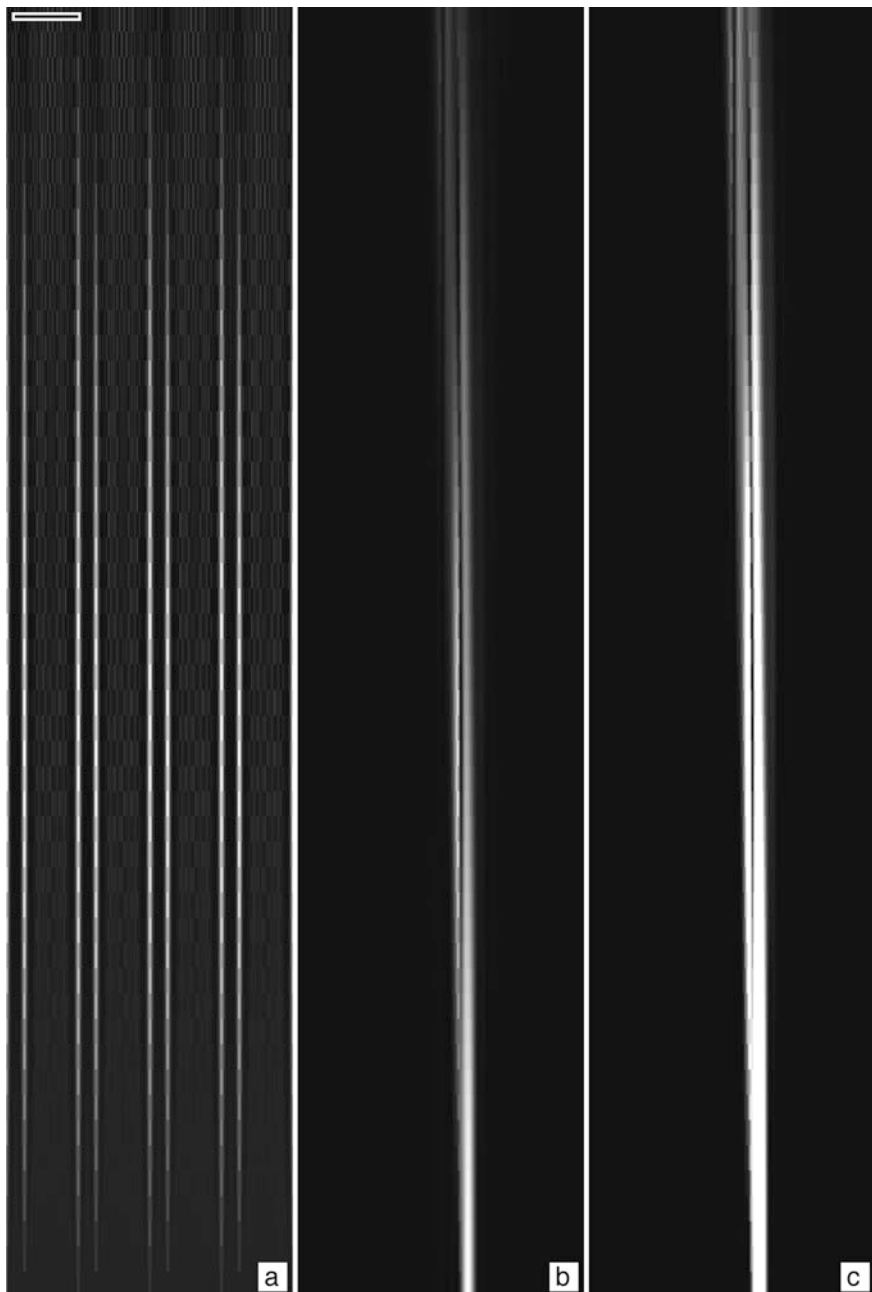


Fig. 7.8 Calculated electron intensity in 110 GaAs at an electron energy of 100 keV. (a) Plane wave incident. (b) Aberration-corrected probe in between atom pairs ($C_{S3} = C_{S5} = \Delta f = 0$, objective aperture of 25 mrad). (c) Same as (b) but with smaller gray scale range to bring out the low intensity portion of the image (at top). The specimen super cell size had dimensions of $6a_0 \times 4b_0$ with 512×512 pixels. The total thickness (bottom to top) was 100 Å and the scale bar in (a) is 5 Å

7.2 Silicon Nitride

Silicon nitride (specifically the β phase, $\beta\text{-Si}_3\text{N}_4$) has a hexagonal unit cell (Wyckoff [539]) as shown in Fig. 7.9. Each side of the unit cell is 7.606 Å and there are two layers with a total repeat length of 2.909 Å (perpendicular to the plane of the paper in Fig. 7.9). The hexagonal unit cell contains 14 atoms (6 silicon atoms and 8 nitrogen atoms).

Silicon nitride is an example of a more complicated unit cell that does not have rectangular symmetry. The multislice method of image simulation is most efficient when the FFT is used and the FFT is separable in x and y . This means that an FFT version of the multislice method works best with a rectangular unit cell. To calculate this specimen it is best to find a larger unit cell with rectangular symmetry. One possible choice is shown in Fig. 7.10. The rectangular unit cell contains 28 atoms (12 silicon atoms and 16 nitrogen atoms). This particular specimen is easy to redefine a larger rectangular unit cell but an arbitrary specimen may be more difficult to describe this way. However this step is required when using a multislice implementation using the FFT (required for an efficient calculation). Each specimen may require a different strategy to generate an equivalent rectangular unit cell.

Figure 7.11 shows the electron wave function after passing through about 50 Å of the specimen. The magnitude in (a) again shows that the electrons are attracted to the positively charged atomic nuclei and the specimen is not a pure phase object. The exit wave function, shown in (b) and (c) has both a strong real part and strong imaginary part. The complex transfer function of the objective lens can mix these two components in rather nonintuitive ways.

Figure 7.12 shows a calculated defocus series of silicon nitride with a thickness of 49.5 Å (stacking sequence 17(ab)). The specimen was modeled as two layers with a stacking sequence of $ababa\dots$. The wave function and potentials were sampled with 256×256 pixels with a size of 38.03×39.52 Å or $5a_0 \times 3b_0$ using the rectangular unit cell defined in Fig. 7.10 (maximum scattering angle of 54 mrad). Partial coherence was modeled using the transmission cross coefficient (see Sect. 5.4.3). The positions of the silicon atoms are initially black in Fig. 7.12a

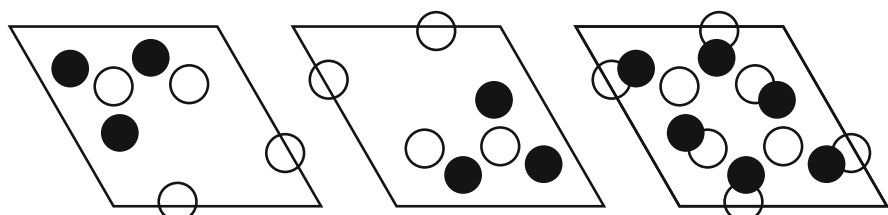


Fig. 7.9 The 001 projection of the hexagonal primitive unit cell of silicon nitride ($\beta\text{-Si}_3\text{N}_4$). The open circles are the positions of the nitrogen atoms and the filled circles are the positions of the silicon atoms. The a layer is on the left, the b layer is in the middle, and the total projection is on the right. The solid line indicates the unit cell boundaries. The side of the unit cell is 7.606 Å

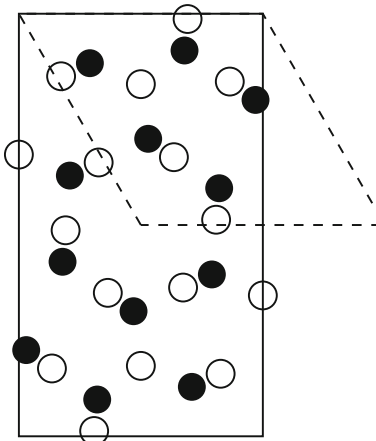


Fig. 7.10 The unit cell of silicon nitride ($\beta\text{-Si}_3\text{N}_4$) expanded to fill a rectangular area suitable for simulating using the multislice method with rectangular FFTs. The open circles are the positions of the nitrogen atoms and the filled circles are the positions of the silicon atoms. The position of the primitive hexagonal unit cell is shown as a dashed line. The unit cell has dimensions of $a_0 = 7.606 \text{ \AA}$, and $b_0 = 13.174 \text{ \AA}$. There are two layers each with a thickness of 1.4545 \AA

but reverse contrast as the defocus is changed, becoming white in Fig. 7.12b, c. Figure 7.13 shows the Scherzer focus image for two different thicknesses of the specimen. The apparent contrast of the silicon atom positions has reversed (black has become white). The sign of the contrast will change periodically with defocus for a given thickness and also periodically with thickness for a given defocus, making image interpretation very difficult. Image simulation is one means of sorting out what is going on in the image.

An aberration-corrected instrument will be corrected to some maximum angle or to some maximum order of aberration (or combination of these). The corrector will add a large negative C_{S3} to balance a large positive C_{S3} from the round objective lens. If the corrector is good to third order there will still be fifth order aberrations (C_{S5} plus all of the parasitic aberrations), which may be minimized to some extent. Just as Scherzer used a lower order aberration (defocus) to partially compensate for the higher order C_{S3} aberration, the fifth order aberrations can be partially offset by the third order aberrations. For simplicity assume that all of the parasitic aberrations ($m \neq 0$) like C_{32} , etc. have been corrected to zero through fifth order. Phase contrast in BF-CTEM and BF-STEM actually require significant amounts of the three $m = 0$ aberrations ($C_{10} = -\Delta f$, $C_{30} = C_{S3}$, and $C_{50} = C_{S5}$) with alternating signs to produce a $\pi/2$ phase plate in the outer regions of the objective aperture to interfere with the unshifted beam in the center of the objective aperture (see Fig. 3.4). A third or higher order corrector should be able to drive the total third order spherical aberration ($C_{S3} = C_{30}$) negative to partially offset a positive fifth order spherical aberration ($C_{S5} = C_{50}$). Similar pairs can be found in most of the parasitic ($m \neq 0$) aberrations (left out from this discussion for simplicity). For

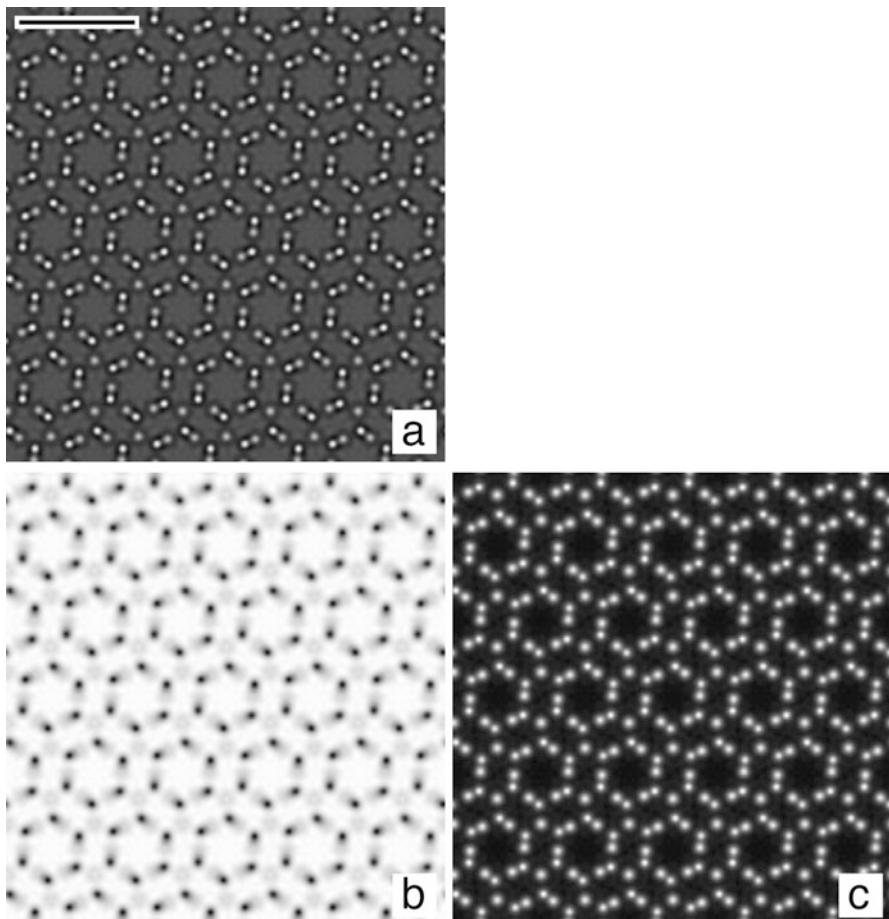


Fig. 7.11 The 200 keV electron wave function after passing through 49.5 Å of 001 silicon nitride (β -Si₃N₄). (a) Magnitude $|\psi(x, y)|$ (b) real part of $\psi(x, y)$ and (c) imaginary part of $\psi(x, y)$. The area of each image corresponds to 5×3 unit cells of the type shown in Fig. 7.10. The numerical range of each image is (a) 0.43–2.84, (b) –1.93–1.04 and (c) 0.01–2.27 (white is a larger positive number). The scale bar in (a) is 10 Å

example, if $C_{S5} = 50$ mm is present at 200 kV, then making third order spherical $C_{S3} = -0.059$ mm and defocus $\Delta f = -C_{10} = -136$ Å allows the transfer function to go out to better than 1 Å (35 mrad) as in Fig. 3.4.

Figure 7.14 shows Si₃N₄ calculated for an aberration-corrected BF-CTEM with three different thickness using 512 by 512 pixels (maximum angle 108 mrad) and a slice thickness of 1.4545 Å. The corrector is assumed to be good to fifth order out to an angle of 35 mrad. Figure 7.14a is very thin (may not be possible in practice) and yields a good representation of the actual specimen structure. As the specimen gets thicker there is only a small change in the image. The atoms mostly stay white.

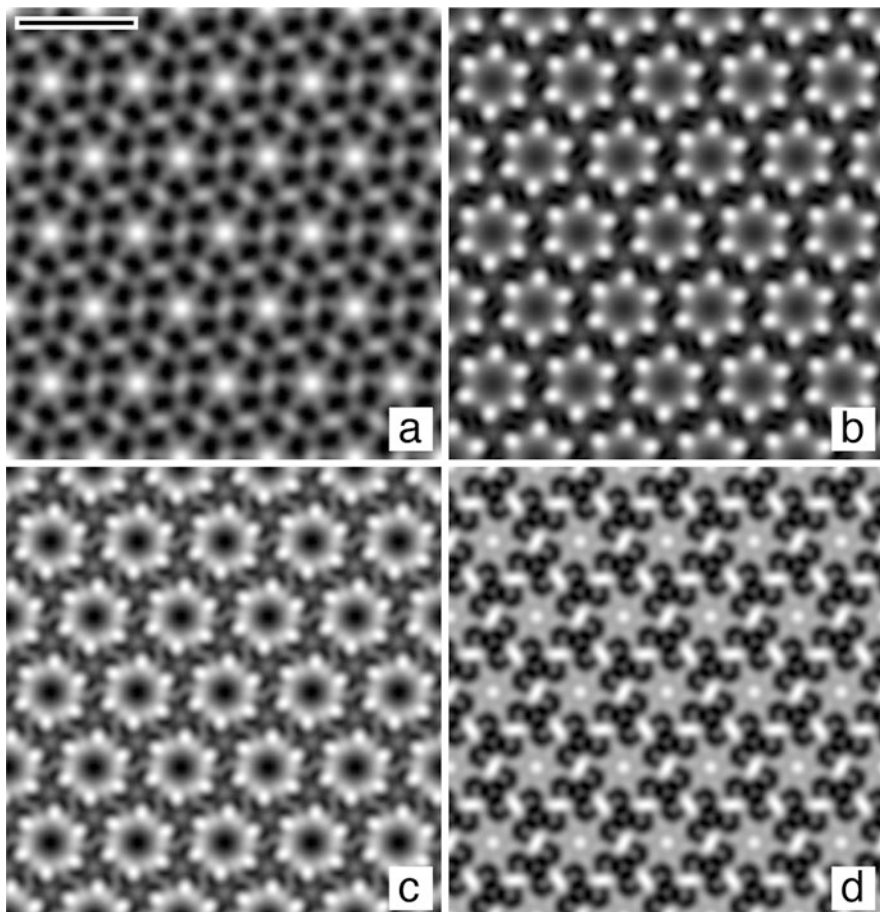


Fig. 7.12 Calculated CTEM defocus series of 001 silicon nitride ($\beta\text{-Si}_3\text{N}_4$), 49.5 Å thick at a beam energy of 200 keV ($C_s = 1.3$ mm, obj. apert. = 12 mrad, condenc. apert = 0.75 mrad, defocus spread = 100 Å). The defocus values are (a) 700 Å (Scherzer focus), (b) 900 Å, (c) 1100 Å and (d) 1300 Å. The scale bar in (a) is 10 Å. The area of each image corresponds to 5×3 unit cells of the type shown in Fig. 7.10. Silicon atom positions appear black in (a)

At this high resolution the depth of focus is only about 30 Å (approximately the resolution divided by the angle), which is less than the specimen thickness. In this calculation defocus is referred to the exit surface. It's not clear which plane is the optimum in this situation. Depth of focus becomes a significant problem as resolution increases. Jia et al. [246], Tillmann et al. [492] and Urban [497] have discussed other possible uses for negative C_{S3} .

Figure 7.15 shows a simulated ADF-STEM defocus series of silicon nitride under similar conditions to that in Fig. 7.12 except that the objective aperture was fixed at 10.37 mrad consistent with Scherzer conditions for a focused probe. The super cell

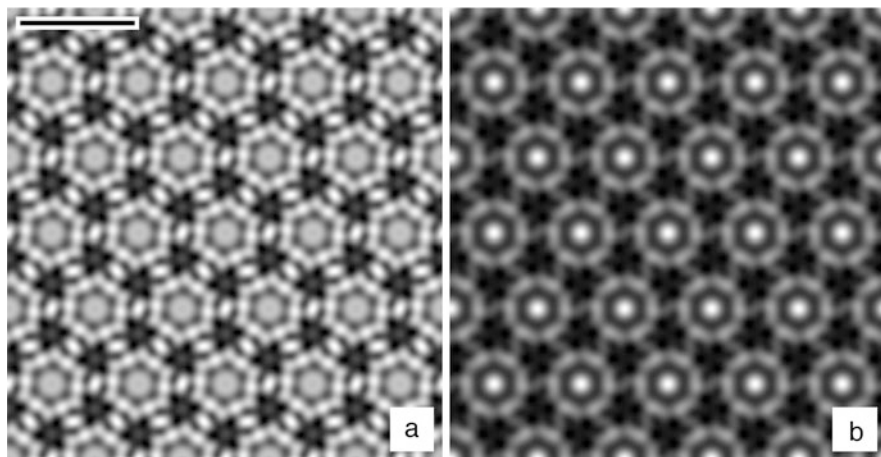


Fig. 7.13 Calculated CTEM images for two different thickness of 001 silicon nitride (β -Si₃N₄), at a beam energy of 200 keV (defocus of 700 Å, $C_s = 1.3$ mm, obj. apert. = 12 mrad, condenc. apert. = 0.75 mrad, defocus spread = 100 Å). The specimen thickness was (a) 102 Å (35(ab) layers), and (b) 151 Å (52(ab) layers) The scale bar in (a) is 10 Å. The area of each image corresponds to 5 × 3 unit cells of the type shown in Fig. 7.10

size was $4a_0 \times 2b_0$ (or 30.4×26.3 Å) with 512×512 pixels to allow a maximum scattering angle of 140 mrad (increased from the CTEM case in Fig. 7.12). The electron wave function was also sampled with 512×512 pixels. To save computer time only the image in one rectangular unit cell was calculated with 32×64 pixels and replicated to fill the same area Fig. 7.12 for comparison. The silicon atom columns appear as white dots in Fig. 7.15a and do not reverse contrast unlike the BF phase contrast image, however there are still significant artifacts in the image that appear as the defocus is increased from Scherzer defocus ($\Delta f = 700$ Å). The artifacts are consistent with the tails of the probe. ADF-STEM is less sensitive to changes in defocus (than BF phase contrast) but there are still significant artifacts produced when defocus is changed. Figures 7.12 and 7.15 clearly indicate that the interpretation of a high-resolution image is not always straightforward in either BF-CTEM or ADF-STEM. Image simulation is one approach to verify that the image is interpreted correctly.

7.3 Two-Dimensional Materials (MoS₂)

MoS₂ is a member of the family of transition metal dichalcogenides (TMD). In a bulk sample it is composed of thin layers stacked on top of each other with a large separation distance. Each layer is only 2 or three atoms thick and can exist as a separate nearly 2D structure. There has been some interest in using this material for

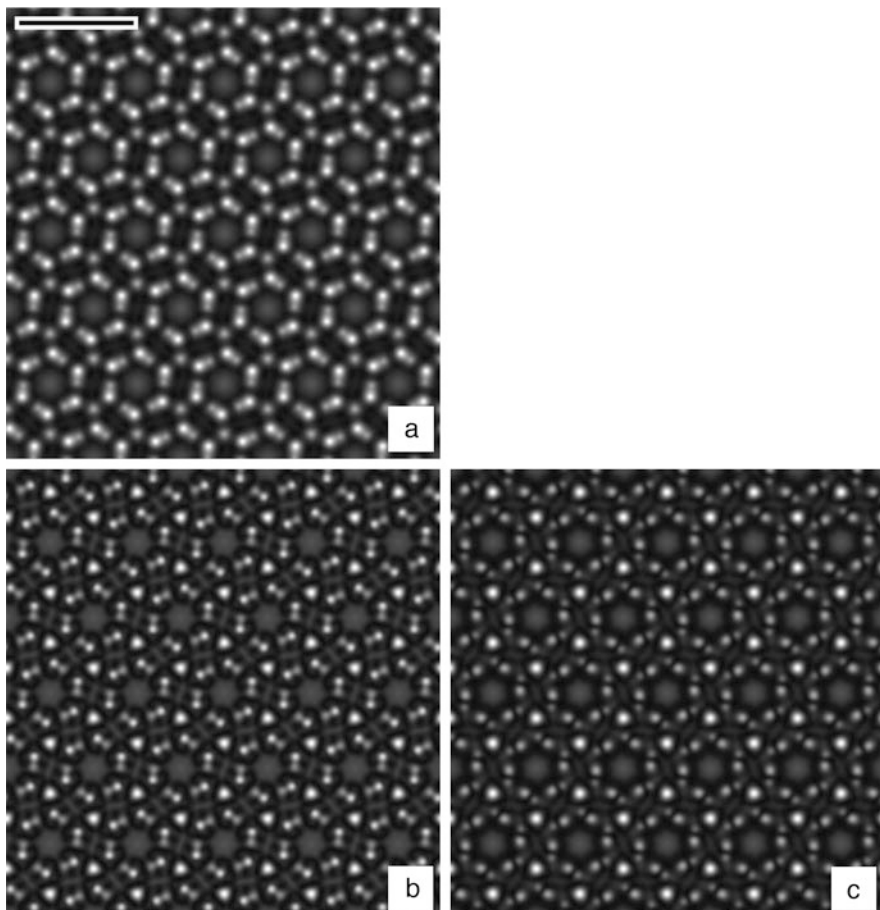


Fig. 7.14 Calculated aberration-corrected BF-CTEM images for three different thickness of 001 silicon nitride ($\beta\text{-Si}_3\text{N}_4$), at a beam energy of 200 keV (defocus of -136 \AA , $C_{S3} = -0.059 \text{ mm}$, $C_{S5} = 50 \text{ mm}$, obj. apert. = 35 mrad, defocus spread = 20 \AA). The specimen thickness was (a) 23 \AA , (b) 102 \AA , and (c) 151 \AA . The scale bar in (a) is 10 \AA . The area of each image corresponds to 5×3 unit cells of the type shown in Fig. 7.10. All other aberrations assumed to be zero

2D electronic devices (for example, Li et al. [313]), and imaging these 2D materials in the electron microscope may also be of interest.

The S atoms in MoS_2 (the 2H lattice) form a basic hexagonal crystal (unit cell $a = b = 3.161 \text{ \AA}$, $c = 12.295 \text{ \AA}$, $\alpha = \beta = 90^\circ$, $\gamma = 120^\circ$) with a single Mo atom near the center of each triangle (position $(2/3, 1/3, 0)$) as described by Schönfeld et al. [449]. There are two layers of S atoms, above and below the layer of Mo atoms ($\pm 0.127c$). This unit cell is not suitable for easy calculation but can be converted into a rectangular unit cell by combining approximately two hexagonal unit cells. The resulting atomic coordinates are listed in Table 7.3. A drawing of

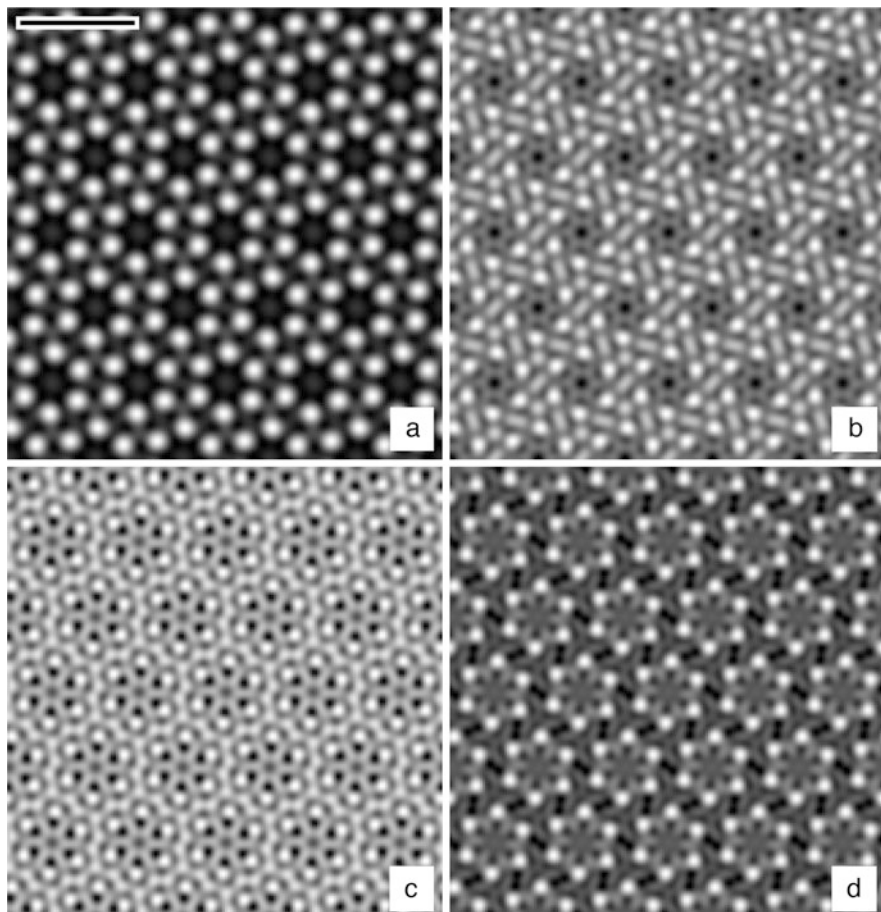


Fig. 7.15 Calculated ADF-STEM defocus series of 001 silicon nitride ($\beta\text{-Si}_3\text{N}_4$), 49.5 Å thick at a beam energy of 200 keV ($C_s = 1.3$ mm, obj. apert. = 10.37 mrad). The defocus values are (a) 700 Å (Scherzer focus), (b) 900 Å, (c) 1100 Å and (d) 1300 Å. The scale bar in (a) is 10 Å. The area of each image corresponds to 5×3 unit cells of the type shown in Fig. 7.10. Silicon atom positions appear white in (a)

the structure projected along the c axis (along the z direction or the optic axis in the microscope) is shown in Fig. 7.16 with one rectangular unit cell outlined in the upper left. The basic hexagonal unit cells may also be combined into a sequence of open hexagonal structures outlined in the lower left (not the same as a single hexagonal unit cell).

A single layer of this specimen is fairly well described by the simple incoherent images model (Eq. 3.70) because the specimen is too thin to have multiple scattering and the atoms are not very heavy. This image model is fast and easy to calculate and flexible enough to add a variety of other features. If the incident beam current and

Table 7.3 Atomic coordinates (in Å) for a unit cell of MoS_2 converted to a rectangular unit cell (from hexagonal form) for calculation

Atom	x	y	z
S	0	0	0
S	1.580500	2.737506	0
Mo	1.580500	0.912502	1.561465
Mo	0	3.650008	1.561465
S	0	0	3.122930
S	1.580500	2.737506	3.122930

The unit cell size is $a_0 = a = 3.161 \text{ \AA}$, $b_0 = a\sqrt{3} = 5.475013 \text{ \AA}$, and $c = 12.295 \text{ \AA}$

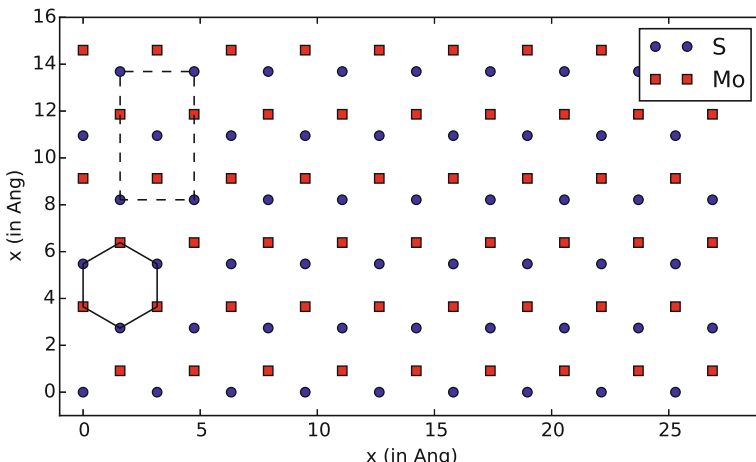


Fig. 7.16 Structure of MoS_2 projected along the c axis. Squares are Mo atoms and circles are S atoms. One hexagonal unit is outlined with a solid line in the lower left, and the rectangular unit cell is outlined with a dashed line in the upper left

dwell time per pixel (point in the scan) are known, then Poisson electron counting noise can be calculated. This is the theoretical best that might be achieved with an ideal detector capable of single electron counting (some are but many are not). An actual experimental image may include a variety of other noise sources in practice, but it is still of interest to estimate what might be achieved in a minimum noise result including only counting noise.

Programming a Poisson distributed random number generator is actually not trivial. To be correct, what is calculated should be referred to as a pseudo random number generator not a true random number generator because it is reproducible in a program but has most of the important properties of random numbers. Most random number generators use clever integer arithmetic and/or bit manipulations to generate a uniformly distributed random number. Random numbers for many other continuous probability distributions can be generated using the basic laws of probability. However, Poisson random numbers are positive integer values not

continuous variable so require some extra steps. Atkinson [1] has given a review of several different method.

An ADF-STEM image of MoS₂ is shown in Fig. 7.17. The specimen is most likely radiation damage sensitive so a low beam energy of 60 kV is used. Figure 7.17a is an ideal image with no noise and no aberrations. Figure 7.17b, c includes noise and Fig. 7.17c also includes small amount of high order aberrations which will be the most difficult to correct and hence likely to still be present. The main effect of small high order aberrations in Fig. 7.17c is to significantly reduce the peak signal with only a small increase in the apparent size of each atom. All images in this figure include a modest source size and defocus spread. This result is similar to what has been experimentally observed (for example, Kang et al. [254] and Li et al. [312]).

7.4 Reciprocity and Z-Contrast

Due to reciprocity, STEM and CTEM are equivalent under certain circumstances (Sect. 2.4). ADF-STEM usually has a simple image interpretation called Z-contrast in which the image intensity varies uniformly with atomic number Z , with little variation with thickness (i.e., it can be thought of as an incoherent imaging process). The price paid is that the signal is small. BF-CTEM has a stronger signal but varies with thickness in a complicated, often nonintuitive manner (it is more of a coherent image process). Reciprocity means that CTEM with a large illumination angle (condenser angle) equal to the detector angles in ADF-STEM should produce Z-contrast similar to ADF-STEM. A large condenser angle effectively washes out the coherence making this mode incoherent BF. Detector angles can be very large (20–200 mrad) compared to illumination angles (up to a few mrad). Most condenser lenses will probably not handle 100 mrad or more but an equivalent signal might be obtained by making illumination angles the same as the hole in the ADF detector. The sum of the signal on the ADF detector plus the signal in the hole must sum to the total beam intensity I_0 (neglecting backscattered electrons) which is constant in most cases. BF-CTEM with a large illumination angle is approximately I_0 minus the ADF signal (chromatic aberration and inelastic scattering enter slightly differently, so this analogy may not be exact).

Figure 7.18 shows calculated (with multislice) ADF-STEM and BF-CTEM images of 110 silicon ($Z = 14$) with a few rows of Si atoms in the middle replaced with As ($Z = 33$) atoms. In the middle, every other Si atom has been replaced with As in the equivalent Ga atom position in GaAs. This specimen is not practical to fabricated and if it were, there would be some lattice relaxation which is also ignored. This specimen is for demonstration purposes only, and conveniently has a large scale structure with different atomic number atoms. Figure 7.18a shows the ADF-STEM image with the higher atomic number As atom columns as bright white spots (Z-contrast). Figure 7.18b shows a typical BF-CTEM image with not much contrast between heavy (As) and light (Si) atoms. Figure 7.18c shows a BF-CTEM with a large condenser angle equal to the size of the hole in the

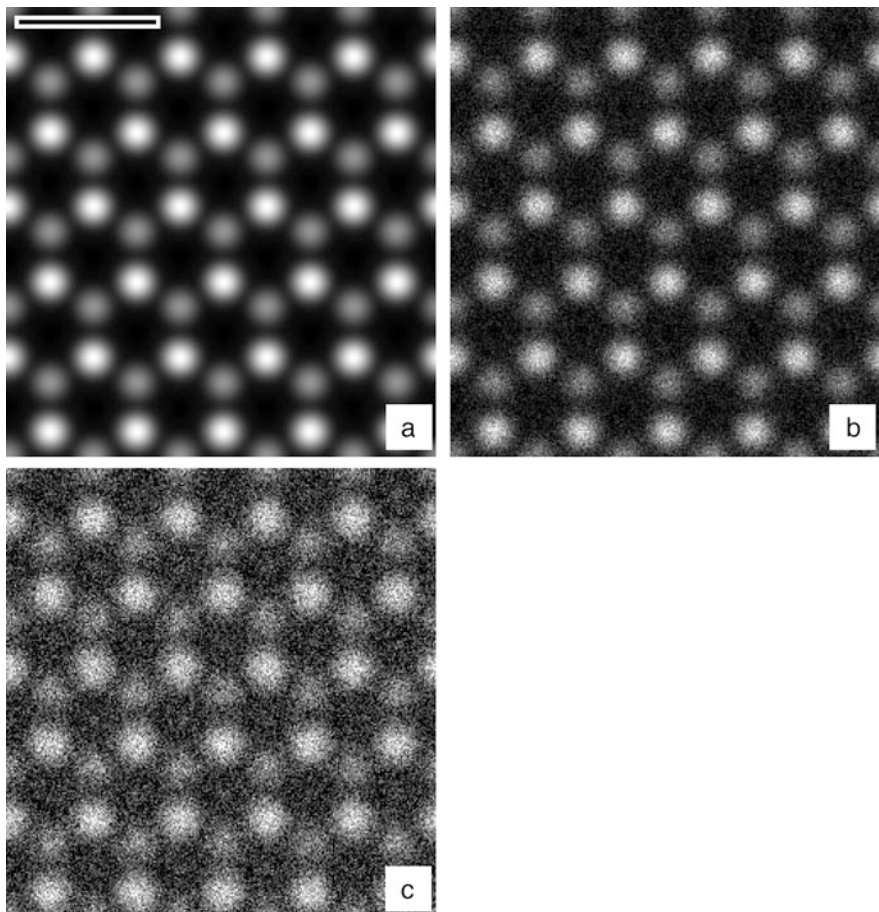


Fig. 7.17 Calculated images of MoS_2 in ADF-STEM at 60 kV, obj. apert. 30 mrad, source size 0.5 \AA , and defocus spread of 50 \AA . (a) No aberrations and noise free, (b) no aberrations with Poisson counting noise for 20 pA beam current and dwell time of $10 \mu\text{s}$, (c) same as (b) but with $C_{45a} = 0.5 \text{ mm}$ and $C_{56a} = 40 \text{ mm}$. The image range is (a) $0.001\text{--}0.024$, (b) $0\text{--}46$ electrons and (c) $0\text{--}29$ electrons. (b) and (c) are slightly saturated to improve visibility. Bright white spots should be Mo atoms and gray spots should be S atoms. The scale bar is 5 \AA .

ADF-STEM image. For each position in the condenser aperture (consistent with periodic boundary conditions) a plane wave (with a tilt determined by position in the condenser aperture) is propagated through the specimen and forms an image (see Sect. 6.10.3). The intensity of all images is added (incoherently). There is an assumption that the condenser aperture is incoherently illuminated which is usually the case. The resulting BF-CTEM image is very similar to the ADF-STEM image except with reverse contrast. The heavier As atoms are now black instead of white as in the ADF-STEM image due to the inverted contrast as discussed above. If ADF-

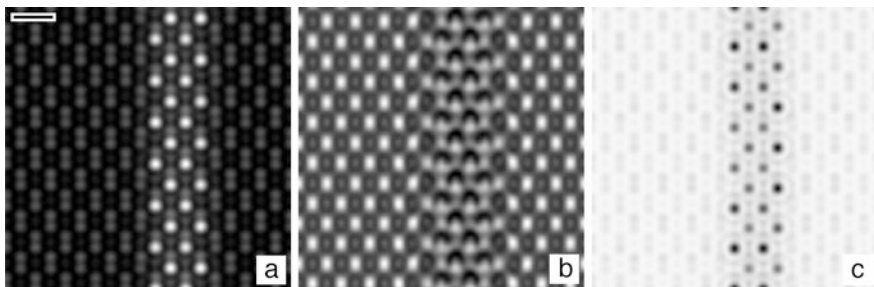


Fig. 7.18 Reciprocity and Z -contrast. Calculated image of 110 silicon (512×512 pixels and 52 \AA thick) with two rows of As atom columns in the middle. 200 keV , $C_{S3} = 0.7 \text{ mm}$, $\Delta f = 510 \text{ \AA}$. (a) ADF-STEM, detector angle $30\text{--}100 \text{ mrad}$. (b) BF-CTEM with parallel illumination. (c) BF-CTEM with large illumination angle of $0\text{--}30 \text{ mrad}$. The range (white is a larger value) of each image is (a) $0.0021\text{--}0.0542$, (b) $0.1547\text{--}2.2018$, (c) $0.1684\text{--}0.1867$. The scale bar is 5 \AA

STEM is said to be Z -contrast, then this form of incoherent BF might be said to be inverted Z -contrast. Z -contrast is possible at least in principle in BF-CTEM utilizing reciprocity. Similar calculated results were shown by Kirkland [272]. This effect has been tested in STEM with two different detectors (unpublished) but has not been tested in BF-CTEM so far it seems.

7.5 CBED Simulations

The CBED or convergent beam electron diffraction pattern is formed when a small focused probe is incident on the specimen. The diffraction pattern is from a microscopic area of the specimen and can also be referred to as the microdiffraction pattern. When the illuminating radiation is convergent (as required to focus on a small area of the specimen) then each diffraction spot is enlarged to the same size as the illumination cone and becomes a disk instead of a spot. The angular diameter of each disk is the same as the angular spread of the incident beam. In the case of the STEM each diffraction disk is the same size as the objective aperture.

The sampling error test (as in Table 7.2 and Fig. 7.5) are only an internal consistency test and do not test for systematic errors in the simulation theory or program implementation. The only real test of the simulation is a comparison to actual experimental data. Once the simulation software and theory have been verified by a detailed comparison to one or more experiments, then it can be used to predict other unknown situations.

Figure 7.19 shows experimentally recorded CBED patterns from 111 silicon at an electron energy of 100 keV (from Kirkland et al. [280]). In this case the probe (about 2.7 \AA diameter) is larger than the lattice spacing (1.92 \AA) so the CBED disks do not overlap and the lattice is not observable (Spence [472]). The outer (white) ring is the HOLZ line. It is thin because the Ewald sphere intersects each diffraction

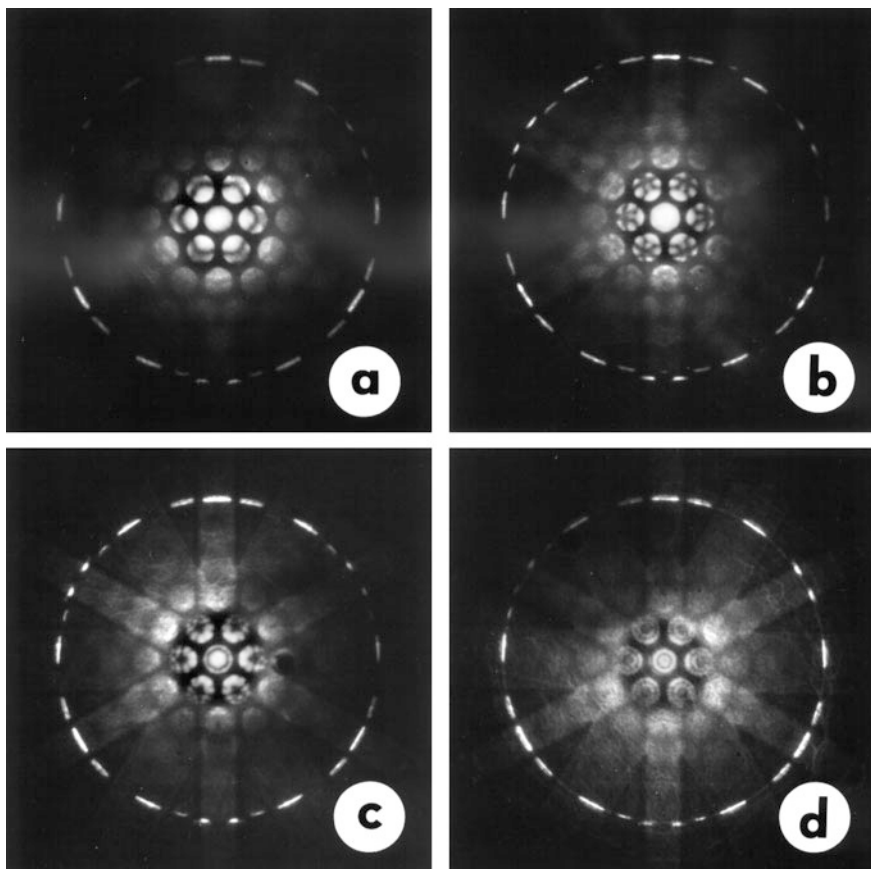


Fig. 7.19 Experimental CBED patterns of 111 silicon recorded in an HB501A STEM at 100 keV, $C_s = 3.3$ mm, with an objective aperture of 8 mrad (Scherzer conditions). The specimen thickness was determined to be (a) 198 Å, (b) 273 Å, (c) 489 Å, (d) 1270 Å (± 30 Å). Reprinted from Kirkland et al. [280] with the permission of *The Minerals, Metals and Materials Society*

disk at a steep angle. The patterns were recorded by photographing the diffraction screen (phosphor screen) with a 35 mm camera (using Kodak Plus-X film, chosen for its long linear region) with an exposure of 2 min. The dynamic range of the CBED pattern is too large to display easily so some old fashioned image processing was applied to the central seven disks (they were photographically *burned in* by a factor of six when the final prints were made in the dark room).

A CBED calculation requires only one multislice calculation like in a BF-CTEM calculation. The initial wave function is a focused probe (instead of a plane wave) and the final image is Fourier transformed into the far field to get a diffraction pattern. Silicon 111 was modeled as a layered structure with a stacking sequence of $abcabca\dots$. The slice thickness (one layer per slice) is 3.135 Å, with a total repeat

length of 9.405 Å. The wave function and specimen potential were sampled with 512×512 pixels and a super cell size of 53.5×53.2 Å. A library of CBED patterns was calculated for various thickness in the range 100–1500 Å at intervals of 10–50 Å. Each experimental CBED pattern was visually matched to a calculated CBED pattern to determine the specimen thickness. It was possible to distinguish the thickness to an accuracy of about ± 30 Å by observing the structure in the low order diffraction disks. The best match is shown in Fig. 7.20 recalculated with a higher resolution of 1024×1024 pixels and 65.2732 Å by 66.504 Å (max. angle 190 mrad) needed for the thick specimen in (d). Only the center portion of the diffraction pattern is shown for simplicity. This calculation does not include temperature (no atomic vibrations) so is missing a few features. Several more rings (HOLZ lines) are visible in the calculation and there are no Kikuchi line (radial spokes). In a more complete calculation the extra HOLTS lines disappear and the Kikuchi lines appear (see the next section).

An EELS (electron energy loss spectroscopy) spectra was recorded for the same region that each CBED pattern was recorded. The ratio of the integrated signal in the first plasmon peak to the intensity in the zero loss peak is a good measure of the thickness of the specimen. Plotting the EELS ratio versus the thickness determined by matching the CBED simulation yielded a straight line with a slope indicating a plasmon mean free path of 1297 ± 25 Å (with an EELS spectrometer collection angle of 8 mrad). The subjective agreement between Figs. 7.19 and 7.20 (overall features and the pattern of dark lines in the low order disks, taking into account the different intensity display scales used) and the measurement of the plasmon mean free path indicate a good agreement between the multislice simulation theory and an actual experiment. This particular experiment ignored the thermal motion of the atoms in the specimen. Later experiments by Loane et al. [317] yielded a plasmon mean free path of 1207 Å including the effects of thermal atomic vibrations. The faint radial bands are called the Kikuchi bands and are also absent when thermal vibrations are ignored (as in Fig. 7.20).

7.6 Thermal Vibrations of the Atoms in the Specimen

All of the simulations considered so far have treated the atoms in the specimen as completely stationary. Most electron microscopy is done at room temperature of about 300°K (some microscopes can be equipped with heating and cooling stages). At room temperature the atoms in the specimen vibrate slightly. These atomic vibrations are quantized and the quantum unit of energy is called a phonon similar to the quantum unit of electromagnetic energy, the photon. Atomic vibrations are small compared to a typical interatomic distance so this effect is expected to be small but can lead to some interesting effects. In particular the thermal vibrations lead to a diffuse background intensity (in the diffraction pattern) in between the

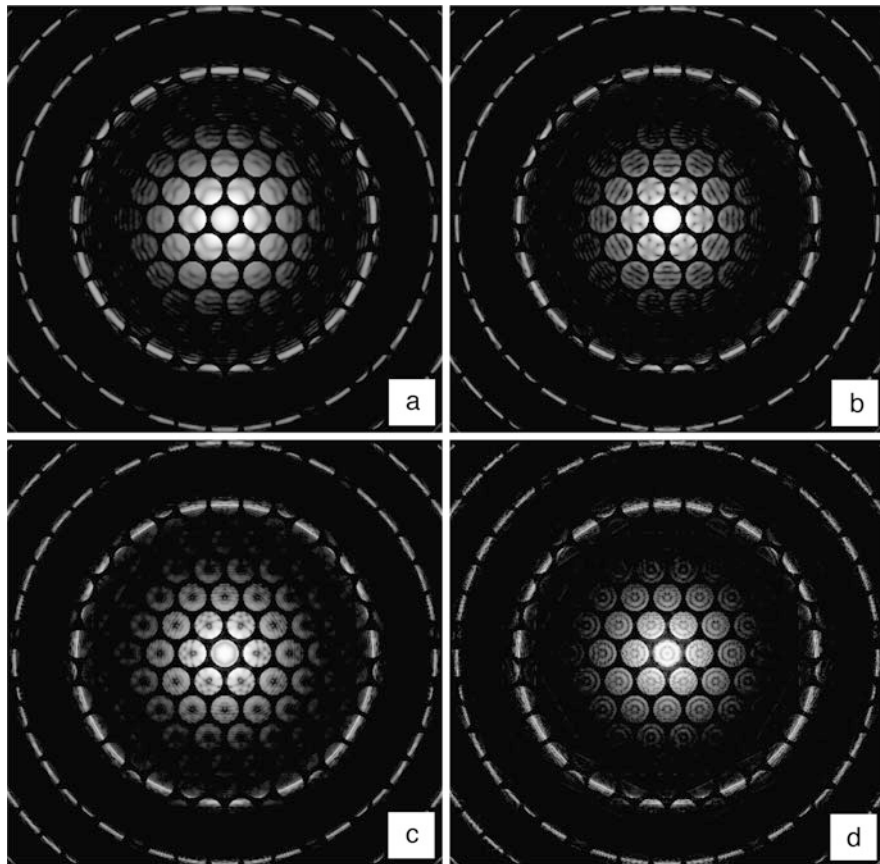


Fig. 7.20 Calculated CBED patterns of 111 silicon at 100 keV, $C_s = 3.3$ mm, with an objective aperture of 8 mrad (Scherzer conditions). The specimen thickness was determined to be (a) 198 Å, (b) 273 Å, (c) 489 Å, (d) 1270 Å (± 30 Å). Each pattern is displayed on a logarithmic scale. The maximum scattering angle is 190 mrad (A higher resolution version of what was given in Kirkland et al. [280])

normal allowed diffraction positions. This type of scattering may be referred to as thermal diffuse scattering or simply TDS.

Typical optical phonons have a frequency no greater than about 10^{12} to 10^{13} Hz (Kittel [286]), and acoustic phonons are significantly lower frequencies. The imaging electrons in the microscope are traveling at about one half the speed of light (1.5×10^{10} cm/s) or greater. At this speed it takes only about 0.7×10^{-16} s. to traverse the specimen which is much smaller than the period of oscillation of the atoms in the specimen. While the imaging electron is inside the specimen the atoms do not change their position significantly. The imaging electrons see the atoms as stationary but slightly offset from their normal lattice positions. The final image or diffraction pattern is made up of the average of many different imaging electrons.

The typical current in the microscope is small enough that the time between two successive imaging electrons passing through the specimen is long compared to the period of oscillation of the thermal phonons in the specimen. Therefore each successive imaging electron sees a slightly different configuration of atoms in the specimen. Each configuration of atoms is uncorrelated with all other configurations so the average over atomic configurations should be done incoherently.

The final image is the time average of many oscillations of the phonons in the specimen. However, only the imaging electron intensity and not the wave function can be averaged. This means that the time average must be performed in the image plane (or diffraction plane if simulating a diffraction pattern) and not in the specimen plane. The detection process (film, CCD, etc.) converts the electron wave function into an intensity (square magnitude of the wave function). It is not appropriate to replace the atomic potential of the specimen by a time averaged potential (or equivalently apply a Debye–Waller factor to the atomic potential) because the phase of the imaging electron wave function must be carried through to the detector plane. It is only in the detector plane that the wave function can be converted to an intensity.

A general theory of imaging and diffraction in the presence of thermal vibrations can be rather involved (for example: Hall and Hirsch [185], Cowley and Pogany [80], Cowley and Murray [79], Rez et al. [420], Cowley [76], Allen and Rossouw [11], Wang and Cowley [523, 524], Wang [519–522], Dinges and Rose [97], Jesson and Pennycook [245], Amali and Rez [14], Mitsuishi et al. [351], Dwyer and Etheridge [107], Croitoru et al. [86]). The theory of TDS scattering of X-rays has been thoroughly reviewed by Warren [525] and is very similar to TDS scattering of electrons. Although a theoretical analysis may be complicated, there is however a simple if somewhat brute force approach to numerically simulate the effects of thermal vibrations in the specimen. Given a list of atomic coordinates in the specimen, offset the position of each atom by a small random amount and then perform a normal multislice simulation to get an image or diffraction pattern. Next repeat this process with a different random offset for each atomic coordinate (each random offset should start from the original unperturbed atom position, so the random offsets are not cumulative). The final image or diffraction pattern is the intensity averaged over several different configurations of atoms with different random offsets (average $|\psi|^2$ and not ψ). This approach is called the frozen phonon approximation (Loane et al. [316], Hillyard and Silcox [207]). There is a similar method in condensed matter calculations with a similar name (for example, Martin [333]) used to calculate phonon behavior but these two methods seem to have appeared independently near the same time. The random offsets can be generated using a random number generator with a Gaussian distribution which is then equivalent to the Einstein model of the density of states for phonons (see, for example, Kittel [286]). This method can also be labeled a Monte-Carlo method because it uses a sequence of computer generated random numbers to perform a simulation. Fan [124], Dinges and Rose [97], and Amali and Rez [14] have proposed slightly different methods.

When all of the atoms in the specimen have a slightly different offset the specimen is no longer periodic in any direction. The specimen is technically amorphous although there is still an approximate periodicity. This simulation requires a different type of multislice simulation. Each slice of the specimen is different so there is no advantage to precalculating the slices, storing them, and reusing the transmission function of each slice (they cannot be reused). This type of multislice simulation first reads in all of the coordinates (in practice the program reads in only the coordinates for one unit cell and then replicates them for many unit cells) and then adds a random offset for each coordinate. Then the atomic coordinates are sorted by depth and cut into thin slices. The transmission function for each successive slice is calculated (one at a time), applied to the transmitted wave function, and then discarded because it cannot be used again.

7.6.1 Silicon 111 CBED with TDS

Thermal vibrations have the most visible effects on the diffraction pattern, generating a diffuse background intensity in between the normal diffraction spots. The steps in a frozen phonon calculation are shown in Fig. 7.21. Each atom was allowed to deviate from its normal lattice position with a Gaussian distribution and an rms deviation of $x_{RMS} = 0.075 \text{ \AA}$ in each of three directions, consistent with a measured Debye–Waller factor B at room temperature (Sears and Selly [451]), $x_{RMS} = \sqrt{B/(8\pi^2)}$. This simulation models a CBED pattern ($|\Psi(k)|^2$) of the 111 projection of silicon. The wave function and potentials were sampled with 512×512 pixels in an area of $34.6 \times 33.3 \text{ \AA}$ (maximum scattering angle 183 mrad). Figure 7.21a shows the CBED pattern without thermal displacements. Figure 7.21b has one particular set of random offsets. The number of different configurations in the average increases to 16 in Fig. 7.21d. Surprisingly, this is enough configurations to produce a smooth pattern. This calculation is completely elastic and there is no inelastic scattering.

This simulation in Fig. 7.21d should match the experimental CBED pattern in Fig. 7.19c. However the scale was changed slightly to improve the sampling. The faint white bands that travel radially outward from the center of the CBED pattern are called the Kikuchi bands and are noticeably absent in the CBED simulation in Fig. 7.20 without thermal vibrations, but are reproduced appropriately in Fig. 7.21. Figure 7.22 shows the average intensity versus scattering angle including thermal atomic vibrations. Notice that the intensity in between the diffraction peaks has become nonzero. The main effect of thermal vibrations is to reduce the intensity in the HOLZ lines and redistribute it more uniformly over the whole range of scattering angles. The ADF-STEM signal integrates over this whole region so there is only a small qualitative effect in the ADF-STEM image. The TDS should be included in ADF-STEM for a good quantitative calculation but usually does not have a qualitative effect on ADF-STEM image (Hillyard and Silcox [207]). Möbus et al. [355] have also added TDS to simulations of BF-CTEM images and conclude

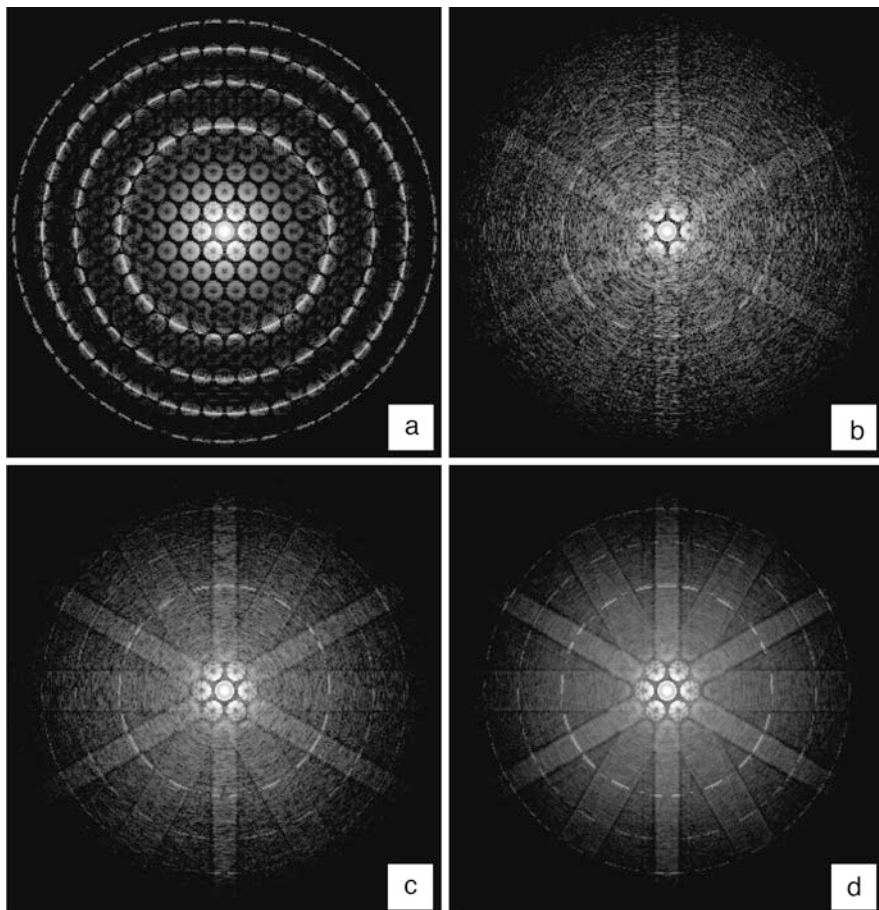


Fig. 7.21 Monte Carlo simulation of the CBED pattern of 111 silicon (489 Å thick) including thermal atomic vibrations (0.075 Å in each direction) at 100 keV ($C_s = 3.3$ mm, obj. aperture 8 mrad. Scherzer conditions). (a) has no thermal vibrations and the other images are the average of successively more sets of random displacements (b) one set, (c) four sets, and (d) 16 sets. Each pattern is displayed on a logarithmic scale. The maximum scattering angle is 183 mrad

that there is no significant effect for thin specimen as are typically used. Muller et al. [365] have performed a more detailed simulation using a set of phonons accurately generated from the measured band structure of the crystal and found that there was no significant deviation from the simple Einstein model with a Gaussian distribution of atomic coordinate offsets. Debye–Waller factors for many different materials can be found in the literature (for example, Reid [412], Krishna and Sirdeshmukh [296] and Schowalter et al. [450])

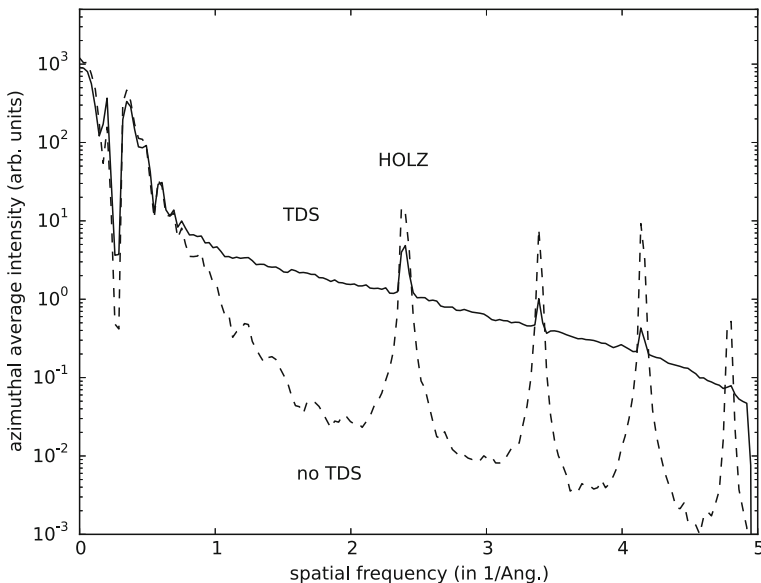


Fig. 7.22 Azimuthal average of the scattered intensity in the simulated CBED diffraction pattern including thermal atomic vibrations in 111 silicon as in Fig. 7.21d. The solid line includes thermal vibrations and the dashed line does not (Fig. 7.21a)

7.6.2 Silicon 110 ADF-STEM with TDS

Generally speaking, the TDS scattering in crystalline specimens reduces the peak intensity in the Bragg peaks on the ADF detector. A significant portion reappears as a diffuse background in between the Bragg peaks, which is still integrated by the ADF detector. Unless there are one or more strong Bragg peaks near the edge of the detector then TDS scattering should not have a large effect on the ADF-STEM image, although it should be included for a good quantitative comparison. Figure 7.23 shows a line scan through the so-called dumbbells (atom col. pair) in the 110 projection of Si (1.36 Å spacing) calculated with and without thermal vibrations (TDS scattering) for an aberration-corrected 100 keV STEM. This calculation used 512 by 512 pixels with a super cell size of approximately 20 Å in each direction and a specimen thickness of about 100 Å. This super cell size includes scattering angles (on the ADF detector) to 290 mrad. The TDS calculation was averaged over 32 phonon configurations. Both calculations include a source size of 0.5 Å (full width half max.), calculated by convolving a 2D image (64 by 256 pixels) with a Gaussian of the appropriate width.

In the top graph (of Fig. 7.23) the atom pairs are nicely resolved and the TDS scattering does not have much effect (overall curve moved up slightly). There is a slight asymmetry due to the stacking order in the two columns, which will likely disappear in practice with surface relaxation of the crystal. The systematic error in

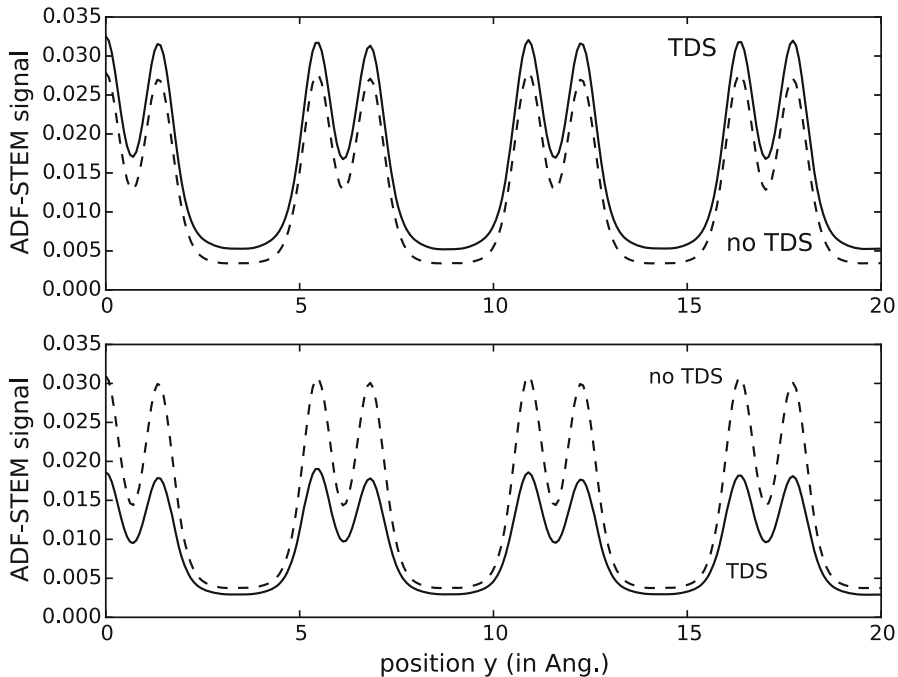


Fig. 7.23 Calculated aberration-corrected ADF-STEM images for the 110 projection of silicon with (solid line) and without (dashed line) TDS scattering, at a beam energy of 100 keV (defocus of 0 \AA , $C_{S5} = 0$, $C_{S3} = 0$, obj. apert. = 35 mrad, source size 0.5 \AA). The specimen thickness was 100 \AA . The area of each image corresponds to 5×4 unit cells of the type shown in Fig. 5.15. The top graph has a detector of 80–200 mrad and the bottom graph has a detector of 120–280 mrad

this calculation may be about the size of the difference between these two curves so there may not be a real difference in the two curves. The bottom graph includes only high angles on the detector and the TDS scattering has the effect of reducing the overall signal which is a little unexpected. It is likely that there is a strong set of Bragg peaks near the inner angle of the detector (the FOLZ line) whose intensity gets scattered off the detector and disappears. It is not always a good idea to restrict the detector to very high angles. Usually it's best to get the FOLZ nicely centered on the detector.

7.7 Specimen Edges or Interfaces

Calculating images of edges and interfaces presents some special problems. The specimen is no longer really periodic. The so-called wrap-around error causes an extra edge or interface to be introduced (see Fig. 6.13). Figure 7.24 shows the image of a sharp edge of copper. There is a pure crystal of copper in the left half and

vacuum in the right half with an atomically sharp edge in the middle. Copper is a simple FCC (face centered cubic) structure with a unit cell size of 3.61 Å. The edge could also be an interface between two different materials, with the same problem. There is one intended edge (or interface) in the center and also an unintended interface on the left and right edges due to the wrap-around effect. The effects of this edge are just visible along the right edge of each image. Usually only the middle interface is of interest and typically only the middle portion of the image (with left and right edges removed) is shown. However the whole image is shown here to help understand the situation.

The trick to calculating an edge or interface which is not strictly periodic using an FFT based multislice method in which the specimen is required to be periodic in the two-dimensional image plane is to make the specimen extra long in the non-periodic direction. The specimen does not have to be periodic along the beam direction (into the page in this example). If it is long enough, the two interfaces are far apart and do not interfere with each other. The new unit cell is called a super cell. In this example the super cell is 72.2 by 36.1 Å and was sampled with 512 by 256 pixels for BF-CTEM and 1024 by 512 pixels for ADF and confocal STEM. The specimen was 50.54 Å thick (thin to reduce thickness effect for simplicity which also reduces the computer time). The STEM probe was sampled with 512 by 512 pixels (which effectively slides around on the larger specimen). Using a smaller sampling for the probe reduces the required computer time (which is significant for this calculation). The final image has 512 by 256 pixels. The atomic columns should appear dark in (a) and (c) and white in (b).

The ADF-STEM image (Fig. 7.24b) is incoherent and the edge appears sharp (white dots at the atom positions). The BF-CTEM image (Fig. 7.24a) is coherent and a well-known Fresnel fringe (oscillations) appears at the edge (both edges) which makes it difficult to determine the exact location of the edge. This particular confocal image is well behaved although confocal is frequently not well behaved (in part because there are twice as many parameters to go wrong).

7.8 Biological Specimens

The multislice method is capable of handling specimens that are nearly amorphous. Each slice of the specimen is calculated independently of the other slices so the specimen can be completely amorphous in the beam direction (z as used in this book). Using a discrete Fourier transform (the FFT) in two dimensions perpendicular to the beam direction forces the unit cell to be repeated infinitely in those two directions (x, y as used in this book). If the specimen is somehow bounded (such as a nano particle or macromolecule) and embedded in a larger supercell such that the repeated copies of the specimen are far apart so they do not interfere with each other, then amorphous objects may be calculated using the multislice method (see Fig. 6.12).

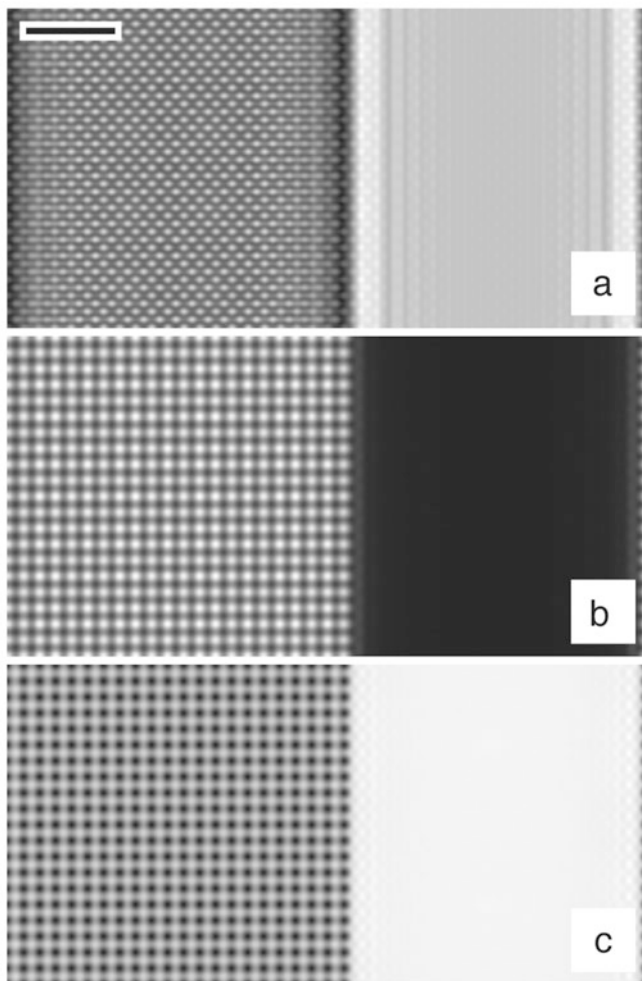


Fig. 7.24 Calculated images of an edge of copper at 200 kV. **(a)** BF-CTEM image, **(b)** ADF-STEM image, **(c)** confocal STEM with a detector radius of 2 Å, and the same parameters for the collector lens as the objective lens. $C_s = 0.7$ mm a defocus of 700 Å, and an objective aperture of 12 mrad. The scale bar is 10 Å

Biological macromolecules or microorganisms are good examples of (nearly) amorphous particles (the method discussed next should also apply to inorganic nano-particles as well). The Protein Data Bank (PDB) is an on-line depository of structure data for proteins and related molecules, many of which come from X-ray diffraction studies of crystallized specimens. Each structure data file in the PDB contains a list of atomic coordinates (in three dimensions) that can be converted to a format used here for a multislice calculation (as done by Wall [517]). Some images of glutamin synthetase (with thallium, PDB identification 1F1H.pdb, Gill

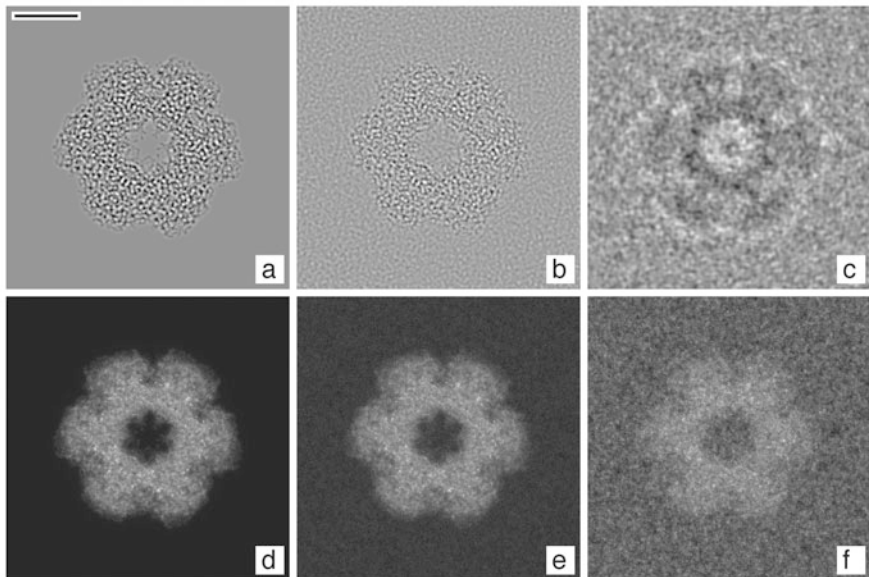


Fig. 7.25 Calculated images of glutamin synthetase (1F1H.pdb, Gill and Eisenberg [156]) using multislice (2 Å slices). (**a–c**) BF-CTEM, (**d–f**) ADF-STEM. (**a, d**) have no support (not physically possible), (**b, e**) have a 20 Å amorphous carbon support and (**c, f**) have 120 Å of amorphous ice support. Electron beam energy 300 keV, $C_S = 1.0$ mm, $\Delta f = 550$ Å (at center of specimen), obj. apert. 13 mrad (BF) and 10 mrad (ADF). (**a–c**) also have an illumination angle of 0.1 mrad and defocus spread of 100 Å, except $\Delta f = 15,000$ Å and defocus spread = 200 Å in (**c**). Radiation damage and low beam dose noise are ignored for simplicity. The scale bar is 50 Å

and Eisenberg et al. [156]) are calculated in Fig. 7.25. This molecule has 45,564 atoms and is projected along the z axis as defined by the PDB file (which seems to be along an interesting direction). Several major effects will be ignored for simplicity. Radiation damage is frequently the primary limiting factor in images of biological specimens. The total beam dose must be limited to some small value. The low dose generates a lot of noise in the image. Part of the specimen may be moved around by the interaction with the beam if it has too large of a current. Both of these effect are ignored here for simplicity, so this result is a little bit of a fantasy.

Figure 7.25a is a BF-CTEM image (512 by 512 pixels) of the molecule with no support (magically suspended in space; not possible). Cryo-EM typically assumes that the biological specimen is a weak phase object (WPO) so that the intensity in the image is easily correlated with atomic density in some way. However, Fig. 7.25a is not really a WPO. The background (outer edges in the image) should be the largest signal (white) but is gray (i.e., the signal is scaled to fill the black to white range). The region in the middle where the specimen is should be smaller (various shades of gray) but has regions larger than the background (white) inconsistent with it being a WPO (a more systematic study may be warranted here, there might be some interaction with defocus as well). Figure 7.25b is a BF-CTEM image of the

molecule with a 20 Å amorphous carbon support, simulated by generating uniformly distributed random numbers used as atomic coordinates for the carbon atoms inside a rectangular slab on the exit surfaces. A minimum separation of 1.4 Å between carbon atoms was maintained using the known density of carbon (2.0 gm/cm³), with a filling fraction of 0.9 (to mimic a rough surface). There were approximately 91,000 atoms in the carbon support. Generating random coordinates inside a rectangular volume is relatively easy, but keeping them a minimum distance apart is not. It is best to keep the coordinates in a list sorted by one coordinate (z was used) using an insertion sort. Then a new random coordinate only need be tested on a few nearby (in z) coordinates (and rejected if it is too close) not the whole list which is an N^2 problem that quickly escalates into a large computational effort. There is essentially nothing visible in the BF image, which is why biological specimens are usually stained with some heavy material (no stain here). In principle multislice can handle a surrounding stain if given a list of coordinates for the atoms in the stain (not easy to get or calculate). Figure 7.25c is a BF-CTEM images with amorphous or vitreous ice surrounding the biological molecule to approximate the cryo-EM specimen techniques. Rapidly frozen water (ice) seems to more closely preserve the state of the biological molecule near its natural state and reduce radiation damage (at the expense of image noise in the support structure). Rapid freezing also prevents crystal formation in the ice which might damage the specimen. Ice has been modeled as successive random coordinates filling the space around the biological molecule (similar to amorphous carbon above) with about the same thickness (in z) as the biological molecule. Random coordinates for the oxygen atom in water were generated in the whole volume keeping a minimum distance (1.4 Å) between all other atoms of water and atoms in the biological molecule. Two hydrogen atoms were added at random positions with the required bond length and all three atoms in H₂O were added to the existing list. For programming simplicity the hydrogen bond angle was ignored which is likely a small effect in projection. Water molecules were added until the average density outside a bounding box surrounding the biological molecule was that of ice (0.92 gm/cm³) with a filling fraction of 1.0. Water molecules may occupy large holes on the surface and inside the biological molecule which is probably true in practice. With normal Scherzer focus conditions the image in ice is just a uniform rough surface with no structure for the biological molecule. As practiced in cryo-EM (for example, Frank [143], Cheng et al. [63]) Fig. 7.25c has been given a very large defocus to push the WPOA transfer function into low spatial frequencies (where more of the structural information seems to be) at the expense of significantly scrambling the high spatial frequencies (high resolution). Cryo-EM images may require deconvolution of the transfer function (not done here).

Figure 7.25d–f are ADF-STEM (30–100 mrad detector) images of the same specimens in Fig. 7.25a–c. The specimen transmission functions (one per 2 Å slice) were sampled with 2048 by 2048 pixels and the probe was 512 by 512 pixels. There are 512 by 512 pixels in the final image. It is interesting that the structure should be visible even without staining in ADF although the signal is much smaller

and radiation damage will be much more of a problem with a larger beam dose. ADF naturally keeps a lot of the low spatial frequencies unlike BF-CTEM in the WPOA. There might be some reason to try this with a low dose technique and a cold stage to reduce radiation damage. For this particular specimen and imaging parameters the simple incoherent image model (Eq. 3.70) yields an image that is subjectively the same as the image in Fig. 7.25d–f, which can be calculated in seconds rather than hours. Engel and Colliex [119] and Engel [118] (amongst many) have reviewed STEM imaging of biological specimens. BF-CTEM imaging of biological specimens has been reviewed by a great many authors.

7.9 Ronchigrams (in STEM)

A Ronchigram is a convenient experimental method of diagnosing the aberrations in a focused probe (in STEM). It originated in light optics for measuring aberrations by passing the light through an optical grating and measuring the distortions. At high resolution in the STEM it is not practical to machine a grating of appropriate size so a thin amorphous specimen (typically carbon) is substituted. If a defocused probe is incident on the specimen, then the beam illuminates a small circular region on the specimen in the shape of the objective aperture. In the far field (calculated with a Fourier transform) a shadow image of the specimen is formed. This image is a curious combination of the real space image of the specimen and angles in the objective aperture. If there are no aberrations, then the rays in the probes are uniform and the resulting shadow image is similar to a BF-CTEM image of this region of the specimen. The aberrations of the instrument cause the ray paths in the probe to be distorted (with a corresponding distortion of the image of the specimen) in a manner determined by each aberration. The resulting pattern is similar in some ways to the calculated aberration structure in Fig. 2.19. If the specimen has a recognizable structure, then these ray distortions can be used to diagnose the aberrations currently present. A Ronchigram is also just the center disk in a CBED pattern, although the outer disks are usually not shown. A Ronchigram is rarely useful (for diagnosing aberrations) from a crystalline specimen which may produce a multitude of Bragg reflections in unhelpful places. Thin amorphous specimens have the advantage of usually producing only one central disk that is strong enough to see.

Figure 7.26 shows several calculated Ronchigrams in a thin amorphous carbon specimen of size $150 \times 150 \text{ \AA}$ and 512×512 pixels (carbon atom positions calculated as described in Sect. 7.8, and 2 \AA thick slices). These were calculated as a CBED pattern with a large specimen area (small pixel size in angle) and a large objective aperture. As defocus is reduced in magnitude the visible area of the specimen would also be reduced. Figure 7.26a is the ideal aberration free Ronchigram. The whole center region is a shadow image of the amorphous carbon and the outer circle is an image of the objective aperture (made large to better see the aberrations). The parasitic aberrations ($m \neq 0$) produce circular lobes around the outer circumference of aperture. There are what may look like several jagged parallel arc in a group

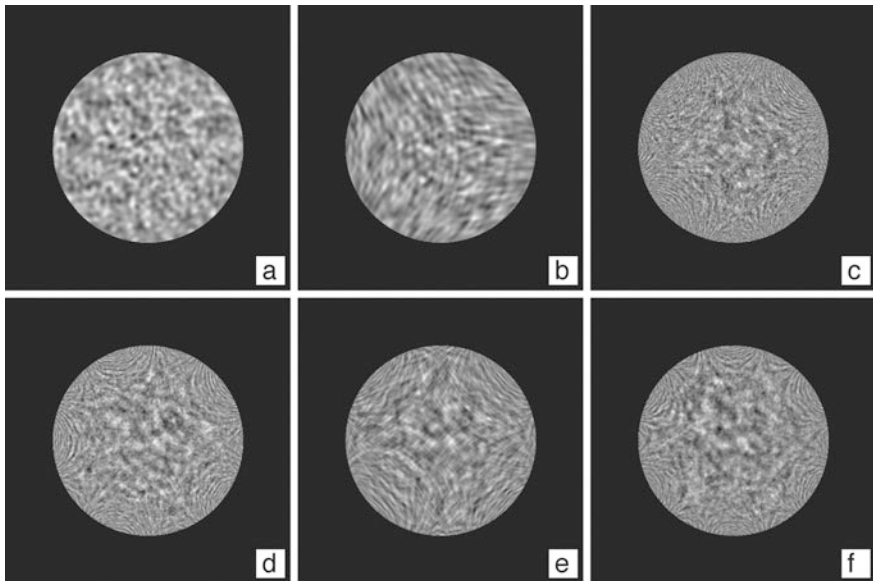


Fig. 7.26 Calculated Ronchigrams through 30 \AA of amorphous carbon for a beam energy of 100 keV, $\Delta f = 300 \text{ \AA}$, objective aperture of 60 mrad. (a) Ideal aberration free, (b) $C_{23a} = 200 \text{ nm}$, (c) $C_{34a} = 50 \mu\text{m}$, (d) $C_{45a} = 0.9 \text{ mm}$, (e) $C_{54a} = 20 \text{ mm}$, (f) $C_{56a} = 20 \text{ mm}$

with the rounded portion pointing toward the center of the circle. Each value of m produces a different number of groups. Figures 7.26b have $m = 3$ and has three groups. Figures 7.26c, e have $m = 4$ with four groups. Figures 7.26d, f have 5 and 6 groups, respectively. Low order aberrations (such as C_{23}) extend far into the center of the disk and high order aberrations tend to be pushed to the outer circumference of the disk (such as C_{56}). There is a small flat undistorted region in the center of Fig. 7.26c, d, f that would be useful to use in an ADF-STEM probe (i.e., put a small objective aperture here).

A calculation such as this has the luxury of choosing the aberrations one at a time with a value that yields an interesting pattern (as done here). However, in practice there may be many different aberrations present that combine into a disturbing mess. In addition the center of the aberration may not be the same as the center of the Ronchigram or the center of the other aberrations adding to the confusion. There has been some progress in using Ronchigrams to diagnose and tune an aberration corrector using sophisticated computer analysis (for example, Lupini [323]).

7.10 Aberration Tuning

A modern aberration-corrected instrument can be quite complicated and requires sophisticated computer control. There are 25 different aberrations through fifth order (see Table 2.1) that must be precisely adjusted for optimum performance. In practice, there will always be some small measurement (or adjustment) errors left leaving a collection of small residual tuning errors. The current practice is to adjust each aberration to yield no more than a $\pi/4$ phase error in the objective aperture per aberration (see Sect. 2.2). Figure 7.27 shows an ADF-STEM line scan through the dumbbells in 110 silicon for the case of perfect aberration correction and different random aberration errors within the maximum allowed error of $\pm\pi/4$ per aberration. Defocus and astigmatism are assumed to be manually adjusted by the operator to their optimum values and hence held at zero, leaving 22 other aberrations with small errors (through fifth order). The optimum defocus (for a maximum peak signal) is at the middle of the specimen (25 Å for a 50 Å thick specimen). The allowed tuning errors produce a random variation of about 20% in the peak amplitude, which may cause significant difficulty in quantitative matching in image intensity. This variation is not reproducible, but will be different every time the microscope is used, unless

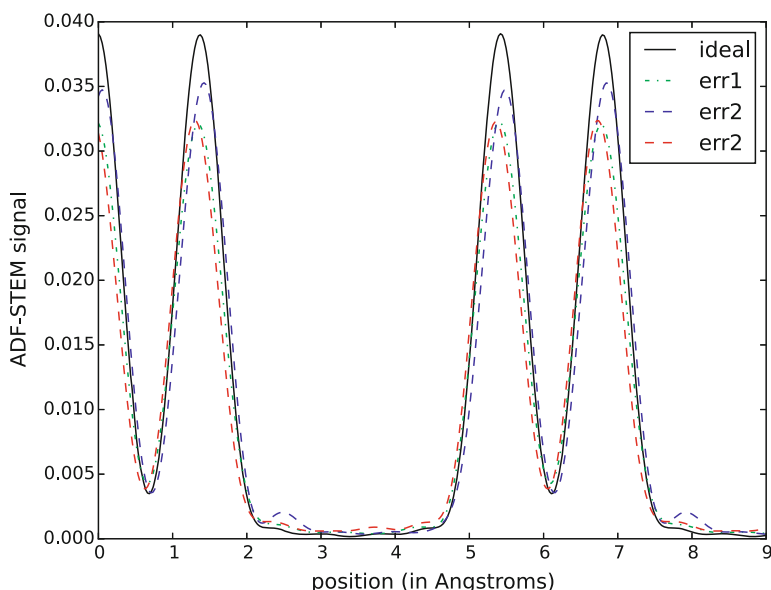


Fig. 7.27 Calculated line scan of 110 silicon (50 Å thick) using aberration-corrected ADF-STEM (100 keV, 30 mrad objective aperture, 80–200 mrad detector angles) with random $\pm\pi/4$ tuning errors (to 5th order, excluding defocus and astigmatism). The solid line has identically zero aberrations (perfectly tuned) and the other dashed and dotted lines have different random errors. Focus was set at the middle of the specimen (25 Å). Source size and defocus spread have been ignored for ease of calculation

tuned to a somewhat tighter tolerance on a regular basis. Aberrations with $m = 1$ (such as C_{21} and C_{41}) may also cause a small shift in the peak position because these are similar to pure shift (C_{01}).

A convenient measure of the total image contrast or signal strength is the total image variance σ^2 normalized to the square of the image mean μ^2 . The variance is just the square of the standard deviation σ . Dividing by the mean squared tends to reduce the sensitivity to small beam current drift and sample thickness variations. If z_{ij} is the value in each pixel, then this figure of merit is:

$$F(C_{nm}) = \frac{\sigma^2}{\mu^2} \quad (7.1)$$

$$\mu = \frac{1}{N} \sum_{ij} z_{ij} \quad (7.2)$$

$$\sigma^2 = \frac{1}{N} \sum_{ij} [z_{ij} - \mu]^2 = \frac{1}{N} \sum_{ij} z_{ij}^2 - \left[\frac{1}{N} \sum_{ij} z_{ij} \right]^2 \quad (7.3)$$

$F(C_{nm})$ is an abbreviation for the dependence on all aberrations C_{nm} and N is the total number of pixels.

Figure 7.28 shows the normalized image variance versus each aberration through third order for an ADF-STEM image of approximately 50 Å (17 unit cells) of Si₃N₄ calculated with a slice thickness of approximately 2 Å, and 512 by 512 pixels. Only one aberration was varied at a time with all others held at zero. The aberrations C_{nm} are normalized to their respective tolerances T_{nm} (Eq. 2.29). The behavior of the b type aberrations C_{nmb} is similar to the a type aberrations and is not shown for simplicity. For some reason the optimum focus for this specimen is about on the exit surface rather than the middle as in other specimens. Coma, C_{21} can be compensated by shift C_{01} which does not have much effect so coma is less sensitive than other aberrations.

The normalized total image variance in ADF-STEM, Fig. 7.28, has a remarkably simple dependence on the aberrations. Also, when the aberrations are normalized to their respective tolerances T_{nm} they produce a similar effect. This simple behavior has been proposed as a means of tuning an aberration corrector using standard N-dimensional optimization algorithms (Kirkland [278]), inspired by earlier work of Erasmus [120] and Smith on automatic focusing and astigmatism adjustment in a SEM. A similar curve given in Kirkland [278] for a slightly different specimen (110 silicon) in the incoherent image model (no thickness) showed a similar shape but decayed quicker as the aberration got larger (possibly a small thickness effect).

Figure 7.29 shows the normalized image variance for a BF-CTEM image of approximately 50 Å (17 unit cells) of Si₃N₄ calculated with a slice thickness of approximately 2 Å, and 512 by 512 pixels, similar to Fig. 7.28 for ADF-STEM. A condenser angle of 0.1 mrad and defocus spread of 20 Å have been included. BF-CTEM has a minimum contrast at Gaussian focus (zero defocus) whereas ADF-

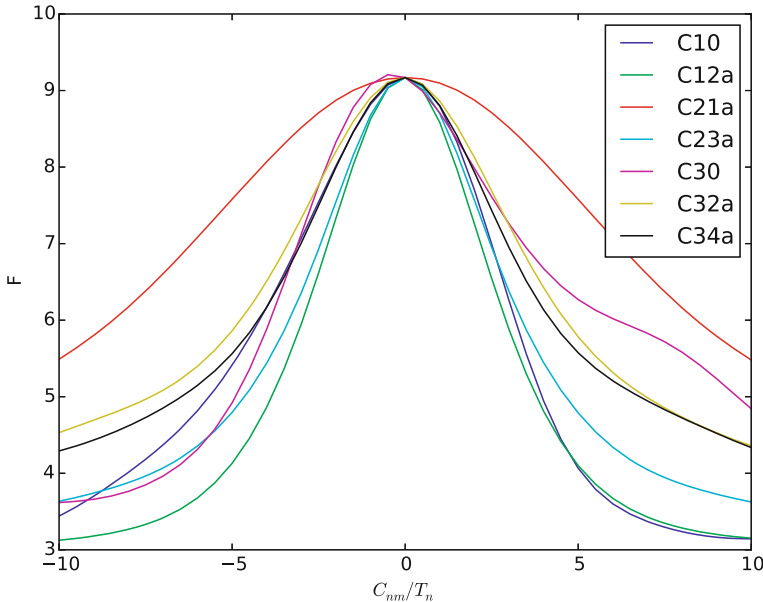


Fig. 7.28 Calculated normalized total image variance (512 by 512 pixels) for ADF-STEM in Si_3N_4 with approximate thickness of 50 Å versus individual aberrations. Beam energy of 100 keV and objective aperture of 30 mrad. Optimum defocus zero was set at 56.7 Å (relative to the entrance surface). Source size and defocus spread have been ignored

STEM has maximum contrast or signal. BF-STEM requires defocus to produce a good signal (plus other $m = 0$ aberrations, C_{30} , C_{50} , etc.) There is an argument for recalculating this figure about a Scherzer focus condition, but this has not been done here.

7.11 Quantitative Image Matching

Most comparisons between theoretically simulated electron micrographs and experimentally recorded electron micrographs are somewhat subjective. The two images are just displayed side by side and pronounced as being in good agreement after subjective visual inspection (Sect. 7.5 is also guilty of this practice). In principle it is possible (indeed recommended) to be more quantitative in comparing simulated and recorded images (vanHeel [508], Barry [22, 23]). An easily definable figure of merit is the Chi-Squared measure of the difference between two images :

$$\chi^2 = \frac{1}{N_x N_y} \sum_{i,j} [f_{\text{exp}}(x_i, y_j) - f_{\text{sim}}(x_i, y_j)]^2 / \sigma_{ij}^2 \quad (7.4)$$

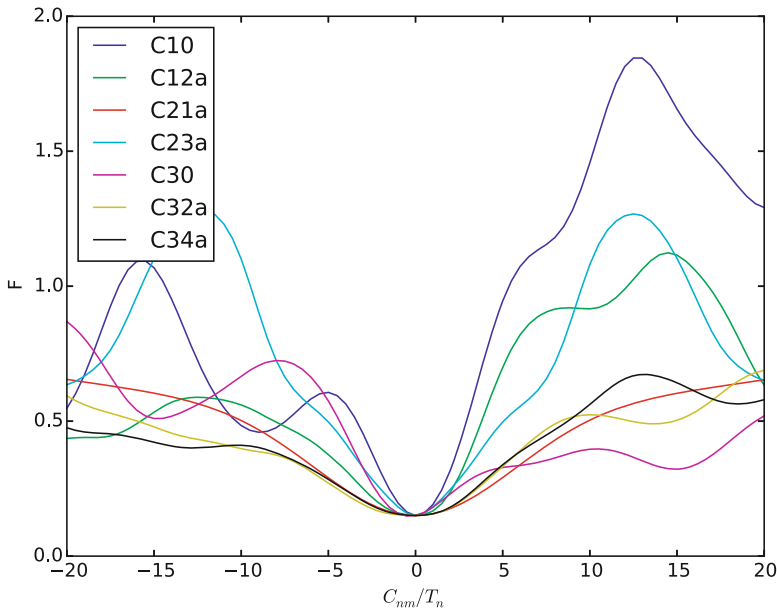


Fig. 7.29 Calculated normalized total image variance for BF-CTEM in Si_3N_4 of approximate thickness of 50 Å versus aberrations to third order. Beam energy of 100 keV and objective aperture of 30 mrad. Optimum focus was set at 25 Å

where $N_x N_y$ is the number of pixels in the image, σ_{ij} is the error associated with pixel (i, j) , $f_{\text{exp}}(x_i, y_j)$ is the experimental image, and $f_{\text{sim}}(x_i, y_j)$ is the simulated image. (This symbol χ should not be confused with the same symbol used for the aberration function.) This definition of χ^2 is technically called the reduced χ^2 because it is normalized to the total number of data points. A value of $\chi^2 \sim 1$ indicates a good fit. The *r*-factor figure of merit (R_1 , or R_2) commonly used in X-ray diffraction could also be used.

$$R_1 = \int |f_{\text{exp}}(x, y) - f_{\text{sim}}(x, y)| dx dy / \int |f_{\text{exp}}(x, y)| dx dy$$

$$R_2 = \int |f_{\text{exp}}(x, y) - f_{\text{sim}}(x, y)|^2 dx dy / \int |f_{\text{exp}}(x, y)|^2 dx dy \quad (7.5)$$

It would be very nice to be able to quote a value of χ^2 or the r-factor for the agreement between a simulated image and an experimentally recorded image. However there are considerable obstacles to overcome to perform a quantitative image match. In practice the two images to be compared can be in different orientations (translation and rotation) and they will never be at exactly the same magnification. Just to begin a quantitative comparison requires fitting these four

degrees of freedom. These properties of the image must be found in spite of the fact that the image may be noisy.

Next the overall scale and background level of the experimental image must be found. Most image detectors (film is particularly difficult to quantify) are designed to provide a linear image which is all that is required for human vision. This means that there are two additional degrees of freedom. The recorded image intensity may have an arbitrary additive and multiplicative constant:

$$f_{\text{exp}}(x, y) = a_{\text{det}} f_{\text{ideal}}(x, y) + b_{\text{det}} \quad (7.6)$$

where a_{det} and b_{det} are constants unique to each detector. These scaling constants can be found by recording the image intensity through a hole in the specimen and the intensity with the beam turned off (ideally at the same time that the image is recorded), but this additional measurement is rarely done. Film and plates notoriously vary with development time and temperature, etc. and are difficult to quantify but more modern CCD imaging systems may make this much easier. With a lot of care an experimental image can be recorded with sufficient detail to quantitatively compare to a simulated image but this extra burden is rarely accepted in practice, so most comparisons are subjective in nature.

Thust and Urban [491] and Möbus and Rühle [356] have also proposed using the cross correlation coefficient such as:

$$C_{\text{cor}}(f_{\text{exp}}, f_{\text{sim}}) = \frac{\sum_{xy} (f_{\text{exp}}(x, y) - f_{e0})(f_{\text{sim}}(x, y) - f_{s0})}{\sqrt{\sum_{x,y} (f_{\text{exp}}(x, y) - f_{e0})^2 \sum_{xy} (f_{\text{sim}}(x, y) - f_{s0})^2}} \quad (7.7)$$

where f_{e0} and f_{s0} are the average values of $f_{\text{exp}}(x, y)$ and $f_{\text{sim}}(x, y)$, respectively. The cross correlation coefficient has the advantage of eliminating the dependence on the scaling parameters of the detector.

Minimizing χ^2 (or maximizing the cross correlation coefficient) with respect to some parameter of the simulation is a method for extracting that parameter from the recorded image. The specific program implementation of a minimization procedure can become rather involved and may involve a multislice simulation for each iteration. Kirkland [284] has used this approach to determine the defocus of the electron micrographs. Wilson et al. [536] have used a semi-quantitative matching technique to determine the optical parameters of the microscope such as spherical aberration C_s and defocus Δf .

Ourazd et al. [392] have used a quantitative pattern matching technique to map the stoichiometry of their specimen. A precalculated set of possible specimen types was quantitatively compared to each unit cell of the specimen to determine its chemical composition. The best match determined the chemical composition of each unit cell. This requires that there be a small number of different unit cells.

King [262] and Möbus and Rühle [356] have performed nonlinear least squares fitting to extract specimen parameter such as tilt and defocus as well as the atomic coordinates. Zhang et al. [547] have used a quantitative fitting procedure to refine

the atomic coordinates at an interface. Möbus [353] and Möbus and Dehm [354] have recently proposed maximizing the cross correlation coefficient instead of minimizing χ^2 to refine the specimen parameters and coordinates. Möbus et al. [357] have presented a general structure retrieval program using image matching.

For the last decade or so many authors have found a significant discrepancy of about a factor of $2\times$ to $3\times$ (principally in the lattice fringe amplitude) between calculated and experimentally measured images that has become known as the “Stobbs factor” (Hÿtch and Stobbs [222], Boothroyd [41]). As discussed above this is a difficult measurement, usually requiring a measurement of the incident beam intensity on an absolute scale, an accurate specimen model, and a well-characterized electron optical column (aberrations and partial coherence) and detector response function. A possible amorphous contamination layer (Mkoyhan et al. [352]) on the specimen (usually organic material from the air or diffusion pumps), crystal tilt (Maccagnano et al. [326]), or inelastic scattering may also confuse the issue. Thust [488] has recently obtained good quantitative agreement of BF-CTEM images using an accurate model of the CCD transfer function. LeBeau et al. [304] have obtained good agreement between theory and experiment in BF-STEM images which should be similar to BF-CTEM via reciprocity. Klenov et al. [288], LeBeau et al. [305–307], and Findlay and LeBeau [134] have also obtained good agreement between measured and calculated ADF-STEM images using Bloch waves and multislice with the frozen phonon approximation. Meyer et al. [343] have found it necessary to include charge redistribution in graphene to obtain good agreement in BF-CTEM. Krause et al. [295] have obtained good agreement in CTEM with small apertures and a small discrepancy for large apertures. There is good reason to believe that the current theory is quantitatively correct with careful attention to experimental details.

7.12 Troubleshooting (What Can Go Wrong)

There are a large number of things that can go wrong in an image simulation. The proposed specimen structure must be specified in some detail, usually in the form of a list of atomic coordinates and atomic numbers in a unit cell. Even less well known is the thickness of the specimen. Usually a large sequence of possible specimen thicknesses are calculated and compared to experiment.

The instrumental (optical) parameters such as the aberration constants (C_s , etc.) and aperture size of the objective lens and lens defocus must be known. Usually defocus is not known very well (particularly in bright field phase contrast). Frequently a *defocus series* is calculated for comparison to experiment. There are also a variety of parameters such as defocus spread, illumination angle, etc. that are hard to estimate but can influence the image.

There are also many parameters that are solely related to the calculation and have very little to do with the microscope or specimen but can dramatically affect the calculation. These parameters include the sampling size (pixel size) in the image and slices and the slice thickness itself.

Multislice almost always uses an FFT to reduce the total CPU time. The FFT is a discrete Fourier transform which repeats the image infinitely in all directions. Although the image is only displayed as a single image you should remember that it is really an infinite array of identical side-by-side images. This produces a strange effect called the *wrap-around error*. The left side of the image in essence touches the right side of the image (and vice versa) and the top of the image touches the bottom of the image (see Fig. 6.12). To use the FFT each image and slice must obey periodic boundary conditions or be an integer number unit cells of the specimen (called a super cell). Interfaces and defects must be imbedded inside a large super cell.

In summary, some of the things that need to be specified correctly are:

Specimen parameters: atomic coordinates and numbers of the specimen and thickness of specimen

Instrumental parameters: defocus, C_s , objective aperture, etc.

Sampling size: number of pixels in the image and slice and the slice thickness.

Ensure that the total integrated intensity is at least 0.9 or higher (1.0 to start). Calculations with slightly higher or lower sampling should yield the same result if the sampling is adequate.

Slice thickness: usually the slices should correspond to the existing atomic layers in the specimen. If the slices are too thick, then the total integrated intensity will decline too much (as in the sampling size issue) and may produce false high order Laue zones corresponding to the slice thickness.

Wrap-around error: each slice must obey periodic boundary conditions

Chapter 8

The Programs



This chapter describes the programs that were used to calculate many of the figures shown in the text. These programs are also available on the associated web site (see link given in the preface). The general organization of the programs and some specific examples of running the programs are given. It describes how to prepare the input data files with the specimen description and how to actually run the programs. Alternately this discussion can be viewed as a description of some possible approaches to implementing programs to perform the calculation described earlier in this book.

There are two groups of programs. The TEMSIM group of programs (for conventional and scanning Transmission Electron Microscope image SIMulation) uses a simple command line user interface and the *computem* program has a more unified graphical user interface (GUI). Most of the basic calculations are separated into independent calculation-only modules with no obvious user interface. TEMSIM and *computem* mostly call the same low level calculation modules to perform the actual calculations, but have different front end user interfaces and different back end file save functions. TEMSIM is organized as several separate programs but *computem* is a large unified program with a GUI which many users find easier to use. Separating TEMSIM into different pieces makes the calculations easier to test and debug before incorporating into *computem*. The TEMSIM group is also easier to script into long sequences of operations (using scripting facilities available in most operating system). The command line interface in TEMSIM has almost no operating system dependence so is more portable.

8.1 TEMSIM Program Organization

The TEMSIM programs are written in a generic no-frills manner using C/C++ (Stroustrup [477]). The code adheres to the standard definition of the language as much as possible so that the programs will run on as many different types of computers as possible. The programs are nearly independent of the operating system used. Their main purpose is to perform the numerical simulation in an efficient manner without being dependent on any specific type or brand of computer. They do not have a very elegant user interface by today's standards, but they are as nearly machine independent as they can be. The programs are intended for people who are comfortable using the simple command line interface available on most operating systems. There is some error checking, but very inappropriate input may cause the programs to crash in an uncivilized manner. They have been compiled and run on a variety of different computers without requiring any changes to the program. They will probably evolve with time or be abandoned in favor of new programs. Some portions of TEMSIM are incorporated into *computem* with a graphical user interface (GUI).

The TEMSIM programs are a group of loosely coupled programs. The basic simulation steps are split into a small number of separate programs with the output of one program being used as the input for the next program. For example, there is one program called *atompot* (for atomic potential) to calculate the projected atomic potential of a two-dimensional slice through the specimen. This program should be run for each slice in the specimen. The output of *atompot* can be read by the program *mulslice* to calculate the wave function that would be transmitted through the specimen using the multislice method. A third program called *image* can then use the results of *mulslice* to calculate a defocused CTEM image. The advantage of splitting the programs this way is that *atompot* and *mulslice* take more computer time than *image* but their output can be reused several times. The program *image* can use the same results of *atompot* and *mulslice* several times to generate a series of images at different defocus in an efficient manner. Furthermore the output of *atompot* can also be used by *stemslic* to simulate a STEM image. The programs in the TEMSIM group can be combined in different ways to produce different results without having to reprogram each specific case or image simulation operation. This obviously requires using a standard disk data file format to store the intermediate images.

There are two possible strategies for describing the specimen structure. One strategy, applicable to specimens with a few repeating layers (periodic along z or the beam axis), is to manually decompose the specimen into a sequence of repeated slices. Simple crystals frequently divide into a small number of repeated layers. The atomic coordinates for each layer are generated by hand and the projected atomic potential of the layer (or slice) is calculated and stored in a disk file. The potentials are then read into memory and used over and over again in the multislice method. The programs *atompot*, *mulslice*, and *stemslic* use this approach. If there are only a few different layers that are repeated many times, then this is the

most efficient method because it avoids recalculating the projected atomic potential of the same layer over and over again. In principle it might be possible to automate this decomposition, but the programs still require this to be done by the human operator. A second strategy, applicable to amorphous specimen with no obvious repeating structure (along the beam direction), is to read in a list of all of the (three dimensional) coordinates of the atoms in the specimen, sort by z (position along the beam axis), and calculate the projected potential for each slice as it is needed and then discard it. If the specimen is completely amorphous, then the potentials cannot be reused so there is no loss of efficiency; however, this calculation can take substantially longer than reusing a small number of repeated layers or slices. The programs *autoslic* and *autostem* use this approach. This can also be used for periodic or semi-periodic structures if computer time is readily available.

autoslic and *autostem* are second generation programs that are split into a separate calculation portion and a separate user interface portion (front end) and file save portion (back end). This allows them to be used in both a command line user interface mode and a graphical user interface (GUI) mode. *incostem* is a fast approximate ADF-STEM calculation that is also organized in this manner.

8.1.1 *Image Display*

The numerical portion of the simulation programs can be written to be independent of the specific computer they are running on but the simple operation of displaying the image on the computer screen is very different on each type of computer and is usually also very difficult to program properly. However there are currently many different image display and manipulation programs available on most popular computer platforms. These programs range from simple display programs (some are distributed free) to complex commercial package with elaborate image manipulations capabilities. Even simple word processing programs can include images if they are in the correct format. There is a rather strong incentive to somehow use the existing image manipulation programs to display and manipulate the results of the image simulation without having to write a display program on each different type of computer. Using an image file format that the available image display programs recognize will allow the TEMSIM results to be feed into the existing image display programs. Each image program has its own constraints on which format the image data should be stored in to use the program. There are a wide variety of image file formats that can be used, ranging from proprietary formats from specific manufacturers to well-described standard formats published in publicly available manuals. Almost all of the available image display software supports the TIFF (or Tagged Image File Format) format. TIFF has been around for many years and is well supported on many different computers (many standards now exist). As of version 6.0, TIFF also has enough features to be usable for multislice image simulation. The TEMSIM package uses the TIFF standard image file format (with the standard extensions to support both 8-bit gray scale images for display and 32

bit floating point images for calculations, see discussion below). The results of the image simulation can be easily manipulated and displayed by a wide variety of available software.

8.1.2 Disk File Format

The TEMSIM package uses the TIFF standard file format to store image data. TIFF was originally designed in the late 1980s to store black and white images for desk top publishing and has evolved into a published standard supporting both black and white images and color images as well as two tone line drawings. Murray and vanRyper [367] have discussed TIFF and cataloged many other standard image formats. TIFF is more powerful and flexible than many other formats, which is both an advantage and a curse because it is also complicated. It can be very difficult to program a good TIFF subroutine library but the format can be extended to do a lot of different things. TIFF has many more features than are needed in any one applications and most applications only support a subset of TIFF features. Simply saying that a file is in TIFF format is not enough to specify the type of data format. The image must also be specified as color or black and white or a simple line drawing and the number of bits per pixel must be identified. The TEMSIM package uses a combination of 8-bit gray scale images and 32 bit floating point images (described in more detail below). When most image processing program say they support TIFF format they typically mean 8-bit gray scale images or occasionally mapped color or true color images.

The first eight bytes or header of a TIFF file specifies the byte ordering scheme the file uses and the byte offset of the first IFD or image file directory in the file. There is a threaded directory structure inside each TIFF file. TIFF files can use either the big-endian or little-endian byte ordering scheme. Byte ordering refers to the order in which the bytes (one byte is eight bits) are addressed within a 32 bit (or four byte) data element (or word). In big-endian byte ordering (used by some microprocessors) the byte address starts at the most significant byte and advances to the least significant byte. Little-endian byte ordering (used on Intel microprocessors) is just the opposite, the address starts at the least significant byte and increase to the most significant byte. All TIFF readers are required to read both byte ordering schemes so that TIFF image files should be transportable between different types of computers. (In practice some application software does not always follow this rule.) Also contained in the TIFF eight byte header is a pointer (or byte offset within the TIFF file) to an IFD or image file directory. The IFD contains a list of data about the image, such as the number of bits per pixel, the number of pixels in x and y , etc. Each data item is identified with a unique tag or eight bit code. TIFF stands for Tagged Image File Format because of this tagged data structure. There are several dozen different tags listed in the TIFF standard but only a small subset of a dozen or so are typically used in a given application. Subroutines that read TIFF files must somehow deal with many different possible tags and this tends to

make TIFF difficult to program. Also contained within the IFD is a list of byte offsets (or pointers) for the raster image data itself and a pointer to the next IFD in the file. If there are no more images in the file, then the next IFD pointer is NULL. Only the eight byte header is in a fixed position in the file. The IFD's and the image data associated with them may be anywhere in the file. The TIFF file has an internal threaded data structure. There can be more than one image, each with its own IFD. The first eight byte header points to the first IFD and its image data. The first IFD then points to the second IFD and its image data, and so forth. To read a TIFF file the computer program must follow all of the pointers as they wind their way through the file. This also presumes that the programming language can address any specific byte within the file (i.e., this essential requires using the C/C++ programming language). Refer to the actual published TIFF standard [70] for a complete description of the data format.

Most software applications that support TIFF images only read the first image in the file. The stated purpose of the second and later images in the TIFF file is for storing higher resolution versions of the image. This feature is very useful for image simulation. As of version 6.0 TIFF also supports a floating point pixel data type (each pixel is one 32 bit IEEE format floating point number). TEMSIM uses this feature to combine an 8 bit image with a 32 bit floating point image. The first image in the TIFF file is an 8-bit gray scale preview version of the image and the second image is the 32 bit floating point version of the image. Most display programs assume square pixels, so the 8 bit image is expanded in one direction if necessary (using bilinear interpolation as in Appendix E) to get square pixels. (Compressing the image using interpolation runs the risk of leaving out sharp points so is not used.) The second image, which is ignored by many image display programs, is a 32 bit floating point image used for numerical simulation. Although it seems as if each data file looks like an 8 bit image it really has 32 bits of precision for numerical calculation. Storing both versions of the image increases the size of the file by about 25% but allows using readily available image display programs. When you look at an intermediate TIFF image used in the TEMSIM package you should be careful not to save it from a standard TIFF application, because this will most likely destroy the hidden 32 bit portion of the image. Stacking the images and using 32 bit floating point pixels data are allowed within the TIFF standard so this type of format may be referred to as an extended TIFF format. When one TEMSIM program reads the results generated by another it is helpful for the image file to contain its parameters like electron energy, etc. This information is transferred in a third image in the TIFF file that is 512 pixels wide and one pixel high. This image is not for display but contains a 512 element array of image parameters. Complex images are stored side by side as two real floating point images. The program file *floatTIFF.cpp* contains a library of TIFF subroutines for reading and writing floating point TIFF images in this format.

Some application programs require that the name of a TIFF file end in “.tif” to be identified as a TIFF file, so it is a good practice to end all image data file names with “.tif.” Also, some display programs put the origin in the upper left corner and some put it in the lower left corner, which is sometimes confusing.

8.2 BF-CTEM Sample Calculations for Periodic Specimens

There are three basic computational steps in simulating a BF-CTEM image. The first step is to calculate the projected atomic potential of each slice of the specimen using the *atompot* program. The second step is to transmit the incident electron wave (usually a plane wave) through the specimen using the program *mulslice*. The third and final step is to form the image with defocus and the objective lens aberration using the program *image*.

This example will simulate an image of strontium titanate (SrTiO_3), which has a cubic perovskite structure with a cubic unit cell size of $a = 3.905 \text{ \AA}$. There are Sr atoms on all of the corners of the cubic and O atoms on center of each face, with a single Ti atom in the center of the cube. (There is an alternate description of this structure with the positions of Sr swapped with that of Ti and the O atoms on the edges instead of the faces.) With the optic axis of the electron microscope along one of the three primary cubic axes this specimen naturally divides into two rectangular slices. One slice is a face of the cube and the other is through the center of the cube.

The examples below list the computer response while each program is running. Each line containing information that the user must supply has a “>” at the beginning of the line. This is to separate the computer response from the user response and should not be entered when the program is actually run. Multiple numbers should be entered separated with spaces and without commas.

8.2.1 Atomic Potentials

The projected atomic potential of the slices in the specimen are calculated using *atompot*. This program calculates the structure factor in reciprocal space using the scattering factors in the first Born approximation and then does an inverse FFT to get the projected atomic potential (see Eq. 5.21). The result stored in the file does not contain the leading factor of $\lambda m/m_0$ so that it is independent of electron energy. The programs *mulslice* and *stemslic* add this factor later when the potential is used.

The *atompot* program can also apply symmetry operations to the atomic position using the following symmetry operation:

$$x_{\text{new}} = S_{\text{xai}}x_{\text{old}} + S_{\text{xbi}} \quad (8.1)$$

$$y_{\text{new}} = S_{\text{yai}}y_{\text{old}} + S_{\text{ybi}} \quad (8.2)$$

where the parameters S_{xai} , S_{xbi} , S_{yai} , and S_{ybi} are supplied for each symmetry operation. $(x, y)_{\text{old}}$ are the specified atomic coordinates and $(x, y)_{\text{new}}$ are the coordinates generated by the symmetry operation. If the specimen has a high degree of symmetry, this feature can greatly reduce the amount of data to type in.

Table 8.1 The format of the input data for *atompot*. There are two different atomic numbers Zatom1 and Zatom2 with n and m coordinates each. There may be an arbitrary number of different atomic numbers and an arbitrary number of coordinates for each atomic number

ax	by	cz		
Ns				
Sxa1	Sxb1	Sya1	Syb1	
Sxa2	Sxb2	Sya2	Syb2	
:	:	:	:	
SxaNs	SxbNs	SyaNs	SybNs	
<blank line>				
Zatom1				
occ1	xpos1	ypos1	wobble1	
:	:	:	:	
occn	xposn	yposn	wobblen	
<blank line>				
Zatom2				
occ1	xpos1	ypos1	wobble1	
:	:	:	:	
occn	xposm	yposm	wobblem	
<blank line>				
<blank line>				

The format of the input data file for *atompot* is shown in abbreviated form in Table 8.1. The first line of the file has three numbers (ax, by, cz) that are the dimensions of the super cell of one slice of the specimen in Angstroms. The slice thickness is cz. The next line has the number of symmetry operations (Ns) for each coordinate, followed by the symmetry operations themselves. There is one line for each symmetry operation and the number of lines must match Ns. If Ns = 0, then no symmetry operations are listed. After the symmetry operations the atomic coordinates of atoms are listed in groups with the same atomic number Zatom. Each line of coordinate data has the reduced coordinates xpos = x/ax and ypos = y/by of each atom. The first number on the coordinate data line is the occupancy (occ) of each atom. The occupancy is typically one but may be set to a fractional value (for example, the symmetry operations may generate several identical atoms at the same location and the occupancy may be used to correct for this duplication). At the end of each coordinate data line is a number labeled wobble signifying the rms random displacement (in Angstroms) for simulating thermal phonons (typically wobble = 0). This value is the rms deviation in each direction and not the 3D rms value. *atompot* uses a random number generator with a Gaussian distribution to simulate random thermal (phonon) displacements. The initial seed for the random number generator is obtained from the *clock()* function, so that each run should produce a different (random) results. This feature is mainly an historical artifact (may be removed in future) and is usually not used (*autoslic* and *autostem* do this much better). When all of the atoms for a particular atomic number have been listed there is a single blank line. Following this blank line is the next atomic number

Table 8.2 The *atompot* input data file srt.a.dat for the a layer of strontium titanate

```
3.9051 3.9051 1.9525
0
38
1.0000 0.0000 0.0000

8
1.0000 0.5000 0.5000
```

This is one face of the cube and has one strontium atom ($Z = 38$) in the corner and one oxygen atom ($Z = 8$) in the center

Table 8.3 The *atompot* input data file srb.dat for the b layer of strontium titanate

```
3.9051 3.9051 1.9525
0
22
1.0000 0.5000 0.5000

8
1.0000 0.5000 0.0000
1.0000 0.0000 0.5000
```

This is a plane through the center of the cube and has one titanium atom ($Z = 22$) in the center and two oxygen atoms ($Z = 8$) on the edges

(Zatom2) and the coordinates for this atomic number are listed in the same format. The input is terminated by two successive blank lines. Two different atomic numbers are shown but there may be any number of different atomic numbers (limited by the amount of computer memory available).

The input coordinates for both of the layers of the SrTiO₃ specimen are shown in Tables 8.2 and 8.3. Layer *a* has two atoms and no symmetry operations and layer *b* has three atoms and no symmetry operations. The input data files may be prepared using standard text editors or word processing programs if the file is saved as “text only.” The input data specifies the coordinates for one unit cell and *atompot* will expand the final potential to an arbitrary (positive) integer number of unit cells. The rms random deviation is left blank because this feature will not be used in this example. The results of running *atompot* on the data is shown below.

```
<---- run program atompot ---->

atompot version dated 5-aug-2017 EJK
Copyright (C) 1998-2017 Earl J. Kirkland
This program is provided AS-IS with ABSOLUTELY NO WARRANTY
under the GNU general public license
```

Warning: this program is obsolete and may be discontinued soon
calculate projected atomic potentials (to use in multislice)
using FFTW

Name of file with input crystal data :
>srtb.dat
Name of file to get binary output of atomic potential :
>srtbpot.tif
Real space dimensions in pixels Nx, Ny :
>512 512
Replicate unit cell by NCELLX,NCELLY,NCELLZ :
>8 8 1
Do you want to add thermal displac. to atomic coord.? (y/n) :
>n
2D lattice constants= 3.9051 x 3.9051 Angstroms
and propagation constant= 1.9525 Angstroms
Unit cell replicated to a= 31.2408, b= 31.2408, c= 1.9525 Ang.
Maximum symmetrical resolution set to 0.122034 Angstroms

64 atoms with Z= 38 (Sr)
64 atoms with Z= 8 (O)

for a grand total of 128 atoms
pix range 0.253792 to 47.6074
103184 fourier coeff. calculated in right half plane
The average real space value was 0.986566
CPU time (excluding set-up) = 0.12 sec.

<---- run program atompot ---->

atompot version dated 5-aug-2017 EJK
Copyright (C) 1998-2017 Earl J. Kirkland
This program is provided AS-IS with ABSOLUTELY NO WARRANTY
under the GNU general public license

Warning: this program is obsolete and may be discontinued soon
calculate projected atomic potentials (to use in multislice)
using FFTW

Name of file with input crystal data :
>srtb.dat
Name of file to get binary output of atomic potential :
>srtbpot.tif
Real space dimensions in pixels Nx, Ny :
>512 512
Replicate unit cell by NCELLX,NCELLY,NCELLZ :
>8 8 1
Do you want to add thermal displac. to atomic coord.? (y/n) :
>n
2D lattice constants= 3.9051 x 3.9051 Angstroms
and propagation constant= 1.9525 Angstroms

```
Unit cell replicated to a= 31.2408, b= 31.2408, c= 1.9525 Ang.
Maximum symmetrical resolution set to 0.122034 Angstroms
```

```
64 atoms with Z= 22 (Ti)
128 atoms with Z= 8 (O)
```

```
for a grand total of 192 atoms
pix range 0.0406346 to 30.2206
103184 fourier coeff. calculated in right half plane
The average real space value was 0.834076
CPU time (excluding set-up) = 0.16 sec.
```

8.2.2 *Multislice*

After the projected atomic potential has been calculated for each layer in the specimen (and stored in a file), the *mulslice* program is run. This program performs a multislice calculation to transmit the electron wave function through the specimen. A sample output using the strontium titanate potentials from Sect. 8.2.1 is shown below. This program allows the incident beam and the crystal to be tilted. The incident beam tilt should obey periodic boundary conditions (i.e., not all angles are allowed) and be small. The crystal tilt is calculated by adding a phase factor to the propagator (Eq. 6.93) and is only valid for small angles of no more than about 1°.

mulslice can also print out a table of values (real and imaginary part) for selected beams versus thickness. The beam (or Fourier coefficient) can be specified by its crystallographic index (h,k). However, this is the index in the super cell which is not necessarily the same as the primitive unit cell. This feature is not used in this example.

```
<---- run program mulslice ---->

mulslice version dated 4-may-2018 ejk
Copyright (C) 1998-2018 Earl J. Kirkland
This program is provided AS-IS with ABSOLUTELY NO WARRANTY
under the GNU general public license

Warning: this program is obsolete and may be discontinued soon

perform traditional CTEM multislice calculation
using FFTW with 4 thread(s)

Type in the stacking sequence :
>12(ab)

Type in the name of 2 atomic potential layers :

Name of file with input atomic potential :a
>srtapot.tif
```

```
Name of file with input atomic potential :b
>srtbpot.tif
Name of file to get binary output of multislice result:
>srtmul.tif
Do you want to include partial coherence (y/n) :
>n
NOTE, the program image must also be run.
Do you want to start from previous result (y/n) :
>n
Incident beam energy in kev:
>400
Crystal tilt x,y in mrad.:
>0 0
Incident beam tilt x,y in mrad.:
>0 0
Do you want to record the (real,imag) value
of selected beams vs. thickness (y/n) :
>n
Wavelength = 0.0164394 Angstroms
layer a, cz = 1.9525
layer b, cz = 1.9525
Size in pixels Nx x Ny= 512 x 512 = 262144 beams
Lattice constant a = 31.2408, b = 31.2408
Total specimen thickness = 46.86 Angstroms
Bandwidth limited to a real space resolution of 0.183052 Ang.
(= 89.8077 mrad) for symmetrical anti-aliasing.
Number of symmetrical non-aliasing beams = 91529
slice 1, layer = a, integrated intensity = 0.999959
slice 2, layer = b, integrated intensity = 0.999935
slice 3, layer = a, integrated intensity = 0.999851
slice 4, layer = b, integrated intensity = 0.999811
slice 5, layer = a, integrated intensity = 0.999658
slice 6, layer = b, integrated intensity = 0.999593
slice 7, layer = a, integrated intensity = 0.999351
slice 8, layer = b, integrated intensity = 0.999253
slice 9, layer = a, integrated intensity = 0.998905
slice 10, layer = b, integrated intensity = 0.998767
slice 11, layer = a, integrated intensity = 0.998303
slice 12, layer = b, integrated intensity = 0.998122
slice 13, layer = a, integrated intensity = 0.997535
slice 14, layer = b, integrated intensity = 0.997307
slice 15, layer = a, integrated intensity = 0.996598
slice 16, layer = b, integrated intensity = 0.996323
slice 17, layer = a, integrated intensity = 0.995502
slice 18, layer = b, integrated intensity = 0.995187
slice 19, layer = a, integrated intensity = 0.994269
slice 20, layer = b, integrated intensity = 0.993912
slice 21, layer = a, integrated intensity = 0.992917
slice 22, layer = b, integrated intensity = 0.992538
slice 23, layer = a, integrated intensity = 0.991511
slice 24, layer = b, integrated intensity = 0.991113
make output pix 512 x 512
pix range -3.95399 to 0.996049 real,
```

```
-1.85484 to 1.76015 imag
Total CPU time = 0.49 sec.
elapsed time = 0 sec.
```

The stacking sequence of the slices or layers of the specimen is entered in symbolic form as 12(ab) in this example. Each layer is given a unique single character name in the order abcd...xyzABCD...XYZ. There are 52 possible layer names (it is case sensitive). Pairs of parenthesis denote a group of slices and the leading number is the number of times that the group in parenthesis is repeated. 12(ab) means that there are twelve repeats of the sequence ab. Parenthesis may be nested up to 100 levels and structures such as 5(2(ab)3(ca)) are possible.

8.2.3 *Image Formation*

The multislice calculation produces the wave function at the exit surface of the specimen. The objective lens images this wave function. The program *image* adds the effects of the objective lens aberrations and defocus and produces an image as it would be observed in the electron microscope. *image* can perform this calculation in a completely coherent mode or add partial coherence. The example shown below is a coherent image. *image* does not change the input data file (from *multslice*) so it can be run several times with the same input file (without running *multslice* again) to produce a whole defocus series.

```
<---- run program image ---->

image version dated 30-jul-2017 (ejk)
Copyright (C) 1998-2017 Earl J. Kirkland
This program is provided AS-IS with ABSOLUTELY NO WARRANTY
under the GNU general public license

calculate TEM images with defocus, using FFTW

Name of file with input multislice result:
>srtmul.tif
Type 0 for coherent real space image,
or 1 for partially coherent real space image,
or 2 for diffraction pattern output:
>0
Name of file to get defocused output:
>srtimg.tif
Spherical aberration Cs3, Cs5 (in mm.):
>1.3 0.0
Defocus in Angstroms:
>566
Objective aperture size in mrad:
>9.33
Mag. and angle of two-fold astig. (in Angst. and degrees):
>0 0
```

```
Mag. and angle of three-fold astig. (in Angst. and degrees) :  
>0 0  
Objective lens and aperture center x,y in mrad  
(i.e. non-zero for dark field):  
>0 0  
Starting pix energy = 400 keV  
Starting pix range -3.95399  0.996049 real  
                           -1.85484  1.76015 imag.  
calculate coherent image....  
There were 989 pixels inside the obj. apert.  
output image  
Pix range 0.0510914 to 1.43728  
Elapsed time = 0.03 sec.
```

8.2.4 Partial Coherence

Partial coherence may be added in two different ways. If the specimen is thin, then the image may be calculated using the transmission cross coefficient as in Sect. 5.4.3 as shown below. The actual simulated image is shown in Fig. 8.1. The black dots correspond to the oxygen atom positions and there is a contrast reversal in the image.

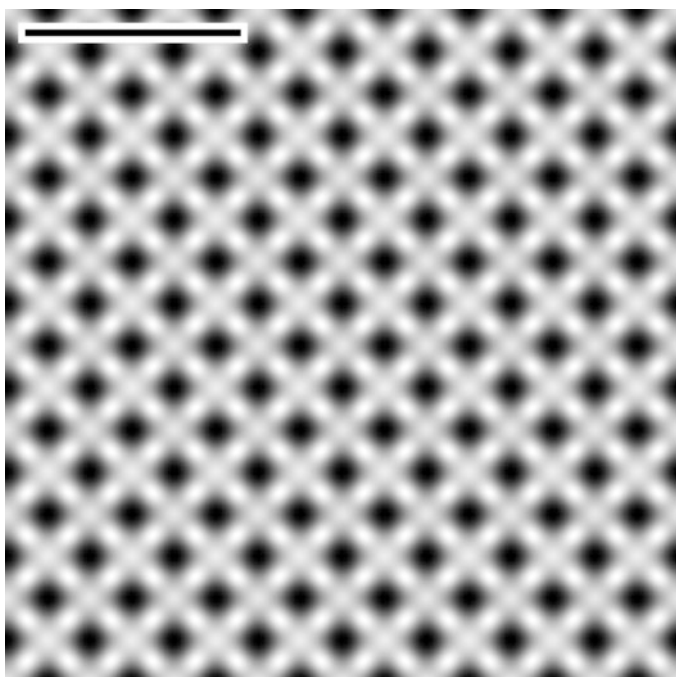


Fig. 8.1 The results of the program *image* for a partially coherent BF-CTEM image of strontium titanate. The scale bar in the upper left corner is 10 Å

```
<---- run program image ---->

image version dated 30-jul-2017 (ejk)
Copyright (C) 1998-2017 Earl J. Kirkland
This program is provided AS-IS with ABSOLUTELY NO WARRANTY
under the GNU general public license

calculate TEM images with defocus, using FFTW

Name of file with input multislice result:
>srtmul.tif
Type 0 for coherent real space image,
or 1 for partially coherent real space image,
or 2 for diffraction pattern output:
>1
Name of file to get defocused output:
>srtimg2.tif
Spherical aberration Cs3, Cs5 (in mm.):
>1.3 0.0
Defocus in Angstroms:
>566
Objective aperture size in mrad:
>12
Illumination semiangle in mrad:
>0.6
Defocus spread in Angstroms:
>50
Starting pix energy = 400 keV
Starting pix range -3.95399 0.996049 real
                           -1.85484 1.76015 imag.
calculate partially coherent image....
output image
Pix range 0.158975 to 1.32719
Elapsed time = 0.17 sec.
```

A more accurate type of calculation (for thick specimen) is shown next. This method performs a multislice calculation for each incident angle (from the condenser illumination system) and sums the resulting images incoherently as described in Eq. 6.98. The program *mulslice* does this calculation as shown below. The allowed incident angles must satisfy periodic boundary conditions so only a few discrete illumination angles can be used.

```
<---- run program mulslice ---->

mulslice version dated 4-may-2018 ejk
Copyright (C) 1998-2018 Earl J. Kirkland
This program is provided AS-IS with ABSOLUTELY NO WARRANTY
under the GNU general public license

Warning: this program is obsolete and may be discontinued soon

perform traditional CTEM multislice calculation
using FFTW with 4 thread(s)
```

```
Type in the stacking sequence :
>12 (ab)

Type in the name of 2 atomic potential layers :

Name of file with input atomic potential :a
>srtapot.tif
Name of file with input atomic potential :b
>srtbpot.tif
Name of file to get binary output of multislice result:
>srtmul2.tif
Do you want to include partial coherence (y/n) :
>y
Illumination angle min, max in mrad:
>0 0.6
Spherical aberration (in mm.):
>1.3
Defocus, mean, standard deviation, and sampling size (in Ang.):
>566 50 10
Objective aperture (in mrad) =
>12
Magnitude and angle of 2-fold astig. (in Ang. and degrees):
>0 0
Magnitude and angle of 3-fold astig. (in Ang. and degrees):
>0 0
Incident beam energy in kev:
>400
Crystal tilt x,y in mrad.:
>0 0
Wavelength = 0.0164394 Angstroms
layer a, cz = 1.9525
layer b, cz = 1.9525
Size in pixels Nx x Ny= 512 x 512 = 262144 beams
Lattice constant a = 31.2408, b = 31.2408
Total specimen thickness = 46.86 Angstroms
Bandwidth limited to a real space resolution of 0.183052 Ang.
(= 89.8077 mrad) for symmetrical anti-aliasing.
Number of symmetrical non-aliasing beams = 91529
Illumination angle sampling (in mrad) = 0.526217, 0.526217

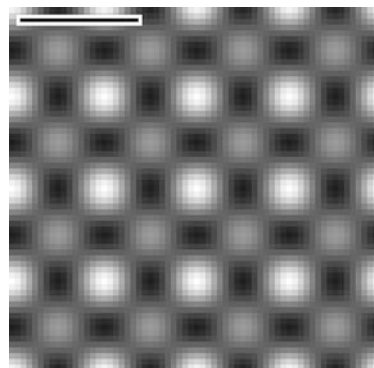
Illum. angle = 0, -0.526217 mrad, total intensity= 0.991149
Illum. angle = -0.526217, 0 mrad, total intensity= 0.99115
Illum. angle = 0, 0 mrad, total intensity= 0.991112
Illum. angle = 0.526217, 0 mrad, total intensity= 0.991149
Illum. angle = 0, 0.526217 mrad, total intensity= 0.991148
Total number of illumination angle = 5
Total number of defocus values = 25
pix range 0.196647 to 1.45265 real,
    0 to 0 imag
Total CPU time = 0.912 sec.
elapsed time = 1 sec.
```

8.3 ADF-STEM Sample Calculations for Periodic Specimens

The program *stemslic* performs a multislice simulation for a STEM image. It generates an incident focused probe wave function at each position of the final image, transmits the wave function through the specimen (using *multislice*), and then integrates the electron intensity on the detector. It can generate the signal for several detectors at the same time. This is obviously a significant increase in computer time relative to a CTEM image because a STEM simulation requires a multislice simulation at each point in the image, whereas a whole CTEM image is calculated in parallel. In response to this problem *stemslic* can generate a one-dimensional line scan or a two-dimensional image. A line scan is relatively quicker to calculate and can yield a significant amount of information about the specimen. *stemslic* uses the same projected atomic potential (produced by *atompot*) for each slice as is required for *multislice*. Modeling interfaces may require a very large number of pixels in the transmission function to avoid periodic interference between interfaces. *stemslic* allows for the number of pixels in the probe wave function to be less than the number of pixels in the transmission function to decrease the required computer time. The pixel size in each must be the same however. A smaller probe wave function slides around inside a larger transmission function (with the periodicity of the transmission function not the probe wave function).

There are two examples shown below. Each uses the projected atomic potential as calculated using *atompot* for the CTEM simulation (Sect. 8.2.1). The first simulation below is a 1D line scan image and the second simulation is a 2D image simulation. As in *multislice*, crystal tilt is calculated by adding a phase factor to the propagator (Eq. 6.93) and is only valid for small angles of no more than about 1° . Both an inner and outer angle may be specified for the objective aperture to model hollow cone and apodization effects (Loane and Silcox [315]) to minimize the probe size. The initial point of the line scan is (x_i, y_i) and the final point is (x_f, y_f) . The simulated ADF-STEM image is shown in Fig. 8.2. The white spots correspond to the Sr atom positions. The gray dot in the middle of four white dots are the Ti atom positions and the black dots are the oxygen positions.

Fig. 8.2 The results of *stemslic* for an ADF-STEM image of strontium titanate. The scale bar in the upper left corner is 5 Å. This image corresponds to the lower left corner of the BF-CTEM image in Fig. 8.1. The Sr atom is in the lower left corner and should be white



```
<---- run program stemslic ---->

stemslic(e) version dated 10-aug-2017 (ejk)
Copyright (C) 1998-2017 Earl J. Kirkland
This program is provided AS-IS with ABSOLUTELY NO WARRANTY
under the GNU general public license

Warning: this program is obsolete and may be discontinued soon

perform STEM multislice using FFTW with 4 thread(s)

Type in the stacking sequence :
>12(ab)

Type in the name of 2 atomic potential layers :

Name of file with input atomic potential a:
>srtapot.tif
Name of file with input atomic potential b:
>srtbpot.tif
STEM prb param.,V0(kv),Cs3(mm),Cs5(mm),df(Ang.),apert1,2(mrad):
>100 1.3 0.0 850 0 11.43
Magnitude and angle of 2-fold astig. (in Ang. and degrees):
>0 0
Magnitude and angle of 3-fold astig. (in Ang. and degrees):
>0 0
wavelength = 0.0370144 Angstroms
Size of probe wavefunction Nx,Ny in pixels :
>512 512
Crystal tilt x,y in mrad. :
>0 0
Do you want to calculate a 1D line scan (y/n) :
>y
Number of detector geometries :
>2
Name of file to get output of 1D STEM multislice result :
>srt100_1d.txt
Detector 1: Type, min,max angles(mrad) of collector :
>50 200
Detector 2: Type, min,max angles(mrad) of collector :
>100 200
xi, xf, yi, yf, nout :
>0 12 0 0 25
layer a, cz = 1.9525
layer b, cz = 1.9525
Size in pixels Nx x Ny = 512 x 512 = 262144 total pixels,
lattice constants a,b = 31.2408 x 31.2408
Total specimen thickness = 46.86 Angstroms
Number of symm. anti-aliasing beams in trans. function = 91529
with a resolution of 0.183052 Angstroms.
Number of symmetrical anti-aliasing beams in probe = 91529
    1           0           0       0.0865097      0.0692008
    2           0.5          0       0.0722205      0.0574117
    3             1          0       0.0421764      0.0327658
```

4	1.5	0	0.0185487	0.0135994
5	2	0	0.011472	0.00792155
6	2.5	0	0.0218633	0.016271
7	3	0	0.0479635	0.0374944
8	3.5	0	0.0768416	0.0612204
9	4	0	0.0859489	0.0687375
10	4.5	0	0.0670029	0.0531162
11	5	0	0.0366695	0.0282767
12	5.5	0	0.0158581	0.0114361
13	6	0	0.0120988	0.00842279
14	6.5	0	0.0257812	0.0194373
15	7	0	0.0538918	0.0423487
16	7.5	0	0.0807025	0.0644054
17	8	0	0.0842883	0.0673658
18	8.5	0	0.0613653	0.0484815
19	9	0	0.031558	0.0241205
20	9.5	0	0.0137998	0.00978486
21	10	0	0.0133547	0.00942819
22	10.5	0	0.0302642	0.0230702
23	11	0	0.0598023	0.0471978
24	11.5	0	0.083662	0.0668486
25	12	0	0.0815915	0.0651392

The total integrated intensity range was:
0.9684 to 0.996714

CPU time = 3.44 sec.
elapsed time = 3 sec.

A two-dimensional image can be calculated as:

<---- run program stemslic ---->

```
stemslic(e) version dated 10-aug-2017 (ejk)
Copyright (C) 1998-2017 Earl J. Kirkland
This program is provided AS-IS with ABSOLUTELY NO WARRANTY
under the GNU general public license
```

Warning: this program is obsolete and may be discontinued soon
perform STEM multislice using FFTW with 4 thread(s)

Type in the stacking sequence :
>12(ab)

Type in the name of 2 atomic potential layers :

```
Name of file with input atomic potential a:  
>srapot.tif
Name of file with input atomic potential b:  
>srbtpot.tif
STEM prb param.,V0(kv),Cs3(mm),Cs5(mm),df(Ang.),apert1,2(mrad):  
>100 1.3 0.0 850 0 11.43
Magnitude and angle of 2-fold astig. (in Ang. and degrees):  
>0 0
Magnitude and angle of 3-fold astig. (in Ang. and degrees):  
>0 0
```

```
wavelength = 0.0370144 Angstroms
Size of probe wavefunction Nx,Ny in pixels :
>512 512
Crystal tilt x,y in mrad. :
>0 0
Do you want to calculate a 1D line scan (y/n) :
>n
Number of detector geometries :
>1
Detector 1: Type, min,max angles(mrad) of collector :
>50 200
Name of file to get output of result for this detector:
>srtadf.tif
xi,xf,yi,yf, nxout,nyout :
>0 15.376 0 15.376 64 64
layer a, cz = 1.9525
layer b, cz = 1.9525
Size in pixels Nx x Ny = 512 x 512 = 262144 total pixels,
lattice constants a,b = 31.2408 x 31.2408
Total specimen thickness = 46.86 Angstroms
Number of symmm. anti-aliasing beams in trans. function = 91529
with a resolution of 0.183052 Angstroms.
Number of symmetrical anti-aliasing beams in probe = 91529
output file size in pixels is 64 x 64
iy= 0, min[0]= 0.0113937, max[0]= 0.0865097
iy= 1, min[0]= 0.0113937, max[0]= 0.0865097
iy= 2, min[0]= 0.0113937, max[0]= 0.0865097
iy= 3, min[0]= 0.0113937, max[0]= 0.0865097
:
:
iy= 56, min[0]= 0.0113937, max[0]= 0.0865097
iy= 57, min[0]= 0.0113937, max[0]= 0.0865097
iy= 58, min[0]= 0.0113937, max[0]= 0.0865097
iy= 59, min[0]= 0.0113937, max[0]= 0.0865097
iy= 60, min[0]= 0.0113937, max[0]= 0.0865097
iy= 61, min[0]= 0.0113937, max[0]= 0.0865097
iy= 62, min[0]= 0.0113937, max[0]= 0.0865097
iy= 63, min[0]= 0.0113937, max[0]= 0.0865097
output pix range : 0.0113937 to 0.0865097
The total integrated intensity range was:
0.9684 to 0.996743

CPU time = 494.344 sec.
elapsed time = 495 sec.
```

8.4 Non-periodic Specimens

Specimens that have no obvious periodic structure along the beam or z direction require another approach to image simulation. The programs *autoslic* and *autostem* implement this strategy. The specimen is described as a sequence of (x, y, z) coordinates with an associated atomic number Z_{atom} . This sequence is first sorted

by depth (along z) and then is automatically sliced into layers of a specified thickness Δz . The projected atomic potential of each slice is calculated, the electron wave function is transmitted through the slice and propagates to the next slice. The atomic potential is discarded after each slice and the process is repeated for each successive slice until the electron wave function has reached the exit surface of the specimen. This approach does not require a possibly tedious effort on the part of the user to decompose the specimen into repeating layers but will take much more computer time than calculations using repeating slices (as in *atompot*, *mulslice*, and *stemslice*). However, if there is no repetitive structure along the beam direction (z), then there is no significant difference in computer time. *autoslic* and *autostem* can be dramatically easier to use than *mulslice* or *stemslice* for specimens with defects or interface or completely amorphous specimens

This approach also uses a different method to calculate the projected atomic potential of each slice (as compared to *atompot*). The computer time for this non-periodic approach to image simulation is dominated by the calculation of the projected atomic potentials of the slices, and this step should be optimized if possible. (A STEM calculation may use the same potential for many probes so may scale differently.) The atomic potential is very localized in real space (see Fig. 5.5, for example) but it is very extended in reciprocal space. It is more efficient to calculate the projected atomic potential in real space using Eq. 5.19 because there are much fewer pixels to fill in (Pan et al. [393]). Each atomic potential is assumed to have a range of no more than 3 Å in real space and the individual projected potentials are calculated from expression (5.11). The transcendental functions involved are time-consuming to calculate so a look up table of cubic spline interpolation coefficients (using the quasi-Hermite spline method of Akima [4, 5]) is generated for the atomic potentials as needed (i.e., only for the specific atomic numbers needed). The potential is sampled on a logarithmic grid to get more points near the origin where the potential is rapidly changing. Using the spline look up table reduces the CPU time by about a factor of three to four on typical specimens. The total projected potential (integrated from minus infinity to plus infinity) has some extent so each slice must be thicker than the range of the potential for a single atom (about one Angstroms).

The input data format to describe a specimen structure is shown in Table 8.4. The first line is a comment line with a brief description of the specimen (ignored by the program). The second line has the unit cell dimensions of the specimen in units of Angstroms. Each following line is the coordinates for one atom. The first number Zatom is the atomic number for the atom. The next three numbers are its three-dimensional coordinates (xpos,ypos,zpos). All of the coordinates are assumed to be between (0,0,0) and (ax,by,cz) (i.e., the coordinates are positive). The fifth number is the occupancy for the atom (as in *atompot*). The last number on the line, wobble, is the standard deviation (in Angstroms) of the rms displacement if random thermal displacements are used. (This is the rms value in each direction and not the 3D rms value.) These displacements are generated using a random number generator with a

Table 8.4 The format of the input data for *autoslic* and *autostem* and *incostem*. The first line is a comment line (ignored by the program)

<comment line>

ax	by	cz			
Zatom1	xpos1	ypos1	zpos1	occ1	wobble1
Zatom2	xpos2	ypos2	zpos2	occ2	wobble2
:	:	:	:	:	:
ZatomN	xposN	yposN	zposN	occN	wobbleN
-1					

The second line is the unit cell dimensions of the specimen. Each line following the second line is the atomic number and position of one atom in the specimen. There may be an arbitrary number of different atoms, each with its own atomic number, position, and thermal vibration amplitude

Gaussian distribution. The initial seed for the random number generator is obtained from the *clock()* function, and should produce a different (pseudo-random) result each time the program is run.

The specimen can be expanded to an arbitrary number of unit cells using the unit cell dimensions. The specimen would then be periodic and it would be better to use *mulslice*. However this feature is useful for simulating the effects of random thermal vibration, because random displacements can be added to the replicated unit cell coordinates to generate an essentially non-periodic structure. The random thermal displacements can be scaled with a semi-classical temperature law as:

$$\text{wobble} = \text{wobble}_0 \sqrt{\frac{T}{300}} \quad (8.3)$$

where wobble_0 is the value appearing in the input file. Although this is not very rigorous it provides a simple methods of changing all of the thermal displacements with a single control variable. The apparent temperature can be set to some nonphysical value to get the actual scaling for a more appropriate scaling law if necessary.

autoslic can print out a table of values for selected beams versus thickness. The beam (or Fourier coefficient) is specified by its crystallographic index (h,k) ; however, this is the index in the super cell which is not necessarily the same as the primitive unit cell.

8.4.1 Fixed Beam Calculation

The previous examples were calculations of real space images. This example will use *autoslic* to calculate a convergent beam diffraction (CBED) pattern of a specimen with thermal vibrations. This program is not limited to diffraction patterns and can calculate images as well, just as *atompot* and *mulslice* can

calculate diffraction patterns as well as images. Higher order aberrations may also be included.

The program *autoslic* can calculate a CBED pattern including thermal vibrations. A focused probe at a specified position is transmitted through the specimen and the square modulus of the Fourier transform of the exit wave function is the CBED pattern. A conventional electron diffraction pattern can also be calculated if the incident wave function were a plane wave (possible with this program but is not shown here). Thermal diffuse scattering (TDS) can be modeled by adding a set of random Gaussian thermal offsets in the atomic positions to produce a snapshot of one phonon configuration in the frozen phonon approach. One set of displacements produces one noisy CBED pattern. Averaging the CBED over several different sets of random displacements produces a time averaged TDS CBED pattern. Each set of random displacements is by definition independent so it is computationally convenient to calculate each CBED pattern in parallel, one thread (or CPU) per each set of displacements (using openMP).

A sample run is shown below and the resulting CBED pattern is shown in Fig. 8.3. The input data for this run is in the file si100.xyz shown in Table 8.5. Each silicon atom is given an rms random displacement of 0.078 Å, to simulate thermal diffuse scattering. Each phonon configuration is launched independently at about the same time. Each CPU echoes its configuration index at about the same time so the final thread order is listed in more or less random order (which looks odd).

Fig. 8.3 The results of the *autoslic* for a convergent beam diffraction pattern of 100 silicon averaged over 16 phonon configurations. The image intensities are shown on a logarithmic scale

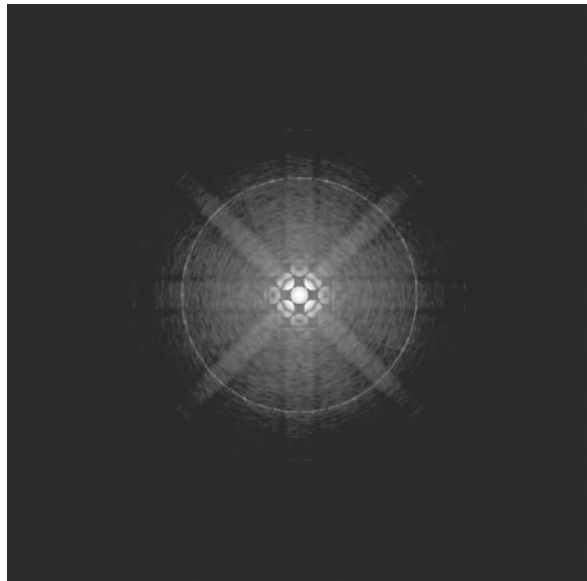


Table 8.5 The *autoslic* input data for 100 silicon in xyz format

```

one unit cell of 100 silicon
      5.43    5.43    5.43
 14  0.0000  0.0000  0.0000  1.0  0.078
 14  2.7150  2.7150  0.0000  1.0  0.078
 14  1.3575  4.0725  1.3575  1.0  0.078
 14  4.0725  1.3575  1.3575  1.0  0.078
 14  2.7150  0.0000  2.7150  1.0  0.078
 14  0.0000  2.7150  2.7150  1.0  0.078
 14  1.3575  1.3575  4.0725  1.0  0.078
 14  4.0725  4.0725  4.0725  1.0  0.078
-1

<---- run program autoslic ---->

autoslic(e) version dated 28-mar-2019 (ejk)
Copyright (C) 1998-2019 Earl J. Kirkland
This program is provided AS-IS with ABSOLUTELY NO WARRANTY
under the GNU general public license

perform CTEM multislice with automatic slicing and FFTW
and multithreaded using openMP

Name of file with input atomic coord. in x,y,z format:
>si100.xyz
Replicate unit cell by NCELLX,NCELLY,NCELLZ :
>6 6 40
Name of file to get binary output of multislice result:
>sicbed.tif
Do you want to include partial coherence (y/n) :
>n
Do you want to calculate CBED with TDS (y/n) :
>y
Spherical aberration Cs3, Cs5(in mm.) :
>1.3  0.0
Defocus (in Angstroms) =
>555
Objective aperture (in mrad) =
>8.91
type higher order aber. name (as C32a, etc.) followed
by a value in mm. (END to end)
>END
CBED probe position (in Ang.):
>17.0 16.0
Incident beam energy in kev:
>100
Wavefunction size in pixels, Nx,Ny:
>512 512
Crystal tilt x,y in mrad.:
>0  0

```

```
Slice thickness (in Angstroms) :  
>1.3575  
Do you want to include thermal vibrations (y/n) :  
>y  
Type the temperature in degrees K:  
>300  
Type number of configurations to average over:  
>16  
Random number seed initialized to 1561944323  
Do you want to output intensity on a log scale (y/n) :  
>y  
electron wavelength = 0.0370144 Angstroms  
11520 atomic coordinates read in  
one unit cell of 100 silicon  
Size in pixels Nx, Ny= 512 x 512 = 262144 beams  
Lattice constant a,b = 32.58, 32.58  
Total specimen range is  
0 to 31.2225 in x  
0 to 31.2225 in y  
0 to 215.842 in z  
Range of thermal rms displacements (300K) = 0.076 to 0.076  
calculate CBED  
fit from r= 0.01 to r= 5  
193 pixels in obj. apert.  
configuration # 1  
configuration # 11configuration # 5  
  
configuration # 14  
configuration # 9  
configuration # 10  
configuration # 12  
configuration # 3  
configuration # 15  
configuration # 13  
configuration # 7  
configuration # 16  
# 3 total intensity = 0.988375  
configuration # 4  
# 12 total intensity = 0.988954  
# 9 total intensity = 0.987783  
# 15 total intensity = 0.988593  
# 10 total intensity = 0.987985  
# 11 total intensity = 0.988536  
# 16 total intensity = 0.98732  
# 1 total intensity = 0.988416  
configuration # 2  
# 7 total intensity = 0.988016  
configuration # 8  
# 14 total intensity = 0.988587  
# 13 total intensity = 0.987927  
# 5 total intensity = 0.987747  
configuration # 6  
# 4 total intensity = 0.988971  
# 2 total intensity = 0.989023
```

```
# 6 total intensity = 0.988558
# 8 total intensity = 0.987621
write azimuthal averaged intensity vs.
    spatial frequency k, into file azimuth.dat
pix range -1.88946 to 7.00333 real,
    0 to 0 imag
Total CPU time = 13.372 sec.
wall time = 13.372 sec.
```

8.4.2 Scanned Beam Calculation

The program *autostem* calculates a high-resolution ADF-STEM or scanning confocal image of a specimen that is described by a list of atoms and their positions. In ADF mode the detector geometry may be described as an annulus bounded by two polar angles or a segment bounded by two azimuthal angles and two polar angles. The resulting signals may be combined using *sumpix* to produce a variety of shaped detectors. The *atan2()* function is used to denote the segments in the azimuthal direction, which is defined only for angle between -180 and $+180^\circ$, so the segments cannot cross this boundary (although two adjacent segments might be added together to achieve a similar result).

autostem is a combination of *autoslic* and *stemslic* with a few extra tricks to dramatically reduce the CPU time and make it easier to produce ADF STEM images with the frozen phonon approximation. A large fraction of the CPU time is used in the calculation of the transmission functions for each slice, which are all different with phonons. *stemslic* reuses many identical slices to reduce CPU time, but this does not work with the frozen phonon method or amorphous specimens. *autostem* reduces the CPU time by reusing the transmission function for several probes (using lots of CPU memory). For an image it will do a whole line of the image at one time using the same transmission function. The statistics seem to work out if there are enough phonon configurations (i.e., adjacent probe positions are not really independent for phonons). This produces a large improvement in speed, making this calculation practical (close to the same time for one phonon configuration as *stemslic*). *autostem* also does all of the averaging (over phonon configurations) in memory with a single simple output file rather than requiring the user to calculate the average with a separate program. This process is generally transparent to the user (except for being much faster). For example, to calculate a 128×128 image, *autostem* will propagate 128 probes (each 512×512 typically) at once (using a lot more memory) and repeat for 128 lines and also repeat both steps for each phonon configuration.

This program can save multiple thicknesses in one run to avoid multiple runs for intermediate thickness and includes higher order aberrations for an aberration-corrected microscope. The thickness levels are measured from the beginning of the specimen (unit cell). It propagates many probes at once which is much faster but uses much more memory (it is not hard to run out of memory on a 32 bit computer).

In addition this program is multithreaded. If running on a computer with more than one processor in a shared memory configuration (SMP), the program will use all available CPUs (up to one per probe) to reduce the total computation time (using openMP). Although it may still take a lot of CPU time for some specimens, it is much faster than other approaches (for ADF-STEM with TDS) and can run by itself most of the time. There is also a GPU version of *autostem* that further reduces the CPU time.

Confocal mode has a lot in common with ADF-STEM so this program can calculate confocal results by just adding an extra lens on the exit.

8.4.2.1 Atomic Coordinates

This program reads in a 3D atomic coord. in *xyz* format (Table 8.4), automatically slices the specimen (as *autoslic*), calculates ADF-STEM images and line scans (as *stemslice*), and integrates over phonon configurations if needed. The atomic coordinates may be randomly displaced to simulate thermal motion (the frozen phonon approx.) and then sorted by *z* as in *autoslic*. The calculation starts slightly before the beginning of the specimen (lowest *z*) with the specified defocus value, and continues until slightly past the specimen (covering a distance slightly larger than the super cell of the specimen).

8.4.2.2 Sample Run

Below is an example of running *autostem* in one mode. Lines beginning with *>* are typed in by the user (without the *>*). The other lines are printed by the program. There are many (almost too many) different modes of this program. It can produce a single line scan or a whole image. There is also an *xz* mode in which the line scan is saved at all thickness levels and output in image form, which is a convenient visual representation of the fringe contrast versus depth. This example uses only two phonon configurations for simplicity which is not sufficient. In practice something like 10–20 configurations should be used (averaged over). Figure 8.4 shows the results for *xz* mode (other figures in this book use other modes). Two detector geometries are for ADF-STEM and one is for a confocal detector, which adds some extra questions on the collector lens and a little CPU time for this extra step. The initial point of the line scan is (x_i, y_i) and the final point is (x_f, y_f). Several output files are generated (different thickness levels, different detectors, etc.). The output “.txt” file lists which files correspond to which parameters. The “.dat” file has the line scan data and the “.tif” files have image data.

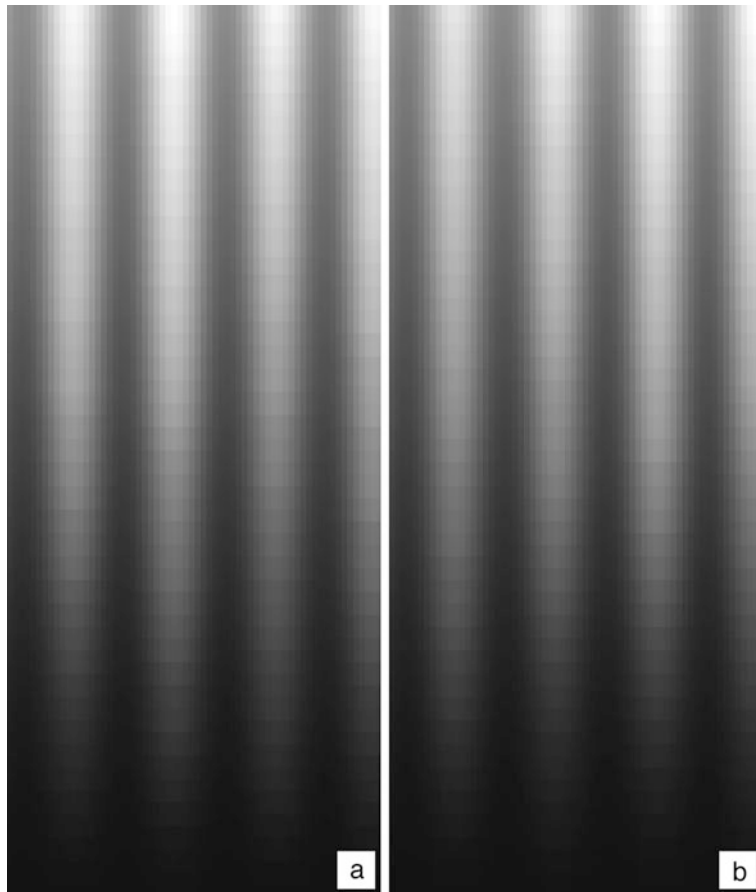


Fig. 8.4 Example of *autostem* in xz mode (line scan vs. thickness), with the start of the specimen (thin) at the bottom and the end (thick part) at the top. This illustrates how the lattice intensity increases with thickness. The horizontal and vertical scales may be different. In this case, the scale is 10 Å in the horizontal directions and 206 Å in the vertical direction. **(a)** First ADF detector and **(b)** second ADF detector

```
<---- run program autostem ---->

autostem (ADF,confocal,segmented) version dated 30-jan-2019
(ejk)
Copyright (C) 1998-2019 Earl J. Kirkland
This program is provided AS-IS with ABSOLUTELY NO WARRANTY
under the GNU general public license

Calculate STEM images using FFTW
and multithreaded using openMP
```

```
To calculate 2D pos. aver. CBED, include a file name on
command line.
Name of file with input atomic potential in x,y,z format:
>si100.xyz
Replicate unit cell by NCELLX,NCELLY,NCELLZ :
>5 5 38
STEM probe parameters, V0(kv), Cs3(mm), Cs5(mm),
df(Angstroms), apert1,2(mrad) :
>200 1 0 450 0 10
type higher order aber. name (as C32a, etc.) followed
by a value in mm. (END to end)
>END
Do you want to add random pi/4 tunning errors for orders
2 to 5 (y/n) :
>n
wavelength = 0.0250793 Angstroms
Size of specimen transmission function Nx,Ny in pixels :
>512 512

Size of probe wave function Nx,Ny in pixels :
>512 512
Crystal tilt x,y in mrad. :
>0 0
Do you want to calculate a 1D line scan (y/n) :
>y
Do you want to save all depth information as xz image (y/n) :
>y
File name prefix to get output of STEM multislice result
    (no extension) :
>test1dbig
Number of detector geometries (>=1):
>3
Detector 1, type: min max polar angles(mrad) or radius(Ang.)
followed by m, A, or seg (ADF, confocal, segmented-mrad)
add phimin phimax (degrees) if segmented
>50 200 m
normal ADF detector
Detector 2, type: min max polar angles(mrad) or radius(Ang.)
followed by m, A, or seg (ADF, confocal, segmented-mrad)
add phimin phimax (degrees) if segmented
>80 200 m
normal ADF detector
Detector 3, type: min max polar angles(mrad) or radius(Ang.)
followed by m, A, or seg (ADF, confocal, segmented-mrad)
add phimin phimax (degrees) if segmented
>0 3 A
confocal detector
Collector lens parameters, Cs3(mm), Cs5(mm), df(Angstroms),
apert1,2(mrad) :
>1.3 0 700 0 10.37
Magnitude and angle of 2-fold astigmatism (in Ang. and
degrees) :
>0 0
```

```
Magnitude and angle of 3-fold astigmatism (in Ang. and
degrees) :
>0 0
xi, xf, yi, yf, nout :
>1 11 5.43 5.43 64
Slice thickness (in Angstroms) :
>1.36
Do you want to include thermal vibrations (y/n) :
>y
Type the temperature in degrees K:
>300
Type number of configurations to average over:
>2
Random number seed initialized to 1549075158
electron wavelength = 0.0250793 Angstroms
7600 atomic coordinates read in
one unit cell of 100 silicon
Lattice constant a,b,c = 27.15, 27.15, 206.34
save up to 152 thickness levels
Total specimen range is
 0 to 25.7925 in x
 0 to 25.7925 in y
 0 to 204.982 in z
Range of thermal rms displacements (300K) = 0.076 to 0.076
Bandwidth limited to a real space resolution of 0.159082
  Angstroms
  (= 157.65 mrad) for symmetrical anti-aliasing.
Number of symmetrical anti-aliasing beams in probe = 91529
Number of beams in probe aperture = 373
output file size in pixels is 1 x 64
fit from r= 0.01 to r= 5
configuration # 1
The new range of z is -0.126899 to 205.178
configuration # 2
The new range of z is -0.115034 to 205.119
output file= test1dbig.dat
output file= test1dbig0.tif
test1dbig0.tif: output pix range : 2.35557e-005 to 0.0441806
output file= test1dbig1.tif
test1dbig1.tif: output pix range : 7.76159e-006 to 0.0198969
output file= test1dbig2.tif
test1dbig2.tif: output pix range : 0.18399 to 0.621195
Number of symmetrical anti-aliasing beams in trans. function
= 91529
The total integrated intensity range was:

  0.99344 to 0.997537

CPU time = 85.421 sec.
wall time = 85.4213 sec.
```

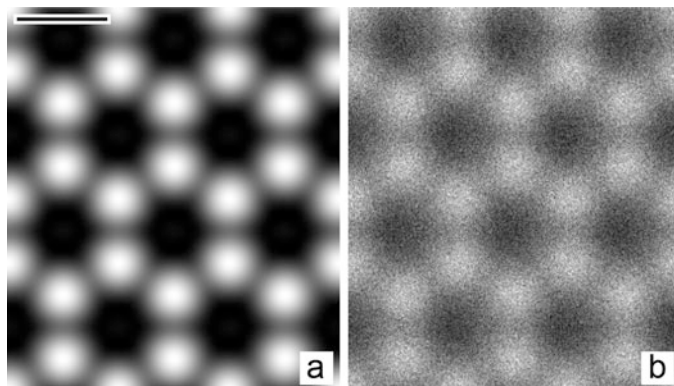


Fig. 8.5 Example of *incostem* calculation of graphene for 60 keV with an objective aperture of 30 mrad, a source size of 0.5 Å, and a defocus spread of 50 Å. (a) Ideal aberration free image without noise and (b) $C_{45a} = 0.3$ mm, $C_{56a} = 20$ mm (all other geometric aberration assumed zero), probe current 100 pAmp, dwell time 80 µs. The scalebar is 2 Å

8.5 Program Incostem

A full ADF-STEM calculation can require a large amount of computer time. With a large angle ADF detector the ADF-STEM image is mostly incoherent and fairly well behaved which permits some approximations. The program *incostem* can calculate an approximate ADF-STEM image very quickly using a simple incoherent approximation as in Eq. 3.70. The partial scattering cross section for an individual atom is calculated in the Moliere approx. (Eq. 5.18) and placed at the (x, y) position of this atom. The intensity may be spread onto a few adjacent pixels if the atom does not happen to be exactly on a single pixel. The position in z along the beam direction is ignored. This produces a collections of small dots in the (x, y) plane with the intensity of each dot proportional to the scattering cross section. This image is then convolved with the STEM probe intensity. The final result is usually qualitatively correct and very fast. Generally speaking, it is mostly correct, most of the time. This approx. can be very helpful in getting a quick idea of how the image behaves as the image parameters are changed and to debug the specimen structure file (i.e., are all of the atoms in the right places). This approximation makes the program easier to manage so a variety of extra features such as source size, defocus spread, and noise can be added with a modest effort. The ADF-STEM signal is very small by definition, so the minimum noise is due to the Poisson counting noise from the small number of electrons in each pixel. There may be more noise from other sources but this counting noise is the theoretical minimum noise.

This incoherent approximation is usually not quantitatively accurate for most specimen. However, for the class of 2D specimens such as graphene this approximation is fairly accurate if the probe is small enough to illuminate only one atom at a time. A sample run is shown below and the resulting images are shown in Fig. 8.5. The run for the ideal image in Fig. 8.5a is not shown.

```
<---- run program incostem ---->

incostem version dated 6-jul-2016 ejk
calculate ADF-STEM images for very thin specimens
using the incoherent image model
Copyright (C) 1998-2016 Earl J. Kirkland
This program is provided AS-IS with ABSOLUTELY NO WARRANTY
under the GNU general public license

Name of file with input atomic potential in x,y,z format:
>graphene.xyz
Replicate unit cell by NCELLX,NCELLY,NCELLZ :
>3 2 1
Name of file to get binary output of adf-stem result:
>graphene60noise.tif
Image size, Nx,Ny in pixels :
>256 256
STEM probe parameters, V0(kv), Cs3(mm), Cs5(mm),
    df(Angstroms), apert(mrad):
>60 0 0 0 30
ADF detector angles thetamin, thetamax (in mrad) =
>60 200
type higher order aber. name (as C32a, etc.) followed
by a value in mm. (END to end)
>C45a 0.3
>C56a 20.0
>END
Source size at specimen (FWHM in Ang.):
>0.5
Defocus spread (FWHM in Ang.):
>50
Do you want to add electron counting noise (y/n) :
>y
Type total probe current (in pAmp) and dwell time
    (in microSec):
>100 80
electron wavelength = 0.0486606 Angstroms
24 atomic coordinates read in
one unit cell of graphene
Lattice constant a= 7.368, b= 8.50783
Total specimen range is 0 to 7.368 in x
0 to 7.08986 in y
1.674 to 1.674 in z
probe size (FWHM-II) = 1.76572 Ang.
calculate the 2D specimen function...
the partial cross section for Z = 6 is 0.00117954 sq-Ang
CPU time = 0.034 sec.
final pix range: 0.000184443 to 0.000750999 (real)
    -5.02552e-011 to 4.86611e-011 (imag)
scale by 49931.7
scaled pix range: 9.20956 to 37.4987 (counts)
Poisson noise added to 65536 out of 65536 pixels
final pix range: 0 to 58 (counts)
output only the real part
all done
```

8.6 Program Computem

The set of programs above are all run from the command line. Many people interested in high-resolution transmission electron microscopy may not be fond of using the command line and prefer a graphical user interface (GUI). The program *computem* combines most of the above programs under a simple to use GUI. Programming a GUI on one computer platform can be as much work as programming the numerical simulations. Every different computer platform (operating system) uses a different programming interface. Rather than repeat this effort on every different platform it is easier to use what is called a cross-platform software package of which there are several available. The GUI program uses a common programming interface, which is then translated into the platform in use. Writing a cross-platform package is itself a significant effort but some generous programmers have done this already and make them available. Two popular examples are WxWidgets [459] and QT [38]. *computem* uses the WxWidgets package and can be compiled and run on several different common operating systems. A sample screenshot is shown in Fig. 8.6. WxWidgets attempts to make the GUI appearance and behavior conform to the host system so it looks like other applications on that system. This make the programming effort somewhat easier, but one drawback is that the available features are limited to those that are available on all target systems.

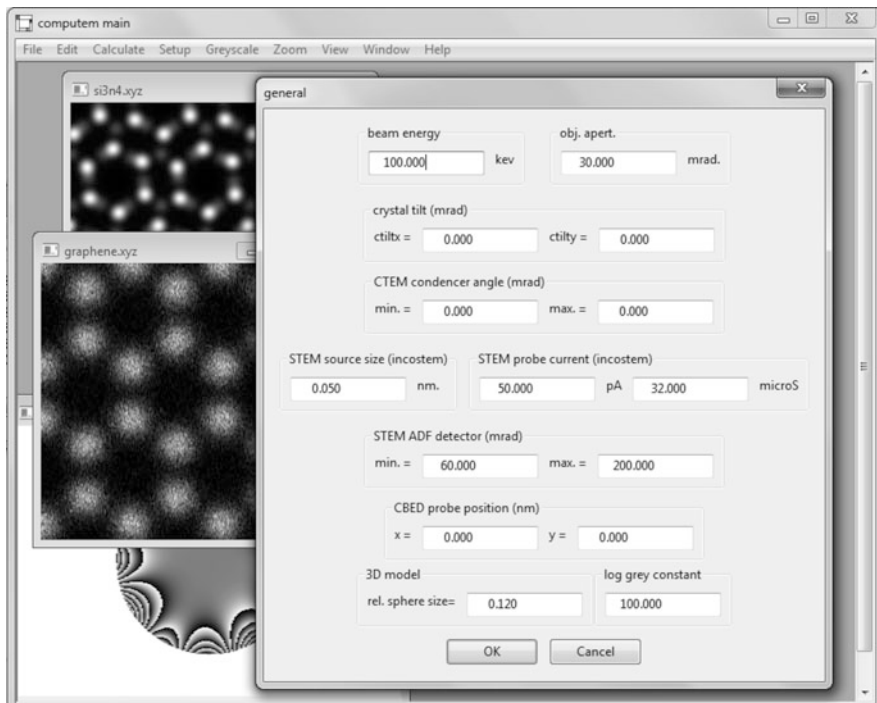


Fig. 8.6 Example of *computem* graphical user interface (GUI) on a Microsoft Windows operating system

Appendix A

Plotting Transfer Functions

The following scripts interactively calculate and plot transfer functions for the CTEM and STEM on the screen or in publication quality hardcopy using Octave, which is a free open-source package. Octave is relatively easy to use and provides a graphical output on many popular computers in a nearly machine independent manner. It is a complete programming language and has a variety of sophisticated mathematical functions and procedures. Octave's ease of use comes at a price, however. It is mostly an interpreted language (newer versions may have a just-in-time compiler that improves performance) with the inherent speed penalty. However, Octave's fundamental operations are on matrices and vectors. If the problem is vectorized (i.e., the operation is on a whole array or vector of numbers at one time), then the performance penalty typically associated with an interpreted language is partially overcome. Octave is well suited for small to medium calculations (such as calculating and plotting transfer functions) but probably should not be used for large numerical simulation.

Each of the three Octave programs ctemtf.m, stempsf.m, and stemmtf.m should be called directly from the Octave command line. All files should be in the default directory. The Octave functions do not need to be called directly but are called from the other three programs. Each program first asks for the electron optical parameters. Then it calculates and plots the appropriate function on the screen. The STEM programs may take significantly longer time because they must calculate a Fourier-Bessel transform. Once the graph appears on the screen it can be printed from the command line using the standard Octave print command.

A.1 CTEM

There is one Octave program and one Octave function (each is a separate file). A sample output of each program is shown below (Fig. A.1) along with the source listing.

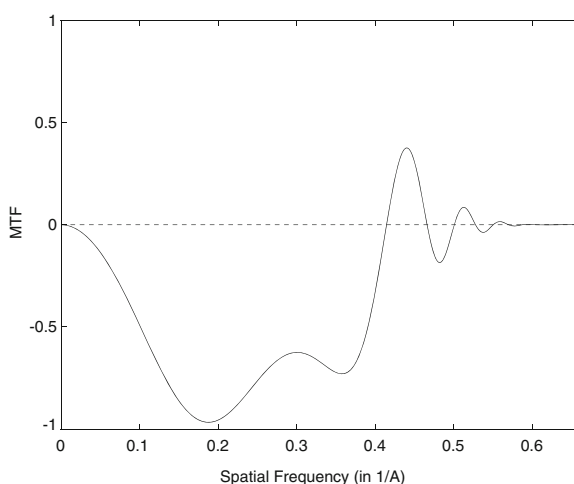
- **ctemtf.m** Plot CTEM transfer function (calls ctemh.m below).
- **ctemh.m** Calculate the CTEM transfer function (see Eq. 3.44).

ctemtf.m

```
%  
% Octave script ctemtf.m to plot CTEM transfer functions  
% this script calls ctemh.m  
%  
% Cs3,5 = Spherical Aberration  
% df = defocus  
% kev = electron energy in keV  
% ddf = chromatic aberation defocus spread  
% beta = spread in illumination angles  
%  
disp( 'Plot CTEM transfer function' );  
p.kev = input('Type electron energy in keV : ' );  
p.Cs3 = input('Type spherical aberration Cs3 in mm : ' );  
p.Cs5 = input('Type spherical aberration Cs5 in mm : ' );  
p.df = input('Type defocus df in Angstroms : ' );  
p.ddf = input('Type defocus spread ddf in Angs. : ' );  
p.beta = input('Type illumination semiangle in mrad : ' );  
%  
% electron wavelength  
wav = 12.3986/sqrt((2*511.0+p.kev)*p.kev);
```

Fig. A.1 Example of CTEM transfer function from the Octave program **ctemtf.m**

E= 200keV, Cs3= 1.3mm, Cs5= 0mm, df= 700A, Beta= 0.5mrad, ddf= 100A



```

Cs = abs(p.Cs3);
if( Cs < 0.1 )
    Cs = 0.1;
end
ds = sqrt( sqrt( Cs*1.0e7*wav*wav*wav ) );
kmax = 2.5/ds;
k = 0.:(kmax/500):kmax; % 500 points
sinw = ctemh( k, p, 0 );
plot( k, sinw, 'k-' );
axis([0, kmax, -1, +1]);
xlabel( 'Spatial Frequency (in 1/A)' );
ylabel( 'MTF' );
s1 = sprintf('E= %gkeV, Cs3= %gmm, ', p.kev, p.Cs3);
s2 = sprintf(' Cs5= %gmm, df= %gA, ', p.Cs5, p.df);
s3 = sprintf('Beta= %gmrad, ddf= %gA', p.beta, p.ddf);
title([s1 s2 s3]);
hold on; % plot line through zero
x = [0, kmax];
y = [0, 0];
plot( x, y, 'k--' );
hold off;

```

ctemh.m

```

function y = ctemh(k,params,type)
%
% Octave function ctemh.m to calculate CTEM bright
% field phase contrast transfer function with partial
% coherence for weak phase objects
% input array k has the spatial freq. values (in 1/A)
% input array params has the optical parameters
% params = [Cs, df, kev, ddf, beta]
% input type = 0 for phase contrast
%           and 1 for amplitude contrast
% output array contains the transfer function vs k
%
% params.Cs3,5 = spherical aberration (in mm)
% params.df = defocus (in Angstroms)
% params.kev = electron energy (in keV)
% params.ddf = chrom. aberr. def. spread (in Angst.)
% params.beta = spread in illum. angles (in mrad)
%
% reference
% R. H. Wade and J. Frank, Optik 49 (1977) p.81
%
Cs3 = params.Cs3*1.0e7;
Cs5 = params.Cs5*1.0e7;
df = params.df;
kev = params.kev;
ddf = params.ddf;
beta = params.beta*0.001;
mo = 511.0; % electron rest mass in keV
hc = 12.3986; % in keV-Angstroms
wav = (2*mo)+kev;

```

```

wav = hc/sqrt(wav*kev);
wavsq = wav*wav;
w1 = pi*Cs3*wavsq*wav;
w2 = pi*wav*df;
w3 = pi*Cs5*wavsq*wavsq*wav;
e0 = (pi*beta*ddf)^2;
k2 = k .* k;
wr = ((w3.*k2+w1).*k2-w2).*k*beta/wav;
wi = pi*wav*ddf.*k2;
wi = wr.*wr + 0.25.*wi.*wi;
wi = exp(-wi./(1+e0.*k2));
wr = w3*(1-2.0*e0.*k2)/3.0;
wr = wr.*k2 + 0.5*w1.* (1-e0.*k2);
wr = (wr.*k2 - w2).*k2./(1+e0.*k2);
if type == 0
    y = sin(wr).* wi;
else
    y = cos(wr).* wi;
end;
endfunction

```

A.2 STEM

There are two Octave programs and three Octave functions (each is a separate file). The first integral over the lens aberration function is not well behaved, so an Octave adaptive quadrature routine is used to gain efficiency and accuracy (in stemhr.m). A sample output of each program is shown below (Figs. A.2 and A.3) along with the source listing.

- **stempsf.m** Plot the STEM probe profile (calls stemhr.m below).
- **stemtf.m** Plot the STEM transfer function (calls stemhr.m and stemhk.m below).
- **stemhr.m** Calculate the STEM probe profile (see Eq. 3.74).
- **stemhk.m** Calculate the STEM transfer function (see Eq. 3.75, calls stemhr.m).

stempsf.m

```

% stempsf.m
% Octave file to plot the STEM probe profile
% this script calls stemhr.m
%
clear;
disp( 'Plot STEM probe intensity' );
p.kev = input( 'Type electron energy in keV : ' );
p.Cs3 = input( 'Type spherical aberration Cs3 in mm : ' );
p.Cs5 = input( 'Type spherical aberration Cs5 in mm : ' );
p.df = input( 'Type defocus df in Angstroms : ' );
p.amax = input( 'Type obj. apert. semiangle in mrad : ' );
%
% electron wavelength
wav = 12.3986/sqrt((2*511.0+p.kev)*p.kev);

```

Fig. A.2 Example of STEM probe intensity profile output from the Octave program **stempsf.m**

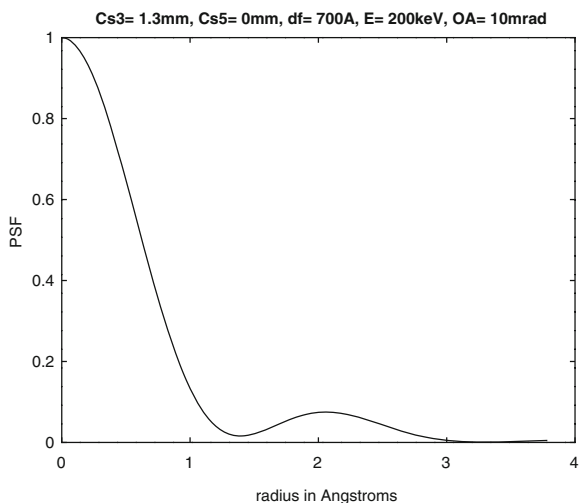
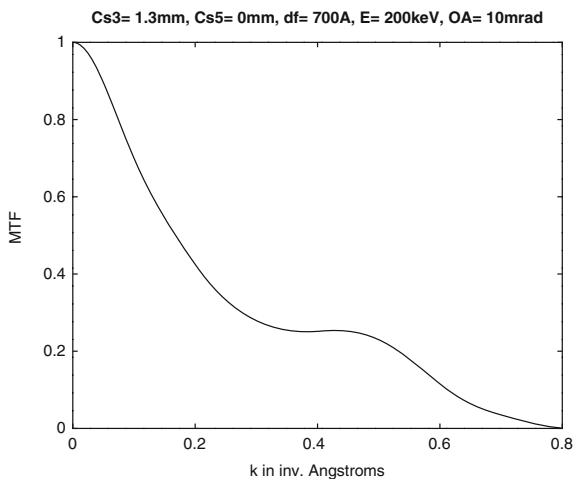


Fig. A.3 Example of the STEM transfer function output from the Octave program **stemtf.m**



```

Cs = abs(p.Cs3);
if( Cs < 0.1 )
    Cs = 0.1;
end
rmax = sqrt( sqrt( Cs*1.0e7*wav*wav*wav ) );
npts = 300; % number of points in curve
r = 0:(rmax/npts):rmax;
psf = stemhr( r, p );
plot( r, psf, 'k-' );
xlabel( 'radius in Angstroms' );
ylabel( 'PSF' );
s1 = sprintf('Cs3= %gmm, Cs5= %gmm, ', p.Cs3, p.Cs5 );
s2 = sprintf(' df= %gA, ', p.df);

```

```
s3 = sprintf('E= %gkeV, OA= %gmrad', p.kev, p.amax);
title([s1 s2 s3]);
```

stemtf.m

```
%  stemtf.m
%  Octave file to plot the STEM probe mtf
%  this script calls stemhk.m
%
clear;
disp( 'Plot STEM transfer function' );
p.kev = input( 'Type electron energy in keV : ' );
p.Cs3 = input( 'Type spherical aberration Cs3 in mm : ' );
p.Cs5 = input( 'Type spherical aberration Cs5 in mm : ' );
p.df = input( 'Type defocus df in Angstroms : ' );
p.amax = input( 'Type obj. apert. semiangle in mrad : ' );
%
% electron wavelength
wav = 12.3986/sqrt((2*511.0+p.kev)*p.kev);
kmax = 2*0.001*p.amax/wav;
npts = 500; % number of points
k = 0:(kmax/npts):kmax;
mtf = stemhk( k, p );
plot( k, mtf, 'k-' );
xlabel( 'k in inv. Angstroms' );
ylabel( 'MTF' );
s1 = sprintf('Cs3= %gmm, Cs5= %gmm, ', p.Cs3, p.Cs5 );
s2 = sprintf(' df= %gA, ', p.df);
s3 = sprintf('E= %gkeV, OA= %gmrad', p.kev, p.amax);
title([s1 s2 s3]);
```

stemhr.m

```
function psf = stemhr(r,params)
%
%  Octave function stemhr.m to calculate
%  STEM probe profile vs. r
%  input array r has the radial positions (in Angs.)
%  input variable params has the optical parameters
%  <Cs, df, kev, amax> as elements
%  output array contains the transfer function
%
% param.Cs3 = third order spherical aberration (in mm)
% param.Cs5 = fifth order spherical aberration (in mm)
% param.df = defocus (in Angstroms)
% param.kev = electron energy (in keV)
% param.amax = objective aperture (in mrad)
%
global w2 w4 w6 intr; % constants for lensr,i
df = params.df;
kev = params.kev;
amax = params.amax*0.001;
% electron wavelength
wav = 12.3986/sqrt((2*511.0+kev)*kev);
```

```

kmax = amax/wav;
w2 = wav*pi*df;
w4 = 0.5*pi*params.Cs3*1.0e7*wav*wav*wav;
w6 = pi*params.Cs5*1.0e7*wav*wav*wav*wav*wav /3.0;
nr = length( r );
for ir=1:nr,
    intr = 2*pi*r(ir);
    tol = [1.0e-7, 1.0e-7]; % rel, abs tolerance
    % use adaptive quadrature because integrand
    % not well behaved
    hr(ir) = quadcc( @lensr, 0, kmax, tol );
    hi(ir) = quadcc( @lensi, 0, kmax, tol );
end;
psf = hr.^2 + hi.^2;
a = max(psf);
psf = psf/a; % norm. probe intensity to a max. of 1
endfunction
%
% dummy functions to integrate (used by stempsf.m)
% Octave function lens.m to calculate complex
% aberr. function
% input k (in 1/angs.), wav = electron wavelength
%
chi = pi*wav*k^2*[ 0.5*Cs3*wav^2*k^2
                    + (1/3)*Cs5*wav^4*k^4 - df ];
return exp( -i*chi )
%
% globals:
% w2 = pi*defocus*wav
% w4 = 0.5*pi*Cs3*wav^3
% w6 = (1/3)*pi*Cs5*wav^5
% intr = 2*pi*r
%
function expchi = lensr(k) % real part
    global w2 w4 w6 intr; % constants from stemhr.m
    k2 = k.*k;
    w = ( (w6.*k2 + w4) .*k2 - w2 ).*k2;
    expchi = cos(w) .* besselj( 0, intr.*k ).*k;
endfunction

function expchi = lensi(k) % imag. part
    global w2 w4 w6 intr; % constants from stemhr.m
    k2 = k.*k;
    w = ( (w6.*k2 + w4) .*k2 - w2 ).*k2;
    expchi = sin(-w) .* besselj( 0, intr.*k ).*k;
endfunction

```

stemhk.m

```

function mtf = stemhk( k, params )
%
% Octave function stemhk.m to calculate STEM mtf vs. k
% input array k has the spatial freq. (in inv. Angs.)
% input variable params has the optical parameters
% [Cs, df, kev, amax] as elements
% output array contains the transfer function
%
% param.Cs3 = third order spherical aberration (in mm)
% param.Cs5 = fifth order spherical aberration (in mm)
% param.df = defocus (in Angstroms)
% param.kev = electron energy (in keV)
% param.amax = objective aperture (in mrad)
%
Cs3 = params.Cs3;
df = params.df;
kev = params.kev;
amax = params.amax*0.001;
% first calculate the psf using stemhr()
nr = 500; % number of points in integral over r
wav = 12.3986/sqrt((2*511.0+kev)*kev); % elect. wavelength
Cs = abs(Cs3);
if( Cs < 0.1 ) % guess if Cs3=0
    Cs = 0.1;
end
rmax = 2.0*sqrt( sqrt( Cs*1.0e7*wav*wav*wav) );
r = 0:(rmax/nr):rmax;
psf = stemhr( r, params );
% next inverse psf to get mtf
nk = length( k );
for ik=1:nk,
    h = psf .* besselj( 0, 2*pi*r*k(ik) ) .*r;
    mtf(ik) = sum(h);
end;
a = mtf(1);
mtf = mtf/a; % normalize mtf(0)=1
endfunction

```

Appendix B

The Fourier Projection Theorem

It seems like a two-dimensional inverse Fourier transform should never be applied to a function of three dimensions. However, the inverse two-dimensional transform of a three-dimensional object will end up producing the desired inverse transform with respect to two of the dimensions and integrating (or projecting) along the third dimension.

To see that this is true, define a function $f(x, y, z)$ that is a function of three spatial coordinates x, y, z . The three-dimensional Fourier transform of this function will be $F(k_x, k_y, k_z)$ which is a function of three reciprocal space coordinates k_x, k_y, k_z .

$$\begin{aligned} F(k_x, k_y, k_z) &= FT_{3D}[f(x, y, z)] \\ &= \int_{x,y,z} f(x, y, z) \exp[2\pi i(xk_x + yk_y + zk_z)] dx dy dz \quad (\text{B.1}) \end{aligned}$$

Next calculate the inverse Fourier transform in two dimensions of the three-dimensional object $F(k_x, k_y, k_z)$:

$$FT_{2D}^{-1}[F(k_x, k_y, k_z)] = \int_{k_x, k_y} F(k_x, k_y, k_z) \exp[-2\pi i(xk_x + yk_y)] dk_x dk_y \quad (\text{B.2})$$

and then substitute the original expression for $F(k_x, k_y, k_z)$ from Eq. B.1 using dummy variable r, s, t in place of x, y, z for the second occurrence of the spatial coordinates inside the integrand:

$$\begin{aligned} FT_{2D}^{-1}[F(k_x, k_y, k_z)] &= \int_{k_x, k_y} \left\{ \int_{r,s,t} f(r, s, t) \exp[2\pi i(rk_x + sk_y + tk_z)] dr ds dt \right\} \\ &\quad \times \exp[-2\pi i(xk_x + yk_y)] dk_x dk_y \end{aligned}$$

$$\begin{aligned}
&= \int_{r,s,t} f(r, s, t) \left\{ \int_{k_x} \exp[2\pi i(r-x)k_x] dk_x \right\} \\
&\quad \times \left\{ \int_{k_y} \exp[2\pi i(s-y)k_y] dk_y \right\} \exp[2\pi itk_z] dr ds dt \\
&= \int_{r,s,t} f(r, s, t) \delta(r-x) \delta(s-y) \exp[2\pi itk_z] dr ds dt \\
&= \int_t f(x, y, t) \exp[2\pi itk_z] dt
\end{aligned} \tag{B.3}$$

where $\delta(x)$ is the Dirac delta function. Finally if $k_z = 0$ and z is substituted for the dummy variable t this leaves:

$$FT_{2D}^{-1}[F(k_x, k_y, k_z = 0)] = \int_z f(x, y, z) dz \tag{B.4}$$

Therefore if a two-dimensional inverse Fourier transform is applied to a function of three dimensions the result is an inverse transform over the appropriate two dimensions and a projection (or integral) over the third dimension if the missing third reciprocal space coordinate (k_z above) is set to zero.

Appendix C

Atomic Potentials and Scattering Factors

The projected atomic potential of the atoms in the specimen is a necessary starting point for the calculation of an electron microscope image. The basic principles of quantum mechanics enable a well-defined calculation of the atomic potentials for single isolated atoms. The potentials for all of the atoms in the periodic chart have been calculated and the results are tabulated below. Treating the specimen as a collection of single isolated atoms neglects the change in electronic structure due to bonding etc. in the solid. This should be a small effect because electron scattering is mainly from the nucleus with the core and valence electrons screening the nucleus. However, the low angle scattering may be in error due to this approximation. This might give rise to problems with phase contrast bright field images; however, high angle annular dark field (STEM) images should be more accurate. A rigorous calculation of the electronic structure of solids including bonding is currently an active area of research. Including the effects of bonding in a rigorous and general manner in the calculation of electron microscope images is beyond the capability of generally available computers at present and is not considered here.

Herman and Skillman [203] tabulated the electron wave functions resulting from Hartree–Fock calculations. The atomic scattering factors for X-rays and electrons have been tabulated in many places and a representative sample is given in Table C.1. The data given by Doyle and Turner [100] and Doyle and Cowley [99] (using the program of Coulthard [71]) is generally considered to be the most accurate. However, Doyle and Turner do not calculate the whole periodic chart and Doyle and Cowley do not calculate the scattering factors for high angles. Rez et al. [417–419] have recently published a new set of scattering factors that covers the whole periodic chart and includes high angle scattering. The scattering factor table presented below is most similar to that of Doyle and Turner [100], Doyle and Cowley [99], and Rez et al. [417, 418] (i.e., all of these use a relativistic Hartree–Fock calculation) and covers the whole periodic chart including high scattering angles. Bonham and Fink [40] have also reviewed electronic structure calculations for electron scattering in an energy range appropriate for electron microscopy.

Table C.1 Some tabulations of atomic potentials and scattering factors

Author	Year	Quantity	Z	Comments
Bragg and West [47]	1929	fx	8, 9, 11–14, 17, 19, 20, 26	
James and Brindley [242]	1931	fx	1–22, 29, 37	TF, H
McWeeny et al. [339]	1951	fx	1–10	Analytical
Vand et al. [511]	1957	fx	1–100	Param.
Ibers [223]	1958	fe	1–12, 18, 20, 25–80	TFD, H, HF
Freeman [146, 147]	1959	fx	3, 4, 6–11, 13, 14 17, 19, 20, 22 23, 25, 26, 31, 81	H, HF
Forsyth and Wells [139]	1959	fx	1–92	Param.
Dawson [91]	1961	fe	9–20, 36	HF
Ibers and Vainshtein [224]	1962	fx	1–104	HF, TF
Smith and Burge [464]	1962	fe	1–18, 20–104	Param.
Cromer and Waber [88, 89]	1965	fx	2–103	RHF, TF
Mott and Massey [364]	1965	pce	3–36, 47, 74, 80	HF
Cox and Bonham [82]	1967	fe	1–54	Param.
Cromer and Mann [87]	1968	fx	2–103	HF
Doyle and Turner [100]	1968	fx,fe	2–38, 42, 47–56, 63, 79, 80–83, 86, 92	RHF
Hasse [176–178]	1968	fe	1–92	HF, TF
Doyle and Cowley [99]	1974	fe	2–98	HF, RHF
Fox et al. [140]	1989	fx	2–98	Param.
Weickenmeier and Kohl [530]	1991	fx	2–98	Param.
Rez et al. [417–419]	1994	fx	2–92	RHF
Waasmaier and Kirfel [513]	1995	fx	2–92	Param.
Peng et al. [395]	1996	fe	1–98	Param.
Wang et al. [518]	1996	fx	2–18	RHF
Su and Coppens [479]	1997	fx	1–54	RHF, Param.
Lobato and van Dyck [318]	2014	fx, fe	1–103	RHF, param.

TF Thomas Fermi, *TFD* Thomas-Fermi-Dirac, *H* Hartree, *HF* Hartree-Fock, *RHF* Relativistic Hartree, *fx* X-ray, *fe* electron scattering factor, *pce* partial cross section (electrons), *param.* parameterized

C.1 Atomic Charge Distribution

The distribution of charge in an atom must be found from a quantum mechanical description of the electrons and nucleus of the atom. Unfortunately the hydrogen atom is the only element in the periodic chart that can be solved analytically.

With more than one electron the atom becomes a many-body problem and requires a numerical solution with suitably approximations. The Hartree–Fock procedure (see for example Hartree [190], Froese-Fischer [151], Froese-Fischer et al. [137], and Cowan [72]) is a method of calculating the electron wave functions of all of the electrons in an atom assuming a central potential model. It is a variational calculation to minimize the total energy of the many-electron atomic system, and includes the interaction of the electrons with each other and with the nucleus. The total wave function is fashioned so that it is antisymmetric on the exchange of identical electrons, which leads to the so-called exchange terms. Hartree–Fock starts with an initial guess of the electron wave functions (such as the hydrogenic analytical form). From this guess a net potential for each electron orbital is calculated due to the other electrons and the nucleus (each orbital sees a slightly different potential because it does not interact with itself). From this potential a new set of wave functions is calculated and the process repeats until a self-consistent answer is obtained. Each orbital produces one coupled integral-differential equation (one equation per orbital). With the assumption of a central potential the angular integrations may be done analytically, so it is only the radial portion of the wave function that need to be calculated. The wave function is sampled on a discrete grid versus radius.

The kinetic energy of the inner shell electrons of the heavier elements such as gold is of the order of 100 keV, which produces some relativistic effects. A relativistic form of the Hartree–Fock procedure uses the Dirac relativistic wave equation instead of the nonrelativistic Schrödinger equation. Grant [165, 166] has given a thorough discussion of relativistic Hartree–Fock theory. With the Dirac equation the wave function for each electron has two components $P(r)$ and $Q(r)$ instead of one and there is a separate orbital for each spin state of the electron. This produces roughly twice as many sets of coupled integro-differential equations to solve and generally increases the amount of computation significantly. Desclaux [95], Grant et al. [167], and Dyall et al. [108] have published extensive Dirac-Fock programs.

A program based on the average configuration theory (Grant [166]) was used to calculate the relativistic wave functions for all atoms in the periodic chart (atomic number $Z = 3$ to $Z = 103$) except hydrogen (which is known analytically). Helium ($Z = 2$) was calculated nonrelativistically. The atomic radial charge distribution, X-ray and electron scattering factors, and the projected atomic potential were then calculated from the electron wave functions. The configurations of the electrons in each atom were obtained from standard tables (for example, Wiese and Martin [532], appendix 5 of Morrison et al. [361], table 19.3a of Haken and Wolf [183]). The wave functions vary rapidly near the nucleus, so it is more efficient to change the independent variable from r to $t = \log r$ with equal spacings in t . This produces a fine sampling (small grid size) at small r where the wave function is changing rapidly but keeps the total number of grid points manageable by increasing the grid size at large r where the wave function varies slowly. Each wave function was sampled with 500 points in each component (1000 points all together). The wave functions are initially set to the relativistic hydrogenic wave functions that are

known analytically (Burke and Grant [50]). At each iteration the effective electron-electron interaction is calculated from the current electron wave functions and a new set of electron wave functions is then calculated. The calculation proceeded until the energy eigenvalues changed by less than one part in 1×10^6 . The minimum radius was set to $r = 1 \times 10^{-6}a_0$ and the maximum radius varied between $8a_0$ and $15a_0$ (where $a_0 = 0.5292\text{\AA}$ is the Bohr radii). The energy and size ($\langle r^2 \rangle$) of each orbital are in good agreement with those tabulated by Desclaux [94].

For historical reasons it was more convenient to use the radial charge density (calculated from the electron wave functions) than to produce the atomic potentials directly. First the X-ray scattering factors were calculated from the wave functions. Then the electron scattering factors and hence the projected atomic potential were obtained from the X-ray scattering factors via the Mott–Bethe formula (i.e., the electron scattering factor in the first Born approximation is the Fourier transform of the atomic potential).

The relativistic electron wave function of each atomic orbital i consists of two components $Q_i(r)$ and $P_i(r)$ of the radial portion of the Dirac wave equation and an occupancy c_i for each atomic orbital. The radial distribution of the electron charge $\rho(r)$ is calculated from the wave function as:

$$4\pi r^2 \rho(r) = \sum_i c_i \left[|Q_i(r)|^2 + |P_i(r)|^2 \right] \quad (\text{C.1})$$

Both sides of this equation have units of electrons per Angstrom. r is the three-dimensional radial coordinate. The wave functions are sampled on an exponential grid to get more points near the nucleus where the wave function is changing rapidly. The r coordinates are defined on a grid as:

$$r_n = R_{\min} e^{n\Delta t} \quad ; \quad n = 0, 1, 2, \dots, (N_r - 1) \quad (\text{C.2})$$

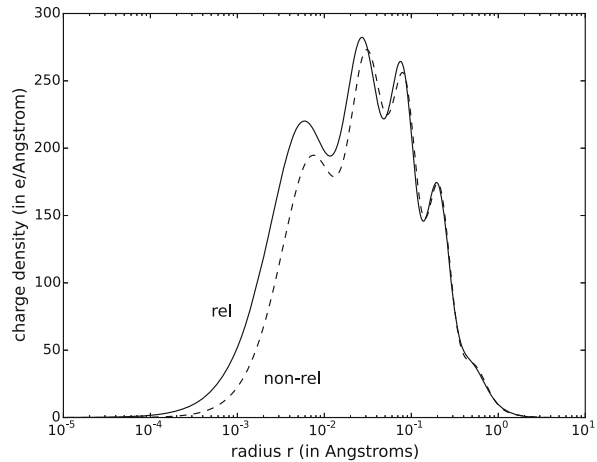
R_{\min} is the minimum radius and Δt is a logarithmic spacing ($t = \log(r)$) in the radial coordinate r . This is equivalent to changing the independent variable from r to $\log(r)$. Remember that $Q_i(0) = P_i(0) = 0$.

An example of the radial charge distribution of mercury ($Z = 80$) is shown in Fig. C.1 for both a relativistic and nonrelativistic calculation (using the average configuration theory as defined by Cowan [72]). The main effect of relativity is that the inner electron shell moves closer to the nucleus. This changes the effective screening of the nucleus and can have a large effect on the valence shell energies for heavy elements.

C.2 X-ray Scattering Factors

The X-ray scattering factor for a spherically symmetric charge distributions is defined as:

Fig. C.1 The radial electron charge density $4\pi r^2 \rho(r)$ versus radius for Hg ($Z = 80$) calculated relativistically (solid line) and nonrelativistically (dashed line)



$$f_X(q) = 4\pi \int r^2 \rho(r) \frac{\sin(2\pi qr)}{2\pi qr} dr \quad (\text{C.3})$$

where $q = \sin(\alpha)/\lambda$ is the magnitude of the three-dimensional wavevector that is the difference between the incident and scattered X-ray. λ is wavelength and α is the scattering semi-angle. $f_X(q)$ is a dimensionless quantity corresponding to the number of electrons. Most numerical integration formulas for tabulated data assume that the data is sampled on a regularly spaced grid and not an exponential grid as used here. The integral can however be converted to a regular spacing in the independent variable by changing the integration variable from dr to $d(\ln r) = dr/r$.

$$f_X(q) = \int [4\pi r^2 \rho(r)] \frac{\sin(2\pi qr)}{2\pi q} d(\ln r) \quad (\text{C.4})$$

The integrand is now sampled at regularly spaced intervals of $\Delta t = \Delta \ln(r)$ and can be easily integrated numerically. Simpson's three point formula was used here.

For neutral atoms $f_X(0) = Z$ where Z is the atomic number, so integrating the charge distribution to find $f_X(0)$ is only a test of the program.

C.3 Electron Scattering Factors

It is traditional to tabulate the electron scattering factor $f_e(q)$ in the first Born approximation. The scattering factor is the amplitude for scattering of a single electron by a single atom. The first Born approximation is totally inadequate for calculating electron scattering and electron microscope image (Zeitler [543, 544], Glauber and Shoemaker [157]). However, the first Born approximation is useful

because it is the three-dimensional Fourier transform of the atomic potential (see for example section 38 of Schiff [444]):

$$\begin{aligned} f_e(\mathbf{q}) &= \frac{2\pi m_0 e}{h^2} \int V(\mathbf{r}) \exp(2\pi i \mathbf{q} \cdot \mathbf{r}) d^3 r \\ &= \frac{1}{2\pi e a_0} \int V(\mathbf{r}) \exp(2\pi i \mathbf{q} \cdot \mathbf{r}) d^3 r \end{aligned} \quad (\text{C.5})$$

where $V(\mathbf{r})$ is the 3D atomic potential of the atom, m_0 is the rest mass of the electron, e is the charge of the electron, h is Planck's constant, and $a_0 = \hbar^2/m_0 e^2 = 0.5292 \text{ \AA}$ is the Bohr radius. $f_e(q)$ is in units of \AA . For the case where the atom is spherically symmetric this reduces to:

$$f_e(q) = \frac{1}{\pi e a_0 q} \int_0^\infty V(r) \sin(2\pi qr) r dr \quad (\text{C.6})$$

The electron scattering factor in the first Born approximation is also simply related to the X-ray scattering factor for an atom with atomic number Z using the Mott–Bethe [32, 34, 363, 364] formula:

$$f_e(q) = \frac{2m_0 e^2}{h^2} \left(\frac{Z - f_X(q)}{q^2} \right) = \frac{1}{2\pi^2 a_0} \left(\frac{Z - f_X(q)}{q^2} \right) \quad (\text{C.7})$$

(Bethe [33] has recently given an English language translation of his original German publication.) There is a singularity at $q = 0$, so the Mott–Bethe formula must be replaced by the following expression due to Ibers [223]:

$$f_e(0) = \frac{4\pi^2 m_0 e^2}{3h^2} Z \langle r^2 \rangle = \frac{Z}{3a_0} \langle r^2 \rangle \quad (\text{C.8})$$

$$\langle r^2 \rangle = \frac{\int_0^\infty r^2 [4\pi r^2 \rho(r)] dr}{\int_0^\infty [4\pi r^2 \rho(r)] dr} \quad (\text{C.9})$$

where $\langle r^2 \rangle$ is the mean square radius of the electrons in the atom. Note that neutral atoms also satisfy:

$$Z = \int_0^\infty [4\pi r^2 \rho(r)] dr \quad (\text{C.10})$$

The Mott–Bethe formula is equivalent to solving Poisson's equation in reciprocal space to obtain the potential distribution from the charge distribution (including the point charge of the nucleus). For historical reasons it is more convenient to calculate the atomic potentials in a round-about manner from the Mott–Bethe formula and the X-ray scattering factors.

If the valence shell electrons are not in the s ($l = 0$) angular momentum state, then the charge distribution in the atom is not necessarily spherically symmetric as assumed in the expressions for the scattering factors. McWeeny [339, 340] and Freeman [146, 147] have shown that the X-ray scattering from aspherical atoms (p-state valence shells) may vary by approximately 5–10% with azimuthal angle in low Z atoms. This difference shows up mainly at low scattering angles. The Mott–Bethe formula also implies that high angle electron scattering is mainly due to the nucleus and becomes insensitive to the X-ray scattering factor at high scattering angles. Bonding in the solid should produce a similar order of magnitude error in the electron scattering factor at small scattering angles. This 5–10% error should be regarded as an estimate of the error in image simulation produced by treating a solid as a collection of isolated (nonbonded) spherically symmetric atoms (i.e., by using the values tabulated here).

C.4 Parameterization

The electron and X-ray scattering factors for all neutral atoms with atomic numbers $Z = 2$ through $Z = 103$ were calculated using the relativistic Hartree–Fock program as outlined above. The results were tabulated for scattering angles $0 < q < 12\text{\AA}^{-1}$ (equivalent to $0 < s < 6$ in the notation of Doyle and Turner [100]) at intervals of 0.05\AA^{-1} and parameterized to make it easy to hard code into the subroutine library used for the main programs. $f_e(q)$ is in units of \AA and $f_x(q)$ is in dimensionless units of electron number. A few low atomic number atoms ($2 \leq Z \leq 6$) do not scatter appreciably at this high angle and so were stopped when $f_x(q) < 0.010$.

Hydrogen is the only atom that can be solved analytically. The (nonrelativistic) electron distribution for hydrogen is:

$$\rho(r) = |\psi(r)|^2 = \frac{1}{\pi a_0^3} \exp(-2r/a_0) \quad (\text{C.11})$$

Using this expression yields:

$$f_X(q) = (1 + \pi^2 a_0^2 q^2)^{-2} \quad (\text{C.12})$$

$$\langle r^2 \rangle = 3a_0^2 \quad (\text{C.13})$$

$$f_e(q = 0) = a_0 \quad (\text{C.14})$$

These analytical expressions for the scattering from hydrogen were also fit to the same parameters as the rest of the atoms in the periodic chart for completeness, although not strictly necessary.

There is a relatively large amount of data to represent the scattering factors. The simulation programs could read in a large tabulation and interpolate it to

obtain the potentials or scattering factors at every required point. Parameterizing the scattering factors can considerably reduce the amount of required data and also allow for easier analytical calculations although it is not necessarily required for a simulation program. Any parameterization should have the correct asymptotic form at high and low angles. Because the electron charge distribution in the atom has a nonzero size the X-ray scattering factor $f_x(q)$ must approach zero at high angles. The Mott–Bethe formula then implies that the electron scattering factor must approach $f_e(q) \propto s^{-2}$ at high angles. The parameterization must also approach a constant value at $q = 0$. Doyle and Turner [100] had some success in fitting linear combinations of Gaussians to the tabulated data. Gaussians fit well at low scattering angles but fall off too rapidly at high angles. Weickenmeier and Kohl [530] have proposed an alternate form that has the appropriate form at high angles, but is more complicated to work with analytically. The following form has the appropriate form at large and small angles and can be transformed analytically (see Eq. C.20):

$$f_e(q) = \sum_{i=1}^{N_L} \frac{a_i}{q^2 + b_i} + \sum_{i=1}^{N_G} c_i \exp(-d_i q^2) \quad (\text{C.15})$$

where $N_L = 3$ is the number of Lorenzians (first summation) and $N_G = 3$ is the number of Gaussians (second summation). The Lorenzians have the correct behavior at high angles and the Gaussians empirically fit the behavior at low angles. It is best to parameterize $f_e(q)$ and not $f_x(q)$ because of the singularity in the Mott–Bethe formula. The inverse Mott–Bethe formula:

$$f_x(q) = Z - 2\pi^2 a_0 q^2 f_e(q) \quad (\text{C.16})$$

is however well behaved everywhere, so if $f_e(q)$ is known, then it is easy to calculate $f_x(q)$. Peng and Cowley [394] have shown that serious errors may result from applying the Mott–Bethe formula to parameterize X-ray scattering factors. It is much better to parameterize the electron scattering factors than the X-ray scattering factors.

The actual parameters (a_i, b_i, c_i, d_i) are found by performing a nonlinear least squares fit of the numerical tabulation of the X-ray scattering factor f_{xj} and electron scattering factors f_{ej} at the angle q_j to the form of $f_e(q_j)$ given in Eq. C.15. The combined reduced χ^2 fit:

$$\begin{aligned} \chi^2 &= \frac{1}{2N_q - 2N_L - 2N_G} \sum_{j=1}^{N_q} \left\{ \left[\frac{f_{xj} - f_x(q_j)}{\sigma_{xj}} \right]^2 + \left[\frac{f_{ej} - f_e(q_j)}{\sigma_{ej}} \right]^2 \right\} \\ &= \text{minimum} \end{aligned} \quad (\text{C.17})$$

is minimized. N_q is the number of points in the q direction and $f_x(q_j)$ is calculated from the inverse Mott–Bethe formula and $f_e(q_j)$. The effective error of each data point was set to:

$$\begin{aligned}\sigma_{xj} &= 10^{-3} f_x(0) \\ \sigma_{ej} &= 10^{-3} f_e(0)\end{aligned}\quad (\text{C.18})$$

$f_e(q)$ and $f_x(q)$ sometimes differ by a factor or two or more (at the same q), so each must be scaled before summing in the figure of merit χ^2 to give equal weight to the X-ray and electron scattering factors. This choice of errors gives a slight preference for matching the scattering factors at low scattering angle but in practice does not seem to hinder the fit at high scattering angles either. A value of $\chi^2 \sim 1$ means that the parameterization is good to about three significant figures on average at low scattering angle (where f_e and f_x are a maximum).

The actual fit was performed with the Levenberg–Marquardt algorithm (for example, see Press et al. [406]). The parameters were constrained to be positive by fitting the square root of the parameters (and then squaring them in Eq. C.15). The Levenberg–Marquardt algorithm is reasonably robust if it is started relatively close to the correct values of the parameters. With a large number of degrees of freedom (i.e., many free parameters) the algorithm frequently converges to an incorrect answer (i.e., it is not globally convergent). The fit was greatly improved by trying several different starting points and keeping only the best one. In practice several hundred different starting points were generated for each atomic number using a random number generator (with appropriate scaling). Also in many cases the correct parameters are very close to the parameters for other atomic numbers, so each fit was also tried by starting from the best-fit parameters for all other atoms. There is one additional failure mode in which $b_i \gg 1$ and $a_i \gg 1$ but $a_i/b_i \sim 1$. This results in a constant value of f_e at large angles which is not correct. Therefore any fit with $|b_i| > 200$ was rejected (in practice only a small number of cases produce this response). The resulting parameters fit the tabulated values very well in most cases but it should be noted that the parameters are probably not unique. This fitting procedure is a relatively brute force solution but it only has to be done once so it is not worth optimizing this procedure.

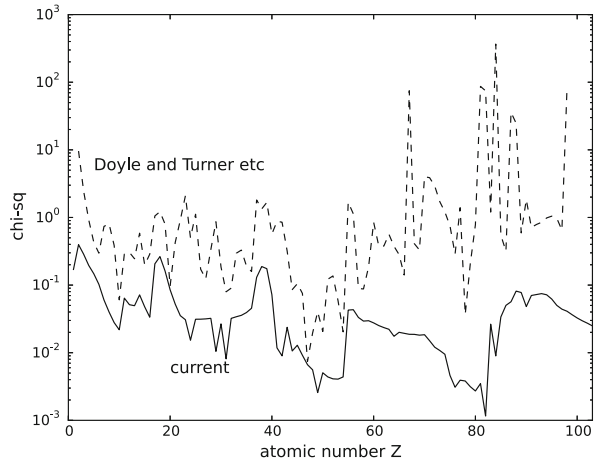
The resulting parameterization with 12 parameters (for each neutral atom) is tabulated below. The parameters are listed for each atomic number Z at the end of this chapter in the following order:

Z=	6,	chisq=	0.143335
a1	b1	a2	b2
a3	b3	c1	d1
c2	d2	c3	d3

a_i , b_i , c_i , and d_i have units of \AA^{-1} , \AA^{-2} , \AA , and \AA^2 respectively. Although this may seem like a large number of parameters they can be used for both X-ray and electron scattering factors as well as the atomic potential. Some atoms such as He ($Z = 2$) produce $b_1 \sim b_2 \sim b_3$ which means that there is really only one Lorenzian. However, other atoms require all six independent functions.

The figure of merit χ^2 (Eq. C.17) is shown versus atomic number Z in Fig. C.2 as a solid line. Most atomic numbers have $\chi^2 < 0.1$ indicating a very good fit. The

Fig. C.2 The figure of merit χ^2 of the parameterized form of the X-ray and electron scattering factors versus atomic number Z . The parameters are compared to the data of Doyle and Turner, Doyle and Cowley, and Fox et al. in the dashed line curve and to the current calculation in the solid line curve



error introduced by using the parameterized form instead of the tabulated form is significantly less than the error introduced by ignoring the effects of bonding in the solid.

If the previously tabulated values of $f_x(s)$ and $f_e(s)$ given by Doyle and Turner [100], Doyle and Cowley [99], Cromer and Waber [89], and Fox et al. [140] are considered as one data set, then the effective χ^2 formed by comparing this data set to the new parameters is shown in Fig. C.2 as a dashed line. Each of the old tabulations were typed in from the published literature (6076 values of $f_x(s)$ and 5432 values for $f_e(s)$). The data was entered twice and compared to find any typing errors. Because the new parameters fit the new tabulation relatively well this χ^2 is a measure of the agreement between the two Hartree–Fock programs. Many atomic numbers agree to $\chi^2 < 1.0$ which is good. However, some disagree significantly. The maximum disagreement occurs for $Z = 84$ with $\chi^2 = 367$. This corresponds to an average relative error of $0.1\sqrt{\chi^2} = 1.9\%$ (with the definitions of the error terms σ_x and σ_e in Eq. C.18). The largest percentage error (of about 10%) is in $f_e(0)$. The inverse Mott–Bethe formula constrains $f_x(0)$ to be exact. The scattering factors agree fairly well at high angles.

The particular parameterization was chosen to be a combination of relatively simple functions so that it can be inverse Fourier transformed analytically. The three-dimensional atomic potential $V(\mathbf{r}) = V(x, y, z)$ is:

$$\begin{aligned} V(x, y, z) &= 2\pi a_0 e \int f_e(q) \exp(-2\pi i \mathbf{q} \cdot \mathbf{r}) d^3 r \\ &= 2\pi^2 a_0 e \sum_i \frac{a_i}{r} \exp(-2\pi r \sqrt{b_i}) + 2\pi^{5/2} a_0 e \sum_i c_i d_i^{-3/2} \exp(-\pi^2 r^2 / d_i) \\ \text{with } r^2 &= x^2 + y^2 + z^2 \end{aligned} \quad (\text{C.19})$$

and the projected atomic potential is:

$$\begin{aligned}
 V_z(x, y) &= \int_{-\infty}^{+\infty} V(x, y, z) dz \\
 &= 4\pi^2 a_0 e \sum_i a_i K_0(2\pi r \sqrt{b_i}) + 2\pi^2 a_0 e \sum_i \frac{c_i}{d_i} \exp(-\pi^2 r^2 / d_i) \\
 \text{with } r^2 &= x^2 + y^2
 \end{aligned} \tag{C.20}$$

where $K_0(x)$ is the modified Bessel function. The integral for the first summation was helped by expression 3.387.6 of Gradshteyn and Ryzhik [163]. Abramowitz and Stegun [2] (section 9.8) give a convenient numerical expression for evaluating $K_0(x)$. The right-hand side of the expression for $V_z(x, y)$ (Eq. C.20) has units of the electron charge e . By combining the Rydberg constant $Ry = 0.5e^2/a_0$ ($Ry/e = 13.6$ V) and the Bohr radius $a_0 = 0.529$ Å the electron charge can be written in an unconventional set of units as $e = 14.4$ V-Å which is more convenient for evaluating $V_z(x, y)$.

Z= 1, chisq=	0.170190			
4.20298324e-003	2.25350888e-001	6.27762505e-002	2.25366950e-001	
3.00907347e-002	2.25331756e-001	6.77756695e-002	4.38854001e+000	
3.56609237e-003	4.03848423e-001	2.76135815e-002	1.44490166e+000	
Z= 2, chisq=	0.396634			
1.87543704e-005	2.12427997e-001	4.10595800e-004	3.32212279e-001	
1.96300059e-001	5.17325152e-001	8.36015738e-003	3.66668239e-001	
2.95102022e-002	1.37171827e+000	4.65928982e-007	3.75768025e+004	
Z= 3, chisq=	0.286232			
7.45843816e-002	8.81151424e-001	7.15382250e-002	4.59142904e-002	
1.45315229e-001	8.81301714e-001	1.12125769e+000	1.88483665e+001	
2.51736525e-003	1.59189995e-001	3.58434971e-001	6.12371000e+000	
Z= 4, chisq=	0.195442			
6.11642897e-002	9.90182132e-002	1.25755034e-001	9.90272412e-002	
2.00831548e-001	1.87392509e+000	7.87242876e-001	9.32794929e+000	
1.58847850e-003	8.91900236e-002	2.73962031e-001	3.20687658e+000	
Z= 5, chisq=	0.146989			
1.25716066e-001	1.48258830e-001	1.73314452e-001	1.48257216e-001	
1.84774811e-001	3.34227311e+000	1.95250221e-001	1.97339463e+000	
5.29642075e-001	5.70035553e+000	1.08230500e-003	5.64857237e-002	
Z= 6, chisq=	0.102440			
2.12080767e-001	2.08605417e-001	1.99811865e-001	2.08610186e-001	
1.68254385e-001	5.57870773e+000	1.42048360e-001	1.33311887e+000	
3.63830672e-001	3.80800263e+000	8.35012044e-004	4.03982620e-002	
Z= 7, chisq=	0.060249			
5.33015554e-001	2.90952515e-001	5.29008883e-002	1.03547896e+001	
9.24159648e-002	1.03540028e+001	2.61799101e-001	2.76252723e+000	
8.80262108e-004	3.47681236e-002	1.10166555e-001	9.93421736e-001	
Z= 8, chisq=	0.039944			
3.39969204e-001	3.81570280e-001	3.07570172e-001	3.81571436e-001	
1.30369702e-001	1.91919745e+001	8.83326058e-002	7.60635525e-001	
1.96586700e-001	2.07401094e+000	9.96220028e-004	3.03266869e-002	

Z= 9, chisq=	0.027866			
2.30560593e-001	4.80754213e-001	5.26889648e-001	4.80763895e-001	
1.24346755e-001	3.95306720e+001	1.24616894e-003	2.62181803e-002	
7.20452555e-002	5.92495593e-001	1.53075777e-001	1.59127671e+000	
Z= 10, chisq=	0.021836			
4.08371771e-001	5.88228627e-001	4.54418858e-001	5.88288655e-001	
1.44564923e-001	1.21246013e+002	5.91531395e-002	4.63963540e-001	
1.24003718e-001	1.23413025e+000	1.64986037e-003	2.05869217e-002	
Z= 11, chisq=	0.064136			
1.36471662e-001	4.99965301e-002	7.70677865e-001	8.81899664e-001	
1.56862014e-001	1.61768579e+001	9.96821513e-001	2.00132610e+001	
3.80304670e-002	2.60516254e-001	1.27685089e-001	6.99559329e-001	
Z= 12, chisq=	0.051303			
3.04384121e-001	8.42014377e-002	7.56270563e-001	1.64065598e+000	
1.01164809e-001	2.97142975e+001	3.45203403e-002	2.16596094e-001	
9.71751327e-001	1.21236852e+001	1.20593012e-001	5.60865838e-001	
Z= 13, chisq=	0.049529			
7.77419424e-001	2.71058227e+000	5.78312036e-002	7.17532098e+001	
4.26386499e-001	9.13331555e-002	1.13407220e-001	4.48867451e-001	
7.90114035e-001	8.66366718e+000	3.23293496e-002	1.78503463e-001	
Z= 14, chisq=	0.071667			
1.06543892e+000	1.04118455e+000	1.20143691e-001	6.87113368e+001	
1.80915263e-001	8.87533926e-002	1.12065620e+000	3.70062619e+000	
3.05452816e-002	2.14097897e-001	1.59963502e+000	9.99096638e+000	
Z= 15, chisq=	0.047673			
1.05284447e+000	1.31962590e+000	2.99440284e-001	1.28460520e-001	
1.17460748e-001	1.02190163e+002	9.60643452e-001	2.87477555e+000	
2.63555748e-002	1.82076844e-001	1.38059330e+000	7.49165526e+000	
Z= 16, chisq=	0.033482			
1.01646916e+000	1.69181965e+000	4.41766748e-001	1.74180288e-001	
1.21503863e-001	1.67011091e+002	8.27966670e-001	2.30342810e+000	
2.33022533e-002	1.56954150e-001	1.18302846e+000	5.85782891e+000	
Z= 17, chisq=	0.206186			
9.44221116e-001	2.40052374e-001	4.37322049e-001	9.30510439e+000	
2.54547926e-001	9.30486346e+000	5.47763323e-002	1.68655688e-001	
8.00087488e-001	2.97849774e+000	1.07488641e-002	6.84240646e-002	
Z= 18, chisq=	0.263904			
1.06983288e+000	2.87791022e-001	4.24631786e-001	1.24156957e+001	
2.43897949e-001	1.24158868e+001	4.79446296e-002	1.36979796e-001	
7.64958952e-001	2.43940729e+000	8.23128431e-003	5.27258749e-002	
Z= 19, chisq=	0.161900			
6.92717865e-001	7.10849990e+000	9.65161085e-001	3.57532901e-001	
1.48466588e-001	3.93763275e-002	2.64645027e-002	1.03591321e-001	
1.80883768e+000	3.22845199e+001	5.43900018e-001	1.67791374e+000	
Z= 20, chisq=	0.085209			
3.66902871e-001	6.14274129e-002	8.66378999e-001	5.70881727e-001	
6.67203300e-001	7.82965639e+000	4.87743636e-001	1.32531318e+000	
1.82406314e+000	2.10056032e+001	2.20248453e-002	9.11853450e-002	
Z= 21, chisq=	0.052352			
3.78871777e-001	6.98910162e-002	9.00022505e-001	5.21061541e-001	
7.15288914e-001	7.87707920e+000	1.88640973e-002	8.17512708e-002	
4.07945949e-001	1.11141388e+000	1.61786540e+000	1.80840759e+001	

```

Z= 22, chisq= 0.035298
 3.62383267e-001 7.54707114e-002 9.84232966e-001 4.97757309e-001
 7.41715642e-001 8.17659391e+000 3.62555269e-001 9.55524906e-001
 1.49159390e+000 1.62221677e+001 1.61659509e-002 7.33140839e-002

Z= 23, chisq= 0.030745
 3.52961378e-001 8.19204103e-002 7.46791014e-001 8.81189511e+000
 1.08364068e+000 5.10646075e-001 1.39013610e+000 1.48901841e+001
 3.31273356e-001 8.38543079e-001 1.40422612e-002 6.57432678e-002

Z= 24, chisq= 0.015287
 1.34348379e+000 1.25814353e+000 5.07040328e-001 1.15042811e+001
 4.26358955e-001 8.53660389e-002 1.17241826e-002 6.00177061e-002
 5.11966516e-001 1.53772451e+000 3.38285828e-001 6.62418319e-001

Z= 25, chisq= 0.031274
 3.26697613e-001 8.88813083e-002 7.17297000e-001 1.11300198e+001
 1.33212464e+000 5.82141104e-001 2.80801702e-001 6.71583145e-001
 1.15499241e+000 1.26825395e+001 1.11984488e-002 5.32334467e-002

Z= 26, chisq= 0.031315
 3.13454847e-001 8.99325756e-002 6.89290016e-001 1.30366038e+001
 1.47141531e+000 6.33345291e-001 1.03298688e+000 1.16783425e+001
 2.58280285e-001 6.09116446e-001 1.03460690e-002 4.81610627e-002

Z= 27, chisq= 0.031643
 3.15878278e-001 9.46683246e-002 1.60139005e+000 6.99436449e-001
 6.56394338e-001 1.56954403e+001 9.36746624e-001 1.09392410e+001
 9.77562646e-003 4.37446816e-002 2.38378578e-001 5.56286483e-001

Z= 28, chisq= 0.032245
 1.72254630e+000 7.76606908e-001 3.29543044e-001 1.02262360e-001
 6.23007200e-001 1.94156207e+001 9.43496513e-003 3.98684596e-002
 8.54063515e-001 1.04078166e+001 2.21073515e-001 5.10869330e-001

Z= 29, chisq= 0.010467
 3.58774531e-001 1.06153463e-001 1.76181348e+000 1.01640995e+000
 6.36905053e-001 1.53659093e+001 7.44930667e-003 3.85345989e-002
 1.89002347e-001 3.98427790e-001 2.29619589e-001 9.01419843e-001

Z= 30, chisq= 0.026698
 5.70893973e-001 1.26534614e-001 1.98908856e+000 2.17781965e+000
 3.06060585e-001 3.78619003e+001 2.35600223e-001 3.67019041e-001
 3.97061102e-001 8.66419596e-001 6.85657228e-003 3.35778823e-002

Z= 31, chisq= 0.008110
 6.25528464e-001 1.10005650e-001 2.05302901e+000 2.41095786e+000
 2.89608120e-001 4.78685736e+001 2.07910594e-001 3.27807224e-001
 3.45079617e-001 7.43139061e-001 6.55634298e-003 3.09411369e-002

Z= 32, chisq= 0.032198
 5.90952690e-001 1.18375976e-001 5.39980660e-001 7.18937433e+001
 2.00626188e+000 1.39304889e+000 7.49705041e-001 6.89943350e+000
 1.83581347e-001 3.64667232e-001 9.52190743e-003 2.69888650e-002

Z= 33, chisq= 0.034014
 7.77875218e-001 1.50733157e-001 5.93848150e-001 1.42882209e+002
 1.95918751e+000 1.74750339e+000 1.79880226e-001 3.31800852e-001
 8.63267222e-001 5.85490274e+000 9.59053427e-003 2.33777569e-002

Z= 34, chisq= 0.035703
 9.58390681e-001 1.83775557e-001 6.03851342e-001 1.96819224e+002
 1.90828931e+000 2.15082053e+000 1.73885956e-001 3.00006024e-001
 9.35265145e-001 4.92471215e+000 8.62254658e-003 2.12308108e-002

```

Z= 35,	chisq=	0.039250		
1.14136170e+000	2.18708710e-001	5.18118737e-001	1.93916682e+002	
1.85731975e+000	2.65755396e+000	1.68217399e-001	2.71719918e-001	
9.75705606e-001	4.19482500e+000	7.24187871e-003	1.99325718e-002	
Z= 36,	chisq=	0.045421		
3.24386970e-001	6.31317973e+001	1.31732163e+000	2.54706036e-001	
1.79912614e+000	3.23668394e+000	4.29961425e-003	1.98965610e-002	
1.00429433e+000	3.61094513e+000	1.62188197e-001	2.45583672e-001	
Z= 37,	chisq=	0.130044		
2.90445351e-001	3.68420227e-002	2.44201329e+000	1.16013332e+000	
7.69435449e-001	1.69591472e+001	1.58687000e+000	2.53082574e+000	
2.81617593e-003	1.88577417e-002	1.28663830e-001	2.10753969e-001	
Z= 38,	chisq=	0.188055		
1.37373086e-002	1.87469061e-002	1.97548672e+000	6.36079230e+000	
1.59261029e+000	2.21992482e-001	1.73263882e-001	2.01624958e-001	
4.66280378e+000	2.53027803e+001	1.61265063e-003	1.53610568e-002	
Z= 39,	chisq=	0.174927		
6.75302747e-001	6.54331847e-002	4.70286720e-001	1.06108709e+002	
2.63497677e+000	2.06643540e+000	1.09621746e-001	1.93131925e-001	
9.60348773e-001	1.63310938e+000	5.28921555e-003	1.66083821e-002	
Z= 40,	chisq=	0.072078		
2.64365505e+000	2.20202699e+000	5.54225147e-001	1.78260107e+002	
7.61376625e-001	7.67218745e-002	6.02946891e-003	1.55143296e-002	
9.91630530e-002	1.76175995e-001	9.56782020e-001	1.54330682e+000	
Z= 41,	chisq=	0.011800		
6.59532875e-001	8.66145490e-002	1.84545854e+000	5.94774398e+000	
1.25584405e+000	6.40851475e-001	1.22253422e-001	1.66646050e-001	
7.06638328e-001	1.62853268e+000	2.62381591e-003	8.26257859e-003	
Z= 42,	chisq=	0.008976		
6.10160120e-001	9.11628054e-002	1.26544000e+000	5.06776025e-001	
1.97428762e+000	5.89590381e+000	6.48028962e-001	1.46634108e+000	
2.60380817e-003	7.84336311e-003	1.13887493e-001	1.55114340e-001	
Z= 43,	chisq=	0.023771		
8.55189183e-001	1.02962151e-001	1.66219641e+000	7.64907000e+000	
1.45575475e+000	1.01639987e+000	1.05445664e-001	1.42303338e-001	
7.71657112e-001	1.34659349e+000	2.20992635e-003	7.90358976e-003	
Z= 44,	chisq=	0.010613		
4.70847093e-001	9.33029874e-002	1.58180781e+000	4.52831347e-001	
2.02419818e+000	7.11489023e+000	1.97036257e-003	7.56181595e-003	
6.26912639e-001	1.25399858e+000	1.02641320e-001	1.33786087e-001	
Z= 45,	chisq=	0.012895		
4.20051553e-001	9.38882628e-002	1.76266507e+000	4.64441687e-001	
2.02735641e+000	8.19346046e+000	1.45487176e-003	7.82704517e-003	
6.22809600e-001	1.17194153e+000	9.91529915e-002	1.24532839e-001	
Z= 46,	chisq=	0.009172		
2.10475155e+000	8.68606470e+000	2.03884487e+000	3.78924449e-001	
1.82067264e-001	1.42921634e-001	9.52040948e-002	1.17125900e-001	
5.91445248e-001	1.07843808e+000	1.13328676e-003	7.80252092e-003	
Z= 47,	chisq=	0.006648		
2.07981390e+000	9.92540297e+000	4.43170726e-001	1.04920104e-001	
1.96515215e+000	6.40103839e-001	5.96130591e-001	8.89594790e-001	
4.78016333e-001	1.98509407e+000	9.46458470e-002	1.12744464e-001	

```

Z= 48, chisq= 0.005588
 1.63657549e+000 1.24540381e+001 2.17927989e+000 1.45134660e+000
 7.71300690e-001 1.26695757e-001 6.64193880e-001 7.77659202e-001
 7.64563285e-001 1.66075210e+000 8.61126689e-002 1.05728357e-001

Z= 49, chisq= 0.002569
 2.24820632e+000 1.51913507e+000 1.64706864e+000 1.30113424e+001
 7.88679265e-001 1.06128184e-001 8.12579069e-002 9.94045620e-002
 6.68280346e-001 1.49742063e+000 6.38467475e-001 7.18422635e-001

Z= 50, chisq= 0.005051
 2.16644620e+000 1.13174909e+001 6.88691021e-001 1.10131285e-001
 1.92431751e+000 6.74464853e-001 5.65359888e-001 7.33564610e-001
 9.18683861e-001 1.02310312e+001 7.80542213e-002 9.31104308e-002

Z= 51, chisq= 0.004383
 1.73662114e+000 8.84334719e-001 9.99871380e-001 1.38462121e-001
 2.13972409e+000 1.19666432e+001 5.60566526e-001 6.72672880e-001
 9.93772747e-001 8.72330411e+000 7.37374982e-002 8.78577715e-002

Z= 52, chisq= 0.004105
 2.09383882e+000 1.26856869e+001 1.56940519e+000 1.21236537e+000
 1.30941993e+000 1.66633292e-001 6.98067804e-002 8.30817576e-002
 1.04969537e+000 7.43147857e+000 5.55594354e-001 6.17487676e-001

Z= 53, chisq= 0.004068
 1.60186925e+000 1.95031538e-001 1.98510264e+000 1.36976183e+001
 1.48226200e+000 1.80304795e+000 5.53807199e-001 5.67912340e-001
 1.11728722e+000 6.40879878e+000 6.60720847e-002 7.86615429e-002

Z= 54, chisq= 0.004381
 1.60015487e+000 2.92913354e+000 1.71644581e+000 1.55882990e+001
 1.84968351e+000 2.22525983e-001 6.23813648e-002 7.45581223e-002
 1.21387555e+000 5.56013271e+000 5.54051946e-001 5.21994521e-001

Z= 55, chisq= 0.042676
 2.95236854e+000 6.01461952e+000 4.28105721e-001 4.64151246e+001
 1.89599233e+000 1.80109756e-001 5.48012938e-002 7.12799633e-002
 4.70838600e+000 4.56702799e+001 5.90356719e-001 4.70236310e-001

Z= 56, chisq= 0.043267
 3.19434243e+000 9.27352241e+000 1.98289586e+000 2.28741632e-001
 1.55121052e-001 3.82000231e-002 6.73222354e-002 7.30961745e-002
 4.48474211e+000 2.95703565e+001 5.42674414e-001 4.08647015e-001

Z= 57, chisq= 0.033249
 2.05036425e+000 2.20348417e-001 1.42114311e-001 3.96438056e-002
 3.23538151e+000 9.56979169e+000 6.34683429e-002 6.92443091e-002
 3.97960586e+000 2.53178406e+001 5.20116711e-001 3.83614098e-001

Z= 58, chisq= 0.029355
 3.22990759e+000 9.94660135e+000 1.57618307e-001 4.15378676e-002
 2.13477838e+000 2.40480572e-001 5.01907609e-001 3.66252019e-001
 3.80889010e+000 2.43275968e+001 5.96625028e-002 6.59653503e-002

Z= 59, chisq= 0.029725
 1.58189324e-001 3.91309056e-002 3.18141995e+000 1.04139545e+001
 2.27622140e+000 2.81671757e-001 3.97705472e+000 2.61872978e+001
 5.58448277e-002 6.30921695e-002 4.85207954e-001 3.54234369e-001

Z= 60, chisq= 0.027597
 1.81379417e-001 4.37324793e-002 3.17616396e+000 1.07842572e+001
 2.35221519e+000 3.05571833e-001 3.83125763e+000 2.54745408e+001
 5.25889976e-002 6.02676073e-002 4.70090742e-001 3.39017003e-001

```

```

Z= 61, chisq= 0.025208
 1.92986811e-001 4.37785970e-002 2.43756023e+000 3.29336996e-001
 3.17248504e+000 1.11259996e+001 3.58105414e+000 2.46709586e+001
 4.56529394e-001 3.24990282e-001 4.94812177e-002 5.76553100e-002

Z= 62, chisq= 0.023540
 2.12002595e-001 4.57703608e-002 3.16891754e+000 1.14536599e+001
 2.51503494e+000 3.55561054e-001 4.44080845e-001 3.11953363e-001
 3.36742101e+000 2.40291435e+001 4.65652543e-002 5.52266819e-002

Z= 63, chisq= 0.022204
 2.59355002e+000 3.82452612e-001 3.16557522e+000 1.17675155e+001
 2.29402652e-001 4.76642249e-002 4.32257780e-001 2.99719833e-001
 3.17261920e+000 2.34462738e+001 4.37958317e-002 5.29440680e-002

Z= 64, chisq= 0.017492
 3.19144939e+000 1.20224655e+001 2.55766431e+000 4.08338876e-001
 3.32681934e-001 5.85819814e-002 4.14243130e-002 5.06771477e-002
 2.61036728e+000 1.99344244e+001 4.20526863e-001 2.85686240e-001

Z= 65, chisq= 0.020036
 2.59407462e-001 5.04689354e-002 3.16177855e+000 1.23140183e+001
 2.75095751e+000 4.38337626e-001 2.79247686e+000 2.23797309e+001
 3.85931001e-002 4.87920992e-002 4.10881708e-001 2.77622892e-001

Z= 66, chisq= 0.019351
 3.16055396e+000 1.25470414e+001 2.82751709e+000 4.67899094e-001
 2.75140255e-001 5.23226982e-002 4.00967160e-001 2.67614884e-001
 2.63110834e+000 2.19498166e+001 3.61333817e-002 4.68871497e-002

Z= 67, chisq= 0.018720
 2.88642467e-001 5.40507687e-002 2.90567296e+000 4.97581077e-001
 3.15960159e+000 1.27599505e+001 3.91280259e-001 2.58151831e-001
 2.48596038e+000 2.15400972e+001 3.37664478e-002 4.50664323e-002

Z= 68, chisq= 0.018677
 3.15573213e+000 1.29729009e+001 3.11519560e-001 5.81399387e-002
 2.97722406e+000 5.31213394e-001 3.81563854e-001 2.49195776e-001
 2.40247532e+000 2.13627616e+001 3.15224214e-002 4.33253257e-002

Z= 69, chisq= 0.018176
 3.15591970e+000 1.31232407e+001 3.22544710e-001 5.97223323e-002
 3.05569053e+000 5.61876773e-001 2.92845100e-002 4.16534255e-002
 3.72487205e-001 2.40821967e-001 2.27833695e+000 2.10034185e+001

Z= 70, chisq= 0.018460
 3.10794704e+000 6.06347847e-001 3.14091221e+000 1.33705269e+001
 3.75660454e-001 7.29814740e-002 3.61901097e-001 2.32652051e-001
 2.45409082e+000 2.12695209e+001 2.72383990e-002 3.99969597e-002

Z= 71, chisq= 0.015021
 3.11446863e+000 1.38968881e+001 5.39634353e-001 8.91708508e-002
 3.06460915e+000 6.79919563e-001 2.58563745e-002 3.82808522e-002
 2.13983556e+000 1.80078788e+001 3.47788231e-001 2.22706591e-001

Z= 72, chisq= 0.012070
 3.01166899e+000 7.10401889e-001 3.16284788e+000 1.38262192e+001
 6.33421771e-001 9.48486572e-002 3.41417198e-001 2.14129678e-001
 1.53566013e+000 1.55298698e+001 2.40723773e-002 3.67833690e-002

Z= 73, chisq= 0.010775
 3.20236821e+000 1.38446369e+001 8.30098413e-001 1.18381581e-001
 2.86552297e+000 7.66369118e-001 2.24813887e-002 3.52934622e-002
 1.40165263e+000 1.46148877e+001 3.33740596e-001 2.05704486e-001

```

```

Z= 74, chisq= 0.009479
 9.24906855e-001 1.2863377e-001 2.75554557e+000 7.65826479e-001
 3.3044006e+000 1.34471170e+001 3.29973862e-001 1.98218895e-001
 1.09916444e+000 1.35087534e+001 2.06498883e-002 3.38918459e-002

Z= 75, chisq= 0.004620
 1.96952105e+000 4.98830620e+001 1.21726619e+000 1.33243809e-001
 4.10391685e+000 1.84396916e+000 2.90791978e-002 2.84192813e-002
 2.30696669e-001 1.90968784e-001 6.08840299e-001 1.37090356e+000

Z= 76, chisq= 0.003085
 2.06385867e+000 4.05671697e+001 1.29603406e+000 1.46559047e-001
 3.96920673e+000 1.82561596e+000 2.69835487e-002 2.84172045e-002
 2.31083999e-001 1.79765184e-001 6.30466774e-001 1.38911543e+000

Z= 77, chisq= 0.003924
 2.21522726e+000 3.24464090e+001 1.37573155e+000 1.60920048e-001
 3.78244405e+000 1.78756553e+000 2.44643240e-002 2.82909938e-002
 2.36932016e-001 1.70692368e-001 6.48471412e-001 1.37928390e+000

Z= 78, chisq= 0.003817
 9.84697940e-001 1.60910839e-001 2.73987079e+000 7.18971667e-001
 3.61696715e+000 1.29281016e+001 3.02885602e-001 1.70134854e-001
 2.78370726e-001 1.49862703e+000 1.52124129e-002 2.83510822e-002

Z= 79, chisq= 0.003143
 9.61263398e-001 1.70932277e-001 3.69581030e+000 1.29335319e+001
 2.77567491e+000 6.89997070e-001 2.95414176e-001 1.63525510e-001
 3.11475743e-001 1.39200901e+000 1.43237267e-002 2.71265337e-002

Z= 80, chisq= 0.002717
 1.29200491e+000 1.83432865e-001 2.75161478e+000 9.42368371e-001
 3.49387949e+000 1.46235654e+001 2.77304636e-001 1.55110144e-001
 4.30232810e-001 1.28871670e+000 1.48294351e-002 2.61903834e-002

Z= 81, chisq= 0.003492
 3.75964730e+000 1.35041513e+001 3.21195904e+000 6.66330993e-001
 6.47767825e-001 9.22518234e-002 2.76123274e-001 1.50312897e-001
 3.18838810e-001 1.12565588e+000 1.31668419e-002 2.48879842e-002

Z= 82, chisq= 0.001158
 1.00795975e+000 1.17268427e-001 3.09796153e+000 8.80453235e-001
 3.61296864e+000 1.47325812e+001 2.62401476e-001 1.43491014e-001
 4.05621995e-001 1.04103506e+000 1.31812509e-002 2.39575415e-002

Z= 83, chisq= 0.026436
 1.59826875e+000 1.56897471e-001 4.38233925e+000 2.47094692e+000
 2.06074719e+000 5.72438972e+001 1.94426023e-001 1.32979109e-001
 8.22704978e-001 9.56532528e-001 2.33226953e-002 2.23038435e-002

Z= 84, chisq= 0.008962
 1.71463223e+000 9.79262841e+001 2.14115960e+000 2.10193717e-001
 4.37512413e+000 3.66948812e+000 2.16216680e-002 1.98456144e-002
 1.97843837e-001 1.33758807e-001 6.52047920e-001 7.80432104e-001

Z= 85, chisq= 0.033776
 1.48047794e+000 1.25943919e+002 2.09174630e+000 1.83803008e-001
 4.75246033e+000 4.19890596e+000 1.85643958e-002 1.81383503e-002
 2.05859375e-001 1.33035404e-001 7.13540948e-001 7.03031938e-001

Z= 86, chisq= 0.050132
 6.30022295e-001 1.40909762e-001 3.80962881e+000 3.08515540e+001
 3.89756067e+000 6.51559763e-001 2.40755100e-001 1.08899672e-001
 2.62868577e+000 6.42383261e+000 3.14285931e-002 2.42346699e-002

```

Z= 87, chisq=	0.056720			
5.23288135e+000	8.60599536e+000	2.48604205e+000	3.04543982e-001	
3.23431354e-001	3.87759096e-002	2.55403596e-001	1.28717724e-001	
5.53607228e-001	5.36977452e-001	5.75278889e-003	1.29417790e-002	
Z= 88, chisq=	0.081498			
1.44192685e+000	1.18740873e-001	3.55291725e+000	1.01739750e+000	
3.91259586e+000	6.31814783e+001	2.16173519e-001	9.55806441e-002	
3.94191605e+000	3.50602732e+001	4.60422605e-002	2.20850385e-002	
Z= 89, chisq=	0.077643			
1.45864127e+000	1.07760494e-001	4.18945405e+000	8.89090649e+001	
3.65866182e+000	1.05088931e+000	2.08479229e-001	9.09335557e-002	
3.16528117e+000	3.13297788e+001	5.23892556e-002	2.08807697e-002	
Z= 90, chisq=	0.048096			
1.19014064e+000	7.73468729e-002	2.55380607e+000	6.59693681e-001	
4.68110181e+000	1.28013896e+001	2.26121303e-001	1.08632194e-001	
3.58250545e-001	4.56765664e-001	7.82263950e-003	1.62623474e-002	
Z= 91, chisq=	0.070186			
4.68537504e+000	1.44503632e+001	2.98413708e+000	5.56438592e-001	
8.91988061e-001	6.69512914e-002	2.24825384e-001	1.03235396e-001	
3.04444846e-001	4.27255647e-001	9.48162708e-003	1.77730611e-002	
Z= 92, chisq=	0.072478			
4.63343606e+000	1.63377267e+001	3.18157056e+000	5.69517868e-001	
8.76455075e-001	6.88860012e-002	2.21685477e-001	9.84254550e-002	
2.72917100e-001	4.09470917e-001	1.11737298e-002	1.86215410e-002	
Z= 93, chisq=	0.074792			
4.56773888e+000	1.90992795e+001	3.40325179e+000	5.90099634e-001	
8.61841923e-001	7.03204851e-002	2.19728870e-001	9.36334280e-002	
2.38176903e-001	3.93554882e-001	1.38306499e-002	1.94437286e-002	
Z= 94, chisq=	0.071877			
5.45671123e+000	1.01892720e+001	1.11687906e-001	3.98131313e-002	
3.30260343e+000	3.14622212e-001	1.84568319e-001	1.04220860e-001	
4.93644263e-001	4.63080540e-001	3.57484743e+000	2.19369542e+001	
Z= 95, chisq=	0.062156			
5.38321999e+000	1.07289857e+001	1.23343236e-001	4.15137806e-002	
3.46469090e+000	3.39326208e-001	1.75437132e-001	9.98932346e-002	
3.3980073e+000	2.11601535e+001	4.69459519e-001	4.51996970e-001	
Z= 96, chisq=	0.050111			
5.38402377e+000	1.11211419e+001	3.49861264e+000	3.56750210e-001	
1.88039547e-001	5.39853583e-002	1.69143137e-001	9.60082633e-002	
3.19595016e+000	1.80694389e+001	4.64393059e-001	4.36318197e-001	
Z= 97, chisq=	0.044081			
3.66090688e+000	3.84420906e-001	2.03054678e-001	5.48547131e-002	
5.30697515e+000	1.17150262e+001	1.60934046e-001	9.21020329e-002	
3.04808401e+000	1.73525367e+001	4.43610295e-001	4.27132359e-001	
Z= 98, chisq=	0.041053			
3.94150390e+000	4.18246722e-001	5.16915345e+000	1.25201788e+001	
1.61941074e-001	4.81540117e-002	4.15299561e-001	4.24913856e-001	
2.91761325e+000	1.90899693e+001	1.51474927e-001	8.81568925e-002	
Z= 99, chisq=	0.036478			
4.09780623e+000	4.46021145e-001	5.10079393e+000	1.31768613e+001	
1.74617289e-001	5.02742829e-002	2.76774658e+000	1.84815393e+001	
1.44496639e-001	8.46232592e-002	4.02772109e-001	4.17640100e-001	

Z=100, chisq=	0.032651			
4.24934820e+000	4.75263933e-001	5.03556594e+000	1.38570834e+001	
1.88920613e-001	5.26975158e-002	3.94356058e-001	4.11193751e-001	
2.61213100e+000	1.78537905e+001	1.38001927e-001	8.12774434e-002	
Z=101, chisq=	0.029668			
2.00942931e-001	5.48366518e-002	4.40119869e+000	5.04248434e-001	
4.97250102e+000	1.45721366e+001	2.47530599e+000	1.72978308e+001	
3.86883197e-001	4.05043898e-001	1.31936095e-001	7.80821071e-002	
Z=102, chisq=	0.027320			
2.16052899e-001	5.83584058e-002	4.91106799e+000	1.53264212e+001	
4.54862870e+000	5.34434760e-001	2.36114249e+000	1.68164803e+001	
1.26277292e-001	7.50304633e-002	3.81364501e-001	3.99305852e-001	
Z=103, chisq=	0.024894			
4.86738014e+000	1.60320520e+001	3.19974401e-001	6.70871138e-002	
4.58872425e+000	5.77039373e-001	1.21482448e-001	7.22275899e-002	
2.31639872e+000	1.41279737e+001	3.79258137e-001	3.89973484e-001	

Appendix D

The Inverse Problem

Most of the discussions up to here have focused on the basic understanding of image formation in the TEM and how to calculate the expected images from first principles which might be labeled the “forward problem.” Understanding what in the image is real and what is an artifact is important. The so-called “inverse problem” is a calculation in the opposite direction. That is, start from the recorded image (or other related data) and work backwards to uncover the original specimen structure (or other related information about the specimen). The inverse problem usually requires a good understanding of the forward problem and is typically much harder and equally important. The inverse problem might warrant a whole second volume but time and space limitations only permit a short summary here. Some discussion has also been given by Kirkland [277].

The calculations involved in the inverse problem are usually much harder than the forward problem. The inverse problem is usually said to be ill-conditioned because it usually leads to some mathematical ambiguity such as a singular matrix or division by zero. Subtle algorithms with clever mathematical manipulations are usually required to circumvent these problems. Adding to these difficulties, the input data may have significant random noise from the measurement process which further complicates the calculation. The quality of the result typically depends on the SNR (signal to noise ratio) of the original data. The larger the SNR, the better the result.

The inverse problem originated from the desire to uncover the specimen structure from an X-ray or electron diffraction pattern. There has been a large amount of effort and publications on developing computational methods for the problem of inverting a diffraction pattern, but will not be reviewed significantly here.

The corresponding inverse problem for electron microscope images was initiated by Schiske [445] (English translation [446]) with reconstruction from a defocus series of BF-CTEM images. Each image in a defocus series contains a little different information about the specimen compared to other images. Recombining the information from all images in the series may result in an improved image with

more information than a single image. Schiske's original work assumed a linear image model and was studied in depth by Frank [141]. When the ideal image is modeled as a general complex object, then the reconstructed image is identified as the exit wave (or transmission function for thin specimens). The whole process can then be called "exit wave reconstruction" (EWR). Later efforts by Kirkland et al. [266, 267, 270, 282–284] extended the theory to properly handle the singularity found in the original Schiske formula and include nonlinear effects with a complex image in the MIMAP method. Coene et al. [66, 67, 490] proposed a modification valid in some cases that improves the speed of this method (the MAL method). Kirkland et al. [265, 344, 345] have also shown how a series of images at different tilt angles may be used for image reconstruction. If the exit wave is properly reconstructed the imaginary (or anomalous) portion has a strong variation with atomic number similar to that in ADF-STEM (Kirkland and Siegel [281]). Exit wave reconstruction methods have been reviewed by Kirkland [263] and Ophus [389].

If the exit wave has been reconstructed, then the next step in the inverse problem would be to invert the three-dimensional structure of the specimen in an inverse multislice calculation (or inverse Bloch wave calculation) which is even more difficult. Some methods have been proposed by Gribelyuk [168], Beeching [27, 28], Spargo [467], Allen [7, 9, 10], Spence [469, 471], and O'Leary [385], but there has not been much practical application as yet.

The inverse method known as tomography uses a set of 2D images (CTEM or STEM) taken at different tilt angles to reconstruct the 3D structure of the specimen (for example, Midgley [346], Ercius et al. [121]). Cryo-EM uses a large number of low dose images of single (identical) biological particles at random orientations (a serendipitous tilt series) to effectively perform tomography on 3D biological particles (for example, Frank [143], Cheng et al. [63], Nogales [374]).

Reconstructing specimen information from a large 4D data set is called ptychography. The whole diffraction pattern (CBED) is recorded at each position of the probe in STEM, generating a prodigious amount of data that has only recently become practical to record using large disk drives and fast detectors. The CBED pattern is recorded in two dimensions and the probe is scanned in two dimensions, so this is an effective 4D data set. This large data set includes a variety of useful information that might be exploited. Ptychography and has been discussed by many authors, for example, Rodenburg and Bates [423], Nellist and Rodenburg [370], Plamann and Rodenburg [403], Maiden et al. [328, 329], and D'Alfonso et al. [90]. Jiang et al. [247] have recently reported remarkable resolution in 2D materials using ptychography.

There are many available software packages for the inverse problem in electron microscopy. Some of them are listed in Table D.1. Many of the newer programs are for reconstructing cryo-EM images into 3D biological structures. Smith and Carragher [466] have given a recent review of software developments for analysis of biological electron microscope images. An online listing is maintained at wikipedia (en.wikibooks.org/wiki/Software_Tools_For_Molecular_Microscopy) under the title /Software_Tools_For_Molecular_Microscopy.

Table D.1 Some available image analysis software packages for electron microscopy

Program	Author	Year	Type	Comments
IMPROC	Saxton [436]	1978	IP	
SEMPER	Saxton [437, 438]	1979, 1996	IP	
SPIDER	Frank et al. [145]	1981	BIP	
SPIDER/WEB	Frank et al. [144]	1996	BIP	
EM	Hegerl [200, 201]	1982, 1996	IP	
CRISP	Hovmöller [217]	1992	DA	
IMAGIC	van Heel et al. [509, 510]	1981, 1996	BIP	
Xmipp	Marabini et al. [330]	1996	BIP	
EMAN	Ludtke et al. [321]	1999	BIP	
TRICE	Zou et al. [548]	2004	DA	
EDM	Kilaas et al. [259]	2005	DA	
serialEM	Mastronarde [334]	2005	TOM	
EMAN2	Tang et al. [484]	2007	BIP	
SPIRE	Baxter et al. [26]	2007	BIP	
SPARX	Hohn et al. [209]	2007	BIP	Python
FREALIGN	Grigorieff [169]	2007	BIP	
imageJ	Schneider et al. [447]	2012	IP	
SIMPLE	Elmlund and Elmlund [116]	2012	BIP	
RELION	Scheres [440]	2012	BIP	
Xmipp3	de la Rosa-Trevín et al. [93]	2013	BIP	
tomviz	Hovden et al. [214, 310]	2015	TOM	
RELION2	Kimanius et al. [261]	2016	BIP	GPU
GENFIRE	Pryor et al. [407]	2017	TOM	3D atomic imaging

IP is image processing, BIP is biological image processing, DA is diffraction analysis, and TOM is tomography. Some may be commercial and other private programs likely exist. Some older programs may no longer be available. Apologies to the authors of many other programs that may have been left out

Appendix E

Bilinear Interpolation

It is frequently necessary to combine or compare two different digital images with different sampling sizes (Δx or Δy). Interpolation in two dimensions is one method of reconciling the difference in sampling sizes. For example, most simulated electron microscope images will have a rectangular pixel with unequal spacings in x and y (to match the underlying periodicity of the specimen) but many image display devices (computer screens) will have square pixels with equal spacings in x and y . To properly display an image with rectangular pixels on a device with square pixels will require resampling the image.

The basic problem can be stated as: Given a set of image intensities sampled on a two-dimensional grid with spacing Δx_a and Δy_a generate another set of image intensities on a grid with a different spacing Δx_b and Δy_b . Interpolating the initial grid in two dimensions generates a function of two independent variables $f(x, y)$ that is continuous but may not have continuous derivatives. Calculating this function at each point in the new grid effectively samples the first image onto the second grid. This procedure works best if the first and second grids are nearly the same spacing. If the spacings are dramatically different (i.e., more than about a factor of two different), then various artifacts can be produced.

The basic geometry of interpolation on a grid is shown in Fig. E.1. The initial image is only given at discrete points in (x, y) . To find an interpolated value at an arbitrary point requires first locating the four grid points surrounding the point (x, y) . In Fig. E.1 the new point is located between x_1 and x_2 in x and between y_1 and y_2 in y . The values of the initial image at the four grid points surrounding (x, y) are f_{11} , f_{12} , f_{21} , and f_{22} .

With four points there are four known conditions and the best interpolation available is a bilinear form:

$$f(x, y) = a + bx + cy + dxy \quad (\text{E.1})$$

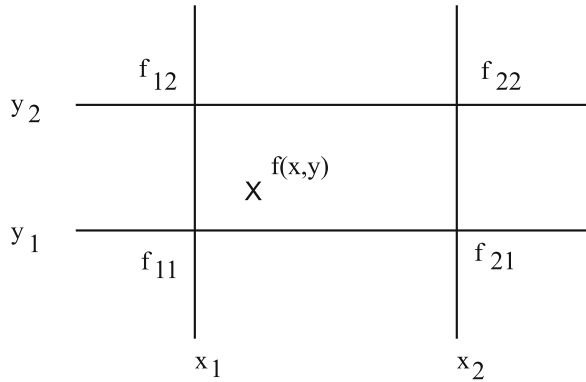


Fig. E.1 Interpolation in a two-dimensional rectangular grid. The function $f(x, y)$ can be found at an arbitrary point (x, y) given only the values sampled at discrete values of $x = x_1, x_2$ and $y = y_1, y_2$ surrounding point (x, y) . The spacing in x does not need to be the same as that in y

The a, b, c , and d coefficients are determined by the surrounding image values as:

$$\begin{aligned}f_{11} &= a + bx_1 + cy_1 + dx_1y_1 \\f_{12} &= a + bx_1 + cy_2 + dx_1y_2 \\f_{22} &= a + bx_2 + cy_2 + dx_2y_2 \\f_{21} &= a + bx_2 + cy_1 + dx_2y_1\end{aligned}\tag{E.2}$$

Combining pairs of equations yields:

$$\begin{aligned}(f_{11} - f_{12}) &= (c + dx_1)(y_1 - y_2) \\(f_{21} - f_{22}) &= (c + dx_2)(y_1 - y_2)\end{aligned}\tag{E.3}$$

The coefficients may be found one at a time. Subtracting Eqs. E.3 yields a value for d :

$$d = \frac{f_{11} - f_{12} - f_{21} + f_{22}}{(x_1 - x_2)(y_1 - y_2)}\tag{E.4}$$

Using this value for d and one of Eqs. E.3 yields a value for c :

$$c = \left(\frac{f_{11} - f_{12}}{y_1 - y_2} \right) - dx_1\tag{E.5}$$

Next combining Eqs. E.2 in a slightly different order gives:

$$f_{11} - f_{21} = b(x_1 - x_2) + dy_1(x_1 - x_2)\tag{E.6}$$

from which the a and b coefficients can be found.

$$b = \left(\frac{f_{11} - f_{21}}{x_1 - x_2} \right) - dy_1 \quad (\text{E.7})$$

$$a = f_{11} - bx_1 - cy_1 - dx_1y_1 \quad (\text{E.8})$$

Now given a value for all four coefficients (a , b , c , and d) a value for the function $f(x, y)$ at any point inside the four grid points may be obtained from Eq. E.1. Repeating this process at each point of the second grid yields an interpolated value of the first image at each grid point of the second image.

Appendix F

3D Perspective View

The specimen is clearly three dimensional (3D) but the electron microscope image is two dimensional (2D). The three-dimensional structure of the specimen is projected into the final two-dimensional image making it difficult to determine if the original three-dimensional structure of the specimen was properly described. The electron microscope image is in an x , y plane but the crystal structure is a set of (x_i, y_i, z_i) coordinates. The third dimension z can have a significant influence on the scattering within the specimen and influence the final image in rather nonintuitive ways. It is important to check that the full three-dimensional structure of the specimen has been entered correctly.

A crystalline or amorphous specimen must be described as a detailed numerical list of atomic coordinates before an electron microscope image of the specimen can be simulated in the computer. Generating this set of numbers can be a rather tedious and difficult task. It is difficult to generate this list and even more difficult to determine if it is correct in the first place.

One particular type of diagnostic tool to determine if the specimen description is correct is to render a 3D perspective view of the entire specimen structure. Each atom can be drawn as a simple hard sphere and the entire structure can be rotated and viewed to inspect its three-dimensional structure. A full rendering with shading and hidden surfaces can be difficult to calculate. There are a variety of sophisticated programs available for this procedure (for example, RasMol [439], jmol [248], and VESTA [359]). However, if some approximations are made there is a simple way to draw a reasonable approximation of the full 3D structure.

The specimen is assumed to be a collection of atoms in 3D. Each atom is drawn as a hard sphere at a particular set of coordinates (x_i, y_i, z_i) in 3D. This structure is viewed from a particular point in space as shown in Fig. F.1. The image seen by the viewer must be projected into a 2D image (the computer screen or a piece of paper). If the viewer is close, then the structure will appear more distorted than if the viewer is far away. By varying the relative viewing position the three-dimensional nature of the structure can be investigated.

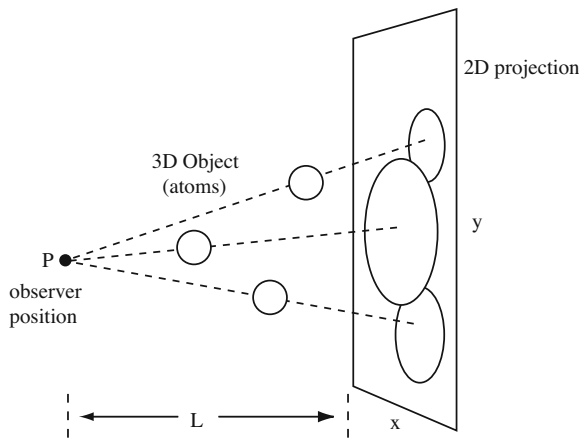


Fig. F.1 3D geometry of viewing a three-dimensional collection of atoms (a specimen) as a two-dimensional projection

There are several approximations that make the 2D image simple to generate. First approximate a 3D sphere as a shaded circle. In 3D some atoms will be in front of other atoms and fully or partially hide those atoms in the back from the viewer. This is the so-called hidden surface problem. A simple approach to drawing hidden surfaces is to sort by depth and draw from the back forward. This is not particularly efficient but is simple to program and does a reasonable job of hiding the appropriate atoms. One particular situation that is not handled properly is the case where two adjacent atoms are at the same depth. One atom will be arbitrarily drawn on top of the other. This approach is simply enough to program on relatively simple and inexpensive personal computers Kirkland [268].

A 3D perspective view of the specimen is more useful if it can be rotated to see it from different angles. This should be done before drawing the 2D image for obvious reasons. Given a rotation angle ϕ and the tilt angle θ the initial set of atom coordinates (x_i, y_i, z_i) can be rotated about the point (x_0, y_0, z_0) (usually the center of the crystal) in two steps. First rotate by ϕ as:

$$\begin{aligned} x'_i &= (x_i - x_0) \cos \phi - (y_i - y_0) \sin \phi \\ y'_i &= (x_i - x_0) \sin \phi + (y_i - y_0) \cos \phi \end{aligned} \quad (\text{F.1})$$

then tilt by θ as:

$$\begin{aligned} y''_i &= y'_i \cos \theta + (z_i - z_0) \sin \theta \\ z'_i &= -y'_i \sin \theta + (z_i - z_0) \cos \theta \end{aligned} \quad (\text{F.2})$$

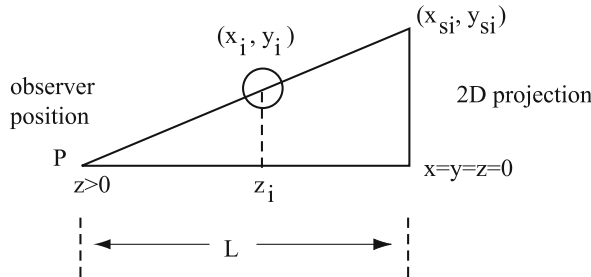


Fig. F.2 Similar triangles used to calculate the relative coordinates in a 3D perspective view

Rotating and tilting produce a new set of coordinates (x'_i, y''_i, z'_i) . An angle of $(\phi, \theta) = (0, 0)$ generates a view down the beam direction (the optic axis of the electron microscope). After rotating and tilting the z'_i coordinates are offset to yield $z > 0$ at the top or entrance surface and $z = 0$ at the bottom or exit surface. In Fig. F.1 the electrons are traveling from left to right with $z = 0$ on the right.

The position of each atom on the 2D viewing screen is not simply (x'_i, y''_i) . The three-dimensional geometry between the viewer, the specimen, and 2D viewing screen must be taken into account (for example, Newman and Sproull [372]). If L is the distance from the viewer to the viewing screen and the specimen is in between the viewer and the viewing screen (as in Fig. F.1), then the actual coordinates on the viewing screen $(x_i, y_i)_s$ are:

$$\begin{aligned} x_{si} &= \frac{Lx'_i}{L - z'_i} \\ y_{si} &= \frac{Ly''_i}{L - z'_i} \end{aligned} \quad (\text{F.3})$$

by comparison of similar triangles as in Fig. F.2. The apparent size of each atom must also be scaled in a similar manner. If the actual 3D diameter of the atom is d_i , then the diameter of the 2D circle is:

$$d_{si} = \frac{Ld_i}{L - z'_i} \quad (\text{F.4})$$

The final set of coordinates is sorted by depth z'_i and drawn from negative z'_i to positive z'_i . The sorting method of Shell is relatively easy to program and efficient enough for this purpose (Shell [455] and Press et al. [406]). After sorting, each

atom is drawn as a shaded circle. Each successive layer of atoms will overwrite the previous layer taking care of the hidden surface problem. Drawing a simple shaded circle is relatively easy and can mimic an actual 3D shaded sphere in a convincing manner. There are several possible ways to do this and two empirical schemes are listed below. If the output 2D perspective image is encoded as eight bits per pixel (integer valued) with 255 being white and 0 being black, then the gray scale intensity g inside each circle can follow:

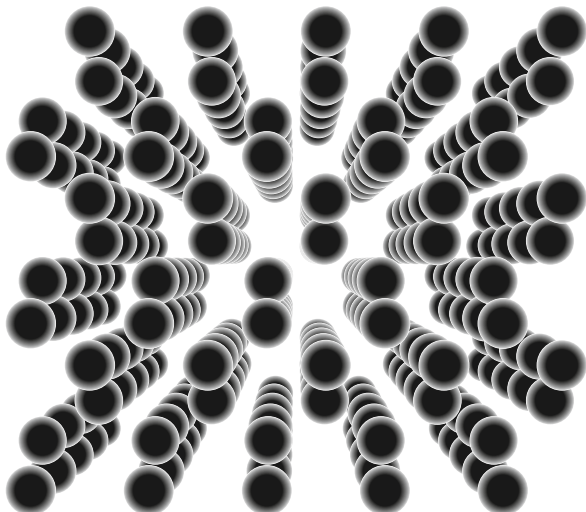
$$g = 255 - 150 \frac{r^2}{r_{\max}^2} \quad (\text{F.5})$$

where r is the radius of the circle, and r_{\max} is its maximum radius. This generates a white shaded circle on a black background. The entire background should be set to black before drawing any of the atoms. Alternately if an image is generated for printing on a postscript printer, then the following postscript macros (Adobe Reference manual [225]) generate a black shaded circle on a white background:

```
%  
% macro to make a unit circle at (0,0)  
%  
/circle {newpath 0 0 1 0 360 arc  
closepath fill} def  
  
%  
% macro to make a shaded sphere  
% call as--> xscale yscale xpos ypos sp  
%  
/sp { gsave translate scale  
0.0 0.04 1 { sqrt 1 exch sub setgray circle  
0.98 0.98 scale } for grestore } def
```

The first macro called “circle” draw a circle and fills it in with the current color or gray level. The second macros called “sp” draws a series of solid circle one on top of the other. Each successive circle is slightly smaller and slightly blacker to generate the shading. The “sp” macro is given a short name because it must be called many times and a shorter name will use less disk space and transfer quicker to the printer. Figure F.3 shows an example of a 3D view looking down the 110 direction of the silicon lattice.

Fig. F.3 A 3D perspective view looking down the (110) direction of silicon (drawn in postscript format). Each silicon atom is drawn as a shaded hard sphere (black)



References

1. Atkinson A. C. The computer generation of Poisson random variable. *J. Royal Statistical Society, Series C (Applied Statistics)*, 28:29–35, 1979.
2. M. Abramowitz and I. A. Stegun. *Handbook of Mathematical Functions*. Dover, New York, 1965.
3. G. P. Agrawal. *Nonlinear Fiber Optics*. Academic Press, San Diego, 2nd edition, 1995.
4. H. Akima. A new method of interpolation and smooth curve fitting based on local procedures. *Journal of the Association for Computing Machinery*, 17:589–602, 1970.
5. H. Akima. Algorithm 433: Interpolation and smooth curve fitting based on local procedures. *Communications of the Association for Computing Machinery*, 15:914–918, 1972.
6. L. J. Allen, A. J. D’Alfonso, and S. D. Findlay. Modeling the inelastic scattering of fast electrons. *Ultramicroscopy*, 151:11–22, 2015.
7. L. J. Allen, H. M. L. Faulkner, and H. Leeb. Inversion of dynamical electron diffraction data including adsorption. *Acta Cryst.*, A56:119–126, 2000.
8. L. J. Allen, S. D. Findlay, M. P. Oxley, and C. J. Rossouw. Lattice-resolution contrast from a focused coherent electron probe. Part I. *Ultramicroscopy*, 96:47–63, 2003.
9. L. J. Allen, T. W. Josefsson, and H. Leeb. Obtaining the crystal potential by inversion from electron scattering intensities. *Acta Cryst.*, A54:388–398, 1998.
10. L. J. Allen, H. Leeb, and A. E. C. Spargo. Retrieval of the projected potential by inversion from the scattering matrix in electron-crystal scattering. *Acta Cryst.*, A55:105–111, 1999.
11. L. J. Allen and C. J. Rossouw. Absorptive potentials due to ionization and thermal diffuse scattering by fast electrons in crystals. *Phys. Rev. B*, 42:11644–11654, 1990.
12. J. G. Allpress, E. A. Hewat, A. F. Moodie, and J. V. Sanders. n-beam lattice images. I. experimental and computed images of $\text{W}_4\text{Nb}_{26}\text{O}_{77}$. *Acta Cryst.*, A28:528–536, 1972.
13. J. G. Allpress and J. V. Sanders. The direct observation of the structure of real crystals by lattice imaging. *J. Appl. Cryst.*, 6:165–190, 1973.
14. A. Amali and P. Rez. Theory of lattice resolution in high-angle annular dark-field images. *Microscopy and Microanalysis*, 3:28–46, 1997.
15. E. Anderson, Z. Bai, C. Bischof, S. Blackford, J. Demmel, J. Dongarra, J. Du Croz, A. Greenbaum, S. Hammarling, A. McKenney, and D. Sorensen. *LAPACK Users’ Guide*. Society for Industrial and Applied Mathematics, Philadelphia, PA, third edition, 1999.
16. H. C. Andrews and B. R. Hunt. *Digital Image Restoration*. Prentice Hall, New Jersey, 1977.
17. G. R. Anstis. The s-state analysis applied to high-angle, annular dark-field image interpretation when can we use it? *Microscopy and Microanalysis*, 10:4–8, 2004.
18. G. R. Anstis, D. Q. Cai, and D. J. H. Cockayne. Limitations on the s-state approach to the interpretation of sub-angstrom resolution electron microscope images and microanalysis. *Ultramicroscopy*, 94:309–327, 2003.

19. G. R. Anstis and D. J. H. Cockayne. The calculation and interpretation of high-resolution electron microscope images of lattice defects. *Acta Cryst.*, A35:511–524, 1979.
20. N. W. Ashcroft and N. D. Mermin. *Solid State Physics*. Holt, Rinehart and Winston, New York, 1976.
21. R. Barakat and A. Houston. Transfer function of an annular aperture in the presence of spherical aberration. *J. Optical Soc. Amer.*, 55:538–541, 1965.
22. J. C. Barry. Semiquantitative image matching in HRTEM. In W. Krakow and M. O’Keefe, editors, *Computer Simulation of Electron Microscope Diffraction and Images*, pages 57–78, Warrendale, Penn., 1989. The Minerals, Metals and Materials Society.
23. J. C. Barry. Image-matching as a means of atomic structure evaluation in high resolution transmission electron microscopy. In P. W. Hawkes, editor, *Signal and Image Processing in Microscopy and Microanalysis, Scanning Microscopy, Supplement 6*, pages 209–221, Chicago, 1992. Scanning Microscopy Intern.
24. J. Barthel. Dr. Probe: A software for high-resolution STEM image simulation. *Ultramicroscopy*, 193:1–11, 2018.
25. B. W. Batterman and H. Cole. Dynamical diffraction of X-rays by perfect crystals. *Reviews of Modern Physics*, 36:681–717, 1964.
26. W. T. Baxter, A. Leith, and J. Frank. SPIRE: The SPIDER reconstruction engine. *J. Structural Biology*, 157:56–63, 2007.
27. M. J. Beeching and A. E. C. Spargo. A method for crystal potential retrieval in HRTEM. *Ultramicroscopy*, 52:243–247, 1993.
28. M. J. Beeching and A. E. C. Spargo. Inversion of nonperiodic wavefields to determine localized defect structure. *J. Microscopy*, 190:262–266, 1998.
29. G. Behan, E. C. Cosgriff, Angus I. Kirkland, and Peter D. Nellist. Three-dimensional imaging by optical sectioning in the aberration-corrected scanning transmission electron microscope. *Phil. Trans. R. Soc. A*, 367:3825–3844, 2009.
30. H. M. Berman, J. Westbrook, Z. Feng, G. Gilliland, T. N. Bhat, H. Weissig, I. N. Shindyalov, and P. E. Bourne. The protein data bank. *Nucleic Acids Research*, 28:235–242, 2000. www.rcsb.org.
31. H. Bethe. Theorie der beugung von elektronen an kristallen. *Annalen der Physik*, 87:55–129, 1928.
32. H. Bethe. Zur theorie des durchgangs schneller korpuskularstrahlen durch materie. *Annalen der Physik*, 5:325–400, 1930.
33. H. A. Bethe. *Selected Works of Hans A. Bethe*. World Scientific, Singapore, 1997.
34. H. A. Bethe and R. W. Jackiw. *Intermediate Quantum Mechanics*. Benjamin, Reading, Mass., 2nd edition, 1968.
35. G. Binnig and H. Rohrer. Scanning tunneling microscopy - from birth to adolescence. *Rev. Modern Physics*, 59:615–625, 1987.
36. D. M. Bird. Theory of zone axis electron diffraction. *J. of Elect. Microsc. Tech.*, 13:77–97, 1989.
37. G. Black and E. H. Linfoot. Spherical aberration and the information content of optical images. *Proc. Royal Society London*, A239:522–540, 1957.
38. Jasmine Blanchette and Mark Summerfield. *C++ GUI Programming with Qt 4*. Prentice Hall, Westford, Mass., second edition, 2008. www.qt.io.
39. J. E. Bonevich and L. D. Marks. Contrast transfer theory for non-linear imaging. *Ultramicroscopy*, 26:313–320, 1988.
40. R. A. Bonham and M. Fink. *High Energy Electron Scattering*. Van Nostrand Reinhold, New York, 1974.
41. C. B. Boothroyd. Why don’t high-resolution simulations and images match? *J. Microscopy*, 190:99–108, 1998.
42. M. Born and E. Wolf. *Principles of Optics*. Pergamon Press, Oxford, 6th edition, 1980.
43. Eric G. T. Bosch and Ivan Lazić. Analysis of HR-STEM theory for thin specimens. *Ultramicroscopy*, 156:59–72, 2015.
44. D. K. Bowen and C. R. Hall. *Microscopy of Materials*. MacMillan Press, London, 1975.

45. J. J. Bozzola and L. D. Russell. *Electron Microscopy, Princ. and Tech. for Biologists*, 2nd edit. Jones and Bartlett, Sudbury, Mass., 1999.
46. R. N. Bracewell. *The Fourier Transform and Its Applications*. McGraw-Hill, New York, 2nd edition, 1986.
47. W. L. Bragg and J. West. A technique for the X-ray examination of crystal structures with many parameters. *Zeit. fur Kristallographie*, 69:118–148, 1929.
48. E. O. Brigham. *The Fast Fourier Transform*. Prentice-Hall, Englewood Cliffs, New Jersey, 1988.
49. T. F. Budinger and R. M. Glaeser. Measurement of focus and spherical aberration of an electron microscope objective lens. *Ultramicroscopy*, 2:31–41, 1976.
50. V. M. Burke and I. P. Grant. The effect of relativity on atomic wave functions. *Proc. Phys. Soc.*, 90:297–314, 1967.
51. L. A. Bursill and A. R. Wilson. Electron-optical imaging of the hollandite structure at 3 Å resolution. *Acta Cryst.*, A33:672–676, 1977.
52. P. R. Buseck, J. M. Cowley, and L. Eyring, editors. *High-Resolution Transmission Electron Microscopy*. Oxford Univ. Press, New York, 1988.
53. B. F. Buxton, J. E. Loveluck, and J. W. Steeds. Bloch waves and their corresponding atomic and molecular orbitals in high energy electron diffraction. *Philosophical Magazine A*, 38:259–278, 1978.
54. C. Cai and J. Chen. An accurate multislice method for low-energy transmission electron microscopy. *Micron*, 43:374–379, 2012.
55. Can Ying Cai, Song Jun Zeng, Hong Rong Liu, and Qi Bin Yang. Computational comparison of the conventional multislice method and the real space multislice method for simulating exit wavefunctions. *Micron*, 40:313–319, 2009.
56. Ewen Callaway. Molecular-imaging pioneers scoop nobel. *Nature*, 550:167, 2017.
57. E. Carlini, V. Grillo, and P. Palazzari. Accurate and fast multislice simulations of HAADF image contrast by parallel computing. In A. G. Cullis and P. A. Midgley, editors, *Springer Proc. in Phys.*, volume 120, pages 177–180, 2008.
58. K. R. Castleman. *Digital Image Processing*. Prentice Hall, Englewood Cliffs, New Jersey, 1979.
59. L. Y. Chang, A. I. Kirkland, and J. M. Titchmarsh. On the importance of fifth-order spherical aberration for fully corrected electron microscopy. *Ultramicroscopy*, 106:301–306, 2006.
60. J. H. Chen and D. Van Dyck. Accurate multislice theory for elastic electron scattering in transmission electron microscopy. *Ultramicroscopy*, 70:29–44, 1997.
61. J. H. Chen, D. Van Dyck, and M. Op de Beck. Multislice method for large beam tilt with applications to HOLZ effects in triclinic and monoclinic crystals. *Acta Cryst.*, A53:576–589, 1997.
62. J. H. Chen, D. Van Dyck, M. Op de Beck, and J. Van Landuyt. Computational comparisons between the conventional multislice method and the third-order multislice method for calculating high-energy electron diffraction and imaging. *Ultramicroscopy*, 69:219–240, 1997.
63. Yifan Cheng, Nikolaus Grigorieff, Pawel A. Penczek, and Thomas Waltz. A primer on single-particle cryo-electron microscopy. *Cell*, 161:439–449, 2015.
64. W. Coene and D. Van Dyck. The real space method for dynamical electron diffraction calculation in high resolution electron microscopy, II. critical analysis of the dependency on the input parameters. *Ultramicroscopy*, 15:41–50, 1984.
65. W. Coene and D. Van Dyck. The real space method for dynamical electron diffraction calculations in high resolution electron microscopy III. a computational algorithm for the electron propagation with practical applications. *Ultramicroscopy*, 15:287–300, 1984.
66. W. Coene, G. Janssen, M. Op de Beck, and D. Van Dyck. Phase retrieval through focus variation for ultra-resolution in field-emission transmission electron microscopy. *Phys. Rev. Letters*, 69:3743–3746, 1992.

67. W. M. J. Coene, A. Thust, M. Op de Beck, and D. van Dyck. Maximum-likelihood method for focus-variation image reconstruction in high resolution transmission electron microscopy. *Ultramicroscopy*, 64:109–135, 1996.
68. J. W. Cooley and J. W. Tukey. An algorithm for the machine calculation of complex Fourier series. *Mathematics of Computation*, 19:297–301, 1965.
69. J. M. Cordes, A. Pidwerbetsky, and R. V. E. Lovelace. Refractive and diffractive scattering in the interstellar medium. *The Astrophysical J.*, 310:737–767, 1986.
70. Adobe Corp. *TIFF, Revision 6.0*. Adobe Corp., Mountain View, CA, 1992.
71. M. A. Coulthard. A relativistic Hartree-Fock atomic field calculation. *Proc. Phys. Soc.*, 91:44–49, 1967.
72. R. D. Cowan. *The Theory of Atomic Structure and Spectra*. Univ. of California Press, Berkeley, 1981.
73. J. M. Cowley. Image contrast in a transmission scanning electron microscope. *Appl. Phys. Letters*, 15:58–59, 1969.
74. J. M. Cowley. *Diffraction Physics*. North-Holland, Amsterdam, 2nd edition, 1975.
75. J. M. Cowley. Scanning transmission electron microscopy of thin specimens. *Ultramicroscopy*, 2:3–16, 1976.
76. J. M. Cowley. Electron microscopy of crystals with time-dependent perturbations. *Acta Cryst.*, A44:847–853, 1988.
77. J. M. Cowley and S. Iijima. Electron microscope image contrast for thin crystals. *Z. Naturforsch.*, 27a:445–451, 1972.
78. J. M. Cowley and A. F. Moodie. The scattering of electrons by atoms and crystals. I. a new theoretical approach. *Acta Cryst.*, 10:609–619, 1957.
79. J. M. Cowley and R. J. Murray. Diffuse scattering in electron diffraction patterns, II. short-range order scattering. *Acta Cryst.*, A24:329–336, 1968.
80. J. M. Cowley and A. P. Pogany. Diffuse scattering in electron diffraction patterns, I. general theory and computational methods. *Acta Cryst.*, A24:109–116, 1968.
81. J. M. Cowley and J. C. H. Spence. Innovative imaging and microdiffraction in STEM. *Ultramicroscopy*, 3:433–438, 1979.
82. H. L. Cox and R. A. Bonham. Elastic electron scattering amplitudes for neutral atoms calculated using the partial wave method at 10, 40, 70, and 100 kV for $Z = 1$ to $Z = 54$. *J. Chem. Phys.*, 47:2599–2608, 1967.
83. A. V. Crewe, J. P. Langmore, and M. S. Isaacson. Resolution and contrast in the scanning transmission electron microscope. In B. M. Siegel and D. R. Beaman, editors, *Physical Aspects of Electron Microscopy and Microbeam Analysis*, pages 47–62. Wiley, New York, 1975.
84. A. V. Crewe and D. B. Salzman. On the optimum resolution for a corrected STEM. *Ultramicroscopy*, 9:373–378, 1982.
85. A. V. Crewe, J. Wall, and L. M. Welter. A high-resolution scanning transmission electron microscope. *J. Applied Physics*, 39:5861–5868, 1968.
86. M. D. Croitoru, D. Van Dyck, S. Van Aert, S. Bals, and J. Verbeeck. An efficient way of including thermal diffuse scattering in simulation of scanning transmission electron microscope images. *Ultramicroscopy*, 106:933–940, 2006.
87. D. T. Cromer and J. B. Mann. X-ray scattering factors computed from numerical Hartree-Fock wave functions. *Acta Cryst.*, A24:321–324, 1968.
88. D. T. Cromer and J. T. Waber. Scattering factors computed from relativistic Dirac-Slater wave functions. *Acta Cryst.*, 18:104–109, 1965.
89. D. T. Cromer and J. T. Waber. Atomic scattering factors for X-rays. In J. A. Ibers and W. C. Hamilton, editors, *International Tables for X-Ray Crystallography, Vol. IV, Section 2.2*, pages 71–147. Kynoch Press, Birmingham, 1974.
90. A. J. D’Alfonso, A. J. Morgan, A. W. C. Yan, P. Wang, H. Sawada, A. I. Kirkland, and L. J. Allen. Deterministic electron ptychography at atomic resolution. *Phys. Rev. B*, 89:064101, 2014.

91. B. Dawson. Atomic scattering amplitudes for electrons for some of the lighter elements. *Acta Cryst.*, 14:1120–1124, 1961.
92. M. Op de Beck. Comments on the use of the relativistic Schrodinger equation in high-energy electron diffraction. In G. W. Bailey and C. L. Rieder, editors, *Proceedings of the 51th Annual Meeting of the Microscopy Society of America*, pages 1212–1213. San Francisco Press, 1993.
93. J. M. de la Rosa-Trevín, J. Otón, R. Marabini, A. Zaldívar, J. Vargas, J. M. Carazo, and C. O. S. Sorzano. Xmipp 3.0: An improved software suite for image processing in electron microscopy. *J. Structural Biology*, 184:321–328, 2013.
94. J. P. Desclaux. Relativistic Dirac-Fock expectation values for atoms with $Z = 1$ to $Z = 120$. *Atomic Data and Nuclear Data Tables*, 12:311–406, 1973.
95. J. P. Desclaux. A multiconfiguration relativistic Dirac-Fock program. *Computer Physics Communications*, 9:31–45, 1975.
96. J. Desseaux, A. Renault, and A. Bourret. Multi-beam images of germanium oriented in (011). *Phil. Mag.*, 35:357–372, 1977.
97. C. Dinges and H. Rose. Simulation of filtered and unfiltered TEM images and diffraction patterns. *Phys. Stat. Sol. (A)*, 150:23–30, 1995.
98. K. H. Downing and D. A. Grano. Analysis of photographic emulsions for electron microscopy of two-dimensional crystalline specimens. *Ultramicroscopy*, 7:381–404, 1982.
99. P. A. Doyle and J. M. Cowley. Scattering factors for the diffraction of electrons by crystalline solids. In J. A. Ibers and W. C. Hamilton, editors, *International Tables for X-Ray Crystallography, Vol. IV, Section 2.4*, pages 152–175. Kynoch Press, Birmingham, 1974.
100. P. A. Doyle and P. S. Turner. Relativistic Hartree-Fock x-ray and electron scattering factors. *Acta Cryst.*, A24:390–397, 1968.
101. D. Drouin, A. R. Couture, D. Joly, X. Tastet, V. Aimez, and R. Gauvin. CASINO V 2.42 - a fast and easy-to-use modeling tool for scanning electron microscopy and microanalysis users. *Scanning*, 29:92–101, 2007.
102. D. Drouin, P. Hovington, and R. Gauvin. CASINO: A new Monte Carlo code in C language for electron beam interaction—part II: Tabulated values of the Mott cross section. *Scanning*, 19:20–28, 1997.
103. D. E. Dudgeon and R. M. Mersereau. *Multidimensional Digital Signal Processing*. Prentice Halls, New Jersey, 1984.
104. B. J. Dulong, R. D. Haynes, and M. D. Robertson. A study in the computation time required for the inclusion of strain field effects in Bloch-wave simulations of TEM diffraction contrast images. *Ultramicroscopy*, 108:415–425, 2008.
105. C. Dwyer. Multislice simulation of scanning transmission electron microscope images. In L. N. Brewer, S. McKernan, J. P. Shields, F. E. Schmidt Jr, J. H. Woodward, and N. J. Zaluzec, editors, *Microscopy and Microanalysis 2009*, volume 15, suppl. 2, pages 754–755, Cambridge, UK, 2009. Cambridge Univ. Press.
106. C. Dwyer. Simulation of scanning transmission electron microscope images on desktop computers. *Ultramicroscopy*, 110:195–198, 2010.
107. C. Dwyer and J. Etheridge. Scattering of Å-scale electron probes in silicon. *Ultramicroscopy*, 96:343–360, 2003.
108. K. G. Dyall, I. P. Grant, C. T. Johnson, F. A. Parpia, and E. P. Plummer. Grasp: A general-purpose relativistic atomic structure program. *Computer Physics Communications*, 55:425–456, 1989.
109. J. W. Edington. *Practical Electron Microscopy in Materials Science*. Van Nostrand Reinhold, New York, 1976.
110. A. S. Eggeman, A. London, and P. A. Midgley. Ultrafast electron diffraction pattern simulations using GPU technology. applications to lattice vibrations. *Ultramicroscopy*, 134:44–47, 2013.
111. J. J. Einspahr and P. M. Voyles. Prospects for 3D, nanometer-resolution imaging by confocal STEM. *Ultramicroscopy*, 106:1041–1052, 2006.
112. R. Eisberg and R. Resnick. *Quantum Physics of Atoms, Molecules, Solids, Nuclei, and Particles*. Wiley, New York, 2nd edition, 1985.

113. C. B. Eisenhandler and B. M. Siegel. Imaging of single atoms with the electron microscope by phase contrast. *J. Applied Physics*, 37:1613–1620, 1966.
114. C. B. Eisenhandler and B. M. Siegel. A zone-plate aperture for enhancing resolution in phase contrast electron microscopy. *Applied Physics Letters*, 8:258–260, 1966.
115. A. B. El-Kareh and J. C. J. El-Kareh. *Electron Beams, Lenses, and Optics*, Vol. 1,2. Academic Press, New York, 1970.
116. Dominika Elmlund and Hans Elmlund. SIMPLE: software for *ab initio* reconstruction of heterogeneous single-particles. *J. Structural Biology*, 180:420–427, 2012.
117. A. Engel. The principle of reciprocity and its application to conventional and scanning dark field electron microscopy. *Optik*, 41:117–126, 1974.
118. A. Engel. Scanning transmission electron microscopy: Biological application. In P. W. Hawkes, editor, *Adv. in Imaging and Electron Physics*, vol. 159, pages 357–386. Academic Press, San Diego, 2009.
119. A. Engel and C. Colliex. Application of scanning transmission electron microscopy to the study of biological structure. *Current Opinion in Biotechnology*, 4:403–411, 1993.
120. S. J. Erasmus and K. C. A. Smith. An automatic focusing and astigmatism correction system for the SEM and CTEM. *J. Microscopy*, 127:185–199, 1982.
121. Peter Ercius, Osama Alaidi, Matthew J. Rames, and Gang Ren. Electron tomography: A three-dimensional analytic tool for hard and soft material research. *Adv. Materials*, 27:5638–5663, 2015.
122. H. P. Erikson. The Fourier transform of an electron micrograph - first order and second order theory of image formation. In R. Barer and V. E. Cosslett, editors, *Adv. in Optical and Electron Microscopy*, Vol. 5, pages 163–199. Academic Press, London, 1973.
123. R. Erni. *Aberration-Corrected Imaging in Transmission Electron Microscopy*. Imperial College Press, London, 2nd edition, 2015.
124. G. Y. Fan. Multislice calculation of kikuchi patterns. In G. W. Bailey, editor, *Proceedings of the 47th Annual Meeting of the Microscopy Society of America*, pages 52–53. San Francisco Press, 1989.
125. G. Y. Fan, P. J. Mercurio, S. J. Young, and M. H. Ellisman. Telemicroscopy. *Ultramicroscopy*, 52:499–503, 1993.
126. M. D. Feit and J. A. Fleck. Light propagation in graded-index optical fibers. *Applied Optics*, 17:3990–3998, 1978.
127. P. L. Fejes. Approximations for the calculation of high resolution electron microscope images of thin films. *Acta Cryst.*, A33:109–113, 1977.
128. J. Fertig and H. Rose. Resolution and contrast of crystalline objects in high-resolution scanning transmission electron microscopy. *Optik*, 59:407–429, 1981.
129. H. A. Ferwerda, B. J. Hoenders, and C. H. Slump. The fully relativistic foundation of linear transfer theory in electron optics based on the Dirac equation. *Optica Acta*, 33:159–183, 1986.
130. H. A. Ferwerda, B. J. Hoenders, and C. H. Slump. Fully relativistic treatment of electron-optical image formation based on the Dirac equation. *Optica Acta*, 33:145–157, 1986.
131. H. A. Ferwerda and F. P. C. Visser. Applications of Glauber's scattering theory to the scattering of electrons by heavy elements. In P. W. Hawkes, editor, *Image Processing and Computer-Aided Design in Electron Optics*, pages 212–219. Academic Press, London, 1973.
132. R. P. Feynman. An operator calculus having applications in quantum electrodynamics. *Phys. Rev.*, 84:108–128, 1951.
133. P. M. Fields and J. M. Cowley. Computed electron microscope images of atomic defects in fcc metals. *Acta Cryst.*, A34:103–112, 1978.
134. S. D. Findlay and J. M. LeBeau. Detector non-uniformity in scanning transmission electron microscopy. *Ultramicroscopy*, 124:52–60, 2013.
135. S. D. Findlay, N. Shibata, H. Sawada, E. Okunishi, Y. Kondo, and Y. Ikuhara. Dynamics of annular bright field scanning transmission electron microscopy. *Ultramicroscopy*, 110:903–923, 2010.

136. S. D. Findlay, N. Shibata, H. Sawada, E. Okunishi, Y. Kondo, T. Yamamoto, and Y. Ikuhara. Robust atomic resolution imaging of light elements using scanning transmission electron microscopy. *Appl. Phys. Lett.*, 95:191913, 2009.
137. C. Froese Fischer, T. Brage, and P. Jönsson. *Computational Atomic Structure, an MCDF Approach*. Institute of Physics Publishing, Bristol and London, 1997.
138. J. A. Fleck(Jr.), J. R. Morris, and M. D. Feit. Time-dependent propagation of high energy laser beams through the atmosphere. *Appl. Phys.*, 10:129–160, 1976.
139. J. B. Forsyth and M. Wells. On the analytical approx. to the atomic scattering factor. *Acta Cryst.*, 12:412–415, 1959.
140. A. G. Fox, M. A. O'Keefe, and M. A. Tabbernор. Relativistic Hartree-Fock X-ray and electron atomic scattering factors at high angles. *Acta Cryst.*, A45:786–793, 1989.
141. J. Frank. A study on heavy/light atom discrimination in bright-field electron microscopy. *Biophysical J.*, 12:484–511, 1972.
142. J. Frank. The envelope of electron microscope transfer functions for partially coherent illumination. *Optik*, 38:519–536, 1973.
143. J. Frank. *Three Dimensional Electron Microscopy of Macromolecular Assemblies*. Oxford Univ. Press, New York, 2006.
144. J. Frank, M. Radermacher, P. Penczek, J. Zhu, Y. Li, M. Ladjadj, and Ardean Leith. SPIDER and WEB: Processing and visualization of images in 3D electron microscopy and related fields. *J. Structural Biology*, 116:190–199, 1996.
145. J. Frank, B. Shimkin, and H. Dowse. SPIDER - a modular software system for image processing. *Ultramicroscopy*, 6:343–358, 1981.
146. A. J. Freeman. Atomic scattering factors for spherical and aspherical charge distributions. *Acta Cryst.*, 12:261–270, 1959.
147. A. J. Freeman and J. H. Wood. An atomic scattering factor for iron. *Acta Cryst.*, 12:271–273, 1959.
148. R. G. French and R. V. E. Lovelace. Strong turbulence and atmospheric waves in stellar occultations. *Icarus*, 56:122–146, 1983.
149. Matteo Frigo and Steven G. Johnson. The design and implementation of FFTW3. *Proc. of the IEEE*, 93:216–231, 2005. www.fftw.org.
150. S. P. Frigo, Z. H. Levine, and N. J. Zaluzec. Submicron imaging of buried integrated circuit structures using scanning confocal electron microscopy. *Applied Physics Letters*, 81:2112–2114, 2002.
151. C. Froese-Fischer. *The Hartree-Fock Method for Atoms*. Wiley, New York, 1977.
152. F. Fujimoto. Dynamical theory of electron diffraction in Laue-case I. general theory. *J. Physical Soc. Japan*, 14:1558–1568, 1959.
153. K. Fujiwara. Relativistic dynamical theory of electron diffraction. *J. Physical Society of Japan*, 16:2226–2238, 1961.
154. B. Fultz and J. M. Howe. *Transmission Electron Microscopy and Diffractometry of Materials*. Springer-Verlag, Berlin, fourth edition, 2013.
155. D. Gabor. A new microscopic principle. *Nature*, 161:777–778, 1948.
156. Harindarpal S. Gill and David Eisenberg. The crystal structure of phosphinothricin in the active site of glutamine synthetase illuminates the mechanism of enzymatic inhibition. *Biochemistry*, 40:1903–1912, 2001.
157. R. Glauber and V. Schomaker. The theory of electron diffraction. *Phys. Rev.*, 89:667–671, 1953.
158. Joseph I. Goldstein, Dale E. Newbury, Joseph R. Michael, Nicholas W. M. Ritchie, John Henry J. Scott, and David C. Joy. *Scanning Electron Microscopy and X-Ray Microanalysis*. Springer, New York, fourth edition, 2018.
159. A. Gómez-Rodríguez, L. M. Beltrán-del-Río, and R. Herrera-Becerra. SimulaTEM: Multi-slice simulations for general objects. *Ultramicroscopy*, 110:95–104, 2010.
160. R. C. Gonzalez and R. E. Woods. *Digital Image Processing*. Prentice Hall, New York, 3rd edition, 2008.

161. J. W. Goodman. *Intro. to Fourier Optics*. Roberts and Co., Englewood, Colorado, 3rd edition, 2005.
162. P. Goodman and A. F. Moodie. Numerical evaluation of N-beam wave functions in electron scattering by the multislice method. *Acta Cryst.*, A30:280–290, 1974.
163. I. S. Gradshteyn and I. M. Ryzhik. *Table of Integrals, Series, and Products*. Academic Press, San Diego, 5th edition, 1994.
164. M. De Graf. *Intro. to Conventional Transmission Electron Microscopy*. Cambridge Univ. Press, Cambridge, UK, 2003.
165. I. P. Grant. Relativistic self-consistent fields. *Proc. Royal Society A*, 262:555–576, 1961.
166. I. P. Grant. Relativistic calculation of atomic structures. *Advances in Physics*, 19:747–811, 1970.
167. I. P. Grant, B. J. McKenzie, P. H. Norrington, D. F. Mayers, and N. C. Pyper. An atomic multiconfigurational Dirac-Fock package. *Computer Physics Communications*, 21:207–231, 1980.
168. M. A. Gribelyuk. Structure retrieval in HREM. *Acta Cryst.*, A47:715–723, 1991.
169. Nikolaus Grigorieff. FREALIGN: High-resolution refinement of single particle structure. *J. Structural Biology*, 157:117–125, 2007.
170. V. Grillo, E. Carlino, and F. Glas. Influence of the static atomic displacement on atomic resolution Z-contrast imaging. *Phys. Rev. B*, 77:054103, 2008.
171. V. Grillo and F. Rossi. STEM_CELL: a software tool for electron microscopy: Part ii analysis of crystalline materials. *Ultramicroscopy*, 125:112–129, 2013.
172. V. Grillo and E. Rotunno. STEM_CELL: a software tool for electron microscopy: Part i simulations. *Ultramicroscopy*, 125:97–111, 2013.
173. G. R. Grinton and J. M. Cowley. Phase and amplitude contrast in electron microscopy of biological materials. *Optik*, 34:221–233, 1971.
174. P. Grivet. *Electron Optics, Parts 1 and 2*. Pergamon, Oxford, 2nd English edition, 1972.
175. Bahadir K. Gunturk and Xin Li, editors. *Image Restoration, Fundamentals and Advances*. CRC Press, NY, 2013.
176. J. Haase. Berechnung der komplexen atomaren streufaktoren für schnelle elektronen unter verwendung von Hartree-Fock-atompotentialen. *Zeitschrift fur Naturforschung*, 23a:1000–1019, 1968.
177. J. Haase. Zusammenstellung der koefizienten für die anpassung komplexer atomarer streufaktoren für schnelle elektron durch polynome 1. mitteilung: Hartree-Fock fall. *Zeitschrift fur Naturforschung*, 25a:936–945, 1970.
178. J. Haase. Zusammenstellung der koefizienten für die anpassung komplexer atomarer streufaktoren für schnelle elektron durch polynome 2. mitteilung: Thomas-Fermi-Dirac-fall. *Zeitschrift fur Naturforschung*, 25a:1219–1235, 1970.
179. F. Haguenau, P. W. Hawkes, J. L. Hutchison, B. Satiat-Jeunemaître, and G. T. Simon. Key events in the history of electron microscopy. *Micros. and Microanal.*, 9:96–138, 2003.
180. M. Haider, A. Epstein, P. Jarron, and C. Boulin. A versatile, software configurable multichannel STEM detector for angle-resolved imaging. *Ultramicroscopy*, 54:41–59, 1994.
181. M. Haider, P. Hartel, H. Müller, S. Uhlemann, and J. Zach. Current and future aberration correctors for the improvement of resolution in electron microscopy. *Phil. Trans. R. Soc. A*, 367:3665–3682, 2009.
182. M. Haider, S. Uhlemann, and J. Zach. Upper limits for the residual aberrations of a high-resolution aberration-corrected STEM. *Ultramicroscopy*, 81:163–175, 2000.
183. H. Haken and H. C. Wolf. *Atomic and Quantum Physics*. Springer-Verlag, Berlin, 1984.
184. C. E. Hall. *Introduction to Electron Microscopy*. McGraw-Hill, New York, 2nd edition, 1966.
185. C. R. Hall and P. B. Hirsch. Effect of thermal diffuse scattering on propagation of high energy electrons through crystals. *Proc. Roy. Soc. London*, A286:158–177, 1965.
186. E. L. Hall. *Computer Image Processing and Recognition*. Academic Press, New York, 1979.
187. T. Hanai, H. Yoshida, and M. Hibino. Characteristics and effectiveness of a foil lens for correction of spherical aberration in scanning transmission electron microscopy. *J. Elect. Microsc.*, 47:185–192, 1998.

188. K.-J. Hanszen. The optical transfer theory of the electron microscope: fundamental principles and applications. In R. Barer and V. E. Cosslett, editors, *Adv. in Optical and Electron Microscopy*, Vol. 4, pages 1–84. Academic Press, New York, 1971.
189. K.-J. Hanszen and L.Trepte. Die kontrastübertragung im elektronenmikroskop bei partiell koharenter beleuchtung. *Optik*, 33:166–198, 1971.
190. D. R. Hartree. *The Calculation of Atomic Structure*. John Wiley and Sons, New York, 1957.
191. A. Hashimoto, M. Shimojo, K. Mitsuishi, and Masaki Takeguchi. Three-dimensional optical sectioning by scanning confocal electron microscopy with stage-scanning system. *Micros. and Microanal.*, 16:233–238, 2010.
192. P. W. Hawkes, editor. *The Beginnings of Electron Microscopy*. Adv. in Electronics and Electron Physics, Suppl. 16. Academic Press, London, 1985.
193. P. W. Hawkes, editor. *Aberration-corrected Electron Microscopy*. Adv. in Imaging and Electron Physics, Vol. 153. Academic Press, Amsterdam, 2008.
194. P. W. Hawkes. Aberration correction past and present. *Phil. Trans. Roy. Soc. A*, 367:3637–3664, 2009.
195. P. W. Hawkes. The correction of electron lens aberrations. *Ultramicroscopy*, 156:A1–A64, 2015.
196. P. W. Hawkes and E. Kasper. *Principles of Electron Optics*, volume 1. Academic Press, San Diego, 1989. Basic Geometrical Optics.
197. P. W. Hawkes and E. Kasper. *Principles of Electron Optics*, volume 2. Academic Press, San Diego, 1989. Applied Geometrical Optics.
198. P. W. Hawkes and E. Kasper. *Principles of Electron Optics*, volume 3. Academic Press, San Diego, 1994. Wave Optics.
199. E. Hecht. *Optics*. Addison-Wesley, San Francisco, 4th edition, 2002.
200. R. Hegerl and A. Altbauer. The EM program system. *Ultramicroscopy*, 9:109–116, 1982.
201. Reiner Hegerl. The EM program package: A platform for image processing in biological electron microscopy. *J. Structural Biology*, 116:30–34, 1996.
202. R. D. Heidenreich. *Fundamentals of Transmission Electron Microscopy*. Wiley, New York, 1964.
203. F. Herman and S. Skillman. *Atomic Structure Calculations*. Prentice-Hall, Englewood Cliffs, NJ, 1963.
204. K.-H. Herrmann. The present state of instrumentation in high-resolution electron microscopy. *J. Phys. E: Sci. Instrum.*, 11:1076–1091, 1978.
205. K.-H. Herrmann. Instrumentational requirements for high resolution imaging. *J. of Microscopy*, 131:67–78, 1983.
206. S. C. Hiller, E. T. Robertson, G. D. Reid, R. D. Haynes, and M. D. Robertson. On the role of the second-order derivative term in the calculation of convergent beam diffraction patterns. *Ultramicroscopy*, 179:73–80, 2017.
207. S. Hillyard and J. Silcox. Detector geometry, thermal diffuse scattering and strain effects in ADF-STEM imaging. *Ultramicroscopy*, 58:6–17, 1995.
208. P. Hirsch, A. Howie, R. B. Nicholson, D. W. Pashley, and M. J. Whelan. *Electron Microscopy of Thin Crystals*. Krieger, Huntington, New York, second edition, 1977.
209. Michael Hohn, Grant Tang, Grant Goodyear, P. R. Baldwin, Zhong Huang, Pawel A. Penczek, Chao Yang, Robert M. Glaeser, Paul D. Adams, and Steven J. Ludtke. SPARX, a new environment for cryo-EM image processing. *J. Structural Biology*, 157:47–55, 2007.
210. W. Hoppe. Prin. of electron structure research at atomic resolution using conventional electron microscopes for the measurement of amplitudes and phases. *Acta Cryst.*, A26:414–426, 1970.
211. S. Horiuchi. *Fundamentals of High Resolution Transmission Electron Microscopy*. North-Holland, Amsterdam, 1994.
212. F. Hosakawa, T. Shinkawa, Y. Arai, and T. Sannomiya. Benchmark test of accelerated multi-slice simulation by GPGPU. *Ultramicroscopy*, 158:56–64, 2015.
213. R. Hovden, H. L. Xin, and D. A. Muller. Channeling of a subangstrom electron beam in a crystal mapped to two-dimensional molecular orbitals. *Phys. Rev. B*, 86:195415, 2012.

214. Robert Hovden, Marcus D. Hanwell, Utkarsh Ayachit, Yi Jiang, Robert Maynard, and David Muller. Repeatable and transferable processing for electron tomography: An open platform for visualization and reconstruction of 3D materials. *Microsc. Microanal.*, 21 suppl. 3:2407–2408, 2015.
215. P. Hovington, D. Drouin, and R. Gauvin. CASINO: A new Monte Carlo code in C language for electron beam interaction—part I: Description of the program. *Scanning*, 19:1–14, 1997.
216. P. Hovington, D. Drouin, R. Gauvin, D. C. Joy, and N. Evans. CASINO: A new Monte Carlo code in C language for electron beam interaction—part III: Stopping power at low energies. *Scanning*, 19:29–35, 1997.
217. Sven Hovmöller. CRISP: Crystallographic image processing on a personal computer. *Ultramicroscopy*, 41:121–135, 1992. www.calidris-em.com.
218. A. Howie and Z. S. Basinski. Approx. of the dynamical theory of diffraction contrast. *Phil. Mag.*, 17:1039–1063, 1968.
219. A. Howie and M. J. Whelan. Diffraction contrast of electron microscope images of crystal lattice defects, II. the development of a dynamical theory. *Proc. Royal Society of London*, A263:217–237, 1961.
220. C. J. Humphreys. The scattering of fast electrons by crystals. *Rep. Prog. Phys.*, 42:1825–1887, 1979.
221. J. L. Hutchison and W. G. Waddington. Atomic images of silicon? *Ultramicroscopy*, 25:93–96, 1988.
222. M. J. Hýtch and W. M. Stobbs. Quantitative comparison of high resolution TEM images with image simulation. *Ultramicroscopy*, 53:191–203, 1994.
223. J. A. Ibers. Atomic scattering amplitudes for electrons. *Acta Cryst.*, 11:178–183, 1958.
224. J. A. Ibers and B. K. Vainshtein. Section 3.3.3. In C. H. MacGillavry, G. D. Rieck, and K. Lonsdale, editors, *International Tables for X-Ray Crystallography*, Vol. III, pages 216–227. Kynoch Press, Birmingham, 1962.
225. Adobe Systems Inc. *Postscript Language Reference Manual*. Addison-Wesley, Reading, Mass., 2nd edition, 1990.
226. Varat Intaraprasornk, Huolin L. Xin, and David A. Muller. Analytic derivation of optimal imaging conditions for incoherent imaging in aberration-corrected electron microscopes. *Ultramicroscopy*, 108:1454–1466, 2008.
227. M. S. Isaacson, J. Langmore, N. W. Parker, D. Kopf, and M. Utlaut. The study of the adsorption and diffusion of heavy atoms on light element substrates by means of the atomic resolution STEM. *Ultramicroscopy*, 1:359–376, 1976.
228. R. Ishikawa, E. Okunishi, H. Sawada, Y. Kondo, F. Hosokawa, and E. Abe. Direct imaging of hydrogen-atom columns in a crystal by annular bright-field electron microscopy. *Nature Mat.*, 10:278–281, 2011.
229. Ryo Ishikawa, Andrew R. Lupini, Scott D. Findlay, and Stephen J. Pennycook. Quantitative annular dark field electron microscopy using electron signals. *Microscopy and Microanalysis*, 20:99–110, 2014.
230. K. Ishizuka. Contrast transfer of crystal images in TEM. *Ultramicroscopy*, 5:55–65, 1980.
231. K. Ishizuka. Multislice formula for inclined illumination. *Acta Cryst.*, A38:773–779, 1982.
232. K. Ishizuka. Coma-free alignment of a high-resolution electron microscope with three-fold astigmatism. *Ultramicroscopy*, 55:407–418, 1994.
233. K. Ishizuka. A practical approach for STEM image simulation based on the FFT multislice method. *Ultramicroscopy*, 90:71–83, 2002.
234. K. Ishizuka. FFT multislice method - the silver anniversary. *Microsc. and Microanalysis*, 10:34–40, 2004.
235. K. Ishizuka, 2006. www.hremresearch.com.
236. K. Ishizuka and N. Uyeda. A new theoretical and practical approach to the multislice method. *Acta Cryst.*, A33:740–749, 1977.
237. K. Izui, S. Furuno, and H. Otsu. Observations of crystal structure images of silicon. *Jap. J. Elect. Microsc.*, 26:129–132, 1977.

238. R. Jagannathan. Quantum theory of electron lenses based on the Dirac equation. *Phys. Rev. A*, 42:6674–6689, 1990.
239. R. Jagannathan, R. Simon, E. C. G. Sudarshan, and N. Mukunda. Quantum theory of magnetic electron lenses based on the Dirac equation. *Physics Letters A*, 134:457–464, 1989.
240. B. Jähne. *Digital Image Processing*. Springer, Berlin, 3rd edition, 1995.
241. A. K. Jain. *Fundamentals of Digital Image Processing*. Prentice Hall, Englewood Cliffs, NJ, 1989.
242. R. W. James and G. W. Brindley. Some numerical calculations of atomic scattering factors. *Phil. Mag.*, 12:81–112, 1931.
243. B. K. Jap and R. M. Glaeser. The scattering of high-energy electrons. I. Feynman path-integral formulation. *Acta Cryst.*, A34:94–102, 1978.
244. D. E. Jesson and S. J. Pennycook. Incoherent imaging of thin specimens using coherent scattered electrons. *Proc. R. Soc. Lond. A*, 441:261–281, 1993.
245. D. E. Jesson and S. J. Pennycook. Incoherent imaging of crystals using thermally scattered electrons. *Proc. R. Soc. Lond. A*, 449:273–293, 1995.
246. C.-L. Jia, M. Lentzen, and K. Urban. High-resolution transmission electron microscopy using negative spherical aberration. *Microsc. and Microanalysis*, 10:174–184, 2004.
247. Yi Jiang, Zhen Chen, Yimo Han, Pratiti Deb, Hui Gao, Saien Xie, Prafull Purohit, Mark W. Tate, Jiwoong Park, Sol M. Gruner, Veit Elser, and David A Muller. Electron ptychography of 2D materials to deep sub-ångstrom resolution. *Nature*, 559:343–349, 2018.
248. Jmol. Jmol: an open-source java viewer for chemical structure in 3d, 2008. www.jmol.org.
249. Lewys Jones and Peter D. Nellist. Testing the accuracy of the two-dimensional object model in HAADF-STEM. *Micron*, 63:47–51, 2014.
250. David C. Joy. *Monte Carlo Modeling for Electron Microscopy and Analysis*. Oxford Univ. Press, New York, 1995.
251. Nicholas H. Julian, Tian T. Li, Robert E. Rudd, and Jaime Martian. MS-STEM-FEM: A parallelized multi-slice fluctuation TEM simulation tool. *Ultramicroscopy*, 194:117–125, 2018.
252. K. Kambe, G. Lehmpfuhl, and F. Fujimoto. Interpretation of electron channeling by the dynamical theory of electron diffraction. *Z. Naturforsch.*, 29 a:1034–1044, 1974.
253. T. Kaneko, A. Saitow, T. Fujino, E. Okunishi, and H. Sawada. Development of a high-efficiency DF-STEM detector. *J. Phys: Conference Series*, 522:012050, 2014.
254. Kibum Kang, Saien Xie, Lujie Huang, Yimo Han, Pinshane Y. Huang, Kin Fai Mak, Cheol-Joo Kim, David Muller, and Jiwoong Park. High-mobility three-atom-thick semiconducting films with wafer-scale homogeneity. *Nature*, 520:656–660, 2015.
255. R. J. Keyse, A. J. Garratt-Reed, P. J. Goodhew, and G. W. Lorimer. *Intro. to Scanning Transmission Electron Microscopy*. Springer-Verlag, New York, 1998.
256. R. Kilaas. Interactive simulation of high-resolution electron micrographs. In G. W. Bailey, editor, *Proceedings of the 45th Annual Meeting of the Microscopy Society of America*, pages 66–69. San Francisco Press, 1987.
257. R. Kilaas, 2006. www.totalresolution.com/index.html.
258. R. Kilaas and R. Gronsky. Real space image simulation in high resolution electron microscopy. *Ultramicroscopy*, 11:289–298, 1983.
259. R. Kilaas, L. D. Marks, and C. S. Own. EDM 1.0: Electron direct methods. *Ultramicroscopy*, 102:233–237, 2005.
260. R. Kilaas, M. A. O’Keefe, and K. M. Krishman. On the inclusion of upper Laue layers in computational methods in high resolution transmission electron microscopy. *Ultramicroscopy*, 21:47–62, 1987.
261. Dari Kimanius, Björn O. Forsberg, Sjors H. W. Scheres, and Erik Lindahl. Accelerated cryo-EM structure determination with parallelisation using GPUs in RELION-2. *eLife*, 5:e18722, 2016.
262. W. E. King and G. H. Campbell. Quantitative HREM using non-linear least-squares methods. *Ultramicroscopy*, 56:46–53, 1994.

263. A. I. Kirkland and R. R. Meyer. Indirect high-resolution transmission electron microscopy: Aberration measurement and wavefunction reconstruction. *Microscopy ad Microanalysis*, 10:401–413, 2004.
264. A. I. Kirkland, P. D. Nellist, Lan-Yun Chang, and S. J. Haigh. Aberration-corrected imaging in conventional transmission electron microscopy and scanning transmission electron microscopy. In P. W. Hawkes, editor, *Aberration-corrected Electron Microscopy*, volume 153 of *Adv. in Imaging and Electron Physics*, pages 283–325. Academic Press, Amsterdam, 2008.
265. A. I. Kirkland, W. O. Saxton, K.-L. Chau, K. Tsuno, and M. Kawasaki. Super-resolution by aperture synthesis: tilt series reconstruction in CTEM. *Ultramicroscopy*, 57:355–374, 1995.
266. E. J. Kirkland. Nonlinear high resolution image processing of conventional transmission electron micrographs, I. theory. *Ultramicroscopy*, 9:45–64, 1982.
267. E. J. Kirkland. Improved high resolution image processing of bright field electron micrographs I. theory. *Ultramicroscopy*, 15:151–172, 1984.
268. E. J. Kirkland. Viewing molecules with the Macintosh. *Byte Magazine*, Feb.:251–259, 1985.
269. E. J. Kirkland. Digital restoration of ADF-STEM images. In G. W. Bailey, editor, *Proceedings of the 46th Annual Meeting of the Electron Microscopy Society of America*, pages 832–833. San Francisco Press, 1988.
270. E. J. Kirkland. High resolution image processing of electron micrographs. In P. W. Hawkes, F. P. Ottensmeyer, W. O. Saxton, and A. Rosenfeld, editors, *Image and Signal Processing in Electron Microscopy, Scanning Microscopy, Supplement 2*, pages 139–147, Chicago, 1988. Scanning Microscopy Intern.
271. E. J. Kirkland. An image and spectrum acquisition system for a VG HB501 STEM using a color graphics workstation. *Ultramicroscopy*, 32:349–364, 1990.
272. E. J. Kirkland. Z-contrast in a conventional TEM. In G. W. Bailey, R. V. W. Dimlich, K. B. Alexander, J. J. McCarthy, and T. P. Pretlow, editors, *Proceedings Microscopy and Microanalysis 1997*, pages 1147–1148, New York, 1997. Springer.
273. E. J. Kirkland. *Advanced Computing in Electron Microscopy*. Plenum, New York, 1998.
274. E. J. Kirkland. Some effects of electron channeling on electron energy loss spectroscopy. *Ultramicroscopy*, 102:199–207, 2005.
275. E. J. Kirkland. On the optimum probe in aberration corrected ADF-STEM. *Ultramicroscopy*, 111:1523–1530, 2011.
276. E. J. Kirkland, 2013. www.sourceforge.com/computem.
277. E. J. Kirkland. Computation in electron microscopy. *Acta Cryst. A*, 72:1–27, 2016.
278. E. J. Kirkland. Fine tuning an aberration corrected ADF-STEM. *Ultramicroscopy*, 186:62–65, 2018.
279. E. J. Kirkland, R. F. Loane, and J. Silcox. Simulation of annular dark field STEM images using a modified multislice method. *Ultramicroscopy*, 23:77–96, 1987.
280. E. J. Kirkland, R. F. Loane, P. Xu, and J. Silcox. Multislice simulation of ADF-STEM and CBED images. In W. Krakow and M. O’Keefe, editors, *Computer Simulation of Electron Microscope Diffraction and Images*, pages 13–31, Warrendale, Penn., 1989. The Minerals, Metals and Materials Society.
281. E. J. Kirkland and B. M. Siegel. Linear image processing and anomalous scattering. *Ultramicroscopy*, 6:169–180, 1981.
282. E. J. Kirkland, B. M. Siegel, N. Uyeda, and Y. Fujiyoshi. Digital reconstruction of bright field phase contrast images from high resolution electron micrographs. *Ultramicroscopy*, 5:479–503, 1980.
283. E. J. Kirkland, B. M. Siegel, N. Uyeda, and Y. Fujiyoshi. Nonlinear high resolution image processing of conventional transmission electron micrographs, II. experiment. *Ultramicroscopy*, 9:65–74, 1982.
284. E. J. Kirkland, B. M. Siegel, N. Uyeda, and Y. Fujiyoshi. Improved high resolution image processing of bright field electron micrographs II. experiment. *Ultramicroscopy*, 17:87–104, 1985.
285. E. J. Kirkland and M. G. Thomas. A high efficiency annular dark field detector for STEM. *Ultramicroscopy*, 62:79–88, 1996.

286. C. Kittel. *Intro. to Solid State Physics*. Wiley, New York, 7th edition, 1996.
287. O. Klemperer and M. E. Barnett. *Electron Optics*. Cambridge Univ. Press, Cambridge, Great Britain, third edition, 1971.
288. D. O. Klenov, S. D. Findlay, L. J. Allen, and S. Stemmer. Influence of orientation on the contrast of high-angle annular dark-field images of silicon. *Phys. Rev. B*, 76:014111, 2007.
289. M. Knoll and E. Ruska. Das elektronenmikroskop. *Z. fur Physik*, 78:318–339, 1932.
290. C. Koch, 2015. elim.physik.uni-ulm.de.
291. H. Koops. Aberration correction in electron microscopy. In J. M. Sturgess, editor, *Proceedings of the Ninth International Congress on Electron Microscopy*, volume 3, pages 185–196, Ontario, Canada, 1978. Imperial Press.
292. D. Kosloff and R. Kosloff. A Fourier method solution for the time dependent Schrodinger equation as a tool in molecular dynamics. *J. Comp. Phys.*, 52:35–53, 1983.
293. R. Kosloff. Time-dependent quantum-mechanical methods for molecular dynamics. *J. Phys. Chem.*, 92:2087–2100, 1988.
294. L. Fitting Kourkoutis, J. M. Plitzko, and W. Baumeister. Electron microscopy of biological materials at the nanometer scale. *Annu. Rev. Mater. Res.*, 42:33–58, 2012.
295. Florian F. Krause, Knut Müller, Dennis Zillmann, Jacob Jansen, and Marco Schowalter. Comparison of intensity and absolute contrast of simulated and experimental high-resolution transmission electron microscopy images for different multislice simulation methods. *Ultramicroscopy*, 134:94–101, 2013.
296. N. G. Krishna and D. B. Sirdeshmukh. Compilation of temperature factors of hexagonal close packed elements. *Acta Cryst.*, A54:513–514, 1998.
297. O. L. Krivanek. A method for determining the coefficient of spherical aberration from a single electron micrograph. *Optik*, 45:97–101, 1976.
298. O. L. Krivanek. Three fold astigmatism in high resolution transmission electron microscopy. *Ultramicroscopy*, 55:419–433, 1994.
299. O. L. Krivanek, G. J. Corbin, N. Dellby, B. F. Elson, R. J. Keyse, M. F. Murfit, C. S. Own, Z. S. Szilagi, and J. W. Woodruff. An electron microscope for the aberration-corrected era. *Ultramicroscopy*, 108:179–195, 2008.
300. O.L. Krivanek, N. Dellby, and A.R. Lupini. Towards sub-Å electron beams. *Ultramicroscopy*, 78:1–11, 1999.
301. Ondrej L. Krivanek, Niklas Dellby, and Matthew F. Murfit. Aberration correction in electron microscopy. In J. Orloff, editor, *Handbook of Charged Particle Optics*, 2nd edit., pages 601–640. CRC Press, Taylor and Francis, Boca Raton, 2009.
302. W. Kunath, F. Zemlin, and K. Weiss. Apodization in phase-contrast electron microscopy realized with hollow-cone illumination. *Ultramicroscopy*, 16:123–138, 1985.
303. J. P. Langmore. Electron microscopy of atoms. In M. A. Hayat, editor, *Princ. and Tech. of Electron Microscopy (Biol. App.)*, Vol. 9, pages 1–63. Van Nostrand, New York, 1978.
304. J. M. LeBeau, A. J. D’Alfonso, S. D. Findlay, S. Stemmer, and L. J. Allen. Quantitative comparisons of contrast in experimental and simulated bright-field scanning transmission electron microscopy images. *Phys. Rev. B*, 80:174106, 2009.
305. J. M. LeBeau, S. D. Findlay, L. J. Allen, and S. Stemmer. Quantitative atomic resolution scanning transmission electron microscopy. *Phys. Rev. Lett.*, 100:206101, 2008.
306. J. M. LeBeau, S. D. Findlay, X. Wang, A. J. Jacobson, L. J. Allen, and S. Stemmer. High-angle scattering of fast electrons from crystal containing heavy element: Simulation and experiment. *Phys. Rev. B*, 79:214110, 2009.
307. J. M. LeBeau and S. Stemmer. Experimental quantification of annular dark-field images in scanning transmission electron microscopy. *Ultramicroscopy*, 108:1653–1658, 2008.
308. M. Lentzen. Contrast transfer and resolution limits for sub-angstrom high-resolution transmission electron microscopy. *Micros. and Microanal.*, 14:16–26, 2008.
309. F. A. Lenz. Transfer of image information in the electron microscope. In U. Valdre, editor, *Electron Microscopy in Materials Science*, pages 541–569. Academic Press, New York, 1971.

310. Barnaby D. A. Levin, Yi Jiang, Elliot Padgett, Shawn Waldon, Cory Quammen, Chris Harris, Utkarsh Ayachit, Marcus Hanwell, Peter Ercius, David Muller, and Robert Hovden. Tutorial on the visualization of volumetric data using *tomviz*. *Microscopy Today*, January:12–16, 2018.
311. A. L. Lewis, R. B. Hammond, and R. E. Villagrana. The importance of second-order partial derivatives in the theory of high-energy-electron diffraction from imperfect crystals. *Acta Cryst.*, A31:221–227, 1975.
312. Ming-Yang Li, Yumeng Shi, Chia-Chin Cheng, Li-Syuan Lu, Yung-Chang Lin, Hao-Lin Tang, Meng-Li Tsai, Chih-Wei Chu, Kung-Hwa Wei, Jr-Hau He, Wen-Hao Chang, Kazu Suenaga, and Lain-Jong Li. Epitaxial growth of a monolayer WSe₂-MoS₂ lateral p-n junction with an atomically sharp interface. *Science*, 349:524–528, 2015.
313. Xinxing Li, Li Tao, Zefeng Chen, Hui Fang, Xuesong Li, Xinran Wang, Jian-Bin Xu, and Hongwei Zhu. Graphene and related two-dimensional materials: Structure-property relationships for electronics and optoelectronics. *Applied Physics Reviews*, 4:021306, 2017.
314. Hannes Lichte. Electron holography approaching atomic resolution. *Ultramicroscopy*, 20:293–304, 1986.
315. R. F. Loane and J. Silcox. Hollow-cone illumination in simulated ADF STEM. In G. W. Bailey, editor, *Proceedings of the 47th Annual Meeting of the Microscopy Society of America*, pages 124–125. San Francisco Press, 1989.
316. R. F. Loane, P. Xu, and J. Silcox. Thermal vibrations in convergent-beam electron diffraction. *Acta Cryst.*, A47:267–278, 1991.
317. R. F. Loane, P. Xu, and J. Silcox. Incoherent imaging of zone axis crystals with ADF STEM. *Ultramicroscopy*, 40:121–138, 1992.
318. I. Lobato and D. van Dyck. An accurate parameterization for scattering factors, electron densities and electrostatic potentials for neutral atoms that obey all physical constraints. *Acta Cryst.*, A70:636–649, 2014.
319. I. Lobato and D. van Dyck. MULTEM: a new multislice program to perform accurate and fast electron diffraction and imaging simulations using graphics processing unit with CUDA. *Ultramicroscopy*, 156:9–17, 2015.
320. L. B. Lucy. An iterative technique for the rectification of observed distributions. *The Astronomical Journal*, 79:745–754, 1974.
321. S. J. Ludtke, P. R. Baldwin, and W. Chiu. EMAN: Semiautomated software for high-resolution single-particle reconstructions. *J. Structural Biology*, 128:82–97, 1999.
322. A. R. Lupini, A. Y. Borisevich, J. C. Idrobo, H. M. Christen, M. Biegalski, and S. J. Pennycook. Characterizing the two- and three-dimensional resolution of an improved aberration-corrected STEM. *Microsc. and Microanal.*, 15:441–453, 2009.
323. Andrew R. Lupini. The electron Ronchigram. In Stephen J. Pennycook and Peter D. Nellist, editors, *Scanning Transmission Electron Microscopy, Imaging and Analysis*, pages 117–482. Springer, New York, 2011.
324. D. F. Lynch and A. F. Moodie. Numerical evaluation of low energy electron diffraction intensities I. the perfect crystal with no upper layer lines and no absorption. *Surface Science*, 32:422–438, 1972.
325. D. F. Lynch and M. A. O’Keefe. n-beam lattice images II. methods of calculation. *Acta Cryst.*, A28:536–548, 1972.
326. S. E. Maccagnano-Zacher, K. A. Mkhoyen, E. J. Kirkland, and J. Silcox. Effects of tilt on high-resolution ADF-STEM imaging. *Ultramicroscopy*, 108:718–726, 2008.
327. D. S. MacLagan, L. A. Bursill, and A. E. C. Spargo. Experimental and calculated images of planar defects at high resolution. *Phil. Mag.*, 35:757–780, 1977.
328. A. M. Maiden, M. J. Humphry, and J. M. Rodenbury. Ptychographic transmission microscopy in three dimensions using a multi-slice approach. *J. Opt. Soc. Am. A*, 29:1606–1614, 2012.
329. A. M. Maiden, M. J. Humphry, F. Zhang, and J. M. Rodenbury. Superresolution imaging via ptychography. *J. Opt. Soc. Am. A*, 28:604–612, 2011.
330. R. Marabini, I. M. Masegosa, M. C. San Martín, S. Marco, J. J. Fernández, L. G. de la Fraga, C. Vaquerizo, and J. M. Carazo. Xmipp: An image processing package for electron microscopy. *J. Structural Biology*, 116:237–240, 1996.

331. A. Maréchal. Étude des effects combinés de la diffraction et des aberrations géométriques sur l'image d'un point lumineux. *Rev. Opt.*, 26:257–277, 1947.
332. L. Marks and R. Kilass, 2006. www.numis.northwestern.edu/edm/documentation/edm.htm.
333. Richard M. Martin. *Electronic Structure, Basic Theory and Practice*. Cambridge Univ. Press, New York, 2004.
334. David N. Mastronarde. Automated electron microscope tomography using robust prediction of specimen movements. *J. Structural Biology*, 152:36–51, 2005.
335. H. Matsuhata, D. Van Dyck, J. Van Lanuyt, and S. Amelincx. A practical approach to the periodic continuation method for the simulation of high resolution TEM images of isolated crystal defects. *Ultramicroscopy*, 13:343–348, 1984.
336. D. McMullan. Scanning electron microscopy 1928–1965. *Scanning*, 17:175–185, 1995.
337. G. McMullan, A. T. Clark, R. Turchetta, and A. R. Faruqi. Enhanced imaging in low dose electron microscopy using electron counting. *Ultramicroscopy*, 109:1411–1416, 2009.
338. G. McMullan, A. R. Faruqi, D. Clare, and R. Henderson. Comparison of optimal performance at 300 keV of three direct electron detectors for use in low electron microscopy. *Ultramicroscopy*, 147:156–163, 2014.
339. R. McWeeny. X-ray scattering by aggregates of bonded atoms, I. analytical approximations in single atom scattering. *Acta Cryst.*, 4:513–519, 1951.
340. R. McWeeny. X-ray scattering by aggregates of bonded atoms, II. the effects of bonds with applications to H_2 . *Acta Cryst.*, 5:463–468, 1952.
341. G. A. Meek. *Practical Electron Microscopy for Biologists*. Wiley, London, second edition, 1976.
342. H. D. Megaw. *Crystal Structures: A Working Approach*. Saunders, Philadelphia, 1973.
343. J. C. Meyer, S. Kurasch, H. J. Park, V. Skakalova, D. Künzel, A. Groß, A. Chuvilin, G. Algara-Siller, S. Roth, T. Iwasaki, U. Starke, J. H. Smet, and U. Kaiser. Experimental analysis of charge redistribution due to chemical bonding by high-resolution transmission electron microscopy. *Nature Materials*, 10:209–215, 2011.
344. R. R. Meyer, A. I. Kirkland, and W. O. Saxton. A new method for the determination of the wave aberration function for high resolution TEM 1. measurement of the symmetric aberrations. *Ultramicroscopy*, 92:89–109, 2002.
345. R. R. Meyer, A. I. Kirkland, and W. O. Saxton. A new method for the determination of the wave aberration function for high resolution TEM 2. measurement of the antisymmetric aberrations. *Ultramicroscopy*, 99:115–123, 2004.
346. P. A. Midgley and M. Weyland. 3D electron microscopy in the physical sciences: the development of Z-contrast and EFTEM. *Ultramicroscopy*, 96:413–431, 2003.
347. W. Q. Ming and J. H. Chen. Validities of three multislice algorithms for quantitative low-energy transmission electron microscopy. *Ultramicroscopy*, 134:135–143, 2013.
348. D. L. Misell, G. W. Stroke, and M. Halioua. Coherent and incoherent imaging in the scanning transmission electron microscope. *J. Phys. D: Appl. Phys.*, 7:L113–L117, 1974.
349. D. L. Misell. *Image Analysis, Enhancement and Interpretation*, volume 7 of *Prac. Methods in Electron Microscopy*. North Holland, Amsterdam, 1978.
350. K. Mitsuishi, K. Iakoubovskii, M. Takeguchi, M. Shimojo, A. Hashimoto, and K. Furuya. Bloch wave-based calculations of imaging properties of high-resolution scanning confocal electron microscopy. *Ultramicroscopy*, 108:981–988, 2008.
351. K. Mitsuishi, M. Takeguchi, H. Yasuda, and K. Furuya. New scheme for calculation of annular dark-field STEM image including both elastically diffracted and TDS waves. *J. Electron Microscopy*, 50:157–162, 2001.
352. K. A. Mkhoyan, S. E. Maccagnano-Zacher, E. J. Kirkland, and J. Silcox. Effects of amorphous layers ADF-STEM imaging. *Ultramicroscopy*, 108:791–803, 2008.
353. G. Möbus. Retrieval of crystal defect structures from HRTEM images by simulated evolution I. basic technique. *Ultramicroscopy*, 65:205–216, 1996.
354. G. Möbus and G. Dehm. Retrieval of crystal defect structures from HRTEM images by simulated evolution II. experimental image evaluation. *Ultramicroscopy*, 65:217–228, 1996.

355. G. Möbus, T. Gemming, and P. Gumbsch. The influence of phonon scattering on HREM images. *Acta Cryst.*, A54:83–90, 1998.
356. G. Möbus and M. Rühle. Structure determination of metal-ceramic interfaces by numerical contrast evaluation of HRTEM micrographs. *Ultramicroscopy*, 56:54–70, 1994.
357. G. Möbus, R. Schweinfest, T. Gemming, T. Wagner, and M. Rühle. Iterative structure retrieval techniques in HREM: a comparative study and a modular program package. *J. Microscopy*, 190:109–130, 1998.
358. G. Moliere. Theorie der streuung schneller gelandener teilchen I. einzelstreuung am abgeschirmten coulomb-field. *Z. für Naturforsch*, 2A:133–145, 1947.
359. Koichi Momma and Fujio Izumi. VESTA 3 for three-dimensional visualization of crystal, volumetric and morphology data. *J. Applied Crystallography*, 44:1272–1276, 2011.
360. Gordon E. Moore. Cramming more components onto integrated circuits. *Proc. IEEE*, 86:82–85, 1998. reprinted from Electronics, April 19, 1965, p. 114–117.
361. M. A. Morrison, T. L. Estle, and N. F. Lane. *Quantum States of Atoms, Molecules, and Solids*. Prentice-Hall, Englewood Cliffs, New Jersey, 1976.
362. C. Mory, C. Colliex, and J. M. Cowley. Optimum defocus for STEM imaging and microanalysis. *Ultramicroscopy*, 21:171–178, 1987.
363. N. F. Mott. The scattering of electrons by atoms. *Proc. Royal Society*, A127:658–665, 1930.
364. N. F. Mott and H. S. W. Massey. *The Theory of Atomic Collisions*. Clarendon Press, Oxford, 3rd edition, 1965.
365. D. A. Muller, B. Edwards, E. J. Kirkland, and J. Silcox. Detailed calculations of thermal diffuse scattering. In G. W. Bailey, R. V. W. Dimlich, K. B. Alexander, J. J. McCarthy, and T. P. Pretlow, editors, *Proceedings Microscopy and Microanalysis 1997*, pages 1153–1154, New York, 1997. Springer.
366. T. Mulvey, editor. *The Growth of Electron Microscopy*, volume 96 of *Adv. in Imaging and Electron Physics*. Academic Press, San Diego, 1996.
367. J. D. Murray and W. vanRyper. *Encyclopedia of Graphics File Format*. O'Reilly and Assoc., Sebastopol, CA, 2nd edition, 1996.
368. P. D. Nellist and S. J. Pennycook. Incoherent imaging using dynamically scattered coherent electrons. *Ultramicroscopy*, 78:111–124, 1999.
369. P. D. Nellist and S. J. Pennycook. The principles and interpretation of annular dark-field Z-contrast imaging. In P. W. Hawkes, editor, *Adv. in Imaging and Electron Physics*, vol. 113, pages 147–203. Academic Press, San Diego, 2000.
370. P. D. Nellist and J. M. Rodenburg. Electron ptychography. I. experimental demonstration beyond the conventional resolution limits. *Acta Cryst.*, A54:49–6, 1998.
371. P.D. Nellist, E.C. Cosgriff, G. Behan, and A.I. Kirkland. Imaging modes for scanning confocal electron microscopy in a double aberration-corrected transmission electron microscope. *Microsc. and Microanal.*, 14:82–88, 2008.
372. W. M. Newman and R. F. Sproull. *Princ. of Interactive Computer Graphics*. McGraw-Hill, New York, 2nd edition, 1979.
373. H. Niehrs and E. H. Wagner. Die amplituden der wellenfelder bei elektroneninterferenzen im Laue-fall. *Z. Physik*, 143:285–299, 1955.
374. Eva Nogales. The development of cryo-EM into a mainstream structural biology technique. *Nature Methods*, 13:24–27, 2016.
375. C. W. Oatley, D. McMullan, and K. C. A. Smith. The development of the scanning electron microscope. In L. Marton and C. Marton, editors, *Advances in Electronics and Electron Physics*, Suppl. 16, pages 443–482. Academic Press, New York, 1985.
376. Jan Oliver Oelerich, Lennart Duschek, Jürgen Belz, Andreas Beyer, Sergei D. Baranovskii, and Kerstin Volz. STEMsalabim: A high-performance computing cluster friendly code for scanning transmission electron microscopy image simulations of thin specimens. *Ultramicroscopy*, 177:91–96, 2017.
377. M. A. O'Keefe. Resolution-damping functions in non-linear imaging. In G. W. Bailey, editor, *Proceedings of the 37st Annual Meeting of the Electron Microscopy Society of America*, pages 556–557, Baton Rouge, 1979. Claitor's Publishing.

378. M. A. O'Keefe. Advances in image simulation for high resolution TEM. In G. W. Bailey, M. H. Ellisman, R. A. Hennigar, and N. J. Zaluzec, editors, *Proc. Micros. and Microanal.* 1995, pages 38–39, New York, 1995. Jones and Begell.
379. M. A. O'Keefe and P. R. Buseck. Computation of high resolution TEM images of materials. *Trans. American Crystallography Assoc.*, 15:27–46, 1979.
380. M. A. O'Keefe, P. R. Buseck, and S. Iijima. Computed crystal structure images for high resolution electron microscopy. *Nature*, 274:322–324, 1978.
381. M. A. O'Keefe and R. Kilaas. Advances in high-resolution image simulation. In P. W. Hawkes, F. P. Ottensmeyer, W. O. Saxton, and A. Rosenfeld, editors, *Image and Signal Processing in Electron Microscopy, Scanning Microscopy, Supplement 2*, pages 225–244, Chicago, 1988. Scanning Microscopy Intern.
382. M. A. O'Keefe and J. V. Sanders. n-beam lattice images. VI. degradation of image resolution by a combination of incident-beam divergence and spherical aberration. *Acta Cryst.*, A31:307–310, 1975.
383. M. A. O'Keefe, J. Taylor, D. Owen, K. H. Westmacott, W. Johnston, and U. Dahmen. Remote on-line control of a high-voltage in situ transmission electron microscope with a rational user interface. In G. W. Bailey, J. M. Corbett, R. V. W. Dimlich, J. R. Michael, and N. J. Zaluzec, editors, *Proceedings of the 54th Annual Meeting of the Microscopy Society of America*, pages 384–385. San Francisco Press, 1996.
384. L. C. Oldfield. Computer design of high frequency electron-optical systems. In P. W. Hawkes, editor, *Image Processing and Computer-Aided Design in Electron Optics*, pages 370–399. Academic Press, London, 1973.
385. N. L. O'Leary and L. J. Allen. Quantitative structure retrieval at atomic resolution. *Acta Cryst.*, A61:252–259, 2005.
386. Edward L. O'Neil. *Intro. Statistical Optics*. Addison-Wesley (Dover reprinted 1992), Reading, Mass., 1963.
387. Colin Ophus. A fast image simulation algorithm for scanning transmission electron microscopy. *Advanced Structural and Chemical Imaging*, 3:13, 2017.
388. Colin Ophus. Four-dimensional scanning transmission electron microscopy (4D-STEM): From scanning nanodiffraction to ptychography and beyond. *Microscopy and Microanalysis*, 25:563–582, 2019.
389. Colin Ophus and Timo Ewalds. Guidelines for quantitative reconstruction of complex exit waves in HRTEM. *Ultramicroscopy*, 113:88–95, 2012.
390. J. Orloff, editor. *Handbook of Charged Particle Optics*, 2nd edit. CRC Press, Taylor and Francis, Boca Raton, 2009.
391. M. T. Otten and W. M. J. Coene. High resolution imaging on a field emission TEM. *Ultramicroscopy*, 48:77–91, 1993.
392. A. Ourmazd, F. H. Baumann, M. Bode, and Y. Kim. Quantitative chemical lattice matching: Theory and practice. *Ultramicroscopy*, 34:237–255, 1990.
393. M. Pan, P. Rez, and J. M. Cowley. A new method of computing the phase-grating function in multislice calculation. In G. W. Bailey, editor, *Proceedings of the 47th Annual Meeting of the Microscopy Society of America*, pages 478–479. San Francisco Press, 1989.
394. L. M. Peng and J. M. Cowley. Errors arising from numerical use of the Mott formula in electron image simulation. *Acta Cryst.*, A44:1–5, 1988.
395. L. M. Peng, G. Ren, S. L. Dudarev, and M. J. Whelan. Robust parameterization of elastic and absorptive electron atomic scattering factors. *Acta Cryst.*, A52:257–276, 1996.
396. S. J. Pennycook. Z-contrast STEM materials science. *Ultramicroscopy*, 30:58–69, 1989.
397. S. J. Pennycook. Z-contrast transmission electron microscopy: Direct atomic imaging of materials. *Ann. Rev. Mater. Sci.*, 22:171–195, 1992.
398. S. J. Pennycook and D. E. Jesson. High-resolution incoherent imaging of crystals. *Phys. Rev. Lett.*, 64:938–941, 1990.
399. S. J. Pennycook and D. E. Jesson. High resolution Z-contrast imaging of crystals. *Ultramicroscopy*, 37:14–38, 1991.

400. S. J. Pennycook and D. E. Jesson. Atomic resolution Z-contrast imaging of interfaces. *Acta Metall. Mater.*, 40:S149–S159, 1992.
401. Stephen J. Pennycook and Peter D. Nellist, editors. *Scanning Transmission Electron Microscopy, Imaging and Analysis*. Springer, NY, 2011.
402. A. Pidwerbetsky and R. V. E. Lovelace. Chaotic wave propagation in a random medium. *Physics Letters A*, 140:411–415, 1989.
403. T. Plamann and J. M. Rodenburg. Electron ptychography. II. theory of three-dimensional propagation effects. *Acta Cryst.*, A54:61–73, 1998.
404. A. P. Pogany and P. S. Turner. Reciprocity in electron diffraction and microscopy. *Acta Cryst.*, A24:103–109, 1968.
405. W. K. Pratt. *Digital Image Processing*. Wiley, New York, 1978.
406. W. H. Press, S. A. Teukolsky, W. T. Vetterling, and B. P. Flannery. *Numerical Recipes*. Cambridge University Press, Cambridge, 3rd edition, 2007.
407. A. Pryor Jr., Y. Yang, A. Rana, M. Gallagher-Jones, J. Zhou, Y. H. Lo, G. Melinte, W. Chiu, J. A. Rodriguez, and J. Miao. GENFIRE: A generalized Fourier iterative reconstruction algorithm for high-resolution 3D imaging. *Scientific Reports*, 7:10409, 2017.
408. H. Pulvermacher. Der transmissions-kreuz-koeffizient fur die elektronenmikroskopische abbildung bei partiell koharenter beleuchtung und elektischer instabilitat. *Optik*, 60:45–60, 1981.
409. M. J. Quinn. *Parallel Programming in C with MPI and openMP*. McGraw Hill, New York, 2004.
410. M. Radek, J.-G. Tenberge, S. Hilke, G. Wilde, and M. Peterlechner. STEMcl- a multi-GPU multislice algorithm for simulation of large structure and imaging parameter series. *Ultramicroscopy*, 188:24–30, 2018.
411. Lord Rayleigh. On the theory of optical images, with special reference to the microscope. *Phil. Mag.*, XLII-fifth series:167–195, 1896.
412. John S. Reid. Debye–Waller factors of zinc-blende-structure materials - a lattice dynamical comparison. *Acta Cryst.*, A39:1–13, 1983.
413. L. Reimer. *Scanning Electron Microscopy*, volume 45 of *Spring Series in Optical Sciences*. Springer-Verlag, New York, 1985.
414. L. Reimer. *Transmission Electron Microscopy*, volume 36 of *Spring Series in Optical Sciences*. Springer-Verlag, New York, third edition, 1993.
415. L. Reimer. *Energy-Filtering Transmission Electron Microscopy*, volume 71 of *Spring Series in Optical Sciences*. Springer-Verlag, New York, 1995.
416. L. Reimer and H. Gilde. Scattering theory and image formation in the electron microscope. In P. W. Hawkes, editor, *Image Processing and Computer-Aided Design in Electron Optics*, pages 138–167. Academic Press, London, 1973.
417. D. Rez and P. Rez. Dirac-Fock calculations of scattering factors and mean inner potentials for neutral and ionized atoms. In G. W. Bailey and C. L. Rieder, editors, *Proceedings of the 51st Annual Meeting of the Microscopy Society of America*, pages 1202–1203. San Francisco Press, 1993.
418. D. Rez, P. Rez, and I. Grant. Dirac-Fock calculations of X-ray scattering factors and contributions to the mean inner potential for electron scattering. *Acta Cryst.*, A50:481–497, 1994.
419. D. Rez, P. Rez, and I. Grant. Dirac-Fock calculations of X-ray scattering factors and contributions to the mean inner potential for electron scattering. erratum. *Acta Cryst.*, A53:522, 1997.
420. P. Rez, C. J. Humphreys, and M. J. Whelan. The distribution of intensity in electron diffraction patterns due to phonon scattering. *Phil. Mag.*, 35:81–96, 1977.
421. W. H. Richardson. Bayesian-based iterative method of image restoration. *J. Opt. Soc. Amer.*, 62:55–59, 1972.

422. M. D. Robertson, J. C. Bennett, M. M. J. Burns, and D. Currie. The simulation of annular dark field images of InAs/InP quantum dots. In P. Kotula, M. Marko, J.-H. Scott, R. Gauvin, D. Beniac, G. Lucas, S. McKernan, and J. Shields, editors, *Microscopy and Microanalysis 2006*, volume 12, suppl. 2, pages 714–715, Cambridge, UK, 2006. Cambridge Univ. Press.
423. J. M. Rodenburg and R. H. T. Bates. The theory of super-resolution electron microscopy via Wigner-distribution deconvolution. *Phil. Trans. Roy. Soc. Lond. A*, 339:521–553, 1992.
424. H. Rose. Nonstandard imaging methods in electron microscopy. *Ultramicroscopy*, 2:251–267, 1977.
425. H. Rose. Correction of aperture aberrations in magnetic systems with threefold symmetry. *Nuclear Instruments and Methods*, 187:187–199, 1981.
426. H. Rose. Outline of a spherically corrected semiaplanatic medium-voltage transmission electron microscope. *Optik*, 85:19–24, 1990.
427. H. Rose. History of direct aberration correction. In *Aberration-corrected Electron Microscopy*, volume 153 of *Adv. in Imaging and Electron Physics*, pages 3–39. Academic Press, Amsterdam, 2008.
428. H. H. Rose. Historical aspects of aberrations correction. *J. Elect. Microsc.*, 58:77–85, 2009.
429. Harald Rose. *Geometrical Charged-Particle Optics*. Springer, New York, second edition, 2012.
430. Axel Rother and Kurt Scheerschmidt. Relativistic effects in elastic scattering of electrons in TEM. *Ultramicroscopy*, 109:154–160, 2009.
431. H. Rullgård, L.-G. Öfverstedt, S. Masich, B. Daneholt, and O. Öktem. Simulation of transmission electron microscope images of biological specimens. *J. Microscopy*, 243:234–256, 2011.
432. E. Ruska. The development of the electron microscope and of electron microscopy. *Rev. Modern Physics*, 59:627–638, 1987.
433. Jason Sanders and Edward Kandrot. *CUDA by Example, An Intr. to General-Purpose GPU Programming*. Addison-Wesley, Boston, 2011.
434. H. Sawada, T. Sannomiya, F. Hosokawa, T. Nakamichi, T. Kaneyama, T. Tomita, Y. Kondo, T. Tanaka, Y. Oshima, Y. Tanishiro, and K. Takayanagi. Measurement method of aberration from ronchigram by autocorrelation function. *Ultramicroscopy*, 108:1467–1475, 2008.
435. H. Sawada, T. Sasaki, F. Hosokawa, S. Yuasa, M. Terao, M. Kawazoe, T. Nakamichi, T. Kaneyama, Y. Kondo, Koji Kimoto, and K. Suenaga. Correction of higher order geometrical aberration by triple 3-fold astigmatism field. *J. Elect. Microsc.*, 58:341–347, 2009.
436. W. O. Saxton. *Computer Techniques for Image Processing in Electron Microscopy*. Adv. in Electronics and Electron Physics, Supplement 10. Academic Press, New York, 1978.
437. W. O. Saxton. Semper: Distortion compensation, selective averaging, 3d reconstruction, and transfer function correction in a highly programmable system. *J. Structural Biology*, 116:230–236, 1996.
438. W. O. Saxton, T. J. Pitt, and M. Horner. Digital image processing: The SEMPER system. *Ultramicroscopy*, 4:343–354, 1979.
439. Roger Sayle. RasMol and OpenRasMol, 1999. rasmol.org.
440. Sjors H. W. Scheres. RELION: implementation of a Bayesian approach to cryo-EM structure determination. *J. Structural Biology*, 180:519–530, 2012.
441. O. Scherzer. Sphaerische und chromatische korrektur von elektronenlinsen. *Optik*, 2:114–132, 1947.
442. O. Scherzer. The theoretical resolution limit of the electron microscope. *J. Applied Physics*, 20:20–29, 1949.
443. O. Scherzer. Die strahlenschädigung der objekte als grenze für die hochauflösende elektro-nenmikroskopie. *Berichte der Bunsen. Phys. Chem.*, 74:1154–1167, 1970.
444. L. I. Schiff. *Quantum Mechanics*. McGraw-Hill, New York, third edition, 1968.
445. P. Schiske. Image reconstruction by means of focus series (in German). In Daria Steve Bocciarelli, editor, *Proc. of the Fourth Regional Congress on Electron Microscopy, Rome*, volume I, pages 145–146, 1968.

446. P. Schiske. Image reconstruction by means of focus series (English translation of Schiske 1968). *Journal of Microscopy*, 207:154, 2002.
447. C. A. Schneider, W. S. Rasband, and W. K. Eliceiri. NIH image to ImageJ: 25 years of image analysis. *Nature Methods*, 9:671–675, 2012. imagej.nih.gov/ij.
448. Noah Schnitzer, Suk Hyun Sung, and Robert Hovden. Intro. to the ronchigram and its calculation with ronchigram.com. *Microscopy Today*, May:12–15, 2019.
449. B. Schönfeld, J. J. Huang, and S. C. Moss. Anisotropic mean-square displacements (MSD) in single crystals of 2H- and 3R-MoS₂. *Acta Cryst. B*, 39:404–407, 1983.
450. M. Schowalter, A. Rosenauer, J. T. Titanth, and D. Lamoen. Computation and parametrization of the temperature dependence of Debye–Waller factors for group IV, III-V and II-VI semiconductors. *Acta Cryst. A*65:1–13, 2008.
451. V. F. Sears and S. A. Shelley. Debye–Waller factor for elemental crystals. *Acta Cryst.*, A47:441–446, 1991.
452. P. G. Self, M. A. O’Keefe, P. R. Buseck, and A. E. C. Spargo. Practical computation of amplitudes and phases in electron diffraction. *Ultramicroscopy*, 11:35–52, 1983.
453. A. Septier. The struggle to overcome spherical aberration in electron optics. In *Adv. in Optical and Electron Microscopy*, volume 1, pages 204–274. Academic Press, London, 1966.
454. A. Septier, editor. *Applied Charged Particle Optics*, volume 13A,B of *Adv. in Electronics and Electron Physics*. Academic Press, New York, 1980.
455. D. L. Shell. A high speed sorting procedure. *Comm. of the ACM*, 2:30–32, 1959.
456. C. J. R. Sheppard and T. Wilson. Image formation in scanning microscopes with partially coherent source and detector. *Optica Acta*, 25:315–325, 1978.
457. Colin J. R. Sheppard. Orthogonal aberration functions for high-aperture optical systems. *J. Opt. Soc. Am. A*, 21:832–838, 2004.
458. A. J. Skarnulis. A computer system for on-line image capture and analysis. *J. Microscopy*, 127:39–46, 1982.
459. Julian Smart, Kevin Hock, and Stefan Csomor. *Cross Platform GUI Programming wxWidgets*. Prentice Hall, NJ, 2006. wxwidgets.org.
460. D. J. Smith. Instrumentation and operation for high-resolution electron microscopy. In T. Mulvey and C. J. R. Sheppard, editors, *Adv. in Optical and Electron Microscopy*, volume 11, pages 1–55. Academic Press, London, 1989.
461. D. J. Smith. The realization of atomic resolution with the electron microscope. *Rep. Prog. Physics*, 60:1513–1580, 1997.
462. D. J. Smith. Development of aberration-corrected electron microscopy. *Microsc. and Microanalysis*, 14:2–15, 2008.
463. D. J. Smith. Progress and perspectives for atomic-resolution electron microscopy. *Ultramicroscopy*, 108:159–166, 2008.
464. G. H. Smith and R. E. Burge. The analytical representation of atomic scattering amplitudes for electrons. *Acta Cryst.*, 15:182–186, 1962.
465. K. C. A. Smith. On-line digital computer techniques in electron microscopy: general intro. *J. Microscopy*, 127:3–16, 1982.
466. Ross Smith and Bridget Carragher. Software tools for molecular microscopy. *J. Structural Biology*, 163:224–228, 2008.
467. A. E. C. Spargo, M. J. Beeching, and L. J. Allen. Inversion of electron scattering intensity for crystal structure analysis. *Ultramicroscopy*, 55:329–333, 1994.
468. M. C. Sparrow. On spectroscopic resolving power. *Astrophysical J.*, 44:76–86, 1916.
469. J. C. H. Spence. Direct inversion of dynamical electron diffraction patterns to structure factors. *Acta Cryst.*, A54:7–18, 1998.
470. J. C. H. Spence. *High-Resolution Electron Microscopy*. Oxford University Press, New York, fourth edition, 2013.
471. J. C. H. Spence, B. Calef, and J. M. Zuo. Dynamic inversion by the method of generalized projections. *Acta Cryst.*, A55:112–118, 1999.
472. J. C. H. Spence and J. M. Cowley. Lattice imaging in STEM. *Optik*, 50:129–142, 1978.

473. J. C. H. Spence, M. A. O'Keefe, and H. Kolar. High resolution image interpretation in crystalline germanium. *Optik*, 49:307–323, 1977.
474. J. C. H. Spence and J. M. Zuo. *Electron Microdiffraction*. Plenum Press, New York, 1992.
475. P. A. Stadelmann. EMS - a software package for electron diffraction analysis and HREM image simulation in materials science. *Ultramicroscopy*, 21:131–146, 1987.
476. P. A. Stadelmann. JEMS - EMS java version, 2004. cimewww.epfl.ch/people/stadelmann/jemsWebSite/jems.html.
477. Bjarne Stroustrup. *The C++ Programming Language*. Addison-Wesley, Reading Mass., second edition, 1991.
478. L. Sturkey. The calculation of electron diffraction intensities. *Proc. Phys. Soc.*, 80:321–354, 1962.
479. Z. Su and P. Coppens. Relativistic X-ray elastic scattering factors for neutral atoms Z=1–54 from multiconfiguration Dirac-Fock wavefunctions in the 0–12 Å⁻¹ sin θ/λ range, and six-Gaussian analytical expressions in the 0–6 Å⁻¹ range. *Acta Cryst.*, A53:749–762, 1997.
480. Toma Susi, Jacob Madsen, Ursula Ludacka, Jens Jørgen Mortensen, Timothy J. Pennycook, Zhongbo Lee, Jani Kotakoski, Ute Kaiser, and Jannik C. Meyer. Efficient first principles simulation of electron scattering factors for transmission electron microscopy. *Ultramicroscopy*, 197:16–22, 2019.
481. L. Szasz. *The Electronic Structure of Atoms*. Wiley, New York, 1992.
482. Masaki Takeguchi¹, Ayako Hashimoto¹, Masayuki Shimojo, Kazutaka Mitsuishi, and Kazuo Furuya. Development of a stage-scanning system for high-resolution confocal STEM. *J. Electron Micr.*, 57:123–127, 2008.
483. Nobuo Tanaka, editor. *Scanning Transmission Electron Microscopy of Nanomaterials*. Imperial College Press, London, 2015.
484. G. Tang, L. Peng, P. R. Baldwin, D. S. Mann, W. Jiang, I. Rees, and S. J. Ludtke. EMAN2: An extensible image processing suite for electron microscopy. *J. Structural Biology*, 157:38–46, 2007.
485. M. W. Tate, P. Purohit, D. Chamberlain, K. X. Nguyen, R. Hovden, C. S. Chang, P. Deb, E. Turgut, J. T. Heron, D. G. Schlom, D. C. Ralph, G. D. Fuchs, K. S. Shanks, H. T. Philipp, D. A. Muller, and S. M. Gruner. High dynamic range pixel array detector for scanning transmission electron microscope. *Microscopy and Microanalysis*, 22:237–249, 2016.
486. M. G. R. Thomson. Resolution and contrast in the conventional and the scanning high resolution transmission electron microscope. *Optik*, 39:15–38, 1973.
487. F. Thon. Phase contrast electron microscopy. In U. Valdre, editor, *Electron Microscopy in Materials Science*, pages 571–625. Academic Press, New York, 1971.
488. A. Thust. High-resolution transmission electron microscopy on an absolute contrast scale. *Phys. Rev. Lett.*, 102:220801, 2009.
489. A. Thust, J. Barthel, L. Houben, C. L. Jia, M. Lentzen, K. Tillmann, and K. Urban. Strategies for aberration control in sub-angstrom HRTEM. *Microscopy and Microanalysis*, 11 suppl. 2:58–59, 2005.
490. A. Thust, W. M. J. Coene, M. Op de Beck, and D. van Dyck. Focal-series reconstruction in HRTEM: simulation studies on non-periodic objects. *Ultramicroscopy*, 64:211–230, 1996.
491. A. Thust and K. Urban. Quantitative high-speed matching of high-resolution electron microscopy images. *Ultramicroscopy*, 45:23–42, 1992.
492. K. Tillmann, A. Thust, and K. Urban. Spherical aberration correction in tandem with exit-plane wave function reconstruction: Interlocking tools for atomic scale imaging of lattice defects in GaAs. *Microsc. and Microanalysis*, 10:185–198, 2004.
493. M. Tournaire. Recent developments of the matrical and semi-reciprocal formulation in the field of dynamical theory. *J. of the Physical Society of Japan, Suppl. B II*, 17:98–100, 1962.
494. M. M. J. Treacy and J. M. Gibson. Coherence and multiple scattering in Z-contrast images. *Ultramicroscopy*, 52:31–53, 1993.
495. Michael M. J. Treacy. Z dependence of electron scattering by single atoms into annular dark-field detectors. *Microscopy and Microanalysis*, 17:847–858, 2011.

496. S. Uhlemann and M. Haider. Residual wave aberrations in the first spherical aberration corrected transmission electron microscope. *Ultramicroscopy*, 72:109–119, 1998.
497. K. Urban. Studying atomic structures by aberration-corrected transmission electron microscopy. *Science*, 321:506–510, 2008.
498. B. K. Vainshtein. *Modern Crystallography I, Fundamentals of Crystals*. Springer-Verlag, Berlin, 2nd edition, 1994.
499. B. K. Vainshtein, V. M. Fridkin, and V. L. Indenbom. *Modern Crystallography II, Structure of Crystals*. Springer-Verlag, Berlin, 1982.
500. W. van den Broek, X. Jiang, and C. T. Koch. FDES, a GPU-based multislice algorithm with increased efficiency of the computation of the potential. *Ultramicroscopy*, 158:89–97, 2015.
501. D. van Dyck. The path integral formalism as a new description for the diffraction of high-energy electrons in crystals. *Phys. Stat. Sol.*, B72:321–336, 1975.
502. D. van Dyck. On the optimisation of methods for the computation of many-beam structure images. In J. M. Sturgess, V. I. Kalnins, F. P. Ottensmeyer, and G. T. Simon, editors, *Electron Microscopy 1978, Vol. 1, Ninth Intern. Congress on Electron Microscopy (Toronto)*, pages 196–197, Ontario, 1978. The Imperial Press.
503. D. van Dyck. Improved methods for the high speed calculation of electron microscopic structure images. *Phys. Stat. Sol.*, A52:283–292, 1979.
504. D. van Dyck. Fast computational procedures for the simulation of structures in complex or disordered crystal: A new approach. *J. of Microscopy*, 119:141–152, 1980.
505. D. van Dyck. High-speed computation techniques for the simulation of high resolution electron micrographs. *J. of Microscopy*, 132:31–42, 1983.
506. D. van Dyck. Image calculations in high-resolution electron microscopy: Problems, progress, and prospects. In P. W. Hawkes, editor, *Advances in Electronics and Electron Physics*, Vol. 65, pages 295–355. Academic Press, Orlando, 1985.
507. D. van Dyck and W. Coene. The real space method for dynamical electron diffraction calculation in high resolution electron microscopy, I. principles of the method. *Ultramicroscopy*, 15:29–40, 1984.
508. M. van Heel. Similarity measures between images. *Ultramicroscopy*, 21:95–100, 1987.
509. M. van Heel, G. Harauz, E. V. Orlova, R. Schmidt, and M. Schatz. A new generation of the IMAGIC image processing system. *J. Structural Biology*, 116:17–24, 1996.
510. M. van Heel and W. Keegstra. IMAGIC: A fast flexible and friendly image analysis software system. *Ultramicroscopy*, 7:113–130, 1981.
511. V. Vand, P. F. Eiland, and R. Pepinsky. Analytical representation of atomic scattering factors. *Acta Cryst.*, 10:303–306, 1957.
512. M. von Ardenne. Das elektronen-rastermikroskop. *Z. fur Physik*, 109:553–572, 1938.
513. D. Waasmaier and A. Kirfel. New analytical scattering-factor functions for free atoms and ions. *Acta Cryst. A*, 51:416–431, 1995.
514. C. Wacker and R. R. Schröder. Multislice algorithms revisited: Solving the Schrödinger equation numerically for imaging electrons. *Ultramicroscopy*, 151:211–223, 2015.
515. R. H. Wade and J. Frank. Electron microscope transfer functions for partially coherent axial illumination and chromatic defocus spread. *Optik*, 49:81–92, 1977.
516. James S. Walker. *Fast Fourier Transforms*. CRC Press, Boca Raton, 2nd edition, 1996.
517. J. Wall. Simulation of coherent scattering in STEM. In P. Kotula, M. Marko, J.-H. Scott, R. Gauvin, D. Beniac, G. Lucas, S. McKernan, and J. Shields, editors, *Microscopy and Microanalysis 2006*, volume 12, suppl. 2, pages 1350–1351, Cambridge, UK, 2006. Cambridge Univ. Press.
518. J. Wang, V. H. Smith, C. F. Bunge, and R. Jauregui. Relativistic X-ray elastic scattering factors for He-Ar from Dirac-Hartree-Fock wave functions. *Acta Cryst.*, A52:649–658, 1996.
519. Z. L. Wang. Dynamics of thermal diffuse scattering in high-energy electron diffraction and imaging: Theory and experiments. *Phil. Mag.*, B65:559–587, 1992.
520. Z. L. Wang. Dynamical theories of dark-field imaging using diffusely scattered electrons in STEM and TEM. *Acta Cryst.*, A51:569–585, 1995.

521. Z. L. Wang. Electron statistical dynamical diffuse scattering in crystals containing short range order point defects. *Acta Cryst.*, A52:717–729, 1996.
522. Z. L. Wang. An optical potential approach to incoherent multiple thermal diffuse scattering in quantitative HRTEM. *Ultramicroscopy*, 74:7–26, 1998.
523. Z. L. Wang and J. M. Cowley. Simulating high-angle annular dark-field STEM images including inelastic thermal diffuse scattering. *Ultramicroscopy*, 31:437–454, 1989.
524. Z. L. Wang and J. M. Cowley. Dynamical theory of high-angle annular dark-field STEM lattice images for a Ge/Si interface. *Ultramicroscopy*, 32:275–289, 1990.
525. B. E. Warren. *X-ray Diffraction*. Dover, New York, 1969, 1990.
526. K. Watanabe. n-beam dynamical calculations. In P. W. Hawkes, editor, *Advances in Electronics and Electron Physics*, Vol. 86, pages 173–224. Academic Press, San Diego, 1993.
527. K. Watanabe, Y. Kikuchi, K. Hiratsuka, and H. Yamaguchi. A new approach for n-beam lattice image calculation. *Phys. Status Solidi*, A109:119–126, 1988.
528. K. Watanabe, Y. Kikuchi, K. Hiratsuka, and H. Yamaguchi. A new approach for n-beam dynamical calculations. *Acta Cryst.*, A46:94–98, 1990.
529. K. Watanabe, T. Yamazaki, I. Hashimoto, and M. Shiojiri. Atomic-resolution annular dark-field STEM image calculations. *Phys. Rev. B*, 64:115432, 2001.
530. A. Weickenmeier and H. Kohl. Computation of absorptive form factors for high-energy electron diffraction. *Acta Cryst.*, A47:590–597, 1991.
531. G. H. Weiss and A. A. Maradudin. The Baker-Hausdorff formula and a problem in crystal physics. *J. Math. Phys.*, 3:771–777, 1962.
532. W. L. Wiese and G. A. Martin. Atomic spectroscopy. In H. L. Anderson, editor, *A Physicist's Desk Reference, the second edition of Physics Vade Mecum*, pages 92–102. American Institute of Physics, New York, 1989.
533. R. M. Wilcox. Exponential operators and parameter differentiation in quantum physics. *J. Math. Physics*, 8:962–982, 1967.
534. D. B. Williams and C. B. Carter. *Transmission Electron Microscopy, A Textbook for Materials Science*. Springer, New York, second edition, 2009.
535. A. R. Wilson and A. E. C. Spargo. Calculation of the scattering from defects using periodic continuation methods. *Phil. Mag.*, A46:435–449, 1982.
536. A. R. Wilson, A. E. C. Spargo, and D. J. Smith. The characterisation of instrumental parameters in high resolution electron microscopy. *Optik*, 61:63–78, 1982.
537. T. Wilson and C. Sheppard. *Theory and Practice of Scanning Optical Microscopy*. Academic Press, London, 1984.
538. K. Wong, E. Kirkland, P. Xu, R. Loane, and J. Silcox. Measurement of spherical aberration in STEM. *Ultramicroscopy*, 40:139–150, 1992.
539. R. W. G. Wyckoff. *Crystal Structures*, Vol. 1 and 2. Wiley, New York, 2nd edition, 1963, 64.
540. Huolin L. Xin and D. A. Muller. Three-dimensional imaging in aberration-corrected electron microscope. *Microsc. and Microanal.*, 16:445–455, 2010.
541. N. J. Zaluzec. Tele-presence microscopy/labspace: An interactive collaboratory for use in education and research. In G. W. Bailey, J. M. Corbett, R. V. W. Dimlich, J. R. Michael, and N. J. Zaluzec, editors, *Proceedings of the 54th Annual Meeting of the Microscopy Society of America*, pages 382–383. San Francisco Press, 1996.
542. N. J. Zaluzec. The scanning confocal electron microscope. *Microscopy Today*, Nov./Dec.:8–12, 2003.
543. E. Zeitler and H. Olsen. Screening effects in elastic scattering. *Physical Review*, 136:A1546–A1552, 1964.
544. E. Zeitler and H. Olsen. Complex scattering amplitudes in elastic electron scattering. *Physical Review*, 162:1439–1447, 1967.
545. E. Zeitler and M. G. R. Thomson. Scanning transmission electron microscopy. *Optik*, 31:258–366, 1970.
546. F. Zemlin, K. Weiss, P. Schiske, W. Kunath, and K.-H. Herrman. Coma free alignment of high resolution electron microscopes with the aid of optical diffractograms. *Ultramicroscopy*, 3:49–60, 1978.

547. H. Zhang, L. D. Marks, Y. Y. Wang, H. Zhang, V. P. Dravid, P. Han, and D. A. Payne. Structure of planar defects in $(\text{Sr}_{0.9}\text{Ca}_{0.3})_{1.1}\text{CuO}_2$ infinite-layer superconductors by quantitative high-resolution electron microscopy. *Ultramicroscopy*, 57:103–111, 1995.
548. Xiaodong Zou, Anders Hovmöller, and Sven Hovmöller. TRICE- a program for reconstructing 3D reciprocal space and determining unit-cell parameters. *Ultramicroscopy*, 98:187–193, 2004.
549. J. M. Zuo. Web electron microscopy applications software (WebEMAPS), 2009. emaps.mrl.uiuc.edu/.
550. Jian Min Zuo and John C. H. Spence. *Advanced Transmission Electron Microscopy, Imaging and Diffraction in Nanoscience*. Springer, New York, 2017.

Author Index

A

A. C. Atkinson, 216
Abe, E., 13, 135
Abramowitz, M., 69, 293
Adams, Paul D., 305
Aert, S. Van, 222
Agrawal, G. P., 145
Aimez, V., 180
Akima, H., 260
Alaïdi, Osama, 4, 304
Algara-Siller, G., 112, 238
Allen, L. J., 15, 146, 180, 222, 238, 304
Allpress, J. G., 144
Altbauer, A., 305
Amali, A., 222
Amelincx, S., 178
Anderson, E., 152
Andrews, H. C., 61
Anstis, G. R., 178, 206
Arai, Y., 187
Ashcroft, N. W., 143
Ayachit, Utkarsh, 305

B

Bai, Z., 152
Baldwin, P. R., 305
Bals, S., 222
Barakat, R., 65
Baranovskii, Sergei D., 180
Barnett, M. E., 36
Barry, J. C., 235
Barthel, J., 33, 180
Basinski, Z. S., 159
Bates, R. H. T., 15, 304

Batterman, B. W., 143
Baumann, F. H., 237
Baumeister, W., 4
Baxter, W. T., 305
Beeching, M. J., 146, 304
Behan, G., 22, 76
Beltrán-del-Río, L. M., 180
Belz, Jürgen, 180
Bennett, J. C., 187
Berman, H. M., 197
Bethe, H., 2, 103, 143, 146, 288
Bethe, H. A., 103, 288
Beyer, Andreas, 180
Bhat, T. N., 197
Biegalski, M., 22
Binnig, G., 9
Bird, D. M., 159
Bischof, C., 152
Black, G., 56, 65
Blackford, S., 152
Blanchette, Jasmine, 272
Bode, M., 237
Bonevich, J. E., 126
Bonham, R. A., 283, 284
Boothroyd, C. B., 238
Borisovich, A. Y., 22
Born, M., 21, 32, 53, 125, 169
Bosch, Eric G. T., 135
Boulin, C., 15
Bourne, P. E., 197
Bourret, A., 123
Bowen, D. K., 35
Bozzola, J. J., 35
Bracewell, R. N., 88
Brage, T., 103, 285

- Bragg, W. L., 284
 Brigham, E. O., 88, 90, 98
 Brindley, G. W., 284
 Budinger, T. F., 23
 Bunge, C. F., 284
 Burge, R. E., 284
 Burke, V. M., 286
 Burns, M. M. J., 187
 Bursill, L. A., 144, 170, 178
 Buseck, P. R., 39, 144, 145, 177, 180
 Buxton, B. F., 206
- C**
 Cai, C., 189
 Cai, Can Ying, 189
 Cai, D. Q., 206
 Calef, B., 146, 304
 Callaway, Ewen, 9
 Campbell, G. H., 237
 Carazo, J. M., 305
 Carlino, E., 187
 Carragher, Bridget, 304
 Carter, C. B., 35
 Castleman, K. R., 97
 Chamberlain, D., 15
 Chang, C. S., 15
 Chang, L. Y., 44
 Chang, Lan-Yun, 73
 Chang, Wen-Hao, 216
 Chau, K.-L., 304
 Chen, J., 189
 Chen, J. H., 181, 189, 190
 Chen, Zefeng, 213
 Chen, Zhen, 304
 Cheng, Chia-Chin, 216
 Cheng, Yifan, 4, 230, 304
 Chiu, W., 305
 Christen, H. M., 22
 Chu, Chih-Wei, 216
 Chuvilin, A., 112, 238
 Clare, D., 10
 Clark, A. T., 10
 Cockayne, D. J. H., 178, 206
 Coene, W., 4, 128, 144, 304
 Coene, W. M. J., 4, 10, 304
 Cole, H., 143
 Colliex, C., 65, 231
 Cooley, J. W., 88
 Coppens, P., 284
 Corbin, G. J., 29, 33, 65
 Cordes, J. M., 145
 Corp., Adobe, 245
 Cosgriff, E. C., 22
- Cosgriff, E.C., 76
 Coulthard, M. A., 283
 Couture, A. R., 180
 Cowan, R. D., 103, 285, 286
 Cowley, J. M., 2, 18, 60, 65, 102, 144, 168,
 178, 181, 218, 222, 260, 283, 284, 290,
 292
 Cox, H. L., 284
 Crewe, A. V., 9, 65, 131
 Croitoru, M. D., 222
 Cromer, D. T., 284, 292
 Csomor, Stefan, 272
 Currie, D., 187
- D**
 Dahmen, U., 4
 D'Alfonso, A. J., 15, 180, 238, 304
 Daneholt, B., 180
 Dawson, B., 284
 de Beck, M. Op, 4, 17, 128, 181, 189, 190,
 304
 de la Fraga, L. G., 305
 de la Rosa-Trevín, J. M., 305
 Deb, P., 15
 Deb, Pratiti, 304
 Dehm, G., 238
 Dellby, N., 29, 32, 33, 65
 Dellby, Niklas, 32
 Demmel, J., 152
 Desclaux, J. P., 285, 286
 Desseaux, J., 123
 Dinges, C., 222
 Dongarra, J., 152
 Downing, K. H., 53
 Dowse, H., 305
 Doyle, P. A., 109, 283, 284, 289, 290, 292
 Dravid, V. P., 237
 Drouin, D., 180
 Du Croz, J., 152
 Dudarev, S. L., 284
 Dudgeon, D. E., 171
 Dulong, B. J., 189
 Duscheck, Lennart, 180
 Dwyer, C., 187, 222
 Dyall, K. G., 285
 Dyck, D. Van, 4, 128, 144, 178, 181, 189, 190,
 222, 304
- E**
 Edington, J. W., 35, 124
 Edwards, B., 224
 Eggeman, A. S., 187

- Eiland, P. F., 284
Einspahr, J. J., 22
Eisberg, R., 103
Eisenberg, David, 229
Eisenhandler, C. B., 41, 117
El-Kareh, A. B., 36
El-Kareh, J. C. J., 36
Eliceiri, W. K., 305
Ellisman, M. H., 4
Elmlund, Dominika, 305
Elmlund, Hans, 305
Elser, Veit, 304
Elson, B. F., 29, 33, 65
Engel, A., 18, 58, 231
Epstein, A., 15
Erasmus, S. J., 4, 234
Ercius, Peter, 4, 304, 305
Erikson, H. P., 38
Erni, R., 35, 44
Estle, T. L., 285
Etheridge, J., 222
Evans, N., 180
Ewalds, Timo, 304
- F**
Fan, G. Y., 4, 222
Fang, Hui, 213
Faruqi, A. R., 10
Faulkner, H. M. L., 146, 304
Feit, M. D., 145, 190
Fejes, P. L., 44
Feng, Z., 197
Fernández, J. J., 305
Fertig, J., 144, 146
Ferwerda, H. A., 17, 110
Feynman, R. P., 163
Fields, P. M., 178
Findlay, S. D., 10, 13, 135, 146, 180, 238
Findlay, Scott D., 10
Fink, M., 283
Fischer, C. Froese, 103, 285
Flannery, B. P., 69, 90, 92, 145, 157, 160, 166, 194, 291, 313
Fleck, J. A., 145
Fleck(Jr.), J. A., 145, 190
Forsberg, Björn O., 305
Forsyth, J. B., 284
Fox, A. G., 284, 292
Frank, J., 4, 35, 44, 110, 111, 230, 304, 305
Freeman, A. J., 112, 284, 289
French, R. G., 145
Fridkin, V. M., 197
Frigo, Matteo, 90, 156
Frigo, S. P., 19
Froese-Fischer, C., 103, 285
Fuchs, G. D., 15
Fujimoto, F., 144, 206
Fujino, T., 10
Fujiwara, K., 17
Fujiyoshi, Y., 4, 41, 237, 304
Fultz, B., 35
Furuno, S., 122
Furuya, K., 146, 222
Furuya, Kazuo, 19
- G**
Gabor, D., 40
Gallagher-Jones, M., 305
Gao, Hui, 304
Garrett-Reed, A. J., 35
Gauvin, R., 180
Gemming, T., 223, 238
Gibson, J. M., 60
Gilde, H., 110, 117
Gill, Harindarpal S., 229
Gilliland, G., 197
Glaeser, Robert M., 305
Glaeser, R. M., 23, 144
Glas, F., 187
Glauber, R., 109, 287
Goldstein, Joseph I., 10
Gómez-Rodríguez, A., 180
Gonzalez, R. C., 93, 97
Goodhew, P. J., 35
Goodman, J. W., 37, 58, 98
Goodman, P., 2, 144, 145, 163, 173
Goodyear, Grant, 305
Gradshteyn, I. S., 293
Graf, M. De, 35, 146, 150, 180
Grano, D. A., 53
Grant, I., 283, 284
Grant, I. P., 285, 286
Greenbaum, A., 152
Gribelyuk, M. A., 146, 304
Grigorieff, Nikolaus, 4, 230, 304, 305
Grillo, V., 180, 187
Grinton, G. R., 178
Grivet, P., 36
Gronsky, R., 144
Groß, A., 112, 238
Gruner, S. M., 15
Gruner, Sol M., 304
Gumsch, P., 223

H

Haase, J., 284

Haguenau, F., 9

Haider, M., 15, 29, 30, 33

Haigh, S. J., 73

Haken, H., 285

Halioua, M., 60

Hall, C. E., 9, 35

Hall, C. R., 35, 222

Hall, E. L., 98

Hammarling, S., 152

Hammond, R. B., 159

Han, P., 237

Han, Yimo, 216, 304

Hanai, T., 27

Hanszen, K.-J., 38, 58

Hanwell, Marcus, 305

Hanwell, Marcus D., 305

Harauz, G., 305

Harris, Chris, 305

Hartel, P., 29, 30, 33

Hartree, D. R., 285

Hashimoto, A., 22, 146

Hashimoto, I., 146

Hashimoto1, Ayako, 19

Hawkes, P. W., 4, 9, 20, 28, 36

Haynes, R. D., 189

He, Jr-Hau, 216

Hecht, E., 65

Hegerl, R., 305

Hegerl, Reiner, 305

Heidenreich, R. D., 9, 35

Henderson, R., 10

Herman, F., 283

Heron, J. T., 15

Herrera-Becerra, R., 180

Herrman, K.-H., 24

Herrmann, K.-H., 13

Hewat, E. A., 144

Hibino, M., 27

Hilke, S., 180

Hiller, S. C., 189

Hillyard, S., 222, 223

Hiratsuka, K., 161, 189

Hirsch, F., 35, 161

Hirsch, P. B., 222

Hock, Kevin, 272

Hoenders, B. J., 17

Hohn, Michael, 305

Hoppe, W., 38, 41

Horiuchi, S., 35

Horner, M., 305

Hosakawa, F., 187

Hosokawa, F., 13, 29, 30, 33, 135

Houben, L., 33

Houston, A., 65

Hovden, R., 15, 206

Hovden, Robert, 180, 305

Hovington, P., 180

Hovmöller, Anders, 305

Hovmöller, Sven, 305

Howe, J. M., 35

Howie, A., 2, 35, 144, 159–161

Huang, J. J., 213

Huang, Lujie, 216

Huang, Pinshane Y., 216

Huang, Zhong, 305

Humphreys, C. J., 146, 222

Humphry, M. J., 304

Hunt, B. R., 61

Hutchison, J. L., 9, 122

Hýtch, M. J., 238

I

Iakoubovskii, K., 146

Ibers, J. A., 284, 288

Idrobo, J. C., 22

Iijima, S., 102, 144

Ikuhara, Y., 13, 135

Inc., Adobe Systems, 314

Indenbom, V. L., 197

Intaraprasong, Varat, 65, 66

Isaacson, M. S., 131

Ishikawa, R., 13, 135

Ishikawa, Ryo, 10

Ishizuka, K., 2, 24, 126, 144, 170, 180, 181

Iwasaki, T., 112, 238

Izui, K., 122

Izumi, Fujio, 311

J

Jackiw, R. W., 103, 288

Jacobson, A. J., 238

Jagannathan, R., 17

Jähne, B., 98

Jain, A. K., 98

James, R. W., 284

Jansen, Jacob, 180, 238

Janssen, G., 4, 128, 304

Jap, B. K., 144

Jarron, P., 15

Jauregui, R., 284

Jesson, D. E., 60, 144, 146, 206, 222

Jia, C.-L., 211

Jiang, W., 305

Jiang, X., 180

- Jiang, Yi, 304, 305
Jmol, 311
Johnson, C. T., 285
Johnson, Steven G., 90, 156
Johnston, W., 4
Joly, D., 180
Jones, Lewys, 60
Jönsson, P., 103, 285
Josefsson, T. W., 146, 304
Joy, D. C., 180
Joy, David C., 10
Julian, Nicholas H., 180
Koslof, D., 193
Kosloff, R., 145, 193
Kotakoski, Jani, 112
Kourkoutis, L. Fitting, 4
Krause, Florian F., 180, 238
Krishman, K. M., 175
Krishna, N. G., 224
Krivanek, O. L., 23, 24, 29, 33, 65
Krivanek, O.L., 32, 33
Krivanek, Ondrej L., 32
Kunath, W., 15, 24, 135
Künzel, D., 112, 238
Kurasch, S., 112, 238

K

- Kaiser, U., 112, 238
Kaiser, Ute, 112
Kambe, K., 206
Kandrot, Edward, 187
Kaneko, T., 10
Kaneyama, T., 29, 30, 33
Kang, Kibum, 216
Kasper, E., 4, 20, 36
Kawasaki, M., 304
Kawazoe, M., 29, 30, 33
Keegstra, W., 305
Keyse, R. J., 29, 33, 35, 65
Kikuchi, Y., 161, 189
Kilaas, R., 144, 175, 178, 180, 305
Kilass, R., 180
Kim, Cheol-Joo, 216
Kim, Y., 237
Kimanius, Dari, 305
Kimoto, Koji, 29, 30, 33
King, W. E., 237
Kirfel, A., 284
Kirkland, A. I., 15, 44, 73, 304
Kirkland, A.I., 76
Kirkland, Angus I., 22
Kirkland, E., 18
Kirkland, E. J., 4, 10, 41, 58, 61, 63, 65, 71,
144, 180, 189, 206, 218, 219, 221, 224,
234, 237, 238, 303, 304, 312
Kittel, C., 143, 221, 222
Klemperer, O., 36
Klenov, D. O., 238
Knoll, M., 9
Koch, C., 180
Koch, C. T., 180
Kohl, H., 284, 290
Kolar, H., 123
Kondo, Y., 13, 29, 30, 33, 135
Koops, H., 28
Kopf, D., 131

L

- Ladjadj, M., 305
Lamoen, D., 224
Landuyt, J. Van, 189, 190
Lane, N. F., 285
Langmore, J., 131
Langmore, J. P., 131
Lanuyt, J. Van, 178
Lazić, Ivan, 135
LeBeau, J. M., 10, 238
Lee, Zhongbo, 112
Leeb, H., 146, 304
Lehmpfuhl, G., 206
Leith, A., 305
Leith, Ardean, 305
Lentzen, M., 33, 44, 211
Lenz, F. A., 38
Levin, Barnaby D. A., 305
Levine, Z. H., 19
Lewis, A. L., 159
Li, Lain-Jong, 216
Li, Ming-Yang, 216
Li, Tian T., 180
Li, Ximming, 213
Li, Xuesong, 213
Li, Y., 305
Lichte, Hannes, 4
Lin, Yung-Chang, 216
Lindahl, Erik, 305
Linfoot, E. H., 56, 65
Liu, Hong Rong, 189
Lo, Y. H., 305
Loane, R., 18
Loane, R. F., 60, 144, 218–222, 256
Lobato, I., 180, 187, 284
London, A., 187
Lorimer, G. W., 35
Lovelace, R. V. E., 145
Loveluck, J. E., 206

- L.Trepte, 58
 Lu, Li-Syuan, 216
 Lucy, L. B., 61
 Ludacka, Ursula, 112
 Ludtke, S. J., 305
 Ludtke, Steven J., 305
 Lupini, A. R., 22
 Lupini, Andrew R., 10, 232
 Lupini, A.R., 32, 33
 Lynch, D. F., 2, 144, 159
- M**
 Maccagnano-Zacher, S. E., 63, 238
 MacLagan, D. S., 178
 Madsen, Jacob, 112
 Maiden, A. M., 304
 Mak, Kin Fai, 216
 Mann, D. S., 305
 Mann, J. B., 284
 Marabini, R., 305
 Maradudin, A. A., 163
 Marco, S., 305
 Maréchal, A., 65
 Marks, L., 180
 Marks, L. D., 126, 237, 305
 Martian, Jaime, 180
 Martin, G. A., 285
 Martin, Richard M., 222
 Masegosa, I. M., 305
 Masich, S., 180
 Massey, H. S. W., 103, 284, 288
 Mastronarde, David N., 305
 Matsuhata, H., 178
 Mayers, D. F., 285
 Maynard, Robert, 305
 McKenney, A., 152
 McKenzie, B. J., 285
 McMulan, D., 10
 McMullan, D., 10
 McMullan, G., 10
 McWeeny, R., 112, 284, 289
 Meek, G. A., 35
 Megaw, H. D., 197
 Melinte, G., 305
 Mercurio, P. J., 4
 Mermin, N. D., 143
 Mersereau, R. M., 171
 Meyer, J. C., 112, 238
 Meyer, Jannik C., 112
 Meyer, R. R., 304
 Miao, J., 305
 Michael, Joseph R., 10
 Midgley, P. A., 4, 187, 304
- Ming, W. Q., 189
 Misell, D. L., 60
 Missel, D. L., 98
 Mitsuishi, K., 22, 146, 222
 Mitsuishi, Kazutaka, 19
 Mkhoyan, K. A., 238
 Mkhoyen, K. A., 63, 238
 Möbus, G., 223, 237, 238
 Moliere, G., 39, 109
 Momma, Koichi, 311
 Moodie, A. F., 2, 144, 145, 159, 163, 168,
 173
 Moore, Gordon E., 185
 Morgan, A. J., 15, 304
 Morris, J. R., 145, 190
 Morrison, M. A., 285
 Mortensen, Jens Jørgen, 112
 Mory, C., 65
 Moss, S. C., 213
 Mott, N. F., 103, 284, 288
 Mukunda, N., 17
 Muller, D. A., 15, 22, 206, 224
 Muller, David, 216, 305
 Muller, David A., 304
 Müller, H., 29, 30, 33
 Müller, Knut, 180, 238
 Murfit, M. F., 29, 33, 65
 Murfit, Matthew F., 32
 Murray, J. D., 244
 Murray, R. J., 222
- N**
 Nakamichi, T., 29, 30, 33
 Nellist, P. D., 15, 73, 144, 146, 304
 Nellist, P.D., 76
 Nellist, Peter D., 22, 60
 Newbury, Dale E., 10
 Newman, W. M., 313
 Nguyen, K. X., 15
 Nicholson, R. B., 35, 161
 Niehrs, H., 144
 Nogales, Eva, 4, 304
 Norrington, P. H., 285
- O**
 Oatley, C. W., 10
 Oelerich, Jan Oliver, 180
 Öfverstedt, L.-G., 180
 O'Keefe, M. A., 2, 4, 39, 123, 126, 144, 145,
 175, 177, 178, 180, 185, 284, 292
 Öktem, O., 180
 Okunishi, E., 10, 13, 135

Oldfield, L. C., 27
O'Leary, N. L., 146, 304
Olsen, H., 109, 110, 287
O'Neil, Edward L., 65
Op de Beck, M., 4, 304
Ophus, Colin, 15, 180, 304
Orlova, E. V., 305
Oshima, Y., 33
Otón, J., 305
Otsu, H., 122
Otten, M. T., 10
Ourmazd, A., 237
Owen, D., 4
Own, C. S., 29, 33, 65, 305
Oxley, M. P., 146

P

Padgett, Elliot, 305
Palazzari, P., 187
Pan, M., 260
Park, H. J., 112, 238
Park, Jiwoong, 216, 304
Parker, N. W., 131
Parpia, F. A., 285
Pashley, D. W., 35, 161
Payne, D. A., 237
Penczek, P., 305
Penczek, Paweł A., 4, 230, 304, 305
Peng, L., 305
Peng, L. M., 284, 290
Pennycook, S. J., 22, 60, 131, 144, 146, 206,
 222
Pennycook, Stephen J., 10
Pennycook, Timothy J., 112
Pepinsky, R., 284
Peterlechner, M., 180
Philipp, H. T., 15
Pidwerbetsky, A., 145
Pitt, T. J., 305
Plamann, T., 15, 304
Plitzko, J. M., 4
Plummer, E. P., 285
Pogany, A. P., 18, 222
Pratt, W. K., 93, 98
Press, W. H., 69, 90, 92, 145, 157, 160, 166,
 194, 291, 313
Pryor Jr., A., 305
Pulvermacher, H., 126
Purohit, P., 15
Purohit, Prafull, 304
Pyper, N. C., 285

Q

Quammen, Cory, 305
Quinn, M. J., 187

R

Radek, M., 180
Radermacher, M., 305
Ralph, D. C., 15
Rames, Matthew J., 4, 304
Rana, A., 305
Rasband, W. S., 305
Rayleigh, Lord, 58
Rees, I., 305
Reid, G. D., 189
Reid, John S., 224
Reimer, L., 10, 13, 35, 110, 117, 161
Ren, G., 284
Ren, Gang, 4, 304
Renault, A., 123
Resnick, R., 103
Rez, D., 283, 284
Rez, P., 222, 260, 283, 284
Richardson, W. H., 61
Ritchie, Nicholas W. M., 10
Robertson, E. T., 189
Robertson, M. D., 187, 189
Rodenburg, J. M., 15, 304
Rodenburg, J. M., 304
Rodriguez, J. A., 305
Rohrer, H., 9
Rose, H., 15, 28–30, 135, 144, 146, 222
Rose, H. H., 28, 29

Rose, Harald, 36
Rosenauer, A., 224
Rossi, F., 180
Rossouw, C. J., 146, 222
Roth, S., 112, 238
Rother, Axel, 17
Rotunno, E., 180
Rudd, Robert E., 180
Rühle, M., 237, 238
Rullgård, H., 180
Ruska, E., 9
Russell, L. D., 35
Ryzhik, I. M., 293

S

Saitow, A., 10
Salzman, D. B., 65
San Martín, M. C., 305

- Sanders, J. V., 144, 185
 Sanders, Jason, 187
 Sannomiya, T., 33, 187
 Sasaki, T., 29, 30, 33
 Satiat-Jeunemaître, B., 9
 Sawada, H., 10, 13, 15, 29, 30, 33, 135, 304
 Saxton, W. O., 98, 304, 305
 Sayle, Roger, 311
 Schatz, M., 305
 Scheerschmidt, Kurt, 17
 Scheres, Sjors H. W., 305
 Scherzer, O., 23, 28, 29, 38, 42, 44, 66
 Schiff, L. I., 39, 103, 108–110, 288
 Schiske, P., 24, 303
 Schlom, D. G., 15
 Schmidt, R., 305
 Schneider, C. A., 305
 Schnitzer, Noah, 180
 Schomaker, V., 109, 287
 Schönfeld, B., 213
 Schowalter, M., 224
 Schowalter, Marco, 180, 238
 Schröder, R. R., 189
 Schweinfest, R., 238
 Scott, John Henry J., 10
 Sears, V. F., 223
 Self, P. G., 39, 144, 145, 177
 Septier, A., 28
 Shanks, K. S., 15
 Shell, D. L., 313
 Shelley, S. A., 223
 Sheppard, C., 10, 76
 Sheppard, C. J. R., 69
 Sheppard, Colin J. R., 32
 Shi, Yumeng, 216
 Shibata, N., 13, 135
 Shimkin, B., 305
 Shimojo, M., 22, 146
 Shimojo, Masayuki, 19
 Shindyarov, I. N., 197
 Shinkawa, T., 187
 Shiojiri, M., 146
 Siegel, B. M., 4, 41, 117, 237, 304
 Silcox, J., 18, 60, 63, 144, 218–224, 238, 256
 Simon, G. T., 9
 Simon, R., 17
 Sirdeshmukh, D. B., 224
 Skakalova, V., 112, 238
 Skarnulis, A. J., 4
 Skillman, S., 283
 Slump, C. H., 17
 Smart, Julian, 272
 Smet, J. H., 112, 238
 Smith, D. J., 13, 28, 237
 Smith, G. H., 284
 Smith, K. C. A., 4, 10, 234
 Smith, Ross, 304
 Smith, V. H., 284
 Sorensen, D., 152
 Sorzano, C. O. S., 305
 Spargo, A. E. C., 39, 144–146, 177, 178, 237,
 304
 Sparrow, M. C., 65
 Spence, J. C. H., 35, 60, 123, 144, 146, 180,
 218, 304
 Spence, John C. H., 35, 146
 Sproull, R. F., 313
 Stadelmann, P. A., 180
 Starke, U., 112, 238
 Steeds, J. W., 206
 Stegun, I. A., 69, 293
 Stemmer, S., 238
 Stobbs, W. M., 238
 Stroke, G. W., 60
 Stroustrup, Bjarne, 242
 Sturkey, L., 144, 154
 Su, Z., 284
 Sudarshan, E. C. G., 17
 Suenaga, K., 29, 30, 33
 Suenaga, Kazu, 216
 Summerfield, Mark, 272
 Sung, Suk Hyun, 180
 Susi, Toma, 112
 Szasz, L., 103
 Szilagi, Z. S., 29, 33, 65
- T**
- Tabbernor, M. A., 284, 292
 Takayanagi, K., 33
 Takeguchi, M., 146, 222
 Takeguchi, Masaki, 22
 Takeguchi1, Masaki, 19
 Tanaka, T., 33
 Tang, G., 305
 Tang, Grant, 305
 Tang, Hao-Lin, 216
 Tanishiro, Y., 33
 Tao, Li, 213
 Tastet, X., 180
 Tate, M. W., 15
 Tate, Mark W., 304
 Taylor, J., 4
 Tenberge, J.-G., 180
 Terao, M., 29, 30, 33
 Teukolsky, S. A., 69, 90, 92, 145, 157, 160,
 166, 194, 291, 313
 Thomas, M. G., 10

- Thomson, M. G. R., 18, 58
Thon, F., 38
Thust, A., 4, 33, 53, 211, 237, 238, 304
Tillmann, K., 33, 211
Titantah, J. T., 224
Titchmarsh, J. M., 44
Tomita, T., 33
Tournaire, M., 144
Treacy, M. M. J., 60
Treacy, Michael M. J., 131
Tsai, Meng-Li, 216
Tsuno, K., 304
Tukey, J. W., 88
Turchetta, R., 10
Turgut, E., 15
Turner, P. S., 18, 109, 283, 284, 289, 290, 292
- U**
Uhlemann, S., 29, 30, 33
Urban, K., 33, 211, 237
Utlaut, M., 131
Uyeda, N., 2, 4, 41, 144, 170, 237, 304
- V**
Vainshtein, B. K., 197, 284
van den Broek, W., 180
van Dyck, D., 4, 144, 180, 187, 190, 284, 304
van Heel, M., 305
Vand, V., 284
vanRyper, W., 244
Vaquerizo, C., 305
Vargas, J., 305
Verbeeck, J., 222
Vetterling, W. T., 69, 90, 92, 145, 157, 160, 166, 194, 291, 313
Villagrana, R. E., 159
Visser, F. P. C., 110
Volz, Kerstin, 180
vonArdenne, M., 9
Voyles, P. M., 22
- W**
Waasmaier, D., 284
Waber, J. T., 284, 292
Wacker, C., 189
Waddington, W. G., 122
Wade, R. H., 44
Wagner, E. H., 144
Wagner, T., 238
Waldon, Shawn, 305
Walker, James S., 98
Wall, J., 9, 228
Waltz, Thomas, 4, 230, 304
Wang, J., 284
Wang, P., 15, 304
Wang, X., 238
Wang, Xinran, 213
Wang, Y. Y., 237
Wang, Z. L., 222
Warren, B. E., 222
Watanabe, K., 144, 146, 161, 175, 189
Wei, Kung-Hwa, 216
Weickenmeier, A., 284, 290
Weiss, G. H., 163
Weiss, K., 15, 24, 135
Weissig, H., 197
Wells, M., 284
Welter, L. M., 9
West, J., 284
Westbrook, J., 197
Westmacott, K. H., 4
Weyland, M., 4, 304
Whelan, M. J., 2, 35, 144, 160, 161, 222, 284
Wiese, W. L., 285
Wilcox, R. M., 163
Wilde, G., 180
Williams, D. B., 35
Wilson, A. R., 144, 170, 178, 237
Wilson, T., 10, 69, 76
Wolf, E., 21, 32, 53, 125, 169
Wolf, H. C., 285
Wong, K., 18
Wood, J. H., 112, 284, 289
Woodruff, J. W., 29, 33, 65
Woods, R. E., 93, 97
Wyckoff, R. W. G., 197, 208
- X**
Xie, Saien, 216, 304
Xin, H. L., 206
Xin, Huolin L., 22, 65, 66
Xu, Jian-Bin, 213
Xu, P., 18, 60, 218–222
- Y**
Yamaguchi, H., 161, 189
Yamamoto, T., 13, 135
Yamazaki, T., 146
Yan, A. W. C., 15, 304
Yang, Chao, 305
Yang, Qi Bin, 189
Yang, Y., 305

Yasuda, H., 222

Yoshida, H., 27

Young, S. J., 4

Yuasa, S., 29, 30, 33

Z

Zach, J., 29, 30, 33

Zaldívar, A., 305

Zaluzec, N. J., 4, 19

Zeitler, E., 18, 109, 110, 287

Zemlin, F., 15, 24, 135

Zeng, Song Jun, 189

Zhang, F., 304

Zhang, H., 237

Zhou, J., 305

Zhu, Hongwei, 213

Zhu, J., 305

Zillmann, Dennis, 180, 238

Zou, Xiaodong, 305

Zuo, J. M., 146, 180, 304

Zuo, Jian Min, 35, 146

Subject Index

Symbols

3D perspective view, 311

4D STEM, 15

A

Aberrations, 20

balancing, 65

correction, 26

corrector, 44

function, 23, 24

high order, 30

Aberration tuning, 34, 233

Aberration tunning errors (ADF),
69

Acronyms, 5

Airy disk, 117

Aliasing, 83, 170, 175, 177

Amplitude contrast, 78

Annular bright field (ABF), 7, 13, 135

Annular dark field (ADF), 7, 13, 58

Aperture function, 115

Aspherical atoms, 289

Astigmatism, 24

Atomic charge distribution, 284

Atomic potentials, 103, 283

Atomic size, 106

Atompot, 242, 248

Autoslic, 243, 262

Autostem, 243

B

Backscattered electrons, 151

Bandwidth limit, 115, 177

BF-CTEM

calculation, 246

Bilinear interpolation, 307

Biological specimens, 227

Bloch waves, 2, 143, 146

Bloch wave solution, 159

Bonding in specimen, 112

Born approximation, 108, 287

Bragg reflections, 113

Bright field (BF), 7, 13, 38

Bright field image, 40

Byte ordering, 244

C

C_s , 22

C_{s3} , 22

C_{ss} , 22

CBED example, 262

Central processing unit (CPU), 7

Centro-symmetric, 149

Channeling, 205

Cold field emission gun (CFEG), 7

Compensation, 72

Computem, 241, 272

Confocal, 19, 76

Contrast transfer function (CTF), 7

Conventional transmission electron microscope
(CTEM), 7, 9, 13

BF, 114

image calculation, 116

model, 13

Convergence test, 183

Convergent beam electron diffraction (CBED),
7, 60, 218

Convolution, 37, 176

Cryo-EM, 230

Cryo-microscopy, 1, 4, 9

D

Data archiving and analysis, 2

Debye–Waller factor, 223, 224

Defects, 178

Defocus, 22–24, 41, 61, 65, 170

Defocus spread, 69

Depth of focus (DOF), 7, 22

Depth sectioning, 22

Detector influence, 53

Detectors, 10

Differential phase contrast (DPC), 7

Diffraction pattern, 93

Dirac equation, 17

Dirac wave equation, 285

Discrete Fourier Transform (DFT), 7, 86

Dynamical diffraction, 144

Dynamical scattering, 143

E

Eigenvalue, 146, 152

Eigenvector, 152

Eikonal approximation, 109

Einstein model, 222

Electron energy loss spectroscopy (EELS), 7

Electron scattering factors, 287

Electron source, 10

Electron velocity, 16

Electron wavelength, 17

Error term, 165

Ewald sphere, 160

Excitation error, 151

Exit wave reconstruction (EWR), 7, 304

Extinction distance, 201, 204

Extra high tension (EHT), 7

F

Fast Fourier transform (FFT), 7, 88, 170

FFT (in C), 95

FFTW, 90

Field emission gun (FEG), 7

Finite difference solution, 166

Finite precision arithmetic, 85

First Born approx., 287

First order Laue zone (FOLZ), 174

FloatTIFF.cpp, 245

Forward problem, 303

Fourier projection theorem, 281

Fourier transform (FT), 7, 87

Free space propagation, 167

Fresnel–Kirchhoff diffraction, 169

Frozen phonon, 262, 266

Frozen phonon approx., 222

G

Gallium arsenide, 197

Gaussians, 290

Global error, 165, 193

Graphical user interface (GUI), 7, 241, 272

Graphics processing unit (GPU), 7, 266

H

Hartree–Fock, 283, 285

High energy approx., 151, 159

High-angle annular dark-field (HAADF), 7

Higher order Laue zones (HOLZ), 174

High-resolution transmission electron microscopy (HREM), 7

History, 9, 144

Hollow cone, 15, 135

Holography, 4

Howie–Whelan equations, 160

Huygen's principle, 168

Hydrogen, 289

I

Image, 242, 252, 254

 matching, 235

 model, 37

 processing, 1

 simulation, 1

Impact parameter, 110

Incoherent image model, 58, 60

Incoherent imaging, 53

Incostem, 243

Incostem.cpp, 270

Independent atom model (IAM), 7, 112

In-line hologram, 40

Instrument design, 2

Interaction parameter, 101

Interfaces, 178

Inverse problem, 146, 303

K

Kinematical image approximation, 99

Kinematical scattering, 143

L

Levenberg–Marquardt algorithm, 291
Linear image model, 37
Local error, 165, 193
Lorenzians, 290
Low-angle annular dark field (LAADF), 7

M

Message passing interface (MPI), 7
Minimum probe conditions, 65
Minimum slice thickness, 175
Modulation transfer function (MTF), 7, 37
Moliere approximation, 109
Monte-Carlo methods, 222
Moore’s law, 185
 MoS_2 , 212
Mott–Bethe formula, 103, 288
Mulslice, 242, 250, 254
 equation, 165, 170
 interpretation, 167
 method, 2, 144
 solution, 162

N

N-beam calculation, 152
Nobel Prize, 9
Non-periodic specimens, 259
Nyquist sampling limit, 83

O

Octave, 273
On-line control, 2
OpenMP, 262, 266
Operator solution, 162
Optical theorem, 110
Optimum probe, 65

P

Parallel computing, 185
Parameterization, 289
Parasitic aberrations, 32
Paraxial approximation, 21
Paraxial Schrödinger equation, 159
Partial coherence, 44, 184
 aberration corrector, 51
Periodic continuation, 178
Periodic potential, 148
Phase contrast, 78
Phase grating approximation, 99
Phase grating calculation, 116

Phonon, 220

Pixels, 81
Point spread function (PSF), 7, 37
Poisson random number generator, 215
Probe, 65
Projected atomic potential, 283
Propagation function, 181
Propagator function, 164, 170
Protein data bank (PDB), 228
Ptychography, 1, 4, 15
Ptycography, 304

Q

QT, 272
Quantitative image matching, 235

R

Radial charge distribution, 103, 286
Radix-2, 88
Radix-4, 89
RasMol, 311
Rayleigh criteria, 65
Real space method, 144
Real to complex FFT, 92
Reciprocity, 18, 216
Relativistic electrons, 15
Relativistic Hartree–Fock, 285
Relativistic Schrödinger equation, 17
Relativistic wave function, 286
Remote access, 4
Ronchigrams, 231
Rotation, 313
Roundoff error, 85
Row-column decomposition, 87
Ruska, 9

S

S-state, 206
 s_G , 151
Scaling diffraction patterns, 93
Scanning electron microscope (SEM), 7, 9
Scanning transmission electron microscope (STEM), 7, 9, 13, 58
 ABF, 13, 135
 ADF, 13, 128
 BF, 13
 dedicated, 10
 detector, 130
 image calculation, 130
 incoherent image model, 60
 model, 15
 probe wave function, 128

Scattering factors, 108, 283
 Scherzer aperture, 43
 Scherzer focus, 41
 Scherzer's theorem, 23
 Schrödinger equation, 157
 Second order Laue zone (SOLZ), 174
 Second order multislice, 190
 Shared memory processor (SMP), 7, 186
 Signal to noise ratio (SNR), 7
 Sign convention, 39
 Silicon, 95, 121, 223, 314
 Silicon nitride, 208
 Single atom images, 116, 130
 Size of atoms, 106
 Slicing the specimen, 171
 Source size, 67
 Sparrow criteria, 65
 Sparrow resolution, 71
 Spatial frequency, 23
 Specimen
 edges, 226
 interaction parameter, 101
 tilt, 181
 transmission function, 128
 Spherical aberration, 21–23
 Stemslic, 242
 Stobbs factor, 238
 Structure factor, 113
 Super cell, 178
 Symbol definitions, 5
 Symmetrical bandwidth limit, 115

T

Telemicroscopy, 4
 TEMSIM, 241, 242
 Thermal diffuse scattering (TDS), 7, 114, 220,
 221, 262
 Thermal vibrations, 220

Thick phase grating, 99
 Threads, 187
 Tilt, 181, 313
 Tomography, 1, 4, 304
 Transfer function, 37
 Transmission cross coefficient, 125
 Transmission function, 128
 Troubleshooting, 238
 Tuning errors (ADF), 69
 Tuning tolerance, 34

V

Velocity, 16
 VESTA, 311
 Von Ardenne, 9

W

Wave equation, 157
 Wavelength, 17
 Weak phase object, 38, 39, 99, 102
 Weak phase object approximation (WPOA), 7,
 40
 Wrap around error, 90, 172
 Wrap-around edge, 226
 WxWidgets, 272

X

X-ray scattering factor, 286

Z

Zassenhaus theorem, 163
 Z-contrast, 131, 216
 Zemlin tableau, 24
 Zero order Laue zone (ZOLZ), 174